NIST Technical Note 1523

# Trapped Ions and Laser Cooling, V

Edited by

James C. Bergquist
John J. Bollinger
Wayne M. Itano
David J. Wineland

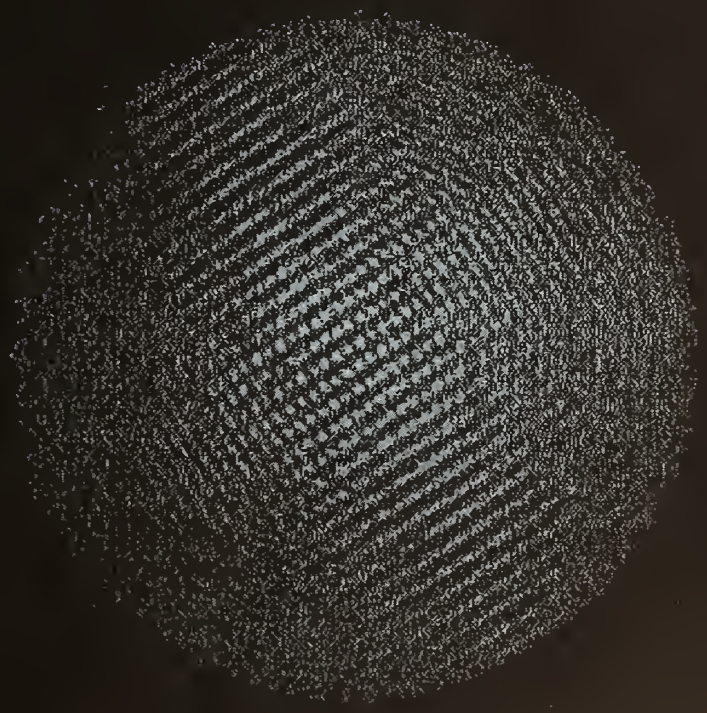

*Selected publications of the Ion Storage Group*
*NIST Time and Frequency Division*

NIST
National Institute of Standards and Technology
Technology Administration, U.S. Department of Commerce

# NIST Technical Note 1523

# Trapped Ions and Laser Cooling, V
## Selected publications of the Ion Storage Group NIST Time and Frequency Division


Edited by

James C. Bergquist
John J. Bollinger
Wayne M. Itano
David J. Wineland

*Time and Frequency Division*
*Physics Laboratory*
*National Institute of Standards and Technology*
*325 Broadway*
*Boulder, Colorado 80305*



February 2002

**U.S. Department of Commerce**
*Donald L. Evans, Secretary*

**Technology Administration**
*Phillip J. Bond, Under Secretary of Commerce for Technology*

**National Institute of Standards and Technology**
*Arden L. Bement, Jr., Director*

National Institute of Standards and Technology Technical Note 1523
Natl. Inst. Stand. Technol. Tech. Note 1523, 203 pages (February 2002)
CODEN: NTNOEF

U.S. GOVERNMENT PRINTING OFFICE
WASHINGTON: 2002

---

For sale by the Superintendent of Documents, U.S. Government Printing Office
Internet: bookstore.gpo.gov Phone: (202) 512-1800 Fax: (202) 512-2250
Mail: Stop SSOP, Washington, DC 20402-0001

**CONTENTS**

## ADDITIONAL PUBLICATIONS

The following publications were published during the period between February 1996 and December 1998 but are not included in this Technical Note.


1. "An all solid-state Hg+ optical frequency standard," F.C. Cruz, M. Rauner, J.H. Marquardt, L. Hollberg, and J.C. Bergquist, Proc., Fifth Symposium on Frequency Standards and Metrology, J.C. Bergquist, ed., Singapore: World Scientific (1996), pp. 511-513.

2. "Primary atomic-frequency standards: new developments," R.E. Drullinger, S.L. Rolston, and W.M. Itano, Review of Radio Science, 1993-1996, New York, NY: Oxford Univ. Press (1996), pp. 11-41.

3. "Manipulating the motion of a single trapped atom," C. Monroe, D.M. Meekhof, B.E. King, D. Leibfried, W.M. Itano, and D.J. Wineland, Acct. Chem. Res. **29**, 585-590 (1996).

4. "High-accuracy $Hg^+$ microwave and optical frequency standards in cryogenic linear ion traps," D.J. Berkeland, J.D. Miller, F.C. Cruz, J.C. Bergquist, W.M. Itano, and D.J. Wineland, Proc., Workshop on the Scientific Applications of Clocks in Space, JPL Publication 97-15, Pasadena, CA: Jet Propulsion Laboratory (1997), pp. 133-142.

5. "Experimental creation and measurement of motional quantum states of a trapped ion," D.M. Meekhof, D. Leibfried, C. Monroe, B.E. King, W.M. Itano, and D.J. Wineland, Brazilian J. Phys., **27**, 178-192 (1997).

6. "Atomic physics in ion traps," C.J. Monroe and J.J. Bollinger, Phys. World **10**, 37-42 (March 1997).

7. "High-accuracy frequency standards using laser-cooled Hg+ ions," D.J. Berkeland, J.D. Miller, B.C. Young, J.C. Bergquist, W.M. Itano, and D.J. Wineland, Methods for Ultrasensitive Detection, Bryan L. Fearey, ed., Proc., SPIE **3270**, 138-146 (1998).

8. "High-accuracy microwave and optical frequency standards using laser-cooled $Hg^+$ ions," D.J. Berkeland, J.D. Miller, F.C. Cruz, B.C. Young, J.C. Bergquist, W.M. Itano, and D.J. Wineland, Proc., Second Int. Symp. on Modern Problems of Laser Physics, Sergei N. Bagayev and Vladimir I. Denisov, eds., Laser Physics **8**, 673-678 (1998).

9. "Formation and control of coulomb crystals in trapped ion plasmas," X.-P. Huang, J.J. Bollinger, W.M. Itano, J.N. Tan, B. Jelenković, T.B. Mitchell, and D.J. Wineland, Strongly Coupled Coulomb Systems, Kalman, et al., eds., New York, NY: Plenum, New York (1998), p. 429-432.

10. "Structure and control of coulomb crystals in a penning trap," X.-P. Huang, J.J. Bollinger, W.M. Itano, J.N. Tan, B. Jelenković, T.B Mitchell, and D.J. Wineland, Hyperfine Interact. **115**, 41-45 (1998).

11. "Quantum state manipulation of trapped atomic ions," D.J. Wineland, C. Monroe, D.M. Meekhof, B.E. King, D. Leibfried, W.M. Itano, J.C. Bergquist, D. Berkeland, J.J. Bollinger, J. Miller, Proc., Workshop on Quantum Computing, Proc. R. Soc. **454**, 411-429 (1998).

12. "Coherent quantum state manipulation of trapped atomic ions," D.J. Wineland, C. Monroe, D.M. Meekhof, B.E. King, D. Leibfried, W.M. Itano, J.C. Bergquist, D. Berkeland, J.J. Bollinger, J. Miller, Proc., Symp. on Modern Trends in Atomic Physics, Adv. Quant. Chem. **30**, 41-64 (1998).

13. "Experimental issues in coherent quantum-state manipulation of trapped atomic ions," D.J. Wineland, C. Monroe, W.M. Itano, D. Leibfried, B.E. King, and D.M. Meekhof, J. Res. Natl. Inst. Stand. Technol. **103** (3), 259-328 (1998) (available at **www.nist.gov/jres**).

## PREFACE

This collection of papers represents the work of the Ion Storage Group, Time and Frequency Division, National Institute of Standards and Technology, from February 1996 to December 1998. It follows the similar collections of papers contained in the previous Tech Notes:

NBS Technical Note 1086, *Trapped Ions and Laser Cooling I* (June 1985)
NIST Technical Note 1324, *Trapped Ions and Laser Cooling II* (September 1988)
NIST Technical Note 1353, *Trapped Ions and Laser Cooling III* (April 1992)
NIST Technical Note 1380, *Trapped Ions and Laser Cooling IV* (February, 1996)

Papers listed on page v were published during the period from February 1996 to December 1998, but are not included here. Copies can be obtained on request. We hope this collection of papers will be useful to our colleagues in this and related fields.

We acknowledge our ion-trap/laser-cooling colleagues whose contributions made this work possible. These include: Jim Beall, Dana Berkeland, Flavio Cruz, Dan Dubin, Dan Heinzen, Leo Hollberg, Pei Huang, Brana Jelenković, David Kielpinski, Brian King, Didi Leibfried, John Marquardt, Dawn Meekhof, John Miller, Travis Mitchell, Chris Myatt, Amy Newbury, Chris Oates, Max Rauner, Andy Steinbach, Michelle Stephens, Joseph Tan, Quentin Turchette, Chris Wood, Brent Young, and in particular, Chris Monroe (now at University of Michigan). We gratefully acknowledge the support of the U.S. Office of Naval Research (ONR), the U.S. Army Research Office (ARO), and the U.S. National Security Agency (NSA). We thank Eyvon Petty and Edie DeWeese for assembling this collection.

James C. Bergquist
John J. Bollinger
Wayne M. Itano
David J. Wineland

Boulder, Colorado
December 2001

# Optimal frequency measurements with maximally correlated states

J. J . Bollinger, Wayne M. Itano, and D. J. Wineland
*Time and Frequency Division, National Institute of Standards and Technology, Boulder, Colorado 80303*

D. J. Heinzen
*Physics Department, University of Texas, Austin, Texas 78712*

(Received 16 August 1996)

We show how maximally correlated states of $N$ two-level particles can be used in spectroscopy to yield a frequency uncertainty equal to $(NT)^{-1}$, where $T$ is the time of a single measurement. From the time-energy uncertainty relation we show that this is the best precision possible. We rephrase these results in the language of particle interferometry and obtain a state and detection operator which can be used to achieve a phase uncertainty exactly equal to the $1/N$ Heisenberg limit, where $N$ is the number of particles used in the measurement. [S1050-2947(96)50712-2]

PACS number(s): 42.50.Dv, 06.30.Ft, 03.65.Bz, 39.30.+w

Quantum limits to noise in spectroscopy [1–4] and interferometry [5–13] have been a subject of fundamental, and to an increasing degree, practical interest. This is especially true for spectroscopy on trapped atoms or ions where the number of particles $N$ is fixed and kept small to reduce undesired perturbations. Naively, the uncertainty of a spectroscopic or interferometric measurement is limited by counting statistics to be inversely proportional to $N^{1/2}$. However, a number of proposals have shown that by introducing quantum correlations between the particles, the measurement uncertainty can be reduced so that it scales inversely with $N$ rather than $N^{1/2}$ [2–13]. None of the ideas discussed so far, however, have realized the fundamental limit for quantum noise in the measurement of atomic or interferometric phase, which we show to be precisely equal to $1/N$. In the present work we realize this fundamental quantum limit for any $N$ with an approach that examines a different type of correlation and measures a different operator than previously considered.

We start by considering the spectroscopy of $N$ two-level particles. In an equivalent spin representation [1,14], let $|J=N/2,M_J=-N/2\rangle$ denote the state where all the particles are in the ground (spin-down) state $|g\rangle$ (with energy $E_g$) and $|N/2,N/2\rangle$ denote the state where all the particles are in the excited (spin-up) state $|e\rangle$ (with energy $E_e$). We show how the state

$$|\Psi_M\rangle \equiv \{|N/2,N/2\rangle + |N/2,-N/2\rangle\}/\sqrt{2} \tag{1}$$

can be used to measure $\omega_0=(E_e-E_g)/\hbar$ with a frequency uncertainty equal to $(NT)^{-1}$, where $T$ is the time of a single measurement. This state is "maximally correlated" in the sense that a measurement of any one atom's energy eigenstate determines the state of all of the others. It is an $N$-particle version of the two-particle states discussed in the Einstein-Podolsky-Rosen experiments [15]. The use of $|\Psi_M\rangle$ requires measuring a different operator than customary in spectroscopy. We find a measurement operator which yields a $1/(NT)$ uncertainty and discuss how this measurement operator and $|\Psi_M\rangle$ can be realized with small numbers of trapped ions. Our arguments are phrased in the language of spectroscopy by the Ramsey technique of separated oscillating fields [16]. The Ramsey technique is formally equivalent to Mach-Zehnder interferometry [4,6]. Therefore, after obtaining our results for optimal frequency measurements, we rephrase them in terms of interferometry.

References [2] and [4] discuss the basic idea of using correlated or squeezed spin states to improve the precision in spectroscopy for the Ramsey technique of separated oscillating fields. We briefly review the idea here and start by considering the case of $N$ uncorrelated particles where each particle is initially prepared in its ground state $|g\rangle$. The initial state of the composite system for this case is equivalent to the $|J=N/2, M_J=-N/2\rangle$ state of a $J=N/2$ spin. This initial ($t=0$) state has $\langle J_z\rangle_0=-N/2$, $\langle J_x\rangle_0=\langle J_y\rangle_0=0$, and $\Delta J_x(0)=\Delta J_y(0)=N^{1/2}/2$. [Here $\langle A\rangle_t$ denotes the expectation value of an operator $A$ at time $t$ and $\Delta A(t) \equiv \langle \Delta A^2\rangle_t^{1/2}$, where $\Delta A^2 \equiv A^2-\langle A\rangle^2$.] The Hamiltonian for the equivalent spin system is $H=-\vec{\mu}\cdot\vec{B}$, where $\vec{\mu}=\mu_0\vec{J}$ is the magnetic moment of the composite system and $\vec{B}$ is the applied field. Here $\vec{B}=B_0\hat{z}+\vec{B}_1$, where $B_0=-\hbar\omega_0/\mu_0$ (we assume $\mu_0<0$) and $\vec{B}_1$ is an applied field used to perform spectroscopy. We assume that $\vec{B}_1$ is perpendicular to and rotates about the $z$ axis according to $\vec{B}_1=B_1[-\hat{x}\sin\omega t+\hat{y}\cos\omega t]$. In the Ramsey technique [16], $B_1$ is applied (is nonzero) for two periods of length $t_{\pi/2}=\pi/(2\Omega_R)$, where $\Omega_R=|\mu_0 B_1|/\hbar$ is the Rabi frequency, separated by a period of length $T$ during which $B_1=0$. It is convenient to describe the Ramsey technique in a frame of reference rotating with $\vec{B}_1$. With the assumption $\Omega_R \gg |\omega_0-\omega|$, the first pulse rotates the spin vector about $B_1$ (the $y$ axis in the rotating frame) by 90°. The spin vector then precesses about the $z$ axis during the field-free period, acquiring an angle $(\omega_0-\omega)T$ relative to its initial direction (the $-x$ axis) in the rotating frame. This angle could be read out by measuring, for example, $J_x$ in the rotating frame. Experimentally this is done by applying the second $\pi/2$ pulse, which rotates the spin vector by 90° about the $\vec{B}_1$ axis, and then measuring the number of atoms in $|e\rangle$. This final measurement is equivalent to measuring $J_z$. We obtain

$$\langle J_z\rangle_{t_f}=(N/2)\cos(\omega_0-\omega)T, \tag{2}$$

where $t_f = 2t_{\pi/2} + T$. Throughout this paper we assume $T \gg t_{\pi/2}$ so that $t_f \simeq T$.

Measurements of $J_z$ as a function of $\omega$, along with Eq. (2), can be used to estimate the frequency $\omega_0$. [We assume that $\omega_0$ is sufficiently well known that $\omega$ can be chosen on the central fringe of Eq. (2). This is true for atomic frequency standards and clocks.] Because of the statistical nature of quantum mechanics, the number of particles which are observed to make a transition to $|e\rangle$ from measurement to measurement will fluctuate by $\Delta J_z(t_f)$ [1,2,4]. This produces an uncertainty in the estimate of $\omega_0$ of $|\Delta\omega| \equiv \Delta J_z(t_f)/|\partial\langle J_z\rangle_{t_f}/\partial\omega|$ [4]. For the initial $|N/2,-N/2\rangle$ state of uncorrelated particles, we obtain $|\Delta\omega(\text{uncorrelated})| = \Delta J_y(0)/[T|\langle J_z\rangle_0|] = N^{-1/2}T^{-1}$ independent of $\omega$. [Experimental measurements are usually made with $\omega \sim \omega_0 \pm \pi/(2T)$, where Eq. (2) has its steepest slope. This minimizes the contribution of any added noise.] With correlations between the internal states of the particles it is possible to start with a state $\langle\vec{J}\rangle = \hat{z}\langle J_z\rangle_0$ such that $\Delta J_y(0) < N^{1/2}/2$. Such "spin-squeezed" states can be used to improve the resolution in Ramsey spectroscopy if $\Delta J_y(0)/|\langle J_z\rangle_0| < (2J)^{-1/2} = N^{-1/2}$.

Some correlated states, such as $|\Psi_M\rangle$ in Eq. (1), have a mean spin vector $\langle\vec{J}\rangle = 0$. In this case the previous description of the Ramsey technique in terms of the precession of a mean spin vector is inadequate. In order to motivate how the maximally correlated state $|\Psi_M\rangle$ can improve the precision of Ramsey spectroscopy, recall that for a single particle the precession angle $(\omega_0 - \omega)T$ that is measured in the Ramsey method is, in the rotating frame, just the phase factor $e^{-i(\omega_0-\omega)T}$ that the excited state $|e\rangle$ acquires relative to the ground state $|g\rangle$ during the freed precession period $T$. Consequently, it may be possible to improve the precision of Ramsey spectroscopy with a state which, when rotated by the first $\pi/2$ pulse, is a coherent superposition of two energy eigenstates whose energies differ by more than $\hbar(\omega_0 - \omega)$. For $N$ two-level particles the eigenstates $|N/2,-N/2\rangle$ and $|N/2,N/2\rangle$ provide the largest energy difference, with an accumulated phase difference over the free precession period which is $N$ times greater than for a single particle. However, because $\langle\Psi_M|\vec{J}|\Psi_M\rangle = 0$, some operator other than $J_z$ must be detected after the final $\pi/2$ pulse.

Consider the operator $\tilde{O} = \Pi_{i=1}^{N}\sigma_{z_i}$, where $\sigma_{z_i}$ is the $z$ Pauli spin matrix for the $i$th atom. For $J = N/2$ this operator is diagonal in the $|J,M_J\rangle$ basis with eigenvalues $(-1)^{J-M_J}$. It can be detected by measuring the number of particles in either the spin-up or spin-down state. Experimentally this can be done with nearly 100% efficiency using electron shelving and quantum jump detection [1]. If $N_g$ particles are measured in the spin-down state (the ground state), the result of this measurement is assigned the value $(-1)^{N_g}$ [17]. Suppose the initial state is $\exp\{i\pi J_y/2\}|\Psi_M\rangle$, so that at the end of the first $\pi/2$ pulse the state $|\Psi_M\rangle$ is created. We want to calculate $\langle\tilde{O}\rangle_{t_f} \equiv \langle\Psi_f|\tilde{O}|\Psi_f\rangle$, where

$$|\Psi_f\rangle = e^{-i(\pi/2)J_y}e^{-i(\omega_0-\omega)TJ_z}|\Psi_M\rangle. \tag{3}$$

Let $|e\rangle_i$ and $|g\rangle_i$ denote the excited and ground states of the $i$th atom and $S_{y_i} = \sigma_{y_i}/2$, where $\sigma_{y_i}$ is the $y$ Pauli spin matrix for the $i$th atom. The state $|\Psi_f\rangle$ can be written

$$|\Psi_f\rangle = \frac{1}{\sqrt{2}}\left\{e^{-iN\phi}\prod_{i=1}^{N} e^{-i(\pi/2)S_{y_i}}|e\rangle_i + e^{iN\phi}\prod_{i=1}^{N} e^{-i(\pi/2)S_{y_i}}|g\rangle_i\right\}, \tag{4}$$

where $\phi = (\omega_0 - \omega)T/2$. With $\exp[-i(\pi/2)S_{y_i}] = (1 - S_{+_i} + S_{-_i})/\sqrt{2}$, Eq. (4) can be rewritten as

$$|\Psi_f\rangle = \frac{1}{2^{(N+1)/2}}\left\{e^{-iN\phi}\prod_{i=1}^{N}(|e\rangle_i + |g\rangle_i) + e^{iN\phi}\prod_{i=1}^{N}(-|e\rangle_i + |g\rangle_i)\right\}. \tag{5}$$

Explicit computation then yields $\langle\tilde{O}\rangle_{t_f} = (-1)^N\cos[N(\omega_0 - \omega)T]$ and, because $\tilde{O}^2 = 1$, $\langle\Delta\tilde{O}^2\rangle_{t_f} = \sin^2[N(\omega_0 - \omega)T]$. Note that $\langle\tilde{O}\rangle_{t_f}$ has the same form as that of a single, two-level system with frequency interval $N\omega_0$. The state $|\Psi_M\rangle$ can therefore be used in spectroscopy with a frequency uncertainty $|\Delta\omega| = \Delta\tilde{O}(t_f)/|\partial\langle\tilde{O}\rangle_{t_f}/\partial\omega| = (NT)^{-1}$ independent of $\omega$.

The Ramsey method measures $\omega_0$ by measuring the free precession of $N$ identical two-level particles; that is, $\omega_0$ is measured by observing the free time evolution of the system. With the state $|\Psi_M\rangle$ a frequency uncertainty of $(NT)^{-1}$ is obtained. We show that this is the best precision that can be obtained on $N$ identical two-level particles which undergo free time evoloution for a period of length $T$. This follows from an application of the time-energy uncertainty principle

$$\delta t^2\langle\Delta H^2\rangle \geq \hbar^2/4, \tag{6}$$

where $\langle\Delta H^2\rangle$ is the variance of the Hamiltonian and $\delta t^2$ is the variance in estimating time from a measurement on the system. (Measurements of an operator $A$ can be used to determine time with an uncertainty $\Delta A/|d\langle A\rangle/dt|$. See Ref. [18] for a simple proof of the time-energy uncertainty relation and Ref. [19] for additional rigorous discussions.) For the system of $N$ identical two-level particles, Eq. (6) can be reexpressed in terms of dimensionless quantities

$$\delta\varphi^2\langle\Delta h^2\rangle \geq \tfrac{1}{4}, \tag{7}$$

where $\varphi = \omega_0 t$ and $h = \Sigma_{i=1}^{N}\{\frac{1}{2}|e\rangle_{ii}\langle e| - \frac{1}{2}|g\rangle_{ii}\langle g|\}$. Note that we are here considering the full $2^N$-dimensional Hilbert space and not just the $J = N/2$ subspace discussed earlier. We can establish an upper limit $\langle\Delta h^2\rangle \leq N^2/4$ from $\langle\Delta h^2\rangle = \langle h^2\rangle - \langle h\rangle^2 \leq \langle h^2\rangle$ and $\langle h^2\rangle \leq N^2/4$. The last inequality follows because the maximum eigenvalue of $h^2$ is $N^2/4$. These inequalities and Eq. (7) imply $\delta\varphi \geq N^{-1}$. An uncertainty $\delta\varphi$ in determining $\varphi$ after a free time evolution of duration $T$ results in an uncertainty $\delta\omega_0 = \delta\varphi/T$ in the determination of $\omega_0$. From the previous discussion, $\delta\omega_0$ must satisfy

$$\delta\omega_0 \geq \frac{1}{NT}. \tag{8}$$

Ramsey spectroscopy is formally equivalent to Mach-Zehnder interferometry. In Mach-Zehnder interferometry, schemes [5–13] which use nonclassical input states to approach the $1/N$ Heisenberg limit for large $N$ have been proposed [20]. Examples include the illumination of one of the input ports by a squeezed vacuum [5] where experiment has shown improvement over the shot-noise limit [8], the use of correlated input states [6,7,9], and the use of two Fock states containing equal numbers of particles as inputs [12]. Reference [13] also considers the dual Fock input state, but with a phase measurement scheme that has been optimized according to quantum information theory. Most of these cases show an asymptotic phase sensitivity proportional to $1/N$. In general, the constant of proportionality is $>1$. By rephrasing our results for spectroscopy in terms of Mach-Zehnder interferometry, we obtain an input state and detection scheme that achieve a sensitivity *equal* to $1/N$ even for small $N$. The state after the first beam splitter that is formally equivalent to $|\Psi_M\rangle$ is $|\Psi_M\rangle_{\rm int}=\{|N\rangle_a|0\rangle_b+|0\rangle_a|N\rangle_b\}/\sqrt{2}$, where $a$ and $b$ denote the modes of the two arms of the interferometer, $|N\rangle$ denotes the state with $N$ particles, and $|0\rangle$ denotes the vacuum. (The particles can be bosons or fermions [7].) The operator $\tilde{O}$ can be detected by measuring the number of particles $N_{b'}$ in the $b'$ output mode of the second beam splitter. The result of such a measurement is assigned the value $(-1)^{N_{b'}}$.

Cirac and Zoller [21] have recently described a method for preparing general quantum states of a string of $N$ laser-cooled ions in a linear rf trap. The method uses a well-focused laser beam to couple the internal states of individual ions with a mode of the ion string. The mode is assumed to be a quantized harmonic oscillator and is initially prepared in the $|n=0\rangle$ state. Reference [21] discusses the steps needed to prepare the state $|\Psi_M\rangle$. Coupling the internal state of an individual ion with a mode of the ion string without perturbing the state of the neighboring ions may be difficult. Typical ion spacings are approximately 10 $\mu$m [22] and, because the frequency differences between the modes increase with decreasing ion separation, small ion spacings are desirable.

Here we discuss a different method for making $|\Psi_M\rangle$ that does *not* require interacting with individual ions. This method refines and extends the techniques discussed in Refs. [2] and [4]. In these references, ions in a linear rf trap were assumed to be prepared in either one of the $|N/2,\pm N/2\rangle$ states. This was followed by a resonant coupling of the internal states of all the ions (with identical interaction strength) with a center-of-mass (c.m.) mode. This coupling can take the form $\hbar\Omega(J_+a+J_-a^\dagger)$ or $\hbar\Omega(J_+a^\dagger+J_-a)$, where $a^\dagger$ ($a$) is the raising (lowering) operator for the c.m. mode, and $J_+$ ($J_-$) is the raising (lowering) operator for the $J=N/2$ ladder of atomic states. If the c.m. mode is initially prepared in a coherent state or a squeezed state, Refs. [2] and [4] show that correlated atomic states can be made. In order to make the state $|\Psi_M\rangle$, we consider the second-order sideband interactions

$$\begin{aligned} H_2' &= \hbar\Omega'(J_+a^\dagger b+J_-ab^\dagger), \\ H_2'' &= \hbar\Omega''(J_+ab^\dagger+J_-a^\dagger b), \\ H_3 &= \hbar\Omega_3(b^\dagger c+bc^\dagger), \end{aligned} \tag{9}$$

where $b$ and $c$ denote the lowering operator for the second and third c.m. modes. Suppose the system is initially prepared in the state $|J=N/2,-J\rangle|0\rangle_a|1\rangle_b|0\rangle_c$. Application of a $\pi/2$ pulse with $H_2'$ generates the coherent superposition

$$\{|J,-J\rangle|0\rangle_a|1\rangle_b|0\rangle_c+|J,-J+1\rangle|1\rangle_a|0\rangle_b|0\rangle_c\}/\sqrt{2}. \tag{10}$$

We now "shelve" the first term of Eq. (10) with a $\pi$ pulse of the $H_3$ interaction. This swaps the wave functions of the $b$ and $c$ c.m. modes with the result that the second term in Eq. (10) remains unchanged but the first term becomes $|J,-J\rangle|0\rangle_a|0\rangle_b|1\rangle_c$. A $\pi$ pulse with $H_2''$ can now be used to increase $M_J$ by 1 in the second term of Eq. (10) without affecting the first term. This is then followed by a $\pi$ pulse of $H_2'$, which further increases $M_J$ by 1. In this manner, by alternating $H_2'$ and $H_2''$ $\pi$ pulses, $M_J$ in the second term of Eq. (10) can be increased to $J-1$ with an $n=1$ Fock state in one of the $a$ or $b$ modes and $n=0$ states in the other c.m. modes. Suppose this term is $|J,J-1\rangle|1\rangle_a|0\rangle_b|0\rangle_c$. (A similar argument follows if the $n=1$ Fock state is in the $b$ mode.) Application of another $\pi$ pulse with $H_3$ results in the state

$$\{|J,-J\rangle|0\rangle_a|1\rangle_b|0\rangle_c+|J,J-1\rangle|1\rangle_a|0\rangle_b|0\rangle_c\}/\sqrt{2}. \tag{11}$$

A $\pi$ pulse with $H_2''$ now results in the desired state $|\Psi_M\rangle|0\rangle_a|1\rangle_b|0\rangle_c$.

Realization of the above scheme appears feasible with a string of ions in a linear rf trap. The second-order sideband interactions $H_2'$ and $H_2''$ can be realized for the two c.m. modes corresponding to motion orthogonal to the ion string axis. For example, if $\omega_0$ is a ground-state hyperfine transition, then $H_2'$ and $H_2''$ can be realized by stimulated Raman transitions tuned to $\omega_0+\omega_a-\omega_b$ and $\omega_0-\omega_a+\omega_b$, respectively. (We assume $\omega_a\neq\omega_b$ and require that the laser beam waists be large compared to the ion string.) Parametric mode coupling has been used in mass spectroscopy experiments [23] to generate $H_3$ and exchange the states of two c.m. modes (in a classical regime). It has also been discussed in the quantum regime [24]. Preparation of $n=1$ Fock states has been realized with a single trapped ion [25]. By preparing a state where one of the ions is shelved in an auxiliary level, these single-ion techniques can be used to create an $n=1$ Fock state for the c.m. mode of a string of ions. Alternately, a coupled trap [24] could possibly be used to transfer an $n=1$ Fock state from a single trapped ion to the c.m. mode of a string of ions.

Current proposals for accurate microwave frequency standards based on trapped ions include linear ion traps with a small number ($N<50$) of trapped ions [26]. Therefore the preparation of $|\Psi_M\rangle$ and its use in frequency metrology is of important practical interest even for small $N$. Models for the decay of quantum coherence predict that the coherence in $|\Psi_M\rangle$ may decay up to $N^2$ times faster than for a single ion

[27]. In one experiment, a lower limit of 10 min has been obtained for the coherence time of an individual ion [28]; coherence times more than an order of magnitude longer than this are anticipated [29]. Therefore, for $N<50$, coherence times for $|\Psi_M\rangle$ on the order of 10 s or longer appear feasible in trapped ion experiments. This is comparable to measurement times used in current trapped ion experiments (where the length of the measurement time can be limited by the local oscillator stability). In addition, it is long enough to provide a means to study the decoherence of a large quantum system.

In summary, we have shown how the maximally correlated state $|\Psi_M\rangle$ can be used in spectroscopy to yield a frequency uncertainty equal to $(NT)^{-1}$. This is the least uncertainty that can be achieved by observing the free time evolution of $N$ two-level atoms. Preparation of $|\Psi_M\rangle$ and its use in frequency metrology appear feasible for small numbers of ions in a linear rf trap.

We gratefully acknowledge the support of the Office of Naval Research and the U.S. Army Research Office. We thank D. Leibfried, D. J. Berkeland, and M. Young for useful comments on the manuscript.

[1] W. M. Itano *et al.*, Phys. Rev. A **47**, 3554 (1993).
[2] D. J. Wineland, J. J. Bollinger, W. M. Itano, F. L. Moore, and D. J. Heinzen, Phys. Rev. A **46**, R6797 (1992).
[3] G. S. Agarwal and R. R. Puri, Phys. Rev. A **49**, 4968 (1994).
[4] D. J. Wineland, J. J. Bollinger, W. M. Itano, and D. J. Heinzen, Phys. Rev. A **50**, 67 (1994).
[5] C. M. Caves, Phys. Rev. D **23**, 1693 (1981).
[6] B. Yurke, S. L. McCall, and J. R. Klauder, Phys. Rev. A **33**, 4033 (1986).
[7] B. Yurke, Phys. Rev. Lett. **56**, 1515 (1986).
[8] M. Xiao, L.-A. Wu, and H. J. Kimble, Phys. Rev. Lett. **59**, 278 (1987).
[9] M. Kitagawa and M. Ueda, Phys. Rev. Lett. **67**, 1852 (1991); Phys. Rev. A **47**, 5138 (1993).
[10] S. L. Braunstein, A. S. Lane, and C. M. Caves, Phys. Rev. Lett. **69**, 2153 (1992).
[11] S. L. Braunstein, Phys. Rev. Lett. **69**, 3598 (1992).
[12] M. J. Holland and K. Burnett, Phys. Rev. Lett. **71**, 1355 (1993).
[13] B. C. Sanders and G. J. Milburn, Phys. Rev. Lett. **75**, 2944 (1995).
[14] R. P. Feynman, F. L. Vernon, Jr., and R. W. Hellwarth, J. Appl. Phys. **28**, 49 (1957).
[15] D. Bohm, *Quantum Theory* (Prentice-Hall, Englewood Cliffs, NJ, 1951), p. 611; D. M. Greenberger, M. Horne, and A. Zeilinger, in *Bell's Theorem, Quantum Theory, and Conceptions of the Universe*, edited by M. Kafatos (Kluwer Academic, Dordrecht, The Netherlands, 1989), p. 69.
[16] N. F. Ramsey, *Molecular Beams* (Oxford, London, 1963), p. 124.
[17] In order that the signal-to-noise ratio of the detection of $\tilde{O}$ not be degraded, the measurement error of the number of particles in the spin-down (or spin-up) state must be $\ll 1$ atom. This is satisfied with small numbers of trapped ions.
[18] A. Messiah, *Quantum Mechanics* (North-Holland, Amsterdam, 1961), Vol. I, pp. 319 and 320.
[19] C. W. Helstrom, *Quantum Detection and Estimation Theory* (Academic, New York, 1976), Chaps. VIII.2.c and VIII.4.c; S. L. Braunstein and C. M. Caves, Phys. Rev. Lett. **72**, 3439 (1994).
[20] Heisenberg limited sensitivity has also been discussed in a different approach which uses coherent input states and a nonstandard beam splitter. See J. Jacobson, G. Björk, I. Chuang, and Y. Yamamoto, Phys. Rev. Lett. **74**, 4835 (1995).
[21] J. I. Cirac and P. Zoller, Phys. Rev. Lett. **74**, 4091 (1995).
[22] U. Eichmann *et al.*, Phys. Rev. Lett. **70**, 2359 (1993).
[23] E. A. Cornell, R. M. Weiskoff, K. R. Boyce, and D. E. Pritchard, Phys. Rev. A **41**, 312 (1990).
[24] D. J. Heinzen and D. J. Wineland, Phys. Rev. A **42**, 2977 (1990).
[25] D. M. Meekhof *et al.*, Phys. Rev. Lett. **76**, 1796 (1996).
[26] M. E. Poitzsch, J. C. Bergquist, W. M. Itano, and D. J. Wineland, Rev. Sci. Instrum. **67**, 129 (1996).
[27] R. Alicki, Phys. Lett. **103A**, 247 (1984); D. F. Walls and G. J. Milburn, Phys. Rev. A **31**, 2403 (1985).
[28] J. J. Bollinger *et al.*, IEEE Trans Instrum. Meas. **40**, 126 (1991).
[29] D. J. Wineland *et al.*, Ann. Phys. (Paris) **10**, 737 (1985).

# Laser-Cooled Mercury Ion Frequency Standard

D. J. Berkeland, J. D. Miller,* J. C. Bergquist, W. M. Itano, and D. J. Wineland
*National Institute of Standards and Technology, 325 Broadway, Boulder, Colorado 80303*
(Received 27 October 1997)

A stable and accurate frequency standard based on the 40.5 GHz ground-state hyperfine transition in $^{199}Hg^+$ ions is described. The ions are confined in a cryogenic linear Paul (rf) trap and laser cooled to form a linear crystal. With seven ions and a Ramsey interrogation time of 100 s, the fractional frequency stability is 3.3 (2) $\times 10^{-13}\tau^{-1/2}$ for measurement times $\tau < 2$ h. The ground-state hyperfine interval is measured to be 40 507 347 996.841 59 (14) (41) Hz, where the first number in the parentheses is the uncertainty due to statistical and systematic effects, and the second is the uncertainty in the frequency of the time scale to which our standard is compared. [S0031-9007(98)05392-7]

PACS numbers: 32.80.Pj, 06.30.Ft, 32.10.Fn

Atomic frequency standards [1,2] play vital roles in physics, such as defining the unit of time and other basic units, realizing fundamental constants, and testing basic physical phenomena [3]. A good frequency standard requires that the uncertainty of all systematic effects be small, and that a high measurement precision can be reached in a practical time. Here, we describe a frequency standard based on a laser-cooled linear crystal of $^{199}Hg^+$ ions confined in a linear Paul (rf) trap, which satisfies these requirements. The uncertainty from systematic effects (3.4 parts in $10^{15}$) is approximately equal to the best values reported, from a cesium beam clock (5 parts in $10^{15}$) [4], and a cesium fountain clock (2 parts in $10^{15}$) [5], and can be significantly reduced in future experiments.

An important systematic effect for high-resolution spectroscopy and atomic clocks is the second-order Doppler (time-dilation) shift caused by atomic motion. Laser cooling can reduce this shift and has been applied to accurate atomic clocks based on hyperfine transitions in trapped $^9Be^+$ ions [6] and Cs atoms in a fountain clock [5]. Unfortunately, for trapped ions, part of the atomic motion is due to the trap's electromagnetic field and is not directly affected by laser cooling. In the linear Paul trap [7], driven motion (termed "micromotion") can be significantly reduced by confining the ions near the nodal line of the rf electric field. A limiting case is a linear crystal of ions confined along the field nodal line. For example, if $Hg^+$ ions are laser cooled to the Doppler limit, the magnitude of the time-dilation shift is $2 \times 10^{-18}$ [8].

Fluctuations in frequency measurements are typically expressed by the two-sample Allan variance [9]

$$\sigma_y^2(\tau) \equiv \frac{1}{2(K-1)} \sum_{k=1}^{K-1} \frac{(\langle\omega_k\rangle_\tau - \langle\omega_{k+1}\rangle_\tau)^2}{\omega_0^2}, \quad (1)$$

where $\omega_0$ is the angular frequency, and $\langle\omega_k\rangle_\tau$ is the $k$th measurement of frequency averaged over time $\tau$. The quantity $\sigma_y(\tau)$ is usually called the frequency stability. If measurement of the atomic states is limited by quantum noise [10], the frequency stability is given by [11]

$$\sigma_y(\tau) = \frac{1}{\omega_0\sqrt{NT_R}}\tau^{-1/2}. \quad (2)$$

In this expression, we assume the atomic transition is driven using Ramsey's method of separated fields [12] with time $T_R$ between applications of radiation pulses, $\omega_0$ is the angular frequency of the atomic transition, and $N$ is the number of atoms (assumed constant). Atoms or ions that have a relatively large hyperfine frequency are particularly attractive since good frequency stability is possible even for small $N$. Cigar-shaped clouds of ions whose long axes coincide with the nodal line of a linear Paul trap have been employed to realize very stable $[\sigma_y(\tau) \cong 5 \times 10^{-14}\tau^{-1/2}]$ $^{199}Hg^+$ [13] and $^{171}Yb^+$ [14] microwave clocks using approximately $10^6$ ions cooled by a buffer gas. However, the fractional systematic frequency uncertainty in these clocks from the second-order Doppler shift is about $4 \times 10^{-14}$ [15]. The standard described here demonstrates both good frequency stability and accuracy by using laser-cooled ions that are all confined to the field nodal line.

Figure 1 shows a partial energy level diagram of $^{199}Hg^+$. A small magnetic field $[(1-5) \times 10^{-7}$ T] is applied to break the degeneracy of the $F = 1$ states, isolating the $^2S_{1/2}$ $(F = 0, m_F = 0) \rightarrow (1, 0)$ hyperfine clock transition ($\omega_0 \cong 2\pi \times 40.5$ GHz). Measurements of the Doppler-broadened width of the 282 nm electric quadrupole transition give the temperature of the ions and their heating rate in the absence of laser cooling. Sum-frequency-generated 194 nm light beams [16] drive the indicated electric dipole transitions, which are used to cool the ions. For Doppler cooling, the frequency of a primary 194 nm beam $p$ is tuned slightly below that of transition $p$. Although this is a cycling transition, beam $p$ can excite off-resonantly the ions into the $^2P_{1/2}$, $F = 1$ level, from which they can decay into the $^2S_{1/2}$, $F = 0$ level. To maintain fluorescence, the frequency of a weaker repumping 194 nm beam $r$ is nearly resonant with that of transition $r$. Beams $p$ and $r$ are overlapped to form a single beam, then split into beams $a$ and $b$, which intersect at the site of the ions. To prevent pumping into

0031-9007/98/80(10)/2089(4)$15.00  

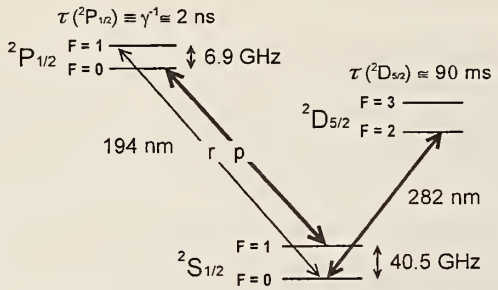


FIG. 1. Partial energy level diagram of $^{199}Hg^+$ in zero magnetic field.

dark states in the $F = 1$ manifold, beam $a$ is linearly polarized in the plane formed by beams $a$ and $b$, and beam $b$ has its polarization continuously modulated (at a frequency comparable to the maximum Rabi frequency) between right and left circular.

The ions are stored in the linear Paul trap depicted in Fig. 2 [17]. To confine the ions radially, we apply a potential $V \cong V_0 \cos \Omega t$ to two diagonally opposite rods while holding the remaining two rods at ground potential. Typically, $V_0 \cong 150$ V and $\Omega \cong 2\pi \times 8.5$ MHz, giving a radial secular frequency $\omega_r = 2\pi \times 230$ kHz. A potential $U_0 \cong +10$ V is applied to the two cylindrical end caps to confine the ions axially ($\omega_z \cong 2\pi \times 15$ kHz). The ions form a linear crystal along the nodal line of the rf electric field at the center of the trap. The trap is placed in an enclosure whose top is also the bottom of a liquid helium Dewar [17]. The cryogenic environment eliminates ion loss and suppresses frequency shifts caused by collisions with background gas. To reduce Doppler and Stark shifts induced by the trap's rf electric field, we detect and minimize ion micromotion in three noncoplanar directions [18].

We use the Ramsey technique of separated oscillatory fields to probe the clock transition [12]. First, the ions are cooled with both beams $p$ and $r$ for approximately 300 ms. Next, beam $r$ is blocked for about 60 ms to optically pump the ions into the $^2S_{1/2}$, $F = 0$ level. Both beams are then blocked during the Ramsey microwave interrogation period, which consists of two $\pi/2$ microwave pulses of duration $t_R = 250$ ms separated by the free precession period $T_R$, which we vary from 2 to 100 s in separate runs. Transitions to the $F = 1$ state are detected by reapplying only beam $p$ until the ion is pumped optically

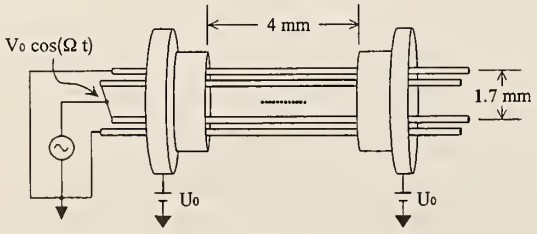


FIG. 2. Schematic diagram of the linear trap. The trap is formed by four parallel rods of radius $r = 0.38$ mm, and two end caps 4 mm apart. A string of ions is depicted at the trap center.

into the $F = 0$ state ($\cong$10–20 ms), while we count the number of detected scattered photons (typically about 150 per ion). This process completes one measurement cycle.

We synthesize the microwave frequency from a low-noise quartz oscillator locked to a reference hydrogen maser [19]. To steer the average microwave frequency into resonance with the clock transition, we step the frequency by $+\Delta f$, then $-\Delta f$, about frequency $f_M$ ($\cong \omega_0/2\pi$), and complete a measurement cycle after each step. Usually, the stepped frequencies lie near the half-maximum points of the central Ramsey fringe. On successive measurement pairs, we alternate the signs of the frequency steps to avoid any bias from linear drifts in, for example, the signal amplitude. The difference between the number of detected photons for the pair of measurement cycles gives the error signal $\varepsilon_M$. A digital servo adjusts the average frequency according to

$$f_{M+1} = f_0 + g_p \varepsilon_M + g_i \sum_{m=1}^{M} \varepsilon_m , \qquad (3)$$

where $f_0$ is the initial value of the frequency, and the proportional gain $g_p$ and the integral gain $g_i$ are independent of each other. Typically, the maximum value of $M$ for a single run is about 130. The average frequency for each run is calculated after discarding the first four recorded frequencies $f_i$, to remove initial frequency offsets.

The stability of the steered microwave frequency when $N = 7$ and $T_R = 100$ s is $\sigma_y(\tau) \cong 3.3\ (2) \times 10^{-13} \tau^{-1/2}$, for $\tau \leq 2$ h. Consistently, $\sigma_y(\tau)$ is about twice the value expected from Eq. (2), primarily due to fluctuations in the intensity of beam $p$. The measured frequency stability is comparable to those of the Cs beam standard NIST-7, for which $\sigma_y(\tau) \cong 8 \times 10^{-13} \tau^{-1/2}$ [20], and the Cs fountain standard, for which $\sigma_y(\tau) \cong 2 \times 10^{-13} \tau^{-1/2}$ [21].

The average frequency for each run is corrected for the systematic effects shown in Table I. We first correct the average frequency of a run for the quadratic Zeeman shift due to the static magnetic field $B_s$. From the measured values of $g_J$ [22] and the $^{199}$Hg nuclear magnetic moment [23], the fractional shift is $1.219\,873\ (5) \times 10^{-21} \nu_{\pm}^2$, where $\nu_{\pm}$ ($\cong 1.4 \times 10^{10} B_s$, where $B_s$ is expressed in teslas) is the frequency separation in hertz of the $^2S_{1/2}$ $[(0,0) \rightarrow (1, \pm 1)]$ field-dependent transitions from the clock transition. The peak-to-peak variation in the static magnetic field between the beginning and the end of a run is, at most, $1 \times 10^{-8}$ T. Since $B_s \cong 3 \times 10^{-7}$ T, an upper bound on the uncertainty in this Zeeman shift is $1.4 \times 10^{-15}$. We observe no sidebands on the $\Delta m_F = \pm 1$ hyperfine transitions from power line-induced 60 Hz fluctuations in the magnetic field. The corresponding upper limit on the Zeeman shift is $< 2 \times 10^{-20}$ when the static field is $3 \times 10^{-7}$ T.

We also correct for an ac Zeeman shift that depends linearly on the rf power $P_{\mathrm{rf}}$ delivered to the trap. The uncertainty in this correction dominates the overall systematic uncertainty of the clock frequency. This shift can be caused by magnetic fields due to currents at frequency

TABLE I. Systematic shifts of the clock transition frequency, expressed fractionally. The magnitudes are calculated using $P_{\rm rf} = 20$ mW, $T_R = 100$ s, $B_s = 3 \times 10^{-7}$ T, and $T_{\rm ambient} = 300$ K. Here, $B_{60}$ and $B_\Omega$ are the magnetic field components of 60 Hz and $\Omega$, $I_p$ is the intensity of beam $p$ during the Ramsey interrogation time, $\delta_p$ is the detuning of the frequency of beam $p$ from that of transition $p$, $\gamma$ is the linewidth of the cooling transition, and $dS/df$ is the slope of the background added to the Ramsey fringe. Other symbols are defined in the text.

| Shift | Scaling | Magnitude of effect | Overall uncertainty in effect |
|---|---|---|---|
| Quadratic Zeeman (static) | $+\langle B_s^2\rangle$ | $2 \times 10^{-14}$ | $1.4 \times 10^{-15}$ |
| Quadratic Zeeman (60 Hz) | $+\langle B_{60}^2\rangle$ | $<2 \times 10^{-20}$ | $<2 \times 10^{-20}$ |
| Quadratic Zeeman ($\Omega$) | $+\langle B_\Omega^2\rangle$ | $5 \times 10^{-15}$ | $3.2 \times 10^{-15}$ |
| Blackbody ac Stark | $-T_{\rm ambient}^4$ | $<1.0 \times 10^{-16}$ | $<1.0 \times 10^{-16}$ |
| Blackbody ac Zeeman [23] | $+T_{\rm ambient}^2$ | $<1.3 \times 10^{-17}$ | $<1.3 \times 10^{-17}$ |
| Light shift from 194 nm radiation | $I_p\delta_p/(\delta_p^2 + \frac{1}{4}\gamma^2)$ | $<3 \times 10^{-16}$ | $<3 \times 10^{-16}$ |
| ac Stark (from trap fields) | $-\langle E_{\rm rf}^2\rangle$ | $<2 \times 10^{-18}$ | $<2 \times 10^{-18}$ |
| Second-order Doppler | $-\langle v^2/c^2\rangle$ | $<3 \times 10^{-17}$ | $<3 \times 10^{-17}$ |
| Background slope | $-(dS/df)/T_R^2$ | $<2 \times 10^{-19}$ | $<2 \times 10^{-19}$ |
| Neighboring transitions | $1/(Bt_R T_R)$ | $<1 \times 10^{-17}$ | $<1 \times 10^{-17}$ |
| Microwave chirp, leakage and spectrum asymmetries | $1/T_R$ | $3 \times 10^{-16}$ | $8 \times 10^{-16}$ |
| Helium pressure shift | $-n_{\rm He}$ | $<1 \times 10^{-19}$ | $<1 \times 10^{-19}$ |

$\Omega$ in the trap electrodes that are asymmetric with respect to the trap nodal line. (In an ideal trap, these asymmetric currents are absent.) Allowing for this asymmetry to vary for different ion crystals, we measure the average transition frequency for $P_{\rm rf}$ ranging from about 17 mW ($V_0 \cong 140$ V) to 68 mW ($V_0 \cong 270$ V) for each ion crystal. A fit to these data gives the frequency shift $(d\omega/dP_{\rm rf})/\omega_0$ and the extrapolated frequency at zero rf power $\omega_0$, for that ion crystal. Typically, $(d\omega/dP_{\rm rf})/\omega_0 \cong (2.5 \pm 2.1) \times 10^{-16}$ mW$^{-1}$ (within the error, this value is the same for each ion crystal), and the uncertainty in the extrapolated frequency averaged over the five ion crystals used in the frequency measurement is $3.2 \times 10^{-15}$. The additional uncertainty due to possible rf power measurement inaccuracies is about $3 \times 10^{-16}$.

The ac Stark shift due to blackbody radiation at 300 K is $1.0 \times 10^{-16}$ [24], but should be much less in the cryogenic environment. From the measured 194 nm intensity at the site of the ions when the 194 nm sources are blocked, the ac Stark shift due to stray 194 nm light present during the Ramsey interrogation time is $<3 \times 10^{-16}$. Because the ion micromotion is minimized, the velocity $v$ of the ion motion and the electric field $E_{\rm rf}$ that the ions experience can be determined from the measured secular temperature [18]. We find that, after the 194 nm beams have been off for 100 s, the secular temperature $T$ is less than 25 mK. The corresponding electric field causes a shift of magnitude $<2 \times 10^{-18}$. This temperature also corresponds to a fractional second-order Doppler shift of magnitude $\leq 3 \times 10^{-17}$.

We search for an added sloping background signal by increasing $\Delta f$ to $4.25\Delta f_R$ when $T_R = 10$ s, and $10.25\Delta f_R$ when $T_R = 25$ s, where $\Delta f_R$ is the frequency separation between Ramsey fringes. The extrapolated fractional frequency shift is $<2 \times 10^{-19}$ when locking to the central fringe ($\Delta f = 0.25\Delta f_R$) and $T_R = 100$ s. To estimate the effects of the neighboring field-dependent hyperfine transitions, we assume the microwave field coupling strength of the $(0,0) \rightarrow (1,1)$ transition equals that of the $(0,0) \rightarrow (1,0)$ transition, while the coupling strength of the $(0,0) \rightarrow (1,-1)$ transition is zero. The corresponding shift is dominated by the ac Zeeman shift, and is less than $1 \times 10^{-17}$ when $T_R = 100$ s and $B_s = 3 \times 10^{-7}$ T. Frequency shifts due to the phase chirp of the microwaves as they are switched on and off (combined with a possible leakage microwave field present during the free precession time $T_R$), and to asymmetries in the microwave spectrum, scale as $1/T_R$. By varying $T_R$, we measure the frequency shift from these combined effects to be $-3(3) \times 10^{-14}/T_R$.

At 4 K, the partial pressure of most gases is negligible [25], with the possible exception of helium. An upper limit on the collision rate with helium background gas can be inferred from the ions' temperature after the cooling beams have been off for 100 s, where we assume that any heating is caused by collisions with helium atoms. We further assume that the helium collision rate for heating is the same as that which causes frequency shifts; we approximate these rates as the helium density $n_{\rm He}$ times the Langevin rate [26]. Using Cutler's measurement of the helium pressure shift for $^{199}Hg^+$ [27], we can estimate a maximum shift of $<1 \times 10^{-19}$.

The fits to the transition frequencies as a function of rf power give the extrapolated frequency $\omega_0$ at zero rf power. This value is reproducible over 18 days, with 42 runs and five different ion crystals. The normalized $\chi^2$ for the measurements of $\omega_0$ from these five ion crystals is 0.77. If we assume that the frequency depends linearly on time, a fit to the data gives a drift of $-5(9) \times 10^{-16}$ per day, consistent with zero.

The hydrogen maser frequency is referenced to primary frequency standards through International Atomic Time (TAI) [3] to obtain the average value $\omega_0 = 2\pi \times 40\,507\,347\,996.841\,59$ (13) (5) (41) Hz. The first uncertainty is due to the statistical uncertainty in the extrapolation of zero rf power, and the second to the other systematic shifts shown in Table I combined in quadrature. The third, due to the frequency comparison, is dominated by the published uncertainty in the frequency of TAI [28]. This value of $\omega_0$ is to be compared with the previous most accurate measurement, which gave $\omega_0 = 2\pi \times 40\,507\,347\,996.9$ (3) Hz [29].

The uncertainty in our measurement is limited primarily by the uncertainty in the Zeeman shift due to fields at the trap frequency $\Omega$. It can be reduced with more measurements of $\omega_0$, and by decreasing $\Omega$ and the trap dimensions, thus reducing $V_0$ for a given $\omega_r$. Better magnetic shielding will reduce fluctuations in the static magnetic field, and use of a smaller, more tightly confining trap will allow linear crystals with more ions. By monitoring each ion individually, we can determine their internal states with negligible uncertainty, which will eliminate noise due to laser frequency and intensity fluctuations. Finally, we are also investigating the use of entangled states to reduce $\sigma_y(\tau)$ [30].

This work was funded by ONR and ARO. We are grateful to R. Drullinger, S. Jefferts, D. Lee, T. Parker, and F. Walls for useful discussions. We thank F. Walls for providing the microwave frequency synthesizer [19], and T. Parker for frequency comparisons to TAI. We thank P. Huang, D. Lee, M. Lombardi, D. Sullivan, and M. Young for carefully reading this manuscript.

*Present address: KLA, Austin, TX.

[1] *Proceedings of the 5th Symposium on Frequency Standards and Metrology,* edited by J.C. Bergquist (World Scientific, Singapore, 1996).
[2] P.T.H. Fisk, Rep. Prog. Phys. **60**, 761 (1997).
[3] Special Issue on Time and Frequency [Proc. IEEE **79** (1991)].
[4] R.E. Drullinger, J.H. Shirley, and W.D. Lee, in *Proceedings of the 28th Annual PTTI Applications and Planning Meeting* (U.S. Naval Observatory, Washington, DC, 1997), p. 255.
[5] E. Simon, P. Laurent, C. Mandache, and A. Clairon, in *Proceedings of the 11th European Frequency and Time Forum* (Swiss Foundation for Research in Microtechnology, Neuchâtel, Switzerland, 1997), p. 43.
[6] J.J. Bollinger, J.D. Prestage, W.M. Itano, and D.J. Wineland, Phys. Rev. Lett. **54**, 1000 (1985).
[7] J. Drees and W. Paul, Z. Phys. **180**, 340 (1964).
[8] D.J. Wineland, J.C. Bergquist, J.J. Bollinger, W.M. Itano, D.J. Heinzen, S.L. Gilbert, C.H. Manney, and M.G. Raizen, IEEE Trans. Ultrason. Ferroelec. Freq. Contr. **37**, 515 (1990).
[9] J.A. Barnes, A.R. Chi, L.S. Cutler, D.J. Healey, D.B. Leeson, T.E. McGunigal, J.A. Mullen, Jr., W.L. Smith, R.L. Sydnor, R.F.C. Vessot, and G.M.R. Winkler, IEEE Trans. Instrum. Meas. **20**, 105 (1971).
[10] W.M. Itano, J.C. Bergquist, J.J. Bollinger, J.M. Gilligan, D.J. Heinzen, F.L. Moore, M.G. Raizen, and D.J. Wineland, Phys. Rev. A **47**, 3554 (1993).
[11] D.J. Wineland, W.M. Itano, J.C. Bergquist, J.J. Bollinger, F. Diedrich, and S.L. Gilbert, in *Proceedings of the 4th Symposium on Frequency Standards and Metrology,* edited by A. Demarchi (Springer-Verlag, Heidelberg, 1989), p. 71.
[12] N.F. Ramsey, *Molecular Beams* (Oxford University Press, London, 1956).
[13] R.L. Tjoelker, J.D. Prestage, and L. Maleki, in Ref. [1], p. 33.
[14] P.T.H. Fisk, M.J. Sellars, M.A. Lawn, and C. Coles, in Ref. [1], p. 27.
[15] R.L. Tjoelker, J.D. Prestage, G.J. Dick, and L. Maleki, in *Proceedings of the 1993 IEEE International Frequency Control Symposium* (IEEE, Piscataway, NJ, 1993), p. 132.
[16] D.J. Berkeland, F.C. Cruz, and J.C. Bergquist, Appl. Opt. **2006**, 4159 (1997).
[17] M.E. Poitzsch, J.C. Bergquist, W.M. Itano, and D.J. Wineland, Rev. Sci. Instrum. **67**, 129 (1996).
[18] D.J. Berkeland, J.D. Miller, J.C. Bergquist, W.M. Itano, and D.J. Wineland, J. Appl. Phys. (to be published).
[19] C.W. Nelson, F.L. Walls, F.G. Ascarrunz, and P.A. Pond, in *Proceedings of the 1992 IEEE Frequency Control Symposium* (IEEE, Piscataway, NJ, 1992), p. 64.
[20] W.D. Lee, J.H. Shirley, J.P. Lowe, and R.E. Drullinger, IEEE Trans. Instrum. Meas. **44**, 120 (1995).
[21] A. Clairon, S. Ghezali, G. Santarelli, Ph. Laurent, S.N. Lea, M. Bahoura, E. Simon, S. Weyers, and K. Szymaniec, in Ref. [1], p. 49.
[22] W.M. Itano, J.C. Bergquist, and D.J. Wineland, J. Opt. Soc. Am. B **2**, 1392 (1985).
[23] B. Cagnac, Ann. Phys. (Paris) **6**, 467 (1961).
[24] W.M. Itano, L.L. Lewis, and D.J. Wineland, Phys. Rev. A **25**, 1233 (1982).
[25] G. Gabrielse, X. Fei, W. Jhe, L.A. Orozco, J. Tan, R.L. Tjoelker, J. Haas, H. Kalinowsky, T.A. Trainor, and W. Kells, Am. Inst. Phys. Conf. Ser. **233**, 549 (1991).
[26] J.B. Hasted, *Physics of Atomic Collisions* (American Elsevier, New York, 1972).
[27] L.S. Cutler, R.P. Giffard, and M.D. McGuire, in *Proceedings of the 37th Annual Symposium on Frequency Control* (Systematics General Corp., Wall Township, NJ, 1983), p. 32.
[28] Circular T, No. 113 (Bureau International des Poids et Mesures, Sèvres, France, 1997), p. 4.
[29] L.S. Cutler, R.P. Giffard, and M.D. McGuire, in *Proceedings of the 13th Annual PTTI Applications and Planning Meeting*, NASA [Conference] Publication No. 2220 (NASA, Washington, DC, 1982), p. 563.
[30] J.J. Bollinger, W.M. Itano, D.J. Wineland, and D.J. Heinzen, Phys. Rev. A **54**, R4649 (1996).

# Phase-Locked Rotation of Crystallized Non-neutral Plasmas by Rotating Electric Fields

X.-P. Huang, J. J. Bollinger, T. B. Mitchell, and Wayne M. Itano
*Time & Frequency Division, National Institute of Standards and Technology, 325 Broadway, Boulder, Colorado 80303*
(Received 29 August 1997)

We report the precise control of the rotation frequency of strongly coupled non-neutral plasmas by rotating electric fields. These plasmas of up to $10^6$ $^9Be^+$ ions are trapped in a Penning trap and laser cooled into crystallized structures which undergo a rigid-body rotation. Bragg diffraction shows that the crystalline lattice can be stable for longer than 30 min ($\sim 10^8$ rotations), and that the plasma rotation can be phase locked to the applied field without any slip. These corotating plasmas are in a novel global thermal equilibrium whose asymmetric surface shape (triaxial ellipsoid) has been measured. [S0031-9007(97)04919-3]

PACS numbers: 52.25.Wz, 32.80.Pj

Large numbers of particles with a single sign of charge can be trapped and cooled in Penning traps [1,2], which use a combination of static electric and magnetic fields for particle confinement. The global rotation of these non-neutral plasmas about the magnetic field axis is necessary for the radial confinement [3]. Active control of this rotation prevents plasmas from spinning down under the ambient drag from static field errors and background neutrals, and is important for a number of experiments including Coulomb crystal studies [4,5], precision spectroscopy [6–8], measurements of particle and energy transport [9], trapping of antimatter plasmas [10,11], and storage of highly stripped ions [12]. As an example, the second-order Doppler (time dilation) shift due to rotational velocity in a Penning trap atomic clock can be minimized by stabilizing the rotation at a particular frequency [7]. Radiation pressure from laser beams has been used to vary the plasma rotation frequency [13,14]. However, this method is limited to the few ion species whose atomic transitions are accessible by a laser, and is not precise due to laser power, frequency, and pointing fluctuations. Recently, rotating azimuthally asymmetric ("rotating wall") electric fields have been used to apply a torque on $Mg^+$ plasmas with temperatures ranging from 1 K to $5 \times 10^4$ K (4 eV), resulting in steady-state confinement and density compression [15,16]. For these uncorrelated plasmas, the stabilized rotation frequency is somewhat less than that of the rotating field, with a slip which increases with the plasma temperature.

In this Letter, we demonstrate that rotating wall electric fields applied to a Penning trap with quadratic potentials can control the rotation of laser-cooled, crystallized $^9Be^+$ plasmas without slip, thus extending the applicability of this technique from uncorrelated plasmas to strongly coupled systems. Both rotating dipole and quadrupole fields perpendicular to the magnetic field are used to provide this precise control of the plasma rotation. We will concentrate on quadrupole field results, since the dipole configuration apparently requires multiple species or other nonideal effects to be effective and is therefore less general. The rotating quadrupole field interacts with charges near the plasma surface, creating a small-amplitude traveling wave. The torque due to this wave is then transferred to the plasma interior through Coulomb interactions, which act to bring the plasma to the same rotation frequency as the applied field [17]. For temperatures up to $\sim 10$ K, side-view images show that the plasma shape, which is determined by the rotation frequency, can be varied by gradually changing the rotating field frequency. When the plasma is sufficiently cold and crystalline lattices are formed, Bragg diffraction provides a more accurate measurement of the rotation frequency. It is observed that the lattice and its orientation with respect to the axial laser beam can be stable for longer than 30 min ($\sim 10^8$ rotations), and its rotation can be phase locked to the rotating field during this time. In essence, these corotating plasmas have reached a new kind of global thermal equilibrium [17], where the rotation frequency (and hence the density) is precisely set by an external drive. We have observed the predicted triaxial ellipsoidal surface of this equilibrium state for oblate (pancakelike) plasmas.

Figure 1 shows the apparatus and the rotating quadrupole field. The trap consists of a 127 mm long stack of cylindrical electrodes at room temperature with an inner diameter of 40.6 mm, enclosed in a $10^{-8}$ Pa vacuum chamber. The uniform magnetic field $B_0 = 4.46$ T is aligned parallel to the trap axis within 0.01°, giving a $^9Be^+$ (charge $e$ and mass $m$) cyclotron frequency $\Omega = eB_0/m = 2\pi \times 7.61$ MHz. A quadratic axisymmetric potential $(m\omega_z^2/2e)[z^2 - (x^2 + y^2)/2]$ is generated near the trap center by biasing the central electrodes to a negative voltage $-V_0$. At $V_0 = 1$ kV, the single-particle axial frequency $\omega_z = 2\pi \times 799$ kHz and the magnetron frequency $\omega_m = (\Omega - \sqrt{\Omega^2 - 2\omega_z^2})/2 = 2\pi \times 42.2$ kHz. The rotating quadrupole field, which has a potential $\propto (y^2 - x^2)\cos(2\omega_w t) + 2xy \sin(2\omega_w t)$, is generated by applying properly phased sinusoidal voltages of amplitude $V_w$ to the sixfold azimuthal sectors of the compensation electrodes [15].

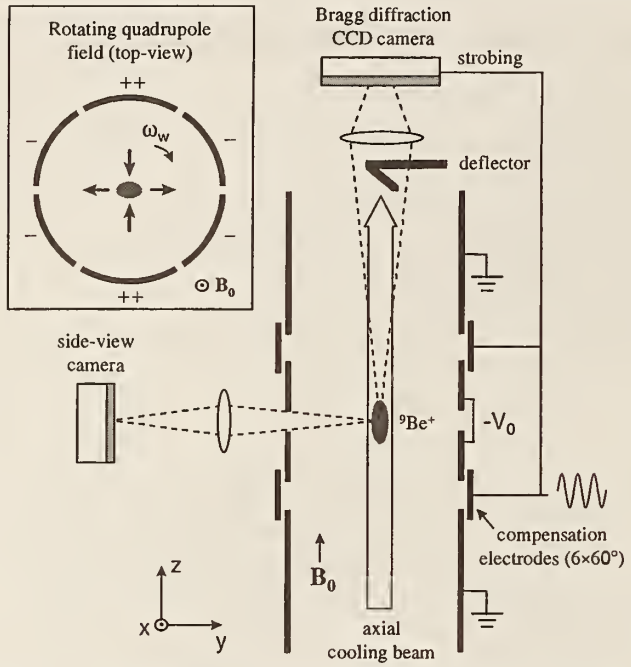


FIG. 1. Schematic side view of the cylindrical trap with real-space imaging optics and Bragg diffraction detection system. Cross section of the rotating quadrupole field (in the $x$-$y$ plane) is shown in the inset.

We create $^9Be^+$ plasmas by ionizing neutral Be atoms in a separate trap (not shown) and then transferring the ions to the main trap for experimentation [4,14]. This procedure can be repeated several times to accumulate up to $10^6$ ions. Immediately after loading, less than 5% are contaminant ions, but this fraction grows on a 20 h time scale due to $^9Be^+$ reactions with neutrals forming ions with smaller charge-to-mass ratio. The trapped $^9Be^+$ ions are Doppler cooled by two laser beams at wavelength $\lambda \approx 313.11$ nm. From previous experiments [13,14], we estimate that temperatures $T \lesssim 10$ mK can be obtained. Here, $k_B T$ refers to the average ion thermal energy in a frame rotating with the plasma which is typically much smaller than the average kinetic energy in the global rotation ($\sim 10^2$ K). The axial cooling beam, directed parallel to $\mathbf{B}_0$, only cools the ion thermal motion while not affecting the global rotation. A second beam propagating perpendicular to $\mathbf{B}_0$ (not shown and turned off during the Bragg scattering measurements) is used to vary the rotation frequency.

When the cloud reaches thermal equilibrium at these cryogenic temperatures, it forms a uniform density spheroid, bounded by $z^2/z_0^2 + (x^2 + y^2)/r_0^2 = 1$, with a rigid-body rotation frequency $\omega_r$ in the range $\omega_m < \omega_r < \Omega - \omega_m$ [14]. The particle density $n_0$ is determined from $\omega_r$ according to $\omega_p^2 \equiv e^2 n_0/\epsilon_0 m = 2\omega_r(\Omega - \omega_r)$, where $\omega_p$ is the plasma frequency [14]. Since the influence of image charges is negligible here, the effective trapping potential in the frame rotating with the plasma, $(x_r, y_r, z)$, is $\Phi_r = (m\omega_z^2/2e)[z^2 + \beta(x_r^2 + y_r^2)]$, where radial trapping strength $\beta \equiv (\omega_p^2 - \omega_z^2)/2\omega_z^2 = \omega_r(\Omega - \omega_r)/\omega_z^2 - 1/2 > 0$ determines the aspect ratio $\alpha \equiv z_0/r_0$ [14,17]. An $f/5$ imaging system detects resonantly scattered photons from the axial cooling beam (diameter $\approx 0.4$ mm, power $\approx 50$ $\mu$W) to produce a side-view image of the $^9Be^+$ ions, from which we measure $\alpha$ to obtain $\omega_r$ and $n_0$.

For the typical condition of $T \lesssim 10$ mK and $n_0 \gtrsim 4 \times 10^8$ cm$^{-3}$, we obtain a Coulomb coupling parameter $\Gamma \equiv (e^2/4\pi\epsilon_0 a_{WS})(k_B T)^{-1} > 200$, where Wigner-Seitz radius $a_{WS}$ is defined by $4\pi a_{WS}^3/3 \equiv n_0^{-1}$. The strong ion-ion coupling results in the formation of crystalline lattices, which are typically body-centered cubic (bcc), in nearly spherical plasmas ($\alpha \approx 1$) with ion number $N \gtrsim 2 \times 10^5$ [4,5]. As shown in Fig. 1, Bragg-scattered light from the axial cooling beam is detected with a second camera near the forward-scattering direction since $\lambda \ll a_{WS}$ [4].

When the rotating fields are first applied, their frequency $\omega_w$ is set close to $\omega_r$ so that they interact strongly with the plasma. By measuring the photon scattering rate from the cooling beam for a fixed laser frequency, we observe that the ion temperature does not change significantly with the application of the rotating fields. Since the rotating quadrupole field typically causes less than 1% shape distortion to the plasma (see later discussions), $\omega_r$ can still be inferred from aspect ratio $\alpha$ within the 5% uncertainty of the method. With $V_w$ sufficiently large, we are able to vary $\omega_r$ by gradually changing $\omega_w$. By tuning the laser frequency far below the resonance or blocking the laser for short periods of time ($\sim 1$ min), we can increase $T$ up to $\sim 10$ K such that the plasma is weakly correlated ($\Gamma \approx 0.2$ for $n_0 \approx 4 \times 10^8$ cm$^{-3}$), and still be able to control $\omega_r$. Figure 2 shows $\omega_r$ versus $\omega_w$

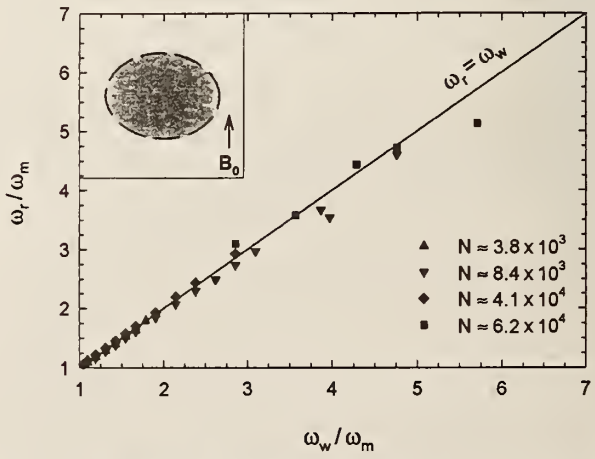


FIG. 2. The plasma rotation frequency $\omega_r$ versus the quadrupole field rotation frequency $\omega_w$. The frequency $\omega_r$ is determined from the aspect ratio $\alpha$ of several plasmas with $200 \le V_0 \le 500$ V. The inset shows a typical side-view image and its boundary fit to an ellipse (dashed line), giving $\alpha$ and $\omega_r$.

for several plasmas with $N < 7 \times 10^4$ and $\omega_r \ll \Omega/2$ ($\omega_r = \Omega/2$ is the Brillouin flow with maximal density $n_B = 5.9 \times 10^9$ cm$^{-3}$). The plasma rotation frequency $\omega_r$ tracks $\omega_w$ closely within the experimental accuracy, demonstrating external control of the plasma rotation by the rotating quadrupole field with both weak and strong Coulomb coupling.

For a more accurate determination of $\omega_r$, we detect the time dependence of Bragg-scattered light from rotating crystals by strobing the diffraction camera with a gateable image intensifier [4,5]. Figure 3(a) shows a time-averaged diffraction pattern of concentric rings from an approximately spherical plasma with $N \approx 7.5 \times 10^5$. Even if this pattern is from a single crystal, rings are observed because of the plasma rotation about the axial laser beam [4]. With the rotating field applied and controlling the plasma rotation, we trigger the intensifier synchronously with the rotating field to open the camera for 50 ns each $2\pi/\omega_w$ period. This enables the camera to record the diffraction pattern in the rest frame of the rotating field. Figure 3(b) shows such a time-resolved pattern taken nearly simultaneously with Fig. 3(a) and accumulated over $\sim 10^6$ rotations. The well-defined rectangular dot pattern demonstrates that the crystal is phase locked to the rotating field. This phase-locked rotation is routinely obtained when $\mathbf{B}_0$ is aligned within 0.01° of the trap axis. In addition, the crystalline lattice and its orientation with respect to the laser beam can last longer than 30 min under this rotation control.

With the rotating quadrupole field, the plasma surface is actually a spinning triaxial ellipsoid with three principal axes differing in length [17]. This particular shape results in a total electric field having only the radial component so that the plasma undergoes a purely azimuthal motion with a uniform rotation frequency. Since $\omega_r = \omega_w$, the combined effective trapping potential in the rotating frame becomes $\Phi_r' = (m\omega_z^2/2e)[z^2 + (\beta - \delta)x_r^2 + (\beta + \delta)y_r^2]$, where $\delta \equiv f_g V_w/V_0 \geq 0$ is the relative strength of the rotating field and $f_g$ depends only on the trap geometry. The thermal equilibrium state in the frame rotating with the plasma is bounded by $z^2/z_0^2 + x_r^2/x_0^2 + y_r^2/y_0^2 = 1$ with $x_0 \geq y_0$, and the parallel and perpendicular aspect ratios ($\alpha_\parallel \equiv z_0/y_0, \alpha_\perp \equiv x_0/y_0$) are determined by $\beta$ and $\delta$ [17].

To maximize $\delta/\beta$, we reduce $V_0$ to less than 200 V and set $\omega_w$ close to $\omega_m$. Side-view images of the plasma are obtained at different phases of the rotating field. In the laboratory frame, the plasma radius along the $x$ axis is expected to oscillate at $2\omega_w$, with an amplitude proportional to $x_0 - y_0$. Figure 4 shows such a plasma with $\alpha_\parallel \approx 0.15$ and $\alpha_\perp \approx 1.4$ rotating at 2.5 kHz ($V_0 = 50$ V, $V_w \approx 185$ V). Excellent agreement between the theory and data is exhibited, showing that the plasma is indeed equilibrated with the rotating field.

We have measured the dependence of $\alpha_\perp$ on parameters $\delta$ and $\beta$. Figure 5(a) shows $\alpha_\perp$ versus $\delta$ at fixed $\beta = 0.103$. Good agreement with the theory is obtained by fitting this data for $f_g$ with the result $f_g \approx 6.38 \times 10^{-3}$. Figure 5(b) shows $\alpha_\perp$ versus $\beta$ for fixed $\delta \approx 0.0159$ using the calibrated $f_g$ value. Excellent agreement is again observed, showing the rapid decrease to unity for $\alpha_\perp$ as $\beta$ is increased. Under typical conditions ($V_0 \geq 500$ V, $V_w \leq 50$ V, and $\omega_w \geq 1.1\omega_m$, giving $\delta < 7 \times 10^{-4}$ and $\beta > 0.1$), $\alpha_\perp - 1$ is less than 1%, but this small distortion apparently generates sufficient torque to phase lock the plasma rotation.

We have also examined rotation control using the dipole field with a potential $\propto y \sin(\omega_w t) - x \cos(\omega_w t)$. Theoretically, this field should not control the plasma rotation, because for a single-species plasma in a quadratic trap it only causes a center-of-mass orbital motion about the trap axis and is thus decoupled from the internal plasma rotation. Experimentally, phase-locked rotation control similar to that by the quadrupole field is obtained. In addition, because larger dipole fields can be applied,

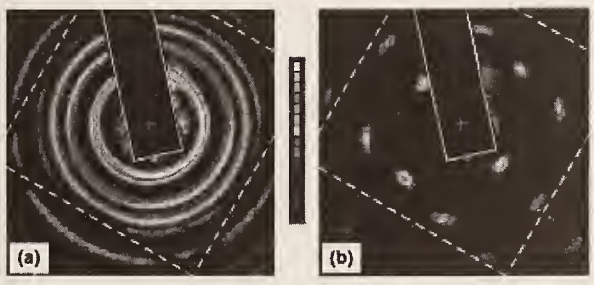


FIG. 3(color). Bragg diffraction from a crystalline lattice (bcc with a {110} plane $\perp$ to $z$ axis) in a plasma phase locked to the rotating field ($\omega_r = \omega_w = 2\pi \times 140$ kHz, $n_0 \approx 4.3 \times 10^8$ cm$^{-3}$, $\alpha \approx 1.1$). (a) 1 s time-averaged pattern; (b) time-resolved pattern by strobing the camera with the rotating field (integration time $\approx$5 s). Both graphs are in false color with logarithmic photon count scales. The long rectangular shadow is from the deflector for the incident beam; four line shadows that form a square are due to a wire mesh at the exit window of the vacuum chamber.

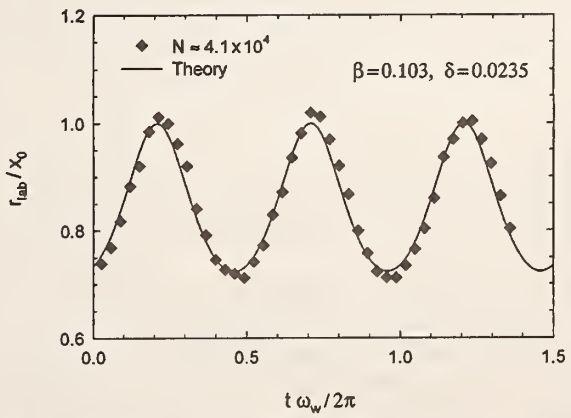


FIG. 4. Oscillation of the plasma radius $r_{lab}$ in 1.5 rotation periods. The theory curve is calculated using the calibrated $f_g$ from Fig. 5(a). The relative phase between the theory and data is not adjusted.

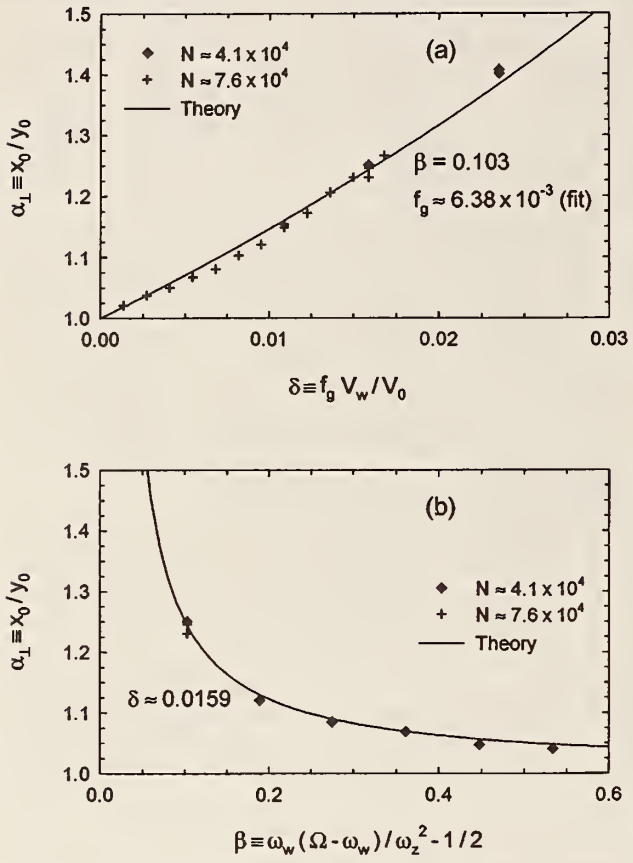


FIG. 5. Dependence of perpendicular aspect ratio $\alpha_\perp$ versus (a) rotating field strength $\delta$ and (b) radial trapping strength $\beta$. Two plasmas are used with $50 \leq V_0 \leq 100$ V and $15 \leq V_w \leq 185$ V. The geometric factor $f_g$ is calibrated in (a).

rotation stabilization in the range $\omega_m < \omega_r \lesssim 0.9(\Omega - \omega_m)$, which includes Brillouin flow, has been achieved. Experimental evidence suggests that the coupling between the center-of-mass motion and plasma rotation can be provided by the contaminant ions which have a slightly larger center-of-mass displacement than $^9Be^+$ due to centrifugal inertia. By measuring the plasma dynamic response under sudden change of $\omega_w$ [15], we have observed that the torque from the dipole field increases with time, presumably due to the growing number of contaminant ions. This observation, however, does not exclude the possibility that other nonideal effects can also provide the coupling.

In the future, direct imaging of individual ions in a crystallized plasma may be possible because of the phase-locked rotation. Furthermore, the increased crystal stability improves the prospect of observing the solid-liquid phase transition.

We thank D. Wineland, D. Dubin, T. O'Neil, and C. F. Driscoll for discussions; B. Jelenković, J. Tan, J. Bergquist, and L. Hollberg for technical assistance; and D. Leibfried, C. Myatt, M. Young, and D. Sullivan for useful comments. This work is supported by the Office of Naval Research.

[1] J. H. Malmberg, C. F. Driscoll, B. Beck, D. L. Eggleston, J. Fajans, K. Fine, X.-P. Huang, and A. W. Hyatt, in *Non-neutral Plasma Physics,* edited by C. W. Roberson and C. F. Driscoll (AIP, New York, 1988), p. 28.

[2] J. J. Bollinger, D. J. Wineland, and D. H. E. Dubin, Phys. Plasmas **1**, 1403 (1994).

[3] T. M. O'Neil, Phys. Fluids **23**, 2216 (1980).

[4] J. N. Tan, J. J. Bollinger, B. Jelenkovic, and D. J. Wineland, Phys. Rev. Lett. **75**, 4198 (1995); J. N. Tan, J. J. Bollinger, B. Jelenkovic, W. M. Itano, and D. J. Wineland, in *Physics of Strongly Coupled Plasmas,* edited by W. D. Kraeft and M. Schlanges (World Scientific, Singapore, 1996), p. 387.

[5] W. M. Itano, J. J. Bollinger, J. N. Tan, B. Jelenkovic, X.-P. Huang, and D. J. Wineland, "Bragg Diffraction from Crystallized Ion Plasmas," Science (to be published).

[6] R. Blatt, P. Gill, and R. C. Thompson, J. Mod. Opt. **39**, 193 (1992); R. C. Thompson, Adv. At. Mol. Phys. **31**, 63 (1993).

[7] J. N. Tan, J. J. Bollinger, and D. J. Wineland, IEEE Trans. Instrum. Meas. **44**, 144 (1995).

[8] G. Savard, St. Becker, G. Bollen, H.-J. Kluge, R. B. Moore, Th. Otto, L. Schweikhard, H. Stolzenberg, and U. Wiess, Phys. Lett. A **158**, 247 (1991); S. Guan, X. Xiang, and A. G. Marshall, Int. J. Mass Spectrom. Ion Process. **124**, 53 (1993).

[9] F. Anderegg, X.-P. Huang, C. F. Driscoll, E. M. Hollmann, T. M. O'Neil, and D. H. E. Dubin, Phys. Rev. Lett. **78**, 2128 (1997).

[10] G. Gabrielse, X. Fei, L. A. Orozco, R. L. Tjoelker, J. Hass, H. Kalinowsky, T. A. Trainer, and W. Kells, Phys. Rev. Lett. **65**, 1317 (1990).

[11] R. G. Greaves and C. M. Surko, Phys. Plasmas **4**, 1528 (1997).

[12] D. Schneider, D. A. Church, G. Weinberg, A. J. Steiger, B. Beck, J. McDonald, E. Magee, and D. Knapp, Rev. Sci. Instrum. **65**, 3472 (1994).

[13] J. J. Bollinger and D. J. Wineland, Phys. Rev. Lett. **53**, 348 (1984).

[14] L. R. Brewer, J. D. Prestage, J. J. Bollinger, W. M. Itano, D. J. Larson, and D. J. Wineland, Phys. Rev. A **38**, 859 (1988); D. J. Heinzen, J. J. Bollinger, F. L. Moore, W. M. Itano, and D. J. Wineland, Phys. Rev. Lett. **66**, 2080 (1991).

[15] X.-P. Huang, F. Anderegg, E. M. Hollmann, C. F. Driscoll, and T. M. O'Neil, Phys. Rev. Lett. **78**, 875 (1997).

[16] Preliminary results on pure electron plasmas are in R. E. Pollock and F. Anderegg, in *Non-neutral Plasma Physics II,* edited by J. Fajans and D. H. E. Dubin (AIP, New York, 1995), p. 139.

[17] D. H. E. Dubin and T. M. O'Neil,"Trapped Non-neutral Plasmas, Liquids, and Crystals (the Thermal Equilibrium States)," Rev. Mod. Phys. (to be published).

ratory experiments for their penetrating power, propagation over intergalactic distances is not without hurdles. A diffuse isotropic infrared background (DIRB) was produced when the first galaxies formed. Massive stars in early galaxies produced large amounts of dust in their winds, reprocessing the visual and ultraviolet light from the stars into infrared (IR) light. By colliding with these ample IR photons, $\gamma$ ray photons can disappear and turn into electron-positron pairs (*23–25*). The most numerous IR photons above the threshold for pair production with 10-TeV $\gamma$ rays have wavelengths ~25 μm. The mean free path ($\lambda_{\gamma\gamma}$) for pair creation at multi-TeV energies is of the order of the distance $d$ of Mrk 501. The exact value depends on the DIRB, which is difficult to measure directly because of the presence of zodiacal light and galactic cirrus clouds.

One can use the observed power law spectrum (*2*) to put a limit on the maximum allowed pair attenuation, assuming that the observed power law is the unattenuated spectrum emitted by the source (consistent with the proton-based model). In general, only contrived intrinsic spectra would look like a smooth power law after the quasi-exponential attenuation. The maximum allowed deviation from the power law $[1 - \exp(-d/\lambda_{\gamma\gamma})]$ is taken to be the size of the statistical error bar at 10 TeV, yielding an optical depth $\tau_{\gamma\gamma} = d/\lambda_{\gamma\gamma} < 0.7$. This limit can be relaxed by a factor not larger than ~2, admitting for weakly absorbed spectra that still approximate a power law (dashed line in Fig. 1). There is some dependence of the attenuation on the shape of the DIRB spectrum. Useful models for the spectral shape can be found in (*23–25*) and yield a similar limit for the 25-μm DIRB normalization $\nu I_\nu$ (25 μm) < (2 to 4) nW m$^{-2}$ sr$^{-1}$. The absence of $\gamma$ ray attenuation in Mrk 501 is consistent with no contribution to the DIRB other than from the optically selected galaxies, for which one expects ~10% of their optical emission to be reprocessed by warm dust, yielding $\nu I_\nu$ (25 μm) ~1 nW m$^{-2}$ sr$^{-1}$ (*26*), but would also allow a DIRB that is stronger by a factor of 2 to 4. A DIRB of at least ~3 nW m$^{-2}$ sr$^{-1}$ is suggested by faint IR galaxy counts and indicates contributions from dust-enshrouded galaxies at red shifts of $z \sim 3$ to 4 (*24*). Electron-based models for the $\gamma$ ray emission from Mrk 501 (*9*) predict deviations from a power law in the multi-TeV range even without external attenuation and therefore impose an upper limit on the DIRB that is below the lower limit from faint IR galaxy counts. If both methods of estimating the DIRB (deviations from a power law spectrum in the multi-TeV range and faint IR galaxy counts) use correct assumptions, a cutoff in the $\gamma$ ray spectrum of Mrk 501 must be present in the energy range 10 to 30 TeV.

## REFERENCES AND NOTES


1. M. F. Cawley and T. C. Weekes, *Exp. Astron.* **6**, 7 (1995).
2. F. Aharonian *et al.*, *Astron. Astrophys.* **327**, L5 (1997).
3. C. D. Dermer and R. Schlickeiser, *Science* **257**, 1642 (1992).
4. P. O. Lagage and C. J. Cesarsky, *Astron. Astrophys.* **125**, 249 (1983); B. Wiebel-Sooth, P. L. Biermann, H. Meyer, *ibid.*, in press.
5. J. R. Jokipii, *Astrophys. J.* **313**, 842 (1987); J. Bednartz and M. Ostrowski, *Mon. Not. R. Astron. Soc.* **283**, 447 (1996).
6. S. R. Reynolds, *Astrophys. J.* **459**, L13 (1996).
7. O. C. De Jager *et al.*, *ibid.* **457**, 253 (1996).
8. K. Koyama *et al.*, *Nature* **378**, 255 (1995).
9. M. Catanese *et al.*, *Astrophys. J.* **487**, L143 (1997); J. Quinn *et al.*, *ibid.* **456**, L83 (1996); E. Pian *et al.*, *Astrophys. J. Lett*, in press.
10. G. Ghisellini, P. Padovani, A. Celotti, L. Maraschi, *Astrophys. J.* **407**, 65 (1993).
11. F. Krennrich *et al.*, *ibid.* **481**, 758 (1997).
12. D. E. Harris, C. L. Carilli, R. A. Perley, *Nature* **367**, 713 (1994).
13. C. M. Urry and P. Padovani, *Pub. Astron. Soc. Pacific* **107**, 803 (1995).
14. P. L. Biermann and P. A. Strittmatter, *Astrophys. J.* **322**, 643 (1987).
15. A. Dar and A. Laor, *ibid.* **478**, L5 (1997).
16. K. Mannheim, P. L. Biermann, W. M. Krülls, *Astron. Astrophys.* **251**, 723 (1991); K. Mannheim, *ibid.* **269**, 67 (1993).
17. K. Mannheim, S. Westerhoff, H. Meyer, H.-H. Fink, *ibid.* **315**, 77 (1996).
18. D. A. Kniffen *et al.*, *Astron. Astrophys. Suppl.* **120**, 615 (1996); P. Padovani, G. Ghisellini, A. C. Fabian, A. Celotti, *Mon. Not. R. Astron. Soc.* **260**, L21 (1993); C. Impey, *Astron. J.* **112**, 2667 (1996).
19. R. J. Protheroe and P. A. Johnson, *Astroparticle Phys.* **5**, 215 (1996).
20. T. Stanev, P. L. Biermann, J. Lloyd-Evans, J. P. Rachen, A. A. Watson, *Phys. Rev. Lett.* **75**, 3065 (1995).
21. J. P. Rachen, T. Stanev, P. L. Biermann, *Astron. Astrophys.* **273**, 377 (1993); N. Hayashida *et al.*, *Phys. Rev. Lett.* **77**, 1000 (1996).
22. T. K. Gaisser, F. Halzen, T. Stanev, *Phys. Rep.* **258**, 173 (1995).
23. D. MacMinn and J. R. Primack, *Space Sci. Rev.* **75**, 413 (1996).
24. A. Franceschini *et al.*, *Astron. Astrophys. Suppl.* **89**, 285 (1991); A. Franceschini *et al.*, in *ESA FIRST Symposium* (European Space Agency special publication 401), in press; T. Stanev and A. Franceschini, in preparation.
25. F. W. Stecker and M. A. Malkan, *Astrophys. J.*, in press.
26. P. Madau *et al.*, *Mon. Not. R. Astron. Soc.* **283**, 1388 (1996); B. T. Soifer and G. Neugebauer, *Astron. J.* **101**, 354 (1991).
27. D. Petry *et al.*, in *Proceedings of the 25th International Cosmic Ray Conference*, Durban, South Africa, August 1997, P. A. Evenson *et al.*, Eds. (International Union of Pure and Applied Physics, in press); S. M. Bradbury *et al.*, *Astron. Astrophys.* **320**, L5 (1997).


28. I thank P. Biermann, A. Dar, J. Kirk, H. Meyer, J. Primack, W. Rhode, F. Rieger, and the referees for their critical reading and suggestions for improvement of the manuscript. This research was generously supported by the Deutsche Forschungsgemeinschaft under travel grant DFG/Ma 1545/6-1.

3 September 1997; accepted 25 November 1997


# Bragg Diffraction from Crystallized Ion Plasmas


W. M. Itano,* J. J. Bollinger, J. N. Tan,† B. Jelenković,‡ X.-P. Huang, D. J. Wineland



Single crystals of a one-component plasma were observed by optical Bragg diffraction. The plasmas contained $10^5$ to $10^6$ single-positive beryllium-9 ions ($^9Be^+$) at particle densities of $10^8$ to $10^9$ per cubic centimeter. In approximately spherical plasmas, single body-centered cubic (bcc) crystals or, in some cases, two or more bcc crystals having fixed orientations with respect to each other were observed. In some oblate plasmas, a mixture of bcc and face-centered cubic ordering was seen. Knowledge of the properties of one-component plasma crystals is required for models of white dwarfs and neutron stars, which are believed to contain matter in that form.


Plasmas, the ionized states of matter, are usually hot and gaseous. However, a sufficiently cold or dense plasma can be liquid or solid. A one-component plasma (OCP) consists of a single charged species embedded in a uniform, neutralizing background charge (*1*). Aside from its intrinsic interest as a simple model of matter, the OCP may be a good model for some dense astrophysical plasmas (*2*), such as the crusts of neutron stars or the interiors of white dwarfs, where the nuclei are embedded in a degenerate electron gas. According to calculations, a classical, infinite OCP freezes into a bcc lattice when the Coulomb coupling parameter

$$\Gamma \equiv \frac{1}{4\pi\epsilon_0}\frac{e^2}{a_{WS}k_BT} \qquad (1)$$

is approximately equal to 170 (*3*). Here, $\epsilon_0$ is the permittivity of the vacuum, $e$ is the charge of an ion, $k_B$ is Boltzmann's con-


Time and Frequency Division, National Institute of Standards and Technology, Boulder, CO 80303, USA.

*To whom correspondence should be addressed. E-mail: witano@nist.gov

†Present address: Frequency & Time Systems, Beverly, MA 01915, USA.

‡On leave from the Institute of Physics, University of Belgrade, Belgrade, Yugoslavia.

stant, $T$ is the temperature, and $a_{WS}$ is the Wigner-Seitz radius, defined by $4\pi a_{WS}^3/3 = 1/n_0$, where $n_0$ is the particle density; $\Gamma$ is the ratio of the Coulomb potential energy of neighboring ions to the kinetic energy per ion.

Ion plasmas can be confined and brought to thermal equilibrium in Penning traps. Such systems have static thermal equilibrium properties equivalent to those of an OCP, where the magnetic field takes the place of the background charge (*4*–*6*). Calculations (*7*) and experiments (*8*) for approximately spherical plasmas having $N \approx 10^3$ to $10^4$ ions show concentric shell structures, dominated by surface effects. Calculations by Dubin and O'Neil (*9*, *10*) suggest that a bcc lattice might begin to form in the center when the number of concentric shells is greater than about 30, which corresponds, for a spherical plasma, to $N \approx 10^5$. Ordered structures of tens of thousands of ions have been observed in a radio-frequency (rf) quadrupole storage ring (*11*) and in a linear rf trap (*12*) but, because of the elongated shapes of these structures, surface effects dominated and bulk structure was not observed.

Tan *et al.* have reported Bragg diffraction patterns from laser-cooled ions in a Penning trap (*13*). For approximately spherical plasmas with 200,000 ions or more, the patterns were consistent with bcc ordering but not with face-centered cubic (fcc) ordering. However, the Bragg patterns were smeared into circles by the rotation of the plasma about the magnetic field axis, so it was not possible to distinguish between scattering by a single crystal and scattering by several crystals or to determine the orientation of the crystals. Here we report the observation of time-resolved (stroboscopic) Bragg diffraction patterns, from which the effect of the plasma rotation is removed (*14*).

In our experiment (Fig. 1), the $^9Be^+$ ions were confined in a cylindrical Penning trap, consisting of an electrostatic quadrupolar potential and a uniform magnetic field $B$ = 4.465 T, parallel to the $z$ axis. The radial electric field leads to a rotation, at frequency $\omega_r$, of the plasma about the $z$ axis. For a given $N$, an equilibrium state of the plasma can be parameterized by $T$ and $\omega_r$ (*4*–*6*). In the limit of low $T$, approached in our experiments, the plasmas are uniform-density spheroids. For $N = 10^6$, a spherical plasma at a typical density of $4 \times 10^8$ cm$^{-3}$ has a diameter of 1.7 mm.

The ions are cooled by a laser beam propagating along the $z$ axis and tuned slightly lower in frequency than a hyperfine-Zeeman component of the $2s\ ^2S_{1/2}$ to $2p\ ^2P_{3/2}$ resonance at 313 nm. The laser power is approximately 50 μW and is focused at the ion plasma to a diameter of about 0.5 mm. We estimate that $T \lesssim 10$ mK (*15*, *16*). For a typical value of $n_0 = 4 \times 10^8$ cm$^{-3}$, this results in $\Gamma \gtrsim 200$. A series of lenses forms an image of the diffraction pattern on an imaging photodetector.

We used two methods to derive a timing signal for stroboscopic detection of the Bragg diffraction patterns. The first (passive method) is based on detecting a photon from a diffracted beam after it has passed through an aperture (Fig. 1). The second (active method) is based on phase-locking the rotation of the plasma to an applied rotating electric field (*17*, *18*).

Two types of imaging detectors were used. One (the MCP-RA detector) is an imaging photomultiplier tube (PMT) based on a microchannel-plate (MCP) electron multiplier and a multielectrode resistive anode (RA) for position sensing. For each photon, the position coordinates are derived from the current pulses collected from the different parts of the RA. The other is a charge-coupled device (CCD) camera coupled to an electronically gateable image intensifier.

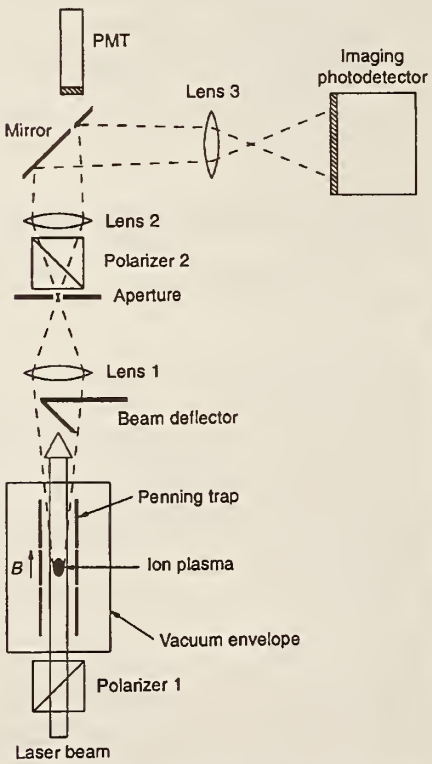


**Fig. 1.** Experimental setup. Laser light is directed through the ion plasma in the Penning trap. A diffraction pattern is created at a plane beyond lens 2, where rays that are parallel leaving the plasma are focused to a point. A mirror, placed near that plane, deflects the light to an imaging photodetector. An aperture placed inside a hole in the mirror allows diffracted light to be detected by a photomultiplier tube (PMT). The aperture is placed off the axis of the optical system, so the PMT generates a timing signal as the diffraction pattern rotates.

Time-integrated diffraction patterns were obtained with both the MCP-RA detector and the CCD camera. Before attempting to observe crystal diffraction patterns, we tuned the frequency of the laser beam from several gigahertz to ~10 MHz below resonance, causing $T$ to vary from above to below the liquid-solid transition temperature. The duration of the frequency sweep was about 10 to 30 s. About 30% of the time, we observed a pattern consisting of several sharp rings, indicating that a crystal had been formed (*13*, *14*). Figure 2, which is consistent with a bcc lattice rotating about a ⟨100⟩ (fourfold symmetry) axis (*19*), is an example of such a pattern.

In order to compare quantitatively the observed Bragg diffraction pattern to a calculated one, it is necessary to know $n_0$, which can be determined from $\omega_r$ [equation 10 of Bollinger *et al.* (*6*)]. In (*13*), $\omega_r$ and $n_0$ were determined from the aspect ratio $\alpha = z_0/r_0$, where $2r_0$ and $2z_0$ are, respectively, the radial and axial diameters of the plasmas [equation 16 of Bollinger *et al.* (*6*)]. The uncertainty in $\omega_r$ determined by fitting the side-view images is ~5%. If there are discrete Bragg diffraction peaks, $\omega_r$ can be determined accurately (to about 0.1%) from time correlations between scattered photons (Fig. 1). A typical correlation spectrum is shown in figure 4(a) of Tan *et al.* (*14*).

As reported in (*13*), 14 time-integrated

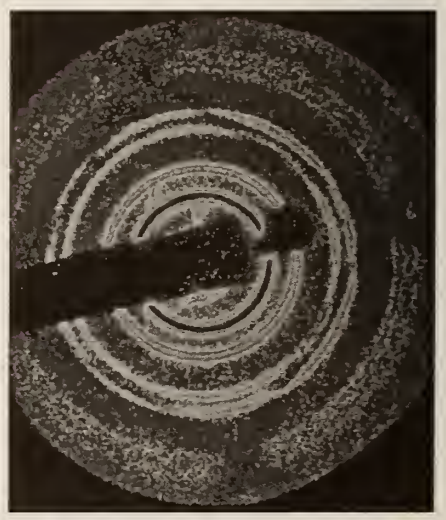

**Fig. 2.** Time-integrated Bragg diffraction pattern obtained with the CCD camera. Rotation of the plasma causes the diffraction spots to be smeared into circles. The long rectangular shadow is due to the laser beam deflector. The small circular shadow is due to the hole in the mirror. The four linear shadows forming a large square are due to a wire mesh. Here, $\omega_r = 2\pi \times 128$ kHz, $n_0 = 3.90 \times 10^8$ cm$^{-3}$, $N = 5 \times 10^5$, $\alpha = 1.00$, and $2r_0 = 1.35$ mm.

Bragg diffraction patterns were analyzed for an approximately spherical plasma having 270,000 ions. Patterns for a larger data set, in which $\omega_r$ was determined by photon correlation, are shown in Fig. 3. The positions of the peaks agree with those calculated for a bcc lattice, to within the 2.5% uncertainty of the angular calibration. They disagree by about 10% with the values calculated for an fcc lattice. The ratios of the peak positions of the first five peaks agree to within about 1% with the calculated ratios for a bcc lattice. The scatter of the data is much reduced relative to that of figure 3 of Tan *et al.* (*13*), reflecting the more accurate $\omega_r$ determination.

In principle, Fig. 3 provides information on the orientations of the crystals. If the crystals formed with random orientations, we would expect Fig. 3 to show a greater number of diffraction peaks at C ({211} Bragg reflections) than at D ({220} Bragg reflections), whereas it actually shows the reverse. This data set showed a preference for alignment of the crystals with a ⟨100⟩ axis along the magnetic field direction. Preliminary observations indicate that the degree to which the magnetic field direction coincides with the symmetry axis of the trap electrodes influences the crystal orientations.

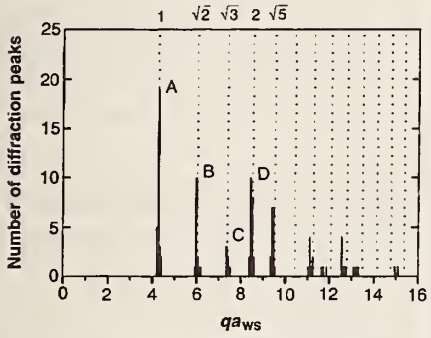


**Fig. 3.** Histogram representing the numbers of peaks (not intensities) observed as a function of $qa_{WS}$, where $\mathbf{q} = \mathbf{k}_s - \mathbf{k}_i$ is the difference between the incident ($\mathbf{k}_i$) and scattered ($\mathbf{k}_s$) photon wave vectors. We analyzed 30 Bragg diffraction patterns from two approximately spherical plasmas having 270,000 and 470,000 ions. The dotted lines show the expected peak positions, normalized to the center of gravity of the peak at A ({110} Bragg reflections).

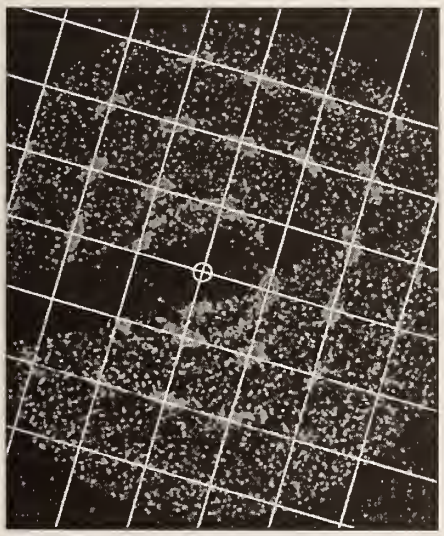

**Fig. 4.** Time-resolved Bragg diffraction pattern of the same plasma as in Fig. 2. Here and in Figs. 5 and 6 the small open circle marks the position of the undeflected laser beam. A bcc lattice, aligned along a ⟨100⟩ axis, would generate a spot at each intersection of the grid lines overlaid on the image. The grid spacing corresponds to an angular deviation of $2.54 \times 10^{-2}$ rad. Here, $\omega_r = 2\pi \times 125.6$ kHz, $n_0 = 3.83 \times 10^8$ cm$^{-3}$, $N = 5 \times 10^5$, $\alpha = 0.98$, and $2r_0 = 1.36$ mm.

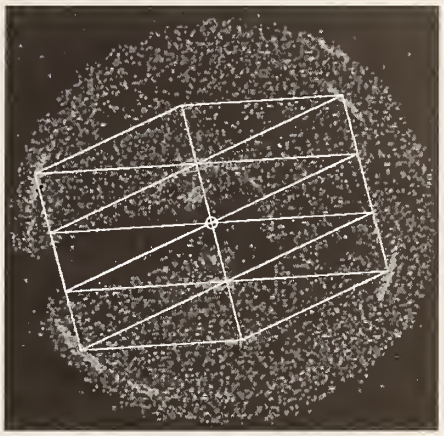

**Fig. 5.** A Bragg diffraction pattern with twofold symmetry. It matches the pattern expected for a bcc lattice oriented along a ⟨115⟩ direction. A diffraction spot is predicted at each intersection of the grid lines. The passive timing method and the MCP-RA detector were used. Here, $\omega_r = 2\pi \times 149$ kHz, $n_0 = 4.53 \times 10^8$ cm$^{-3}$, $N = 4 \times 10^5$, $\alpha = 1.20$, and $2r_0 = 1.12$ mm.

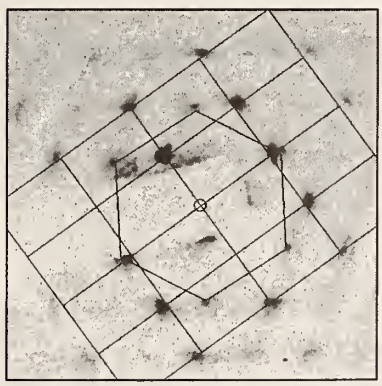

**Fig. 6.** Time-resolved Bragg diffraction pattern showing a superposition of twofold and sixfold symmetric patterns. The rectangular grid connects the points for which diffraction spots are predicted for a bcc lattice oriented along a ⟨110⟩ direction. An fcc lattice oriented along a ⟨111⟩ direction would generate diffraction spots at the vertices of the hexagon. The orientation of the hexagon has been adjusted to fit the data, and it differs by about 3° from that of the rectangular grid. The active timing method and the CCD camera were used. Here, $\omega_r = 2\pi \times 70$ kHz, $n_0 = 2.15 \times 10^8$ cm$^{-3}$, $N = 5 \times 10^5$, and $2r_0 = 2.27$ mm.

Tan *et al.* have noted (*13*) that not all of the diffraction rings allowed for various orientations of a bcc lattice were seen at any given time. This indicated that the portion of the plasma having bcc ordering included at most a few crystals rather than many randomly oriented crystallites. Figure 4 is an example of a time-resolved diffraction pattern obtained with the passive timing method and the CCD camera. In this case, the diffraction spots all line up on a square grid, consistent with a single bcc crystal oriented so that the incident laser beam is along a ⟨100⟩ axis. For these data, an angular calibration was made with an uncertainty of less than 1% with a mask. The agreement between the observed and calculated grid spacing was ~1%.

In order for a diffracted beam to form, $\mathbf{k}_s$ and $\mathbf{k}_i$ must differ by a reciprocal lattice vector (Laue condition) (*20*). In a typical x-ray crystal diffraction case, satisfying the Laue condition for many spots requires that the incident radiation have a continuous range of wavelengths. Here, the Laue condition is relaxed because of the small size of the crystal, so a pattern is obtained even with monochromatic radiation. If the diameter of the region of the plasma having crystalline order is $L$, the mismatch in reciprocal space can be about $2\pi/L$. The diameter of this plasma was ~1.36 mm. In Tan *et al.* (*13*), approximate lower limits for $L$ of 150 μm and 240 μm were determined from the widths and intensities of the Bragg peaks, respectively. For this plasma, $a_{WS} = 8.5$ μm, and the cubic lattice spacing is 17 μm. A cube 240 μm wide would be about 14 lattice spacings in diameter and would contain about 6000 ions.

We also observed patterns that were consistent with single bcc crystals nearly aligned along other directions, including ⟨111⟩, ⟨115⟩, ⟨012⟩, ⟨113⟩, ⟨110⟩, and ⟨013⟩. A pattern consistent with a single bcc crystal oriented along a ⟨115⟩ direction is shown in Fig. 5. Some time-resolved patterns were observed that were not consistent with a single crystal but were consistent with two or more crystals having a fixed relative orientation.

With approximately spherical plasmas (α between 0.6 and 1.4), different diffrac-

tion patterns were observed on different cooling cycles. With more oblate plasmas, the same pattern was observed each time. A very oblate plasma resembles the planar geometry considered by Dubin and O'Neil (*9*, *10*), in which a stack of bcc (110) planes was predicted to have the lowest energy when there are about 60 or more planes. For some cases with fewer planes, a stack of fcc (111) planes has lower energy. In a time-resolved diffraction pattern from a plasma having $\alpha = 0.38$ (Fig. 6), the most intense diffraction spots form a rectangular array, consistent with a bcc lattice oriented along a ⟨110⟩ direction, that is, a stack of (110) planes. Weaker diffraction spots, forming a hexagon, are also seen. These appear at the lowest temperatures. The expected positions of the spots for the {220} Bragg reflections of an fcc lattice oriented along a ⟨111⟩ direction, that is, a stack of (111) planes, are at the vertices of the hexagon overlay. An ideal hexagonal close-packed lattice, oriented along the [001] direction, would generate the same hexagonal spot pattern. However, it would also generate another hexagonal spot pattern at a smaller radius, which is not observed.

Simulations of ion plasmas show hexagonal patterns resembling fcc (111) planes on the layers nearest the surface (*7*). The hexagonal diffraction pattern in Fig. 6 could be the result of scattering from surface layers, and the rectangular pattern could result from scattering from the central region. Some spots in Fig. 6 do not match either the rectangular grid or a hexagonal lattice. They may be due to scattering from a transition region that is neither bcc nor fcc. Further examination of oblate plasmas with different thicknesses may enable the transition from surface-dominated structure to bulk behavior in a finite, strongly coupled OCP to be studied.

### REFERENCES AND NOTES


1. S. Ichimaru, *Rev. Mod. Phys.* **54**, 1017 (1982).
2. H. M. Van Horn, *Science* 252, 384 (1991).
3. E. L. Pollock and J. P. Hansen, *Phys. Rev. A* **8**, 3110 (1973); W. L. Slattery, G. D. Doolen, H. E. DeWitt, *ibid.* **21**, 2087 (1980); *ibid.* **26**, 2255 (1982); S. Ogata and S. Ichimaru, *ibid.* **36**, 5451 (1987); G. S. Stringfellow and H. E. DeWitt, *ibid.* **41**, 1105 (1990); D. H. E. Dubin, *ibid.* **42**, 4972 (1990).
4. R. C. Davidson, *Physics of Nonneutral Plasmas* (Addison-Wesley, Redwood City, CA, 1990), chap. 3.3.
5. J. H. Malmberg and T. M. O'Neil, *Phys. Rev. Lett.* 39, 1333 (1977).
6. J. J. Bollinger, D. J. Wineland, D. H. E. Dubin, *Phys. Plasmas* **1**, 1403 (1994).
7. A. Rahman and J. P. Schiffer, *Phys. Rev. Lett.* **57**, 1133 (1986); H. Totsuji, in *Strongly Coupled Plasma Physics*, F. J. Rogers and H. E. DeWitt, Eds. (Plenum, New York, 1987), p. 19; D. H. E. Dubin and T. M. O'Neil, *Phys. Rev. Lett.* **60**, 511 (1988); J. P. Schiffer, *ibid.* **61**, 1843 (1988); R. W. Hasse and V. V. Avilov, *Phys. Rev. A* 44, 4506 (1991); J. P. Schiffer, in *Non-neutral Plasma Physics II*, F. Fajans and D. H. E. Dubin, Eds. (American Institute of Physics (AIP) Conference Proceedings 331, AIP Press, New York, 1995), p. 191.
8. S. L. Gilbert, J. J. Bollinger, D. J. Wineland, *Phys. Rev. Lett.* **60**, 2022 (1988).
9. D. H. E. Dubin, *Phys. Rev. A* **40**, 1140 (1989).
10. ——— and T. M. O'Neil, in *Strongly Coupled Plasma Physics*, S. Ichimaru, Ed. (Elsevier, Amsterdam, 1990), p. 189.
11. G. Birkl, S. Kassner, H. Walther, *Nature* **357**, 310 (1992).
12. M. Drewsen, C. Brodersen, L. Hornekær, J. S. Hangst, J. P. Schiffer, in preparation.
13. J. N. Tan, J. J. Bollinger, B. Jelenković, D. J. Wineland, *Phys. Rev. Lett.* **72**, 4198 (1995).
14. A preliminary report of the time-resolved detection has appeared [J. N. Tan, J. J. Bollinger, B. Jelenković, W. M. Itano, D. J. Wineland, in *Physics of Strongly Coupled Plasmas*, Proceedings of the International Conference, Binz, Germany, W. D. Kraeft and M. Schlanges, Eds. (World Scientific, Singapore, 1996), p. 387].
15. J. J. Bollinger and D. J. Wineland, *Phys. Rev. Lett.* **53**, 348 (1984).
16. L. R. Brewer *et al.*, *Phys. Rev. A* **38**, 859 (1988).
17. X.-P. Huang, F. Anderegg, E. M. Hollman, C. F. Driscoll, T. M. O'Neil, *Phys. Rev. Lett.* **78**, 875 (1997).
18. X.-P. Huang, J. J. Bollinger, T. B. Mitchell, W. M. Itano, *ibid.* **80**, 73 (1998).
19. The notation refers to the conventional cubic unit cells for the bcc and fcc lattices. A lattice plane specified by Miller indices $h$, $k$, and $\ell$ is denoted by $(hk\ell)$; a direction specified by components $n_1$, $n_2$, and $n_3$ is denoted by $[n_1n_2n_3]$; a set of planes that are equivalent by symmetry is denoted by $\{hk\ell\}$; and a set of directions that are equivalent by symmetry is denoted by $\langle n_1n_2n_3\rangle$. See, for example, N. W. Ashcroft and N. D. Mermin, *Solid State Physics* (Saunders College, Philadelphia, PA, 1976), chap. 5.
20. N. W. Ashcroft and N. D. Mermin, *ibid.*, chap. 6.


21. This manuscript is a work of the U.S. government. It is not subject to U.S. copyright. We acknowledge financial support from the Office of Naval Research.

29 August 1997; accepted 14 November 1997


# Changes in the West Antarctic Ice Sheet Since 1963 from Declassified Satellite Photography


Robert Bindschadler* and Patricia Vornberger



Comparison of declassified satellite photography taken in 1963 with more recent satellite imagery reveals that large changes have occurred in the region where an active ice stream enters the Ross Ice Shelf. Ice stream B has widened by 4 kilometers, at a rate much faster than suggested by models, and has decreased in speed by 50 percent. The ice ridge between ice streams B and C has eroded 14 kilometers. These changes, along with changes in the crevassing around Crary Ice Rise, imply that this region's velocity field shifted during this century.


One of the major uncertainties in the Intergovernmental Panel on Climate Change's projection of future sea level is the uncertain behavior of the West Antarctic Ice Sheet (*1*). It was much larger during the last glacial maximum 20,000 years ago, and its retreat since then has been rapid at times (*2*). Current behavior does not indicate that it is now retreating rapidly, but areas of rapid change have been discovered and the potential for unstable behavior remains under study.

The thick West Antarctic Ice Sheet is grounded on a submarine bed contained in an extensional rift basin coated with thick marine sediments and is subject to high geothermal heat flow (*3*). Discharge of West Antarctic ice is dominated by rapidly moving ice streams. These ice streams feed floating ice shelves; the transition from grounded to floating ice occurs at the "grounding line." Occasionally ice shelves ground, forming ice rises that the ice shelf must flow around. Between ice streams, the ice accumulates to form higher elevation ridges that slowly flow laterally into the ice streams across heavily crevassed shear margins.

Declassified intelligence satellite photography (DISP) recently made available affords a direct view of the ice sheet's configuration in the early 1960s, greatly extending the limited surface observations made during the International Geophysical Year in 1958 to 1959. Here, we analyzed changes in the mouth of ice stream B: from the downstream tip of ridge B/C (between streams B and C) to the area just downstream of Crary Ice Rise (Fig. 1) (*4*).

The DISP data were collected on 29 and 31 October 1963 (*5*). The DISP frames we used were 4 inch by 5 inch (10.16 cm by 12.7 cm) contact negatives, which we scanned at 600 dots per inch to convert them to digital form. They were collected by the cartographic camera onboard a Corona mission satellite and have a ground spatial resolution of about 150 m. Our second data set is a mosaic of two images from the advanced very high resolution radiometer (AVHRR) collected on 12 November 1980 and 8 December 1992. These images were obtained from the U.S. Geological Survey (USGS) World Wide Web site as part of an Antarctic mosaic and have a


R. Bindschadler, Code 971, NASA–Goddard Space Flight Center, Greenbelt, MD 20771, USA.
P. Vornberger, General Sciences Corporation, 6100 Chevy Chase Drive, Laurel, MD 20727, USA.
*To whom correspondence should be addressed.




TN-16

# Doppler imaging of plasma modes in a Penning trap†

**T. B. Mitchell, J. J. Bollinger, X.-P. Huang, and W. M. Itano**

*Time and Frequency Division, National Institute of Standards and Technology, Boulder, CO 80303*

*travis.mitchell@nist.gov*

**Abstract:** We describe a technique and present results for imaging the modes of a laser-cooled plasma of $^9Be^+$ ions in a Penning trap. The modes are excited by sinusoidally time-varying potentials applied to the trap electrodes. They are imaged by changes in the ion resonance fluorescence produced by Doppler shifts from the coherent ion velocities of the mode. For the geometry and conditions of this experiment, the mode frequencies and eigenfunctions have been calculated analytically. A comparison between theory and experiment for some of the azimuthally symmetric modes shows good agreement.



**OCIS codes:** (350.5400) Plasmas; (120.7250) Velocimetry; (140.3320) Laser cooling; (300.6520) Spectroscopy, trapped ion



## References

1. *Non-Neutral Plasma Physics II*, eds. J. Fajans and D. H. E. Dubin (AIP, New York, 1995).
2. J. H. Malmberg and T. M. O'Neil, "Pure electron plasma, liquid, and crystal," *Phys. Rev. Lett.* **39**, 1333-1336 (1977).
3. C. F. Driscoll, J. H. Malmberg, and K. S. Fine, "Observation of transport to thermal equilibrium in pure electron plasmas," *Phys. Rev. Lett.* **60**, 1290-1293 (1988).
4. L. R. Brewer, J. D. Prestage, J. J. Bollinger, W. M. Itano, D. J. Larson, and D. J. Wineland, "Static properties of a non-neutral $^9Be^+$ ion plasma," *Phys. Rev. A* **38**, 859-873 (1988).
5. J. J. Bollinger, D. J. Wineland, and D. H. E. Dubin, "Non-neutral ion plasmas and crystals, laser cooling, and atomic clocks," *Phys. Plasmas* **1**, 1403-1414 (1994).
6. D. H. E. Dubin,"Theory of electrostatic fluid modes in a cold spheroidal non-neutral plasma," *Phys. Rev. Lett.* **66**, 2076-2079 (1991).
7. J. J. Bollinger, D. J. Heinzen, F. L. Moore, W. M. Itano, D. J. Wineland, and D. H. E. Dubin, "Electrostatic modes of ion-trap plasmas," *Phys. Rev. A* **48**, 525-545 (1993).
8. R. G. Greaves and C. M. Surko, "Antimatter plasmas and antihydrogen," *Phys. Plasmas* **4**, 1528-1543 (1997).
9. G. Gabrielse, X. Fei, L. A. Orozco, R. L. Tjoelker, J. Haas, H. Kalinowsky, T. A. Trainor, and W. Kells, "Cooling and slowing of trapped antiprotons below 100 meV," *Phys. Rev. Lett.* **63**, 1360 (1989).
10. M. H. Holzscheiter, X. Feng, T. Goldman, N. S. P. King, R. A. Lewis, M. M. Nieto, and G. A. Smith, "Are antiprotons forever?," *Phys. Lett. A* **214**, 279 (1996).
11. D. J. Heinzen, J. J. Bollinger, F. L. Moore, W. M. Itano, and D. J. Wineland, "Rotational equilibria and low-order modes of a non-neutral ion plasma," *Phys. Rev. Lett.* **66**, 2080-2083 (1991).
12. X.-P. Huang, J. J. Bollinger, T. B. Mitchell, and W. M. Itano, "Phase-locked rotation of crystallized non-neutral plasmas by rotating electric fields," *Phys. Rev. Lett.* **80**, 73-76 (1998).
13. D. H. E. Dubin and J. P. Schiffer, "Normal modes of cold confined one-component plasmas," *Phys. Rev. E* **53**, 5249-5267 (1996).

#4417 - $15.00 US
Received January 13, 1998

14. D. H. E. Dubin, "Effects of correlations on the thermal equilibrium and normal modes of a non-neutral plasma," *Phys. Rev. E* **53**, 5268-5290 (1996).

15. C. S. Weimer, J. J. Bollinger, F. L. Moore, and D. J. Wineland, "Electrostatic modes as a diagnostic in Penning trap experiments," *Phys. Rev. A* **49**, 3842-3853 (1994).

16. M. D. Tinkle, R. G. Greaves, and C. M. Surko, "Low-order longitudinal modes of single-component plasmas," *Phys. Plasmas* **2**, 2880-2894 (1995).

17. R. G. Greaves, M. D. Tinkle, and C. M. Surko, "Modes of a pure ion plasma at the Brillouin limit," *Phys. Rev. Lett.* **74**, 90-93 (1995).

18. C. F. Driscoll, "Observation of an unstable $m = 1$ diocotron mode on a hollow electron column," *Phys. Rev. Lett.* **64**, 1528-1543 (1990).

19. J. N. Tan, J. J. Bollinger, B. Jelenković, and D. J. Wineland, "Long-range order in laser-cooled, atomic-ion Wigner crystals observed by Bragg scattering," *Phys. Rev. Lett.* **75**, 4198-4201 (1995).

20. W. M. Itano, J. J. Bollinger, J. N. Tan, B. Jelenković, X.-P. Huang, and D. J. Wineland, "Bragg diffraction from crystallized ion plasmas," *Science* **279**, 686-689 (1998).

21. Here $\omega_{lm}$ is the mode frequency in a frame rotating with the plasma. For the $m = 0$ modes discussed here this distinction is not necessary because their frequency is the same in either the laboratory or rotating frame.

22. Information on the mode eigenfunction can be obtained from the side-view images even when there is a change in the phase-averaged ion fluorescence. However, the images may no longer provide a linear measure of the mode axial velocity.

23. R. C. Thompson, K. Dholakia, J-L. Hernandez-Pozos, G. Zs. K. Horvath, J. Rink, and D. M. Segal, "Spectroscopy and quantum optics with ion traps," *Phys. Scr.* **T72**, 24-33 (1997).

## 1. Introduction

Non-neutral plasmas consisting exclusively of particles of a single sign of charge have been used to study many basic processes in plasma physics [1], partly because non-neutral (as opposed to neutral or quasi-neutral) plasmas can be confined by static electric and magnetic fields and also be in a state of global thermal equilibrium [2–4]. A particularly simple confinement geometry for non-neutral plasmas is the quadratic Penning trap, which uses a strong uniform magnetic field $\mathbf{B_0} = B_0\hat{\mathbf{z}}$ superimposed on a quadratic electrostatic potential

$$\phi_T(r,z) = \frac{m\omega_z^2}{2q}\left(z^2 - \frac{r^2}{2}\right). \tag{1}$$

Here $m$ and $q$ are the mass and charge of a trapped ion, and $\omega_z$ is the axial frequency of a single ion in the trap. The global thermal equilibrium state for a single charged species in a quadratic Penning trap has been well studied [4,5]. For sufficiently low temperatures, the plasma takes on the simple shape of a uniform density spheroid. An interesting result is that all of the electrostatic modes of a magnetized, uniform density spheroidal plasma can be calculated analytically [6,7]. This is the only finite length geometry for which exact plasma mode frequencies and eigenfunctions have been calculated for a realistic thermal equilibrium state. In this manuscript we describe a technique for measuring these frequencies and eigenfunctions, and compare theory predictions and experimental results for some of the azimuthally symmetric modes.

The modes have several potential applications in Penning trap experiments. In general, the mode frequencies depend on the density and shape of the plasma spheroid. Therefore measurement of a mode frequency provides a non-destructive method for obtaining basic diagnostic information about the plasma. This is especially important in anti-matter plasmas [8–10], where conventional techniques for obtaining information about these plasmas involve ejecting the plasma from the trap. Other applications arise from the fact that the modes can strongly influence the dynamical behavior of trapped

#4417 - $15.00 US
Received January 13, 1998

plasmas. For example, certain azimuthally asymmetric modes can have zero frequency in the laboratory frame and be excited by a static field error of the trap. These zero frequency modes can strongly limit the achievable density in a Penning trap [11]. Similarly, the plasma angular momentum can be changed through the deliberate excitation of azimuthally asymmetric modes, and the applied torque can be much greater than that from the "rotating wall" perturbation [12], which is not mode-resonant. Finally, the modes may provide useful information on the internal state of a plasma. For example, measurement of the damping of the modes can provide information on the plasma's viscosity. This measurement could presumably be done in the interesting regime where the plasma is strongly correlated [13,14].

Previous experimental mode studies on spheroidal plasmas have been limited to frequency measurements on a small class of modes. With laser-cooled $Be^+$ ion plasmas, some quadrupole mode frequencies have been measured and agree well with theory [7,11]. Mode frequencies have also been measured on spheroidal cryogenic electron plasmas [15], 0.025–0.5 eV electron and positron plasmas [16], and room temperature $Ar^+$ ion plasmas [17]. In these cases qualitative agreement with theory was observed and the modes provided some basic diagnostic information. However, deviations from the model of a constant density spheroid in a quadratic trap limited the comparison with the ideal linear theory. Here, in addition to measuring mode frequencies, we also measure the mode eigenfunctions. The eigenfunctions permit direct identification of the modes. In addition, they contain much more information than the frequencies and therefore may be useful for observing nonlinear effects such as mode couplings. Mode eigenfunctions have been measured for low frequency, $z$-independent (diocotron) modes on cylindrical electron columns [18]. In that work, the mode measurements were important in identifying two coexisting modes.

## 2. Experimental apparatus

Figure 1 shows a sketch of the apparatus [19,20] used for the mode measurements. The trap consists of a 127 mm long stack of cylindrical electrodes at room temperature with an inner diameter of 40.6 mm, enclosed in a $10^{-8}$ Pa vacuum chamber. A uniform magnetic field $B_0 = 4.465$ T is aligned parallel to the trap axis within 0.01°, and results in a $^9Be^+$ cyclotron frequency $\Omega = qB_0/m = 2\pi \times 7.608$ MHz. The magnetic field alignment is accomplished by minimizing the excitation of zero-frequency modes produced by a tilt of the magnetic field with respect to the trap electrode symmetry axis [7,11]. Positive ions are confined in this trap by biasing the central "ring" electrode to a negative voltage $-V_0$ with respect to the endcaps. Because the dimensions of the $Be^+$ plasmas ($\lesssim 2$ mm) are small compared to the diameter of the trap electrodes, the quadratic potential of Eq. (1) is a good approximation for the trap potential. For the work reported here, $V_0 = 2.00$ kV which results in $\omega_z = 2\pi \times 1.13$ MHz and a single particle magnetron frequency $\omega_m = [\Omega - (\Omega^2 - 2\omega_z^2)^{\frac{1}{2}}]/2 = 2\pi \times 84.9$ kHz.

We create a $Be^+$ plasma by ionizing neutral Be atoms in a separate trap (not shown) and then transferring the ions to the main trap. For the mode work discussed here, the number of ions was typically $6 \times 10^4$. While the total charge in the trap is conserved after loading, the relative abundance of contaminant, heavier-mass ions increases, presumably due to reactions between $Be^+$ ions and background neutral molecules. Because we analyze our experimental results using an existing theory [6] for the electrostatic modes of a single-species plasma, we took data only with relatively clean clouds (< 3% impurity ions). The plasmas were cleaned approximately every 30 minutes by transferring the ions to the load trap where, with a shallow 3 V deep well, contaminant ions were driven out of the trap by exciting their axial frequencies. Cleaning therefore results in a decrease in the number of trapped ions. Over a 12–14 hour period, the num-

#4417 - $15.00 US
Received January 13, 1998

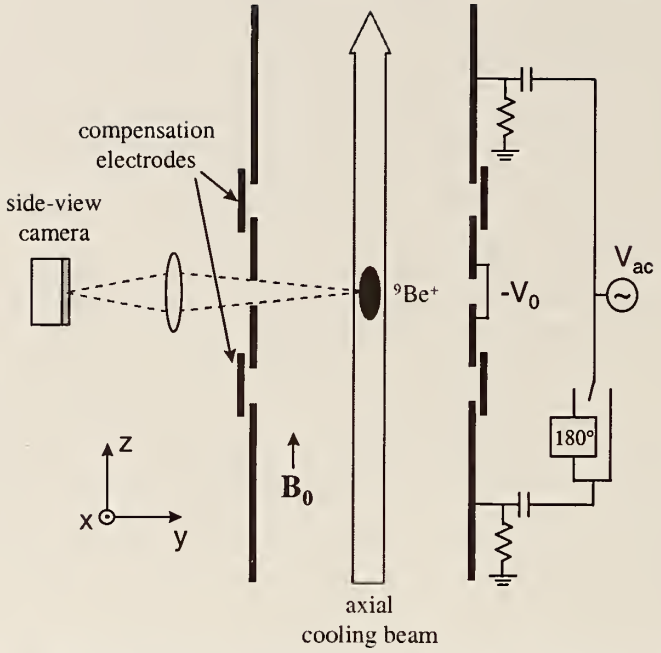


Figure 1. Sketch of the experimental apparatus. Modes were excited by applying in-phase or 180° out-of-phase sinusoidal potentials to the trap endcaps.

ber of ions is reduced by a factor of 2. Because the mode frequencies and eigenfunctions in a quadratic trap are independent of the number of ions, the measurements described here are not affected.

The trapped $Be^+$ ions are Doppler-cooled by two laser beams at wavelength $\lambda \approx 313.11$ nm. The main cooling beam is directed parallel to $\mathbf{B_0}$ as shown in Fig. 1, and a second beam propagating perpendicular to $\mathbf{B_0}$ (not shown and turned off during the mode eigenfunction measurements) is also used to compress the plasma by applying a radiation pressure torque [4,11]. For mode measurements the axial cooling-laser frequency is fixed about one natural linewidth ($\sim$ 20 MHz) below the transition frequency. Ions which, due to excitation of a mode, have an axial velocity $v_z < 0$ therefore fluoresce more strongly than ions with $v_z > 0$. The ion temperature was not measured; however, based on previous work [4], we expect $T \lesssim 20$ mK.

An $f/5$ imaging system detects the $Be^+$ resonance fluorescence scattered perpendicularly from the axial cooling beam (waist $\approx 0.5$ mm, power $\approx 50\,\mu$W) to produce a side-view image of the $Be^+$ ions. The side-view image is obtained with a photon-counting camera system which records the spatial and temporal coordinates of the detected photons. This data is processed to obtain the mode eigenfunctions by constructing side-view images as a function of the phase of the external drive used to excite the modes.

### 3. Electrostatic modes of a cryogenic plasma

The constant-density, spheroidal plasma model is a good approximation for our work. In thermal equilibrium, a Penning trap plasma rotates as a rigid body at frequency $\omega_r$, where $\omega_m < \omega_r < \Omega - \omega_m$, about the trap's $\hat{\mathbf{z}}$ axis [2,5]. In this work the rotation frequency was precisely set by a rotating dipole electric field [12]. As the ions rotate through the magnetic field they experience a Lorentz force which provides the radial

#4417 - $15.00 US
Received January 13, 1998

confining force of the trap. This $\omega_r$-dependent confinement results in an $\omega_r$-dependent ion density and plasma shape. At the low temperatures of this work, the plasma density is uniform over distances large compared to the interparticle spacing ($\sim$ 10 $\mu$m) and is given by $n_0 = \epsilon_0 m\omega_p^2/q^2$ where $\omega_p = [2\omega_r(\Omega - \omega_r)]^{\frac{1}{2}}$ is the plasma frequency. With the confining potential of Eq. (1), the plasma is spheroidal with boundary $z^2/z_0^2 + x^2/r_0^2 + y^2/r_0^2 = 1$. The spheroid aspect ratio $\alpha \equiv z_0/r_0$ is determined by $\omega_r$ [4,5]. We have neglected the effect of image charges, because the plasma dimensions are small compared to the trap dimensions.

The modes of these spheroidal plasmas can be classified by integers $(l, m)$, where $l \geq 1$ and $0 \leq m \leq l$ [6,7]. For an $(l, m)$ mode with frequency $\omega_{lm}$ [21], the perturbed potential of the mode inside the plasma is given by a symmetric product of Legendre functions,

$$\Psi^{lm} \propto P_l^m(\bar{\xi}_1/\bar{d}) P_l^m(\bar{\xi}_2) e^{i(m\phi - \omega_{lm}t)}. \quad (2)$$

Here $\bar{\xi}_1$ and $\bar{\xi}_2$, discussed in Ref. [6], are scaled spheroidal coordinates where the scaling factor depends on the frequencies $\omega_r$, $\Omega$, and $\omega_{lm}$, and $\bar{d}$ is a shape-dependent parameter which also depends on these frequencies. In general, for a given $(l, m)$ there are many different modes. In this paper we report measurements of the mode frequencies and eigenfunctions of a few magnetized plasma modes, which are defined as those modes with frequencies $|\omega_{lm}| < |\Omega - 2\omega_r|$ [6,7]. In addition, we only discuss measurements of azimuthally symmetric ($m = 0$) modes. For $\omega_r \ll \Omega/2$, these modes principally consist of oscillations parallel to the magnetic field at a frequency on the order of $\omega_z$. In the experiment we detect the axial velocity of a mode. In the linear theory, this is proportional to $\partial\Psi^{lm}/\partial z$.

We excite plasma modes by applying sinusoidally time-varying potentials to the trap electrodes. Azimuthally symmetric ($m = 0$) even $l$ modes are excited by applying in-phase potentials to the endcaps (even drive), while odd $l$ modes are excited by applying 180° out-of-phase potentials to the endcaps (odd drive). Azimuthally asymmetric ($m \neq 0$) modes can be excited by applying time-varying potentials to the compensation electrodes, which have 6-fold azimuthal symmetry. In Refs. [7, 11] quadrupole ($l = 2$) mode frequencies were measured by observing the change in the total ion fluorescence from the plasma, averaged over the phase of the drive, which occurred when the drive frequency equaled the mode frequency. However, in order to observe such a change, the mode excitation must be large enough so that either the fluorescence from an ion non-linearly depends on its velocity or there is some heating of the plasma by the mode. The larger amplitude drive required by this technique decreases the precision of the mode measurements.

The new technique reported here entails reducing the drive amplitude until the change in the phase-averaged ion fluorescence is negligible, and detecting the mode's coherent ion velocities by recording side-view images as a function of the phase and frequency of the external drive. These Doppler images provide direct measurements of the mode's axial-velocity eigenfunction [22]. In addition, an accurate measurement of the mode's frequency can be obtained from the line center of the mode amplitude as a function of drive frequency. High order modes have been excited and detected with this technique, such as the $(11, 0)$ and $(12, 1)$ modes. We note that for the (1,0) and (1,1) modes, imaging is not required because there is no spatial variation in their eigenfunction. The driven mode amplitude and phase of these center-of-mass modes can therefore be obtained by coherently detecting the spatially-integrated fluorescence as a function of the phase of the external drive [23].

#4417 - $15.00 US

Received January 13, 1998

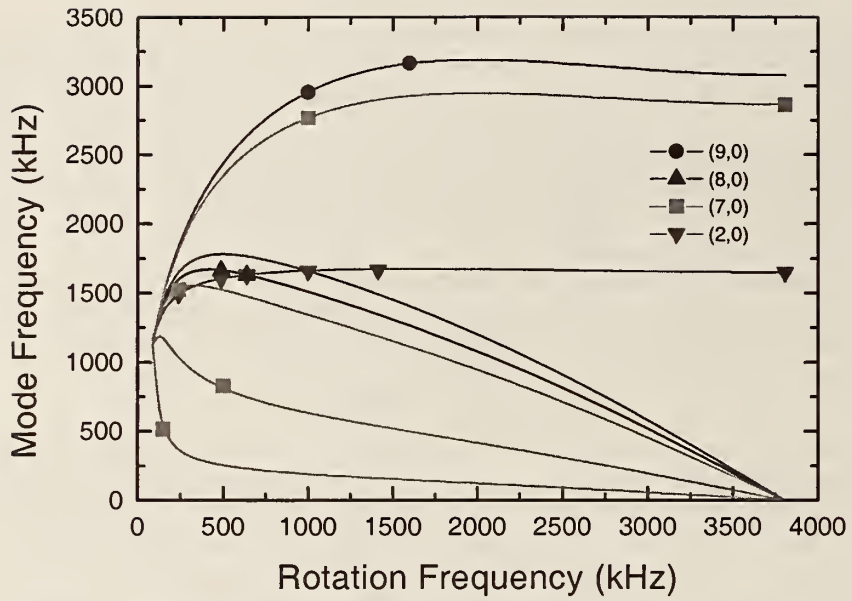


Figure 2. Plots of the frequencies of several magnetized plasma modes as a function of rotation frequency for $\Omega/2\pi$=7.608 MHz and $\omega_z/2\pi$=1.13 MHz. The solid lines are the theoretical predictions and the symbols are experimental measurements. Only the highest frequency $(9,0)$ plasma mode and the second highest frequency $(8,0)$ plasma mode are plotted.

## 4. Experimental results

In Fig. 2 we plot several measured mode frequencies, along with the theoretical predictions, for azimuthally symmetric magnetized plasma modes as a function of $\omega_r$ for $\omega_z/2\pi = 1.13$ MHz and $\Omega/2\pi = 7.608$ MHz. Many different mode frequencies at various values of $\omega_z$ have been measured, and on clean clouds agreement between the observed and predicted mode frequencies is typically better than 1%. In this manuscript we concentrate on describing the images obtained of the $(2,0)$ and the highest frequency $(9,0)$ magnetized plasma modes. For a given $(l, 0)$, the highest frequency magnetized plasma mode does not have any radial nodes.

Figure 3 demonstrates the phase-coherent detection of the $(2,0)$ mode. This is one of the simplest modes that is not merely a center-of-mass oscillation of the plasma. In this mode the plasma stays spheroidal but the aspect ratio (and density) oscillate at $\omega_{2,0}$. For $\omega_r \ll \Omega/2$, the oscillation in $r_0$ is very small, so the mode principally consists of oscillations in $z_0$ at $\omega_{2,0}$. Ions above the $z = 0$ plane oscillate 180° out of phase with ions below $z = 0$.

Figure 3(a) shows a sequence of 18 side-view images as a function of the phase of the mode drive at $\omega_{2,0}/2\pi = 1.656$ MHz. The plasma's rotation frequency was set to $\omega_r/2\pi = 1.00$ MHz and the $m = 0$ even drive rms amplitude was 7.07 mV. In the images, the magnetic field and the axial laser beam point up. As expected for the $(2,0)$ mode, the detected fluorescence in the upper half of the plasma is bright when the lower half is dark and vice versa. We analyze the data of Fig. 3(a) by performing a least-squares fit of the intensity at each point to $A_0 + A_{2,0}\cos(\omega_{2,0}t + \varphi_{2,0})$. Figures 3(b) and 3(c) show the resultant images of the measured mode amplitude $A_{2,0}(x,z)$ and phase $\varphi_{2,0}(x,z)$. These are compared with the theoretically predicted values of these quantities. Because the plasma is optically thin, the theoretical predictions were obtained by integrating $\partial\Psi^{lm}/\partial z$ over $y$. The amplitude of the theoretical prediction is scaled to match the

#4417 - $15.00 US
Received January 13, 1998

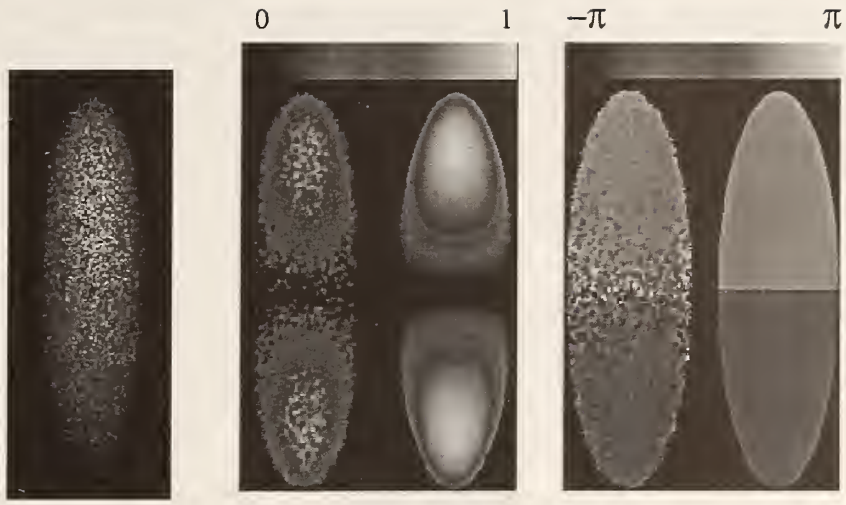


Figure 3. (a) Movie of sideview image data obtained on a plasma with $\omega_r/2\pi=$ 1.00 MHz while driving a (2,0) mode at $\omega_{2,0}/2\pi$=1.656 MHz. The magnetic field and axial laser beam point up. The ion cloud dimensions are $2z_0 = 0.76$ mm and $2r_0 = 0.24$ mm, and the density $n_0 = 2.70 \times 10^9$ cm$^{-3}$. Comparison of the amplitude (b) and phase (c) extracted from the $(2,0)$ mode in (a) with the predictions of linear theory. The theory predictions are on the right.

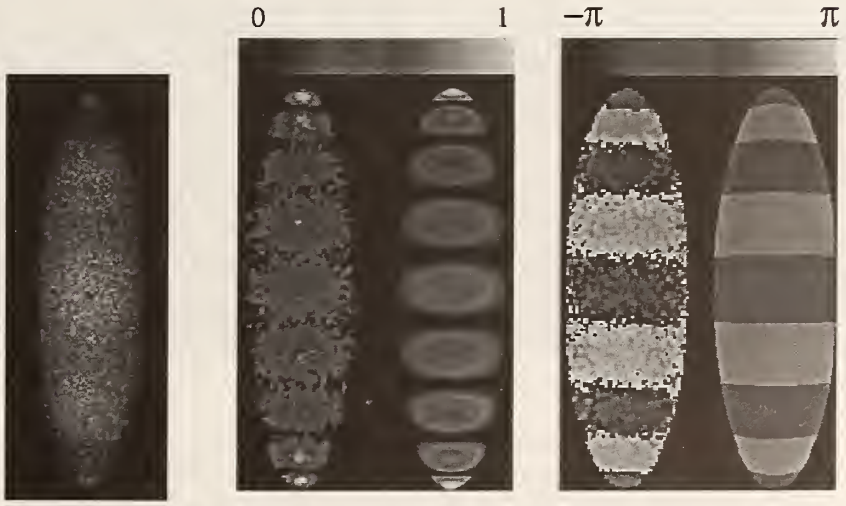


Figure 4. (a) Movie of sideview image data obtained on the plasma of Fig. 3 with $\omega_r/2\pi=$ 1.00 MHz while driving a (9,0) mode at $\omega_{9,0}/2\pi$=2.952 MHz. Comparison of the amplitude (b) and phase (c) extracted from the $(9,0)$ mode in (a) with the predictions of linear theory. The theory predictions are on the right.

experiment, and both amplitudes are normalized to one.

From the fitted values of $A_{2,0}$ and $A_0$ we can estimate the coherent ion mode velocities if the dependence of the ion fluorescence on velocity (through Doppler shifts)

#4417 - $15.00 US
Received January 13, 1998

is known. For the low temperatures of this experiment a good approximation is to assume a Lorentzian profile with a 19 MHz full-width-at-half-maximum due to the natural linewidth of the optical cooling transition. With the 20 MHz detuning used in this experiment, we estimate for the data of Fig. 3 that the maximum coherent mode velocity, which occurs at $z = \pm z_0$, is $\sim$1.5 m/s. The spatial and density changes in the plasma spheroid for this excitation are too small to be resolved ($\Delta z/z_0, \Delta n/n_0 < 10^{-3}$). Therefore the observed variation in the fluorescence intensity is entirely due to Doppler shifts induced by the coherent ion velocities of the mode.

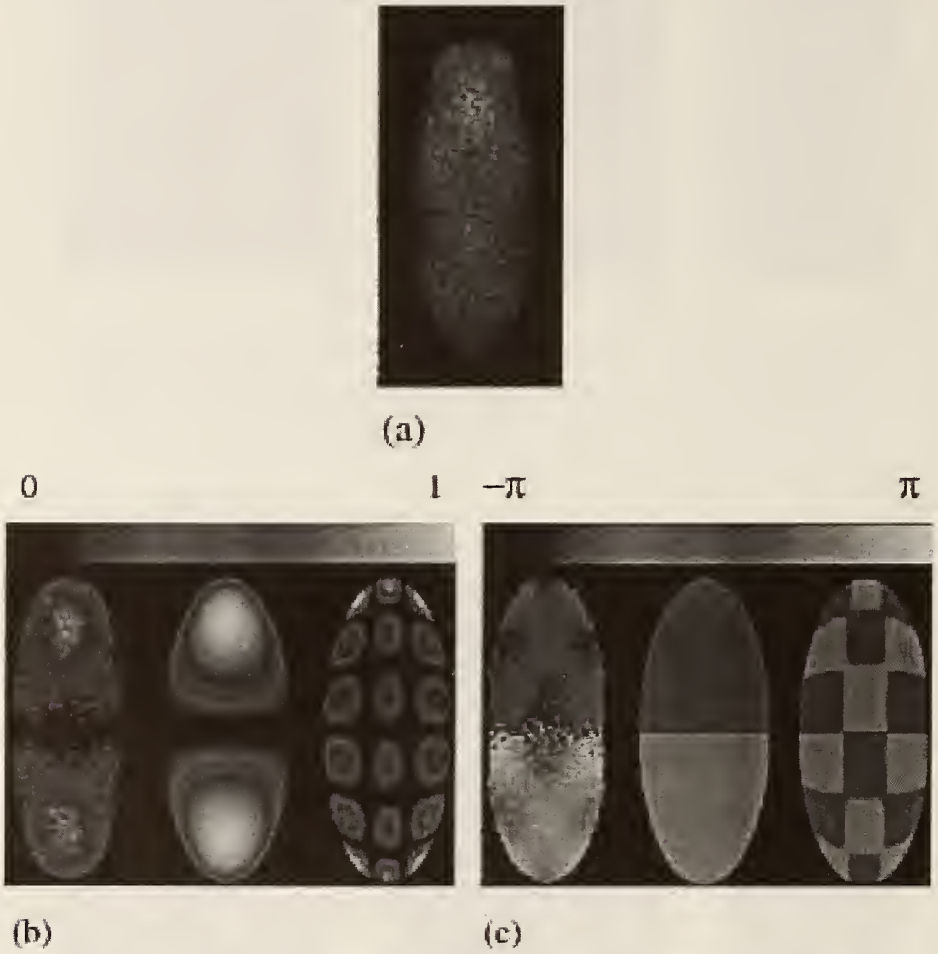


Figure 5. (a) Movie of sideview image data obtained on a plasma with $\omega_r/2\pi$= 638 kHz while driving with an even drive at 1.619 MHz. At this rotation frequency there is a crossing of the $(2,0)$ mode and an $(8,0)$ mode with a radial node. Comparison of the amplitude (b) and phase (c) extracted from the data in (a) with the predictions of linear theory. The predictions of both the $(2,0)$ and $(8,0)$ modes are given. For this plasma $2z_0 = 0.70$ mm and $2r_0 = 0.29$ mm.

We have measured the mode eigenfunctions of a number of different azimuthally symmetric ($m$=0) modes including the $l$=2,3,4,5,7 and 9 modes. Like the data of Fig. 3, good agreement with the predicted eigenfunction amplitude and phase distribution is obtained in the limit of low laser power and drive amplitude. Surprisingly high-order odd modes could be excited with the odd drive on the trap endcaps. Figure 4(a)

#4417 - $15.00 US
Received January 13, 1998

shows a sequence of 18 sideview images obtained with the $(9,0)$ excited by a drive at $\omega_{9,0}/2\pi = 2.952$ MHz. Figures 4(b) and 4(c) show the fitted amplitude and phase from this sequence, along with the predictions from theory. Similar high-order even $(l,0)$ modes are more difficult to excite.

Finally, Fig. 5 shows images from a plasma with $\omega_r/2\pi = 638$ kHz driven by an even drive at 1.619 MHz. This case demonstrates the utility of the Doppler imaging diagnostic. These data were initially taken during a survey of the $(2,0)$ mode eigenfunction as a function of the plasma's rotation frequency. Analysis of the phase-coherent data revealed additional, higher-order structure. An examination of the predictions for the mode frequencies revealed that at this particular rotation frequency, as shown in Fig. 2, both the $(2,0)$ mode and an $(8,0)$ mode with a radial node have similar frequencies. Characteristics of both modes are seen in the data. Measurements of the $(2,0)$ mode frequency near this crossing indicate that any frequency shifts due to a non-linear coupling with the $(8,0)$ mode are less than a few kilohertz. We note that the $(2,0)$ mode driven in Fig. 3 occurs near a crossing with a $(9,0)$ mode (see Fig. 2). In this case, no evidence for the excitation of a $(9,0)$ is observed, presumably because this is an odd mode.

## 5. Summary and conclusion

We have described a technique for imaging the eigenfunctions of a laser-cooled ion plasma. In general, for the azimuthally symmetric modes on spheroidal plasmas discussed here, good agreement is obtained between linear theory and experimental measurements made with low mode drive amplitude and laser power. The technique should be a useful tool for studying deviations from the linear theory, such as large amplitude frequency shifts and non-linear corrections to the mode eigenfunction. Data like that of Fig. 5 should be useful for studying the coupling between modes. Finally, the width of the resonant lineshape of the mode amplitude as a function of the drive frequency provides a measurement of the mode damping. With low laser power and a sufficiently clean plasma this should provide information on the viscosity of a strongly correlated plasma.

## 6. Acknowledgments

We thank D. H. E. Dubin and D. J. Wineland for useful discussions, and B. Jelenković, R. Rafac and S. Robertson for useful comments on the manuscript. This work is supported by the Office of Naval Research.

#4417 - $15.00 US
Received January 13, 1998

## Invited Papers

# Precise control of the global rotation of strongly coupled ion plasmas in a Penning trap*

X.-P. Huang,† J. J. Bollinger, T. B. Mitchell, and W. M. Itano
*Time & Frequency Division, National Institute of Standards and Technology, Boulder, Colorado 80303*

D. H. E. Dubin
*Department of Physics, University of California at San Diego, La Jolla, California 92093*

(Received 13 November 1997; accepted 5 January 1998)

Rotating asymmetric electric fields have been applied to control the rotation frequency (and hence the density) of non-neutral plasmas, which are confined in Penning-type traps and have relaxed close to thermal equilibrium characterized by a global rigid-body rotation. "Infinite" confinement times and density compression were first reported for uncorrelated plasmas of $\sim 10^8$ $Mg^+$ ions with temperatures ranging from 1 K to $5\times10^4$ K (4 eV) [Huang *et al.*, Phys. Rev. Lett. **78**, 875 (1997)]. In this paper, the rotating field technique has been applied to control strongly coupled plasmas of $\sim 10^5$ $^9Be^+$ ions which are laser-cooled to millikelvin temperatures so that the plasma freezes into a solid with a crystalline lattice. Here, Bragg diffraction peaks from crystals provide an accurate way of measuring the rotation frequency, and it is observed that the plasma rotation can be phase locked to the applied rotating field without any slip. In essence, these corotating plasmas have reached thermal equilibrium with the rotating field, and the azimuthally asymmetric boundaries of the equilibrium states have been measured experimentally. Both rotating dipole and quadrupole fields have been used to provide this precise control of the plasma rotation. However, the effectiveness of the dipole field depends on the presence of multiple ion species. With the rotating dipole field, density compression to near the Brillouin limit and increase of the rotation frequency to near the cyclotron frequency have been achieved. [S1070-664X(98)91105-3]

### I. INTRODUCTION

Unneutralized plasmas with a single sign of charge are often confined in Penning-type traps[1,2] for a variety of experiments including plasma physics,[3] Coulomb crystal studies,[4,5] precision spectroscopy,[6,7] antimatter research,[8,9] and storage of highly charged ions.[10] Since there is an average radial electric field, these trapped non-neutral plasmas undergo a global ($\mathbf{E}\times\mathbf{B}$) rotation about the magnetic field axis. In principle, perfect confinement can be obtained in an ideal trap with cylindrical symmetry due to conservation of (canonical) angular momentum.[11] In practice, background neutral molecules[12–14] and static field asymmetries[12,15–18] exert an ambient drag on the rotating plasma, causing slow expansion and eventual particle loss. Radiation pressure from laser beams has been used to balance the angular momentum loss and to vary the plasma rotation frequency.[19,20] However, this method is limited to the few ion species whose atomic transitions are accessible by a laser, and is not precise due to laser power, frequency, and pointing fluctuations. Recently, azimuthally asymmetric ("rotating wall") electric fields rotating in the same sense as the plasma have been used to exert a torque on $Mg^+$ plasmas with temperatures ranging from 1 K to $5\times10^4$ K (4 eV), resulting in steady-state confinement and density compression.[21–23] For these uncorrelated plasmas, the stabilized rotation frequency is somewhat less than that of the rotating field, with a slip frequency which increases with the plasma temperature.[22]

In this paper we show that rotating wall electric fields applied to a Penning trap with quadratic potentials can control the rotation of laser-cooled, crystallized $^9Be^+$ plasmas without slip, thus extending the applicability of this technique from uncorrelated plasmas to strongly coupled systems.[24] Precise control of the plasma rotation is important for some applications. As an example, the second-order Doppler (time dilation) shift due to rotational velocity in a Penning trap atomic clock can be minimized by stabilizing the rotation at a particular frequency.[7] Both axially independent dipole and quadrupole fields in the plane perpendicular to the magnetic field have been used to provide this precise control of the plasma rotation. However, experimental evidence suggests that the effectiveness of the dipole field requires the presence of more than one ion species or other nonideal effects.

The rotating field control, which relies on ion-ion interactions, is fundamentally different from the sideband cooling or "axialization" techniques, where rf fields convert single-

*Paper gTua12-2 Bull. Am. Phys. Soc. **42**, 1876 (1997).
†Invited speaker.

particle magnetron motion into damped axial or cyclotron motions.[25–27] The steady-state sideband-cooled radius of the magnetron motion depends on the strength of the rf field and the damping rate of the motion to which the magnetron motion is being coupled. In general, the rotation control will be of limited precision and may be effective only for low rotation frequencies where the space-charge field is weak.[28] In contrast, the rotating fields interact with ions near the plasma surface, creating a small-amplitude traveling wave. The torque due to this wave is then transferred to the plasma interior through "viscosity" or strong ion-ion Coulomb coupling, which acts to bring the plasma to the same rotation frequency as the applied field.[29]

In the present experiment, side-view images show that the plasma shape, which is determined by the rotation frequency, can be varied by slowly changing the rotating field frequency for both weakly and strongly coupled plasmas. When the plasma is sufficiently cold and crystalline lattices are formed, Bragg diffraction provides a more accurate measurement of the rotation frequency. It is observed that the lattice and its orientation can be stable for longer than 30 min ($\sim 10^8$ rotations), and its rotation can be phase locked to the rotating field during this time. In essence, these corotating plasmas have reached a novel global thermal equilibrium,[29] where the rotation frequency (and hence the density) is set precisely by the external drive. For the rotating quadrupole field we have measured the triaxial ellipsoidal surface of this equilibrium state for oblate (pancake-like) plasmas, and found quantitative agreement with the analytical theory. For the rotating dipole field applied to plasmas with contaminant ions we have observed the expected asymmetric distribution of the $^9Be^+$ ions in close agreement with Monte Carlo simulations. Control of the global rotation has been achieved for nearly all allowed rotation frequencies with the use of the rotating dipole field.

## II. EXPERIMENTAL SETUP

Figure 1 shows the apparatus with its optical diagnostics and schematics of the rotating dipole and quadrupole fields. The trap consists of a 127 mm long stack of cylindrical electrodes at room temperature with an inner diameter of 40.6 mm, enclosed in a $10^{-8}$ Pa vacuum chamber. The uniform magnetic field $B_0 = 4.46$ T is aligned parallel to the trap axis within 0.01°, giving a $^9Be^+$ (charge $e$ and mass $m$) cyclotron frequency $\Omega = eB_0/m = 2\pi \times 7.61$ MHz. An axisymmetric trapping potential $(m\omega_z^2/2e)[z^2 - (x^2+y^2)/2]$ is generated near the trap center by biasing the central electrodes to a negative voltage $-V_0$. At $V_0 = 1$ kV, the single-particle axial frequency $\omega_z$ is $2\pi \times 799$ kHz and the magnetron frequency $\omega_m = (\Omega - \sqrt{\Omega^2 - 2\omega_z^2})/2$ is $2\pi \times 42.2$ kHz. The $z$-independent rotating fields are generated by applying properly phased sinusoidal voltages of amplitude $V_w$ to the six-fold azimuthal sectors of the two compensation electrodes, which are positioned symmetrically in the axial direction with respect to the trap center.

We create $^9Be^+$ plasmas by ionizing neutral $^9Be$ atoms in a separate trap (not shown) and then transferring the ions to the main trap for experimentation.[20] This procedure can be

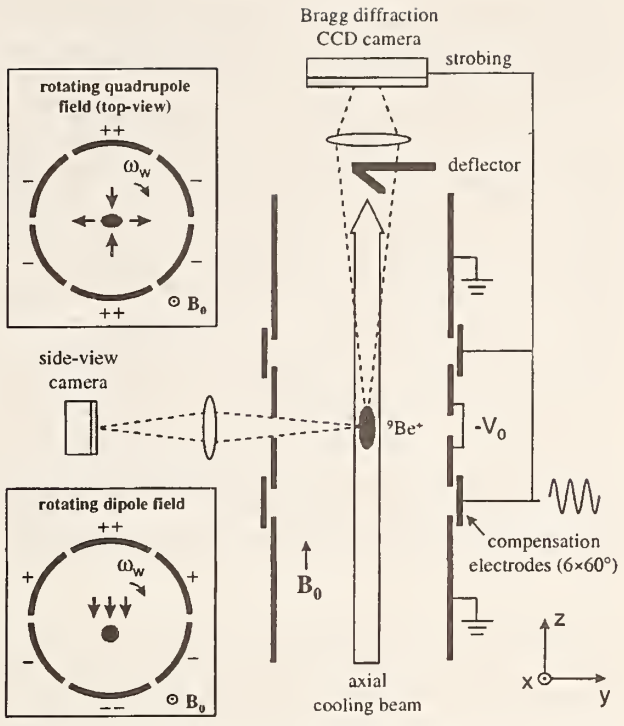


FIG. 1. Schematic side-view of the cylindrical trap with real-space imaging optics and Bragg diffraction detection system. Cross sections of the rotating dipole and quadrupole field (in the $x$-$y$ plane) are shown separately in the two insets.

repeated several times to accumulate up to $10^6$ ions. We expect that essentially all the ions in the trap are singly charged since the formation of doubly charged ions is energetically forbidden. While the total charge in the trap is conserved after loading, the relative abundance of contaminant ions increases from $<5\%$ for a new cloud on a time scale of 20 h, presumably due to reactions between $^9Be^+$ ions and background neutral molecules. By exciting ion cyclotron resonances, we determine that the two main contaminant ion species have mass 10 u and 26 u, where u is the atomic mass unit. These two species are likely to be $BeH^+$ and $BeOH^+$, respectively. Unless noted, data presented in this paper are obtained on relatively clean clouds with $<10\%$ contaminant ions.

The trapped $^9Be^+$ ions are Doppler-cooled by two laser beams tuned slightly below the $2s\ ^2S_{1/2}(M_I = 3/2, M_J = 1/2) \rightarrow 2p\ ^2P_{3/2}(3/2,3/2)$ resonant transition frequency (wavelength $\lambda \approx 313.11$ nm).[19] These laser beams also optically pump most of the ions into the $2s\ ^2S_{1/2}(3/2,1/2)$ state. From previous experiments,[19,20] we estimate that temperatures $T \lesssim 10$ mK can be obtained. Here $k_B T$ refers to the average ion thermal energy in a frame rotating with the plasma, which is typically much smaller than the average kinetic energy in the global rotation ($\sim 10^2$ K). The axial cooling beam (waist diameter $\approx 0.5$ mm, power $\approx 50$ $\mu$W), directed parallel to $\mathbf{B_0}$ as shown in Fig. 1, cools the ion thermal motion while not affecting the global rotation. A second laser beam (not shown in Fig. 1) with a much smaller waist diameter ($\approx 0.07$ mm) is directed perpendicular to $\mathbf{B_0}$ and is used

to compress the plasma and vary the rotation frequency. This beam is turned off during the Bragg scattering measurements.

When the cloud reaches thermal equilibrium at these cryogenic temperatures, the plasma Debye length becomes much smaller than its diameter $2r_0$ and axial length $2z_0$. The influence of image charges is negligible here due to the small dimensions of the plasma compared to the trap radius ($<10\%$). Consequently, the plasma forms a uniform density spheroid, bounded by $z^2/z_0^2+(x^2+y^2)/r_0^2=1$, with a rigid-body rotation frequency $\omega_r$ in the range $\omega_m<\omega_r<(\Omega-\omega_m)$.[20] The particle density $n_0$ is determined from $\omega_r$ according to $\omega_p^2\equiv e^2n_0/\epsilon_0 m=2\omega_r(\Omega-\omega_r)$, where $\omega_p$ is the plasma frequency.[20] The maximum density (Brillouin limit) $n_B\equiv\epsilon_0 B_0^2/2m=5.9\times10^9$ cm$^{-3}$ occurs at $\omega_r=\Omega/2$, the condition for Brillouin flow. In the frame rotating with the plasma, $(x_r,y_r,z)$, the $ev\times B$ Lorentz force gives rise to a radially confining pseudo-potential, and the effective vacuum trapping potential becomes

$$\Phi_r=\frac{m\omega_z^2}{2e}[z^2+\beta(x_r^2+y_r^2)]\,, \tag{1}$$

where $\beta$ is the radial trapping strength defined as

$$\beta\equiv\frac{1}{2}\left(\frac{\omega_p^2}{\omega_z^2}-1\right)=\frac{\omega_r(\Omega-\omega_r)}{\omega_z^2}-\frac{1}{2}>0\,. \tag{2}$$

The parameter $\beta$ determines the aspect ratio $\alpha\equiv z_0/r_0$ of the spheroid.[20,29] We use an f/5 imaging system to detect resonantly scattered photons from the cooling beams and produce a side-view image of the $^9Be^+$ ions. From this side-view image, we measure $\alpha$ and obtain $\omega_r$ and $n_0$.

For the typical conditions of $T\lesssim10$ mK and $n_0\gtrsim4\times10^8$ cm$^{-3}$, we obtain a Coulomb coupling parameter

$$\Gamma\equiv\left(\frac{e^2}{4\pi\epsilon_0\ a_{WS}}\right)\ \frac{1}{k_BT}>200\,, \tag{3}$$

where the Wigner–Seitz radius $a_{WS}$ is defined by $4\pi a_{WS}^3/3\equiv n_0^{-1}$. This strong ion-ion coupling results in the formation of crystalline lattices, which are body-centered cubic (bcc) in nearly spherical plasmas ($\alpha\approx1$) with ion number $N\gtrsim2\times10^5$.[4,5] As shown in Fig. 1, Bragg-scattered light from the axial cooling beam is detected with a charge-coupled device (CCD) camera near the forward-scattering direction since the wavelength is much smaller than the lattice spacing ($\lambda\ll a_{WS}$).[4] After passing through the trap, the axial cooling beam is deflected away from the lenses collecting the Bragg-scattered light.

## III. RESULTS AND ANALYSES

### A. General results for both rotating fields

When the rotating fields are first applied, their rotation frequency $\omega_w$ is set close to $\omega_r$ so that they interact strongly with the plasma. By measuring the photon scattering rate from the cooling beams for a fixed laser frequency, which is a function of the ion temperature, we have established that the ion temperature does not change significantly with the application of the rotating fields. Since the rotating fields typically cause less than 1% shape distortion to the plasma (see later discussions), the plasma rotation frequency $\omega_r$ can still be inferred from the aspect ratio $\alpha$ within the 5% uncertainty of this method. Furthermore, because $\Phi_r$ depends weakly on the ion mass for $\omega_r\ll\Omega/2$ as shown in Eq. (2), a multispecies plasma essentially has the same charge distribution as a pure $^9Be^+$ plasma except for the effect of centrifugal separation, in which the heavier ions tend to occupy positions at larger radii.[30] With a sufficiently large rotating field amplitude $V_w$, we are able to vary the plasma aspect ratio (and hence $\omega_r$) by slowly changing $\omega_w$. Figure 2 shows $\omega_r$ as determined from the side-view images versus $\omega_w$ with both the rotating dipole and quadrupole fields and for several plasmas with particle number $N<7\times10^4$ and $\omega_r\ll\Omega/2$. The plasma rotation frequency $\omega_r$ tracks $\omega_w$ closely within the experimental accuracy, demonstrating external control of the plasma rotation by the rotating fields. The data of Fig. 2 were obtained at low temperatures ($T\lesssim10$ mK) with the axial cooling laser on continuously. However, we are also able to control the plasma rotation with the laser tuned far below the atomic transition frequency or blocked for short periods of time ($\sim1$ min). Under these conditions, we expect significantly higher plasma temperatures (up to $T\sim10$ K) so that the plasma is only weakly correlated ($\Gamma\sim0.2$).

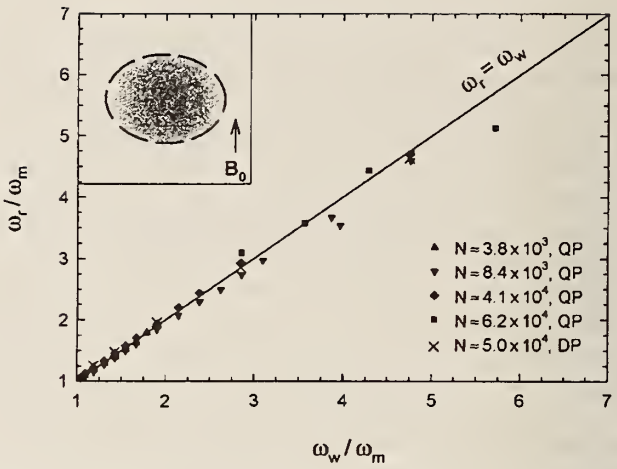


FIG. 2. The plasma rotation frequency $\omega_r$ versus the rotation frequency $\omega_w$ of the rotating fields. The frequency $\omega_r$ is determined from the aspect ratio $\alpha$ of several plasmas with $200\leq V_0\leq1000$ V. Solid symbols are with the quadrupole field and ×'s are with the dipole field. The inset shows a typical side-view image and its boundary fit to an ellipse (dashed line), giving $\alpha$ and $\omega_r$.

For a more accurate determination of $\omega_r$, we use the time dependence of the laser light Bragg-scattered from the rotating crystals.[4,5] A gateable image intensifier, installed in front of the CCD camera, allows the diffraction pattern to be recorded stroboscopically. Figure 3(a) shows a time-averaged diffraction pattern of concentric rings from an approximately spherical plasma with $N\approx7.5\times10^5$. Even if this pattern is from a single crystal, rings are observed because of the plasma rotation about the axial laser beam.[4] With the rotating field applied and controlling the plasma rotation, we trigger the intensifier synchronously with the rotating field opening the camera for 50 ns each $2\pi/\omega_w$ period. This en-

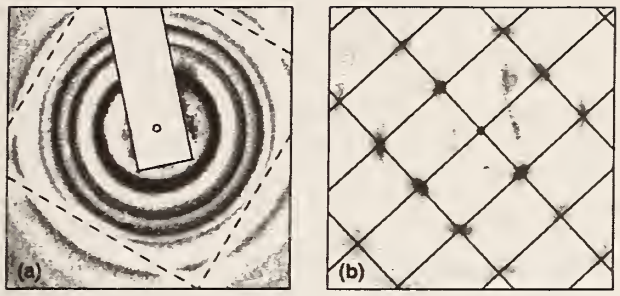


FIG. 3. Bragg diffraction patterns from a plasma phase locked to a rotating quadrupole field ($\omega_r=\omega_w=2\pi\times 140$ kHz, $n_0\approx 4.26\times 10^8$ cm$^{-3}$, $\alpha\approx 1.1$). (a) 1 s time-averaged pattern. The long rectangular shadow is from the deflector for the incident beam; four line shadows that form a square are due to a wire mesh at the exit window of the vacuum chamber. (b) Time-resolved pattern obtained by strobing the camera with the rotating field (integration time $\approx 5$ s). A spot is predicted at each intersection of the rectangular grid lines for a bcc with a {110} plane perpendicular to the axial laser beam. The grid spacings are determined from $n_0$ and are not fitted.

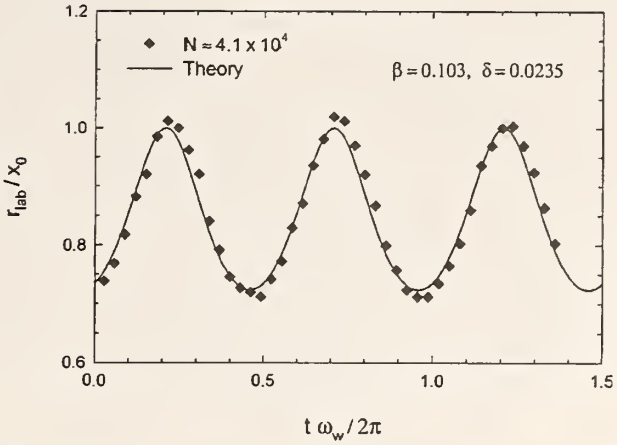


FIG. 4. Oscillation of the plasma radius $r_{\rm lab}$ of the side-view image with the rotating quadrupole field. The theory curve is calculated using the calibrated $f_g$ from Fig. 5(a). The relative phase between the theory and data is not adjusted.

ables the camera to record the diffraction pattern in the rest frame of the rotating field. Figure 3(b) shows such a time-resolved pattern taken nearly simultaneously with Fig. 3(a) and accumulated over $\sim 10^6$ plasma rotations. The well-defined rectangular dot pattern demonstrates that the crystal is phase locked to the rotating field. In this work, we could determine phase-locked rotation when $\mathbf{B_0}$ is aligned within 0.01° of the trap axis and for $\omega_r \lesssim \Omega/20$. This alignment is obtained by minimizing the amplitude of zero-frequency modes of the plasma.[2] Furthermore, the structure and spacings of the crystalline lattice and its orientation with respect to the laser beam can last longer than 30 min under this rotation control. For comparison, a particular Bragg scattering pattern typically changes after $\sim 1$ min without the rotating field control, perhaps due to effects from the plasma spin-down. With a weak rotating field amplitude or when the trap axis is tilted a few hundredth of a degree with respect to $\mathbf{B_0}$, we cannot obtain phase locking but are able to stabilize the plasma rotation frequency close to the rotating field frequency with $\lesssim 1\%$ slippage.

### B. Quadrupole field control

With the rotating quadrupole field, which has a potential $\propto(y^2-x^2)\cos(2\omega_w t)+2xy\sin(2\omega_w t)$, the equilibrium plasma surface is actually a spinning triaxial ellipsoid with three principal axes differing in length.[29] Since the plasma is phase locked with $\omega_r=\omega_w$, the combined vacuum trapping potential in the rotating frame becomes

$$\Phi_r'=\frac{m\omega_z^2}{2e}[z^2+(\beta-\delta)x_r^2+(\beta+\delta)y_r^2]\,, \tag{4}$$

where $\delta=f_g\,V_w/V_0\geqslant 0$ is the relative strength of the quadrupole field and $f_g$ depends only on the trap geometry. Here electric fields from the ambient drag and image charges are neglected. The thermal equilibrium state in the frame rotating with the plasma is bounded by $z^2/z_0^2+x_r^2/x_0^2+y_r^2/y_0^2=1$ with $x_0\geqslant y_0$. The parallel and perpendicular aspect ratios ($\alpha_\parallel\equiv z_0/y_0, \alpha_\perp\equiv x_0/y_0$) are determined by parameters $\beta$ and $\delta$.[29] This shape produces a space-charge potential which cancels $\Phi_r'$ within the equilibrated plasma. In this equilibrium, each individual ion still undergoes a purely rotational average motion as in the ordinary thermal equilibrium state without the rotating field.

To obtain an $\alpha_\perp$ significantly above one, we maximize the ratio $\delta/\beta$ by reducing $V_0$ to less than 200 V and setting $\omega_w$ close to the magnetron frequency $\omega_m$. At these low rotation frequencies and with only the perpendicular cooling beam, the contaminant ions are well mixed with the $^9Be^+$ ions, making the boundary of the fluorescing $^9Be^+$ ions coincide with that of the plasma. Side-view images of the plasma are then recorded stroboscopically at different phases of the rotating field. The radius $r_{\rm lab}$ of the side-view image is expected to oscillate at $2\omega_w$, with an amplitude proportional to $x_0-y_0$. Figure 4 shows a measurement of $r_{\rm lab}$ on a plasma with $\alpha_\parallel\approx 0.15$ and $\alpha_\perp\approx 1.4$, rotating at 2.5 kHz ($V_0=50$ V, $V_w\approx 185$ V). Excellent agreement between the theory and data is exhibited, showing that the plasma is indeed equilibrated with the rotating quadrupole field.

We have measured the dependence of $\alpha_\perp$ on parameters $\delta$ and $\beta$. Figure 5(a) shows $\alpha_\perp$ versus $\delta$ at fixed $\beta=0.103$. Good agreement with the theory is obtained by fitting these data for $f_g$ with the result $f_g\approx 6.38\times 10^{-3}$. Figure 5(b) shows $\alpha_\perp$ versus $\beta$ for fixed $\delta\approx 0.0159$ using the calibrated $f_g$ value. Excellent agreement is again observed, showing the rapid decrease to unity for $\alpha_\perp$ as $\beta$ is increased. Under typical conditions ($V_0\geqslant 500$ V, $V_w\leqslant 50$ V, and $\omega_w\geqslant 1.1\,\omega_m$, giving $\delta<7\times 10^{-4}$ and $\beta>0.1$), $\alpha_\perp-1$ is less than 1%. This small distortion, however, generates sufficient torque to phase lock the plasma rotation when the trap is nearly aligned with the magnetic field.

### C. Dipole field control

We have examined rotation control using the dipole field with a potential $\propto y\sin(\omega_w t)-x\cos(\omega_w t)$. Theoretically, this field is not expected to provide rotation control for a single-species plasma in a quadratic trap. Instead, it drives only a "center-of-mass" orbital motion about the trap axis without

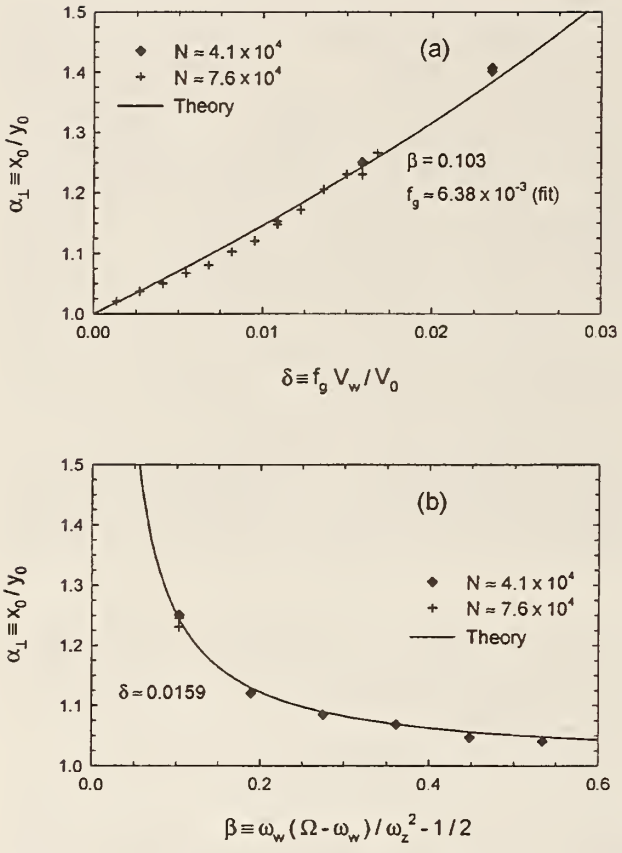


FIG. 5. Dependence of perpendicular aspect ratio $\alpha_\perp$ versus (a) rotating field strength $\delta$ and (b) radial trapping strength $\beta$. Two plasmas are used with $50 \leqslant V_0 \leqslant 100$ V and $15 \leqslant V_w \leqslant 185$ V. The geometric factor $f_g$ is calibrated in (a).

surface distortions and is decoupled from the internal plasma rotation. Experimentally, however, rotation control including phase locking similar to that from the quadrupole field is obtained with the rotating dipole field as discussed in the previous sections. While the asymmetric field from image charges induced by the center-of-mass motion could provide the observed coupling to the plasma rotation, this field is too weak to be effective for our typical trap parameters.

Experimental evidence suggests that the coupling between the center-of-mass motion and plasma rotation is provided by the contaminant ions. By measuring the plasma dynamic response under sudden changes of the dipole field frequency[22] we have observed that the torque from the dipole field increases with time, presumably due to the growing percentage of the contaminant ions. Figure 6 shows the evolution of plasma rotation frequency as $\omega_w/2\pi$ is suddenly changed by $\pm 5$ kHz from 60 kHz (magnetron frequency $\omega_m = 2\pi \times 42.2$ kHz) at $\Delta t = 0$. The initial and final rotation frequencies of the plasma are equal to that of the dipole field as determined from time-resolved Bragg scattering measurements. The intermediate data points are derived from the aspect ratio of the side-view images assuming that the plasma goes through successive thermal equilibrium states during the evolution. The torque from the rotating dipole field has clearly increased from the 1-h-old plasma with ap-

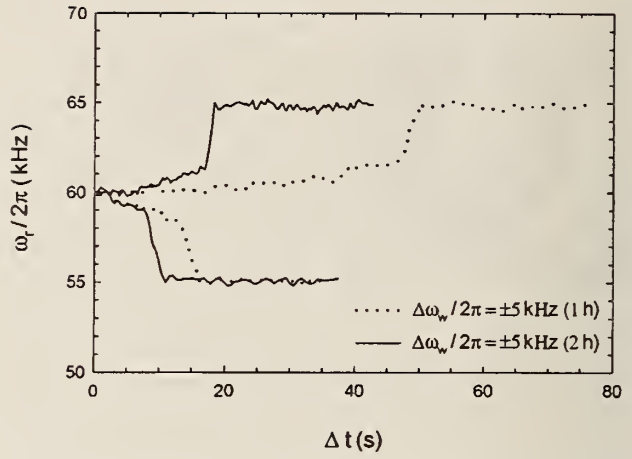


FIG. 6. Time evolution of the plasma rotation frequency under sudden changes of the dipole field frequency. Measurements on the same plasma 1 and 2 h after loading are plotted.

proximately 5% contaminant ions to the 2-h-old plasma with twice as many contaminant ions.

The effect of the contaminant ions on the plasma can be understood in terms of their azimuthally asymmetric distribution with the rotating dipole field. For typical rotation frequencies and laser cooling conditions, these heavier contaminant ions separate radially from the $^9Be^+$ ions and form a nonfluorescent outer cylindrical layer without the rotating field.[30,31] As the plasma undergoes a driven center-of-mass circular motion with the rotating dipole field, the heavier contaminant ions distribute preferentially farther from the trap center than the $^9Be^+$ ions. In order for the contaminant ions to be distributed away from the trap center and to have rigid-body rotation, the plasma rotation frequency must match the rotation frequency of the dipole field (see discussions below). This produces a coupling between the driven center-of-mass motion and the plasma rotation, enabling the rotating dipole field control. When the plasma reaches ther-

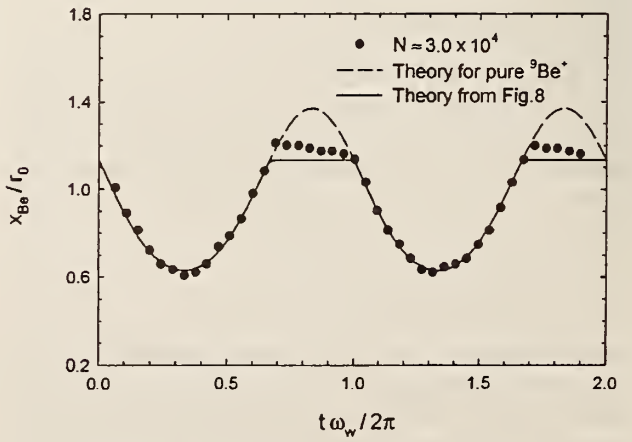


FIG. 7. Oscillation of the positive radial boundary $x_{Be}$ with the rotating dipole field. The dashed curve is calculated for a pure $^9Be^+$ plasma and the solid curve is obtained from the simulation shown in Fig. 8. The dipole field amplitude at the plasma is derived by fitting the data, while the relative phase between the theories and data is not adjusted.

mal equilibrium with the rotating dipole field at $\omega_r = \omega_w$, the average ion motion is simply a rigid-body rotation about the *trap* axis at $\omega_w$.

Figure 7 shows the position $x_{Be}$ of the positive radial boundary (at $z=0$) from the side-view images of a plasma containing about 12% contaminant ions and phased locked with a dipole field rotating at 9 kHz (magnetron frequency is $2\pi \times 8.4$ kHz). This measurement is obtained with the same stroboscopic technique that was used for the quadrupole field results. For these conditions, however, the contaminant ions are well separated from the $^9Be^+$ ions due to the higher rotation frequency. For a pure $^9Be^+$ plasma, a periodic oscillation of $x_{Be}$ at $\omega_w$ is expected due to the center-of-mass motion, as shown in Fig. 7. The data generally follow this prediction except for the "clipping" of $x_{Be}$ at certain phases of the rotating dipole field.

A Monte Carlo simulation on the equilibrium distribution of a two-species plasma (in the rest frame of the dipole field) is shown in Fig. 8. The plasma is made of 1000 particles with 88% $^9Be^+$ (dots) and 12% contaminant ions having mass 26 u (open circles), and is driven by a rotating dipole field resulting in the same relative displacement as in Fig. 7. The plasma has a very oblate shape which enhances its center-of-mass displacement as shown in the side-view of Fig. 8(b). In the $x$-$y$ distribution shown in Fig. 8(a), the overall charge is distributed nearly symmetrically with respect to the shifted plasma axis, while the $^9Be^+$ ions and the contaminant ions are positioned asymmetrically inside the plasma. The boundary of the $^9Be^+$ ions is approximately made of two arcs: one, bordering the vacuum, is centered on the plasma axis (the $\oplus$ symbol), and the other, bordering the contaminant ions, is centered on the trap axis (the cross). This shape explains the observed clipping of $x_{Be}$ in Fig. 7. The small discrepancy between the data and the solid curve in Fig. 7 is likely due to an overestimation of the percentage of the contaminant ions from the side-view images without the rotating field.

When contaminant ions are present, it is advantageous to use the dipole rather than quadrupole field to control the plasma rotation because greater electric field strength at the plasma surface can be obtained for the same amplitude $V_w$ on the compensation electrodes. This is because the plasma dimensions are typically much smaller than the trap radius and the dipole field decays much more gradually from the compensation electrodes than the quadrupole field. Rotation control in the range $\omega_m < \omega_r < (\Omega - \omega_m)$, which includes rotational equilibrium near Brillouin flow ($\omega_r = \Omega/2$), has been achieved using the rotating dipole field. For $\omega_r \sim \Omega/2$, crystalline lattices are generally not observed, and the aspect ratio $\alpha$ depends only weakly on the rotation frequency. However, we can infer $\omega_r$ by measuring the angle of the first Bragg scattering ring, $\theta_{scatt}$, from ions in the shell structures. This angle is related to the Wigner–Seitz radius $a_{WS}$ through

$$\theta_{scatt}\, a_{WS} \approx 4.4 \left( \frac{\lambda}{2\pi} \right), \tag{5}$$

where $\theta_{scatt}$ is in radian (see Ref. 4). The Wigner–Seitz radius in turn is determined by the plasma rotation frequency.

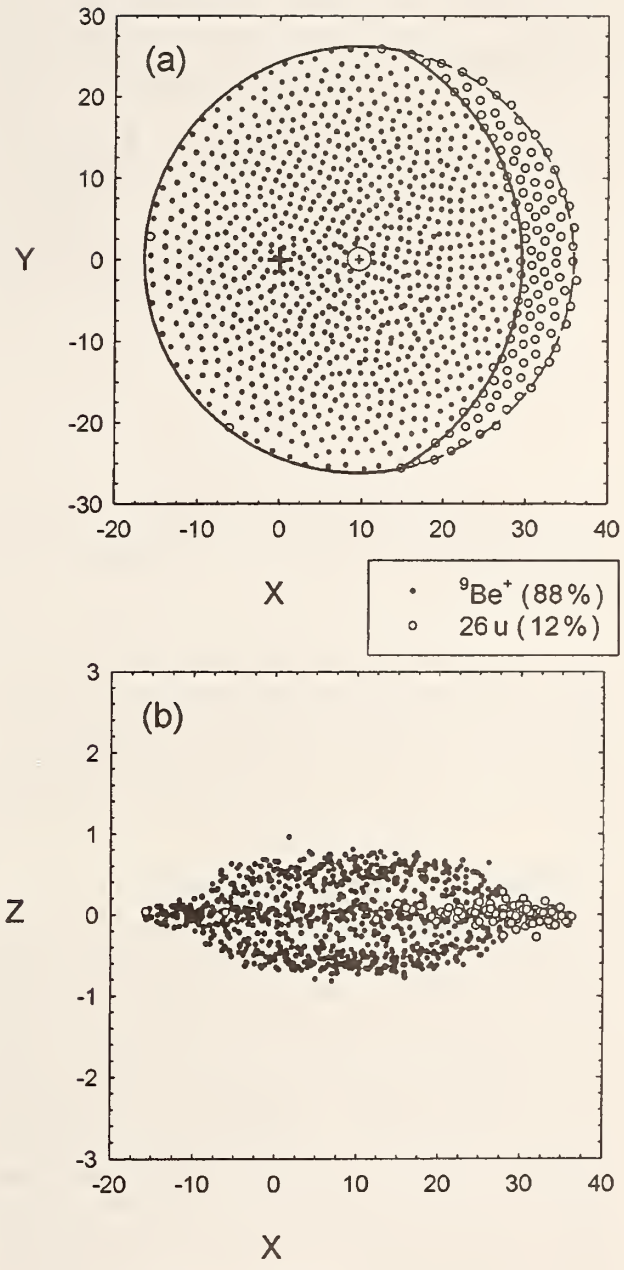


FIG. 8. A Monte Carlo simulation of the thermal equilibrium distribution of a two-species plasma with the rotating dipole field. The plasma is made of 1000 particles with 88% $^9Be^+$ and 12% contaminant ions having mass 26 u, and has a coupling parameter $\Gamma = 40$. The trapping parameters are the same as in Fig. 7. (a) The $x$-$y$ distribution. Solid and dashed lines denote boundaries of the $^9Be^+$ ions and the plasma, respectively. (b) The $x$-$z$ distribution with ten times smaller $z$ scale.

Figure 9 shows the scattering angle $\theta_{scatt}$ as a function of the rotation frequency of the dipole field for two plasmas with different compositions of contaminant ions. With only heavier contaminant ions (dots), we can control the plasma rotation frequency up to about 0.9 $\Omega$ (dotted vertical line) corresponding to the frequency at which ions having mass 10 u can no longer remain in the plasma. If we intentionally create some lighter ions ($\times$'s), we are able to control $\omega_r$

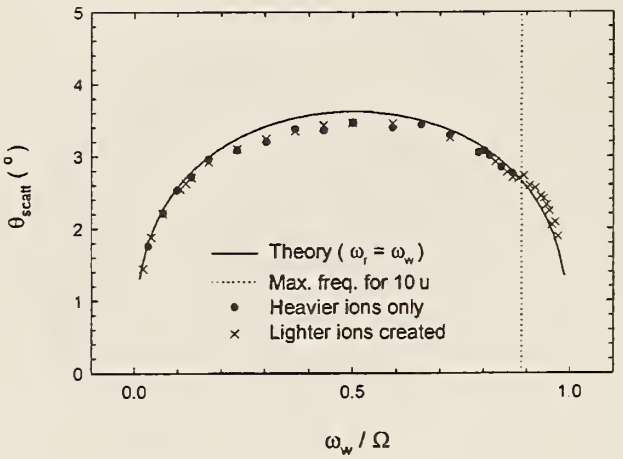


FIG. 9. The angle of the first Bragg scattering ring from shells versus the rotation frequency of the dipole field. Data from a plasma with only heavier contaminant ions are shown as dots. ×'s are data from a plasma with some lighter ions than $^9Be^+$.

through all allowed rotation frequencies. This observation provides further evidence that the contaminant ions are the main coupling mechanism for the rotating dipole field. We cannot, however, exclude the possibility that different non-ideal effects can cause sufficient coupling in other experiments.

## IV. CONCLUSIONS AND DISCUSSION

We have shown experimentally that azimuthally asymmetric electric fields rotating in the same sense as the plasma can exert a torque that balances the ambient drag in both weakly and strongly coupled regimes, resulting in infinite confinement times. The torque from the rotating wall fields acts to bring the plasma to the same rotation frequency as the applied field. For strongly coupled plasmas with laser cooling, we obtain phase-locked rotation with the rotating field even though there is a finite ambient drag on the plasma. This phase-locked rotation is possible presumably because crystallized plasmas are capable of sustaining some stress without structure breakup. As a result of this observation, we are now able to precisely control plasma properties such as density and boundary shape.

There are other methods to inject angular momentum into the plasma and vary the rotation frequency. For example, by exciting an azimuthally asymmetric mode that travels in the same direction but faster than the plasma rotation, $\omega_r$ can be increased very effectively due to the global coherent resonance.[16,32] The challenge of this approach is to remain on resonance with the mode as the plasma rotation frequency is increased. It may also be difficult to balance the heating from the mode excitation. In addition, this method will probably not result in rotation control as precise as the rotating field technique.

Substantial questions remain concerning the theoretical models which give quantitative predictions for the torque from the rotating fields.[33,34] In the strongly coupled regime, such models that describe the experiment are lacking. For uncorrelated plasmas at higher temperatures, two-dimensional rotating fields may not be able to generate enough torque to balance the ambient drag, and electric fields with nonzero $z$ components may be required.[22] Rotating field control of pure electron plasmas also needs further refinement to improve its capability.[23]

In the future, direct imaging of individual ions in a crystallized plasma may be possible because of the phase-locked rotation. In addition, the increased crystal stability improves the prospect of observing the solid–liquid phase transition of strongly coupled plasmas. Dynamics of the Brillouin flow is also an interesting area for investigation. Finally, it may be possible to influence the formation of crystalline lattices with the rotating fields and other perturbations, enabling external control of the crystal orientation.

## ACKNOWLEDGMENTS

We thank D. Wineland, T. O'Neil, and C. F. Driscoll for discussions, and B. Jelenković, R. Rafac, M. Young, M. Lombardi, and D. Sullivan for useful comments on the manuscript.

This work is supported by the Office of Naval Research.

[1] J. H. Malmberg, C. F. Driscoll, B. Beck, D. L. Eggleston, J. Fajans, K. Fine, X.-P. Huang, and A. W. Hyatt, in *Non-neutral Plasma Physics*, edited by C. W. Roberson and C. F. Driscoll (American Institute of Physics, New York, 1988), p. 28.
[2] J. J. Bollinger, D. J. Wineland, and D. H. E. Dubin, Phys. Plasmas **1**, 1403 (1994).
[3] For recent results, see *Non-neutral Plasma Physics II*, edited by J. Fajans and D. H. E. Dubin (American Institute of Physics, New York, 1995).
[4] J. N. Tan, J. J. Bollinger, B. Jelenkovic, and D. J. Wineland, Phys. Rev. Lett. **75**, 4198 (1995); J. N. Tan, J. J. Bollinger, B. Jelenkovic, W. M. Itano, and D. J. Wineland, in *Physics of Strongly Coupled Plasmas*, edited by W. D. Kraeft and M. Schlanges (World Scientific, Singapore, 1996), p. 387.
[5] W. M. Itano, J. J. Bollinger, J. N. Tan, B. Jelenkovic, X.-P. Huang, and D. J. Wineland, Science **279**, 686 (1998).
[6] R. Blatt, P. Gill, and R. C. Thompson, J. Mod. Opt. **39**, 193 (1992); R. C. Thompson, Adv. At. Mol. Phys. **31**, 63 (1993).
[7] J. N. Tan, J. J. Bollinger, and D. J. Wineland, IEEE Trans Instrum. Meas. **44**, 144 (1995).
[8] G. Gabrielse, X. Fei, L. A. Orozco, R. L. Tjoelker, J. Hass, H. Kalinowsky, T. A. Trainer, and W. Kells, Phys. Rev. Lett. **65**, 1317 (1990).
[9] R. G. Greaves and C. M. Surko, Phys. Plasmas **4**, 1528 (1997).
[10] D. Schneider, D. A. Church, G. Weinberg, A. J. Steiger, B. Beck, J. McDonald, E. Magee, and D. Knapp, Rev. Sci. Instrum. **65**, 3472 (1994).
[11] T. M. O'Neil, Phys. Fluids **23**, 2216 (1980).
[12] J. S. DeGrassie and J. H. Malmberg, Phys. Fluids **23**, 63 (1980).
[13] D. A. Moore, R. C. Davidson, S. M. Kaye, and S. F. Paul, in *Non-neutral Plasma Physics II* (Ref. 3), p. 118.
[14] Torques from *rotating* neutral gas are considered in A. J. Peurrung and S. E. Barlow, Phys. Plasmas **3**, 2859 (1996).
[15] J. H. Malmberg and C. F. Driscoll, Phys. Rev. Lett. **44**, 654 (1980); C. F. Driscoll, K. S. Fine, and J. H. Malmberg, Phys. Fluids **29**, 2015 (1986).
[16] D. L. Eggleston, T. M. O'Neil, and J. H. Malmberg, Phys. Rev. Lett. **53**, 982 (1984).
[17] J. Notte and J. Fajans, Phys. Plasmas **1**, 1123 (1994).
[18] D. L. Eggleston, Phys. Plasmas **4**, 1196 (1997).
[19] J. J. Bollinger and D. J. Wineland, Phys. Rev. Lett. **53**, 348 (1984).
[20] L. R. Brewer, J. D. Prestage, J. J. Bollinger, W. M. Itano, D. J. Larson, and D. J. Wineland, Phys. Rev. A **38**, 859 (1988); D. J. Heinzen, J. J. Bollinger, F. L. Moore, W. M. Itano, and D. J. Wineland, Phys. Rev. Lett. **66**, 2080 (1991).
[21] Some preliminary results on $Mg^+$ plasmas are in F. Anderegg, X.-P. Huang, C. F. Driscoll, G. D. Severn, and E. Sarid, in *Non-neutral Plasma Physics II* (Ref. 3), p. 1.

[22]X.-P. Huang, F. Anderegg, E. M. Hollmann, C. F. Driscoll, and T. M. O'Neil, Phys. Rev. Lett. **78**, 875 (1997).
[23]A preliminary work on pure electron plasmas is in R. E. Pollock and F. Anderegg, in *Non-neutral Plasma Physics II* (Ref. 3), p. 139.
[24]X.-P. Huang, J. J. Bollinger, T. B. Mitchell, and W. M. Itano, Phys. Rev. Lett. **80**, 73 (1998).
[25]D. J. Wineland and H. G. Dehmelt, Int. J. Mass Spectrom. Ion Processes **16**, 338 (1974); **19**, 251(E) (1976).
[26]L. S. Brown and G. Gabrielse, Rev. Mod. Phys. **58**, 233 (1986).
[27]G. Savard, St. Becker, G. Bollen, H.-J. Kluge, R. B. Moore, Th. Otto, L. Schweikhard, H. Stolzenberg, and U. Wiess, Phys. Lett. A **158**, 247 (1991); S. Guan, X. Xiang, and A. G. Marshall, Int. J. Mass Spectrom. Ion Processes **124**, 53 (1993).
[28]C. S. Weimer, J. J. Bollinger, F. L. Moore, and D. J. Wineland, Phys. Rev. A **49**, 3842 (1994).
[29]D. H. E. Dubin and T. M. O'Neil, "Trapped non-neutral plasmas, liquids, and crystals (the thermal equilibrium states)," submitted to Rev. Mod. Phys.
[30]T. M. O'Neil, Phys. Fluids **24**, 1447 (1981).
[31]D. J. Larson, J. C. Bergquist, J. J. Bollinger, W. M. Itano, and D. J. Wineland, Phys. Rev. Lett. **57**, 70 (1986).
[32]T. B. Mitchell, Ph.D. thesis, University of California at San Diego, 1993, p. 58.
[33]S. M. Crooks and T. M. O'Neil, Phys. Plasmas **2**, 355 (1995); S. M. Crooks, Ph.D. thesis, University of California at San Diego, 1995, p. 56.
[34]R. Fitzpatrick and E. P. Yu, Phys. Plasmas **4**, 917 (1997).

# Direct Observations of Structural Phase Transitions in Planar Crystallized Ion Plasmas

T. B. Mitchell,* J. J. Bollinger, D. H. E. Dubin, X.-P. Huang, W. M. Itano, R. H. Baughman

Laser-cooled $^9Be^+$ ions confined in two-dimensionally extended lattice planes were directly observed, and the images were used to characterize the structural phases of the ions. Five different stable crystalline phases were observed, and the energetically favored structure could be sensitively tuned by changing the areal density of the confined ions. The experimental results are in good agreement with theoretical predictions for the planar (infinite in two dimensions) one-component plasma. Qualitatively similar structural phase transitions occur, or are predicted to occur, in other experimentally realizable planar systems.

The one-component plasma (OCP) has been a model of condensed matter in statistical physics for over 30 years, and it is used to describe such diverse systems as dense astrophysical matter (*1*) and electrons on the surface of liquid helium (*2*). Laser-cooled trapped ions (*3*) are an excellent experimental realization of the OCP. The phase structures of spatially homogeneous (infinite) (*4*) and cylindrical (infinite in one dimension only) (*5*) OCPs have been explored previously. Here, images of individual ions that were confined in two-dimensionally extended lattice planes are presented and used to characterize the structural phases; the observed structures agree well with the predictions of an analytic theory for the planar OCP.

The OCP model consists of a single charged species embedded in a uniform, neutralizing background charge. In Paul (*6*) or Penning (*6, 7*) traps, which are used to confine charged particles, a (fictitious) neutralizing background is provided by the confining potentials. The thermodynamic properties of the infinite classical OCP are determined by its Coulomb coupling parameter, $\Gamma \equiv [1/(4\pi\epsilon_0)][e^2/(a_{WS}k_BT)]$, which is the ratio of the Coulomb potential energy of neighboring ions to the kinetic energy per ion; $\epsilon_0$ is the permittivity of the vacuum, $e$ is the charge of an ion, $k_B$ is Boltzmann's constant, $T$ is the temperature, and $a_{WS}$ is the Wigner-Seitz radius [defined by $4\pi(a_{WS})^3/3 = 1/n_0$, where $n_0$ is the ion density]. The onset of short-range order for the infinite OCP is predicted (*8*) at $\Gamma \approx 2$, and a phase transition to a body-centered cubic (bcc) lattice is predicted (*8, 9*) at $\Gamma \approx 170$. With an OCP in a planar geometry (infinite in only two dimensions), boundary effects are predicted to cause the formation of a variety of additional structural phases, such as the hexagonal close-packed (hcp) and face-centered cubic (fcc) phases (*10, 11*). Qualitatively similar structural phase transitions occur, or are predicted to occur, in other planar systems with varied interparticle interactions, such as plasma dust crystals (*12*), colloidal suspensions (*13*), semiconductor electron bilayer systems (*14*), and hard spheres (*15*).

The crystallization of small numbers (total number $N < 50$) of laser-cooled ions into Coulomb clusters (*16*) was first observed in Paul traps (*17*). With larger numbers of trapped ions, concentric shells (*18*) were directly observed in Penning (*19*) and Paul traps (*5, 20*). Recently, Bragg diffraction has been used to detect bcc crystals (the predicted infinite volume ordering) in large and spherical ($N > 2 \times 10^5$; radius $r_0 > 60\ a_{WS}$) ion plasmas confined in a Penning trap (*4*).

Measurements were taken from direct images of the central ($r = 0$) structure of pancake-shaped (lenticular) ion plasmas (aspect ratio $\alpha \equiv z_0/r_0 < 0.1$, where $2z_0$ is the plasma center's axial extent). The central region has a disklike geometry with constant areal density $\sigma_0$ (charge density per unit area projected onto the $z = 0$ plane), which facilitates comparison with planar theory. We observed five different stable crystalline phases and found that the energetically favorable central structure can be tuned by changing $\sigma_0$. Both continuous and discontinuous structural phase transitions were observed.

The $^9Be^+$ ions were confined radially in a cylindrical Penning trap (inner trap diameter, 40.6 mm) (Fig. 1) with a uniform magnetic field $B = 4.465$ T in the $\hat{z}$-axis direction. The ions were confined axially by a potential difference of $V_0 = -1.50$ kV, which was applied between the center and end electrodes of the trap. Near the trap center, this axial potential is quadratic and has a value of $1/2(m/e)\omega_z^2 z^2$, where the axial frequency $\omega_z/2\pi = 978$ kHz for $^9Be^+$. The radial electric fields of the trap, as well as the ion space charge, cause the ion plasma to undergo an $\mathbf{E} \times \mathbf{B}$ drift and thus rotate about the trap axis. In thermal equilibrium, this rotation is at a uniform frequency $\omega_r$. The radial binding force of the trap is determined by the Lorentz force caused by the plasma's rotation through the magnetic field. Thus, low $\omega_r$ results in a weak radial binding and a lenticular plasma with a large radius. For $10^4$ trapped ions with $\omega_r/2\pi = 68.5$ kHz (typical for this work), the ion plasma has a density of $2.1 \times 10^8$ cm$^{-3}$ with $2r_0 \approx 1.3$ mm and an aspect ratio $\alpha \approx 0.05$. The rotation frequency was controlled by phase-locking the plasma rotation to an applied "rotating wall" electric field (*21*). At low $\omega_r$, an increase in $\omega_r$ increases both the plasma density and $z_0$, providing a way to sensitively adjust the central areal density of the plasma.

The ions were cooled (*3*) by a laster beam propagating along the $z$ axis and tuned 10 to 20 MHz lower in frequency than a hyperfine-Zeeman component of the $2s\ ^2S_{1/2} \rightarrow 2p\ ^2P_{3/2}$ resonance at 313 nm with a natural linewidth of 19 MHz. The laser power was ~50 μW and was focused at the ion plasma to a diameter of ~0.5 mm. The theoretical cooling limit is 0.5 mK, and an experimental upper bound of $T < 10$ mK has been measured (*22*). For a density of $n_0 = 2 \times 10^8$ cm$^{-3}$, these limits give a range of $160 < \Gamma < 3150$. A series of lenses formed side- and top-view images of the ions, with viewing directions that were perpendicular and parallel to the magnetic field, respectively, on either a gateable charge-coupled device (CCD) camera or on an imaging photomultiplier tube. The resolution of the optical system is ~4 μm, whereas typical interparticle spacings are ~20 μm.

The side-view image insert in Fig. 1, which shows the central region of a lenticular ion plasma with three axial lattice planes, is representative of the flatness and radial extent (<10% of $r_0$) of this region. At large radius, curvature of the planes can cause the side-view images of axial plane positions to blur. This effect was prevented in the measurements reported here by using clouds with sufficient amounts (up to 50%) of nonfluorescing impurity ions. Because these heavier-mass ions are centrifugally separated to larger radii than the $^9Be^+$, the regions of the plasma where curvature begins to be significant can be filled with these ions, which are sympathetically cooled by the $^9Be^+$ (*23*).

With good alignment of the trap with the magnetic field ($<10^{-3}$ rad), the ion plasma

T. B. Mitchell, J. J. Bollinger, X.-P. Huang, W. M. Itano, Time and Frequency Division, National Institute of Standards and Technology, Boulder, CO 80303, USA. D. H. E. Dubin, Department of Physics, University of California at San Diego, La Jolla, CA 92093, USA. R. H. Baughman, Research and Technology, Allied Signal, Morristown, NJ 07962, USA.

*To whom correspondence should be addressed. E-mail: travis.mitchell@nist.gov

rotation is phase-locked with the rotating wall perturbation (*21*). A direct observation of the rotating ion structures was achieved for the first time by gating the top-view CCD camera synchronously with the rotating wall perturbation for brief gate times (<2%) of the plasma rotation period). Total exposure times of ~3 × $10^4$ rotation periods were used for typical images (Fig. 2). For our study of the ion lattice structure, we limited our analysis to the central region, where strong localization and regular ordering of the ions were observed. At larger radius, we observed an increased blurring (due to the plasma rotation), occasional lattice distortions, and, ultimately, the transition to the regions filled by heavier mass ions.

The observed structure of the central crystallized region depends on the central areal density $\sigma_0$ of the plasma. Within a layer, the lattice is characterized by the primitive vectors $\mathbf{a}_1$ and $\mathbf{a}_2$ (which were observed to be equal in magnitude, $|\mathbf{a}_1| = |\mathbf{a}_2| \equiv a$) or, equivalently, by $a$ and the angle $\theta$ ($\leq 90°$) between the primitive vectors. The interlayer structure is characterized by the axial positions $z_n$ of the $n$ lattice planes (measured by the side-view camera) and the interlayer displacement vector $\mathbf{c}_n$ between layers 1 and $n$. Hence, the equilibrium $(x, y)$ positions of ions in axial planes 1 and $n$ are given by $\mathbf{R}_1(i, j) = i\mathbf{a}_1 + j\mathbf{a}_2$ and $\mathbf{R}_n(i, j) = i\mathbf{a}_1 + j\mathbf{a}_2 + \mathbf{c}_n$, where $i$ and $j$ are integers.

Three different types of intralayer ordering were observed: hexagonal ($\theta = 60°$), square ($\theta = 90°$), and rhombic ($90° > \theta \geq 65°$). The square and rhombic layers stack in a staggered fashion, with the upper ions immediately above the centers of the parallelograms below, resulting in an interlayer displacement vector $\mathbf{c}_2 = (\mathbf{a}_1 + \mathbf{a}_2)/2$. Hexagonal layers also stack with ions above the centers of the triangles below, but this stacking can occur in two distinct ways: $3\mathbf{c}_2 = \mathbf{a}_1 + \mathbf{a}_2$ and $3\mathbf{c}_2/2 = \mathbf{a}_1 + \mathbf{a}_2$. With hcp-like stacking, the ions in every other plane lie directly above each other (*abab* . . .), whereas with fcc-like stacking, the ions in every third plane are so aligned (*abcabc* . . .). When there were three or more hexagonal layers, both types of stacking were observed.

The following sequence of phase structures, with lattice parameters defined in Table 1, were observed as the central areal density $\sigma_0$ was increased from where order was first observed: (I) one-layer hexagonal → (III) two-layer staggered square → (IV) two-layer staggered rhombic → (V) two-layer staggered hexagonal. At a critical density, a third layer was formed, resulting in a (III) three-layer staggered square. The process then repeated with minor variations, such as phase III becoming less common. We have followed the classifications used in previous theoretical studies of quantum (*14*) and classical (*11*) electron bilayer systems. Phase II, which is a stable phase of the bilayer systems where the interlayer distance is fixed, is not listed here because it is unstable for the planar OCP, where the interlayer distance can vary.

We have performed an analytical calculation of the energies of these phase structures for the planar OCP (*24*). The calculation minimizes the energy (*25*) of several parallel lattice planes that are infinite and homogeneous in the $(x, y)$ direction but are confined in the $\hat{\mathbf{z}}$ direction by a harmonic external electrostatic confinement potential

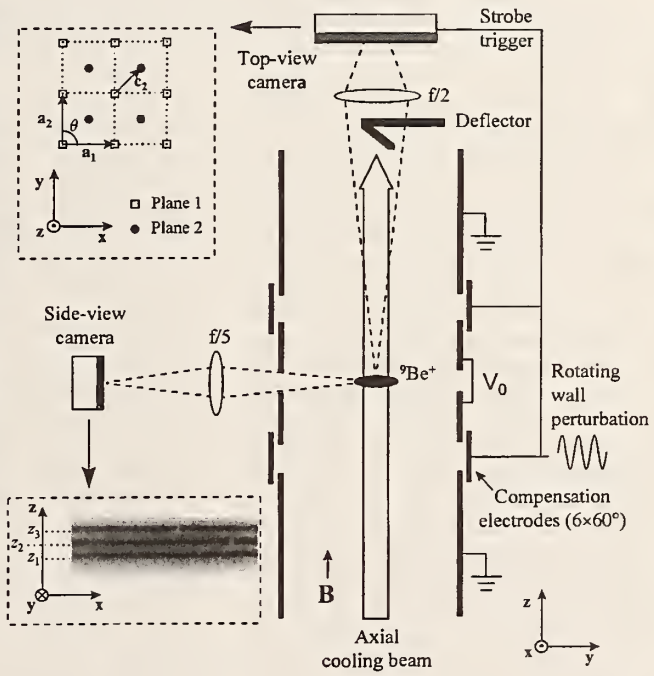


**Fig. 1.** Schematic side view of the cylindrical Penning trap with its side- and top-view imaging optics. The insets show the variables used to characterize the intra- and interlayer structure. The side-view inset also shows the central region of a lenticular ion plasma with three axial lattice planes. The rotation frequency of the ion plasma was controlled by applying properly phased sinusoidally time-varying electric potentials to the sixfold azimuthally segmented compensation electrodes.

**Table 1.** Primitive and interlayer displacement vectors in the $(x, y)$ plane for the observed phases. The primitive vector $\mathbf{a}_1$ defines the $\hat{\mathbf{x}}$ direction, and $|\mathbf{a}_1| = |\mathbf{a}_2| \equiv a$. Dashes, not applicable.

| Phase | Symmetry | Stacking | Vectors | | | |
|---|---|---|---|---|---|---|
| | | | $\mathbf{a}_1$ | $\mathbf{a}_2$ | $\mathbf{c}_2$ | $\mathbf{c}_3$ |
| I | Hexagonal | Single plane | $(a, 0)$ | $(a \cos 60°, a \sin 60°)$ | — | — |
| III | Square | Staggered | $(a, 0)$ | $(0, a)$ | $(\mathbf{a}_1 + \mathbf{a}_2)/2$ | (0, 0) |
| IV | Rhombic | Staggered | $(a, 0)$ | $(a \cos \theta, a \sin \theta)$ | $(\mathbf{a}_1 + \mathbf{a}_2)/2$ | (0, 0) |
| V | Hexagonal | hcp-like | $(a, 0)$ | $(a \cos 60°, a \sin 60°)$ | $(\mathbf{a}_1 + \mathbf{a}_2)/3$ | (0, 0) |
| $V_{fcc}$ | Hexagonal | fcc-like | $(a, 0)$ | $(a \cos 60°, a \sin 60°)$ | $(\mathbf{a}_1 + \mathbf{a}_2)/3$ | $2(\mathbf{a}_1 + \mathbf{a}_2)/3$ |


**Fig. 2.** Top-view $(x, y)$ images of the five structural phases observed in the experiment, with lines showing a fit of the central ions to the indicated structure.



TN-35

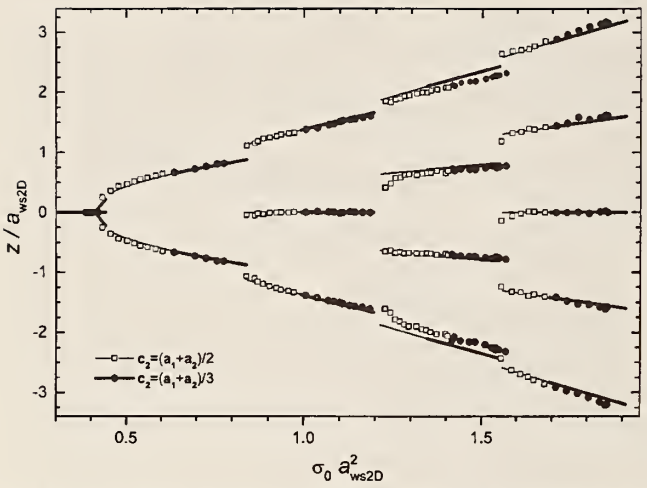


Fig. 3 (left). Interlayer structure (plane axial positions and displacement vectors) of the central region as a function of normalized central areal charge density. The lines show predictions from theory, and symbols show experimental measurements. The symbols indicate whether the lattices had an interlattice displacement vector $\mathbf{c}_2$ that was characteristic of the hexagonal phases (circles) or the square and rhombic phases (squares). Lengths have been normalized by $a_{WS2D} = (3e^2/4\pi\epsilon_0 m\omega_z^2)^{1/3}$ = 10.7 μm, which is the Wigner-Seitz radius in the planar limit.

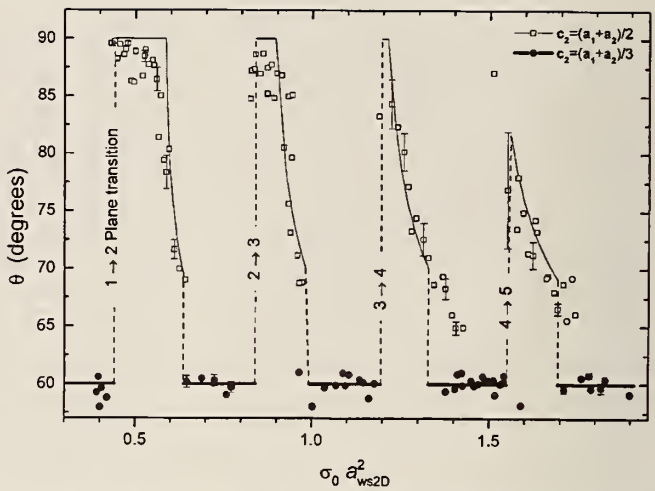


Fig. 4 (right). Intralayer angle θ of the central region as a function of central areal charge density. The solid lines indicate the minimum energy structures that are predicted by the 2D theory. The symbols indicate experimental measurements, which are from the same data sets that were used in Fig. 3. Some representative error bars that indicate the scatter in the measurements are included.

$\phi_e = 1/2(m/e)\omega_z^2 z^2$. Because this potential is identical to the confinement potential of a Penning trap in the $\alpha \rightarrow 0$ planar limit (*26*), this theory should predict the structures that were observed in the central region of the lenticular plasmas of the experiments. The predictions of this two-dimensional (2D) theory, which has no free parameters, were compared directly with our observations by identifying the areal density of the planar OCP with the directly measured central areal density $\sigma_0$ of the lenticular plasmas. For a quantitative analysis of the observed lattice structure, we performed a least squares fit of the positions of the ions in the central region to the relevant phases (shown in Table 1) (lines in Fig. 2). Using the best-fit values of the primitive vector length $a$ and the intralayer angle θ and using the observed number of lattice planes $n$, we calculated the central areal density $\sigma_0 = n/(a^2 \sin\theta)$.

The agreement between the planar OCP theory and experiment, with measurements taken on different plasmas with $N < 10^4$, was good (Figs. 3 and 4). As the central areal density was increased, the lattice planes moved farther apart axially (Fig. 3). Eventually, it became energetically favorable to form an additional lattice plane. However, although the phase $V_{fcc}$ was predicted to be slightly more energetically favorable than phase V, we rarely observed $V_{fcc}$ (~5% of the time). These and other minor discrepancies from theory may be due to the finite radial extent of the ion plasma; we observed a similar preference for hcp stacking in molecular dynamics simulations of small ($N$ = 3000) lenticular ion plasmas.

For the dependence of the angle θ (between the primitive vectors $\mathbf{a}_1$ and $\mathbf{a}_2$) on central areal density $\sigma_0$ (Fig. 4), the general trend is that, when a new lattice plane is formed, θ changes discontinuously from ~60° to a higher value. As $\sigma_0$ of the crystal was further increased, θ smoothly decreased to ~65° until there was a second discontinuous transition to a hexagonal structure. This second transition has been predicted to become continuous, with θ assuming all values $60° \leq \theta \leq 90°$, in liquid ($\Gamma < 80$) bilayer systems (*27*). At central areal charge densities near phase boundaries, both phases can be observed. In these regions, the phase that materializes after the crystal is formed is initially random but tends to persist if the ions are not heated. Where there was no strong preference for one phase over the other, both were plotted (Fig. 4).

Like most materials, the hexagonal and square phases contract in lateral directions when elongated. However, the rhombic phase shows quite different behavior because the intralayer angle θ strongly depends on the $\hat{z}$-axis strain; one rhombus diagonal contracts, and the second expands when the rhombic phase is elongated in the $\hat{z}$-axis direction. The dimensional change for the latter diagonal corresponds to a negative value of the Poisson's ratio (which is the ratio of the lateral contraction to the longitudinal elongation). The present experimental observations substantially expand the mass density range over which negative Poisson's ratios have been established [from ~10 g/cm$^3$ for cubic metals (*28*) and ~0.1 g/cm$^3$ for reentrant foams (*29*) to ~$10^{-15}$ g/cm$^3$ for the present ion crystals].

**References and Notes**


1. H. M. Van Horn, *Science* **252**, 384 (1991).
2. C. C. Grimes and G. Adams, *Phys. Rev. Lett.* **42**, 795 (1979).
3. D. J. Wineland, R. E. Drullinger, F. L. Walls, *ibid.* **40**, 1639 (1978).
4. J. N. Tan, J. J. Bollinger, B. M. Jelenković, D. J. Wineland, *ibid.* **72**, 4198 (1995); W. M. Itano et al., *Science* **279**, 686 (1998).
5. I. Waki, S. Kassner, G. Birkl, H. Walther, *Phys. Rev. Lett.* **68**, 2007 (1992); G. Birkl, S. Kassner, H. Walther, *Nature* **357**, 310 (1992).
6. P. K. Ghosh, *Ion Traps* (Clarendon, Oxford, 1995).
7. C. W. Roberson and C. F. Driscoll, Eds., *Non-Neutral Plasma Physics* (American Institute of Physics, New York, 1988).
8. S. Ichimaru, H. Iyetomi, S. Tanaka, *Phys. Rep.* **149**, 91 (1987).
9. D. H. E. Dubin, *Phys. Rev. E* **42**, 4972 (1990).
10. J. P. Schiffer, *Phys. Rev. Lett.* 70, 818 (1993); D. H. E. Dubin, *ibid.* 71, 2753 (1993).
11. G. Goldoni and F. M. Peeters, *Phys. Rev. B* **53**, 4591 (1996).
12. J. B. Pieper, J. Goree, R. A. Quinn, *J. Vac. Sci. Technol. A* **14**, 519 (1996); H. Totsuji, T. Kishimoto, C. Totsuji, *Phys. Rev. Lett.* **78**, 3113 (1997).
13. D. H. Van Winkle and C. A. Murray, *Phys. Rev. A* **34**, 562 (1986).
14. S. Narasimhan and T.-L. Ho, *Phys. Rev. B* **52**, 12291 (1995); G. Goldoni and F. M. Peeters, *Europhys. Lett.* **37**, 293 (1997).
15. M. Schmidt and H. Löwen, *Phys. Rev. E* **55**, 7228 (1997).
16. R. Rafac, J. P. Schiffer, J. S. Hangst, D. H. E. Dubin, D. J. Wales, *Proc. Natl. Acad. Sci. U.S.A.* **88**, 483 (1991).
17. F. Diedrich, E. Peik, J. M. Chen, W. Quint, H. Walther, *Phys. Rev. Lett.* **59**, 2931 (1987); D. J. Wineland, J. C. Bergquist, W. M. Itano, J. J. Bollinger, C. H. Manney, *ibid.*, p. 2935.
18. A. Rahman and J. P. Schiffer, *ibid.* **57**, 1133 (1986); D. H. E. Dubin and T. M. O'Neil, *ibid.* 60, 511 (1988).
19. S. L. Gilbert, J. J. Bollinger, D. J. Wineland, *ibid.*, p. 2022.
20. M. Drewsen, C. Brodersen, L. Hornekaer, J. S. Hangst, J. P. Schiffer, *ibid.* **81**, 2878 (1998).
21. X.-P. Huang, J. J. Bollinger, T. B. Mitchell, W. M. Itano, *ibid.* 80, 73 (1998); *Phys. Plasmas* **5**, 1656 (1998).
22. L. R. Brewer et al., *Phys. Rev. A* **38**, 859 (1988).
23. T. M. O'Neil, *Phys. Fluids* **24**, 1447 (1981); D. J. Larson et al., *Phys. Rev. Lett.* **57**, 70 (1986).




TN-36

24. T. B. Mitchell, J. J. Bollinger, D. H. E. Dubin, X.-P. Huang, W. M. Itano, in preparation (preprint available at www.boulder.nist.gov/timefreq/ion/penning/pop/pop.pdf).
25. Minimization of the energy was carried out numerically for given areal density by allowing the positions of the planes to vary with respect to one another within the external potential and by varying the lattice structure within the planes. We made the simplifying assumption, which was consistent with the experimental observations, that the lattice structure of each plane was identical. The areal density of the planar OCP is a control parameter that, when varied, leads to transitions in both the number and lattice structure of the planes. This theory focuses on the minimum potential energy states while neglecting finite temperature effects that may be important (particularly effects that are near the continuous phase transitions where large structural fluctuations may occur).
26. T. M. O'Neil and D. H. E. Dubin, *Phys. Plasmas* **5**, 2163 (1998).
27. V. I. Valtchinov, G. Kalman, K. B. Blagoev, *Phys. Rev. E* **56**, 4351 (1997).
28. R. H. Baughman, J. M. Shacklette, A. A. Zakhidov, S. Stafstrom, *Nature* **392**, 362 (1998).
29. R. Lakes, *Science* **235**, 1038 (1987).
30. This manuscript is a work of the U.S. government; it is not subject to U.S. copyright. This research was supported by the Office of Naval Research and NSF (D.H.E.D.). We thank B. King, R. J. Rafac, J. P. Schiffer, and D. J. Wineland for useful comments and B. M. Jelenković and J. N. Tan for technical assistance.

14 August 1998; accepted 14 October 1998

# Controlling Factors for the Brittle-to-Ductile Transition in Tungsten Single Crystals

**Peter Gumbsch,* Joachim Riedle, Alexander Hartmaier, Hellmut F. Fischmeister**

**Materials performance in structural applications is often restricted by a transition from ductile response to brittle fracture with decreasing temperature. This transition is currently viewed as being controlled either by dislocation mobility or by the nucleation of dislocations. Fracture experiments on tungsten single crystals reported here provide evidence for the importance of dislocation nucleation for the fracture toughness in the semibrittle regime. However, it is shown that the transition itself, in general, is controlled by dislocation mobility rather than by nucleation.**

Some materials are brittle and shatter like glass, whereas others are ductile and deformable. Several materials, such as the refractory metals, steels, and semiconductor crystals, exhibit both types of behavior (*1–5*) with a brittle-to-ductile transition (BDT) at a characteristic temperature. A crack introduced into a material may propagate as a brittle crack with an atomically sharp crack front; alternatively, the material near the crack tip may show sufficient plasticity to slow down or arrest the crack. Crack-tip plasticity comprises two distinct processes, nucleation of dislocations at or near the crack tip and their propagation away from the crack. Several models describe the BDT as a nucleation-controlled event (*6, 7*), and others focus on dislocation mobility as the controlling factor (*8–10*).

The experimental evidence on the controlling factors of the BDT, which has been obtained mostly from silicon single crystals, remains inconclusive. On the one hand, the temperature at which the BDT occurs [BDT temperature (BDTT)] is strongly dependent on the strain rate, which allows an activation energy for the BDT to be determined. This activation energy has been shown to be equal to that for dislocation motion (*2, 8, 9*), which suggests a mobility-controlled BDT. On the other hand, specimen size and the availability of dislocation sources have a pronounced influence on the fracture toughness to the degree that they may even switch the material's behavior from brittle to ductile (*11*).

We performed cleavage experiments on tungsten single crystals to determine the controlling factors of the BDT. To exclude disturbances from grain boundaries, single crystals were chosen. Fracture toughness tests were performed on all four low-index crack systems. A crack system is specified by the nominal crack plane and the crack front direction. The four crack systems studied are therefore denoted as {100}<010>, {100}<011>, {110}<1$\bar{1}$0>, and {110}<001> in crystallographic notation. The temperature range covered by the experiments was between the liquid nitrogen temperature (77 K) and 650 K. The toughness tests were performed on high-purity (*12*) tungsten single crystal bars (3 mm by 6 mm by 30 mm) loaded in three-point bending. To obtain a well-defined value for the fracture toughness, a sharp crack front was introduced by precracking at 77 K. Precrack length was evaluated from the compliance and, where possible, was also determined postmortem on the fracture surfaces, where faint arrest lines are visible. The tests were performed with a constant loading rate, which translates into an almost constant stress intensity rate of 0.10 ± 0.02 MPa $m^{1/2}$/s (*13*). More details of the experimental procedure are given in (*14*).

Multiple tests (more than five) were conducted for all four crack systems at room temperature and at 77 K. Several individual tests at other temperatures were performed to determine the temperature dependence of the fracture toughness (Fig. 1). Macroscopically, the transition from brittle to ductile response usually correlates with the maximum in fracture toughness. The temperature at this maximum was taken as the BDTT and was determined from Fig. 1 within 30 to 60 K (Table 1). The so-defined BDTTs fell into an interval of 100 K for all four crack systems, even though both {110} crack systems had a significantly higher room temperature fracture toughness than the {100} systems (Table 1).

Testing at 77 K always resulted in brittle cleavage fracture on the precrack plane for all four crack systems. The load-displacement curves showed perfectly linear behavior up to the load at which fracture occurred. The fracture surfaces were clean except for a few river lines.

At room temperature and above, most of the fracture specimens revealed small deviations from linearity in the load-displacement curves before final fracture, indicating a limited amount of plastic relaxation. The fracture surfaces were significantly rougher than those of the precracks and of the specimens tested at 77 K. Cleavage below the BDTT was always catastrophic. No noticeable amount of slow crack growth was observed.

The preexisting dislocation density and the availability of dislocation sources can be increased by plastic deformation before toughness testing. Specimens with a {110}<1$\bar{1}$0> crack system were deformed by compression along the <110> (long) axis at 400°C to a plastic strain of $\varepsilon_{pl} = 0.1$ before precracking. At low temperatures the predeformed specimens are significantly tougher than the unde-

**Table 1.** BDTT and fracture toughness of tungsten single crystals for the {100} and {110} cleavage planes with different crack front directions. Fracture toughness at room temperature $K^{RT}$ and at liquid nitrogen temperature $K^{77K}$ are mean values from at least five individual measurements (standard deviation in parentheses). Fracture toughness is in MPa $m^{1/2}$.

| Crack system | BDTT (K) | $K^{RT}$ | $K^{77K}$ |
|---|---|---|---|
| {100}<010> | 470 | 8.7 (2.5) | 3.4 (0.6) |
| {100}<011> | 370 | 6.2 (1.7) | 2.4 (0.4) |
| {110}<001> | 430 | 20.2 (5.5) | 3.8 (0.4) |
| {110}<1$\bar{1}$0> | 370 | 12.9 (2.1) | 2.8 (0.2) |

Max-Planck-Institut für Metallforschung, Seestrasse 92, 70174 Stuttgart, Germany.

*To whom correspondence should be addressed. E-mail: gumbsch@finix.mpi-stuttgart.mpg.de

# Generation of Nonclassical Motional States of a Trapped Atom

D. M. Meekhof, C. Monroe, B. E. King, W. M. Itano, and D. J. Wineland
*Time and Frequency Division, National Institute of Standards and Technology, Boulder, Colorado 80303-3328*
(Received 11 October 1995)

We report the creation of thermal, Fock, coherent, and squeezed states of motion of a harmonically bound $^9Be^+$ ion. The last three states are coherently prepared from an ion which has been initially laser cooled to the zero point of motion. The ion is trapped in the regime where the coupling between its motional and internal states, due to applied (classical) radiation, can be described by a Jaynes-Cummings-type interaction. With this coupling, the evolution of the internal atomic state provides a signature of the number state distribution of the motion.

PACS numbers: 42.50.Vk, 32.80.Pj, 32.80.Qk

Nonclassical states of the harmonic oscillator associated with a single mode of the radiation field (for example, squeezed states) have been a subject of considerable interest. One method for analyzing these states has been through the dynamics of a single, two-level atom which radiatively couples to the single mode radiation field. This system, described by the Jaynes-Cummings model (JCM) interaction [1,2], is important to the field of cavity QED [3].

Nonclassical states of motion occur naturally on an atomic scale, for example, for electrons in atoms and atoms in molecules. On a macroscopic scale, the benefits of nonclassical mechanical states, such as squeezed states, for detection of gravitational waves have been appreciated for some time [4], but so far these states have not been realized. More recently, there has been interest in the generation and detection of nonclassical states of motion for an atom confined in a macroscopic, harmonic trap; for trapped ions, see Refs. [5–16]. These states are of interest from the standpoint of quantum measurement concepts and may facilitate other measurements such as sensitive detection [5,7,13] or quantum computation [17].

In this Letter we report the generation and detection of thermal, Fock, coherent, and squeezed states of motion of a single $^9Be^+$ ion confined in an rf (Paul) trap. We detect the state of atomic motion by observing the evolution of the atom's internal levels [6,11] (e.g., collapse and revival) under the influence of a JCM-type interaction realized with the application of external (classical) fields. Under certain conditions, the interaction Hamiltonian is formally equivalent to the JCM Hamiltonian of cavity QED. Here, the harmonic motion of the atom replaces the single mode of the radiation field. The coupling can be realized by applying quasistatic fields [7], traveling-wave fields [6,10,13,15], or standing-wave laser fields [8,9,12]. In each case the coupling $\mathcal{H}_I = -\boldsymbol{\mu} \cdot \mathbf{E}(\mathbf{r})$ between internal and motional states is induced by the atom's motion through the spatially inhomogeneous electromagnetic field $\mathbf{E}(\mathbf{r})$, where $\boldsymbol{\mu}$ is the atomic dipole operator.

In the present experiment, we drive stimulated Raman transitions between two hyperfine ground states by applying a pair of traveling-wave laser beams detuned from an excited electronic state [18]. The resulting interaction between these internal states $|S\rangle$ (denoted $|\downarrow\rangle$ and $|\uparrow\rangle$) and motional harmonic oscillator states $|n\rangle$ and $|n'\rangle$ in the $x$ direction is given by matrix elements

$$\langle S', n'|\mathcal{H}_I|S, n\rangle = \hbar\Omega\langle S', n'|\sigma_+ e^{i\eta(a+a^\dagger)} + \sigma_- e^{-i\eta(a+a^\dagger)}|S, n\rangle \qquad (1)$$

in a frame which rotates at the difference frequency of the laser beams. In this expression, $\sigma_+$ ($\sigma_-$) is the raising (lowering) operator for the internal atomic state, $a^\dagger$ ($a$) is the harmonic oscillator raising (lowering) operator, and $\Omega$ is the Raman coupling parameter [5,13,18]. The Lamb-Dicke parameter is defined by $\eta \equiv \delta k\, x_0$, where $\delta k$ is the wave-vector difference of the two Raman beams along $x$, and $x_0 = \sqrt{\hbar/2m\omega}$ is the spread of the $|n = 0\rangle$ wave function in the harmonic well of frequency $\omega$.

The order $n' - n$ of the vibrational coupling is selected by tuning the Raman beam difference frequency. For example, by tuning to the first red sideband in the Raman spectrum, we resonantly enhance the term which drives transitions between states $|\downarrow, n\rangle$ and $|\uparrow, n-1\rangle$. In the Lamb-Dicke limit [$\delta k\sqrt{\langle x^2\rangle} \ll 1$, $x = x_0(a + a^\dagger)$], the exponentials in Eq. (1) can be expanded to lowest order, resulting in the operator $\eta(a\sigma_+ + a^\dagger\sigma_-)$, which corresponds to the usual JCM operator. We can easily control the strength and duration of the interaction by varying the intensity and time the lasers are applied. By choosing other laser tunings, we can select other operators such as the anti-JCM operator $\eta(a^\dagger\sigma_+ + a\sigma_-)$ at the first blue sideband (which is not present in cavity QED) or the "two-phonon" JCM operator $(\eta^2/2)(a^2\sigma_+ + a^{\dagger 2}\sigma_-)$ at the second red sideband. In this experiment, the higher-order terms in the expansion of the exponential in Eq. (1) must also be taken into account [19]. Reference [20] has explicitly discussed the consequences of these higher-order terms on the trapped ion internal and motional state dynamics.

Additional differences from cavity-QED experiments include the methods of state generation available (described below) and the relatively small decoherence. In all but the case of thermal states, we coherently prepare

the states starting with an ion which has been laser cooled to the $|n = 0\rangle$ ground state of motion [18]; this cooling is crucial to preserve the consistency of the generated states. Decoherence in these experiments is small enough that the atomic population coherence survives for many Rabi cycles of the JCM interaction—the "strong coupling" regime of cavity QED [3].

A single $^9Be^+$ ion is stored in a strong rf Paul trap [21] with a pseudopotential oscillation frequency along $x$ of $\omega/2\pi \approx 11.2$ MHz. The ion is cooled using sideband cooling with stimulated Raman transitions [18] between the $^2S_{1/2}$ $(F = 2, m_F = 2)$ and $^2S_{1/2}$ $(F = 1, m_F = 1)$ hyperfine ground states, which are denoted by $|\downarrow\rangle$ and $|\uparrow\rangle$, respectively, and are separated by $\approx$1.25 GHz. This prepares the ion in the $|S = \downarrow, n = 0\rangle$ state more than 95% of the time. The Raman beam wave vectors point at 45° to the $x$ axis with their wave-vector difference nearly along the $x$ axis of the trap [the Lamb-Dicke parameter is $\eta = 0.202(5)$], so the Raman transitions are highly insensitive to motion in the $y$ or $z$ directions. The beams are detuned $\approx$12 GHz to the red of the $^2P_{1/2}$ excited state with approximately 0.5 mW of power in each beam, so that the Raman transition coupling is $\Omega/2\pi \approx 500$ kHz, and the vibrational structure is clearly resolved.

Once the ion is prepared in the $|\downarrow, 0\rangle$ state, we create the desired motional state as described below. We then acquire the signature of the motional state as follows. The Raman beams are tuned to the first blue sideband and applied for a time $t$. The population of the $|\downarrow\rangle$ level is then measured by applying $\sigma^+$-polarized radiation on the $|\downarrow\rangle \rightarrow {}^2P_{3/2}$ cycling transition and detecting the fluorescence [18]. This experiment is repeated at a rate of a few kilohertz, while $t$ is slowly stepped, accumulating the probability $P_\downarrow(t)$ of occupation in $|\downarrow\rangle$.

Fock states of motion can in principle be produced by quantum jumps [9,16], adiabatic passage [12], or trapping states [14]; here we use an alternate technique. Since the ion is initially cooled to the $|\downarrow, 0\rangle$ Fock state, we create higher-$n$ Fock states by simply applying a sequence of Rabi $\pi$ pulses of laser radiation on the blue sideband, red sideband, or carrier. For example, the $|\uparrow, 2\rangle$ state is prepared by using blue sideband, red sideband, and carrier $\pi$ pulses in succession, so that the ion steps through the states $|\downarrow, 0\rangle$, $|\uparrow, 1\rangle$, $|\downarrow, 2\rangle$, and $|\uparrow, 2\rangle$.

We create a series of Fock states, $|\downarrow, n\rangle$, and record $P_\downarrow(t)$. The expected signal is $P_\downarrow(t) = \cos^2(\Omega_{n,n+1}t)\exp(-\gamma_n t)$, where $\Omega_{n,n+1}$ is the Rabi frequency and $\gamma_n$ is the decoherence rate between levels $|n\rangle$ and $|n + 1\rangle$. The measured $P_\downarrow(t)$ for an initial $|\downarrow, n = 0\rangle$ Fock state is shown in Fig. 1(a) and fitted by this equation, yielding $\Omega_{0,1} = 94(1)$ kHz and $\gamma_0 = 11.9(4)$ kHz. Note that $\Omega_{0,1}$ is much greater than $\gamma_0$, satisfying the strong coupling condition. We believe the decoherence is due to technical problems—primarily intensity fluctuations of the laser beams and instabilities of the trap drive frequency and voltage amplitude. The observed increase of $\gamma_n$ with $n$ [we find $\gamma_n \approx \gamma_0(n + 1)^{0.7}$] is qualitatively consistent with this view. In the Lamb-Dicke limit the Rabi frequency between levels $|\downarrow, n\rangle$ and $|\uparrow, n + 1\rangle$ is $\Omega_{n,n+1} = \sqrt{n + 1}\,\eta\Omega$. If the Lamb-Dicke limit is not satisfied, nonlinear effects in the interaction modify these rates [19,20]. The measured Rabi frequency ratios $\Omega_{n,n+1}/\Omega_{0,1}$ are plotted in Fig. 1(b), showing very good agreement with the JCM for the trap's Lamb-Dicke parameter $\eta = 0.202$.

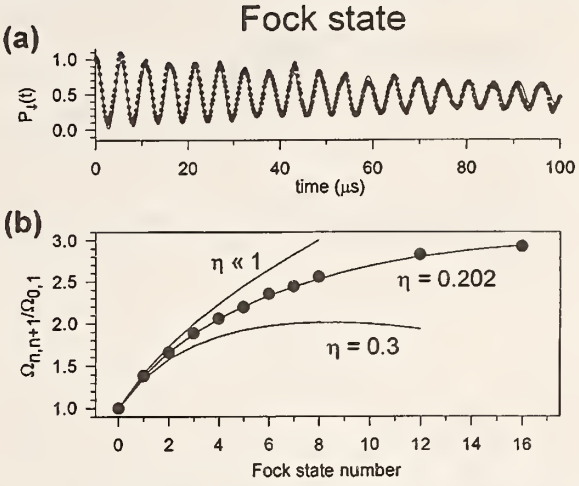


FIG. 1. (a) $P_\downarrow(t)$ for an initial $|\downarrow, 0\rangle$ Fock state driven by a JCM-type interaction provided by tuning the stimulated Raman beams to the first blue sideband. The solid line is a fit by an exponentially decaying sinusoid. (b) The relative Rabi frequencies $\Omega_{n,n+1}/\Omega_{0,1}$ vs the prepared Fock state number $n$. The lines represent the predictions of the nonlinear JCM for certain Lamb-Dicke parameters, showing very good agreement with the known Lamb-Dicke parameter $\eta = 0.202(5)$. The $\eta \ll 1$ line corresponds to the Lamb-Dicke limit: $\Omega_{n,n+1}/\Omega_{0,1} = \sqrt{n + 1}$.

When the ion's motion is not in a Fock state, $P_\downarrow(t)$ shows a more complicated structure. The motional state is characterized by a density operator whose diagonal elements have a number distribution $P_n$ leading to

$$P_\downarrow(t) = \sum_{n=0} P_n \cos^2(\Omega_{n,n+1}t)e^{-\gamma_n t}. \qquad (2)$$

For a thermal distribution $P_n = N[\overline{n}/(1 + \overline{n})]^n$, where $N$ is a normalization constant and $\overline{n}$ is the average vibrational quantum number. By performing Doppler cooling on the $|\downarrow\rangle \rightarrow P_{3/2}$ cycling transition [18], we generate a thermal state of motion [22]. The value of $\overline{n}$ can be controlled by the Doppler detuning. An example of $P_\downarrow(t)$ data for a thermal state of motion is given in Fig. 2. To demonstrate consistency with a thermal state of motion, the time-domain data are fitted by Eq. (2) with a thermal population distribution for $P_n$. The signal scale and $\overline{n}$ are allowed to vary in the fit. Values for the base Rabi frequency $\Omega_{0,1}$ and base decay rate $\gamma_0$ (from which the other rates are scaled using the Fock state data) are obtained from a separate trace of $P_\downarrow(t)$ for an initial $|\downarrow, 0\rangle$ state, as in Fig. 1(a). For Fig. 2, the fit yields $\overline{n} = 1.3 \pm 0.1$. The inset shows the results of

erratum vol. 77, 2346 (1996) → $P_\downarrow(t) = \frac{1}{2}\sum_{n=0} P_n\left(1 + \cos 2\Omega_{n,n+1}t\, e^{-\gamma_n t}\right)$

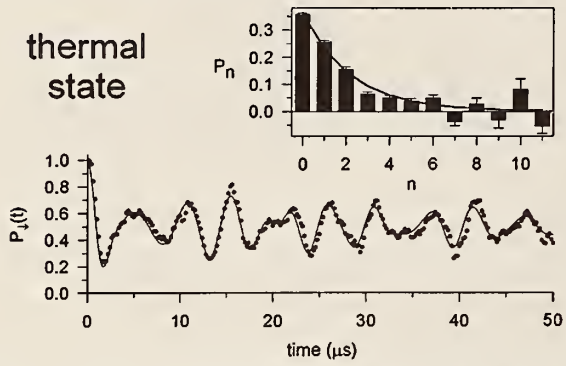


FIG. 2. $P_\downarrow(t)$ for a thermal state. The data (points) are fitted (line) by a superposition of Fock states with $P_n$ given by a thermal state distribution. The fit allows $\overline{n}$ to vary, finding $1.3 \pm 0.1$. The inset shows the decomposition of the data onto the Fock state components (bars) with a fit (line) by the expected exponential distribution, yielding $1.5 \pm 0.1$.

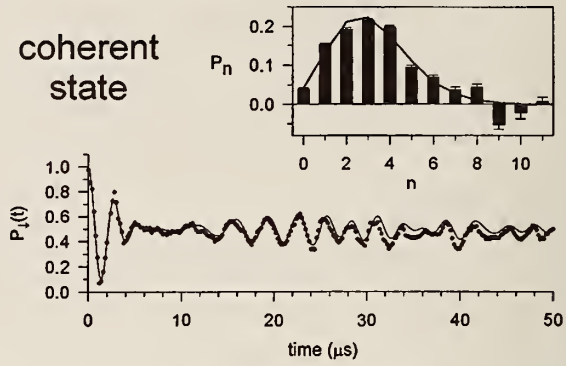


FIG. 3. $P_\downarrow(t)$ for a coherent state, showing collapse and revival. The data are fitted by a coherent state distribution, yielding $\overline{n} = 3.1 \pm 0.1$. The inset shows the decomposition of the data onto the expected Fock state components, fitted by a Poissonian distribution, yielding $\overline{n} = 2.9 \pm 0.1$.

an independent analysis (the frequency-domain analysis). In this case, we directly extract the populations of the various $|n\rangle$ levels. Since the Fock state parameters $\Omega_{n,n+1}$ and $\gamma_n$ are well characterized, the time-domain data can be decomposed into Fock-state components. Equation (2) is linear in the $P_n$, so we use singular-value decomposition [23] to extract the probabilities, shown in the inset to Fig. 2. The probabilities are fitted by an exponential, yielding $\overline{n} = 1.5 \pm 0.1$. Finally, we independently measure $\overline{n}$ by comparing the size of the red and blue sidebands [18], yielding $\overline{n} = 1.5 \pm 0.2$.

A coherent state of motion of the ion corresponds to a displaced zero-point wave packet oscillating in the potential well. The distribution among Fock states is Poissonian, $P_n = (\overline{n}^n e^{-\overline{n}})/n!$. As predicted by the JCM, the internal-state evolution $P_\downarrow(t)$ will undergo quantum collapses and revivals [24]. These revivals are a purely quantum effect due to the discrete energy levels and the narrow distribution of states [2,24].

Coherent states of ion motion can be produced from the $|n = 0\rangle$ state by a spatially uniform classical driving field [25], by a "moving standing wave" [26], by pairs of standing waves [8], or by a sudden shift of the trap center [5]. We have used the first two methods; for the data shown here we use the first. For the classical drive, we apply a sinusoidally varying potential at the trap oscillation frequency on one of the trap compensation electrodes [21] for a fixed time (typically 10 $\mu$s). In Fig. 3 we present an example of $P_\downarrow(t)$ after creation of a coherent state of motion, exhibiting collapse and revival. The time-domain data are fitted by Eq. (2) using a Poissonian distribution and allowing only $\overline{n}$ to vary. All other parameters are measured from a separate trace similar to Fig. 1(a). The inset shows the probabilities of the Fock components, extracted using the frequency-domain analysis described above. These amplitudes display the expected Poissonian dependence on $n$. The observed revival for higher-$\overline{n}$ coherent states is attenuated due to the progressively faster decay rates of the higher-$n$ Fock states, and for states with $\overline{n} \gtrsim 6$ we are unable to see the revival.

A coherent state has a definite phase relationship between the Fock state components. The signal $P_\downarrow(t)$, however, does not contain this phase information. To demonstrate the phase coherence of the created states, we apply a second pulse of classical driving force, which coherently returns the ion to the $|n = 0\rangle$ state, provided the pulse is of the same amplitude as the first and 180° out of phase with the coherent state. As expected, the return of the ion to the $|n = 0\rangle$ state is very sensitive to the phase of the second pulse. However, we are able to reverse the coherent state and return the ion to $|n = 0\rangle$ more than 85% of the time, as indicated by a single frequency component in a subsequent measurement of $P_\downarrow(t)$.

A "vacuum squeezed state" of motion can be created by a parametric drive [5], by a combination of standing- and traveling-wave laser fields [8], or by a nonadiabatic drop in the trap spring constant [5]. Here we irradiate the $|n = 0\rangle$ ion with two Raman beams which differ in frequency by $2\omega$, driving Raman transitions between the even-$n$ levels within the same hyperfine state. The interaction can also be thought of as a parametric drive induced by an optical dipole force modulated at $2\omega$ [26]. The squeeze parameter $\beta$ (defined as the factor by which the variance of the squeezed quadrature is decreased) grows exponentially with the driving time. Figure 4 shows $P_\downarrow(t)$ for a squeezed state prepared in this way. The data are fitted by a vacuum squeezed state distribution, allowing only $\beta$ to vary. The fit of the data in Fig. 4 demonstrates consistency with a squeezed state and finds $\beta = 40 \pm 10$, which corresponds to $\overline{n} \approx 7.1$.

The population distribution for a vacuum squeezed state is relatively flat and is restricted to the even states, $P_{2n} = N(2n)!(\tanh r)^{2n}/(2^n n!)^2$, with $\beta = \exp(2r)$. A squeezed state with $\beta = 40$ has 16% of the population in states above $n = 20$. The Rabi frequency differences of

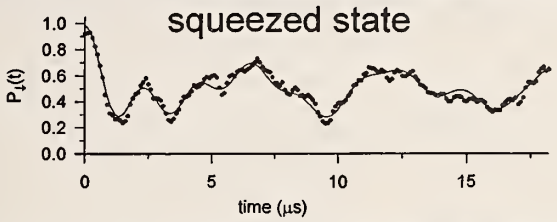


FIG. 4. $P_\downarrow(t)$ for a squeezed state. The data are fitted by a squeezed state population distribution, finding $\beta \approx 40 \pm 10$, which corresponds to $\bar{n} \approx 7.1$.

these high-$n$ levels are small [see Fig. 1(b)], and with the inclusion of nonlinear effects [19,20] the Rabi frequencies begin to decrease with $n$ after $n = 20$. The levels can no longer be distinguished, and the frequency-domain analysis cannot be used to extract the level populations.

In summary, we have created thermal, Fock, coherent, and squeezed states of motion of a trapped ion and examined these states through the evolution of the ion internal state $P_\downarrow(t)$ induced by a (nonlinear) JCM-type interaction. This experiment demonstrates the utility of a trapped ion for the creation of nonclassical states of motion and investigations of the dynamics of Jaynes-Cummings-type interactions. Given a suitable coupling, it should be possible to transfer these nonclassical state properties to other harmonic oscillators including macroscopic oscillators [5]. In addition to work to reduce the decoherence, further efforts will involve the creation of arbitrary quantum states of motion, including macroscopic superposition states (Schrödinger's cat states) [3], investigation of the "two-phonon" Jaynes-Cummings model [27,28], quantum state endoscopy [29], and quantum state tomography [30]. The same interaction can be extended to prepare correlated internal states of two or more trapped ions for sensitive detection [7,13] or quantum computation [17].

This work is supported by the U.S. Office of Naval Research and the U.S. Army Research Office. We acknowledge important contributions by J. C. Bergquist and helpful comments on the manuscript by M. Stephens, C. S. Wood, and M. Young.

[1] E. T. Jaynes and F. W. Cummings, Proc. IEEE **51**, 89 (1963).
[2] B. W. Shore and P. L. Knight, J. Mod. Opt. **40**, 1195 (1993).
[3] *Cavity Quantum Electrodynamics,* edited by P. R. Berman (Academic Press, Boston, MA, 1994).
[4] J. N. Hollenhorst, Phys. Rev. D **19**, 1669 (1979).
[5] D. J. Heinzen and D. J. Wineland, Phys. Rev. A **42**, 2977 (1990).
[6] C. A. Blockley, D. F. Walls, and H. Risken, Europhys. Lett. **17**, 509 (1992).
[7] D. J. Wineland, J. J. Bollinger, W. M. Itano, F. L. Moore, and D. J. Heinzen, Phys. Rev. A **46**, R6797 (1992).
[8] J. I. Cirac, A. S. Parkins, R. Blatt, and P. Zoller, Phys. Rev. Lett. **70**, 556 (1993).
[9] J. I. Cirac, R. Blatt, A. S. Parkins, and P. Zoller, Phys. Rev. Lett. **70**, 762 (1993).
[10] H. Zeng and F. Lin, Phys. Rev. A **48**, 2393 (1993).
[11] J. I. Cirac, R. Blatt, A. S. Parkins, and P. Zoller, Phys. Rev. A **49**, 1202 (1994).
[12] J. I. Cirac, R. Blatt, and P. Zoller, Phys. Rev. A **49**, R3174 (1994).
[13] D. J. Wineland, J. J. Bollinger, W. M. Itano, and D. J. Heinzen, Phys. Rev. A **50**, 67 (1994).
[14] R. Blatt, J. I. Cirac, and P. Zoller, Phys. Rev. A **52**, 518 (1995).
[15] H. Zeng and F. Lin, Phys. Rev. A **52**, 809 (1995).
[16] J. Eschner, B. Appasamy, and P. E. Toschek, Phys. Rev. Lett. **74**, 2435 (1995).
[17] J. I. Cirac and P. Zoller, Phys. Rev. Lett. **74**, 4091 (1995); C. Monroe, D. M. Meekhof, B. E. King, W. Itano, and D. J. Wineland, Phys. Rev. Lett. **75**, 4714 (1995).
[18] C. Monroe, D. M. Meekhof, B. E. King, S. R. Jefferts, W. M. Itano, D. J. Wineland, and P. L. Gould, Phys. Rev. Lett. **75**, 4011 (1995).
[19] See Eq. (31) in D. J. Wineland and W. M. Itano, Phys. Rev. A **20**, 1521 (1979).
[20] W. Vogel and R. L. de Matos Filho, Phys. Rev. A **52**, 4214 (1995).
[21] S. Jefferts, C. Monroe, E. Bell, and D. J. Wineland, Phys. Rev. A **51**, 3112 (1995).
[22] S. Stenholm, Rev. Mod. Phys. **58**, 699 (1986).
[23] W. H. Press, S. A. Teukolsky, W. T. Vetterling, and B. P. Flannery, *Numerical Recipes* (Cambridge University Press, Cambridge, 1992).
[24] J. H. Eberly, N. B. Narozhny, and J. J. Sanchez-Mondragon, Phys. Rev. Lett. **44**, 1323 (1980).
[25] P. Carruthers and M. M. Nieto, Am. J. Phys. **7**, 537 (1965).
[26] D. J. Wineland, J. C. Bergquist, J. J. Bollinger, W. M. Itano, F. L. Moore, J. M. Gilligan, M. G. Raizen, D. J. Heinzen, C. S. Weimer, and C. H. Manney, in *Laser Manipulation of Atoms and Ions,* edited by E. Arimondo, W. D. Phillips, and F. Strumia (North-Holland, Amsterdam, 1992), p. 553.
[27] P. L. Knight, Phys. Scr. **T12**, 51 (1986).
[28] R. L. de Matos Filho and W. Vogel, Phys. Rev. A **50**, R1988 (1994).
[29] P. J. Bardroff, E. Mayr, and W. P. Schleich, Phys. Rev. A **51**, 4963 (1995), and references therein.
[30] K. Vogel and H. Risken, Phys. Rev. A **40**, 2847 (1989); D. T. Smithey, M. Beck, M. G. Raymer, and A. Faridani, Phys. Rev. Lett. **70**, 1244 (1993); T. J. Dunn, I. A. Walmsley, and S. Mukamel, Phys. Rev. Lett. **74**, 884 (1995); S. Wallentowitz and W. Vogel, Phys. Rev. Lett. **75**, 2932 (1995); J. F. Poyatos, R. Walser, J. I. Cirac, P. Zoller, and R. Blatt (to be published).

# A "Schrödinger Cat" Superposition State of an Atom

C. Monroe,* D. M. Meekhof, B. E. King, D. J. Wineland

A "Schrödinger cat"–like state of matter was generated at the single atom level. A trapped $^{9}Be^{+}$ ion was laser-cooled to the zero-point energy and then prepared in a superposition of spatially separated coherent harmonic oscillator states. This state was created by application of a sequence of laser pulses, which entangles internal (electronic) and external (motional) states of the ion. The Schrödinger cat superposition was verified by detection of the quantum mechanical interference between the localized wave packets. This mesoscopic system may provide insight into the fuzzy boundary between the classical and quantum worlds by allowing controlled studies of quantum measurement and quantum decoherence.

Quantum mechanics allows the preparation of physical systems in superposition states, or states that are "smeared" between two or more distinct values. This curious principle of quantum mechanics (*1*) has been extremely successful at describing physical behavior in the microscopic world—from interactions of atoms with photons to interactions at the subnuclear level. But what happens when we extend the quantum superposition principle to macroscopic systems conventionally described by classical physics? Here, superpositions introduce a great amount of conceptual difficulty, as pointed out in 1935 by the celebrated Einstein-Podolsky-Rosen (*2*) and Schrödinger cat (*3*) paradoxes. For example, in Schrödinger's thought experiment (*3*), an unfortunate cat is placed in a quantum superposition of being dead and alive (correlated with a single radioactive atom that has and has not decayed). The state of the system can be represented by the entangled quantum mechanical wave function,

$$\psi = \frac{|\text{☺}\rangle|\uparrow\rangle + |\text{☹}\rangle|\downarrow\rangle}{\sqrt{2}} \qquad (1)$$

where $|\text{☺}\rangle$ and $|\text{☹}\rangle$ refer to the states of a live and dead cat, and $|\downarrow\rangle$ and $|\uparrow\rangle$ refer to the internal states of an atom that has and has not radioactively decayed. This situation defies our sense of reality because we only observe live or dead cats, and we expect that cats are either alive or dead independent of our observation (*4*). Schrödinger's cat paradox is a classic illustration of the conflict between the existence of quantum superpositions and our real-world experience of observation and measurement.

Although superposition states such as Schrödinger's cat do not appear in the macroscopic world, there is great interest in the realization of "Schrödinger cat"–like states in mesoscopic systems, or systems that have both macroscopic and microscopic features. In this context, the "cat" is generalized to

The authors are in the Time and Frequency Division, MS 847, National Institute of Standards and Technology, Boulder, CO 80303, USA.

*To whom correspondence should be addressed.

represent a physical system whose attributes are normally associated with classical concepts, such as the distinguishable position of a particle (instead of the state of livelihood of a real cat). In this article, we report the creation of a mesoscopic "Schrödinger cat" state at the single atom level: An atom was prepared in a quantum superposition of two spatially separated but localized positions. In analogy to Schrödinger's original proposition given by Eq. 1, we created the following state:

$$\psi = \frac{|x_1\rangle|\uparrow\rangle + |x_2\rangle|\downarrow\rangle}{\sqrt{2}} \qquad (2)$$

where $|x_1\rangle$ and $|x_2\rangle$ denote classical-like wave packet states corresponding to separated spatial positions of the atom, and $|\downarrow\rangle$ and $|\uparrow\rangle$ refer to distinct internal electronic quantum states of the atom (5). The wave packets are separated by a mesoscopic distance of more than 80 nm, which is large compared with the size of the individual wave packets (≈7 nm) or the atomic dimension (≈0.1 nm).

Mesoscopic Schrödinger cats may provide an interesting testing ground for the controversial theory of quantum measurement (6). At the core of this historical issue is the question of the universality of quantum mechanics. The "Copenhagen interpretation" of Bohr (7) and Heisenberg (8) holds that the measuring apparatus always involves classical concepts, thus forcing a seemingly arbitrary division between the quantum and classical worlds. Einstein (2) on the other hand argued that for quantum mechanics to be complete, it should describe physical behavior at all scales. One practical approach toward resolving this controversy is the introduction of quantum decoherence, or the environmentally induced reduction of quantum superpositions into statistical mixtures and classical behavior (9). Decoherence is commonly interpreted as a way of quantifying the elusive boundary between classical and quantum worlds and almost always precludes the existence of macroscopic Schrödinger cat states, except at extremely short time scales (9, 10). The creation of mesoscopic Schrödinger cat states may allow controlled studies of quantum decoherence and the quantum-classical boundary. We note that quantum decoherence has received much interest lately because of its importance in proposals for quantum computation (11) and quantum cryptography (12).

Macroscopic superposition states of matter have been realized for electron (13), neutron (14), and atom (15) beam splitters, where these particles are split into superpositions of separated paths. The matter wave packets in these experiments spread in time because the particles are unbound. Spatially separated superpositions of electrons within atoms have been demonstrated by exciting electrons to Rydberg states with pulsed lasers (16). Here, the electron wave packet is also dispersive because of its anharmonic binding potential. There have been related proposals for the creation of macroscopic superposition states of vibration in molecules or crystals (17) and of electrical currents flowing in superconducting rings (18).

The appeal of creating a Schrödinger cat state in a harmonic oscillator is that wave packet dispersion can be negligible. The simple time evolution of a coherent harmonic oscillator wave packet preserves the separation of the superposition and aids in the visualization and interpretation of experiments. There have been several proposals to create mesoscopic Schrödinger cat states in a single mode of the electromagnetic field, which is formally equivalent to a harmonic oscillator. For instance, these states are expected to evolve from the amplitude dispersion of a laser beam propagating in an anharmonic Kerr medium (19). In cavity-quantum-electrodynamics, these states are predicted to emerge by driving a coherent state with a Jaynes-Cummings interaction to the point of collapse (20), by continuously pumping a single cavity mode with polarized two-level atoms (21), or by realizing a dispersive interaction between a single atom and a single cavity mode (22, 23). It has been proposed that Schrödinger cat states of a single harmonically bound atom can be created by driving the atom with a strong laser field and relying on a measurement to project the desired superposition state (24) or by optically pumping the atom to a "dark" state with multiple laser beams (25).

Experimental approach. In the present work, we create a Schrödinger cat state of the harmonic oscillator by forming a superposition of two coherent-state wave packets of a single trapped atom with a sequence of laser pulses. Each wave packet is correlated with a particular internal state of the atom. To analyze this state we apply an additional laser pulse to couple the internal states and then measure the resulting interference of the distinct wave packets (26, 27). The key features of our approach are that (i) we control the harmonic motion of the trapped atom to a high degree by exciting the motion from initial zero-point wave packets to coherent-state wave packets of well-defined amplitude and phase; (ii) we do not rely on a conditional measurement to project out the desired Schrödinger cat state; and (iii) wave packet dispersion of the atomic motion is negligible.

The experimental apparatus is described elsewhere (28, 29). A single $^9Be^+$ ion is confined in a coaxial-resonator radio frequency (RF)–ion trap (28) that provides harmonic oscillation frequencies of $(\omega_x, \omega_y, \omega_z)/2\pi \approx$ (11.2, 18.2, 29.8) MHz along the principal axes of the trap. We laser-cool the ion to the quantum ground state of motion (29) and then coherently manipulate its internal (electronic) and external (motional) state by applying pairs of off-resonant laser beams, which drive two-photon–stimulated Raman transitions (29, 30). As shown in Fig. 1A, the two internal states of interest are the stable $^2S_{1/2}(F = 2, m_F = -2)$ and $^2S_{1/2}(F = 1, m_F = -1)$ hyperfine ground states (denoted by $|\downarrow\rangle_i$ and $|\uparrow\rangle_i$, respectively), separated in frequency by $\omega_{HF}/2\pi \approx 1.250$ GHz. Here, $F$ and $m_F$ are quantum numbers representing the total internal angular momentum of the atom and its projection along a quantization axis. The Raman beams are detuned by $\Delta \approx -12$ GHz from the $^2P_{1/2}(F = 2, m_F = -2)$ excited state,

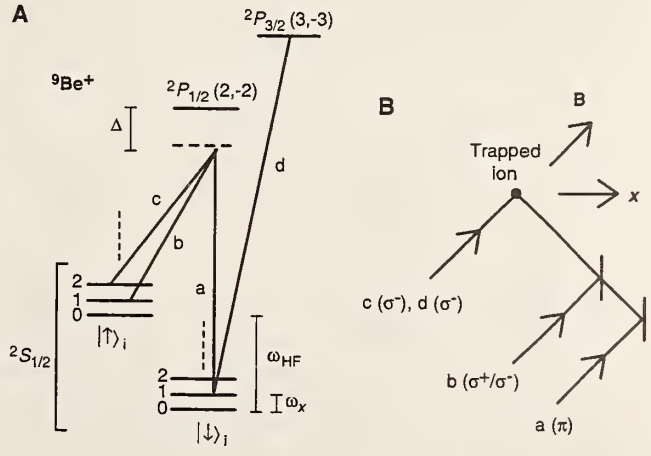


**Fig. 1.** (**A**) Electronic (internal) and motional (external) energy levels (not to scale) of the trapped $^9Be^+$ ion, coupled by the indicated laser beams a through d. The difference frequency of the "carrier" Raman beams a and b is set near $\omega_{HF}/2\pi \approx$ 1.250 GHz, providing a two-photon Raman coupling between the $^2S_{1/2}(F = 2, m_F = -2)$ and $^2S_{1/2}(F = 1, m_F = -1)$ hyperfine ground states (denoted by $|\downarrow\rangle_i$ and $|\uparrow\rangle_i$, respectively). The difference frequency of the "displacement" Raman beams b and c is set to $\omega_x/2\pi \approx 11.2$ MHz. This excites the motion of the ion to a coherent state $|\alpha e^{i\theta}\rangle_e$ from an initial zero-point state of motion $|0\rangle_e$ in the harmonic potential. Because of the polarization of beams b and c, they do not affect motion correlated with the $|\downarrow\rangle_i$ internal state. The three Raman beams (a, b, and c) are detuned $\Delta \approx -12$ GHz from the $^2P_{1/2}(F = 2, m_F = -2)$ excited state (radiative linewidth $\gamma/2\pi \approx 19.4$ MHz). Detection of the internal state is accomplished by first illuminating the ion with $\sigma^-$-polarized "detection" beam d, which drives the cycling $^2S_{1/2}(F = 2, m_F = -2) \rightarrow {}^2P_{3/2}(F = 3, m_F = -3)$ transition, and then observing the scattered fluorescence. (**B**) Geometry of the three Raman laser beams a, b, and c, with polarizations indicated. The quantization axis defined by the applied magnetic field **B** is 45° from the $x$ axis of the harmonic trap potential.

which acts as the virtual level, providing the Raman coupling. The external motional states are characterized by the quantized vibrational harmonic oscillator states $|n\rangle_e$ in the $x$ dimension, separated in frequency by $\omega_x/2\pi \approx 11.2$ MHz.

When we tune the Raman beam difference frequency near $\omega_{HF}$ and apply the "carrier beams" a and b of Fig. 1, the ion experiences a coherent Rabi oscillation between the internal states $|\downarrow\rangle_i$ and $|\uparrow\rangle_i$. By adjusting the exposure time of the carrier beams, we can, for example, "flip" the internal state (a $\pi$-pulse, or one-half of a Rabi cycle) or "split-recombine" the internal state (a $\pi/2$-pulse, or one-fourth of a Rabi cycle). Transitions on the carrier do not significantly affect the state of motion, because beams a and b are copropagating. When we tune the Raman beam difference frequency near $\omega_x$ and apply the "displacement" beams b and c of Fig. 1, the effect is formally equivalent to applying the displacement operator to the state of motion (30). Alternatively, the displacement beams can be thought of as producing a "walking wave" pattern whose time-dependent dipole force resonantly excites the harmonic motion (31). This force promotes an initial zero-point state of motion $|0\rangle_e$ to a coherent state (32)

$$|\beta\rangle_e = \exp(-|\beta|^2/2)\,\Sigma_n\,\beta^n/(n!)^{1/2}|n\rangle_e \quad (3)$$

where $\beta = \alpha e^{i\theta}$ is a dimensionless complex number that represents the amplitude and phase of the motion in the harmonic potential (33). The probability distribution of vibrational levels in a coherent state is Poissonian with mean number of vibrational quanta $\langle n\rangle = \alpha^2$. The coherent state of motion is much like classical motion in a harmonic potential with amplitude $2\alpha x_0$, where $x_0 = (\hbar/2m\omega_x)^{1/2} = 7.1(1)$ nm is the root mean square Gaussian size of the oscillating wave packet, $m$ is the mass of the ion, and $\hbar$ is Planck's constant divided by $2\pi$ (the number in parentheses is the standard error in the last digit).

The polarizations of the three Raman beams a, b, and c produce $\pi$, $\sigma^+/\sigma^-$, and $\sigma^-$ couplings, respectively, with respect to a quantization axis defined by an applied 0.20-mT magnetic field, as indicated in Fig. 1B. As a result, the displacement beams (b and c) affect only the motional state correlated with the $|\uparrow\rangle_i$ internal state, because the $\sigma^-$-polarized beam c cannot couple the internal state $|\downarrow\rangle_i$ to any virtual $^2P_{1/2}$ states (34). This selectivity of the displacement force provides quantum entanglement of the internal state with the external motional state. Although the motional state can be thought of as nearly classical, its entanglement with the internal atomic quantum levels precludes any type of semiclassical analysis.

**Table 1.** Raman beam pulse sequence for the generation of a Schrödinger cat state. The magnitude (phase) of the coherent state is controlled by the duration (phase) of the applied displacement beams in steps 2 and 4. The phases of internal state carrier operations in steps 1, 3, and 5 are relative to step 5. The states created after each step do not include overall phase factors, and the phase appearing in the final state is $\delta \equiv \mu - 2\nu + \pi$.

| Step | Function | Approximate duration ($\mu$s) | Phase | State created (see Fig. 2) (initial state: $|\downarrow\rangle_i|0\rangle_e$) |
|---|---|---|---|---|
| 1 | Carrier $\pi/2$-pulse | 0.5 | $\mu$ | $[|\downarrow\rangle_i|0\rangle_e - ie^{-i\mu}|\uparrow\rangle_i|0\rangle_e]/\sqrt{2}$ |
| 2 | Displacement | $\tau \approx 10.0$ | $-\phi/2$ | $[|\downarrow\rangle_i|0\rangle_e - ie^{-i\mu}|\uparrow\rangle_i|\alpha e^{-i\phi/2}\rangle_e]/\sqrt{2}$ |
| 3 | Carrier $\pi$-pulse | 1.0 | $\nu$ | $[e^{i(\nu-\mu)}|\downarrow\rangle_i|\alpha e^{-i\phi/2}\rangle_e + ie^{-i\nu}|\uparrow\rangle_i|0\rangle_e]/\sqrt{2}$ |
| 4 | Displacement | $\tau \approx 10.0$ | $\phi/2$ | $[e^{i(\nu-\mu)}|\downarrow\rangle_i|\alpha e^{-i\phi/2}\rangle_e + ie^{-i\nu}|\uparrow\rangle_i|\alpha e^{i\phi/2}\rangle_e]/\sqrt{2}$ |
| 5 | Carrier $\pi/2$-pulse | 0.5 | 0 | $1/2|\downarrow\rangle_i[|\alpha e^{-i\phi/2}\rangle_e - e^{i\delta}|\alpha e^{i\phi/2}\rangle_e]$ $-i/2|\uparrow\rangle_i[|\alpha e^{-i\phi/2}\rangle_e + e^{i\delta}|\alpha e^{i\phi/2}\rangle_e]$ |

Each Raman beam contains ≈1 mW of power at ≈313 nm. This results in a two-photon Rabi frequency of $\Omega/2\pi \approx 250$ kHz for the copropagating Raman carrier beams a and b, or a $\pi$-pulse exposure time of about 1 $\mu$s. We apply the displacement Raman beams (b and c) to the ion in directions such that their wave vector difference $\delta\mathbf{k}$ points nearly along the $x$ axis of the trap. Motion in the $y$ or $z$ dimensions is therefore highly insensitive to the displacement beams. When we apply the displacement beams to a zero-point wave packet (correlated with the $|\uparrow\rangle_i$ state) for time $\tau$, we expect to create a coherent state of amplitude $\alpha = \eta\Omega_d\tau$. Here, $\eta = 0.205(5)$ is the Lamb-Dicke parameter (30) and $\Omega_d/2\pi \approx 300$ kHz is the coupling strength of the displacement beams. After each preparation cycle (described below), we detect which internal state ($|\downarrow\rangle_i$ or $|\uparrow\rangle_i$) the atom occupies independent of its state of motion. This is accomplished by applying a few microwatts of $\sigma^-$-polarized light ("detection" beam d of Fig. 1A) resonant with the cycling $|\downarrow\rangle_i \rightarrow {}^2P_{3/2}(F = 3, m_F = -3)$ transition [radiative linewidth $\gamma/2\pi \approx 19.4$ MHz at wavelength ($\lambda$) ≈ 313 nm] and observing the resulting ion fluorescence. Because this radiation does not appreciably couple to the $|\uparrow\rangle_i$ state, the fluorescence reading is proportional to the probability $P_\downarrow$ the ion is in state $|\downarrow\rangle_i$. We collect on average about one photon per measurement cycle when the ion is in the $|\downarrow\rangle_i$ state (29).

**Creation and detection of the Schrödinger cat state.** The ion is first laser-cooled so that the $|\downarrow\rangle_i|n_x = 0\rangle_e$ state is occupied ≈95% of the time as described in (29). We then apply five sequential pulses of the Raman beams (the evolving state of the system is summarized in Table 1 and Fig. 2). In step 1, a $\pi/2$-pulse on the carrier splits the wave function into an equal superposition of states $|\downarrow\rangle_i|0\rangle_e$ and $|\uparrow\rangle_i|0\rangle_e$. In step 2, the displacement beams excite the motion correlated with the $|\uparrow\rangle_i$ component to a coherent state $|\alpha e^{-i\phi/2}\rangle_e$. In step 3, a $\pi$-pulse on the carrier swaps the internal states of the superposition. In step

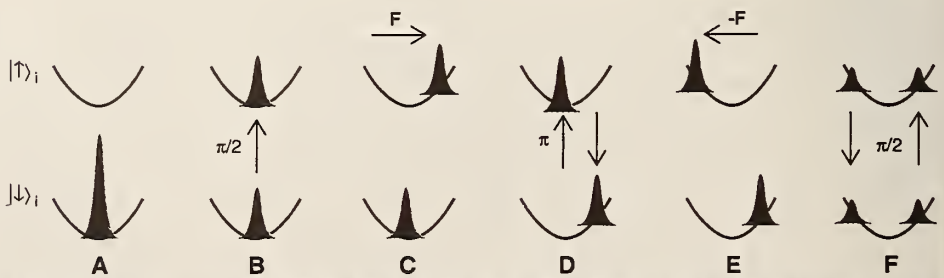


**Fig. 2.** Evolution of the position-space atomic wave packet entangled with the internal states $|\downarrow\rangle_i$ and $|\uparrow\rangle_i$ during creation of a Schrödinger cat state with $\alpha = 3$ and $\phi = \pi$ (see Table 1). The wave packets are snapshots in time, taken when the atom is at the extremum of motion in the harmonic trap (represented by the parabolas). The area of the wave packets corresponds to the probability of finding the atom in the given internal state. (**A**) The initial wave packet corresponds to the quantum ground state of motion after laser-cooling. (**B**) The wave packet is split after a $\pi/2$-pulse on the carrier. (**C**) The $|\uparrow\rangle_i$ wave packet is excited to a coherent state by the force **F** of the displacement beams. Note the force **F** acts only on the $|\uparrow\rangle_i$ wave packet, thereby entangling the internal and motional systems. (**D**) The $|\downarrow\rangle_i$ and $|\uparrow\rangle_i$ wave packets are exchanged following a $\pi$-pulse on the carrier. (**E**) The $|\uparrow\rangle_i$ wave packet is excited to a coherent state by the displacement beam force **−F**, which is out of phase with respect to the force in (C). The state shown in (E) corresponds most closely to Schrödinger's cat (Eqs. 1 and 2). (**F**) The $|\downarrow\rangle_i$ and $|\uparrow\rangle_i$ wave packets are finally combined after a $\pi/2$-pulse on the carrier.

4, the displacement beams excite the motion correlated with the $|\uparrow\rangle_i$ component to a second coherent state $|\alpha e^{i\phi/2}\rangle_e$. In step 5, a final $\pi/2$-pulse on the carrier combines the two coherent states. The relative phases of the above steps are determined by the phases of the RF difference frequencies of the Raman beams (*29*, *30*), which are easily controlled by phase-locking the RF sources.

The state created after step 4 is a superposition of two independent coherent states each correlated with an internal state of the ion, in the spirit of Schrödinger's original thought experiment (Eqs. 1 and 2). We verify this superposition by recombining the coherent wave packets in the final step 5. This creates the following entangled state:

$$|\Psi\rangle = |\downarrow\rangle_i|S_-\rangle_e - i|\uparrow\rangle_i|S_+\rangle_e$$

with

$$|S_\pm\rangle_e \equiv \frac{|\alpha e^{-i\phi/2}\rangle_e \pm e^{i\delta}|\alpha e^{i\phi/2}\rangle_e}{2} \quad (4)$$

For $\phi = \pi$ and $\delta = 0$, the states $|S_\pm\rangle_e$ (when properly normalized) are known as "even" and "odd" Schrödinger cats (*35*).

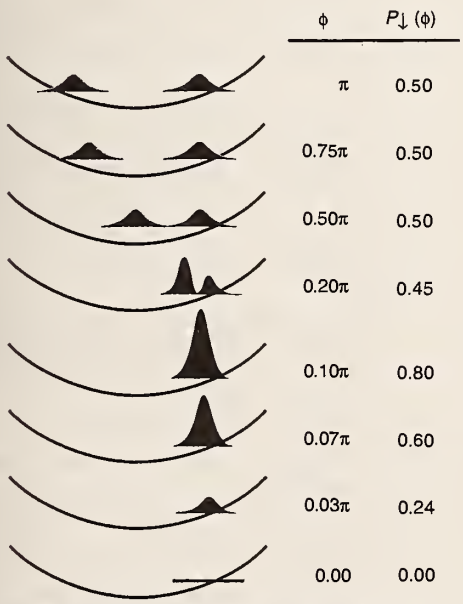


**Fig. 3.** Evolution of the position-space wave packet superposition correlated with the $|\downarrow\rangle_i$ internal state as the phase separation $\phi$ of the two coherent states is varied, for $\alpha = 3$ and $\delta = 0$. The expected signal $P_\downarrow(\phi)$ is the integrated area under these wave packets. Each trace is a snapshot in time, taken when one of the wave packets is at the rightmost turning point in the harmonic trap. The wave packets are maximally separated at $\phi = \pi$ [$P_\downarrow(\phi) \approx 1/2$], but they begin to overlap as $\phi$ gets smaller [$P_\downarrow(\phi)$ oscillates]. Finally, the wave packets destructively interfere at $\phi = 0$ [$P_\downarrow(\phi) = 0$]. This vanishing interference signal is a signature of an odd Schrödinger cat state associated with the $|\downarrow\rangle_i$ state, because $\delta = 0$. Probability conservation is ensured by a similar but constructive interference in the $|\uparrow\rangle_i$ state.

The relative populations of $|\downarrow\rangle_i$ and $|\uparrow\rangle_i$ depend on the motional phase difference $\phi$ between the two coherent wave packets because of the quantum interference between the two coherent states contained in $|S_\pm\rangle_e$. We directly measure this interference by detecting the probability $P_\downarrow(\phi)$ that the ion is in the $|\downarrow\rangle_i$ internal state for a given value of $\phi$. We continuously repeat the experiment—cooling, state preparation, detection—while slowly sweeping the relative coherent state motional phase $\phi$. Figure 3 depicts the expected position basis wave packet $|\langle x|S_-\rangle_e|^2$ correlated with the $|\downarrow\rangle_i$ internal state as a function of $\phi$ for $\delta = 0$ and $\alpha = 3$. The calculated wave packets in the figure are snapshots in time, as each part of the superposition oscillates in the harmonic trap. The measured signal $P_\downarrow(\phi)$ is just the integral of the complete $|\downarrow\rangle_i$ wave packet over space and is time-independent.

$$P_\downarrow(\phi) = \int_{-\infty}^{+\infty} |\langle x|S_-\rangle|^2 dx = \frac{1 - e^{-\alpha^2(1-\cos\phi)}\cos(\delta + \alpha^2\sin\phi)}{2} \quad (5)$$

The wave packets of the superposition are maximally separated in phase space for $\phi \approx \pm\pi$, where the signal is about 1/2 (for large $\alpha$). However, as $\phi$ approaches 0, the wave packets of the superposition begin to overlap, finally interfering completely at $\phi = 0$. For large $\alpha$, the signal $P_\downarrow(\phi)$ acquires oscillations near $\phi = 0$, with the width of the central interference fringe (in $\phi$ space) proportional to $1/\alpha^2$. If the two pieces of the wave packet are not phase-coherent or if the state is a statistical mixture ($\delta$ random between preparations) instead of a coherent superposition of wave packets, the signal would remain constant, $P_\downarrow(\phi) = 1/2$. We experimentally set the phase $\delta$ associated with the internal state superposition by blocking the displacement beams ($\alpha = 0$) and measuring $P_\downarrow = \sin^2(\delta/2)$.

**Superpositions versus mixtures.** In Fig. 4, we display the measured $P_\downarrow(\phi)$ for $\delta = 0$ and a few different values of the coherent state amplitude $\alpha$, which is set by changing the duration $\tau$ of application of the displacement

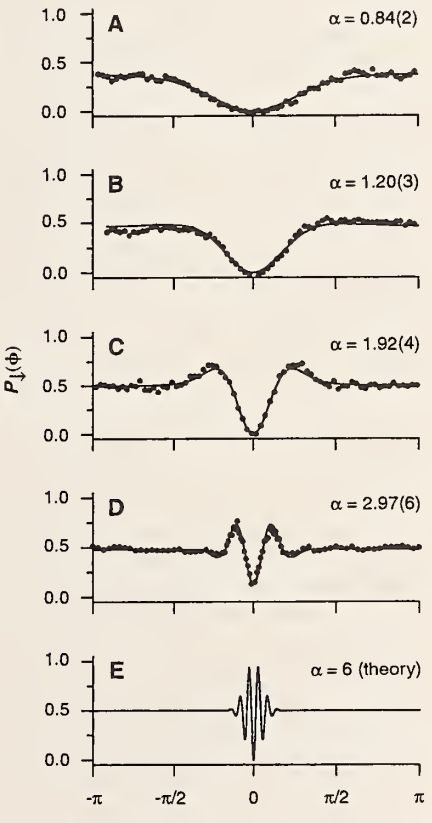


**Fig. 4.** Measured and fit interference signal $P_\downarrow(\phi)$ versus the phase difference $\phi$ of two coherent states for $\delta = 0$. Curves in (**A**) to (**D**) represent measurements for various values of $\tau$ (2, 3, 5, and 15 μs, respectively). As $\tau$ grows, the feature near $\phi = 0$ narrows. The lines are fits of the measurements to the parameter $\alpha$ (Eq. 4), yielding $\alpha$ = 0.84, 1.20, 1.92, and 2.97, respectively. The fit in curve (D) includes a loss of contrast and represents a superposition of two $x_0 \approx 7$-nm wave packets with a maximum separation of $4\alpha x_0 \approx 80$ nm. Curve (**E**) is a theoretical plot for a pair of coherent states with $\alpha = 6$. Each data point in (A) to (D) represents an average of ≈4000 measurements, or 1 s of integration.

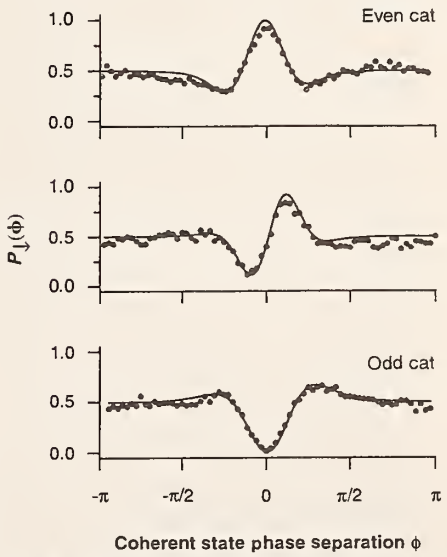


**Fig. 5.** Measured interference signal $P_\downarrow(\phi)$ for three values of $\delta$ ($\alpha \approx 1.5$). The top curve corresponds to $\delta = 1.03\pi$ (approximate even cat state correlated with $|\downarrow\rangle_i$ exhibiting constructive interference), the middle curve to $\delta = 0.48\pi$ [approximate "Yurke-Stoler" cat state (*19*)], and the bottom curve to $\delta = 0.06\pi$ (approximate odd cat state exhibiting destructive interference). Each data point represents an average of ≈4000 measurements, or 1 s of integration.

beams (steps 2 and 4 of Table 1). The presence of the interference feature near $\phi = 0$ verifies that we are producing superposition states instead of statistical mixtures, and the feature clearly narrows as $\alpha$ is increased. We have verified that the interference feature vanishes [$P_\downarrow(\phi) = 1/2$] when $\delta$ is randomized between preparations. In Fig. 5, we present $P_\downarrow(\phi)$ for three different values of the phase $\delta$ while fixing $\tau$. The shape of the interference at $\phi \approx 0$ indicates the parity of the cat state at $\phi = \pm\pi$. Here, we see the transition from an even cat ($\delta \approx \pi$) to the Yurke-Stoler (*19*) cat ($\delta \approx \pi/2$) to an odd cat state ($\delta \approx 0$) correlated with the $|\downarrow\rangle_i$ state.

We extract the amplitude of the Schrödinger cat state by fitting the interference data to the parameter $\alpha$ appearing in Eq. 4. The extracted values of $\alpha$ agree with the independently measured value $\eta\Omega_d\tau$ for short displacement beam durations ($\tau \lesssim 10$ μs) (*36*). We measure coherent-state amplitudes as high as $\alpha \approx 2.97(6)$, corresponding to an average of $\langle n \rangle \approx 9$ vibrational quanta in the state of motion. This indicates a maximum spatial separation of $4\alpha x_0 = 83(3)$ nm, which is significantly larger than the single wave packet size of $x_0 = 7.1(1)$ nm. The individual wave packets are thus clearly separated in phase space.

For longer displacement beam durations ($\tau \gtrsim 10$ μs), the interference signal loses contrast, as evident in Fig. 4D. We believe this is partly due to fluctuations of the ion oscillation frequency $\omega_x$, which causes the motional phase difference $\phi$ to fluctuate from measurement to measurement and wash out narrow interference features. The measured interference signal is sensitive to fluctuations of $\omega_x$ at a time scale that is longer than the time to create the cat ($\tau_c \approx \tau \approx 10$ μs) but shorter than the integrated measurement time (≈1 s per data point in Figs. 4 and 5). The observed loss of contrast indicates a phase fluctuation of $\delta\phi \approx 0.1$ rad, which would be consistent with a fractional ion oscillation frequency fluctuation of $\delta\omega_x/\omega_x \approx 10^{-4}$ in a ≈100-kHz bandwidth. Anharmonicities of the trap (*28*) are expected to contribute to a phase dispersion of only $\approx 10^{-6}$ rad during the creation of the cat.

Decoherence. When a Schrödinger cat consisting of two separated coherent states is coupled to a thermal reservoir, the superposition decays exponentially to a statistical mixture with a rate initially proportional to $\alpha^2$, or the square of the separation of the wave packets (*9*, *10*, *27*). As the separation is made larger (more classical), the lifetime of the superposition shortens. This decoherence process underlies the reason quantum superpositions are not generally seen in the macroscopic world and also illustrates the experimental difficulty in preparing and maintaining even mesoscopic superpositions.

In the experiment, the quantum interference signal is only sensitive to decoherence during the period of time $\tau_c$ between the generation of the two coherent states (steps 2 and 4 of Table 1). This is because only the internal atomic state is detected, and once the second coherent state is produced (step 4), the internal and motional states do not interact, even if the motion equilibrates with an external reservoir. We therefore expect the interference signal (Eq. 4) to exhibit a contrast of $\exp(-\alpha^2\lambda\tau_c)$, where $\lambda$ is the temperature-dependent relaxation rate to the thermal reservoir (*10*). The loss of contrast we observe may involve the onset of decoherence, although it is difficult to make a quantitative comparison because we do not know the spectrum and effective temperature of the supposed reservoir. We note that we have previously measured a heating rate of $\partial\langle n \rangle/\partial t \approx 10^3\ s^{-1}$ (*29*), but because the source of this heating is not understood at the present time, it is difficult to characterize its effect on decoherence.

The next step is to deliberately induce decoherence of the Schrödinger cat by coupling the system to "engineered" reservoirs during the interval $\tau_c$. For instance, a uniform stochastic electric field can be applied, whose coupling to the ion could simulate a thermal reservoir at a controllable temperature. Alternatively, one can pulse the Raman beams and controllably allow spontaneous emission to occur during the interval $\tau_c$ [similar to stimulated Raman cooling (*29*)]. With this coupling, one can simulate thermal, zero-temperature, squeezed, and other reservoirs (*37*). By monitoring the contrast of the interference signal, it should then be possible to study the decoherence of the Schrödinger cat to these known reservoirs. The effects of decoherence might also be measured by mapping the complete density matrix of the Schrödinger cat state, as proposed in recent tomographic schemes (*38*).

We finally note that our technique for preparing Schrödinger cat superpositions of two coherent states in one dimension can easily be extended to create superpositions of more than two coherent states and superpositions in two and three dimensions. This technique may also be useful for the creation of superposition states of the collective motion of many trapped atoms.

## REFERENCES AND NOTES


1. P. A. M. Dirac, *The Principles of Quantum Mechanics* (Clarendon, Oxford, ed. 4, 1984), p. 12.
2. A. Einstein, B. Podolsky, N. Rosen, *Phys. Rev.* **47**, 777 (1935).
3. E. Schrödinger, *Naturwissenschaften* **23**, 807 (1935); translation in (*6*).
4. Issues involving observation by the cat itself (by virtue of its consciousness) are beyond the scope of this article. For our purposes, the cat can be replaced, for example, by an object placed in a superposition of macroscopically separated positions.
5. In the literature, there is not universal agreement about the definition of the "cat" state. As opposed to the definition used in Eqs. 1 and 2 of this article, some authors prefer to define a Schrödinger cat state as $(|x_1\rangle + |x_2\rangle)/\sqrt{2}$, or a superposition of two classical-like states that are not correlated with the state of a second system. In the analysis of the state shown in Eq. 2, we in fact create the state corresponding to this alternate definition.
6. J. A. Wheeler and W. H. Zurek, Eds., *Quantum Theory and Measurement* (Princeton Univ. Press, Princeton, NJ, 1983).
7. N. Bohr, *Nature* **121**, 580 (1928); *Phys. Rev.* **48**, 696 (1935).
8. W. Heisenberg, *Z. Phys.* **43**, 172 (1927); translation in (*6*).
9. W. H. Zurek, *Phys. Today* **44**, 36 (October 1991).
10. D. F. Walls and G. J. Milburn, *Phys. Rev. A* **31**, 2403 (1985); C. M. Savage and D. F. Walls, *ibid.* **32**, 2316 (1985); M. J. Collett, *ibid.* **38**, 2233 (1988).
11. D. P. DiVincenzo, *Science* **270**, 255 (1995); I. L. Chuang, R. Laflamme, P. W. Shor, W. H. Zurek, *ibid.*, p. 1633.
12. C. H. Bennett, *Phys. Today* **48**, 24 (October, 1995).
13. L. Marton, J. Arol Simson, J. A. Suddeth, *Phys. Rev.* **90**, 490 (1954).
14. H. Maier-Leibnitz and T. Springer, *Z. Phys.* **167**, 368 (1962).
15. O. Carnal and J. Mlynek, *Phys. Rev. Lett.* **66**, 2689 (1991); D. W. Keith, C. R. Ekstrom, Q. A. Turchette, D. E. Pritchard, *ibid.*, p. 2693; M. Kasevich and S. Chu, *ibid.* **67**, 181 (1991); J. Lawall *et al.*, *ibid.* **75**, 4194 (1995).
16. L. D. Noordam, D. I. Duncan, T. F. Gallagher, *Phys. Rev. A* **45**, 4734 (1992); R. R. Jones, C. S. Raman, D. W. Schumacher, P. H. Bucksbaum, *Phys. Rev. Lett.* **71**, 2575 (1993); M. W. Noel and C. R. Stroud Jr., *ibid.* **75**, 1252 (1995).
17. J. Janszky, A.V. Vinogradov, T. Kobayashi, Z. Kis, *Phys. Rev. A* **50**, 1777 (1994); I. A. Walmsley and M. G. Raymer, *ibid.* **52**, 681 (1995).
18. A. J. Leggett and A. Garg, *Phys. Rev. Lett.* **54**, 857 (1985).
19. B. Yurke and D. Stoler, *ibid.* **57**, 13 (1986); *Phys. Rev. A* **35**, 4846 (1987); *ibid.* **36**, 1955 (1987).
20. S. J. D. Phoenix and P. L. Knight, *Ann. Phys.* **186**, 381 (1988); J. Gea-Banacloche, *Phys. Rev. Lett.* **65**, 3385 (1990); V. Bužek, H. Moya-Cessa, P. L. Knight, S. J. D. Phoenix, *Phys. Rev. A* **45**, 8190 (1992).
21. J. J. Slosser, P. Meystre, E. M. Wright, *Opt. Lett.* **15**, 233 (1990).
22. C. M. Savage, S. L. Braunstein, D. F. Walls, *ibid.*, p. 628.
23. M. Brune, S. Haroche, J. M. Raimond, L. Davidovich, N. Zagury, *Phys. Rev. A* **45**, 5193 (1992); S. Haroche and J. M. Raimond, in *Cavity Quantum Electrodynamics*, P. Berman, Ed. (Academic Press, New York, 1994), pp. 123–170.
24. J. F. Poyatos, J. I. Cirac, R. Blatt, P. Zoller, in preparation.
25. R. L. de Matos Filho and W. Vogel, *Phys. Rev. Lett.* **76**, 608 (1996).
26. L. Davidovich, A. Maali, M. Brune, J. M. Raimond, S. Haroche, *ibid.* **71**, 2360 (1993).
27. P. Goetsch, R. Graham, F. Haake, *Phys. Rev. A* **51**, 136 (1995).
28. S. R. Jefferts, C. Monroe, E. W. Bell, D. J. Wineland, *ibid.*, p. 3112.
29. C. Monroe *et al.*, *Phys. Rev. Lett.* **75**, 4011 (1995).
30. D. M. Meekhof, C. Monroe, B. E. King, W. M. Itano, D. J. Wineland, *ibid.* **76**, 1796 (1996).
31. D. J. Wineland *et al.*, in *Laser Manipulation of Atoms and Ions*, E. Arimondo, W. D. Phillips, F. Strumia, Eds. (North-Holland, Amsterdam, 1992), pp. 562–563.
32. R. J. Glauber, *Phys. Rev.* **131**, 2766 (1963); *ibid.*, p. 2529.
33. In the laboratory frame, the coherent-state parameter $\beta$ has the periodic time dependence $\beta_L = \alpha e^{i(\theta - \omega t)}$, where $\omega$ is the frequency of the harmonic oscillator. Throughout the article, this time dependence is suppressed by working in an interaction frame where $\beta = \beta_L e^{i\omega t}$.
34. The effects of coupling to the $^2P_{3/2}$ excited state are small (detuning ≈ −210 GHz) and can be neglected here.
35. J. Peřina, *Quantum Statistics of Linear and Nonlinear Optical Phenomena* (Reidel, Dordrecht, 1984).

36. For large values of $\eta\Omega_0\tau$, we expect $\alpha(\tau)$ to saturate because of nonlinear correction factors that limit the amplitude of the coherent state and introduce amplitude squeezing [see (*31*) and W. Vogel and R. L. de Matos Filho, *Phys. Rev. A* **52**, 4214 (1995)]. For the experimental Lamb-Dicke parameter of ~0.2, these corrections are not significant for $\alpha \lesssim 5$.
37. J. F. Poyatos, J. I. Cirac, P. Zoller, in preparation.
38. D. T. Smithey, M. Beck, M. G. Raymer, A. Faridani, *Phys. Rev. Lett.* **70**, 1244 (1993); S. Wallentowitz and W. Vogel, *ibid.* **75**, 2932 (1995); J. I. Cirac and P. Zoller, in preparation.
39. We acknowledge key assistance from W. M. Itano, D. Leibfried, J. C. Bergquist, and J. Erickson and useful discussions with J. I. Cirac, P. Zoller, and D. Walls. We thank M. Young, S. Mechels, and D. Lee for critical comments on the manuscript. This work is supported by the U.S. Office of Naval Research and the U.S. Army Research Office.

2 January 1996; accepted 6 March 1996



TN-47

PHYSICAL REVIEW
LETTERS

VOLUME 77 | 18 NOVEMBER 1996 | NUMBER 21

# Experimental Determination of the Motional Quantum State of a Trapped Atom

D. Leibfried, D. M. Meekhof, B. E. King, C. Monroe, W. M. Itano, and D. J. Wineland
*Time and Frequency Division, National Institute of Standards and Technology, Boulder, Colorado 80303-3328*
(Received 11 July 1996)

We reconstruct the density matrices and Wigner functions for various quantum states of motion of a harmonically bound $^9Be^+$ ion. We apply coherent displacements of different amplitudes and phases to the input state and measure the number state populations. Using novel reconstruction schemes we independently determine both the density matrix in the number state basis and the Wigner function. These reconstructions are sensitive indicators of decoherence in the system. [S0031-9007(96)01713-9]

PACS numbers: 03.65.Bz, 32.80.Qk, 42.50.Vk

In quantum mechanics, once the density matrix of a system is determined, all knowable information is at hand. All the elusive quantum properties, like superpositions and decoherence are reflected in it. Although it is well established that the wave function or density matrix of a single quantum system cannot be determined in general, multiple measurements on an ensemble of identically prepared quantum systems can reveal their density matrix.

Early work on determination of the quantum state in such an ensemble was reviewed by Royer [1]. In quantum optics, numerous reconstruction schemes have been proposed, based on the measurement of probability distributions in different representations [2]. More recently, proposals for determining the motional state of a trapped atom have been published [3–6], partially inspired by the analogy between cavity QED and a trapped atom interacting with laser fields [7–9].

Few experiments have succeeded in determining the density matrices or Wigner functions of quantum systems. Angular momentum density matrices were measured in collisionally produced hydrogen [10], the Wigner function and density matrix of a mode of light was experimentally mapped by optical homodyne tomography [11,12], and the Wigner function of the vibrational degree of freedom of a diatomic molecule was reconstructed [13]. In this Letter we present the theory and experimental demonstration of two novel schemes that allow us to reconstruct both the density matrix in the number state basis and the Wigner function of the motional state of a single trapped atom. A unique feature of our experiment is that we are able to prepare a variety of nonclassical input states [9] which can, for example, exhibit negative values of the Wigner function. To our knowledge these are the first experimental reconstructions revealing a negative Wigner function in position-momentum space.

In order to measure the complete state of motion, we controllably displace the input state to several different locations in phase space. Specifically, a coherent displacement [9,14] $U(-\alpha) = U^\dagger(\alpha) = \exp(\alpha^* a - \alpha a^\dagger)$ ($-\alpha$ is used for convenience below) is first applied to the input motional state. Here $a$ and $a^\dagger$ are the lowering and raising operators of the harmonically bound atom (frequency $\omega_x$), while $\alpha$ is the complex parameter characterizing the coherent amplitude and phase. We then apply radiation to the atom for a time $t$, which induces a resonant exchange between states $|\downarrow\rangle|k\rangle$ and $|\uparrow\rangle|k+1\rangle$ in a Jaynes-Cummings-type interaction [7–9]. Here $|\downarrow\rangle$ and $|\uparrow\rangle$ denote two selected internal states, and $|k\rangle$ is the motional eigenstate with energy $\hbar\omega_x(k + 1/2)$. For each $\alpha$ and time $t$ the population $P_\downarrow(t, \alpha)$ of the $|\downarrow\rangle$ level is then measured by monitoring the fluorescence produced in driving a resonant dipole cycling transition [9]. The internal state at $t = 0$ is always prepared to be $|\downarrow\rangle$, so the signal averaged over many measurements is [15]

$$P_\downarrow(t, \alpha) = \frac{1}{2}\left\{1 + \sum_{k=0}^{\infty} Q_k(\alpha)\cos(2\Omega_{k,k+1}t)e^{-\gamma_k t}\right\}, \quad (1)$$

(where $\Omega_{k,k+1}$ are the Rabi frequencies and $\gamma_k$ their experimentally determined decay constants). Because the Rabi frequency between $|\downarrow\rangle|k\rangle$ and $|\uparrow\rangle|k+1\rangle$ depends on $k$ [9], the populations $Q_k(\alpha)$ of the motional eigenstates after the displacement can be extracted [7–9,16]. We repeat this scheme for several magnitudes and phases of the coherent displacement and finally reconstruct the density matrix and the Wigner function from the measured displaced populations $Q_k(\alpha)$.

To reconstruct the density matrix $\rho$ in the number state base, we use the relation

$$Q_k(\alpha) = \langle k|U^\dagger(\alpha)\rho U(\alpha)|k\rangle . \tag{2}$$

Note that $Q_0(\alpha)/\pi$ is the $Q$-quasi-probability distribution [4]. Rewriting (2) we get

$$Q_k(\alpha) = \frac{1}{k!}\langle 0|a^k U^\dagger(\alpha)\rho U(\alpha)(a^\dagger)^k|0\rangle = \frac{1}{k!}\langle\alpha|(a-\alpha)^k\rho(a^\dagger-\alpha^*)^k|\alpha\rangle = \frac{e^{-|\alpha|^2}|\alpha|^{2k}}{k!}\sum_{n,m=0}^{\infty}\sum_{j,j'=0}^{k}\frac{(\alpha^*)^{n-j}\alpha^{m-j'}}{n!\,m!}$$
$$\times(-1)^{-j-j'}\binom{k}{j}\binom{k}{j'}\sqrt{(m+j)!\,(n+j')!}\,\rho_{n+j',m+j} . \tag{3}$$

To separate the contributions of different matrix elements we may displace the state along a circle,

$$\alpha_p = |\alpha|\exp[i(\pi/N)p], \tag{4}$$

where $p\in\{-N,\ldots,N-1\}$. The number of angles $2N$ on that circle determines the maximum number state $n_{\max} = N-1$ included in the reconstruction. This allows us to perform a discrete Fourier transform of Eq. (3) evaluated at the values $\alpha_p$, and we obtain the matrix equations

$$Q_k^{(l)} \equiv \frac{1}{2N}\sum_{p=-N}^{N-1} Q_k(\alpha_p)e^{-il(\pi/N)p} = \sum_{n=\max(0,-l)}^{\infty}\gamma_{kn}^{(l)}\rho_{n,n+l} , \tag{5}$$

with matrix elements

$$\gamma_{kn}^{(l)} = \frac{e^{-|\alpha|^2}|\alpha|^{2k}}{k!}\sum_{j'=0}^{\min(k,n)}\sum_{j=0}^{\min(k,l+n)}|\alpha|^{2(n-j-j')+l} \times(-1)^{-j-j'}\binom{k}{j}\binom{k}{j'}\frac{\sqrt{(l+n)!\,n!}}{(l+n-j)!\,(n-j')!} , \tag{6}$$

for every diagonal $\rho_{n,n+l}$ of the density matrix. To keep the matrix dimension finite, a cutoff for the maximum $n$ in Eq. (5) is introduced, based on the magnitude of the input state. For an unknown input state an upper bound on $n$ may be extracted from the populations $Q_k(\alpha)$. If these are negligible for $k$'s higher than a certain $k_{\max}$ and all displacements $\alpha$, they are negligible in the input state as well, and it is convenient to truncate Eq. (5) at $n_{\max} = k_{\max}$. The resulting matrix equation is overcomplete for some $l$, but the diagonals $\rho_{n,n+l}$ can still be reconstructed by a general linear least-squares method [17].

The Wigner function for every point $\alpha$ in the complex plane can be determined by the simple sum [16,18],

$$W(\alpha) = \frac{2}{\pi}\sum_{n=0}^{\infty}(-1)^n Q_n(\alpha) . \tag{7}$$

In practice, the sum is carried out only to a finite $n_{\max}$, as described above. In contrast to our density matrix method it provides a direct method to obtain the Wigner function at the point $\alpha$ in phase space, without the need to measure at other values of $\alpha$. This also distinguishes the method from preceding experiments that determined the Wigner function by inversion of integral equations (tomography) [11,13].

In our experiment, the trapped atom is a single $^9Be^+$ ion, stored in a rf Paul trap [19] with a pseudopotential oscillation frequency of $\omega_x/2\pi \approx 11.2$ MHz [20]. The ion is laser cooled using sideband cooling with stimulated Raman transitions [21] between the $^2S_{1/2}$ ($F=2$, $m_F=-2$) and $^2S_{1/2}$ ($F=1$, $m_F=-1$) hyperfine ground states, which are denoted by $|\downarrow\rangle$ and $|\uparrow\rangle$, respectively, and are separated by approximately 1.25 GHz.

The preparation of coherent and number (Fock) states of motion starting from the ground state is described in [9]. The coherent displacement we need for the reconstruction mapping is provided by a spatially uniform classical driving field [14,19] at the trap oscillation frequency. The rf oscillators that create and displace the state are phase locked to control their relative phase. Different displacements are realized by varying the amplitude and the phase of the displacement oscillator. For every displacement $\alpha$, we record $P_\downarrow(t,\alpha)$. $Q_n(\alpha)$ can be found from the measured traces with a singular-value decomposition [9]. To determine the amplitude $|\alpha|$ of each displacement, the same driving field is applied to the $|n=0\rangle$ ground state, and the resulting collapse and revival trace is fitted to that of a coherent state [9].

The accuracy of the reconstruction is limited by the uncertainty in the applied displacements, the errors in the determination of the displaced populations, and decoherence during the measurement. The value of the Wigner function is found by a sum with simple error propagation rules. The density matrix is constructed by a linear least-squares method, and it is straightforward to calculate a covariance matrix [17]. As the size of the input state increases, decoherence and the relative accuracy of the displacements become more critical, thereby increasing their uncertainties.

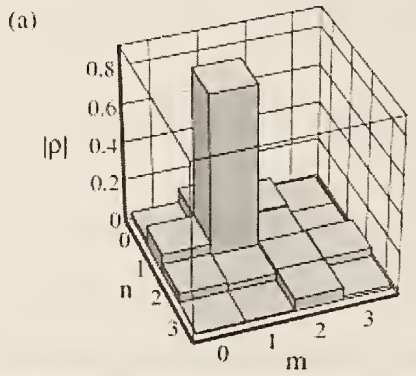


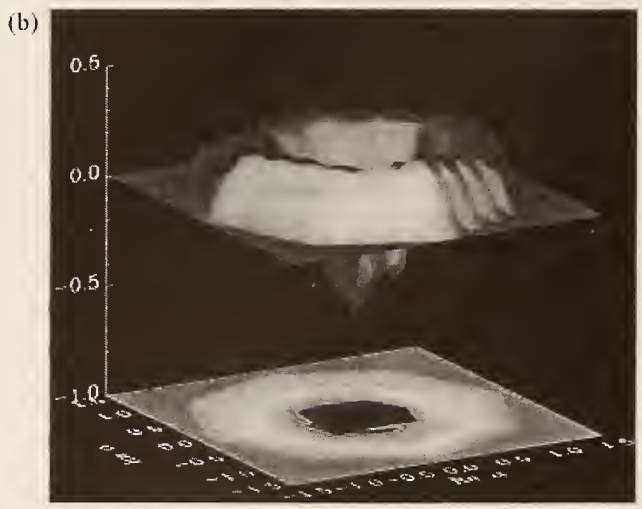


FIG. 1. (a) Reconstructed number-state density matrix amplitudes $\rho_{nm}$ for an approximate $|n = 1\rangle$ number state. The coherent reconstruction displacement amplitude was $|\alpha| = 1.15(3)$. The number of relative phases $N = 4$ in Eq. (4), so $n_{\max} = 3$. (b) (color) Surface and contour plots of the Wigner function $W(\alpha)$ of the $|n = 1\rangle$ number state. The plotted points are the result of fitting a linear interpolation between the actual data points to a 0.1 by 0.1 grid. The octagonal shape is an artifact of the eight measured phases per radius. The white contour represents $W(\alpha) = 0$. The negative values around the origin highlight the nonclassical character of this state.

In Fig. 1, we show the reconstruction of both the number state density matrix (a) and Wigner function (b) of an approximate $|n = 1\rangle$ number state. The large negative part of the Wigner function around the origin highlights the fact that the $|n = 1\rangle$ number state is nonclassical.

In contrast, the state closest to a classical state of motion in a harmonic oscillator is a coherent state. As one example, we have excited and reconstructed a coherent state with amplitude $|\beta| \approx 0.67$. The experimental amplitude and phase of the number state density matrix are depicted in Fig. 2. The off-diagonal elements are generally smaller for the experiment than we would expect from the theory of a pure coherent state. In part, this is due to decoherence during the measurement, so the reconstruction shows a mixed state character rather than a pure coherent state

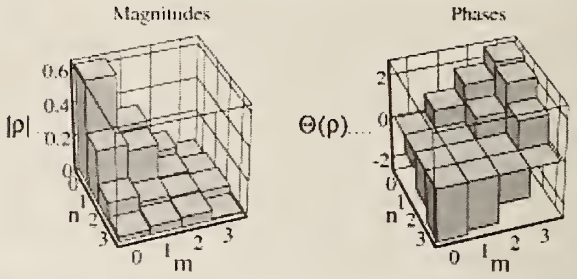


FIG. 2. Experimental amplitudes $\rho_{nm}$ and phases $\Theta(\rho_{nm})$ of the number-state density matrix elements of a $|\beta| \approx 0.67$ coherent state. The state was displaced by $|\alpha| = 0.92$, for $N = 4$ in Eq. (4).

signature. This view is further supported by the fact that farther off-diagonal elements seem to decrease faster than direct neighbors of the diagonal. The reconstructed Wigner function of a coherent state with amplitude $|\beta| \approx 1.5$ is shown in Fig. 3.

Next we created a coherent superposition of $|n = 0\rangle$ and $|n = 2\rangle$ number states. This state is ideally suited to demonstrate the sensitivity of the reconstruction to coherences. The only nonzero off-diagonal elements should be $\rho_{02}$ and $\rho_{20}$, with a magnitude of $|\rho_{02}| = |\rho_{20}| = \sqrt{\rho_{00}\rho_{22}} \approx 0.5$ for a superposition with about equal probability of being measured in the $|n = 0\rangle$ or $|n = 2\rangle$ state. In the reconstruction shown in Fig. 4 the populations $\rho_{00}$ and $\rho_{22}$ are somewhat smaller, due to imperfections in the

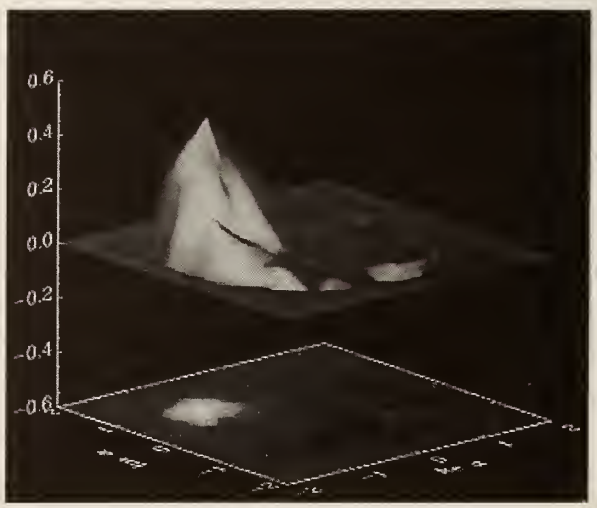


FIG. 3(color). Surface and contour plots of the reconstructed Wigner function of a coherent state. The plotted points are the result of fitting a linear interpolation between the actual data points to a 0.13 by 0.13 grid. The approximately Gaussian minimum uncertainty wave packet is centered around a coherent amplitude of about 1.5 from the origin. The half width at half maximum is about 0.6, in accordance with the minimum uncertainty half width of $\sqrt{(1/2)\ln(2)} \approx 0.59$. To suppress artifacts in the Wigner function summation, we have averaged over $n_{\max} = 5$ and $n_{\max} = 6$ truncations, as suggested by M. Collett.

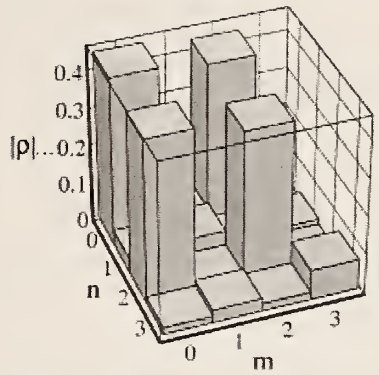


FIG. 4. Reconstructed density matrix amplitudes of an approximate $1/\sqrt{2}(|n=0\rangle - i|n=2\rangle)$ state. The state was displaced by $|\alpha| = 0.79$ for $N = 4$ in Eq. (4). The amplitudes of the coherences indicate that the reconstructed density matrix is close to that of a pure state.

preparation, but the coherence has the expected value of $|\rho_{20}| = |\rho_{02}| \approx \sqrt{\rho_{00}\rho_{22}}$.

In contrast to the above, a thermal state should exhibit no coherences. In the experiment such a state was prepared by (only) Doppler cooling the ion [9]. The reconstruction of the resulting thermal state with mean occupation number $\overline{n} \approx 1.3$ is depicted in Fig. 5. As expected, there are no coherences, and the diagonal, which gives the number state occupation, shows an exponential behavior within the experimental errors.

In summary, we have created number, thermal, coherent, and number-state superposition states of motion of a trapped atom and determined both density matrices in the number-state basis and Wigner functions of these states. The methods are suitable for arbitrary quantum states of motion, including mesoscopic superposition states (Schrödinger's cat states) [22] and could be a useful tool to study decoherence in these states. These methods could also be implemented in cavity-QED experiments to determine the states of an electromagnetic field (using available techniques) [23], or in neutral atom traps where dipole forces could provide the drive for a coherent displacement [9,22]. Another straightforward extension of this work in ion traps would be to perform tomography on entangled motional and internal states of two or more trapped ions, by combining the motional state reconstruction with Ramsey-type and correlation experiments.

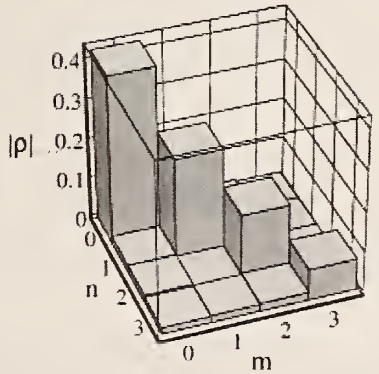


FIG. 5. Reconstructed density matrix of a $\overline{n} \approx 1.3$ thermal state. This state was displaced by $|\alpha| = 0.78$, for $N = 4$ in Eq. (4). As one would expect for a thermal state, no coherences are present within the experimental uncertainties and the populations drop exponentially for higher $n$.

This work is supported by the U.S. National Security Agency, the Office of Naval Research, and the Army Research Office. D. L. acknowledges a Deutsche Forschungsgemeinschaft research grant. D. M. M. is supported by a N. R. C. postdoctoral fellowship. We thank W. Vogel for pointing out the connection of the Wigner function to the displaced populations and J. I. Cirac and P. Zoller for stimulating discussions. We acknowledge important contributions by J. Bergquist and helpful comments on the manuscript by M. Young, J. J. Bollinger, P. Huang, and M. Holland.

*Note added.*—After submission of this work we have learned that Mlynek *et al.* have measured the Wigner function of atoms in an interferometer [24], and that Opatrny *et al.* [25] propose a very similar method to reconstruct the density matrix of a light field in the number-state basis.

[1] A. Royer, Found. Phys. **19**, 3 (1989).
[2] K. Vogel and H. Risken, Phys. Rev. A **40**, 2847 (1989).
[3] S. Wallentowitz and W. Vogel, Phys. Rev. Lett. **75**, 2932 (1995).
[4] J. F. Poyatos, R. Walser, J. I. Cirac, P. Zoller, and R. Blatt, Phys. Rev. A **53**, R1966 (1996).
[5] C. D'Helon and G. J. Milburn, Phys. Rev. A **54**, R25 (1996).
[6] P. J. Bardroff, C. Leichtle, G. Schrade, and W. P. Schleich (to be published).
[7] C. A. Blockley, D. F. Walls, and H. Risken, Europhys. Lett. **77**, 509 (1992).
[8] J. I. Cirac, R. Blatt, A. S. Parkins, and P. Zoller, Phys. Rev. A **49**, 1202 (1994).
[9] D. M. Meekhof, C. Monroe, B. E. King, W. M. Itano, and D. J. Wineland, Phys. Rev. Lett. **76**, 1796 (1996).
[10] J. R. Ashburn, R. A. Cline, P. J. M. van der Burgt, W. B. Westerveldt, and J. S. Risley, Phys. Rev. A **41**, 2407 (1990).
[11] D. T. Smithey, M. Beck, M. G. Raymer, and A. Faridani, Phys. Rev. Lett. **70**, 1244 (1993).
[12] G. Breitenbach, T. Müller, S. F. Pereira, J. Ph. Poizat, S. Schiller, and J. Mlynek, J. Opt. Soc. B **12**, 2304 (1995).
[13] T. J. Dunn, I. A. Walmsley, and S. Mukamel, Phys. Rev. Lett. **74**, 884 (1995).
[14] P. Carruthers and M. M. Nieto, Am. J. Phys. **7**, 537 (1965).
[15] Equation (2) of Ref. [9] is in error and should be replaced by Eq. (1) here.
[16] In this experiment we can consider the internal atomic state to be the detector. If we neglect noise and decoherence in the mapping operations, the motional state information is mapped according to Eq. (1) with unit

efficiency onto the $|\downarrow\rangle$ state. Therefore, to have unit detection efficiency in the experiment, it is not necessary to detect the $|\downarrow\rangle$ state with unit efficiency. The analogy with photon detection would be a 100% efficient detector which is read out only sporadically.

[17] W.H. Press, S.A. Teukolsky, W.T. Vetterling, and B.P. Flannery, *Numerical Recipes* (Cambridge University Press, Cambridge, 1986), Chap. 14.3.

[18] ~~A. Royer,~~ Phys. Rev. Lett. **52**, 1064 (1984); H. Moya-Cessa and P.L. Knight, Phys. Rev. A **48**, 2479 (1993); S. Wallentowitz and W. Vogel, Phys. Rev. A **53**, 4528 (1996); K. Banaszek and K. Wodkiewicz, Phys. Rev. Lett. **76**, 4344 (1996).

[19] S. Jefferts, C. Monroe, E. Bell, and D.J. Wineland, Phys. Rev. A **51**, 3112 (1995).

K. Wódkiewicz

[20] For the parameters of this experiment, the effects of rf "micromotion" are small and can be neglected. A thorough treatment which includes the micromotion is described in Ref. [6].

[21] C. Monroe, D.M. Meekhof, B.E. King, S.R. Jefferts, W.M. Itano, D.J. Wineland, and P.L. Gould, Phys. Rev. Lett. **75**, 4011 (1995).

[22] C. Monroe, D.M. Meekhof, B.E. King, and D.J. Wineland, Science **272**, 1131 (1996).

[23] M. Brune, F. Schmidt-Kaler, A. Maali, J. Dreyer, E. Hagley, J.M. Raymond, and S. Haroche, Phys. Rev. Lett. **76**, 1800 (1996).

[24] J. Mlynek (private communication).

[25] T. Opatrny and D.-G. Welsch (to be published).

Invited Paper

# Quantum harmonic oscillator state synthesis and analysis*

W. M. Itano, C. Monroe, D. M. Meekhof,
D. Leibfried, B. E. King, and D. J. Wineland

Time and Frequency Division
National Institute of Standards and Technology
Boulder, Colorado 80303 USA

## ABSTRACT

We laser-cool single beryllium ions in a Paul trap to the ground ($n = 0$) quantum harmonic oscillator state with greater than 90% probability. From this starting point, we can put the atom into various quantum states of motion by application of optical and rf electric fields. Some of these states resemble classical states (the coherent states), while others are intrinsically quantum, such as number states or squeezed states. We have created entangled position and spin superposition states (Schrödinger cat states), where the atom's spatial wavefunction is split into two widely separated wave packets. We have developed methods to reconstruct the density matrices and Wigner functions of arbitrary motional quantum states. These methods should make it possible to study decoherence of quantum superposition states and the transition from quantum to classical behavior. Calculations of the decoherence of superpositions of coherent states are presented.

**Keywords:** quantum state generation, quantum state tomography, laser cooling, ion storage, quantum computation

## 1. INTRODUCTION

In a series of studies we have prepared single, trapped, $^9Be^+$ ions in various quantum harmonic oscillator states and performed measurements on those states. In this article, we summarize some of the results. Further details are given in the original reports.[1–5]

The quantum states of the simple harmonic oscillator have been studied since the earliest days of quantum mechanics. For example, the harmonic oscillator was among the first applications of the matrix mechanics of Heisenberg[6] and the wave mechanics of Schrödinger.[7] The theoretical interest in harmonic oscillators is partly due to the fact that harmonic oscillator problems often have exact solutions. In addition, physical systems, such as vibrating molecules, mechanical resonators, or modes of the electromagnetic field, can be modeled as harmonic oscillators, so that the theoretical results can be compared to experiments.

A single ion in a Paul trap can be described effectively as a simple harmonic oscillator, even though the Hamiltonian is actually time-dependent, so no stationary states exist. For practical purposes, the system can be treated as if the Hamiltonian were that of an ordinary, time-independent harmonic oscillator (see, e.g., Refs. 8,9).

## 2. SYSTEM AND EFFECTIVE HAMILTONIAN

The effective Hamiltonian for the center-of-mass secular motion is that of an anisotropic three-dimensional harmonic oscillator. If we choose an interaction Hamiltonian which affects only the $x$-motion, then we can deal with the one-dimensional harmonic oscillator Hamiltonian,

$$H_x = \hbar\omega_x a_x^\dagger a_x, \tag{1}$$


Send correspondence to W.M.I. E-mail: witano@nist.gov; telephone: 303-497-5632; fax: 303-497-6461

where $\omega_x$ is the secular frequency for the $x$-motion, and $a_x^\dagger$ and $a_x$ are the creation and annihilation operators for the quanta of the $x$-oscillation mode. The constant term $\hbar\omega_x/2$, which results from the usual quantization procedure, has been left out for convenience. The eigenstates of $H_x$ are $|n_x\rangle$, where

$$H_x|n_x\rangle = n_x\hbar\omega_x|n_x\rangle. \tag{2}$$

The internal states of the $^9Be^+$ ion which are the most important for the experiments are shown in Fig. 1. We are mostly concerned with the hyperfine-Zeeman sublevels of the ground $2s\,^2S_{1/2}$ electronic state, which are denoted by $|2s\,^2S_{1/2}; F, M_F\rangle$, where **F** is the total angular momentum, and $M_F$ is the eigenvalue of $F_z$. The $^9$Be nucleus has spin 3/2. Of chief importance are $|2s\,^2S_{1/2}; 2, 2\rangle$, abbreviated as $|\downarrow\rangle$, and $|2s\,^2S_{1/2}; 1, 1\rangle$, abbreviated as $|\uparrow\rangle$. The hyperfine-Zeeman sublevels of the $2p\,^2P_J$ ($J = 1/2$ or $3/2$) fine-structure multiplet also play a role, either as intermediate states in stimulated Raman transitions or as the final states in resonantly-driven single-photon transitions used for laser cooling or state detection. We denote these states by $|2p\,^2P_J; F, M_F\rangle$. The energy separation of $|\uparrow\rangle$ and $|\downarrow\rangle$ is $\hbar\omega_0$, where $\omega_0 \approx 2\pi \times 1.250$ GHz. They are coupled by laser beams R1 and R2, through the intermediate $|2p\,^2P_{1/2}; 2, 2\rangle$ state. The frequency detuning from the intermediate state is $\Delta$, where $\Delta \approx -2\pi \times 12$ GHz.

If we restrict the internal states to the space spanned by $|\uparrow\rangle$ and $|\downarrow\rangle$, then the internal Hamiltonian can be written as

$$H_{\uparrow\downarrow} = \frac{\hbar\omega_0}{2}\sigma_z, \tag{3}$$

where $\sigma_z$ is a Pauli spin matrix whose nonzero matrix elements are$\langle\uparrow|\sigma_z|\uparrow\rangle = +1$ and $\langle\downarrow|\sigma_z|\downarrow\rangle = -1$.

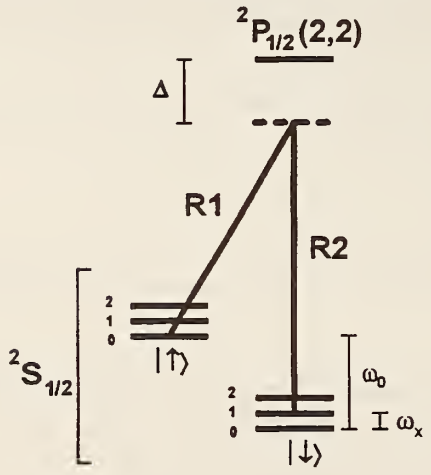


**Figure 1.** Internal and motional energy levels of a $^9Be^+$ ion. The $|\uparrow\rangle$ and $|\downarrow\rangle$ states are particular hyperfine-Zeeman components of the ground $^2S_{1/2}$ state, separated in energy by $\hbar\omega_0$. Each internal state can exist in any of a ladder of vibrational energy states $|n_x\rangle$, where $n_x = 0, 1, 2, \ldots$, separated in energy by $\hbar\omega_x$, where $\omega_x \approx 2\pi \times 11.2$ MHz.

The total effective Hamiltonian for the system consisting of the internal $|\uparrow\rangle$ and $|\downarrow\rangle$ states and the $x$ motional degree of freedom is

$$H = H_{\uparrow\downarrow} + H_x + H_{\rm int}, \tag{4}$$

where $H_{\rm int}$ is the effective interaction Hamiltonian coupling due to the two laser beams R1 and R2 in Fig. 1. We define an interaction-picture operator $\mathcal{O}^I$ in terms of a Schrödinger-picture operator $\mathcal{O}^S$ as

$$\mathcal{O}^I(t) = e^{iH_{\uparrow\downarrow}t/\hbar}\mathcal{O}^S(t)e^{-iH_{\uparrow\downarrow}t/\hbar}. \tag{5}$$

The effective interaction Hamiltonian in the interaction picture and the rotating wave approximation is

$$H_{\rm int}^I = \hbar g\left(\sigma_+ e^{i\eta(a_x^\dagger + a_x) - i\delta t} + \sigma_- e^{-i\eta(a_x^\dagger + a_x) + i\delta t}\right), \tag{6}$$

where $g$ is the interaction strength, $\delta$ is the detuning of the frequency difference of the two laser beams with respect to $\omega_0$, and $\eta = k\sqrt{\hbar/(2m\omega_x)}$ is the Lamb-Dicke parameter, where $k$ is the magnitude of the difference between the wavevectors of the two laser beams, and $m$ is the mass of the ion. The nonzero matrix elements of $\sigma_+$ and $\sigma_-$ are $\langle\uparrow|\sigma_+|\downarrow\rangle = \langle\downarrow|\sigma_-|\uparrow\rangle = 1$.

The detuning $\delta$ can be tuned to multiples of $\omega_x$, $\delta = (n' - n)\omega_x$, so as to resonantly drive transitions between $|\downarrow, n\rangle$ and $|\uparrow, n'\rangle$. We refer to the $\delta = 0$ resonance as the carrier, the $\delta = -\omega_x$ resonance as the first red sideband, and the $\delta = +\omega_x$ resonance as the first blue sideband.

The signal that is detected in the experiments is the probability $P_\downarrow(t)$ that the ion is in the $|\downarrow\rangle$ internal state after a particular preparation. If we irradiate the ion at time $t$ with circularly polarized light, resonant with the electronic transition from $|\downarrow\rangle$ to $|2p\,^2P_{3/2}; 3, 3\rangle$, there will be a high fluorescence intensity if the $|\downarrow\rangle$ state is occupied, since the selection rules only allow that upper state to decay back to the $|\downarrow\rangle$ state, so it can continue to scatter photons. This transition is called a cycling transition. If the ion is in the $|\uparrow\rangle$ state when it is irradiated with the same light, it will scatter a negligible number of photons. Thus, if we repeatedly prepare the ion in the same way, apply radiation resonant with the cycling transition, and detect the fluorescence photons, the average signal will be proportional to $P_\downarrow(t)$.

## 3. CREATION AND PARTIAL MEASUREMENTS OF QUANTUM STATES

### 3.1. Fock states

The ion is prepared in the $n = 0$ state by Raman cooling.[1] (From now on we drop the $x$ label on $n$.) Raman cooling consists of a sequence of laser pulses on the red sideband, driving $|\downarrow, n\rangle$ to $|\uparrow, n-1\rangle$ transitions, followed by laser pulses which recycle the ion back to the $|\downarrow, n-1\rangle$ state. The probability of heating due to recoil during the recycling step is small. At the end of the sequence, the ion is in the $n = 0$ state more than 90% of the time.

A Fock state is another name for an $n$-state. Higher-$n$ Fock states are prepared from the $n = 0$ state by a sequence of $\pi$-pulses on the blue sideband, red sideband, or carrier. For example, the $|\uparrow, 2\rangle$ state is prepared by using blue sideband, red sideband, and carrier $\pi$-pulses in succession, so that the ion steps through the states $|\downarrow, 0\rangle$, $|\uparrow, 1\rangle$, $|\downarrow, 2\rangle$, and $|\uparrow, 2\rangle$.

If the atom is initially in the $|\downarrow, n\rangle$ state, and the first blue sideband is driven, it will oscillate between that state and the $|\uparrow, n+1\rangle$ state. The probability of finding it in the $|\downarrow, n\rangle$ state at a time $t$ is

$$P_{\downarrow}(t) = \frac{1}{2}\left[1 + \cos(2\Omega_{n,n+1}t)e^{-\gamma_n t}\right], \tag{7}$$

where $\Omega_{n,n+1}$, the Rabi flopping rate, is a function of the laser intensities and detunings and $n$, and $\gamma_n$ is a damping factor which is determined empirically. Thus, the frequency of the oscillations of $P_{\downarrow}(t)$ is a signature of the initial value of $n$. Figure 2(a) shows $P_{\downarrow}(t)$ for an initial $|\downarrow, 0\rangle$ state. Figure 2(b) shows the observed ratios of Rabi frequencies compared with the values calculated from the matrix elements of the interaction Hamiltonian [Eq. (6)].

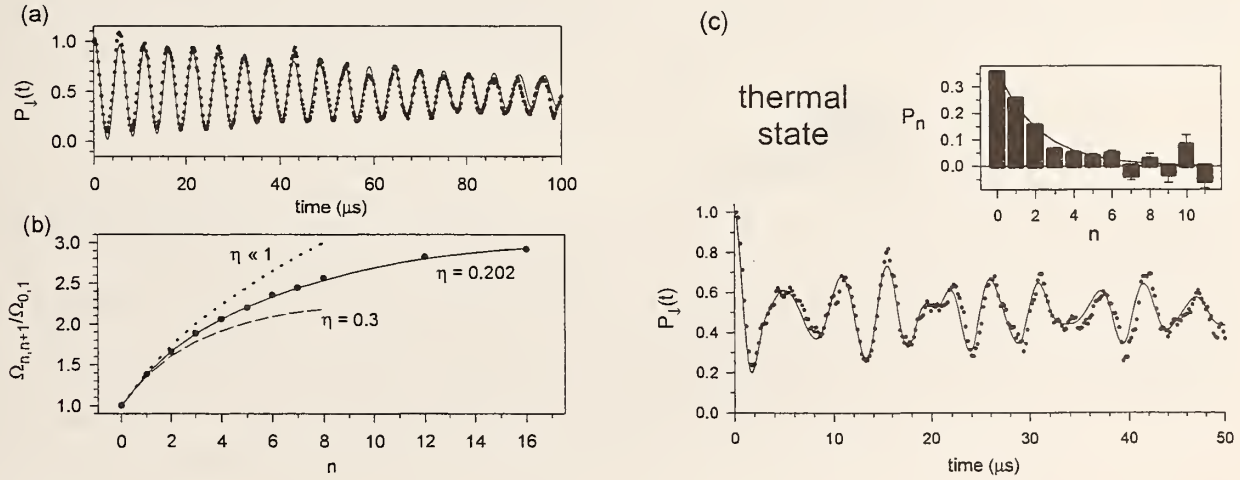


**Figure 2.** (a) $P_{\downarrow}(t)$ for an initial $|\downarrow, 0\rangle$ number state driven by the first blue sideband. The solid line is a fit to an exponentially damped sinusoid. (b) Observed ratios of the Rabi frequencies $\Omega_{n,n+1}/\Omega_{0,1}$ for different values of the initial $n$. The lines represent calculated values for different values of the Lamb-Dicke parameter $\eta$. The value of $\eta$, inferred from other measured quantities, was $0.202 \pm 0.005$. (c) $P_{\downarrow}(t)$ for a thermal state. The solid line is a fit of the data (dots) to a sum of Fock states having a thermal distribution. The fitted value for the mean value of $n$ is $\overline{n} = 1.3 \pm 0.1$. The inset shows the amplitudes of the Fock state components (bars) with a fit to an exponential, corresponding to $\overline{n} = 1.5 \pm 0.1$ (line).

### 3.2. Thermal states

A thermal state of the motion of the ion is not a pure state, but rather must be described by a density matrix, even though there is only one ion. The statistical ensemble which is described by the density matrix is generated by repeatedly preparing the state and making a measurement.

The ion is prepared in a thermal state by Doppler laser cooling.[10] The temperature of the distribution can be controlled by changing the detuning of the cooling laser. When the ion's state is not a Fock state, $P_\downarrow(t)$ has the form

$$P_\downarrow(t) = \frac{1}{2}\left[1 + \sum_{n=0}^{\infty} P_n \cos(2\Omega_{n,n+1}t)e^{-\gamma_n t}\right], \tag{8}$$

where $P_n$ is the probability of finding the ion in the state $|n\rangle$. Figure 2(c) shows $P_\downarrow(t)$ for a thermal state.

### 3.3. Coherent states

Coherent states of the quantum harmonic oscillator were introduced by Schrödinger,[11] with the aim of describing a classical particle with a wavefunction. A coherent state $|\alpha\rangle$ is equal to the following superposition of number states:

$$|\alpha\rangle = e^{-\frac{1}{2}|\alpha|^2} \sum_{n=0}^{\infty} \frac{\alpha^n}{\sqrt{n!}}|n\rangle. \tag{9}$$

In the Schrödinger picture, the absolute square of the wavefunction retains its shape, and its center follows the trajectory of a classical particle in a harmonic well. The mean value of $n$ is $\overline{n} = |\alpha|^2$. A coherent state can be created from the $n = 0$ state (a special case of coherent state) by applying a spatially uniform classical force (see Appendix A). The drive is most effective when its frequency is $\omega_x$. Another method is to apply a "moving standing wave," that is, two laser beams differing in frequency by $\omega_x$ and differing in propagation direction, so that an oscillating dipole force is generated.[12] We have used both of these methods to prepare coherent states. Figure 3(a) shows $P_\downarrow(t)$ for a coherent state. This trace exhibits the phenomenon of collapse and revival.[13]

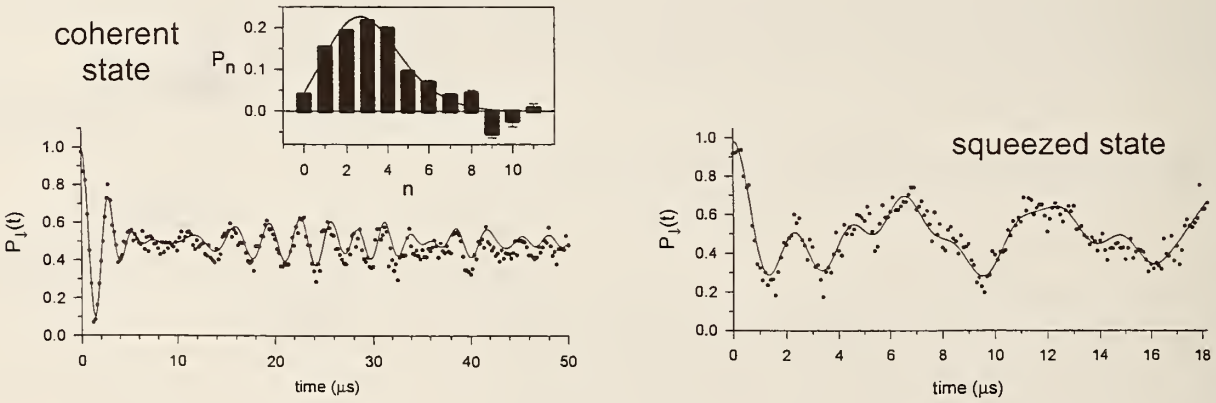


(a) (b)

**Figure 3.** (a) $P_\downarrow(t)$ for a coherent state. The solid line is a fit of the data (dots) to a sum of Fock states having a coherent state distribution. The fitted value for $\overline{n}$ is $3.1 \pm 0.1$. The inset shows the amplitudes of the Fock state components (bars) with a fit to a Poissonian distribution, corresponding to $\overline{n} = 2.9 \pm 0.1$ (line). (b) $P_\downarrow(t)$ for a squeezed state. The solid line is a fit of the data (dots) to a sum of Fock states having a squeezed-state distribution. The fitted value for $\beta$ is $40 \pm 10$, which corresponds to $\overline{n} \approx 7.1$

### 3.4. Squeezed states

A "vacuum squeezed state" can be created by applying an electric field gradient having a frequency of $2\omega_x$ to an ion initially in the $n = 0$ state.[14] Here, the ion was irradiated with two laser beams which differed in frequency by $2\omega_x$. This has the same effect. The squeeze parameter $\beta$ is defined as the factor by which the variance of the squeezed

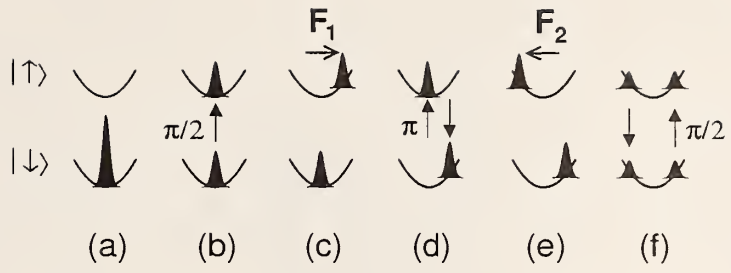


**Figure 4.** Creation of a Schrödinger cat state. See text for details.

quadrature is decreased. It increases exponentially with the time the driving force is applied. The probability distribution of $n$-states is nonzero only for even $n$, for which,

$$P_{2n} = N\frac{(2n)!(\tanh r)^{2n}}{(2^n n!)^2}, \tag{10}$$

where $\beta = e^{2r}$, and $N$ is a normalization constant. Figure 3(b) shows $P_\downarrow(t)$ for a squeezed state having $\beta = 40 \pm 10$.

### 3.5. Schrödinger cat states

The term "Schrödinger cat" is taken here to denote an entangled state which consists of two coherent states of motion correlated with different internal atomic states. A simple example is

$$|\Psi\rangle = \frac{|\uparrow,\alpha\rangle + |\downarrow,-\alpha\rangle}{\sqrt{2}}. \tag{11}$$

Figure 4 shows how such a state is created. (a) The ion is prepared in the $|\downarrow,0\rangle$ state by Raman cooling. (b) A $\pi/2$-pulse on the carrier generates an equal superposition of $|\downarrow,0\rangle$ and $|\uparrow,0\rangle$. (c) The displacement beams generate a force $\mathbf{F_1}$, which excites the component in the $|\uparrow\rangle$ internal state to a coherent state $|\alpha\rangle$. Due to the polarizations of the displacement beams, they do not affect an atom in the $|\downarrow\rangle$ state. (d) A $\pi$-pulse on the carrier exchanges the $|\downarrow\rangle$ and $|\uparrow\rangle$ components. (e) The displacement beams generate a force $\mathbf{F_2}$, which excites the component in the $|\uparrow\rangle$ internal state to a coherent state $|\alpha e^{i\phi}\rangle$, where the phase $\phi$ is controlled by an rf oscillator. The state here is analogous to Schrödinger's cat. (f) The $|\downarrow\rangle$ and $|\uparrow\rangle$ components are combined by a $\pi/2$-pulse on the carrier. At this point, the radiation is applied on the cycling transition, and the signal is recorded.

The predicted signal, for a particular value of $\phi$, is

$$P_\downarrow(\phi) = \frac{1}{2}\left[1 - ce^{-\alpha^2(1-\cos\phi)}\cos(\alpha^2\sin\phi)\right], \tag{12}$$

where $c = 1$ in the absence of decoherence. Figure 5 shows experimental data and fits to Eq. (12) for various values of $\alpha$. In (d), $c$ is clearly less than one, indicating decoherence, although the source is not yet determined.

## 4. COMPLETE MEASUREMENTS OF QUANTUM STATES

The measurements described in the previous Section determine only the $n$-state populations or probabilities, and therefore do not provide a complete description of the motional states. The density matrix $\rho$ does provide a complete description of a state, whether it is a pure or a mixed state. The Wigner function $W(\alpha)$ also provides a complete description. The Wigner function resembles a classical joint probability distribution for position and momentum in some cases. However, it can be negative, unlike a true probability distribution. We have demonstrated experimental methods for reconstructing the density matrix or the Wigner function of a quantum state of motion of a harmonically bound atom.[4]

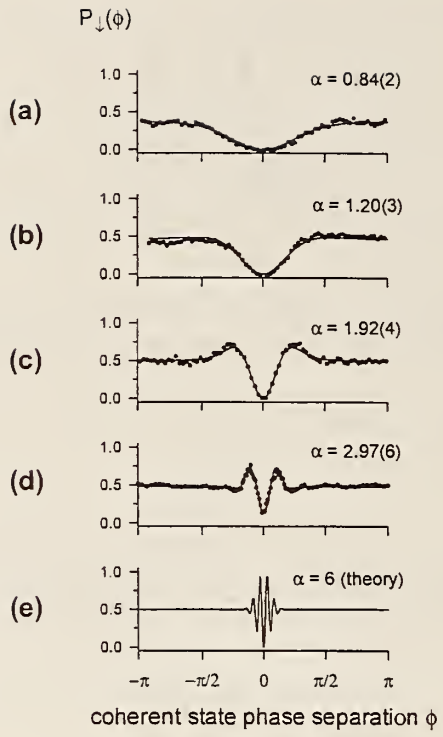


**Figure 5.** Measured and fitted $P_{\downarrow}(\phi)$ interference signals for the Schrödinger cat state. The curves in (a) through (d) represent measurements for different values of the time during which the displacement beams excite the coherent states. The solid lines are fits to Eq. (12), allowing $\alpha$ to vary. In (d), a term representing loss of contrast was included in the fit. The curve in (d) represents a superposition of two $x_0 \approx 7$ nm wave packets with a maximum separation of $4\alpha x_0 \approx 80$ nm. Curve (e) represents a calculation for a pair of coherent states with $\alpha = 6$.

Both of these methods depend on controllably displacing the state in phase space, applying radiation to drive the first blue sideband for time $t$, and then measuring $P_{\downarrow}$. The averaged, normalized, signal is

$$P_{\downarrow}(t,\alpha) = \frac{1}{2}\left[1 + \sum_{k=0}^{\infty} Q_k(\alpha)\cos(2\Omega_{k,k+1}t)e^{-\gamma_k t}\right], \tag{13}$$

where the complex number $\alpha$ represents the amplitude and phase of the displacement, and $Q(\alpha)$ is the occupation probability of the vibrational state $|k\rangle$ for the displaced state.

If the $Q_k(\alpha)$ coefficients are derived for a series of values of $\alpha$ lying in a circle,

$$\alpha_p = |\alpha|\exp[i(\pi/N)p], \tag{14}$$

where $p = -N, \ldots, N-1$, then the density matrix elements $\rho_{nm}$ can be determined for values of $n$ and $m$ up to $N-1$. The details of the numerical procedure are given in Ref. 4.

Figure 6(a) shows the reconstructed density matrix amplitudes for an approximate $n = 1$ state. Figure 6(b) shows the reconstructed density matrix for a coherent state having an amplitude $|\beta| \approx 0.67$.

The Wigner function for a given value of the complex parameter $\alpha$ can be determined from the sum[15–18]

$$W(\alpha) = \frac{2}{\pi}\sum_{n=0}^{\infty}(-1)^n Q_n(\alpha). \tag{15}$$

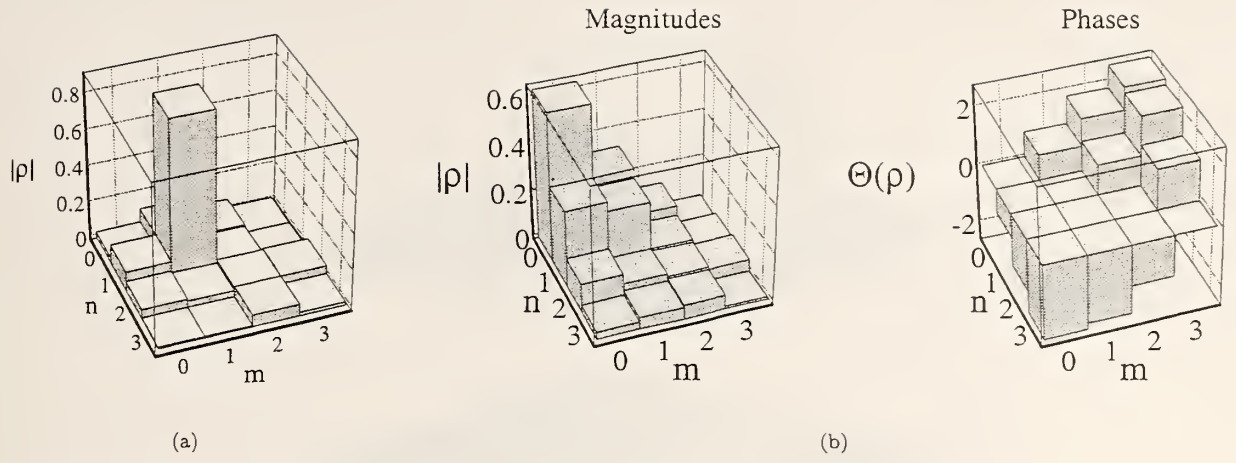


**Figure 6.** (a) Reconstructed number-state density matrix amplitudes $|\rho_{nm}|$ for an approximate $n = 1$ number state. (b) Reconstructed amplitudes $|\rho_{nm}|$ and phases $\Theta(\rho_{nm})$ of a coherent state.

Figure 7 shows the reconstructed Wigner function for an approximate $n = 1$ state. The fact that it is negative in a region around the origin highlights the fact that is a nonclassical state. Figure 8 shows the reconstructed Wigner function for a coherent state with amplitude $|\beta| \approx 1.5$. It is positive, which is not surprising, since the coherent state is the quantum state that most closely approximates a classical state.

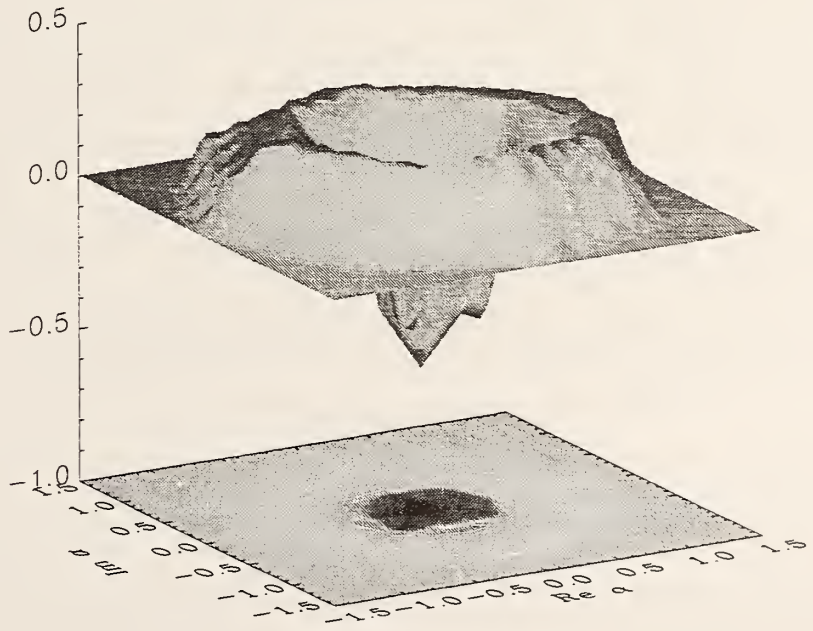


**Figure 7.** Surface and contour plots of the reconstructed Wigner function $W(\alpha)$ of an approximate $n = 1$ number state. The negative values of $W(\alpha)$ around the origin highlight the nonclassical nature of this state.

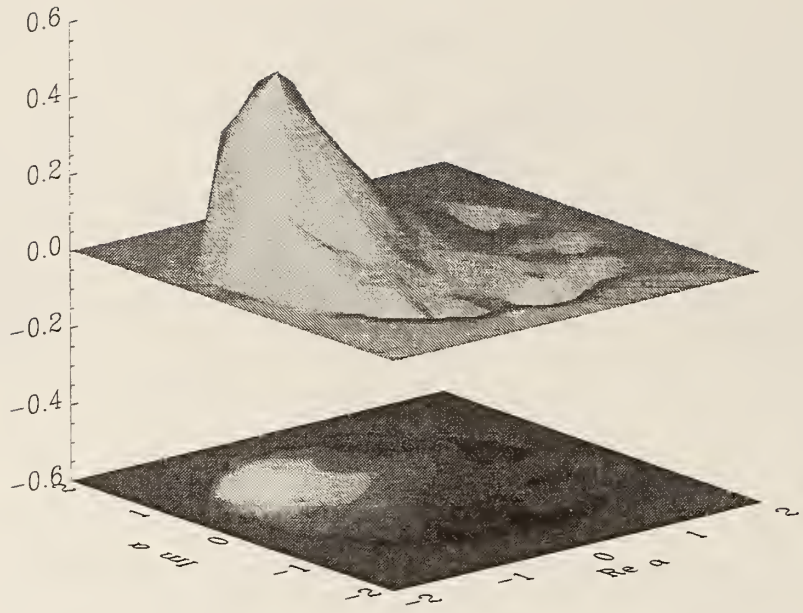


**Figure 8.** Surface and contour plots of the reconstructed Wigner function $W(\alpha)$ of a coherent state. The width is in good agreement with the expected minimum-uncertainty value.

## 5. DECOHERENCE OF A SUPERPOSITION OF COHERENT STATES

Decoherence, the decay of superposition states into mixtures, is of interest because it leads to the familiar classical physics of macroscopic objects (see, e.g. Ref. 19). Experiments are beginning to probe the regime in which decoherence is observable, but not so fast that the dynamics are classical. One example is the observation of the decoherence of a superposition of mesoscopic (few-photon) quantum states of an electromagnetic field having distinct phases by Brune *et al.*[20] In this experiment, as in the Schrödinger cat experiment of Ref. 3, the mesoscopic system was entangled with an internal two-level system of an atom.

A simpler system, which has been well-studied theoretically by others,[21–24] is a superposition of two coherent states of a harmonic oscillator, without entanglement with a two-level system. The system interacts in some way with the environment, leading to decoherence of the superposition state.

Here we carry out a simple calculation of the decoherence of a superposition of two coherent states of a harmonic oscillator. At time $t = 0$, the system is in an equal superposition of two coherent states,

$$|\Psi(0)\rangle = \frac{1}{\sqrt{2}}\left(e^{i\theta_1(0)}|\alpha_1(0)\rangle + e^{i\theta_2(0)}|\alpha_2(0)\rangle\right), \tag{16}$$

where the notation is the same as in Appendix A, and the interaction picture is used. (It is assumed that the two components of the state vector are nearly orthogonal. Otherwise the normalization factor is different.) The system is subjected to a random force, which is uniform over the spatial extent of the system, for example, a uniform electric field acting on a charged particle. In Appendix A, we show that a single coherent state, subjected to such a force, will remain in a coherent state. It follows from the linearity of the Schrödinger equation that the state described by Eq. (16) will, at a later time, still be in an equal superposition of coherent states, although $\alpha_1$, $\alpha_2$, $\theta_1$, and $\theta_2$ will change. Each time the system of Eq. (16) is prepared, $\alpha_1$, $\alpha_2$, $\theta_1$, and $\theta_2$ will have a different time dependence, due to the random force. We can study the decoherence as a function of time by carrying out an ensemble average.

Although both $\alpha_1$ and $\alpha_2$ change with time, their difference does not, since they each change by the same amount. This can be seen from Eq. (45). We define $\Delta\alpha \equiv \alpha_1 - \alpha_2 = \text{constant}$.

Decoherence is due to the changes in the phase difference $[\theta_2(t) - \theta_1(t)]$. We define the change in the phase difference to be

$$\Delta\theta(t) \equiv [\theta_2(t) - \theta_1(t)] - [\theta_2(0) - \theta_1(0)]. \tag{17}$$

Then, from Eq. (48),

$$\Delta\theta(t) = \frac{1}{2}\left[\Delta\alpha \int_0^t f(t')e^{-i\omega_x t'}dt' + \Delta\alpha^* \int_0^t f(t')e^{i\omega_x t'}dt'\right]. \tag{18}$$

The double-integral term in Eq. (48) does not contribute to $\Delta\theta(t)$, since it does not depend on either $\alpha(0)$ or $\theta(0)$, so it makes the same contribution to $\theta_2(t)$ and to $\theta_1(t)$. The square of $\Delta\theta(t)$ is

$$\begin{aligned}(\Delta\theta(t))^2 &= \frac{1}{4}\left[(\Delta\alpha)^2 \int_0^t\int_0^t f(t')f(t'')e^{-i\omega_x t'-i\omega_x t''}dt'dt'' + 2|\Delta\alpha|^2 \int_0^t\int_0^t f(t')f(t'')e^{i\omega_x t'-i\omega_x t''}dt'dt''\right.\\ &\quad \left. + (\Delta\alpha^*)^2 \int_0^t\int_0^t f(t')f(t'')e^{i\omega_x t'+i\omega_x t''}dt'dt''\right],\end{aligned} \tag{19}$$

and its ensemble average is

$$\begin{aligned}\left\langle(\Delta\theta(t))^2\right\rangle &= \frac{1}{4}\left[(\Delta\alpha)^2 \int_0^t\int_0^t \langle f(t')f(t'')\rangle e^{-i\omega_x t'-i\omega_x t''}dt'dt'' + 2|\Delta\alpha|^2 \int_0^t\int_0^t \langle f(t')f(t'')\rangle e^{i\omega_x t'-i\omega_x t''}dt'dt''\right.\\ &\quad \left. + (\Delta\alpha^*)^2 \int_0^t\int_0^t \langle f(t')f(t'')\rangle e^{i\omega_x t'+i\omega_x t''}dt'dt''\right],\end{aligned} \tag{20}$$

where the angular brackets denote an ensemble average. Thus, $\left\langle(\Delta\theta(t))^2\right\rangle$ depends on the autocorrelation function of the random function $f(t)$, which is proportional to the force. If we assume that $f$ is a stationary random variable, then its autocorrelation function

$$R(\tau) = \langle f(t)f(t+\tau)\rangle \tag{21}$$

exists and is independent of $t$. According to the Wiener-Khinchine theorem, the power spectrum $w(\nu)$, defined for $\nu \geq 0$, is

$$w(\nu) = 4\int_0^\infty R(\tau)\cos(2\pi\nu\tau)d\tau. \tag{22}$$

A white-noise spectrum corresponds to $R(\tau) \propto \delta(\tau)$, where $\delta(\tau)$ is the Dirac delta function. If we let $R(\tau) = C\delta(\tau)$, then

$$\begin{aligned}\left\langle(\Delta\theta(t))^2\right\rangle &= \frac{C}{4}\left[(\Delta\alpha)^2 \int_0^t\int_0^t \delta(t''-t')e^{-i\omega_x t'-i\omega_x t''}dt'dt'' + 2|\Delta\alpha|^2 \int_0^t\int_0^t \delta(t''-t')e^{i\omega_x t'-i\omega_x t''}dt'dt''\right.\\ &\quad \left. + (\Delta\alpha^*)^2 \int_0^t\int_0^t \delta(t''-t')e^{i\omega_x t'+i\omega_x t''}dt'dt''\right]\\ &= \frac{C}{4}\left[(\Delta\alpha)^2 \int_0^t e^{-2i\omega_x t'}dt' + 2|\Delta\alpha|^2 \int_0^t dt' + (\Delta\alpha^*)^2 \int_0^t e^{2i\omega_x t'}dt'\right].\end{aligned} \tag{23}$$

The first and third integrals on the right-hand-side of Eq. (23) oscillate, but are bounded, while the second one grows with time, so, for $\omega_x t \gg 1$,

$$\left\langle(\Delta\theta(t))^2\right\rangle \approx \frac{1}{2}C|\Delta\alpha|^2 t. \tag{24}$$

Hence, the decoherence time, that is, the time required for the rms phase difference $\left\langle(\Delta\theta(t))^2\right\rangle^{1/2}$ to increase to about 1 radian, is on the order of $2/\left(C|\Delta\alpha|^2\right)$.

Using the same approximations, we can calculate the rate of change of the amplitude $\alpha_i(t)$ for a single coherent state, where $i$ is 1 or 2. From Eq. (45) in Appendix A,

$$\alpha_i(t) - \alpha_i(0) = i\int_0^t f(t')e^{i\omega_x t'}dt', \tag{25}$$

and

$$|\alpha_i(t) - \alpha_i(0)|^2 = \int_0^t \int_0^t f(t')f(t'')e^{i\omega_x t' - i\omega_x t''} dt' dt''. \tag{26}$$

If $f(t)$ has a white-noise spectrum, as considered previously, the ensemble average is

$$\left\langle |\alpha_i(t) - \alpha_i(0)|^2 \right\rangle = C \int_0^t \int_0^t \delta(t'' - t')e^{i\omega_x t' - i\omega_x t''} dt' dt'' = C \int_0^t dt' = Ct. \tag{27}$$

In the time, $t \approx 2/\left(C|\Delta\alpha|^2\right)$, required for decoherence, the rms change in $\alpha_i$ is $\sqrt{2}/|\Delta\alpha|$. Consider the case $\alpha_1(0) = -\alpha_2(0)$. The energy of a single coherent state is proportional to the square of its amplitude ($\propto |\alpha_i|^2$). The fractional change in the energy is

$$\left|\frac{\Delta|\alpha_i|^2}{|\alpha_i|^2}\right| < \frac{2|\alpha_i(t) - \alpha_i(0)|}{\alpha_i(0)} \approx \frac{2\sqrt{2}}{|\Delta\alpha||\alpha_i(0)|} = \frac{\sqrt{2}}{|\alpha_i(0)|^2}, \tag{28}$$

which becomes small for $|\alpha_i(0)|^2 \gg 1$. Thus, we see that coherent superpositions of macroscopic ($|\alpha_i(0)|^2 \gg 1$) states decohere much more quickly than they change in energy.

We can make a more quantitative statement about the decoherence rate by considering the decay of the off-diagonal density matrix elements. For an initial pure state $2^{-1/2}(|\alpha_1\rangle + |\alpha_2\rangle)$, the density matrix is

$$\rho = \frac{1}{2}\left(|\alpha_1\rangle\langle\alpha_1| + |\alpha_1\rangle\langle\alpha_2| + |\alpha_2\rangle\langle\alpha_1| + |\alpha_2\rangle\langle\alpha_2|\right). \tag{29}$$

If $\Delta\alpha \gg 1$, so that the phase changes are more important than the changes in $\alpha_1$ and $\alpha_2$, then the off-diagonal matrix element $|\alpha_2\rangle\langle\alpha_1|$ evolves to $e^{i\Delta\theta(t)}|\alpha_2\rangle\langle\alpha_1|$. Let us assume that the random variable $\Delta\theta$ at time $t$ has a Gaussian distribution $P(\Delta\theta)$. Given the variance of $\Delta\theta$ from Eq. (24), $P(\Delta\theta)$ must have the form

$$P(\Delta\theta) = \frac{1}{\sqrt{\pi C|\Delta\alpha|^2 t}} \exp\left(-\frac{\Delta\theta^2}{C|\Delta\alpha|^2 t}\right). \tag{30}$$

We evaluate the ensemble average of $e^{i\Delta\theta(t)}$,

$$\left\langle e^{i\Delta\theta(t)} \right\rangle = \int_{-\infty}^{\infty} P(\Delta\theta)e^{i\Delta\theta(t)} d(\Delta\theta) = \exp\left(-\frac{C|\Delta\alpha|^2 t}{4}\right). \tag{31}$$

This yields the basic result, previously derived by others,[21–24] that the off-diagonal matrix element decays exponentially in time, with a time constant that is inversely proportional to $|\Delta\alpha|^2$.

An extension of the experiment of Ref. 3, with a random electric field deliberately applied, might be used to verify these calculations.[3] A means of simulating thermal, zero-temperature, squeezed, and other reservoirs by various combinations of optical fields has been discussed by Poyatos *et al.*[25]

## ACKNOWLEDGMENTS

This work was supported by the National Security Agency, the Army Research Office, and the Office of Naval Research. D. L. acknowledges a Deutsche Forschungsgemeinschaft research grant. D. M. M. was supported by a National Research Council postdoctoral fellowship.

## APPENDIX A. THE FORCED HARMONIC OSCILLATOR

If a coherent state is subjected to a spatially uniform force, it remains a coherent state, though its amplitude changes. This exact result, which is independent of the strength or time-dependence of the force, seems to have been discovered by Husimi[26] and independently by Kerner.[27] For other references on the forced quantum harmonic oscillator, see Ref. 28. The qualitative result stated above is enough to establish that applying a force to the $n = 0$ state will generate a finite-amplitude coherent state, which was required in Sec. 3.3. However, in order to study the decoherence of a superposition of two coherent states, it is useful to have an exact expression for the time-dependent

state vector, given that the state vector is an arbitrary coherent state at $t = 0$. Since the published results of which we are aware do not give this particular result, we give here an elementary derivation.

We consider a Hamiltonian, $H = H_0 + V(t)$, where $H_0 = \hbar\omega_x a_x^\dagger a_x$ is the Hamiltonian of a one-dimensional harmonic oscillator, and $V(t) = -xF(t)$ is a time-dependent potential. Here, $F(t)$ is a real $c$-number function of time and corresponds to a spatially uniform force, and $x = x_0(a_x + a_x^\dagger)$, where $x_0 \equiv (\hbar/2m\omega_x)^{1/2}$. For example, if the particle has charge $q$, and a uniform electric field $\hat{x}E_x(t)$ is applied, then $F(t) = qE_x(t)$.

It is convenient to switch to the interaction picture, where an interaction-picture state vector $|\Psi(t)\rangle^I$ is related to the corresponding Schrödinger-picture state vector $|\Psi(t)\rangle^S$ by

$$|\Psi(t)\rangle^I = e^{iH_0 t/\hbar}|\Psi(t)\rangle^S, \tag{32}$$

and an interaction-picture operator $\mathcal{O}^I(t)$ is related to the corresponding Schrödinger-picture operator $\mathcal{O}^S(t)$ by

$$\mathcal{O}^I(t) = e^{iH_0 t/\hbar}\mathcal{O}^S(t)e^{-iH_0 t/\hbar}. \tag{33}$$

The equation of motion for an interaction-picture operator is

$$\frac{d}{dt}\mathcal{O}^I(t) = -\frac{i}{\hbar}\left[\mathcal{O}^I(t), H_0\right], \tag{34}$$

so

$$\frac{d}{dt}a_x^I(t) = -\frac{i}{\hbar}\left[a_x^I(t), H_0\right] = -i\omega_x a^I(t), \tag{35}$$

$$a_x^I(t) = a_x^I(0)e^{-i\omega_x t}, \tag{36}$$

$$a_x^{\dagger\,I}(t) = a_x^{\dagger\,I}(0)e^{i\omega_x t}. \tag{37}$$

For simplicity, we let $a \equiv a_x^I(0) = a_x^S$ and $a^\dagger \equiv a_x^{\dagger\,I}(0) = a_x^{\dagger\,S}$. The Schrödinger equation in the interaction picture is

$$\frac{\partial}{\partial t}|\Psi(t)\rangle^I = -\frac{i}{\hbar}V^I(t)|\Psi(t)\rangle^I = if(t)\left(ae^{-i\omega_x t} + a^\dagger e^{i\omega_x t}\right)|\Psi(t)\rangle^I, \tag{38}$$

where $f(t) \equiv x_0 F(t)/\hbar$. Note that if $f(t) = 0$, $|\Psi(t)\rangle^I$ is constant.

We impose the initial condition that $|\Psi(0)\rangle^I$ is a coherent state. We make the assumption that $|\Psi(t)\rangle^I$ is also a coherent state for $t > 0$,

$$|\Psi(t)\rangle^I = e^{i\theta(t)}|\alpha(t)\rangle \equiv e^{i\theta(t)}e^{-\frac{1}{2}|\alpha(t)|^2}\sum_{n=0}^{\infty}\frac{\alpha^n(t)}{\sqrt{n!}}|n\rangle, \tag{39}$$

where the $|n\rangle$ are the eigenstates of $a_x^\dagger a_x$ with eigenvalue $n$ at $t = 0$, and $\theta(t)$ is an arbitrary real function, so that ${}^I\langle\Psi(t)|\Psi(t)\rangle^I = 1$. (This assumption must be verified later by substitution of the resulting solution back into Eq. (38).) The problem reduces to finding the complex function $\alpha(t)$ and the real function $\theta(t)$.

The right-hand-side of Eq. (38) is

$$\begin{aligned}
-\frac{i}{\hbar}V^I(t)|\Psi(t)\rangle^I &= if(t)\left(ae^{-i\omega_x t} + a^\dagger e^{i\omega_x t}\right)e^{i\theta(t)}e^{-\frac{1}{2}|\alpha(t)|^2}\sum_{n=0}^{\infty}\frac{\alpha^n(t)}{\sqrt{n!}}|n\rangle \\
&= if(t)e^{i\theta(t)}e^{-\frac{1}{2}|\alpha(t)|^2}\left(e^{-i\omega_x t}\sum_{n=1}^{\infty}\frac{\alpha^n(t)\sqrt{n}}{\sqrt{n!}}|n-1\rangle + e^{i\omega_x t}\sum_{n=0}^{\infty}\frac{\alpha^n(t)\sqrt{n+1}}{\sqrt{n!}}|n+1\rangle\right) \\
&= if(t)e^{i\theta(t)}e^{-\frac{1}{2}|\alpha(t)|^2}\left(e^{-i\omega_x t}\sum_{n=0}^{\infty}\frac{\alpha^{n+1}(t)}{\sqrt{n!}}|n\rangle + e^{i\omega_x t}\sum_{n=1}^{\infty}\frac{\alpha^{n-1}(t)\sqrt{n}}{\sqrt{(n-1)!}}|n\rangle\right).
\end{aligned} \tag{40}$$

The left-hand-side of Eq. (38) is

$$\frac{\partial}{\partial t}|\Psi(t)\rangle^I = i\frac{d\theta}{dt}e^{i\theta(t)}e^{-\frac{1}{2}|\alpha(t)|^2}\sum_{n=0}^{\infty}\frac{\alpha^n(t)}{\sqrt{n!}}|n\rangle + e^{i\theta(t)}\left(-\frac{1}{2}\frac{d\alpha}{dt}\alpha^*(t) - \frac{1}{2}\alpha(t)\frac{d\alpha^*}{dt}\right)e^{-\frac{1}{2}|\alpha(t)|^2}\sum_{n=0}^{\infty}\frac{\alpha^n(t)}{\sqrt{n!}}|n\rangle$$
$$+ ie^{i\theta(t)}e^{-\frac{1}{2}|\alpha(t)|^2}\sum_{n=0}^{\infty}\frac{n\alpha^{n-1}(t)}{\sqrt{n!}}\frac{d\alpha}{dt}|n\rangle. \tag{41}$$

We equate the coefficients of $|n\rangle$ in Eqs. (40) and (41) and divide by a common factor to obtain

$$if(t)\left(e^{-i\omega_x t}\alpha^2(t) + e^{i\omega_x t}n\right) = i\frac{d\theta}{dt}\alpha(t) + \left(-\frac{1}{2}\frac{d\alpha}{dt}\alpha^*(t) - \frac{1}{2}\alpha(t)\frac{d\alpha^*}{dt}\right)\alpha(t) + n\frac{d\alpha}{dt}, \tag{42}$$

which can be rearranged as

$$n\left[\frac{d\alpha}{dt} - if(t)e^{i\omega_x t}\right] + i\alpha(t)\frac{d\theta}{dt} - \frac{1}{2}\alpha(t)\alpha^*(t)\frac{d\alpha}{dt} - \frac{1}{2}\alpha^2(t)\frac{d\alpha^*}{dt} - i\alpha^2(t)f(t)e^{-\omega_x t} = 0 \tag{43}$$

In order for Eq. (43) to be true for all $n$, the expression in the square brackets, which multiplies $n$, must equal zero. Thus, we have the first-order differential equation for $\alpha(t)$,

$$\frac{d\alpha}{dt} - if(t)e^{i\omega_x t} = 0, \tag{44}$$

which has the solution

$$\alpha(t) = \alpha(0) + i\int_0^t f(t')e^{i\omega_x t'}dt'. \tag{45}$$

If the expression in brackets is set to zero, Eq. (43) becomes, after division of both sides by $i\alpha(t)$,

$$\frac{d\theta}{dt} + \frac{i}{2}\alpha^*(t)\frac{d\alpha}{dt} + \frac{i}{2}\alpha(t)\frac{d\alpha^*}{dt} - \alpha(t)f(t)e^{-i\omega_x t} = 0. \tag{46}$$

The imaginary part of Eq. (46) is satisfied as long as Eq. (44) is, so it provides no new information. The real part of Eq. (46) is a first-order differential equation for $\theta(t)$:

$$\begin{aligned}\frac{d\theta}{dt} &= f(t)\left[\mathrm{Re}\,\alpha(t)\cos\omega_x t + \mathrm{Im}\,\alpha(t)\sin\omega_x t\right] \\ &= f(t)\left[\mathrm{Re}\,\alpha(0)\cos\omega_x t + \mathrm{Im}\,\alpha(0)\sin\omega_x t - \cos\omega_x t\int_0^t f(t')\sin\omega_x t'dt' + \sin\omega_x t\int_0^t f(t')\cos\omega_x t'dt'\right] \\ &= f(t)\left[\mathrm{Re}\,\alpha(0)\cos\omega_x t + \mathrm{Im}\,\alpha(0)\sin\omega_x t + \int_0^t f(t')\sin\left[\omega_x(t-t')\right]dt'\right],\end{aligned} \tag{47}$$

where Re and Im stand for the real and imaginary parts. Integrating Eq. (47), we obtain

$$\theta(t) = \theta(0) + \mathrm{Re}\,\alpha(0)\int_0^t f(t')\cos\omega_x t'dt' + \mathrm{Im}\,\alpha(0)\int_0^t f(t')\sin\omega_x t'dt' + \int_0^t dt'f(t')\int_0^{t'}dt''f(t'')\sin\left[\omega_x(t'-t'')\right]. \tag{48}$$

Substitution back into the Schrödinger equation [Eq. (38)] verifies the solution and justifies the original assumption [Eq. (39)].

## REFERENCES


1. C. Monroe, D. M. Meekhof, B. E. King, S. R. Jefferts, W. M. Itano, and D. J. Wineland, "Resolved-sideband Raman cooling of a bound atom to the 3D zero-point energy," *Phys. Rev. Lett.* **75**, pp. 4011–4014, 1995.
2. D. M. Meekhof, C. Monroe, B. E. King, W. M. Itano, and D. J. Wineland, "Generation of nonclassical motional states of a trapped atom," *Phys. Rev. Lett.* **76**, pp. 1796–1799, 1996.

3. C. Monroe, D. M. Meekhof, B. E. King, and D. J. Wineland, "A 'Schrödinger cat' superposition state of an atom," *Science* **272**, pp. 1131–1136, 1996.
4. D. Leibfried, D. M. Meekhof, B. E. King, C. Monroe, W. M. Itano, and D. J. Wineland, "Experimental determination of the motional quantum state of a trapped atom," *Phys. Rev. Lett.* **77**, pp. 4281–4285, 1996.
5. D. Leibfried, D. M. Meekhof, B. E. King, C. Monroe, W. M. Itano, and D. J. Wineland, "Experimental preparation and measurements of quantum states of motion of a trapped atom," *J. Modern Opt. (in press)* .
6. W. Heisenberg, "Über quantentheoretische Umdeutung kinematischer und mechanischer Beziehungen," *Z. Phys.* **33**, pp. 879–893, 1925.
7. E. Schrödinger, "Quantisierung als Eigenwertproblem II," *Ann. Phys. (Leipzig)* **79**, pp. 489–527, 1926.
8. P. J. Bardroff, C. Leichtle, G. Schrade, and W. P. Schleich, "Endoscopy in the Paul trap: Measurement of the vibratory quantum state of a single ion," *Phys. Rev. Lett.* **77**, pp. 2198–2201, 1996.
9. G. Schrade, V. I. Man'ko, W. P. Schleich, and R. J. Glauber, "Wigner functions in the Paul trap," *Quantum Semiclass. Opt.* **7**, pp. 307–325, 1995.
10. S. Stenholm, "The semiclassical theory of laser cooling," *Rev. Mod. Phys.* **58**, pp. 699–739, 1986.
11. E. Schrödinger, "Der stetige Übergang von der Micro- zur Makromechanik," *Die Naturwissenschaften* **14**, pp. 644–666, 1926.
12. D. J. Wineland, J. C. Bergquist, J. J. Bollinger, W. M. Itano, F. L. Moore, J. M. Gilligan, M. G. Raizen, D. J. Heinzen, C. S. Weimer, and C. H. Manney, "Recent experiments on trapped ions at the National Institute of Standards and Technology," in *Laser manipulation of atoms and ions*, E. Arimondo, W. D. Phillips, and F. Strumia, eds., pp. 553–567, North-Holland, Amsterdam, 1992.
13. J. H. Eberly, N. B. Narozhny, and J. J. Sanchez-Mondragon, "Periodic spontaneous collapse and revival in a simple quantum model," *Phys. Rev. Lett.* **44**, pp. 1323–1326, 1980.
14. D. J. Heinzen and D. J. Wineland, "Quantum-limited cooling and detection of radio-frequency oscillations by laser-cooled ions," *Phys. Rev. A* **42**, pp. 2977–2994, 1990.
15. A. Royer, "Measurement of the Wigner function," *Phys. Rev. Lett.* **55**, pp. 2745–2748, 1985.
16. H. Moya-Cessa and P. L. Knight, "Series representations of quantum-field quasiprobabilities," *Phys. Rev. A* **48**, pp. 2479–2485, 1993.
17. S. Wallentowitz and W. Vogel, "Unbalanced homodyning for quantum state measurements," *Phys. Rev. A* **53**, pp. 4528–4533, 1996.
18. K. Banaszek and K. Wódkiewicz, "Direct probing of quantum phase space by photon counting," *Phys. Rev. Lett.* **76**, pp. 4344-4347, 1996.
19. W. H. Zurek, "Decoherence and the transition from quantum to classical," *Phys. Today* **44 (10)**, pp. 35–44, 1991.
20. M. Brune, E. Hagley, J. Dreyer, X. Maître, A. Maali, C. Wunderlich, J. M. Raimond, and S. Haroche, "Observing the progressive decoherence of the 'meter' in a quantum measurement," *Phys. Rev. Lett.* **77**, pp. 4887–4890, 1996.
21. D. F. Walls and G. J. Milburn, "Effect of dissipation on quantum coherence," *Phys. Rev. A* **31**, pp. 2403–2408, 1985.
22. J. P. Paz, S. Habib, and W. H. Zurek, "Reduction of the wave packet: Preferred observable and decoherence time scale," *Phys. Rev. D* **47**, pp. 488–501, 1993.
23. B. M. Garraway and P. L. Knight, "Evolution of quantum superpositions in open environments: Quantum trajectories, jumps, and localization in phase space," *Phys. Rev. A* **50**, pp. 2548–2563, 1994.
24. P. Goetsch, R. Graham, and F. Haake, "Schrödinger cat states and single runs for the damped harmonic oscillator," *Phys. Rev. A* **51**, pp. 136–142, 1995.
25. J. F. Poyatos, J. I. Cirac, and P. Zoller, "Quantum reservoir engineering with laser cooled trapped ions," *Phys. Rev. Lett.* **77**, pp. 4728–4731, 1996.
26. K. Husimi, "Miscellanea in elementary quantum mechanics II," *Prog. Theor. Phys.* **9**, pp. 381–402, 1953.
27. E. H. Kerner, "Note on the forced and damped oscillator in quantum mechanics," *Can. J. Phys.* **36**, pp. 371–377, 1958.
28. Y. Nogami, "Test of the adiabatic approximation in quantum mechanics: Forced harmonic oscillator," *Am. J. Phys.* **59**, pp. 64–68, 1991.

# PHYSICAL REVIEW A

## ATOMIC, MOLECULAR, AND OPTICAL PHYSICS

THIRD SERIES, VOLUME 55, NUMBER 4 APRIL 1997


## RAPID COMMUNICATIONS

*The Rapid Communications section is intended for the accelerated publication of important new results. Since manuscripts submitted to this section are given priority treatment both in the editorial office and in production, authors should explain in their submittal letter why the work justifies this special handling. A Rapid Communication should be no longer than 4 printed pages and must be accompanied by an abstract. Page proofs are sent to authors.*

# Simplified quantum logic with trapped ions


C. Monroe, D. Leibfried, B. E. King, D. M. Meekhof, W. M. Itano, and D. J. Wineland

*National Institute of Standards and Technology, Boulder, Colorado 80303*



(Received 17 December 1996)



We describe a simplified scheme for quantum logic with a collection of laser-cooled trapped atomic ions. Building on the scheme of Cirac and Zoller, we show how the fundamental controlled-NOT gate between a collective mode of ion motion and the internal states of a single ion can be reduced to a single laser pulse, and the need for a third auxiliary internal electronic state can be eliminated. [S1050-2947(97)50904-8]



PACS number(s): 03.65.Bz, 89.70.+c, 32.80.Pj


Lately, much thought has been focused on the implementation of simple quantum logic circuits for quantum computing [1] and other applications such as the generation of multiparticle entangled states for spectroscopy [2]. A promising candidate for quantum logic is based on the work of Cirac and Zoller [3], who showed how to construct universal multibit quantum logic gates in a system of laser-cooled trapped atomic ions. In the simplest form of the ion trap quantum computer, two internal electronic levels of each ion in a collection represent a quantum bit of information, and the quantum bits are "wired" together by virtue of the ions' collective motion in the trap. Trapped ions are attractive for quantum logic applications because their internal levels can be well isolated from the pernicious effects of quantum decoherence [4], while at the same time, the ions strongly interact with one another through their Coulomb repulsion, allowing the formation of entangled states.

Several groups have shown that any quantum computation can be built from a series of one-bit and two-bit quantum logic gates [5]. A fundamental entangling quantum logic gate is the controlled-NOT (CN) gate [6,7], in which one quantum bit is flipped (rotated by $\pi$ radians) depending on the state of a second quantum bit. Cirac and Zoller showed how to realize a CN quantum logic gate in a collection of trapped ions by applying several appropriately tuned laser pulses to the ions and invoking an interaction with a third (auxiliary) internal atomic level. Their scheme was adapted to an experiment on a single $^{9}Be^{+}$ ion and required three laser pulses [8]. This Rapid Communication discusses a simpler CN gate scheme between an ion's internal and motional states that requires only a single laser pulse, while eliminating the requirement of the auxiliary internal electronic level. These simplifications are important for several reasons.

(1) Several popular alkalilike ion candidates, including $^{24}Mg^{+}$, $^{40}Ca^{+}$, $^{88}Sr^{+}$, $^{138}Ba^{+}$, $^{174}Yb^{+}$, and $^{198}Hg^{+}$, do not have a third electronic ground state available for the auxiliary level. These ions have zero nuclear spin with only two Zeeman ground states ($m_s = \pm\frac{1}{2}$). Although excited optical metastable states may be suitable for auxiliary levels in some of these ion species, this places extreme requirements for the frequency stability of the exciting optical field to preserve coherence.

(2) The elimination of an auxiliary ground state removes the possible existence of spectator internal atomic levels, which can act as potential "leaks" from the two levels spanned by the quantum bits (assuming negligible population in excited electronic metastable states). This feature may be important to the success of quantum error-correction schemes [9], which can be degraded when leaks to spectator states are present [10].

(3) The elimination of the auxiliary level can dramatically reduce the sensitivity of a CN quantum logic gate to external magnetic fields fluctuations. It is generally impossible to find three atomic ground states whose splittings are all first-order magnetic-field insensitive. However, for ions possessing hyperfine structure, the transition frequency between two levels can be made first-order magnetic-field insensitive at particular values of an applied magnetic field.

(4) Finally, a reduction of laser pulses simplifies the tuning procedure and may increase the speed of the gate. For example, the gate realized in Ref. [8] required the accurate setting of the phase and frequency of three laser pulses, and the duration of the gate was dominated by the transit through the auxiliary level.

For quantum logic with trapped ions, we assume that each ion has two internal states (denoted by $|\downarrow\rangle$ and $|\uparrow\rangle$ with energy separation $\hbar\omega_0$). We consider the center-of-mass (COM) mode of the ions' collective motion at harmonic frequency $\omega$, described by the ladder of states $|n\rangle$ having vibrational quantum number $n=0,1,2,\ldots$ and energy $\hbar\omega(n+\frac{1}{2})$. In quantum logic applications, we consider only the $|n\rangle=|0\rangle$ and $|n\rangle=|1\rangle$ motional states. The "reduced" CN logic gate flips the internal state of a particular ion $j$ if and only if $|n\rangle=|1\rangle$, summarized in the following truth table and realized on a single ion in Ref. [8]:

$$
\begin{aligned}
&|0\rangle|\downarrow\rangle_j \rightarrow |0\rangle|\downarrow\rangle_j ,\\
&|0\rangle|\uparrow\rangle_j \rightarrow |0\rangle|\uparrow\rangle_j ,\\
&|1\rangle|\downarrow\rangle_j \rightarrow |1\rangle|\uparrow\rangle_j ,\\
&|1\rangle|\uparrow\rangle_j \rightarrow |1\rangle|\downarrow\rangle_j .
\end{aligned}
\tag{1}
$$

When this gate is surrounded by two extra operations that map and reset the internal state of another ion $i$ onto the collective COM state of motion, the result is a more general CN gate that flips the internal state of ion $j$, if and only if, ion $i$ is in state $|\uparrow\rangle_i$ [3]. Below, we show how the reduced CN gate of Eq. (1) can be condensed to a single laser pulse, or, equivalently, how the more general CN gate between two ions can be condensed to three laser pulses.

If $|\downarrow\rangle_j$ and $|\uparrow\rangle_j$ are coupled by a dipole moment operator $\boldsymbol{\mu}_j$, then exposing ion $j$ to a traveling-wave electric field $\mathbf{E}(\mathbf{z})=\mathbf{E}_0\cos(\mathbf{k}\cdot\mathbf{z}-\omega_L t+\phi)$ with frequency $\omega_L$, phase $\phi$, and wave vector $\mathbf{k}$, results in the interaction Hamiltonian:

$$
\mathcal{H}_I^{(j)} = -\boldsymbol{\mu}_j\cdot\mathbf{E}(z) = -\hbar g_j (S_+^{(j)}+S_-^{(j)})(e^{i(\mathbf{k}\cdot\mathbf{z}-\omega_L t-\phi)} + e^{-i(\mathbf{k}\cdot\mathbf{z}-\omega_L t-\phi)}). \tag{2}
$$

In this expression, $g_j=\boldsymbol{\mu}_j\cdot\mathbf{E}_0/2\hbar$ is the resonant Rabi frequency connecting $|\downarrow\rangle_j$ to $|\uparrow\rangle_j$ in the absence of confinement, $S_+^{(j)}$ ($S_-^{(j)}$) is the internal level raising (lowering) operator of the $j$th ion, $\mathbf{z}=z_0\hat{\mathbf{z}}(a+a^\dagger)$ is the COM coordinate operator of the confined motion with associated harmonic raising (lowering) operator $a^\dagger$ ($a$) and zero-point spread $z_0\equiv(\hbar/2M\omega)^{1/2}$, and $M$ is the total mass of the ion collection. If the applied radiation frequency is tuned to $\omega_L=\omega_0+(n'-n)\omega$, thereby coupling the states $|n\rangle|\downarrow\rangle$ and $|n'\rangle|\uparrow\rangle$, $\mathcal{H}_I^{(j)}$ is transformed to

$$
\mathcal{H}_I^{(j)} = -\hbar g_j (S_+^{(j)} e^{i\eta(a+a^\dagger)-i\phi} + S_-^{(j)} e^{-i\eta(a+a^\dagger)+i\phi}) \tag{3}
$$

in a frame rotating at $\omega_L$, where terms oscillating faster than $g_j$ ($g_j \ll \omega,\omega_0$) have been neglected. Here, $\eta\equiv(\mathbf{k}\cdot\hat{\mathbf{z}})z_0$ is the Lamb-Dicke parameter, which controls the amount of coupling between internal and motional states. In the case of two-photon stimulated Raman transitions through a third (virtual) electronic level [11,12], $g_j$ is replaced by $g_{j,1}g_{j,2}/\Delta$, where $g_{j,1}$ and $g_{j,2}$ are the individual Rabi frequencies of the two beams when resonantly coupled to the virtual level and $\Delta$ is the detuning from the virtual level; $\omega_L(\phi)$ is replaced by the difference frequency (phase) of the beams; and $\mathbf{k}$ is replaced by the difference in wave vectors of the two beams $\delta\mathbf{k}=\mathbf{k}_1-\mathbf{k}_2$.

TABLE I. Selected "magic" values of the Lamb-Dicke parameter $\eta$ which satisfy $1-\eta^2=(2k+1)/2m$. When the trapped ion is exposed to the carrier for a particular duration, the result is a "$\pi$-pulse" (mod $2\pi$) between the $|1\rangle|\downarrow\rangle \leftrightarrow |1\rangle|\uparrow\rangle$ states and no net rotation (mod $2\pi$) between the $|0\rangle|\downarrow\rangle \leftrightarrow |0\rangle|\uparrow\rangle$ states.

| $k$ (rotation of $\lvert n\rangle=\lvert 1\rangle$ states) | $m$ (rotation of $\lvert n\rangle=\lvert 0\rangle$ states) | $\eta=[1-(2k+1)/2m]^{1/2}$ |
|---|---|---|
| $0(\pi)$ | $1(2\pi)$ | 0.707 |
| | $2(4\pi)$ | 0.866 |
| | $3(6\pi)$ | 0.913 |
| $1(3\pi)$ | $2(4\pi)$ | 0.500 |
| | $3(6\pi)$ | 0.707 |
| | $4(8\pi)$ | 0.791 |
| $2(5\pi)$ | $3(6\pi)$ | 0.408 |
| | $4(8\pi)$ | 0.612 |
| | $5(10\pi)$ | 0.707 |
| $3(7\pi)$ | $4(8\pi)$ | 0.353 |
| | $5(10\pi)$ | 0.548 |
| | $6(12\pi)$ | 0.645 |
| $4(9\pi)$ | $5(10\pi)$ | 0.316 |
| | $6(12\pi)$ | 0.500 |
| | $7(14\pi)$ | 0.597 |

The CN quantum logic gate [Eq. (1)] can be realized with a single pulse tuned to $\omega_L=\omega_0$ (the "carrier") that couples the states $|n\rangle|\downarrow\rangle$ and $|n\rangle|\uparrow\rangle$ with Rabi frequency [13,14]

$$
\begin{aligned}
\Omega_{n,n} &= \frac{1}{\hbar}|\langle n|\langle\uparrow|\mathcal{H}_I^{(j)}|\downarrow\rangle|n\rangle| \\
&= g_j|\langle n|e^{i\eta(a+a^\dagger)}|n\rangle| \\
&= g_j e^{-\eta^2/2} L_n(\eta^2),
\end{aligned}
\tag{4}
$$

where $L_n(x)$ is a Laguerre polynomial. Specializing to the $|n\rangle=|0\rangle$ and $|n\rangle=|1\rangle$ vibrational levels relevant to quantum logic, we have

$$
\begin{aligned}
\Omega_{0,0} &= g_j e^{-\eta^2/2}, \\
\Omega_{1,1} &= g_j e^{-\eta^2/2}(1-\eta^2).
\end{aligned}
\tag{5}
$$

From Eqs. (4) and (5), the carrier Rabi frequencies depend nonlinearly on the vibrational quantum number $n$, with the nonlinearity mediated by the Lamb-Dicke parameter $\eta$ [15,16]. The reduced CN gate [Eq. (1)] can be achieved in a single pulse by setting $\eta$ so that $\Omega_{1,1}/\Omega_{0,0}=(2k+1)/2m$, with $k$ and $m$ integers satisfying $m>k\geq 0$ [17]. By driving the carrier transition for a duration $\tau$ such that $\Omega_{1,1}\tau=(k+\frac{1}{2})\pi$, or a "$\pi$-pulse" (mod $2\pi$) on the $|n\rangle=|1\rangle$ component,

then $\Omega_{0,0}\tau = m\pi$. Thus the states $|1\rangle|\downarrow\rangle \leftrightarrow |1\rangle|\uparrow\rangle$ are swapped, while the states $|0\rangle|\downarrow\rangle$ and $|0\rangle|\uparrow\rangle$ remain unaffected. The net unitary transformation, in the $\{0\downarrow, 0\uparrow, 1\downarrow, 1\uparrow\}$ basis is

$$\begin{bmatrix} 1 & 0 & 0 & 0 \\ 0 & 1 & 0 & 0 \\ 0 & 0 & 0 & ie^{i\phi}(-1)^{k-m} \\ 0 & 0 & ie^{-i\phi}(-1)^{k-m} & 0 \end{bmatrix}. \quad (6)$$

This transformation is equivalent to the reduced CN of Eq. (1), apart from phase factors that can be eliminated by the appropriate phase settings of subsequent logic operations [7].

The "magic" values of the Lamb-Dicke parameter that allow a single-pulsed reduced CN gate satisfy $L_1(\eta^2) = 1 - \eta^2 = (2k+1)/2m$ and are tabulated in Table I for the first few values [18]. It may be desirable for the reduced CN gate to employ the $|n\rangle = |2\rangle$ or $|n\rangle = |3\rangle$ state instead of the $|n\rangle = |1\rangle$ state for error correction of motional-state decoherence [19]. In these cases, the "magic" Lamb-Dicke parameters satisfy $L_2(\eta^2) = 1 - 2\eta^2 + \eta^4/2 = (2k+1)/2m$ for quantum logic with $|n\rangle = |0\rangle$ and $|2\rangle$, or $L_3(\eta^2) = 1 - 3\eta^2 + 3\eta^4/2 - \eta^6/6 = (2k+1)/2m$ for quantum logic with $|n\rangle = |0\rangle$ and $|3\rangle$.

Finally, we comment on the stability requirements of the Lamb-Dicke parameter in this scheme. Since the mapping pulses surrounding the single-ion CN gate (resulting in the general two-ion CN gate) have interaction strength proportional to $\eta$, this scheme does not place any additional premium on the stability of $\eta$. In this simplified scheme however, the *accuracy* of $\eta$ must also be maintained; otherwise at least one of the two vibrational states will not be rotated by the correct amount. In the two-photon Raman configuration [11,12], the Lamb-Dicke parameter $\eta = |\delta\mathbf{k}|z_0$ can be controlled by both the frequency of the trap (appearing in $z_0$) and by the geometrical wave-vector difference $\delta\mathbf{k}$ of the two Raman beams. Accurate setting of the Lamb-Dicke parameter should therefore not be difficult [16].

We acknowledge support from the U.S. National Security Agency, Office of Naval Research, and Army Research Office. We thank Brana Jelenković, Travis Mitchell, and Matt Young for a critical reading of the manuscript.

[1] D. P. DiVincenzo, Science **270**, 255 (1995); S. Lloyd, Sci. Am. (Int. Ed.) **273**, 140 (1995); A. Ekert and R. Jozsa, Rev. Mod. Phys. **68**, 733 (1996).

[2] D. J. Wineland, J. J. Bollinger, W. M. Itano, and D. J. Heinzen, Phys. Rev. A **50**, 67 (1994); J. J. Bollinger, W. M. Itano, D. J. Wineland, and D. J. Heinzen, *ibid.* **54**, 4649 (1996).

[3] J. I. Cirac and P. Zoller, Phys. Rev. Lett. **74**, 4091 (1995).

[4] W. H. Zurek, Phys. Today **44(10)**, 36 (1991).

[5] D. P. DiVincenzo, Phys. Rev. A **51**, 1015 (1995); A. Barenco *et al.*, *ibid.* **52**, 3457 (1995); S. Lloyd, Phys. Rev. Lett. **75**, 346 (1995).

[6] R. P. Feynman, Opt. News **11**, 11 (1985).

[7] A. Barenco, D. Deutsch, A. Ekert, and R. Jozsa, Phys. Rev. Lett. **74**, 4083 (1995).

[8] C. Monroe, D. Meekhof, B. King, W. Itano, and D. Wineland, Phys. Rev. Lett. **75**, 4714 (1995).

[9] P. W. Shor, Phys. Rev. A **52**, R2493 (1995); A. M. Steane, Phys. Rev. Lett. **77**, 793 (1996); R. Laflamme, C. Miquel, J. P. Paz, and W. H. Zurek, *ibid.* **77**, 198 (1996); D. P. DiVincenzo and P. W. Shor, *ibid.* **77**, 3260 (1996).

[10] M. Plenio and P. Knight (unpublished).

[11] J. E. Thomas, P. R. Hemmer, S. Ezekiel, C. C. Leiby, R. H. Picard, and C. R. Willis, Phys. Rev. Lett. **48**, 867 (1982).

[12] C. Monroe, D. M. Meekhof, B. E. King, S. R. Jefferts, W. M. Itano, D. J. Wineland, and P. Gould, Phys. Rev. Lett. **75**, 4011 (1995).

[13] K. E. Kahill and R. J. Glauber, Phys. Rev. **177**, 1857 (1969).

[14] D. J. Wineland and W. M. Itano, Phys. Rev. A **20**, 1521 (1979).

[15] W. Vogel and R. L. de Matos Filho, Phys. Rev. A **52**, 4214 (1995).

[16] D. M. Meekhof, C. Monroe, B. E. King, W. M. Itano, and D. J. Wineland, Phys. Rev. Lett. **76**, 1796 (1996).

[17] Setting $\Omega_{1,1}/\Omega_{0,0} = 2m/(2k+1)$ will also work, with the roles of the $|0\rangle$ and $|1\rangle$ vibrational states switched in Eq. (1).

[18] For rf (Paul) trap confinement along the COM motional mode, the Rabi frequencies of Eqs. (4) and (5) must be modified to include effects from the micromotion at the rf drive frequency $\omega_{rf}$. In the pseudopotential approximation ($\omega \ll \omega_{rf}$), this correction amounts to replacing the Lamb-Dicke parameter $\eta$ in this paper by $\eta[1 - \omega/(2\sqrt{2}\omega_{rf})]$, as pointed out in P. J. Bardroff, C. Leichtle, G. Schrade, and W. P. Schleich, Acta Phys. Slovaca **46**, 231 (1996). There is no correction if the COM motional mode is confined by static fields (e.g., the axial COM mode of a linear trap).

[19] J. I. Cirac, T. Pellizzari, and P. Zoller, Science **273**, 1207 (1996).

# ENTANGLED STATES OF ATOMIC IONS FOR QUANTUM METROLOGY AND COMPUTATION†

D.J. WINELAND, C. MONROE, D.M. MEEKHOF, B.E. KING, D. LEIBFRIED,
W.M. ITANO, J.C. BERGQUIST, D. BERKELAND, J.J. BOLLINGER, J. MILLER
*Ion Storage Group, Time and Frequency Division, NIST, Boulder, CO, 80303, USA*

A single trapped $^9Be^+$ ion is used to investigate Jaynes-Cummings dynamics for a two-level atomic system coupled to harmonic atomic motion. We create and investigate nonclassical states of motion including "Schrödinger-cat" states. A fundamental quantum logic gate is realized using the quantized motion and internal states as qubits. We explore some of the applications for, and problems in realizing, quantum logic based on multiple trapped ions.

## 1 Introduction

Currently, a major theme in atomic physics is coherent control of quantum states. This theme is manifested in a number of topics such as atom interferometry, atom optics, the atom laser, Bose-Einstein condensation, cavity-QED, electromagnetic-induced transparency, lasing without inversion, quantum computation, quantum cryptography, quantum-state engineering, squeezed states, and wavepacket dynamics. A number of these topics are the subjects of other presentations at this meeting.

In this paper we report related trapped-ion research on (1) the study of Jaynes-Cummings dynamics for a two-level atomic system coupled to harmonic atomic motion, (2) the study of quantum mechanical measurement problems such as the generation of Schrödinger-cat-like superposition states and their relation to various decoherence phenomena, and (3) coherent quantum logic for the investigation of scaling in a quantum computer and for preparation of entangled states useful for spectroscopy.

## 2 Entanglement

An entangled quantum state is one where the wave function of the overall system cannot be written as a product of the wave functions of the subsystems. In this case, a measurement on one of the subsystems will affect the state of the other subsystems. For example, consider a two-level atom bound in a 1-D harmonic well. Suppose we can create the state

$$\Psi = \frac{1}{\sqrt{2}}(|\downarrow\rangle|n\rangle + e^{i\phi}|\uparrow\rangle|n'\rangle), \qquad (1)$$

where the kets $|\downarrow\rangle$ and $|\uparrow\rangle$ denote the two internal eigenstates of the atom (here, we use the spin-½ analog to a two-level system: $\sigma_z|\uparrow\rangle = +|\uparrow\rangle$, etc. ), the second ket denotes a harmonic oscillator eigenstate $|n\rangle$, and $\phi$ is a (controlled) phase factor. If we measure the motional eigenstate of the atom and find it to be in level n, then it must also be found in the $\downarrow$ internal state if we measure $\sigma_z$. Similarly, if we find the atom in the n' motional state, it must be

found in the ↑ internal state. Such correlations are at the heart of the "EPR" experiments[1]. Another state we will consider below is the state for N two-level atoms

$$\Psi = \frac{1}{\sqrt{2}}(|\downarrow\rangle_1|\downarrow\rangle_2...|\downarrow\rangle_N + e^{i\phi}|\uparrow\rangle_1|\uparrow\rangle_2...|\uparrow\rangle_N), \qquad (2)$$

where the subscript i (= 1, 2, ..., N) denotes the ith atom. This state is "maximally entangled" in the sense that a measurement of $\sigma_z$ on any atom automatically determines the value of $\sigma_z$ of all other atoms.

## 3 Jaynes-Cummings-type coupling between internal and motional states

To achieve entanglement from an initially nonentangled system, we need to provide a coupling between subsystems so that the state of one subsystem affects the dynamics of another. Coupling between spins or two-level atoms can, in principle, be achieved through a dipole-dipole interaction (like the hyperfine coupling between electron and proton in the hydrogen atom). In a system of trapped neutral atoms, dipole-dipole coupling may be difficult to control to the desired level; for trapped ions the Coulomb repulsion inhibits strong dipole coupling between ions. However, in the case of trapped ions, the motion can be strongly coupled to the internal levels with the application of inhomogeneous (classical) electromagnetic fields. For example, we consider an atom confined in a 1-D harmonic potential. The atom's dipole moment $\mu$ is assumed to couple to an electric field E(x,t) through the Hamiltonian

$$H_I = -\mu E(x,t) = -\mu\left[E(x=0,t) + \frac{\partial E}{\partial x}x + \frac{1}{2}\frac{\partial^2 E}{\partial x^2}x^2 + \cdots\right]. \qquad (3)$$

We have $\mu \propto \sigma_+ + \sigma_-$, where $\sigma_+$ and $\sigma_-$ are the raising and lowering operators for the internal levels (in the spin-½ analog). In Eq. (3), the position $\mathbf{x}$ is an operator which we write as $\mathbf{x} = x_o(\mathbf{a} + \mathbf{a}^\dagger)$, where $\mathbf{a}$ and $\mathbf{a}^\dagger$ are the usual harmonic oscillator lowering and raising operators, and $x_o$ is the rms spread of the n=0 zero-point state of motion. As a simple example, suppose the field is static and the motional oscillation frequency $\omega$ of the atom is equal to the resonance frequency $\omega_o$ of the internal state transition. In its reference frame, the atom experiences an oscillating field due to the motion through the inhomogeneous field. Since $\omega = \omega_o$, this field resonantly drives transitions between the internal states. If the extent of the atom's motion is small enough that we need only consider the first two terms in Eq. (3), $H_I$ can be approximated as $H_{JCM} = \hbar\Omega(\sigma_+\mathbf{a} + \sigma_-\mathbf{a}^\dagger)$ (in the interaction frame and using the rotating wave approximation) where $\Omega$ is a proportionality constant. This Hamiltonian is also obtained if E is sinusoidally time varying (frequency $\omega_L$) and we satisfy the resonance condition $\omega_L + \omega = \omega_o$. This type of coupling was used to couple the spin and cyclotron motion in the classic electron g - 2 experiments of Dehmelt and coworkers[2]. Formally it is equivalent to the Jaynes-Cummings Hamiltonian of cavity-QED[3,4] which describes the

coupling between a two-level atom and a single mode of the radiation field. This analogy has been pointed out in various papers[5-8]; for a review, see Ref. 9 and further references in Ref. 8.

### *3.1 Realization a Jaynes-Cummings-type coupling for a trapped $^9Be^+$ ion*

To controllably manipulate the internal and vibrational levels of the ion, we must (1) initialize the ion in a well defined internal and motional state and (2) make the vibrational level spacing (trap frequency) much larger than any internal or motional relaxation rates. To accomplish this, we have built an rf (Paul) ion trap which confines a single $^9Be^+$ ion with pseudopotential harmonic trap frequencies of $(\omega_x, \omega_y, \omega_z)/2\pi \approx (11, 19, 29)$ MHz along the three principal axes of the trap[10].

The energy-level structure of $^9Be^+$ is summarized in Fig. 1. Because the ion is harmonically bound, the internal $^9Be^+$ electronic states must include the ladder of external harmonic oscillator levels of energy $E_n = \hbar\omega(n+\frac{1}{2})$, where we have considered only the x-dimension of the oscillator ($\omega \equiv \omega_x$) and its associated quantum number $n \equiv n_x \in (0, 1, 2, ...)$. The two internal levels of interest are the $^2S_{1/2}$ ground state hyperfine levels $|F=2, m_F=2\rangle$ (denoted by $|\downarrow\rangle$) and $|F=1, m_F=1\rangle$ (denoted by $|\uparrow\rangle$), which are separated in frequency by $\omega_o/2\pi \approx 1.25$ GHz. The other Zeeman levels are resolved from the $|\downarrow\rangle$ and $|\uparrow\rangle$ states by the application of a ≈0.2 mT magnetic field[8,11].

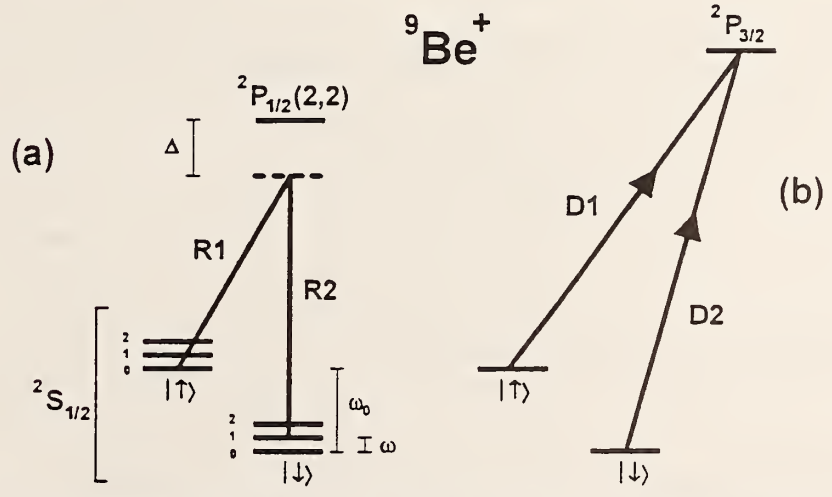


Fig. 1. (a) Electronic (internal) and motional (external) energy levels (not to scale) of the trapped $^9Be^+$ ion, coupled by indicated laser beams R1 and R2. The difference frequency of the Raman beams R1 and R2 is set near $\omega_o/2\pi$ = 1.250 GHz, providing a two-photon Raman coupling between the $^2S_{1/2}(F=2, m_F=2)$ and $^2S_{1/2}(F=1, m_F=1)$ hyperfine ground states (denoted by $|\downarrow\rangle$ and $|\uparrow\rangle$ respectively). The motional energy levels are depicted by a ladder of vibrational states separated in frequency by the trap frequency $\omega/2\pi$ = 11 MHz. The Raman beams are detuned $\Delta/2\pi$ = -12 GHz from the $^2P_{1/2}(F=2, m_F=2)$ excited state. As shown, the Raman beams are tuned to the red sideband. (b) Detection of the internal state is accomplished by illuminating the ion with $\sigma^+$-polarized "detection" beam D2, which drives the cycling $^2S_{1/2}(F=2, m_F=2) - {}^2P_{3/2}(F=3, m_F=3)$ transition, and observing the scattered fluorescence. The vibrational structure is omitted from (b) since it is not resolved. Beam D1, also $\sigma^+$ polarized, provides spontaneous recycling from the $|\uparrow\rangle$ to $|\downarrow\rangle$ state.

Strong field gradients can be obtained with laser fields ($e^{ikx}$ factor). In our experiment, the field corresponding to that in Eq. (3) is provided by two laser fields which drive stimulated-Raman transitions between the levels of interest (R1 and R2 of Fig. 1a). (The use of stimulated-Raman transitions has some technical advantages, but is formally equivalent to driving a narrow single-photon transition.) Two-photon stimulated Raman transitions between the $|\downarrow\rangle$ and $|\uparrow\rangle$ states can be driven by tuning the difference frequency of R1 and R2 to be near $\omega_o$. The two Raman beams ($\lambda \approx 313$ nm) are generated from a single laser source and acousto-optic modulator, allowing excellent stability of their relative frequency and phase. Both beams are detuned $\Delta/2\pi \approx 12$ GHz from the excited $^2P_{1/2}$ electronic state (radiative linewidth $\gamma/2\pi \approx 19.4$ MHz), and the polarizations are set to couple through the $^2P_{1/2}(F=2, m_F=2)$ level (the next nearest levels are the $^2P_{3/2}$ states which are over 200 GHz away and can be neglected). Because $\Delta >> \gamma$, the excited $^2P$ state can be adiabatically eliminated in a theoretical description, resulting in a coupling between the two ground states which exhibits a linewidth inversely proportional to the interaction time. When R1 and R2 are applied to the ion with wavevector difference $\delta\vec{k} = \vec{k}_1 - \vec{k}_2$ along the x-direction, the effective coupling Hamiltonian in the rotating-wave approximation is given by

$$H_I = g\left(\sigma_+ e^{i\eta(a^\dagger + a) - i\delta t} + \sigma_- e^{-i\eta(a^\dagger + a) + i\delta t}\right). \qquad (4)$$

The coupling strength g depends on $\Delta$ and the intensity of the laser beams, $\eta = |\delta\vec{k}|x_0 \approx 0.2$ is the Lamb-Dicke parameter, $x_0 = (\hbar/2m\omega)^{1/2} \approx 7$ nm, and $\delta$ is the difference between the relative frequency of the two Raman beams and $\omega_o$. Setting $\delta\vec{k}$ to be parallel to the x-axis of the trap, yields almost no coupling between the internal states and motion in the y- and z-directions.

If $\delta = \omega(n'-n)$, transitions are resonantly driven between the levels $|\downarrow,n\rangle$ and $|\uparrow,n'\rangle$ at a rate $\Omega_{n,n'}$ which is dependent on n and n'[8]. Starting from the $|\downarrow\rangle|n\rangle$ state, application of a Rabi -$\pi$ pulse coherently transfers the ion to the $|\uparrow\rangle|n'\rangle$ state; this corresponds to applying the Raman beams for a duration $\tau$ such that $\Omega_{n,n'}\cdot\tau = \pi/2$. If we apply the Raman beams for half of this time, we create the entangled state of Eq. (1). Here, we will assume the ion is confined in the Lamb-Dicke limit ($|\delta\vec{k}|\langle x^2\rangle^{1/2} << 1$) and will consider three transitions. The carrier, at $\delta = 0$, drives transitions between states $|\downarrow,n\rangle \leftrightarrow |\uparrow,n\rangle$ with Rabi frequency $\Omega_{n,n} = g$. The "first red sideband," corresponding to $\delta = -\omega$, drives transitions between states $|\downarrow,n\rangle \leftrightarrow |\uparrow,n-1\rangle$ with Rabi frequency $\Omega_{n,n-1} = g\eta\sqrt{n}$. This coupling is analogous to the case in cavity-QED[4] where energy is coherently exchanged between the internal and external degrees of freedom. The "first blue sideband," at $\delta = +\omega$, drives transitions between states $|\downarrow,n\rangle \leftrightarrow |\uparrow,n+1\rangle$ with Rabi frequency $\Omega_{n,n+1} = g\eta(n+1)^{1/2}$.

Preparation of the $|\downarrow\rangle|n=0\rangle$ state is accomplished by first Doppler cooling the ion to $\langle n\rangle \sim 1$, followed by sideband laser cooling using stimulated Raman transitions[11]. For sideband laser cooling, $\pi$ pulses on the first red sideband ($|\downarrow\rangle|n\rangle \rightarrow |\uparrow\rangle|n-1\rangle$) are alternated with repumping cycles using nearly resonant radiation (Fig. 1b) - which results (most probably) in transitions $|\uparrow\rangle|n\rangle \rightarrow |\downarrow\rangle|n\rangle$. These steps are repeated (typically 5 times) until

the ion resides in the $|\downarrow\rangle|0\rangle$ state with high probability (> 0.9).

From the $|\downarrow\rangle|0\rangle$ state, we are able to coherently create states of the form $|\downarrow\rangle\Psi(x)$, where the motional state $\Psi(x) = \Sigma_n C_n e^{-in\omega t}|n\rangle$ and the $C_n$ are complex. We can analyze the motional state created as follows: The Raman beams are pulsed on for a time $\tau$ and the probability $P_\downarrow(\tau)$ that the ion is in the $|\downarrow\rangle$ internal state is measured. The experiment is repeated for a range of $\tau$ values. When the Raman beams are tuned to the first blue sideband, the expected signal is

$$P_\downarrow(\tau) = \frac{1}{2}\left(1 + \sum_{n=0}^{\infty} P_n \cos(2\Omega_{n,n+1}\tau) e^{-\gamma_n \tau}\right), \qquad (5)$$

where $P_n \equiv |C_n|^2$ is the probability of finding the ion in state n and $\gamma_n$ are experimentally determined decay constants. The internal state $|\downarrow\rangle$ is detected by applying near-resonant $\sigma^+$-polarized laser radiation (beam D2, Fig. 1b) between the $|\downarrow\rangle$ and $^2P_{3/2}(F=3, m_F=3)$ energy levels. Because this is a cycling transition, detection efficiency is near unity[8,11]. The measured signal $P_\downarrow(\tau)$ can be inverted (Fourier cosine transform), allowing the extraction of the probability distribution of vibrational state occupation $P_n$. This signal does not show the phase coherences (phase factors of the $C_n$), which must be verified separately[8,12]. The most complete characterization is achieved with a state reconstruction technique[13].

### *3.2 Creation of Coherent and Schrödinger-Cat states*

We have created and analyzed thermal, Fock, squeezed, coherent, Schrödinger-cat states, and superpositions of Fock states[8,12,13]; here we briefly describe the creation and measurements of coherent and Schrödinger-cat states. A coherent state of motion

$$\Psi(x) = |\alpha\rangle \equiv \exp(-|\alpha|^2/2) \sum_{n=0}^{\infty} \frac{\alpha^n}{\sqrt{n!}} |n\rangle, \qquad (6)$$

corresponds to a displaced zero-point wave-packet oscillating in the potential well with amplitude $2|\alpha|x_0$. From Eq. (5), $P_\downarrow(\tau)$ for a coherent state will undergo quantum collapses and revivals[14]. These revivals are a purely quantum effect due to the discrete energy levels and the narrow distribution of states[4,14].

We have produced coherent states of ion motion from the $|\downarrow\rangle|0\rangle$ state by applying either a resonant (frequency $\omega$) classical driving field or a "moving standing wave" of laser radiation which resonantly drives the ion motion through the dipole force[8,12]. In Fig. 2, we show a measurement of $P_\downarrow(\tau)$ after creation of a coherent state of motion, exhibiting the expected collapse and revival signature. (For comparison, see the cavity-QED experiment of Ref. 4.) This data is fitted to Eq. (5) assuming a Poissonian distribution, allowing only $\langle n\rangle$ to vary. The inset shows the results of a separate analysis, which yield the probabilities of the Fock-state components, extracted by applying a Fourier cosine transform to $P_\downarrow(\tau)$ at the known frequencies as described above. These amplitudes display the expected

Poissonian dependence on n.

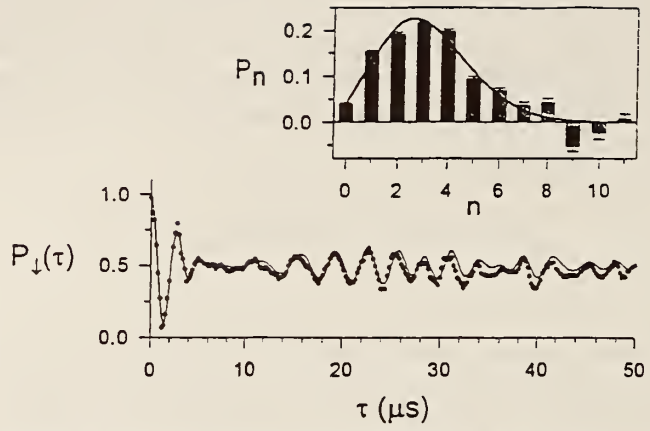


Fig. 2. $P_\downarrow(\tau)$ for a coherent state driven by the first blue sideband interaction, showing collapse and revival behavior. The data are fitted to a coherent state distribution, yielding $\langle n \rangle = 3.1(1)$. The inset shows the results of inverting the time-domain data by employing a Fourier cosine transform at the known Rabi frequencies $\Omega_{n,n+1}$, fitted to a Poissonian distribution, yielding $\langle n \rangle = 2.9(1)$. Each data point represents an average of ≈4000 measurements, or 1 s of integration.

A Schrödinger-cat state is a coherent superposition of classical-like states. In Schrödinger's original thought experiment[15], he described how one could, in principle, entangle a superposition state of an atom with a macroscopic-scale superposition of a live and dead cat. In our experiment[12], we construct an analogous state, on a smaller scale, with a single atom. We create the state

$$\Psi = \frac{1}{\sqrt{2}}(|\downarrow\rangle|\alpha_1\rangle + e^{i\phi}|\uparrow\rangle|\alpha_2\rangle), \tag{7}$$

where $|\alpha_1\rangle$ and $|\alpha_2\rangle$ are coherent motional states and $\phi$ is a (controlled) phase factor. The coherent states of the superposition are spatially separated by mesoscopic distances much greater than the size of the atom wavepacket which has a spread equal to $x_0$.

Analysis of this state is interesting from the point of view of the "quantum measurement problem," an issue that has been debated since the inception of quantum theory by Einstein, Bohr, and others, and continues today[16]. One practical approach toward resolving this controversy is the introduction of quantum decoherence, or the environmentally induced reduction of quantum superpositions into classical statistical mixtures[17]. Decoherence provides a way to quantify the elusive boundary between classical and quantum worlds, and almost always precludes the existence of macroscopic Schrödinger-cat states, except at extremely short time scales. On the other hand, the creation of mesoscopic Schrödinger-cat states like that of Eq. (7) may allow controlled studies of quantum decoherence and the quantum-classical boundary. This problem is directly relevant to quantum computation.

In our experiment, we create a Schrödinger-cat state of the single-ion $^9Be^+$ harmonic oscillator (Eq. (7)) with a sequence of laser pulses[12]. First, we create a state of the form $(|\downarrow\rangle + e^{i\xi}|\uparrow\rangle)|n=0\rangle/\sqrt{2}$ with a $\pi/2$ pulse on the Raman carrier transition (Sec. 3.1). To spatially separate the $|\downarrow\rangle$ and $|\uparrow\rangle$ components of the wave function, we apply a coherent excitation with an optical dipole force which, because of the polarization of the beams used to create the force, selectively excites the motion of only the $|\uparrow\rangle$ state. We then swap the $|\downarrow\rangle$ and $|\uparrow\rangle$ states with a $\pi$-carrier pulse and reapply the dipole force with a different phase to create the state of Eq. (7). In principle, if we could make $|\alpha_{1,2}|$ large enough, we could design a detector which could directly detect the (distinguishable) position of the particle and correlate it with a spin measurement[18]. Instead, to analyze this state in our experiment, we apply an additional laser pulse to couple the internal states, and we measure the resulting interference of the distinct wavepackets. With this interferometer, we can establish the correlations inherent in Eq. (7), the separation of the wavepackets, and the phase coherence $\phi$ between components of the wavefunction. These experiments are described in Ref. 12. The interference signal should be very sensitive to decoherence. As the separation $|\alpha_1 - \alpha_2|$ is made larger, decoherence is expected to exponentially degrade the fringe contrast[4,17].

We remark that other experiments generate Schrödinger-cats in the same sense as in our experiment. Examples are atom interferometers[19,20], and superpositions of electron wavepackets in atoms[21] (also, see additional citations in Ref. 12). However, as opposed to these experiments, the harmonic oscillator cat states of Eq. (7) do not disperse in time. This lack of dispersion provides a simple visualization of the "cat" (e.g., a marble rolling back and forth in a bowl which can be simultaneously at opposite extremes of motion) and should allow controlled studies of decoherence models.

## 4 Quantum Logic

Interest in quantum computation in the atomic physics community was stimulated, in part, by a talk given by Artur Ekert at the last ICAP meeting[22]. Subsequently, Ignacio Cirac and Peter Zoller[23,24] proposed an attractive scheme for a quantum computer which would use a string of ions in a linear trap as "qubits." This proposal has stimulated experimental efforts in several laboratories including those at Innsbruck, Los Alamos National Laboratory, IBM, and NIST.

Each qubit in a quantum computer could be implemented by a two-level atomic system; for the ith qubit, we label these states $|\downarrow\rangle_i$ and $|\uparrow\rangle_i$ as above. In general, any quantum computation can be comprised of a series of single-bit rotations and two-bit "controlled-NOT" (CN) logic operations[22, 25]. We are interested in implementing these two operations in a system of $^9Be^+$ ions. Single-bit rotations are straightforward and correspond to driving Raman carrier transitions (Sec. 3.1) for a controlled time. Such rotations have been achieved in many previous experiments. Next, we describe the demonstration of a nontrivial CN logic gate with a single $^9Be^+$ ion[26].

### *4.1 "Conditional dynamics" and a single-ion controlled-not logic gate*

The key to making a quantum logic gate is to provide conditional dynamics; that is, we

desire to perform on one physical subsystem a unitary transformation which is conditioned upon the quantum state of another subsystem[22]. In the context of cavity QED, the required conditional dynamics at the quantum level has recently been demonstrated[27,28]. For trapped ions, conditional dynamics at the quantum level has been demonstrated in verifications of zero-point laser cooling[11,29]. Recently, we demonstrated a CN logic gate with the ability to prepare arbitrary input states (the "keyboard").

A two-bit quantum CN operation provides the transformation:

$$|\epsilon_1\rangle|\epsilon_2\rangle \rightarrow |\epsilon_1\rangle|\epsilon_1 \oplus \epsilon_2\rangle\,, \tag{8}$$

where $\epsilon_1, \epsilon_2 \in \{0,1\}$ and $\oplus$ is addition modulo 2. The (implicit) phase factor in the transformation is equal to 1. In this expression $\epsilon_1$ is the called the control bit and $\epsilon_2$ is the target bit. If $\epsilon_1 = 0$, the target bit remains unchanged; if $\epsilon_1 = 1$, the target bit flips. In the single-ion experiment of Ref. 26, the control bit is the quantized state of one mode of the ion's motion. If the motional state is $|n=0\rangle$, it is taken to be a $|\epsilon_1=0\rangle$ state; if the motional state is $|n=1\rangle$, it is taken to be a $|\epsilon_1=1\rangle$ state. The target states are two ground-hyperfine states of the ion, the $|\downarrow\rangle$ and $|\uparrow\rangle$ states of Sec. 3.1 with the identification here $|\downarrow\rangle \rightarrow |\epsilon_2=0\rangle$ and $|\uparrow\rangle \rightarrow |\epsilon_2=1\rangle$. Following the notation of Sec. 3.1, the CN operation is realized by applying three Raman laser pulses in succession:

(1a) A "$\pi/2$-pulse" is applied on the spin carrier transition. For a certain choice of initial phase, this corresponds to the operator $V^{\chi}(\pi/2)$ of Ref. 23.

(1b) A $2\pi$-pulse is applied on the first blue sideband transition between levels $|\uparrow\rangle$ and an auxiliary level $|aux\rangle$ in the ion (the $|F=2, M_F=0\rangle$ level in $^9Be^+$). This operator is analogous to the operator $U_n^{21}$ of Ref. 23. This operation provides the conditional dynamics for the controlled-not operation in that it changes the sign of the $|\uparrow\rangle|n=1\rangle$ component of the wavefunction but leaves the sign of the $|\uparrow\rangle|n=0\rangle$ component of the wavefunction unchanged.

(1c) A $\pi/2$-pulse is applied to the spin carrier transition with a 180° phase shift relative to step (1a). This corresponds to the operator $V^{\chi}(-\pi/2)$ of Ref. 23.

Steps (1a) and (1c) can be regarded as two resonant pulses (of opposite phase) in the Ramsey separated-field method of spectroscopy. We can see that if step (b) is active (thereby changing the sign of the $|\uparrow\rangle|n=1\rangle$ component of the wave function) then a spin flip is produced by the Ramsey fields. If step (1b) is inactive, the net effect of the Ramsey fields is to leave the spin state unchanged. This CN operation can be incorporated to provide an overall CN operation between two ions in an ensemble of N ions if we choose the ion oscillator mode to be the center-of-mass (COM) mode of the ensemble. Specifically, to realize a controlled-not $\mathbf{C}_{m,k}$ between two ions (m = control bit, k = target bit), we first assume the COM is prepared in the zero-point state. The initial state of the system is therefore given by

$$\Psi = \left( \sum_{i=1}^{N} \sum_{M_i=\downarrow,\uparrow} C_{M_1,M_2,\ldots M_N} |M_1\rangle_1 |M_2\rangle_2 \ldots |M_N\rangle_N \right) |0\rangle \,. \qquad (9)$$

$\mathbf{C}_{m,k}$ can be accomplished with the following steps:

(2a) Apply a $\pi$-pulse on the red sideband of ion m (the assumption is that ions can be addressed separately[23]). This accomplishes the mapping $(\alpha|\downarrow\rangle_m + \beta|\uparrow\rangle_m)|0\rangle \rightarrow |\downarrow\rangle_m(\alpha|0\rangle - e^{i\phi}\beta|1\rangle)$ , and corresponds to the operator $U_m^{1,0}$ of Ref. 23. We note that in our experiments, we prepare the state $(\alpha|\downarrow\rangle + \beta|\uparrow\rangle)|0\rangle$ using the carrier transition (Sec. 3.1). We can then implement the mapping $(\alpha|\downarrow\rangle + \beta|\uparrow\rangle)|0\rangle \rightarrow |\downarrow\rangle_m(\alpha|0\rangle - e^{i\phi}\beta|1\rangle)$. This is the "keyboard" operation for preparation of arbitrary motional input states for the CN gate of steps 1a - 1c above. Analogous mapping of internal state superpositions to motional state superpositions were demonstrated in Ref. 26.

(2b) Apply the CN operation (steps 1a - 1c above) between the COM motion and ion k.

(2c) Repeat step (2a).

Overall, $\mathbf{C}_{m,k}$ provides the mappings $|\downarrow\rangle_m|\downarrow\rangle_k|0\rangle \rightarrow |\downarrow\rangle_m|\downarrow\rangle_k|0\rangle$, $|\downarrow\rangle_m|\uparrow\rangle_k|0\rangle \rightarrow |\downarrow\rangle_m|\uparrow\rangle_k|0\rangle$, $|\uparrow\rangle_m|\downarrow\rangle_k|0\rangle \rightarrow |\uparrow\rangle_m|\uparrow\rangle_k|0\rangle$ ,and $|\uparrow\rangle_m|\uparrow\rangle_k|0\rangle \rightarrow |\uparrow\rangle_m|\downarrow\rangle_k|0\rangle$ which is the desired logic of Eq. (8). Effectively, $\mathbf{C}_{m,k}$ works by mapping the internal state of ion m onto the COM motion, performing a CN between the motion and ion n, and then mapping the COM state back onto ion m. The resulting CN between ions m and k is not really different from the CN described by Cirac and Zoller[7], because the operations $V^{1/4}(\theta)$ and $U_m^{1,0}$ commute.

### *4.2 Quantum Registers and Schrödinger Cats*

The state represented by Eq. (9) is of the same form as that of Eq. (7). Both involve entangled superpositions and both are subject to the destructive effects of decoherence. Creation of Schrödinger-cats like Eq. (7) is particularly relevant to the ion-based quantum computer because the primary source of decoherence will probably be due to decoherence of the $|n=0,1\rangle$ motional states during the logic operations.

## 5 Potential for, and Problems with, Trapped-Ion Quantum Logic

Quantum computation has received a great deal of attention recently because of the algorithm proposed by Peter Shor for efficient factorization[30]. This has important implications for public-key data encryption where the security of these systems is due to the inability to efficiently factorize large numbers. To accomplish quantum factorization is extremely formidable with any technology; however, other applications of quantum logic may be more tractable.

### *5.1 Positive Aspects of Trapped-Ion Quantum Logic*

Internal state decoherence can be relatively small in experiments on trapped ions. The ions' energy level structure is, of course, perturbed at some level by electric and magnetic fields. However, energy level shifts caused by electric fields (Stark shifts) tend to be quite small and, in many cases, level shifts due to magnetic fields can be controlled well enough. This is evident from trapped-ion atomic clock experiments where linewidths smaller than 0.001 Hz have been achieved[31,32], indicating internal state coherence times exceeding 10 min.

The required laser cooling to $|n=0\rangle$ has been demonstrated[11,29] for single ions. A string of laser-cooled ions (Fig. 3), which could be used as a quantum register, has been achieved in a linear ion trap[33,34], but an immediate future task will be to achieve zero-point cooling (for at least the COM mode) on an ensemble of ions. For a computation performed on an ensemble of ions in a trap, this need not be done extremely well. All we require is that the cooling be sufficient that the ion's COM mode is predominantly in the n=0 state, so the "correct" answer to a computation is obtained most of the time. Similarly, although nearly unit detection efficiency has been achieved with trapped ions[11,35], the basic requirement is that the noise in the "readout" of the quantum register should minimize the number of times the calculation is repeated.

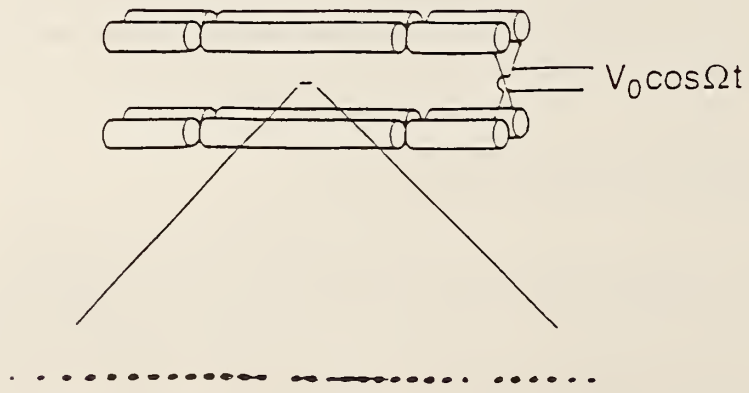


Fig. 3. The upper part of the figure shows a schematic diagram of the electrode configuration for a linear Paul-RF trap (rod spacing ≈ 1 mm)[34]. The lower part of the figure shows an image of a string of $^{199}Hg^+$ ions, illuminated with 194 nm radiation, taken with a UV-sensitive, photon counting imaging tube. The spacing between adjacent ions is approximately 10 μm. The "gaps" in the string are occupied by impurity ions, most likely other isotopes of $Hg^+$, which do not fluoresce because the frequencies of their resonant transitions do not coincide with those of the 194 nm $^2S_{1/2} - {}^2P_{1/2}$ transition of $^{199}Hg^+$.

Estimates of motional decoherence times from the $|n=0,1\rangle$ states, due to fundamental causes, should be very long (more than 100 s)[36]. However, these predictions have not been realized experimentally and the causes of the observed decoherence[11,29] must still be found.

*5.2 Problems and Possible Solutions*

Many problems may conspire to prevent large-scale quantum computation; some of the problems relevant to trapped ions are briefly mentioned here. More complete analyses are given elsewhere,[37, 38].

Motional decoherence can arise from fluctuating trap fields and radiative coupling to the environment. The integrity of the trap electrode structure is expected to play an important role, particularly if the number of ion qubits becomes large. Lithographic techniques for constructing electrodes[39] may be useful to insure accurate dimensional tolerances. With these techniques, it may also be possible to incorporate accurate (Josephson) voltage standards and (superconducting) flux magnetometers into the structure.

Laser power fluctuations will affect the fidelity of the rotations and logic gates (for example, $\pi/2$ rotations become $\pi/2 \pm \epsilon$ rotations where $\epsilon$ is unknown). Although the effects depend on the form of the noise and on the computational algorithm, a conservative estimate is to assume that phase errors accumulate linearly with the number of elemental operations. A computation requiring $10^6$ elemental operations would therefore require an intensity stability of one part in $10^6$ over the time of the computation. With current algorithms, factorization of large numbers will require even more elemental operations, so extreme laser stabilization will be required.

We have noted some of the advantages of using stimulated Raman transitions in quantum logic[26]. One apparent disadvantage is that, since the Raman beams are detuned from a virtual optical level, the energy levels are shifted by AC-Stark effects [see for example Ref. 36]. These effects are absent in single-photon transitions as assumed in Ref. 23. Therefore, if stimulated-Raman transitions are used and if the laser intensities fluctuate, additional Stark-induced phase errors will accumulate. However, we can show[38] that these errors are of the same order as those incurred from the angular errors of the preceding paragraph, if the two Raman laser intensities are approximately equal.

The scheme of Cirac and Zoller[23] assumes that the laser beams can separately address individual ion qubits. This necessitates a tradeoff between two factors. We desire that the ions be well separated spatially to allow a focused laser beam to address only one ion at a time. However, we also desire to spectrally isolate individual modes of the ion motion, to insure the fidelity of the logic. The closer in frequency the "contaminating" transitions (from coupling to other motional modes) are, the slower the logic speed must be to obtain isolation. To give an idea of the problem, we note that the separation of two $^9Be^+$ ions confined in a harmonic well of frequency $\nu \equiv \omega/2\pi$ is given by $d = 9.21\nu^{-2/3}$ where d is in micrometers and $\nu$ in megahertz. For longer strings, the spacing of the central ions becomes closer[40]. Although the focusing predicted with the use of Gaussian beam formulas implies the required isolation could be obtained for $\nu$ up to a few MHz, in practice, stray light intensity will undoubtedly be a problem. With the use of stimulated-Raman transitions [26,36], one solution for this problem is to take advantage of the inherent AC Stark shifts. The basic idea is that the (resonant) Rabi frequencies $g_1, g_2$ of the two Raman beams are made substantially different, say $g_1 >> g_2$. The transition frequency for the selected qubit is therefore shifted from the frequency of adjacent ions so that the adjacent ions are relatively unaffected. Unfortunately, the sensitivity to intensity fluctuations also becomes worse by the

ratio $g_1/g_2$[38].

A large scale computation will require a large qubit register. This makes it extremely hard to isolate unwanted motional mode transitions from the desired one[38]. As noted in Ref. 23, the desired COM trap-axis mode frequency in a linear trap is smaller than other trap axis modes and can therefore be relatively well isolated spectrally. However, as the number of ions in the trap increases, the radial mode frequencies will tend to overlap the COM mode frequency. Also, multi-mode excitations may become a problem when the difference frequency of the modes is close to the COM mode frequency. Therefore, a multiplexing scheme for ion qubit registers seems desirable; we discuss one possibility below.

### *5.3 A 1- or 2-qubit ion accumulator*

One possibility for multiplexing in a trapped-ion quantum computer is to perform all logic in minimal accumulators which hold one or two ions at a time[38]. Ions would be shuffled around in a "super-register" and into and out of the accumulators which are well shielded from the other ions. The shuffling could be accomplished with interconnected linear traps with segmented electrodes; this appears possible with the use of lithographic techniques. Single-bit rotations on the mth ion would be accomplished by moving that ion into an accumulator. Logic operations between ions m and k would be accomplished by first moving these ions into an accumulator. An accumulator would hold a second species of ion (say $Mg^+$) which could be used to provide laser cooling to the $|n=0\rangle$ level (of the mode used for the gate) if necessary. Therefore, for logic operations, an accumulator would hold two computational ions and the auxiliary ion. This scheme should make it easier to select ions with laser beams because it should be straightforward to address one ion while nulling the laser intensity on the other ion, even with very high trap frequencies. The very small number of logic ions in an accumulator (1 or 2) would make extraneous mode coupling much easier to avoid. The main problem appears to be that computational speed is reduced because of the time required to shuffle ions in and out of the accumulator and provide laser cooling with the auxiliary ion, if required. However, energy shifts of the ion's internal structure, due to the electric fields required to move the ion, need not be severe . For example, to move a $^9Be^+$ from rest to a location 1 cm away (and back to rest) in 1 μs would require a field of less than 50 V/cm. Electric fields of this order should give negligible phase shifts in qubits based on hyperfine structure[41]. The phase shift caused by time dilation would be less than 1 μrad.

### *5.4 Perspective on Ion Quantum Computation*

To be useful for factorization, a quantum computer must be able to factorize a 200 digit decimal number. This will require a few thousand ions and perhaps $10^9$ elementary operations[22]. Given the current state-of-the art (one ion and about 10 operations), we should therefore be skeptical. Decoherence will be most decisive in determining the fate of quantum computation. Already, decoherence from spontaneous emission appears to limit the number of operations possible[42,43]. The experiments can be expected to improve

dramatically, but we must hope for more efficient algorithms or ways to patch them (such as error correction schemes[24]) before large scale factorization is possible.

Any quantum system that might be contemplated in quantum computation must be reproducible, stable, and well isolated from the environment. Quantum dots have the potential advantage of large scale integration using microfabrication; however at the present time, they suffer from lack of precise reproducibility and excessive decoherence. Trapped ions are reproducible and relatively immune to environmental perturbations - this is the reason they are candidates for advanced frequency standards[44]. In principle, high information density could be achieved by scaling down the electrodes; however, we must then worry about excessive environmental coupling such as magnetic field perturbations caused by impurities and/or currents in the (nearby) trap electrodes[38]. Electric field perturbations will also become important. Therefore, in terms of scale, the trapped ion system may be close to optimum.

Finally, factorization, discrete logs, and certain other mathematical computations appear to be the hardest problems that quantum logic might be applied to. One of the applications for quantum computation that Richard Feynman originally had in mind was to simulate quantum mechanical calculations[45]. This idea is being explored again with new possibilities in mind[46]. Below, we consider an application to atomic measurement.

## 6 Quantum Logic Applied to Spectroscopy

We conclude by discussing a possible application of quantum logic in the realm of atomic physics. This application has the advantage of being useful with a relatively small number of ions and logic operations.

Entangled atomic states can improve the quantum-limited signal-to-noise ratio in spectroscopy[6,36,47]. In spectroscopy experiments on N atoms, in which changes in atomic populations are detected, we can view the problem in the following way using the spin-½ analogy for two-level atoms. We assume spectroscopy is performed by applying (classical) fields of frequency $\omega_R$ for a time $T_R$ according to the Ramsey method of separated fields[48]. After applying these fields, we measure the final state populations. For example, we might measure the operator $\tilde{N}_\downarrow$ corresponding to the number of atoms in the $|\downarrow\rangle$ state. In the spin-½ analog, this is equivalent to measuring the operator $J_z$, since $\tilde{N}_\downarrow = J\tilde{I} - J_z$ where $\tilde{I}$ is the identity operator.

If all technical sources of noise are eliminated, the signal-to-noise ratio (for repeated measurements) is fundamentally limited by the quantum fluctuations in the number of atoms which are observed to be in the $|\downarrow\rangle$ state. These fluctuations can be called quantum "projection" noise[49]. If spectroscopy is performed on N initially uncorrelated atoms (e.g., $\Psi(t=0) = \Pi_i |\downarrow\rangle_i$), the imprecision in a determination of the frequency of the transition is limited by projection noise to $(\Delta\omega)_{meas.} = 1/(NT_R\tau)^{1/2}$ where $\tau >> T_R$ is the total averaging time. If the atoms can be initially prepared in entangled states, it is possible to achieve $(\Delta\omega)_{meas.} < 1/(NT_R\tau)^{1/2}$. Initial theoretical investigations[6,36] examined the use of correlated states which could achieve $(\Delta\omega)_{meas.} < 1/(NT_R\tau)^{1/2}$ when the population ($J_z$) was measured. More recent theoretical investigations[47] consider the initial state to be one where, after the first Ramsey pulse, the internal state is the maximally entangled state of Eq. (2).

After applying the Ramsey fields, we measure the operator $\tilde{O} = \Pi_i \sigma_{iz}$ instead of $J_z$ (or $\tilde{N}$). For unit detection efficiency, we can achieve $(\Delta\omega)_{min} = 1/(N^2 T_R \tau)^{1/2}$ which is the maximum signal-to-noise ratio possible. For an atomic clock where $T_R$ is fixed by other constraints, this means that the time required to reach a certain measurement precision (stability) is reduced by a factor of N relative to the uncorrelated-atom case. In terms of quantum computation, this amounts to a computation of the function $\cos(N(\omega - \omega_o)T)$. Of course, this computation has special significance for the measurement of $\omega_o$ (an intrinsic computer parameter) but otherwise is much better suited for a classical computer! See Ref. 50 for related work.

Cirac and Zoller[23] have outlined a scheme for producing the state in Eq.(2) using quantum logic gates. Using the notation of Sec. 3.1, we would first apply a $\pi/2$ rotation to ion 1 to create the state $\Psi = 2^{-1/2}(|\downarrow\rangle_1 + e^{i\phi}|\uparrow\rangle_1)|\downarrow\rangle_2|\downarrow\rangle_3 \ldots |\downarrow\rangle_N$. We then apply the CN gate of Eq. (8) sequentially between ion 1 and ions 2 through N to achieve the state of Eq. (2). An alternative method for generating this state, without the need of addressing individual ions is described in Ref. 47.

**Acknowledgments**

We gratefully acknowledge the support of the National Security Agency, the US Office of Naval Research, and the US Army Research Office. We thank P. Huang, M. Lombardi, C. Wood, and M. Young for helpful comments on the manuscript.

**References**

† Contribution of NIST; not subject to US copyright.

1. A. Einstein, B. Podolsky, N. Rosen, *Phys. Rev.* 47, 777 (1935).
2. H. Dehmelt, *Science* 247, 539 (1990).
3. *Cavity Quantum Electrodynamics*, ed. by P.R. Berman (Academic Press, Boston, 1994).
4. S. Haroche, et al., these proceedings.
5. C.A. Blockley, D.F. Walls, and H. Risken, *Europhys. Lett.* 17, 509 (1992).
6. D. J. Wineland, J. J. Bollinger, W. M. Itano, F. L. Moore, and D. J. Heinzen, *Phys. Rev.* A46, R6797 (1992).
7. J.I. Cirac, R. Blatt, A.S. Parkins, and P. Zoller, *Phys. Rev. Lett.* 70, 762 (1993).
8. D.M. Meekhof, C. Monroe, B.E. King, W.M. Itano, and D.J. Wineland, *Phys. Rev. Lett.* 76, 1796 (1996).
9. J.I. Cirac, A.S. Parkins, R. Blatt, P. Zoller, in *Adv. Atomic and Molecular Phys.*, to be published.
10. S. R. Jefferts, C. Monroe, E. W. Bell, and D. J. Wineland, *Phys. Rev.* A51, 3112-3116 (1995).
11. C. Monroe, D. M. Meekhof, B. E. King, S. R. Jefferts, W. M. Itano, D. J. Wineland, and P. Gould, *Phys. Rev. Lett.* 75, 4011 (1995).
12. C. Monroe, D. M. Meekhof, B. E. King, and D. J. Wineland, *Science* 272, 1131

(1996).

13. D. Leibfried, D.M. Meekhof, B.E. King, C. Monroe, W.M. Itano, and D.J. Wineland, submitted.
14. J.H. Eberly, N.B. Narozhny, and J.J. Sanchez-Mondragon, *Phys. Rev. Lett.* 44, 1323 (1980).
15. E. Schrödinger, *Naturwissenschaften* 23, 807 (1935).
16. *Quantum Theory and Measurement*, ed. by J.A. Wheeler, W.H. Zurek (Princeton Univ. Press, Princeton, 1983).
17. W.H. Zurek, *Physics Today*, 44, 36 (1991).
18. J.F. Poyatos, J.I. Cirac, R. Blatt, P. Zoller, *Phys. Rev.* A, to be published.
19. D.E. Pritchard, et al., these proceedings.
20. O. Carnal and J. Mlynek, *Phys. Rev. Lett.* 66, 2689 (1991); D.W. Keith, C.R. Ekstrom, Q.A. Turchette, D.E. Pritchard, *Phys. Rev. Lett.*66, 2693 (1991); M. Kasevich and S. Chu, *Phys. Rev. Lett.* 67, 181 (1991); J. Lawall, S. Kulin, B. Saubamea, N. Bigelow, M. Leduc, and C. Cohen-Tannoudji, *Phys. Rev. Lett.* 75, 4194 (1995).
21. L.D. Noordam, D.I. Duncan, T.F. Gallagher, *Phys. Rev.* A45, 4734 (1992); R.R. Jones, C.S. Raman, S.W. Schumacher, P.H. Bucksbaum, *Phys. Rev. Lett.* 71, 2575 (1993); M.W. Noel and C.R. Stroud, Jr., *Phys. Rev. Lett.* 75, 1252 (1995).
22. A. Ekert, in *Atomic Physics 14*, ed. by D. J. Wineland, C. E. Wieman, and S. J. Smith, (proc. 14th International Conference on Atomic Physics, Boulder, CO, August, 1994), (AIP Press, NY, 1995), p. 450; A. Ekert and R. Jozsa, *Rev. Mod. Phys.*, July, 1996, to be published.
23. J.I. Cirac and P. Zoller, *Phys. Rev. Lett.* 74, 4091 (1995).
24. P. Zoller, et al., these proceedings.
25. D.P. DiVincenzo, *Phys. Rev.* A51, 1051 (1995).
26. C. Monroe, D. M. Meekhof, B. E. King, W. M. Itano, and D. J. Wineland, *Phys. Rev. Lett.* 75, 4714 (1995).
27. M. Brune, P. Nussenzveig, F. Schmidt-Kaler, F. Bernardot, A. Maali, J.M. Raimond, and S. Haroche, *Phys. Rev. Lett.* 72, 3339 (1994).
28. Q. Turchette, C. Hood, W. Lange, H. Mabushi, H.J. Kimble, *Phys. Rev. Lett.* 75, 4710 (1995).
29. F. Diedrich, J.C. Bergquist, W. M. Itano, and D.J. Wineland, *Phys. Rev. Lett.* 62, 403 (1989).
30. P. Shor, Proc. 35th Ann. Symp. on the Foundations of Comp. Sci. (IEEE Comp. Soc. Press, NY, 1994). p. 124.
31. J. J. Bollinger, D. J. Heinzen, W. M. Itano, S. L. Gilbert, and D. J. Wineland, *IEEE Trans. on Instrum. and Meas.* 40, 126 (1991).
32. P.T.H. Fisk, M.J. Sellars, M.A. Lawn, C. Coles, A.G. Mann, and D.G. Blair, *IEEE Trans. Instrum. Meas.* 44, 113 (1995).
33. M. G. Raizen, J. M. Gilligan, J. C. Bergquist, W. M. Itano, and D. J. Wineland, *Phys. Rev.* A45, 6493 (1992).
34. J. Miller, M. E. Poitzsch, F. C. Cruz, D. J. Berkeland, J. C. Bergquist, W. M. Itano. and D. J. Wineland, Proc., 1995 IEEE Intl. Frequency Control Symp., June

1995, pp. 110-112; M. E. Poitzsch, J. C. Bergquist, W. M. Itano, and D. J. Wineland, *Rev. Sci. Instrum.* 67, 129 (1996).

35. W. Nagourney, J. Sandberg, and H.G. Dehmelt, *Phys. Rev. Lett.* 56, 2797 (1986); Th. Sauter, R. Blatt, W. Neuhauser, and P.E. Toschek, *Phys. Rev. Lett.* 57, 1696 (1989); J.C. Bergquist, R.G. Hulet, W.M. Itano, and D.J. Wineland, *Phys. Rev. Lett.* 57, 1699 (1986).
36. D.J. Wineland, J. J. Bollinger, W. M. Itano, and D. J. Heinzen, *Phys. Rev.* A50, 67 (1994).
37. R.J. Hughes, D.F.V. James, E.H. Knill, R. Laflamme, and A.G. Petschek, Los Alamos report LA-UR-96-1266 (1966) (submitted to PRL); Los Alamos eprint archive quant-ph/9604026.
38. D.J. Wineland, et al., in preparation.
39. R. Brewer, R.G. DeVoe, and R. Kallenbach, *Phys. Rev.* A46, R6781 (1992).
40. D. J. Wineland, J. C. Bergquist, J. J. Bollinger, W. M. Itano, D. J. Heinzen, S. L. Gilbert, C. H. Manney, and M. G. Raizen, *IEEE Trans. on Ultrasonics, Ferroelectrics, and Frequency Control* 37, 515 (1990).
41. Wayne M. Itano, L.L. Lewis, and D.J. Wineland, *Phys. Rev.* A25, 1233 (1982).
42. M.B. Plenio and P.L. Knight, Phys. Rev. A53, 2986 (1996).
43. We note that the effects of spontaneous emission are significantly reduced if rf transitions between hyperfine levels are induced with inhomogeneous rf fields (Sec. 3).
44. see: *Proc., Fifth Symp. Freq. Standards and Metrology*, ed. by J.C. Bergquist, Woods Hole, MA, Oct. 1995 (World Scientific, Singapore, 1996).
45. R.P. Feynman, *Int. J. Theor. Phys.* 21, 467 (1982); *Opt. News* 11, 11 (1985); *Found. Phys.* 16, 507 (1986).
46. S. Lloyd, *Science,* to be published.
47. J. J. Bollinger, D. J. Wineland, W. M. Itano, and D. J. Heinzen, *Proc., Fifth Symp. Freq. Standards and Metrology*, ed. by J.C. Bergquist, Woods Hole, MA, Oct. 1995 (World Scientific, Singapore, 1996), p. 107.
48. N.F. Ramsey, *Molecular Beams*, (Oxford University Press, London, 1963).
49. W. M. Itano, J. C. Bergquist, J. J. Bollinger, J. M. Gilligan, D. J. Heinzen, F. L. Moore, M. G. Raizen, and D. J. Wineland, *Phys. Rev.* A47, 3554 (1993).
50. J. Sørensen, J Erland, J. Hald, A. Kuzmich, K. Mølmer, and E.S. Polzik, contributed abstract, this meeting.

JOURNAL OF MODERN OPTICS, 1997, VOL. 44, NO. 11/12, 2485–2505

# Experimental preparation and measurement of quantum states of motion of a trapped atom†

D. LEIBFRIED, D. M. MEEKHOF, C. MONROE, B. E. KING, W. M. ITANO and D. J. WINELAND

Time and Frequency Division, National Institute of Standards and Technology, 325 Broadway, Boulder, CO 80303-3328, USA

(*Received 5 November 1996*)

**Abstract.** We report the creation and full determination of several quantum states of motion of a $^9Be^+$ ion bound in a RF (Paul) trap. The states are coherently prepared from an ion which has been initially laser cooled to the zero-point of motion. We create states having both classical and non-classical character including thermal, number, coherent, squeezed, and 'Schrödinger cat' states. The motional quantum state is fully reconstructed using two novel schemes that determine the density matrix in the number state basis or the Wigner function. Our techniques allow well controlled experiments decoherence and related phenomena on the quantum–classical borderline.

## 1. Introduction

The ability to create and completely characterize a variety of fundamental quantum states has long been sought after in the laboratory since it brings to the forefront issues involving the relationship between quantum and classical physics. Since most theoretical proposals to achieve these goals were put forward in the field of quantum optics, it might seem surprising that some of the first experiments succeeding in both respects were realized on the motion of a trapped atom. However, since both the photon field of quantum optics and the motion of a trapped atom are quantum harmonic oscillators, their couplings to internal atomic levels (described by the Jaynes–Cummings model (JCM) [1, 2]) are quite similar [3, 4]. In addition, for the case of a harmonically-bound atom driven by a light field, there are interactions beyond the simple Jaynes–Cummings coupling, allowing more control over the engineering and measurement of quantum states.

Section 2 will give a brief description of the interaction of a trapped atom with light fields and outline the similarities to the Jaynes–Cummings Hamiltonian studied in quantum optics. Our experimental setup and the cooling of the trapped atom to the motional ground state are described in section 3. We then describe the controlled preparation of both classical and non-classical motional states including a 'Schrödinger-cat' type state in section 4. The complete measurement of either the density matrix in the number state basis or the Wigner function is covered in section 5 and we finally offer some conclusions in section 6.



0950–0340/97 $12·00 

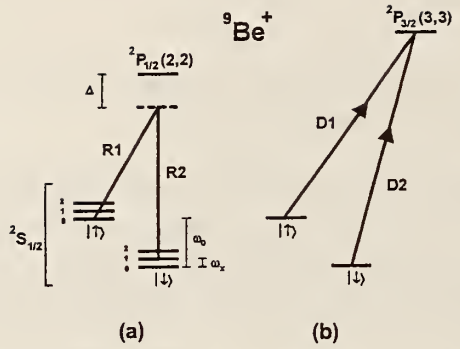


Figure 1. (*a*) Electronic (internal) and motional (external) energy levels of the trapped $Be^+$ ion, coupled by laser beams R1 and R2. The difference frequency of the Raman beams is set near $\omega_0/2\pi \simeq 1{\cdot}250$ GHz, providing a two photon Raman coupling between the $^2S_{1/2}(F=2, m_F=2)$ and $^2S_{1/2}(F=1, m_F=1)$ hyperfine ground states (denoted by $|\downarrow\rangle$ and $|\uparrow\rangle$ respectively). The motional energy levels are depicted by a ladder of vibrational states separated by the trap frequency $\omega_x/(2\pi) \simeq 11{\cdot}2$ MHz. The Raman beams are detuned by $\Delta/(2\pi) \simeq -12$ GHz from the $^2P_{1/2}$ $(F=2, m_F=2)$ excited state. As shown, the Raman beams are tuned to the first red sideband. (*b*) Detection of the internal state is accomplished by illuminating the ion with a $\sigma^+$ polarized 'detection' beam D2, which drives the cycling $^2S_{1/2}$ $(F=2, m_F=2) \rightarrow {}^2P_{3/2}(F=3, m_F=3)$ transition, and observing the scattered fluorescence. The vibrational structure is omitted from (*b*) since it is not resolved. Beam D1, also $\sigma^+$ polarized, provides spontaneous recycling from the $|\uparrow\rangle$ to $|\downarrow\rangle$ state.

## 2. Interaction of a trapped atom with light fields

To describe the interaction of the trapped atom with light fields we make the following assumptions which will be justified below. First we assume that the internal degrees of freedom of the trapped atom are sufficiently described by a two level system, second that the motion of the atom bound in the trap is harmonic in all three dimensions, and finally that the vibrational level spacings (trap frequencies) and internal state transition frequencies are much larger than any internal or motional relaxation rates. Starting from these assumptions we can describe the trapped atom as a two level system with levels labeled $|\downarrow\rangle$, and $|\uparrow\rangle$, dressed by the harmonic oscillator ladders of the external motion with number states $|n_x n_y n_z\rangle$. We will consider coupling to only the $\hat{x}$ dimension harmonic oscillator with number states $|n_x\rangle = |n\rangle$ $[n = 1, 2, \ldots \infty$, see figure 1 (*a*)]. To couple the motional and internal degrees of freedom of the trapped atom, we apply two laser beams whose difference frequency matches the separation of two energy levels, as depicted in figure 1 (*a*). The beams are each sufficiently detuned from short-lived excited electronic states, resulting in two-photon stimulated Raman transitions between the states of interest which are formally equivalent to narrow single photon transitions. By employing two laser beams to drive stimulated Raman transitions, we are able to combine the advantages of strong optical electric-field gradients (allowing manipulation of the state of motion) and microwave stability of the crucial difference frequency.

In the rotating wave approximation in a frame rotating with $\omega_0$, where $\hbar\omega_0$ is the energy difference of the two internal levels, the interaction of the classical laser field with the two levels of the trapped atom is described by the Hamiltonian

$$H_{\text{int}}(t) = \hbar g(\sigma_+ \exp[-i(\delta t - \mathbf{k}\cdot\mathbf{x})] + \sigma_- \exp[i(\delta t - \mathbf{k}\cdot\mathbf{x}]), \tag{1}$$

where $g$ denotes the interaction strength, $\sigma^+$ and $\sigma^-$ are the Pauli spin matrices describing the two level system and $\delta$ the detuning of the frequency difference of the two Raman beams $\omega = \omega_1 - \omega_2$ with respect to $\omega_0$, and $\mathbf{k} = \mathbf{k}_1 - \mathbf{k}_2$ is the difference of the two Raman beam wave-vectors. In these experiments the wave-vector difference was always chosen to be parallel with the $\hat{x}$-direction of the trap, so $\mathbf{k}\cdot\mathbf{x} = kx$ and the interaction couples only the motion in $\hat{x}$-direction to the internal state of the trapped atom.

In our experiment we confine a single beryllium-ion in a RF-(Paul) trap [5], so the trapping potential is not a simple harmonic potential but rather a time dependent potential with the periodicity of the RF field. Based on the full quantum mechanical treatment of Glauber [6], several workers have studied the time dependence of the interaction Hamiltonian (1) [7, 8]. While Bardroff *et al.* [7] give a general expression for the Rabi frequencies, we restrict ourselves to an approximate treatment in the limit where the dimensionless Paul trap parameters $a$ and $q$ related to the static and RF-potential [5] are much smaller than one (in our trap, $a \simeq 0$, $q \simeq 0{\cdot}14$). The main change in the full treatment is a common scaling factor in the interaction strength (Rabi frequencies). This is already taken into account in our experiments, since we scale all our Rabi frequencies with the experimentally determined Rabi frequency $\Omega_{0,1}$ (see below). In the approximation of a simple harmonic oscillator, with creation and destruction operators $a^+$ and $a$, the interaction Hamiltonian (1) reduces to

$$H_{\text{eff}} = \hbar g(\sigma_+ \exp[i\eta(a^\dagger + a) - i\delta t] + \sigma_- \exp[-\eta(a^\dagger + a) + i\delta t]), \tag{2}$$

where $\eta = k[\hbar/(2m\omega_x)]^{1/2}$, $m$ is the mass and $\omega_x$ is the secular frequency of the ion in $\hat{x}$-direction. By tuning the frequency difference $\delta$ to an integer multiple of the secular frequency $\omega_x$, $\delta = (n' - n)\omega_x$, we can resonantly drive transitions from $|\downarrow, n\rangle$ to $|\uparrow, n'\rangle$. In this case $H_{\text{eff}}$ is dominated by a single stationary term. The exponent $\exp[i\eta(a^\dagger + a)]$ in $H_{\text{eff}}$ contains all powers of $a$ and $a^\dagger$. Since their time dependence (in the interaction picture) is $a(t)^m = \tilde{a}(t)^m \exp(-im\omega_x t)$, all contributions with $m \neq n' - n$ oscillate rapidly and average out when $\omega_x$ is much larger than $g$. The biggest stationary term in the Lamb–Dicke limit ($\langle\eta(a + a^\dagger)^2\rangle^{1/2} \ll 1$) is proportional to

$$\bar{H}_{\text{eff}} \sim \hbar g \frac{\eta^{n-n'}}{(n-n')!}(\sigma_+(a^\dagger)^{n-n'} + \sigma_- a^{n-n'}), \tag{3}$$

if $n' - n > 0$, and

$$\bar{H}_{\text{eff}} \sim \hbar g \frac{\eta^{n'-n}}{(n'-n)!}(\sigma_+ a^{n-n'} + \sigma_-(a^\dagger)^{n-n'}), \tag{4}$$

if $n' - n < 0$. In the special case of $n' - n = -1$ ($\delta < 0$, first red sideband) we obtain the familiar Jaynes–Cummings Hamiltonian $\eta(\sigma_+ a + \sigma_- a^\dagger)$. By choosing other detunings we can realize a number of couplings beyond the Jaynes–Cummings coupling; for example a 'two-phonon' coupling $(\eta^2/2)(\sigma_+ a^2 + \sigma_-(a^\dagger)^2)$ for $n - n' = -2$ (second red sideband). The coupling strength to lowest order in $\eta$ is given by the matrix elements (Rabi frequencies)

$$\hbar\Omega_{n,n'} = \langle\downarrow, n|\bar{H}_{\text{eff}}|\uparrow, n'\rangle \simeq \hbar g \frac{\eta^{|n'-n|}}{|n'-n|}[n_>(n_> - 1)\ldots(n_< + 1)]^{\frac{1}{2}}, \tag{5}$$

where $n_>$ ($n_<$) is the greater (lesser) of $n$ and $n'$. The differences are only significant for large $n$ or $n'$. A 'Rabi-π-pulse', which transfers a pure $|\downarrow, n\rangle$ state to a pure $|\uparrow, n'\rangle$ state, corresponds to applying the Raman beams for a time $\tau$, such that $\Omega_{n,n'}\tau = \pi/2$.

## 3. Experimental setup and cooling to the motional ground state

In our experiment, a single $^9Be^+$ ion is stored in a RF Paul trap [9] with a secular frequency along $x$ of $\omega_x/2\pi \approx 11{\cdot}2\,\mathrm{MHz}$, providing a spread of the ground state wavefunction of about $\Delta x_0 \equiv \langle x^2\rangle^{1/2} \approx 7\,\mathrm{nm}$. The $|\downarrow\rangle$ and $|\uparrow\rangle$ levels are the long-lived $^2S_{1/2}(F = 2,\ m_F = 2)$ and $^2S_{1/2}(F = 1,\ m_F = 1)$ hyperfine ground states (see figure 1).

To prepare the ion in the ground state, it is first 'Doppler pre-cooled' by two beams of $\sigma^+$ polarized light detuned by approximately one linewidth ($\Gamma/2\pi = 19{\cdot}4\,\mathrm{MHz}$) to the red of the $^2S_{1/2}(F = 1$ and $2) \rightarrow {}^2P_{3/2}$ transitions. This cools the ion to $\bar{n} \approx 1$, in the $|\downarrow\rangle$ state. To further cool the ion we use narrower Raman transitions in order to be in the resolved sideband limit. One cooling cycle consists of two steps. First we drive stimulated Raman transitions to the $|\uparrow\rangle$ state by applying a pair of travelling-wave laser beams detuned from the $^2P_{1/2}$ state [10]. These Raman beam wave-vectors point at 45° to the $\hat{x}$-axis with their wave-vector difference nearly along the $\hat{x}$-axis of the trap [$\eta_x = 0{\cdot}202(5)$], so the raman transitions are highly insensitive to motion in the $\hat{y}$ or $\hat{z}$ directions. The beams are derived from the same laser with an acousto-optic modulator, reducing the effects of laser frequency jitter. The difference frequency can be tuned near the ground state hyperfine splitting of $\omega_0/2\pi \approx 1{\cdot}25\,\mathrm{GHz}$. The beams are detuned by approximately 12 GHz to the red of the $^2P_{1/2}$ excited state with approximately 0·5 mW in each beam, so that the Raman transition Rabi frequency $\Omega_{0,1}/2\pi$ is approximately 200 kHz, and the vibrational structure is clearly resolved. For cooling, the frequency difference is tuned to the red sideband ($\delta = -\omega_x$), so that one vibrational quantum is lost in the transfer to the $|\uparrow\rangle$ state. The time during which we apply the red-sideband interaction is optimized to leave the internal state as close to a pure $|\uparrow\rangle$ state as possible (Rabi-π-pulse). In the second step of the cooling cycle, we apply lasers tuned to the $|\uparrow\rangle \rightarrow {}^2P_{3/2}$ and $^2S_{1/2}(F = 2,\ m_F = 1) \rightarrow {}^2P_{1/2}$ that repump the atom to the $|\downarrow\rangle$ state. In analogy to the Mössbauer effect, the recoil of the spontaneous emission process in this repumping is absorbed by the whole trap structure with high probability, leaving the motional state of the trapped atom unchanged. Five cycles of this two-step cooling scheme prepare the ion in the $|\downarrow, n = 0\rangle$ state approximately 95% of the time [10].

In the experiments described below we detect the probability of being in one of the states $|\uparrow\rangle$ or $|\downarrow\rangle$. We detect $P_\downarrow$, the probability of finding the $|\downarrow\rangle$-state, by driving a cycling transition to the $^2P_{3/2}$ with $\sigma^+$ polarized light and detecting the emitted fluorescence. The $|\uparrow\rangle$ is not resonantly coupled to an excited state by the light-field, so $P_\downarrow$ is proportional to the number of tries where we see fluorescence when we repeat the experiment. Since the application of the resonant light field effectively reduces the internal state to either $|\uparrow\rangle$ or $|\downarrow\rangle$, we can consider the internal atomic state to be a unit efficiency detector, even if we fail to detect the fluorescence every time. The analogy with photon detection would be a 100% efficient detector which is read out only sporadically.

## 4. Creation of various motional states and measurement of their number state population

### 4.1. *Fock states*

A Fock state $|n\rangle$ is a harmonic oscillator energy eigenstate, designated by the number $n$ of energy quanta. Several techniques for the creation of Fock states of motion have been proposed, using quantum jumps [4, 11], adiabatic passage [12], or trapping states [13]; here we use an alternate technique. Since the ion is initially cooled to the $|\downarrow, 0\rangle$ Fock state, we create higher-$n$ Fock states by simply applying a sequence of Rabi-$\pi$-pulses of laser radiation on the blue sideband, red sideband, or carrier. For example, the $|\uparrow, 2\rangle$ state is prepared by using blue sideband, red sideband, and carrier $\pi$-pulses in succession, so that the ion steps through the states $|\downarrow, 0\rangle$, $|\uparrow, 1\rangle$, $|\downarrow, 2\rangle$, and $|\uparrow, 2\rangle$ [14].

Once the Fock state is created, the signature of the state can be found by driving Rabi transitions on the blue sideband. Specifically, the Raman beams were tuned to the first blue sideband and applied for a time $t$. The probability of finding the $|\downarrow\rangle$ level was then measured by applying $\sigma^+$ polarized radiation on the $|\downarrow\rangle \rightarrow {}^2P_{3/2}$ cycling transition and detecting the fluorescence as described above. The value of $t$ was stepped, and the data $P_\uparrow(t)$ was acquired. The rate of the Rabi flopping, $\Omega_{n,n+1}$ in equation (5), depends on the value of $n$ of the Fock state occupied. The expected signal is

$$P_\downarrow(t) = \tfrac{1}{2}[1 + \cos(2\Omega_{n,n+1}t)\exp(-\gamma_n(t)], \tag{6}$$

where $\gamma_n$ is the decoherence rate between levels $|n\rangle$ and $|n+1\rangle$. The measured $P_\downarrow(t)$ for an initial $|\downarrow, n = 0\rangle$ Fock state is shown in figure 2 (*a*) together with a fit to equation (6), yielding $\Omega_{0,1}/(2\pi) = 94(1)\text{kHz}$ and $\gamma_0 = 11{\cdot}9(4)\,10^3\,\text{s}^{-1}$.

We created a series of Fock states $|\downarrow, n\rangle$ and recorded $P_\downarrow(t)$. The measured Rabi frequency ratios $\Omega_{n,n+1}/\Omega_{0,1}$ are plotted in figure 2 (*b*), showing very good agreement with the theoretical frequencies corrected for the trap's finite Lamb–Dicke parameter $\eta = 0{\cdot}202$. The observed increase of $\gamma_n$ with $n$ (we experimentally find $\gamma_n \approx \gamma_0(n+1)^{0.7}$) is qualitatively consistent with our view that the decoherence is due to technical problems.

### 4.2. *Thermal states*

When the ion's motion is not in a Fock state, $P_\downarrow(t)$ shows a more complicated structure. In this case,

$$P_\downarrow(t) = \tfrac{1}{2}\left[1 + \sum_{n=0}^{\infty} P_n \cos(2\Omega_{n,n+1}t)\exp(-\gamma_n t)\right], \tag{7}$$

where $P_n$ is the probability of finding the atom in the $n$th motional number state. For example, a thermal distribution is found after Doppler cooling [15]. In this case, the probability of occupying the $n$th Fock level is $P_n = [\bar{n}^n/(1+\bar{n})^{n+1}]$, where $\bar{n}$ is the average vibrational quantum number. The value of $\bar{n}$ can be controlled by the detuning during Doppler cooling. An example of $P_\downarrow(t)$ data for a thermal state of motion is given in figure 3. To demonstrate consistency with a thermal state of motion, the time-domain data are fitted to equation (7) with a thermal population distribution for $P_n$. The signal scale and $\bar{n}$ are allowed to vary in the fit. Values for the base Rabi frequency $\Omega_{0,1}$ and base decay rate $\gamma_0$ (from which the other rates are scaled using the dependence found in the Fock state data) are obtained from a

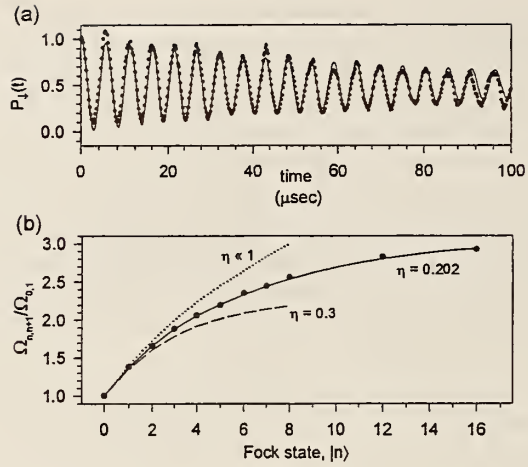


Figure 2. (*a*) $P_\downarrow(t)$ for an initial $|\downarrow, 0\rangle$ Fock state driven by a JCM-type interaction provided by tuning the stimulated Raman beams to the first blue sideband. The solid line is a fit to an exponentially decaying sinusoid. 9*b*) The relative Rabi frequencies $\Omega_{n,n+1}/\Omega_{0,1}$ plotted against the prepared Fock state number $n$. The lines represent the predictions of the nonlinear JCM for certain Lamb–Dicke parameters, showing every good agreement with the known Lamb–Dicke parameter $\eta = 0{\cdot}202(5)$. For $\eta \ll 1$ the ratio of the Rabi frequencies is given by $\Omega_{n,n+1}/\Omega_{0,1} = (n+1)^{\frac{1}{2}}$.

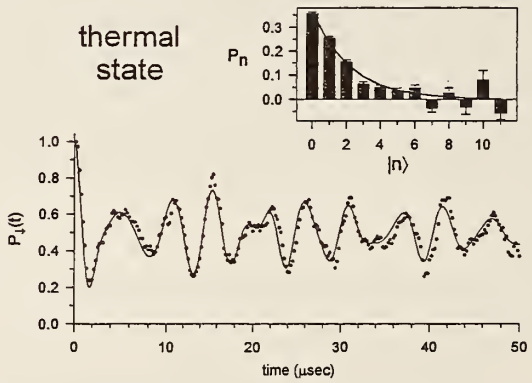


Figure 3. $P_\downarrow(t)$ for a thermal state. The data (points) are fitted (line) to a superposition of Fock states with $P_n$ given by a thermal state distribution. The fit allows $\bar{n}$ to vary, yielding a value of $1{\cdot}3 \pm 0{\cdot}1$. The inset shows the decompostion of the data onto the Fock state components (bars) with a fit (line) to the expected exponential distribution, yielding $1{\cdot}5 \pm 0{\cdot}1$.

separate trace of $P_\downarrow(t)$ for an initial $|\downarrow, 0\rangle$ state. For figure 3, the fit yields $\bar{n} = 1{\cdot}3 \pm 0{\cdot}1$. The inset shows the results of an independent analysis (the frequency domain analysis). In this case, we directly extract the populations of the various $|n\rangle$ levels. Since the Fock state parameters $\Omega_{n,n+1}$ and $\gamma_n$ are well characterized, the time-domain data can be decomposed into Fock-state components. Equation (7) is linear in $P_n$, so we use singular value decomposition [16] to

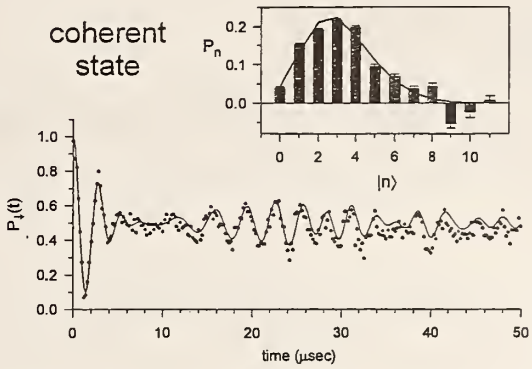


Figure 4. $P_\downarrow(t)$ for a coherent state, showing collapse and revival. The data are fitted to a coherent state distribution, yielding $\bar{n} = 3{\cdot}1 \pm 0{\cdot}1$. The inset shows the decomposition of the data onto the expected Fock state components, fitted to a Poissonian distribution, yielding $\bar{n} = 2{\cdot}9 \pm 0{\cdot}1$.

extract the probabilities, shown in the inset of figure 3. The probabilities are fitted to an exponential, yielding $\bar{n} = 1{\cdot}5 \pm 0{\cdot}1$. A third measure of $\bar{n}$ by comparing the size of the red and blue sidebands [10] yields $\bar{n} = 1{\cdot}5 \pm 0{\cdot}2$.

4.3. *Coherent states*

A coherent state of motion $|\alpha\rangle$ of the ion corresponds to a minimum uncertainty wave-packet whose centre oscillates classically in the harmonic well and retains its shape. The probability distribution among Fock states is Poissonian, $P_n = |\langle n \mid \alpha\rangle|^2 = (\bar{n}^n \exp(-\bar{n}))/n!$ with $\bar{n} = |\alpha|^2$. As predicted by the JCM, the internal state evolution $P_\downarrow(t)$ will undergo collapses and revivals [17], a purely quantum effect [2, 17].

Coherent states of motion can be produced from the $|n = 0\rangle$ state by a spatially uniform classical driving field [18], by a 'moving standing wave' [19] by pairs of standing waves [20], or by a non-adiabatic shift of the trap centre [21]. We have used the first two methods. For the classical drive, we apply a sinusoidally varying potential at the trap oscillation frequency on one of the trap compensation electrodes [9] for a fixed time (typically 10 μs.) For the 'moving standing wave' creation we use two Raman beams which have a frequency difference of only $\omega_x$. Applying these beams couples adjacent oscillator levels within a given internal state. In the Lamb–Dicke limit this interaction is formally equivalent to applying the coherent displacement operator to the state of motion. The Raman beams produce an optical dipole force which is modulated at $\omega_x$ [19], resonantly driving the motion of the atom. On resonance, the magnitude of the coherent state grows linearly with the coupling time.

In figure 4 we present an example of $P_\downarrow(t)$ after creation of a coherent state of motion. Similar behaviour has recently been seen in the context of cavity QED [22]. The time domain data are fitted to equation (7) using a Poissonian distribution and allowing only $\bar{n}$ to vary. All other parameters (signal amplitude, signal offset and decoherence rate) are measured from a separate $|n = 0\rangle$ Fock state trace. The inset shows the probabilities of the Fock components, extracted using the frequency domain analysis described above. The amplitudes display the expected Poissonian dependence on $n$. The observed revival for higher $\bar{n}$ coherent states is

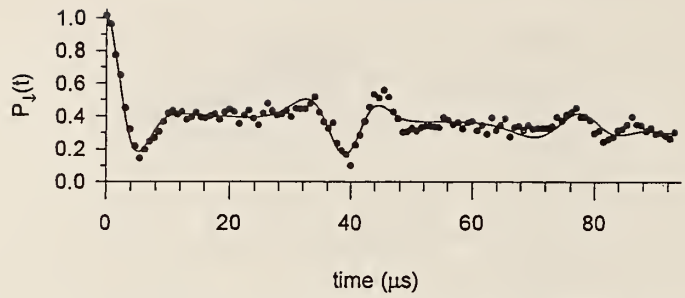


Figure 5. $P_\downarrow(t)$ for a coherent state, driven on the second blue sideband. Since the Rabi frequencies are almost commensurate in this interaction, $P_\downarrow$ shows very sharp collapse and revival features. The solid line is a fit using the exact Rabi frequencies for finite $\eta$. It yields $\bar{n} = 2{\cdot}0 \pm 0{\cdot}1$.

attenuated due to the progressively faster decay rates of the higher-$n$ Fock states, and for states with $\bar{n} \gtrsim 7$ we are unable to see the revival.

We can also realize a different interaction by tuning the frequency difference of the Raman beams to the second blue sideband: $\delta = 2\omega_x$. The interaction Hamilton is then proportional to $(\eta^2/2)(\sigma_+(a^\dagger)^2 + \sigma_- a^2)$ [see equation (3)] and the Rabi frequencies [see equation (5)] are given by

$$\Omega_{n,n+2} \simeq g\frac{\eta^2}{2}[(n+1)(n+2)]^{\frac{1}{2}} \simeq g\frac{\eta^2}{2}(n+\tfrac{3}{2}). \tag{8}$$

Since the last relation holds within 6% for all $n$, the Rabi frequencies in $P_\downarrow(t)$ are almost commensurate, so $P_\downarrow(t)$ shows very sharp collapse and revival features, similar to the two-photon cases discussed by Buck and Sukumar [23] and Knight [24]. Our experimental result is shown in figure 5. The factor $\frac{3}{2}$ in the above approximation leads to an additional $3\pi$ phase shift between successive revivals. This inverts the interference feature from revival to revival. In addition there are small deviations from equation (8), because of the approximation made and the finite Lamb–Dicke parameter $\eta$ which alters the Rabi frequencies [see figure 2 (*b*)].

4.4. *Squeezed states*

A 'vacuum squeezed state' of motion can be created by a parametric drive [21], by a combination of standing- and traveling-wave laser fields [20], or by a non-adiabatic drop in the trap spring constant [21]. Here we irradiate the $|n = 0\rangle$ ion with two Raman beams which differ in frequency by $2\omega$, driving Raman transitions between the even-$n$ levels within the same hyperfine state. The interaction can also be thought of as a parametric drive induced by an optical dipole force modulated at $2\omega$ [19]. The squeeze parameter $\beta$ (defined as the factor by which the variance of the squeezed quadrature is decreased) grows exponentially with the driving time. Figure 6 shows $P_\downarrow(t)$ for a squeezed state prepared in this way. The data are fitted to a vacuum squeezed state distribution, allowing only $\beta$ to vary. The fit of the data in figure 6 demonstrates consistency with a squeezed state and gives $\beta = 40 \pm 10$ (16 dB below the zero point variance), which corresponds to $\bar{n} \approx 7.1$.

The probability distribution for a vacuum squeezed state is restricted to the even states, $P_{2n} = N(2n)!(\tanh r)^{2n}/(2^n n!)^2$, with $\beta = \exp(2r)$. The distribution is very flat; for example, with $\beta = 40$, 16% of the population is in states above $n = 20$. The Rabi frequency differences of these high-$n$ levels are small (see figure 2 (*b*)),

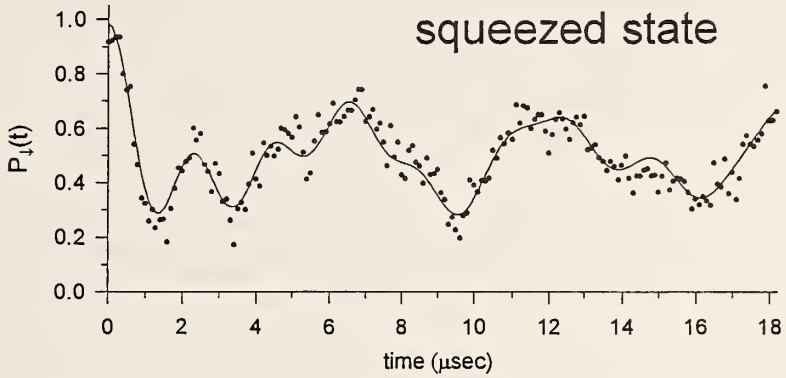


Figure 6. $P_{\downarrow}(t)$ for a squeezed state. The data are fitted to a squeezed state population distribution, yielding $\beta \approx 40 \pm 10$ (16 dB below the zero point variance), which corresponds to $\bar{n} \approx 7{\cdot}1$.

and with $\eta = 0{\cdot}202$ the Rabi frequencies begin to decrease with $n$ after $n = 20$. The levels can no longer be well distinguished by frequency to extract the level populations.

In the above cases, we have checked our state creation through the values of the $P_n$. This information is, of course, incomplete since it does not reveal the coherences. Measurements completely characterizing the quantum state will be discussed below.

### 4.5. *A 'Schrödinger cat' state of motion*

A 'Schrödinger cat' state can be taken as a superposition of classical-like states. In Schrödinger's original thought experiment [25] he describes how we could in principle transform a superposition inside an atom to a large-scale superposition of a live and dead cat. In our experiment [26], we construct an analogous state at the single atom level. A superposition of internal states ($|\uparrow\rangle$ and $|\downarrow\rangle$) is transformed into a superposition of coherent motional states with different phases. The coherent states of the superposition are separated in space by mesoscopic distances much greater than the size of the atom.

This situation is interesting from the point of view of the quantum measurement problem associated with 'wavefunction collapse,' historically debated by Einstein and N. Bohr, among others [27]. One practical approach toward resolving this controversy is the introduction of quantum decoherence, or the environmentally induced reduction of quantum superpositions to statistical mixtures and classical behaviour [28]. Decoherence is commonly interpreted as a way of quantifying the elusive boundary between classical and quantum worlds, and almost always precludes the existence of macroscopic Schrödinger cat states, except at extremely short time scales [28]. The creation of mesoscopic Schrödinger cat states may allow controlled studies of quantum decoherence and the quantum/classical boundary.

In the present work, we create a Schrödinger cat state of the harmonic oscillator by forming a superposition of two coherent state wavepackets of the single trapped atom with a sequence of laser pulses. The coherent states are excited with the use of a pair of Raman laser beams as described above. The key to the

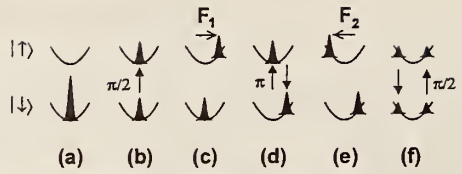


Figure 7. Evolution of the idealized position-space atomic wavepacket entangled with the internal states $|\downarrow\rangle$ and $|\uparrow\rangle$ during the creation of a 'Schrödinger cat' state with $\alpha = 3$ and $\phi = \pi$ (displacement forces in opposite directions). The wavepackets are snapshots in time, taken when the atom is at extrema of motion in the harmonic trap (represented by the parabolas). The area of the wavepackets corresponds to the probability of finding the atom in the given internal state. (*a*) The initial wavepacket corresponds to the quantum ground state of motion following laser cooling. (*b*) The wavepacket is split following a $\frac{\pi}{2}$-pulse on the carrier. (*c*) The $|\uparrow\rangle$ wavepacket is excited to a coherent state by the force $\mathbf{F}_1$ of the displacement beams. Note the force acts only on the $|\uparrow\rangle$ wavepacket, thereby entangling the internal and motional systems. (*d*) The $|\uparrow\rangle$ and the $|\downarrow\rangle$ wavepackets are exchanged, following a $\pi$-pulse on the carrier. (*e*) The $|\downarrow\rangle$ wavepacket is excited to a coherent state by the displacement beam force $\mathbf{F}_2$, which in general has a different phase with respect to the force in (*c*) ($\mathbf{F}_2 = -\mathbf{F}_1$ in the figure). The state shown in (*e*) is analogous to a 'Schrödinger cat' state. (*f*) The $|\uparrow\rangle$ and the $|\downarrow\rangle$ wavepackets are finally combined following a $\frac{\pi}{2}$-pulse on the carrier.

experiment is that the displacement beams are both polarized $\sigma^+$, so that they do not affect the $|\uparrow\rangle$ internal state. It is this selection that allows a superposition of internal states to be transformed into a superposition of motional states.

Following laser cooling to the $|\downarrow\rangle|n = 0\rangle$ state as described above, we create the Schrödinger cat state by applying several sequential pulses of the following Raman beams. (1) A $\pi/2$-pulse on the carrier splits the wavefunction into an equal superposition of states $|\downarrow\rangle|0\rangle$ and $|\uparrow\rangle|0\rangle$. (2) The displacement beams excite the motion correlated with the $|\uparrow\rangle$ component to a coherent state $|\alpha\rangle$. (3) A $\pi$-pulse on the carrier swaps the internal states of the superposition. (4) The displacement beams excite the motion correlated with the new $|\uparrow\rangle$ component to a second coherent state $|\alpha \exp(i\phi)\rangle$. (5) A final $\pi/2$-pulse on the carrier combines the two coherent states (the evolving state of the system is summarized in figure 7). The relative phases ($\phi$ and the phases of steps 1, 3, and 5) of the steps above are determined by the phases of the RF difference frequencies of the Raman beams, which are easily controlled by phase locking the RF sources.

The state created after step 4 is a superposition of two independent coherent states, each correlated with an internal state of the ion (i.e. for $\phi = \pi$),

$$|\Psi\rangle = (|\alpha\rangle\,|\uparrow\rangle + |-\alpha\rangle\,|\downarrow\rangle)/\sqrt{2}, \tag{9}$$

In this state, the widely separated coherent states replace the classical notions of 'dead' and 'alive' in Schrödinger's original thought experiment. We verify this mesoscopic superposition by recombining the coherent wavepackets in the final step 5. This results in an interference of the two wavepackets as the relative phase $\phi$ of the displacement forces (steps 2 and 4) is varied. The nature of the interference depends on the phases of steps (1), (3), and (5), and is set here to cause destructive interference of the wavepackets in the $|\downarrow\rangle$ state. We directly measure this interference by detecting the probability $P_\downarrow(\phi)$ that the ion is in the $|\downarrow\rangle$ internal state for a given value of $\phi$. the signal for particular choices of the phases in 1, 3 and 5 is

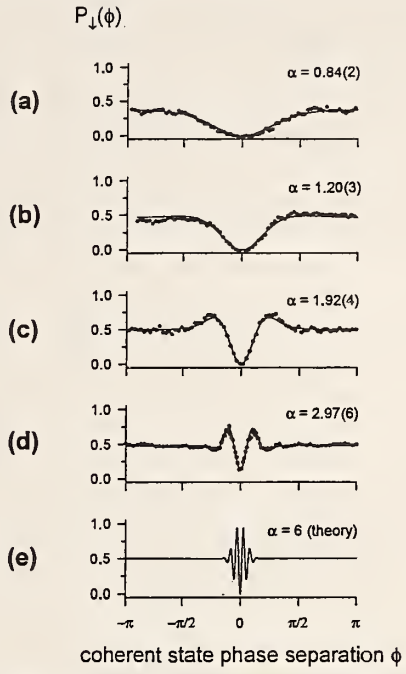


Figure 8. $P_{\downarrow}(\phi)$ interference signal with increasing values of $|\alpha|$. The data are fitted to equation (10), yielding $\alpha = 0{\cdot}84$, $1{\cdot}20$, $1{\cdot}92$ and $2{\cdot}97$. The fit in curve (*d*) includes a term to account for the loss of contrast.

$$P_{\downarrow}(\phi) = \tfrac{1}{2}[1 - C\exp[-\alpha^2(1-\cos\phi)]\cos(\alpha^2\sin\phi)], \tag{10}$$

where $\alpha$ is the magnitude of the coherent states and $C = 1$ is the expected visibility of the fringes in the absence of decoherence. We continuously repeat the experiment—cooling, state preparation, detection—while slowly sweeping the relative coherent state motional phase $\phi$.

In figure 8, we display the measured $P_{\downarrow}(\phi)$ for a few different values of the coherent state amplitude $\alpha$, which is set by changing the duration of application of the displacement beams (steps 2 and 4 from above). The unit visibility of the interference feature near $\phi = 0$ verifies that we are producing superposition states instead of statistical mixtures, and the feature clearly narrows as $\alpha$ is increased. We extract the amplitude of the Schrödinger cat state by fitting the interference data to the expected form of the interference fringe. The extracted values of $\alpha$ agree with an independent calibration of the displacement forces. We measure coherent state amplitudes as high as $a \simeq 2{\cdot}97(6)$, corresponding to an average of $\bar{n} \simeq 9$ vibrational quanta in the state of motion. This indicates a maximum spatial separation of $4\alpha x_0 = 83(3)$ nm, which is significantly larger than the single wavepacket width characterized by $x_0 = 7{\cdot}1(1)$ nm as well as a typical atomic dimension ($\simeq 0{\cdot}1$nm). The individual wavepackets are thus clearly separated in phase space.

Of particular interest is the fact that as the separation of the cat state is made larger, the decay from superposition to statistical mixture (decoherence) becomes faster [29]. In the experiment, decoherence due to coupling to a thermal reservoir is expected to result in a loss of visibility in the interference pattern of $C = \exp(-\alpha^2\lambda t)$ where $\lambda$ is the coupling constant and $t$ the coupling time. The

exponential reduction of coherence with the square of the separation ($\alpha^2$ term) undelies the reason that bigger 'cats' decay faster. In figure 8 (*d*), the observed loss of contrast at the largest observed separation may already indicate the onset of decoherence. Decoherence due to radiative coupling has been observed in cavity QED [29]. The precise control of quantum wavepackets in this version of 'Schrödinger's cat' provides a very sensitive indicator of quantum decoherence, whose characterization is of great interest to quantum measurement theory and applications such as quantum computing [30] and quantum cryptography [31].

## 5. Complete quantum state measurement

The controlled interaction of light and RF electromagnetic fields with the trapped atom allows us not only to prepare very general states of motion, but also to determine these quantum mechanical states using novel techniques. Few experiments have succeeded in determining the density matrices or Wigner functions of quantum systems. The angular momentum density matrices of the substate in principal quantum number $n = 3$ were measured in collisionally produced atomic hydrogen [32]; the Wigner function and density matrix of a mode of light were experimentally mapped by optical homodyne tomography [33, 34]; the Wigner function of the vibrational degree of freedom of a diatomic molecule was reconstructed with a related technique [35]; and, more recently the Wigner function of an atomic beam passing through a double slit was reconstructed [36]. Here we present the theory and experimental demonstration of two distinct schemes that allow us to reconstruct both the density matrix in the number state basis and the Wigner function of the motional state of a single trapped atom [37]. For other proposals to measure the motional state of a trapped atom, see this issue and [38, 39]. As described above, we are able to prepare a variety of non-classical input states [14] which can, for example, exhibit negative values of the Wigner function. Also, comparing the results of the state determination with the state we intended to produce can give an idea of the accuracy of the preparation.

Both of our measurement techniques rely on our ability to displace the input state to several different locations in phase space. Specifically, a coherent displacement [14, 18] $U(-\alpha) = U^{\dagger}(\alpha) = \exp(\alpha^* a - \alpha a^{\dagger})$ ($-\alpha$ is used for convenience below) controlled in phase and amplitude is used in our schemes. We then apply radiation on the blue sideband to the atom for a time $t$, which induces a resonant exchange between the motional and internal degrees of freedom (see section 2). For each $\alpha$ and time $t$, the population $P_{\downarrow}(t, \alpha)$ of the $|\downarrow\rangle$ level is then measured by monitoring the fluorescence produced in driving the resonant dipole cycling transition (see section 2). For these experiments the internal state at $t = 0$ is always prepared to be $|\downarrow\rangle$ for the various input states, so the signal averaged over many measurements is

$$P_{\downarrow}(t, \alpha) = \tfrac{1}{2}\left\{1 + \sum_{k=0}^{\infty} Q_k(\alpha) \cos(2\Omega_{k,k+1} t) \exp(-\gamma_k t)\right\}. \tag{11}$$

Without the coherent displacement we would just recover the previously discussed $P_{\downarrow}(t)$ signal (equation (7)) and would find the populations of the motional eigenstates only. But since we repeat these measurements for several magnitudes

and phases of the coherent displacement, we are able to extract information about the off-diagonal elements of the density matrix and can also reconstruct the Wigner function from the measured displaced populations $Q_k(\alpha)$.

5.1. *Reconstruction of the number state density matrix*

To reconstruct the density marix $\rho$ in the number state basis, we use the relation

$$Q_k(\alpha) = \langle k|U^\dagger(\alpha)\rho U(\alpha)|k\rangle = \langle \alpha, k|\rho|\alpha, k\rangle, \tag{12}$$

where $|\alpha, k\rangle$ is a coherently displaced number state [40]. Hence every $Q_k(\alpha)$ is the population of the displaced number state $|\alpha, k\rangle$ for an ensemble characterized by the input density matrix $\rho$. Rewriting (12) we get

$$\begin{aligned} Q_k(\alpha) &= \frac{1}{k!}\langle 0|a^k U^\dagger(\alpha)\rho U(\alpha)(a^\dagger)^k|0\rangle \\ &= \frac{1}{k!}\langle \alpha|(a-\alpha)^k\rho(a^\dagger-\alpha^*)^k|\alpha\rangle \\ &= \frac{\exp(-|\alpha|^2)|\alpha|^{2k}}{k!}\sum_{n,m=0}^{\infty}\sum_{j,j'=0}^{k}\frac{(\alpha^*)^{n-j}\alpha^{m-j'}}{n!m!} \\ &\quad\times(-1)^{-j-j'}\begin{bmatrix}k\\j\end{bmatrix}\begin{bmatrix}k\\j'\end{bmatrix}[(m+j)!(n+j')!]^{\frac{1}{2}}\rho_{n+j',m+j}. \end{aligned} \tag{13}$$

To separate the contributions of different matrix-elements $\rho_{n,m}$, we may displace the state along a circle,

$$\alpha_p = |\alpha|\exp[i(\pi/N)p], \tag{14}$$

where $p \in \{-N, \ldots, N-1\}$. The number of angles $2N$ on that circle determines the maximum number of states $n_{\max} = N-1$ that can be included in the reconstruction. With a full set of populations of the state displaced along $2N$ points on a circle we can perform a discrete Fournier transform of equation (14) evaluated at the values $\alpha_p$, and we obtain the matrix equations

$$\begin{aligned} Q_k^{(l)} &\equiv \frac{1}{2N}\sum_{p=-N}^{N-1} Q_k(\alpha_p)\exp[-il(\pi/N)p] \\ &= \sum_{n=\max(0,-l)}^{\infty}\gamma_{kn}^{(l)}\rho_{n,n+l}, \end{aligned} \tag{15}$$

with matrix elements

$$\begin{aligned} \gamma_{kn}^{(l)} &= \frac{\exp(-|\alpha|^2)|\alpha|^{2k}}{k!}\sum_{j'=0}^{\min(k,n)}\sum_{j=0}^{\min(k,l+n)}|\alpha|^{2(n-j-j')+l} \\ &\quad\times(-1)^{-j-j'}\begin{bmatrix}k\\j\end{bmatrix}\begin{bmatrix}k\\j'\end{bmatrix}\frac{[(l+n)!n!]^{\frac{1}{2}}}{(l+n-j)!(n-j')!} \end{aligned} \tag{16}$$

for every diagonal $\rho_{n,n+l}$ of the density matrix. To keep the matrix dimension finite, a cutoff for the maximum $n$ in (15) is introduced, based on the magnitude of the

input state. For an unknown input state an upper bound on $n$ may be extracted from the populations $Q_k(\alpha)$. If these are negligible for $k$ higher than a certain $k_{\max}$ and all displacements $\alpha$, they are negligible in the input state as well, and it is convenient to truncate equation (15) at $n_{\max} = k_{\max}$. The resulting matrix equation is overcomplete for some $l$, but the diagonals $\rho_{n,n+l}$ can still be reconstructed by a general linear least squares method [16].

5.2. *Reconstruction of s-parameterized quasiprobability distributions*

As pointed out by several authors, $s$-parametrized quasiprobability distributions $F(\alpha, s)$ have a particularly simple representation when expressed in populations of displaced number states $Q_k(\alpha)$ [40, 41, 42, 43].

$$F(\alpha, s) = \frac{1}{\pi}\sum_{n=0}^{\infty}[(s+1)/2]^n \sum_{k=0}^{n}(-1)^k \begin{bmatrix} n \\ k \end{bmatrix} Q_k(\alpha). \tag{17}$$

For $s = -1$ the sum breaks down to one term and $F(\alpha, -1) = Q_0(\alpha)/\pi$ gives the value of the $Q$ quasi-probability distribution at the complex coordinate $\alpha$ [44]. Also, for $s = 0$, the Wigner function $F(\alpha, 0) = W(\alpha)$ for every point $\alpha$ in the complex plane can be determined by the single sum

$$W(\alpha) = \frac{2}{\pi}\sum_{n=0}^{\infty}(-1)^n Q_n(\alpha). \tag{18}$$

In our reconstruction, the sum is carried out only to a finite $n_{\max}$, as described above. Since truncation of the sum leads to artifacts in the quasi-probability distributions [45], we have averaged our experimental data over different $n_{\max}$. This smoothes out the artifacts to a high degree.

In contrast to the density matrix method described in section 5.1, summing the displaced probabilities with their weight factors provides a direct method to obtain the quasi-probability distribution at the point $\alpha$ in phase space, without the need to measure at other values of $\alpha$. This also distinguishes the method from preceding experiments that determined the Wigner function by inversion of integral equations (tomography) [33, 35].

5.3. *Experimental results*

The coherent displacement needed for the reconstruction mapping is provided by a spatially uniform classical driving field at the trap oscillation frequency. This field is applied on one of the trap compensation electrodes [9] for a time of about 10 μs. The RF oscillators that create and displace the state are phase locked to control their relative phase. Different displacements are realized by varying the amplitude and the phase of the displacement oscillator. For every displacement $\alpha$, we record $P_{\downarrow}(t, \alpha)$. $Q_n(\alpha)$ can be found from the measured traces with a singular value decomposition (see section 4.2). To determine the amplitude $|\alpha|$ of each displacement, the same driving field is applied to the $|n = 0\rangle$ ground state and the resulting collapse and revival trace is fitted to that of a coherent state (see section 4.3).

The accuracy of the reconstruction is limited by the uncertainty in the applied displacements, the errors in the determination of the displaced populations, and decoherence during the measurement. The value of the Wigner function is found

by a sum with simple error propagation rules. The density matrix is reconstructed by a linear least-squares method) and it is straightforward to calculate a covariance matrix [16]. As the size of the input state increases, decoherence and the relative accuracy of the displacements become more critical, thereby increasing their uncertainties.

In figure 9, we show the reconstruction of both the number state density matrix (*a*) and surface and contour plots of the Wigner function (*b*) of an approximate $|n = 1\rangle$ number state. The plotted surface is the result of fitting a linear interpolation between the actual data points to a 0·1 grid. The octagonal shape is an artifact of the eight measured phases per radius. The white contour represents $W(\alpha) = 0$. The negative values around the origin highlight the non-classical character of this state. The Wigner function $W(\alpha)$ is rotationally symmetric within the experimental errors as confirmed by our measured values. Therefore we averaged sets of data with the same value of $|\alpha|$. The averaged points are displayed in figure 9 (*c*), together with a radial slice through the theoretical Wigner function for a pure number state (dashed line) and a thermally contaminated state (solid line) assuming the ion is prepared in a thermal distribution with a probability of finding it in ground state of only ≈90% after cooling and prior to the preparation of the $|n = 1\rangle$ number state. This was independently verified to be the case in our experiment by comparing the magnitude of red and blue sidebands after Raman-sideband cooling to the ground state [10]. Again the large negative part of the Wigner function around the origin highlights the fact that the prepared state is non-classical.

In contrast to the number state, the state closest to a classical state of motion in a harmonic oscillator is a coherent state. As one example, we have excited and reconstructed a small coherent state with amplitude $|\beta| \approx 0{\cdot}67$. The experimental amplitude and phase of the number state density matrix are depicted in figure 10. The off-diagonal elements are generally slightly smaller for the experiment than we would expect from the theory of a pure coherent state. In part this is due to decoherence during the measurement, so the reconstruction shows a mixed state character rather than a pure coherent state signature. This view is further supported by the fact that farther off-diagonal elements seem to decrease faster than direct neighbours of the diagonal.

The reconstructed Wigner function of a second coherent state with amplitude $|\beta| \approx 1.5$ is shown in figure 11. The plotted surface is the result of fitting a linear interpolation between the actual data points to a 0·13 by 0·13 grid. The approximately Gaussian minimum uncertainty wavepacket is centred around a coherent amplitude of about 1·5 from the origin. The half-width at half maximum is about 0·6, in accordance with the minimum uncertainty half-width of $[\ln(2)/2]^{\frac{1}{2}} \approx 0{\cdot}59$. To suppress truncation artifacts in the Wigner function summation (18) [45], we have averaged over $n_{\max} = 5$ and $n_{\max} = 6$.

We have also created a coherent superposition of $|n = 0\rangle$ and $|n = 2\rangle$ number states. This state is ideally suited to demonstrate the sensitivity of the reconstruction to coherences. the only non-zero off-diagonal elements should be $\rho_{02}$ and $\rho_{20}$, with a magnitude of $|\rho_{02}| = |\rho_{20}| = [\rho_{00}\rho_{22}]^{\frac{1}{2}} \approx 0.5$ for a superposition with about equal probability of being measured in the $|n = 0\rangle$ or $|n = 2\rangle$ state. In the reconstruction shown in figure 12 the populations $\rho_{00}$ and $\rho_{22}$ are somewhat smaller, due to imperfections in the preparation, but the coherence has the expected value of $|\rho_{20} = |\rho_{02}| \approx [\rho_{00}\rho_{22}]^{\frac{1}{2}}$.

For a known density matrix one can also find the Wigner function by

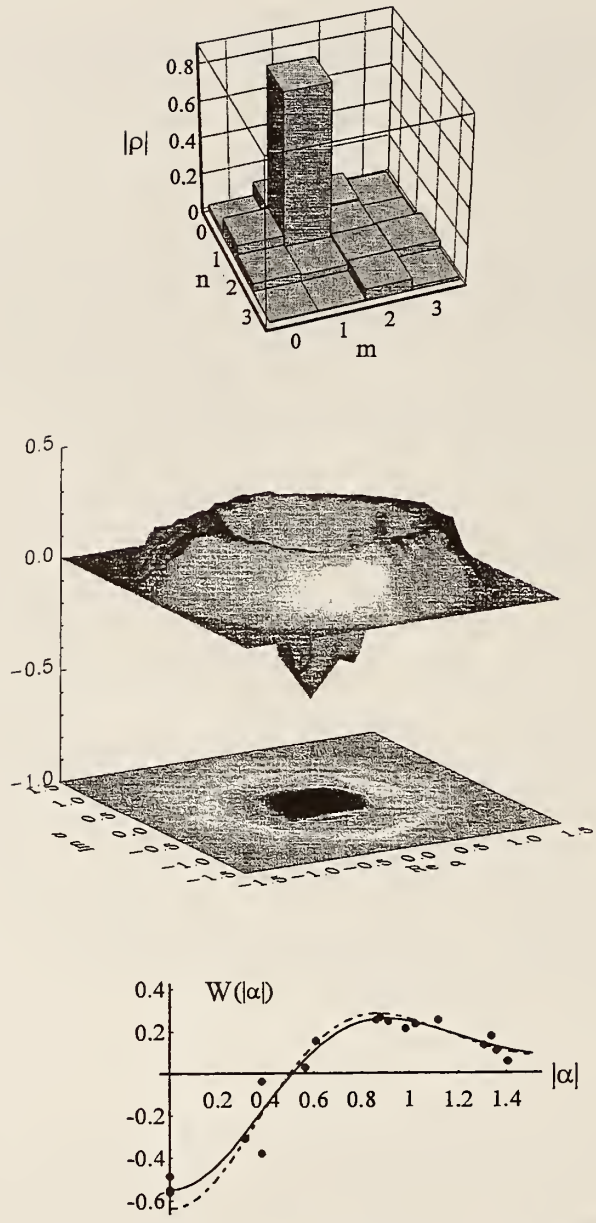


Figure 9. (*a*) reconstructed number state density matrix amplitudes $\rho_{nm}$ for an approximate $|n=1\rangle$ number state. The coherent reconstruction displacement amplitude was $|\alpha| = 1{\cdot}15(3)$. The number of relative phases $N = 4$ in equation (14), so $n_{\max} = 3$. (*b*) Surface and contour plots of the Wigner function $W(\alpha)$ of the $|n=1\rangle$ number state. The white contour represents $W(\alpha) = 0$. The negative values around the origin highlight the non-classical character of this state. (*c*) The Wigner function of the $|n=1\rangle$ number state is rotationally symmetric: $W(\alpha) = W(|\alpha|)$. In this figure we show a radial slice through this function for a pure number state (dashed line) and a thermally contaminated state (solid line) which assumes the ion is in the ground state only ≈90% of the time after cooling. This was independently verified after sideband cooling [10]. The dots are experimentally determined values of the Wigner function, averaged for equal $|\alpha|$.

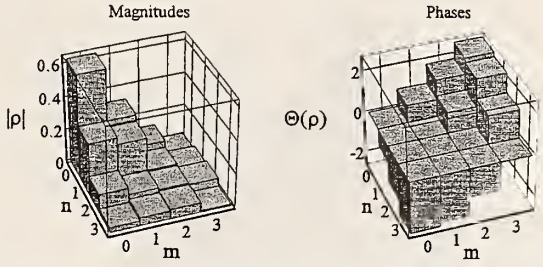


Figure 10. Experimental amplitudes $\rho_{nm}$ and phases $\Theta(\rho_{nm})$ of the number state density matrix elements of a $|\beta| \approx 0{\cdot}67$ coherent state. The state was displaced by $|\alpha| \approx 0.92$, for $N = 4$ in equation (14).

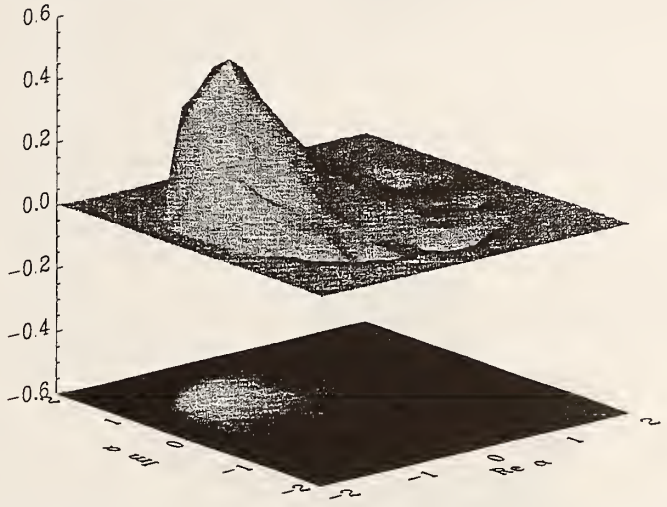

Figure 11. Surface and contour plots of the reconstructed Wigner function of a coherent state. The approximately Gaussian minimum uncertainty wavepacket is centred around a coherent amplitude of about 1·5 from the origin. The half-width at half maximum is about 0·6, in accordance with the minimum uncertainty half-width of $[\ln(2)/2]^{\frac{1}{2}} \approx 0{\cdot}59$.

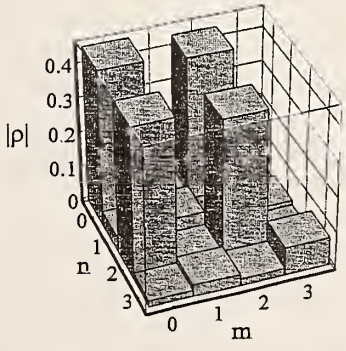


Figure 12. Reconstructed density matrix amplitudes of an approximate $1/\sqrt{2}(|n=0\rangle - i|n=2\rangle)$ state. The state was displaced by $|\alpha| = 0{\cdot}79$ for $N = 4$ in equation (14). The amplitudes of the coherences indicate that the reconstructed density matrix is close to that of a pure state.

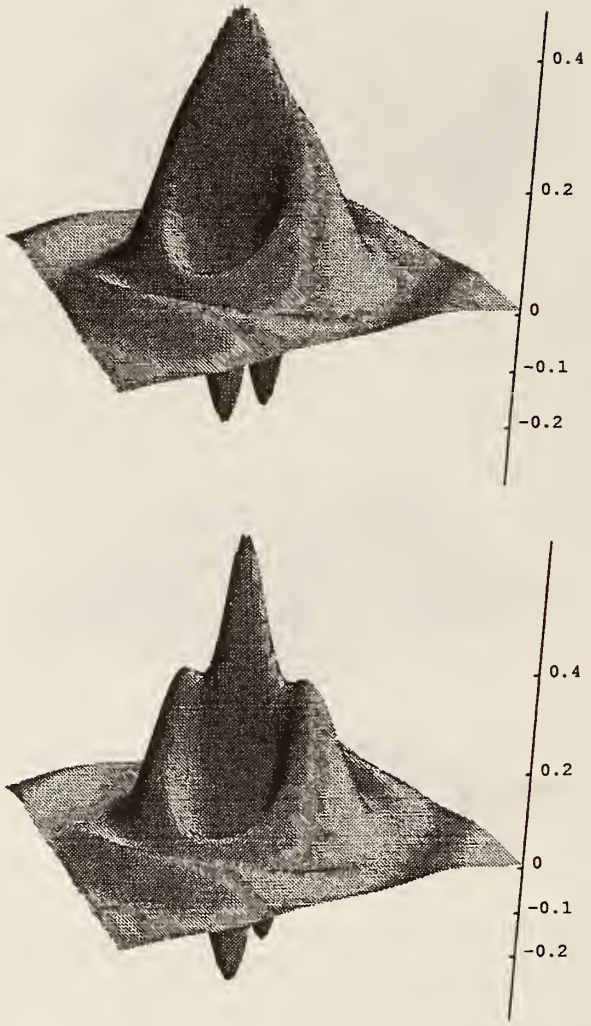


Figure 13. Comparison of the Wigner function of an approximate $1/\sqrt{2}(|n=0\rangle - i|n=2\rangle)$ state transformed from our experimental density matrix data (*a*) with its theoretical counterpart (*b*).

expanding equation (18) in the number state basis,

$$W(\alpha) = \frac{2}{\pi}\sum_{n=0}^{\infty}(-1)^n \sum_{k,l=0}^{\infty}\langle \alpha, n|k\rangle \rho_{kl}\langle l|\alpha, n\rangle, \tag{19}$$

with the matrix elements given by $(l \geqslant n)$ [46]

$$\langle l|\alpha, n\rangle = [n!/l!]^{\frac{1}{2}}\alpha^{l-n}\exp(-1/2|\alpha|^2)\mathcal{L}_n^{(l-n)}(|\alpha|^2), \tag{20}$$

where $\mathcal{L}_n^{(l-n)}$ is a generalized Laguerre polynomial. Using this approach we have generated a plot of the Wigner function using our density matrix data. The result is shown in figure 13 together with the theoretical Wigner function for a $1/\sqrt{2}(|n=0\rangle - i|n=2\rangle)$ state. The differences can be traced to the imperfections

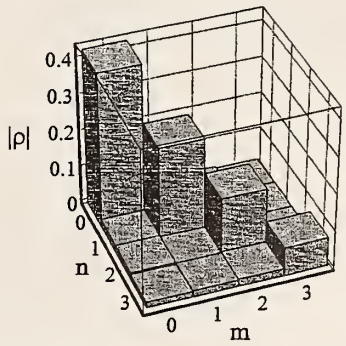


Figure 14. Reconstructed density matrix of an $\bar{n} \approx 1.3$ thermal state. This state was displaced by $|\alpha| = 0{\cdot}78$, for $N = 4$ equation (14). As one would expect for a thermal state, no coherences are present within the experimental uncertainties and the populations drop exponentially for higher $n$.

in the preparation also visible in figure 12; the small but non-zero values of $|\rho_{11}|$ and $|\rho_{33}|$ and the respective coherences lead to the differences in the central feature of the Wigner function.

Finally, we have generated a thermal state by only Doppler-cooling the ion. The reconstruction of the resulting state is depicted in figure 14. As expected, there are no coherences, and the diagonal, which gives the number state occupation, shows an exponential behaviour within the experimental errors, indicating a mean occupation number $\bar{n} \approx 1{\cdot}3$.

## 6. Conclusions

The interaction of a trapped atom with classical light fields can lead to experimental situations that allow us to coherently prepare a multitude of quantum states, both classical-like and non-classical in character. Since the interaction can be tailored to resemble the Jaynes-Cummings model, the system is suited to realizing many proposals originally introduced in the realm of quantum optics and cavity quantum electrodynamics. One special application is the preparation of a state where the internal degree of freedom is entangled with two coherent states, with a separation in phase space much bigger than their spread. This state, bearing many features of 'Schrödinger's cat', is well suited for the study of decoherence phenomena on the boundary of quantum and classical mechanics such as the decoherence of mesoscopic objects. Such studies are especially interesting in our system since we should be able to engineer different couplings and reservoirs by an appropriate choice of the interaction Hamiltonian [47].

Our level of control in the preparation of the states also allows us to prepare the same state many times to a high accuracy. By extending our techniques to several simultaneously trapped ions, we should be able to controllably prepare and manipulate their combined state and thus implement simple quantum logic gates [48, 49]. The techniques described here for characterizing the quantum state of motion, combined with a Ramsey-type spectroscopy on the internal states, seem to lead to a method for completely measuring the internal and motional states of several simultaneously trapped ions (for an alternative method see [50]). Apart

from detecting quantum correlations in these states, this might be a useful way to fully characterize simple quantum logic gates [51].

**Acknowledgments**

This work is supported by the United States National Security Agency, the Office of Naval Research and the Army Research Office. D.L. gratefully acknowledges a deutsche Forschungsgemeinschaft research grant. D.M.M. is supported by an N.R.C. postdoctoral fellowship. We thank W. Vogel, M. Collet, P. Knight, J. I. Cirac and P. Zoller for stimulating discussions. We acknowledge important contributions by J. Bergquist and helpful comments on the manuscript by M. Young, B. Esry and B. Jelenkovic.

**References**

[1] Jaynes, E. T., and Cummings, F. W., 1963, *Proc. IEEE*, **51**, 89.
[2] Shore, B. W., and Knight, P. L., 1993, *J. Mod. Opt.*, **40**, 1195.
[3] Blockley, C. A., Walls, D. F., and Risken, H., 1992, *Europhys. Lett.*, **17**, 509.
[4] Cirac, J. I., Blatt, R., Parkins, A. S., and Zoller, P., 1993, *Phys. Rev. Lett.*, **70**, 762.
[5] Paul, W., 1990, *Rev. Mod. Phys.*, **62**, 531.
[6] Glauber, R. J., 1992, *Laser Manipulation of Atoms and Ions*, Proc. Int. School of Physics 'Enrico Fermi' Course 118, edited by E. Arimondo *et al.*, (Amsterdam: North Holland), p. 643.
[7] Bardroff, P. J., Leichtle, C., Schrade, G., and Schleich, W. P., 1996, *Act. Phys. Slov.*, **46**, 1.
[8] Cirac, J. I., Garay, L. J., Blatt, R., Parkins, A. S., and Zoller, P., 1994, *Phys. Rev.* A, **49**, 421.
[9] Jefferts, S., Monroe, C., Bell, E., and Wineland, D. J., 1994, *Phys. Rev.* A, **51**, 3112.
[10] Monroe, C., Meekhof, D. M., King, B. E., Jefferts, S. R., Itano, W. M., Wineland, D. J., and Gould, P. L., 1995, *Phys. Rev. Lett.*, **75**, 4011.
[11] Eschner, J., Appasamy, B., and Toschek, P. E., 1995, *Phys. Rev. Lett.*, **74**, 2435.
[12] Cirac, J. I., Blatt, R., and Zoller, P., 1994, *Phys. Rev.* A, **49**, R3174.
[13] Blatt, R., Cirac, J. I., and Zoller, P., 1995, *Phys. Rev.* A, **52**, 518.
[14] Meekhof, D. M., Monroe, C., King, B. E., Itano, W. M., and Wineland, D. J., 1996, *Phys. Rev. Lett.*, **76**, 1796; 1996, erratum, *ibid.*, **77**, 2346.
[15] Stenholm, S., 1986, *Rev. Mod. Phys.*, **58**, 699.
[16] Press, W. H., Teukolsky, S. A., Vetterling, W. T., and Flannery, B. P., 1992, *Numerical Recipes* (Cambridge University Press).
[17] von Foerster, T., 1975, *J. Phys.* A, **8**, 95; Eberly, J. H., Narozhny, N. B., and Sanchez-Mondragon, J. J., 1980, *Phys. Rev. Lett.*, **44**, 1323.
[18] Carruthers, P., and Nieto, M. M., 1965, *Am. J. Phys.*, **7**, 537.
[19] Wineland, D. J., Bergquist, J. C., Bollinger, J. J., Itano, W. M., Moore, F. L., Gilligan, J. M., Raizen, M. G., Heinzen, D. J., Weimer, C. S., and Manney, C. H., 1992, *Laser Manipulation of Atoms and Ions*, Proc. Int. School of Physics 'Enrico Fermi' Course 118, edited by E. Arimondo *et al.* (Amsterdam: North Holland), p. 553.
[20] Cirac, J. I., Parkins, A. S., Blatt, R., and Zoller, P., 1993, *Phys. Rev. Lett.*, **70**, 556.
[21] Janszky, J., and Yushin, Y. Y., 1986, *Opt. Comm.*, **59**, 151; Fan Hong Yi and Zaidi, H. R., 1988, *Phys. Rev.* A, **37**, 2985; Heinzen, D. J., and Wineland, D. J., 1990, *Phys. Rev.* A, **42**, 2977.
[22] Brune, M., Schmidt-Kaler, F., Maali, A., Dreyer, J., Hagley, E., Raimond, J. M., and Haroche, S., 1996, *Phys. Rev. Lett.*, **76**, 1800.
[23] Buck, B., Sukumar, C. V., 1981, *Phys. Lett.* A, **81**, 132.
[24] Knight, P., 1986, *Phys. Scr.* T, **12**, 51.
[25] Schrödinger, E., 1935, *Naturwissenschaften*, **23**, 807.

[26] Monroe, C., Meekhof, D. M., King, B. E., and Wineland, D. J., 1996, *Science*, **272,** 1131.
[27] Wheeler, J. A., and Zurek, W. H. (editors), 1983, *Quantum Theory and Measurement* (Princeton NJ: Princeton Univ. Press).
[28] Zurek, W. H., 1991, *Phys. Today*, **44,** 36.
[29] Brune, M., Hagley, E., Dreyer, J., Maitre, X., Maali, A., Wunderlich, C., Raimond, J. M., and Haroche, S., 1996, *Phys. Rev. Lett.*, **77,** 4887.
[30] Ekert, A., and Josza, R., 1966, *Rev. Mod. Phys.*, **68,** 733.
[31] Bennett, C. H., 1996, *Phys. Today*, **48,** 24.
[32] Ashburn, J. R., Cline, R. A., van der Burgt, P. J. M., Westerveldt, W. B., and Risley, J. S., 1990, *Phys. Rev.* A, **41,** 2407.
[33] Smithey, D. T., Beck, M., Raymer, M. G., and Faridani, A., 1993, *Phys. Rev. Lett.*, **70,** 1244.
[34] Breitenbach, G., Möller, T., Pereira, S. F., Poizat, J. Ph., Schiller, S., and Mlynek, J., 1995, *Opt. Soc.* B, **12,** 2304.
[35] Dunn, T. J., Walmsley, I. A., and Mukamel, S., 1995, *Phys. rev. Lett.*, **74,** 884.
[36] Kurtsiefer, C., and Mlynek, J., 1997, *Nature*, **386,** 150.
[37] Leibfried, D., Meekhof, D. M., King, B. E., Monroe, C. M., Itano, W. M., Wineland, D. J., 1996, *Phys. Rev. Lett.*, **77,** 4281.
[38] Wallentowitz, S., and Vogel, W., 1995, *Phys. Rev. Lett.*, **75,** 2932; Poyatos, J. F., Walser, R., Cirac, J. I., Zoller, P., and Blatt, R., 1996, *Phys. Rev.* A, **53,** R1966.
[39] D'Helon, C., and Milburn, G. J., 1996, *Phys. Rev.* A, **54,** R25; Bardroff, P. J., Leichtle, C., Schrade, G., and Schleich, W. P., 1996, *Phys. Rev. Lett.*, **77,** 2198.
[40] Moya-Cessa, H., and Knight, P. L., 1993, *Phys. Rev.* A, **48,** 2479.
[41] Royer, A., 1985, *Phys. Rev. Lett.*, **55,** 2745.
[42] Wallentowitz, S., and Vogel, W., 1996, *Phys. Rev.* A, **53,** 4528.
[43] Banaszek, K., and Wodkiewicz, K., 1996, *Phys. Rev. Lett.*, **76,** 4344.
[44] Poyatos, J. F., Walser, R., Cirac, J. I., Zoller, P., and Blatt, R., 1996, *Phys. Rev.* A, **53,** R1966.
[45] Collett, M., and Walls, D., private communication, July 1996; see also Banaszek, K., and Wodkiewicz, K., this issue, 2441.
[46] Cahill, K. E., Glauber, R. J., 1969, *Phys. Rev.*, **177,** 1857.
[47] Poyatos, J. F., Cirac, J. I., and Zoller, P., 1996, *Phys. Rev. Lett.*, **77,** 4728.
[48] Cirac, J. I., and Zoller, P., 1995, *Phys. Rev. Lett.*, **74,** 4091.
[49] Monroe, C., Meekhof, D. M., King, B. E., Itano, W. M., and Wineland, D. J., 1995, *Phys. Rev. Lett.*, **75,** 4714.
[50] Wallentowitz, S., de Mathos Filho, R., and Vogel, W., Sept. 1996, preprint.
[51] Poyatos, J. F., Cirac, J. I., and Zoller, P., 1997, *Phys. Rev. Lett.*, **78,** 390.

Fortschr. Phys. 46 (1998) 4–5, 363–390

# Experimental Primer on the Trapped Ion Quantum Computer

D.J. Wineland, C. Monroe, W.M. Itano, B.E. King, D. Leibfried, D.M. Meekhof, C. Myatt, and C. Wood

National Institute of Standards and Technology, Boulder, CO 80303

## Abstract

The development of a quantum computer based on a system of trapped atomic ions is described, following the proposal of Cirac and Zoller. Initial results on a two-bit quantum logic gate are presented, and select experimental issues in scaling the system to larger numbers of ions and gates are treated.

PACS numbers: 32.80.Qk, 42.50.Vk, 89.80.+h


## I. Introduction

In its simplest form, a quantum computer is a collection of $N$ two-level quantum systems (quantum bits) which can be prepared in an arbitrary entangled quantum state spanning all $2^N$ basis states [1, 2]. A quantum computer, unlike its classical counterpart, can thus store and simultaneously process superpositions of numbers. Once a measurement is performed on the quantum computer, the superposition collapses to a single number, which in some cases can jointly depend on all of the numbers previously stored. This gives the potential for massive parallelism in particular algorithms [3], most notably an algorithm which factorizes numbers efficiently [2, 4]. Apart from applications to this and other algorithms [5], creating multi-particle entangled states is of great interest in its own right, from the standpoint of quantum measurements [6] and, for example, for improved signal-to-noise ratio in spectroscopy [7, 8].

Unfortunately, there are very few physical systems which are amenable to the task of quantum computation. This is because a quantum computer must (i) interact very weakly with the environment to preserve coherence of the superpositions, and (ii) interact very strongly with other quantum bits to facilitate the construction of quantum logic gates necessary for computing. In addition to these seemingly conflicting requirements, the quantum bits must be able to be controlled and manipulated in a coherent fashion and be read out with high efficiency.

In 1995, Cirac and Zoller showed that a collection of trapped and cooled atomic ions can satisfy these requirements and form an attractive quantum computer architecture [9]. In their proposal, each quantum bit is derived from a pair of internal energy levels of an individual atomic ion. By using laser beams, the quantum bits are coupled to one another

by virtue of the quantized collective motion of the ions in the trap, mediated by the Coulomb interaction. A reduced version of their scheme was implemented in an experiment on a single trapped ion [10].

This paper concentrates on the trapped ion quantum computer architecture, and covers some of the experimental details involved in conducting simple logic operations between small numbers of trapped ions. Following a brief introduction to ion traps and the interaction between internal and motional states of trapped ions in section II, preliminary experiments involving one ion are reviewed in section III, and particular technical problems in the extension of this scheme to $N > 1$ ions are discussed. Section IV considers the problems of addressing individual ions in a string with lasers and the cross-coupling of the $3N$ quantized modes of motion, and section V characterizes some expected sources of decoherence. The topics covered here are by no means exhaustive, but may give an indication of some of the key problems which may lie ahead in the near future. We have attempted a more complete investigation of the problems in Ref. [11]. For more reviews of the trapped ions quantum computer, see Refs. [12, 13]. Other notable physical systems proposed for quantum computation not covered here include cavity-QED [14] and bulk spin nuclear magnetic resonance [15].

## II. Background

### A. Internal states and detection

Ions can be confined for days in an ultra-high-vacuum environment with minimal perturbations to their internal atomic structure, and collisions with background gas can be neglected. Even though the ions interact strongly through their mutual Coulomb interaction, the fact that the ions are localized necessarily means that the time-averaged value of the electric field they experience is zero; therefore electric field perturbations are small. Magnetic field perturbations to internal structure are important; however, the coherence time for superposition states of two internal levels can be very long by operating at fields where the energy separation between levels is at an extremum with respect to field. For example, a coherence time exceeding 10 minutes between a pair of $^9Be^+$ ground state hyperfine levels has been observed [16]. It is also possible to employ a ground and excited (metastable) electronic state of a trapped ion as a quantum bit [9]. This option seems difficult at the present time, primarily because the energy splitting is typically in the optical region, requiring extremely high laser frequency stability to drive coherent transitions.

Figure 1a shows a reduced energy level diagram of a single $^9Be^+$ ion. Although many other ion species would also be suitable for quantum computation, we will concentrate on $^9Be^+$ here for concreteness and to make a connection to the experiments at NIST [10, 17]. We will primarily be interested in two electronic states, the $^2S_{1/2}(F = 2, m_F = 2)$ and $^2S_{1/2}(F = 1, m_F = 1)$ hyperfine ground states (denoted by $|\downarrow\rangle$, and $|\uparrow\rangle$, respectively), separated in energy by $\hbar\omega_0$. These long-lived "spin" states will form the basis for a quantum bit. Detection of the spin states can be accomplished using the technique of quantum jumps [18]. By tuning a polarized laser beam to the $|\downarrow\rangle \leftrightarrow {}^2P_{3/2}$ transition near 313 nm (Fig. 1a), many photons are scattered if the atom is in the $|\downarrow\rangle$ spin state (a "cycling" transition), but essentially no photons are scattered if the atom is in the $|\uparrow\rangle$ spin state. If a modest number of these photons are detected, the efficiency of our ability to discriminate between these two states approaches 100%.

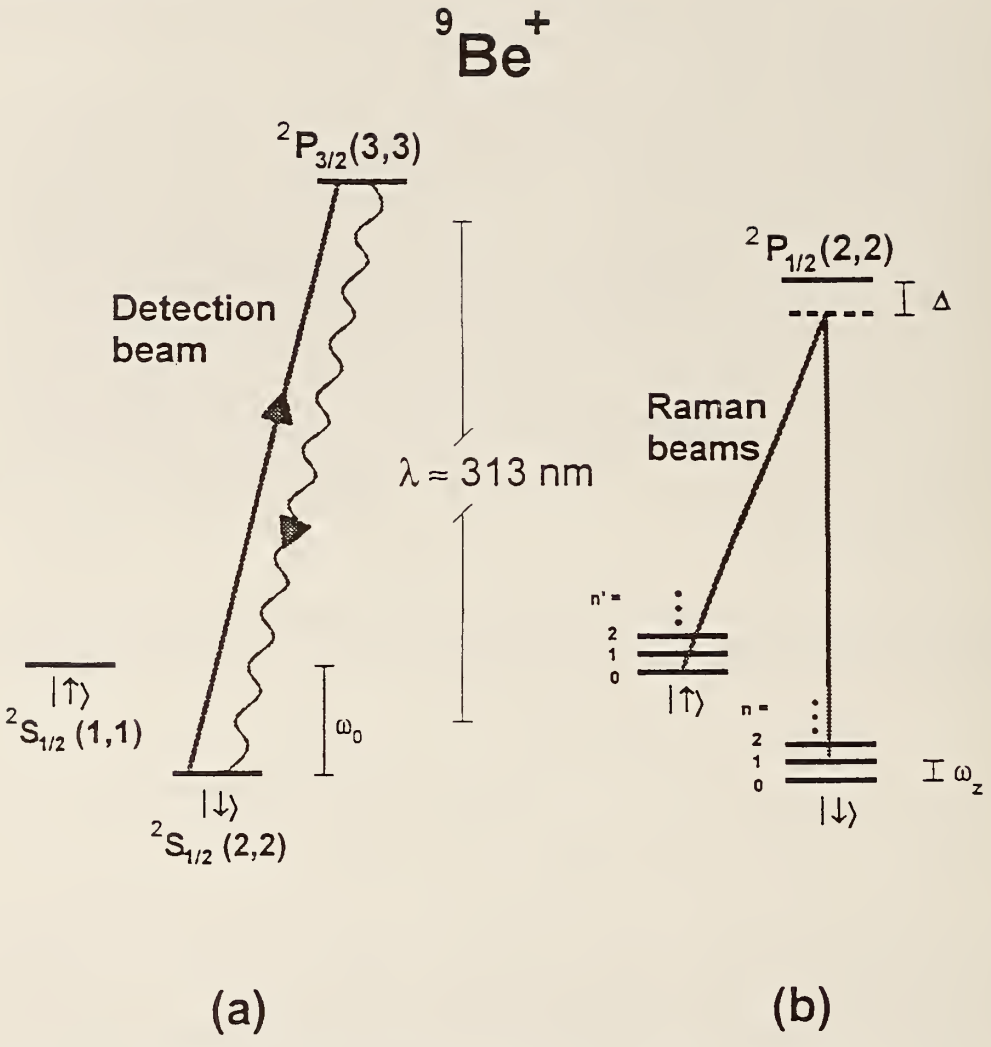


Fig 1: (a) Electronic (internal) energy levels (not to scale) of a $^9Be^+$ ion. The $^2S_{1/2}(F = 2, m_F = 2)$ and $^2S_{1/2}(F = 1, m_F = 1)$ hyperfine ground states (denoted by $|\downarrow\rangle$ and $|\uparrow\rangle$ respectively), separated in frequency by $\omega_0/2\pi \approx 1.250$ GHz, form the basis of a quantum bit. Detection of the internal state is accomplished by illuminating the ion with a $\sigma^-$-polarized "detection" beam near 313 nm, which drives the cycling $^2S_{1/2}(F = 2, m_F = 2) \leftrightarrow {}^2P_{3/2}(F = 3, m_F = 3)$ transition, and observing the scattered fluorescence. The excited $P$ state has radiative linewidth $\gamma/2\pi \approx 19.4$ MHz. (b) Energy levels of a trapped $^9Be^+$ ion, including the motional states of a single mode of harmonic motion, depicted by ladders of vibrational states separated in frequency by the mode frequency $\omega_z$. Two "Raman" beams, both detuned $\Delta \gg \omega_0, \omega_z, \gamma$ ( from the excited $^2P_{1/2}$ state, provide a coherent two-photon coupling between states $|n\rangle|\downarrow\rangle$ and $|n'\rangle|\uparrow\rangle$ by setting the difference frequency $\omega_L$ to match the desired transition frequency. As shown, the Raman beams are tuned to the first red sideband of the $|\downarrow\rangle \leftrightarrow |\uparrow\rangle$ transition ($\omega_L = \omega_0 - \omega_z$).

## B. Ion traps and motional states

In Fig. 2, we show a schematic diagram of a linear Paul trap [19], consisting of four electrode rods. The linear trap is similar to a quadrupole mass filter [20] which is plugged at the ends with static electric potentials. A potential $V_0 \cos \Omega_T t$ is applied between diagonally

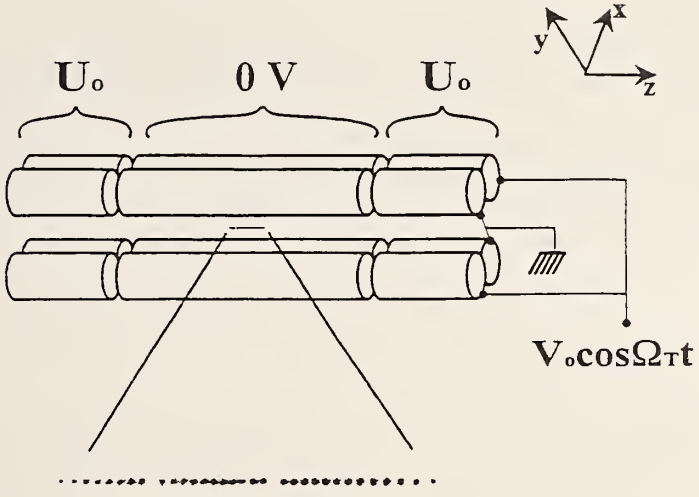


Fig. 2: The upper part of the figure shows a schematic diagram of the electrode configuration for a linear Paul-rf trap (rod spacing $\simeq$1 mm). The lower part of the figure shows an image of a string of $^{199}Hg^+$ ions, illuminated with 194 nm radiation, taken with a UV-sensitive, photon counting imaging tube [22]. The spacing between adjacent ions is approximately 10 μm. The "gaps" in the string are occupied by impurity ions, most likely other isotopes of $Hg^+$, which do not fluoresce because the frequencies of their resonant transitions do not coincide with those of the 194 nm $^2S_{1/2} \rightarrow {}^2P_{1/2}$ transition of $^{199}Hg^+$.

opposite rods, which are fixed in a quadrupolar configuration, as indicated in Fig. 2. To provide confinement along the axial $z$ direction, static potentials $U_0$ are applied to the end segments of the rods as indicated. We assume that the rod segments along the $z$ direction are coupled together with capacitors (not shown) so that the rf potential is constant as a function of $z$. Near the axis of the trap this creates a potential of the form

$$\Phi \simeq \frac{V_0}{2} \cos \Omega_T t \left(1 + \frac{x^2 - y^2}{R^2}\right) + \frac{U_0}{2} \left(\frac{2z^2 - x^2 - y^2}{d^2}\right), \tag{1}$$

where $R$ is equal to the distance from the axis to the surface of the electrode and $d$ is a characteristic axial dimension of the static electrodes. This gives rise to harmonic ponderomotive potentials [21] in the radial ($x$ and $y$) directions accompanied by static harmonic confinement in the axial ($z$) direction resulting in an effective $3D$ harmonic confining potential $U(r) = \frac{1}{2} m\omega_x^2 x^2 + \frac{1}{2} m\omega_y^2 y^2 + \frac{1}{2} m\omega_z^2 z^2$, with

$$\omega_x \approx \omega_y \approx \sqrt{\omega_p^2 - \frac{\omega_z^2}{2}}, \qquad \omega_z = \sqrt{\frac{2qU_0}{md^2}}, \tag{2}$$

where $\omega_p \equiv qV_0/(2^{1/2}\Omega_T m R^2)$ describes the ponderomotive portion of the potential, and $q$ and $m$ are the charge and mass of the ion, respectively. In these expressions, it is assumed that $\omega_p \ll \Omega_T$, a condition known as the "pseudopotential approximation" [21].

Figure 2 also shows an image of a "string" of $^{199}Hg^+$ ions which are confined near the $z$ axis of the trap described in Ref. [22]. This was achieved by making $\omega_x$, $\omega_y \gg \omega_z$, thereby forcing the ions to the axis of the trap. The spacings between individual ions in this string are governed by a balance of the force along the $z$ direction and the mutual Coulomb repulsion of the ions. Example parameters are given in the figure caption.

Of the $3N$ normal modes of small oscillation in a linear trap, we are primarily interested in the $N$ modes associated with axial motion. A remarkable feature of the linear ion trap is that the axial modes frequencies are nearly independent of $N$, offering the possibility that mode interference might be small, even for large numbers of ions [9]. For two ions, the axial normal mode frequencies are at $\omega_z$ and $\sqrt{3}\omega_z$; for three ions they are

$\omega_z$, $\sqrt{3}\,\omega_z$ and $\sqrt{5.4}\,\omega_z$. For $N > 3$ ions, the $N$th axial normal mode can be determined numerically [12, 13, 23]. We will concentrate on the axial center-of-mass (COM) mode, which is the lowest frequency mode and is also the most resolved in frequency from the others. The quantum state of axial COM motion at frequency $\omega_z$ can be described by the ladder of vibrational eigenstates $|n\rangle$, of energy $\hbar\omega_z(n+\frac{1}{2})$ with vibrational index $n$ describing the number of "phonons" contained in the collective harmonic COM motion.

### C. Coupling between internal and motional states

We describe the coupling between the internal levels of a particular ion in the string with the COM axial mode of collective motion when a classical radiation field is applied to that ion. If the internal levels $|\downarrow\rangle_j$ and $|\uparrow\rangle_j$ of the $j$th ion in a string are coupled by a dipole moment operator $\boldsymbol{\mu}_j$ (other couplings can be shown to behave analogously), then exposing this ion to a traveling-wave electric field $\boldsymbol{E}(\boldsymbol{r}) = \boldsymbol{E}_0 \cos(\boldsymbol{k}\cdot\boldsymbol{r} - \omega_L t + \varphi)$ with frequency $\omega_L$, phase $\varphi$, and wavevector $\boldsymbol{k}$, results in the interaction Hamiltonian

$$\mathcal{H}_I^j = -\boldsymbol{\mu}_j \cdot \boldsymbol{E}(\boldsymbol{r}) = \hbar\Omega^j(S_+^j + S_-^j)\,(e^{i(\boldsymbol{k}\cdot z - \omega_L t + \varphi)} + e^{-i(\boldsymbol{k}\cdot z - \omega_L t + \varphi)})\,. \tag{3}$$

In this expression, $\Omega^j = -\langle\uparrow|\boldsymbol{\mu}_j|\downarrow\rangle \cdot \boldsymbol{E}_0/4\hbar$ is the resonant Rabi frequency connecting $|\downarrow\rangle_j$ to $|\uparrow\rangle_j$ in the absence of confinement, $S_+^j(S_-^j)$ is the internal level raising (lowering) operator of the $j$th ion changing $|\downarrow\rangle_j$ to $|\uparrow\rangle_j$ and vice-versa, $z = z_0\hat{z}(ae^{-i\omega_z t} + a^\dagger e^{i\omega_z t})$ is the axial COM coordinate operator of the confined motion with associated harmonic raising (lowering) operator $a^\dagger(a)$ and zero-point spread $z_0 \equiv (\hbar/2Nm\omega_z)^{1/2}$, and $Nm$ is the total mass of the ion collection. If the applied radiation frequency is tuned to $\omega_L = \omega_0 + (n'-n)\,\omega_z$, thereby coupling the states $|n\rangle\,|\downarrow\rangle_j$ and $|n'\rangle\,|\uparrow\rangle_j$, $\mathcal{H}_I^j$ is transformed to

$$\mathcal{H}_I^j = \hbar\Omega^j(S_+^j\, e^{i\eta(a+a^\dagger)+i\varphi} + S_-^j\, e^{-i\eta(a+a^\dagger)-i\varphi}) \tag{4}$$

in a frame rotating at $\omega_L$, where terms oscillating faster than $\Omega^j$ ($\Omega^j \ll \omega_z, \omega_0$) have been neglected. Here, $\eta \equiv (\boldsymbol{k}\cdot\hat{z})\,z_0$ is the Lamb-Dicke parameter, which controls the amount of coupling between internal and COM motional states.

When the coupling of Eq. (4) is applied between the $j$th ion and the COM mode of motion, the system evolves between the two quantum states $|n\rangle\,|\downarrow\rangle_j$ and $|n'\rangle\,|\uparrow\rangle_j$ with Rabi frequency [24, 25]

$$\begin{aligned}\Omega_{n',n}^j &\equiv \frac{1}{\hbar}\,|\langle n'|\langle\uparrow|\,\mathcal{H}_I^j\,|\downarrow\rangle_j\,|n\rangle| \\ &= \Omega^j\,|\langle n'|\,e^{i\eta(a+a^\dagger)}\,|n\rangle| = \Omega^j\eta^{|n'-n|}\,e^{-\eta^2/2}\,\sqrt{\frac{n_<!}{n_>!}}\,L_{n_<}^{|n'-n|}(\eta^2)\,,\end{aligned} \tag{5}$$

where $n_>(n_<)$ is the greater (lesser) of $n$ and $n'$ and $L_n^\alpha(x)$ is a generalized Laguerre polynomial. If the Lamb-Dicke criterion is satisfied, where the amplitude of the ion's motion in the direction of the radiation is much less than $\lambda/2\pi$ (or $n^{1/2}\eta \ll 1$), we can evaluate $\Omega_{n',n}^j$ to lowest order in $\eta$ to obtain

$$\Omega_{n',n}^j = \Omega^j\,\frac{\eta^{|n'-n|}}{|n'-n|!}\,\sqrt{\frac{n_>!}{n_<!}}\,. \tag{6}$$

We will be primarily interested in three types of transitions – the carrier ($n' = n$), the first red sideband ($n' = n - 1$), and the first blue sideband ($n' = n + 1$) whose Rabi frequencies, in the Lamb-Dicke limit, are given from Eq. (6) by $\Omega^j$, $\eta n^{1/2}\Omega^j$, and $\eta(n+1)^{1/2}\Omega^j$ respectively.

In practice, driving direct transitions between $|n\rangle|\downarrow\rangle_j$ and $|n'\rangle|\uparrow\rangle_j$ with rf or microwave radiation is not be feasible, as the sideband operation transition rates (proportional to $\eta = 2\pi z_0/\lambda$) would be extremely slow due to the long wavelength of the radiation. Alternatively, optical fields can be used to drive two-photon stimulated Raman transitions between $|n\rangle|\downarrow\rangle_j$ and $|n'\rangle|\uparrow\rangle_j$ [17, 26]. As depicted in Fig. 1b, two laser beams detuned by $\Delta$ from an excited state of radiative width $\gamma$ are applied to the $j$th ion with their difference frequency matched to the desired transition frequency. For sufficient detuning $|\Delta| \gg \gamma$, the excited state may be adiabatically eliminated, and the above couplings apply, with $\Omega^j$ replaced by $g_1^j g_2^j/\Delta$, where $g_1^j$ and $g_2^j$ are the individual Rabi frequencies of the two beams when resonantly coupled to the excited level. In addition, $\omega_L(\varphi)$ is replaced by the difference frequency (phase) of the beams; and $\boldsymbol{k}$ is replaced by the difference in wavevectors of the two Raman beams $\delta\boldsymbol{k} = \boldsymbol{k}_1 - \boldsymbol{k}_2$. Since the relevant frequency depends only on the microwave difference between the two laser frequencies, both beams can be generated with a single laser source and a modulator, thereby relaxing the constraints of laser frequency stabilization. The use of stimulated Raman transitions thus combines the advantages of the strong couplings with the frequency stability of microwave sources [26, 27].

### D. Laser cooling to the motional ground state

As a starting point for trapped ion quantum computing, the ions must be initialized in known pure states. Using standard optical pumping techniques, we can prepare the ions in the $|\downarrow\rangle$, internal state. Laser cooling in the resolved sideband limit [25] can, for single ions, generate the $|n = 0\rangle$ motional state with reasonable efficiency [17, 28]. This type of laser cooling is usually preceded by a stage of "Doppler" laser cooling [29] which typically cools the ion to $\langle n\rangle \geq 1$, or an equivalent temperature of about 1 mK.

Resolved sideband laser cooling for a single, harmonically-bound atom can be explained as follows: For simplicity, we assume the atom is confined by a 1-D harmonic well of vibration frequency $\omega_z$. We use an optical transition whose radiative linewidth $\gamma$ is relatively narrow, $\gamma \ll \omega_z$ (Doppler laser cooling applies when $\gamma \geq \omega_z$). If a laser beam (frequency $\omega_L$) is incident along the direction of the atomic motion, the bound atom's absorption spectrum is composed of a "carrier" at frequency $\omega_0$ and resolved frequency-modulation sidebands that are spaced by $\omega_z$. These sidebands in the spectrum are generated from the Doppler effect (like vibrational substructure in a molecular optical spectrum). Laser cooling can occur if the laser is tuned to a lower (red) sideband, for example, at $\omega_L = \omega_0 - \omega_z$. In this case, photons of energy $\hbar(\omega_0 - \omega_z)$ are absorbed, and spontaneously emitted photons of average energy $\hbar\omega_0 - R$ return the atom to its initial internal state, where $R \equiv (\hbar k)^2/2m = \hbar\omega_R$ is the photon recoil energy of the atom. Overall, for each scattering event, this reduces the atom's kinetic energy by $\hbar\omega_z$ if $\omega_z \gg \omega_R$, a condition which is satisfied for ions in strong ion traps. Since $\omega_R/\omega_z = \eta^2$ where $\eta$ is the Lamb-Dicke parameter, this simple form of sideband cooling requires that the Lamb-Dicke parameter be small. For example, in $^9Be^+$, if the recoil corresponds to spontaneous emission from the 313 nm $^2P_{1/2} \rightarrow {}^2S_{1/2}$ transition (typically used for laser cooling), $\omega_R/2\pi \simeq 230$ kHz. This is to be compared to trap oscillation frequencies in some laser-cooling experiments of around 10 MHz [17]. Cooling proceeds until the atom's mean vibrational quantum number in the harmonic well is given by $\langle n\rangle_{\min} \simeq (\gamma/2\omega_z)^2 \ll 1$ [29]. As discussed above, it is convenient to use two-photon stimulated Raman transitions for sideband cooling [17, 30], but the basic idea for, and limits to, cooling are essentially the same as for single-photon transitions.

Although laser cooling to the $|n = 0\rangle$ state has been achieved with single ions [17, 28]; a prerequisite to future work is to laser cool a collection of ions (or, at least one mode of the collection) to the zero-point state. Cooling of any of the $3N$ modes of motion of a collection of ions should, in principle, work the same as cooling of a single ion. To cool a particular mode, we tune the cooling radiation to its first lower sideband. If we want to cool all modes, sideband cooling must be cycled through all $3N$ modes more than once, or applied to all $3N$ modes at once, since recoil will heat all modes. For the COM mode, the cooling is essentially the same as cooling a single particle of mass Nm; however, the recoil energy upon re-emission is distributed over all $3N$ modes. Other methods to prepare atoms in the $|n = 0\rangle$ state are discussed in Refs. [31]. In Ref. [32], it is shown that it is not necessary to satisfy the condition $\omega_R \ll \omega_z$ ($\eta \ll 1$) to achieve cooling to $n = 0$.

## III. Quantum Logic with Trapped Ions

Several authors have shown that an arbitrary unitary operation (therefore any quantum computation) on a collection of quantum bits can be broken into a series of fundamental single bit and dual bit quantum logic gates [33]. This is similar to classical computing, where certain families of logic gates are universal (for instance, the single bit NOT and two bit AND gates). One such family of universal quantum logic gates consists of the single bit rotation gate and the two-bit controlled-NOT gate [34]. For brevity, we concentrate on these two gates and how they can be implemented in a system of trapped ions.

The single bit rotation gate [operator $R(\theta, \varphi)$] simply changes the state of a single quantum bit and is characterized by the following transformation:

$$\begin{aligned} |\downarrow\rangle &\rightarrow \cos(\theta/2)\,|\downarrow\rangle - i e^{i\varphi} \sin(\theta/2)\,|\uparrow\rangle \\ |\uparrow\rangle &\rightarrow \cos(\theta/2)\,|\uparrow\rangle - i e^{-i\varphi} \sin(\theta/2)\,|\downarrow\rangle , \end{aligned} \tag{7}$$

where $\theta$ and $\varphi$ are parameters of the gate. This transformation is commonplace in atomic physics and nuclear magnetic resonance, and has been widely applied to two level systems. In the context of trapped ions, the single bit rotation gate is accomplished by tuning to the carrier transition ($\omega_L = \omega_0$) and applying radiation for a time $t$ such that $\theta = 2\Omega^i t$ (Eq. (6)). The parameter $\theta$ describes the "rotation" between the two spin states ($\theta = \pi$ is called a "$\pi$" pulse, etc.), and the parameter $\varphi$ describes the phase of the rotation. Figure 3 depicts the observed Rabi flopping between $|\downarrow\rangle$, and $|\uparrow\rangle$, states in a single trapped $^9Be^+$ ion

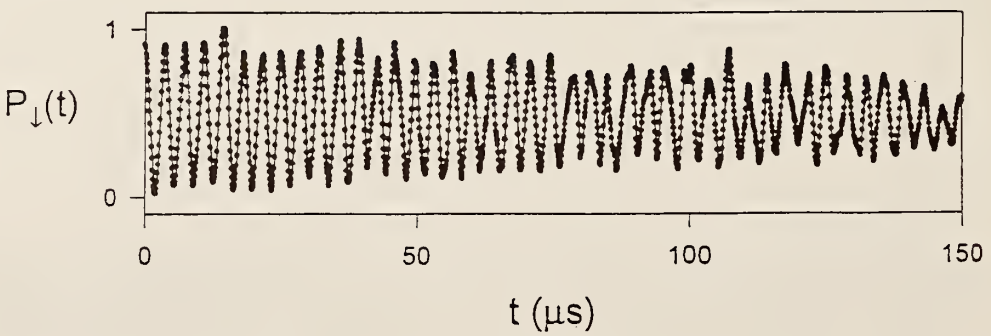


Fig. 3: Experimental plot of the probability $P_\downarrow(t)$ of finding a single $^9Be^+$ ion in the $|\downarrow\rangle$ state after first preparing it in the $|\downarrow\rangle$ state and applying the carrier coupling (Eq. (7)) for a time $t$, with $\theta/2 = \Omega^i t$. $P_\downarrow(t)$ does not follow a perfect sinusoid due to decoherence, described in section IV. Each point represents an average of 4000 observations.

according to the above transformation [35]. The ion is first prepared in the $|\downarrow\rangle$, state, then the carrier transition is applied for a time $t$, and the state ($|\downarrow\rangle$, or $|\uparrow\rangle$) is detected as described above and in Fig. 1a.

A more nontrivial quantum logic gate is the two-bit controlled-NOT (CN) gate [33, 34], reminiscent of the classical XOR gate. This gate flips the spin of ion $k$, the "target bit" ($|\downarrow\rangle_k \leftrightarrow |\uparrow\rangle_k$) if and only if ion $j$, the "control bit," is in state $|\uparrow\rangle$. The transformation of the two quantum bits $j$ and $k$ are as follows:

$$\begin{aligned} |\downarrow\rangle_j |\downarrow\rangle_k &\rightarrow |\downarrow\rangle_j |\downarrow\rangle_k \\ |\downarrow\rangle_j |\uparrow\rangle_k &\rightarrow |\downarrow\rangle_j |\uparrow\rangle_k \\ |\uparrow\rangle_j |\downarrow\rangle_k &\rightarrow |\uparrow\rangle_j |\uparrow\rangle_k \\ |\uparrow\rangle_j |\uparrow\rangle_k &\rightarrow |\uparrow\rangle_j |\downarrow\rangle_k . \end{aligned} \tag{8}$$

CIRAC and ZOLLER [9] showed how the above transformation could be accomplished between two of a collection of trapped ions by utilizing a motional mode (i.e., axial COM mode) as a "data bus" through which the quantum bits are shuttled. As described above, the COM mode is assumed to be initially cooled to the $|n = 0\rangle$ ground state. The scheme is outlined as follows:

(1) Map the state of ion $j$ (spanning the states $|\downarrow\rangle_j$, $|\uparrow\rangle_j$) onto the first two axial COM motional states (spanning the states $|n = 0\rangle$, $|n = 1\rangle$) shared amongst all ions.
(2) Flip the spin state of ion $k$ ($|\downarrow\rangle_k \leftrightarrow |\uparrow\rangle_k$) if and only if there is a phonon in the COM mode.
(3) Reverse step (1): map the state of the motion back onto ion $j$.

The central ingredient here is step (2), which is itself a "reduced" CN gate, with the first two motional states acting as the control bit and ion $k$ acting as the target bit

$$\begin{aligned} |0\rangle |\downarrow\rangle_k &\rightarrow |0\rangle |\downarrow\rangle_k \\ |0\rangle |\uparrow\rangle_k &\rightarrow |0\rangle |\uparrow\rangle_k \\ |1\rangle |\downarrow\rangle_k &\rightarrow |1\rangle |\uparrow\rangle_k \\ |1\rangle |\uparrow\rangle_k &\rightarrow |1\rangle |\downarrow\rangle_k . \end{aligned} \tag{9}$$

This last transformation has been realized on a single trapped ion [10]. In that experiment, performed on a trapped $^9Be^+$ ion, the control bit was one of the three modes of the ion's motion. The reduced CN operation between these states (step (2) above) was realized by applying three laser pulses in succession:

(a) A $\pi/2$ pulse ($\Omega^k t = \pi/4$ in Eq. (6)) is applied on the carrier transition. For a certain choice of initial phase, this corresponds to the rotation operator $R(\theta = \pi/2, \varphi)$.
(b) A $2\pi$ pulse is applied on the first blue sideband transition between levels $|\uparrow\rangle$ and an auxiliary level $|\text{aux}\rangle$ in the ion (the $|F = 2, M_F = 0\rangle$ level in $^9Be^+$; see Fig. 4). This operation provides the "conditional dynamics" for the overall CN operation. It changes the sign of the $|1\rangle |\uparrow\rangle$ component of the wavefunction but leaves the sign of the $|0\rangle |\uparrow\rangle$ component of the wavefunction unchanged; that is, the sign change is conditioned on whether or not the ion is in the $|0\rangle$ or $|1\rangle$ motional state.
(c) A $\pi/2$ pulse is applied to the spin carrier transition with a 180° phase shift relative to step (a). This corresponds to the operator $R(\theta = \pi/2, \varphi + \pi)$.

Steps (a) and (c) can be regarded as two resonant pulses of opposite phase in the RAMSEY separated-field method of spectroscopy [36]. If step (b) is active (thereby changing the sign

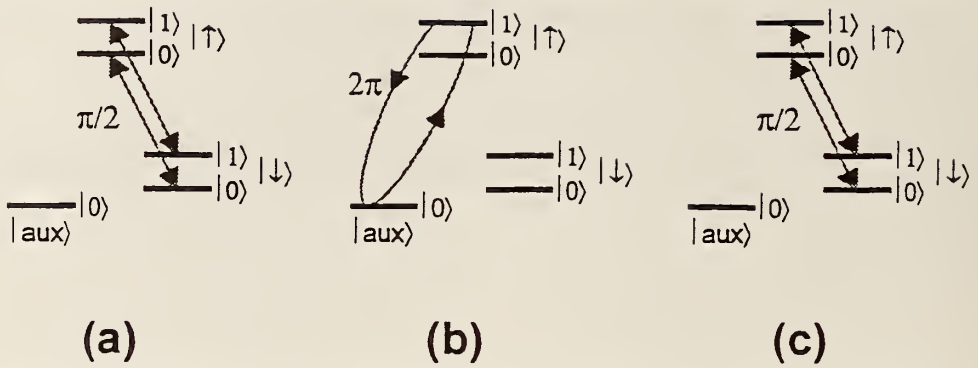


Fig. 4: Energy levels of a single trapped $^9Be^+$ ion, including the internal hyperfine levels $|\downarrow\rangle$ and $|\uparrow\rangle$ and an auxiliary level $|\text{aux}\rangle$ [the $^2S_{1/2}(F = 2, m_F = 0)$ state], each dressed by the lowest two motional quantum harmonic oscillator states $|n\rangle = |0\rangle$ and $|1\rangle$. The controlled-NOT quantum logic gate results in a spin flip ($|\downarrow\rangle \leftrightarrows |\uparrow\rangle$ if and only if $|n\rangle = |1\rangle$. This transformation is realized with a sequence of three pulses of laser light which couple the states indicated by the arrows: **(a)** A $\pi/2$ pulse couples states $|n\rangle|\downarrow\rangle$ to $|n\rangle|\uparrow\rangle$. **(b)** A $2\pi$ pulse couples state $|1\rangle|\uparrow\rangle$ to $|0\rangle|\text{aux}\rangle$, resulting in a sign change of any component in the $|1\rangle|\uparrow\rangle$ state. **(c)** A $-\pi/2$ pulse couples states $|n\rangle|\downarrow\rangle$ to $|n\rangle|\uparrow\rangle$ (same as step (a) with a $\pi$ phase shift). If $|n\rangle = |0\rangle$, then step (b) is inactive since it only affects to the $|1\rangle|\uparrow\rangle$ state, and the two $\pi/2$ pulses cancel, leaving the initial state unaffected. If $|n\rangle = |1\rangle$, then the sign change in step (b) causes the two $\pi/2$ pulses to add, resulting in a net spin flip ($|\downarrow\rangle \leftrightarrows |\uparrow\rangle$). The result is the transformation of Eq. (9).

of the $|1\rangle|\uparrow\rangle$ component of the wavefunction), then a spin flip is induced by the Ramsey fields. If step (b) is inactive, step (c) reverses the effect of step (a).

Instead of the three pulses (a–c above), a simpler CN gate scheme between an ion's internal and motional states can be achieved with a single laser pulse, while eliminating the requirement of the auxiliary internal electronic level [37]. By applying a single pulse tuned to the carrier transition, from Eq. (5), the states $|n\rangle|\downarrow\rangle$ and $|n\rangle|\uparrow\rangle$ are coupled with Rabi frequency

$$\Omega_{n,n} = \Omega\,|\langle n|\, e^{i\eta(a+a^\dagger)}\,|n\rangle| = \Omega\, e^{-\eta^2/2}\,\mathcal{L}_n(\eta^2)\,, \tag{10}$$

where $\mathcal{L}_n(\eta^2) \equiv L_n^0(\eta^2)$ is a Laguerre polynomial. Specializing to the $|n\rangle = |0\rangle$ and $|n\rangle = |1\rangle$ vibrational levels relevant to quantum logic, we have

$$\begin{aligned} \Omega_{0,0} &= \Omega\, e^{-\eta^2/2}, \\ \Omega_{1,1} &= \Omega\, e^{-\eta^2/2}(1-\eta^2)\,. \end{aligned} \tag{11}$$

The CN gate can be achieved in a single pulse by setting $\eta$ so that $\Omega_{1,1}/\Omega_{0,0} = (2k+1)/2m$, with $k$ and $m$ positive integers satisfying $m > k \geq 0$. Setting $\Omega_{1,1}/\Omega_{0,0} = 2m/(2k+1)$ will also work, with the roles of the $|0\rangle$ and $|1\rangle$ motional states switched in Eq. (10). By driving the carrier transition for a duration $\tau$ such that $\Omega_{1,1}\tau = (k+\frac{1}{2})\pi$, or a "$\pi$-pulse" (mod $2\pi$) on the $|n\rangle = |1\rangle$ component, this forces $\Omega_{0,0}\tau = m\pi$. Thus the states $|\downarrow\rangle|1\rangle \leftrightarrow |\uparrow\rangle|1\rangle$ are swapped, while the states $|\downarrow\rangle|0\rangle$ and $|\uparrow\rangle|0\rangle$ remain unaffected. This transformation is equivalent to the reduced CN of Eq. (9), apart from phase factors which can be eliminated by the appropriate settings of the phase of subsequent logic operations.

The mapping steps (steps (1) and (3) above) can be realized by applying a $\pi$-pulse on the red sideband of ion $j$. This accomplishes the mapping $|0\rangle(\alpha|\downarrow\rangle_j + \beta|\uparrow\rangle_j) \rightarrow (\alpha|0\rangle$

$+\beta|1\rangle)|\downarrow\rangle_j$. Analogous mapping of internal state superpositions to motional state superpositions of a trapped ion has also been reported in the generation of a "Schrödinger cat" state of motion [38] and the tomographic measurement of nonclassical states of motion [39].

To complete this section, we give an example of how a "maximally-entangled" state of $N$ ions might be prepared with the use of the quantum logic gates described in this section [9]. We desire to create the state

$$\Phi_{\mathrm{ME}} = \frac{|\downarrow\rangle_1|\downarrow\rangle_2|\downarrow\rangle_3\cdots|\downarrow\rangle_N + e^{i\varphi}|\uparrow\rangle_1|\uparrow\rangle_2|\uparrow\rangle_3\cdots|\uparrow\rangle_N}{\sqrt{2}} \tag{12}$$

(or equivalently, a coherent superposition of the numbers 0 and $2^N - 1$ in binary where we make the identification $|\downarrow\rangle \equiv 0$ and $|\uparrow\rangle \equiv 1$). Starting in an initial state $\Phi_{\mathrm{init}}$ where all spins are in the $|\downarrow\rangle$ state, it is easy to show that one way to prepare Eq. (12) is to operate the following $N$ gates on the initial state:

$$\Phi_{\mathrm{ME}} = [CN_{1,N}][CN_{1,N-1}][CN_{1,N-2}]\cdots[CN_{1,2}][R_1(\pi/2, \varphi)]\,\Phi_{\mathrm{init}}, \tag{13}$$

where $CN_{i,j}$ denotes the controlled-NOT operator with ion $i$ as the control bit and ion $j$ as the target bit, and the rotation operator is applied to the first ion. The state $\Phi_{\mathrm{ME}}$ can be viewed as the $N$-particle generalization of the entangled pair states envisioned by EINSTEIN, PODOLSKY, and ROSEN [40], and may find uses in improved atomic spectroscopy and frequency standards [7, 8].

## IV. Packing Ions into a Trap

The reduced CN gate demonstrated in [10] involved only a single ion, and is therefore not useful for computation. Future experimental work will concentrate on scaling the system up by packing more ions into the trap and improving the gate fidelity, thereby allowing more gates to be coherently performed. In this section, we survey selected experimental problems which may arise in the scaleup. For a more extensive coverage of the scaling problem, see Ref. [11].

### A. Individual ion addressing

One major concern in extending quantum logic to larger numbers of ions is the requirement that ions be individually addressed with laser beams for logic operations. This may be difficult, because the high vibrational frequencies desired for efficient laser cooling and suppression of decoherence also results in closely spaced ions. It can be shown that the minimum separation of adjacent ions in a linear trap between the center ions scales approximately as $s_{\min} \simeq 2sN^{-0.56}$, with $s = (q^2/4\pi\varepsilon_0 m\omega_z^2)^{1/3}$, where $N$ is the number of ions [12, 13]. For $^9Be^+$ ions with an axial COM frequency of $\omega_z/2\pi = 1$ MHz, this separation is about 10 μm for 2 ions, and 4 μm for 10 ions.

The most straightforward method for individual optical addressing is to tightly focus laser beams on the selected ion [9]. The transverse intensity distribution of a Gaussian optical beam of power $P$ is

$$I(r) = \frac{2P}{\pi w_0^2}\exp\left(-\frac{2r^2}{w_0^2}\right), \tag{14}$$

where $w_0 \simeq \lambda(\pi \cdot NA)$ is the beam waist, $\lambda$ the radiation wavelength, and $NA = \tan\theta$ is the numerical aperture of the beam with cone half-angle $\theta$ (the formula for $w_0$ in the paraxial ray approximation is valid only for $NA < 1$) [41]. For large numerical apertures ($NA \approx 0.5$), it appears that laser beams can thus be focussed down to a spot on the order of a wavelength, but this is difficult to realize in the laboratory. If we can realize $w_0 = 5\,\mu\text{m}$ in a Gaussian beam, then at a distance 10 μm from the center of the beam this would imply a relative intensity of about $3 \cdot 10^{-4}$ or a electric field amplitude (proportional to Rabi frequency) of 1.8% relative to the center of the beam. If $w_0 = 2\,\mu\text{m}$ could be obtained, the intensity (electric field) would be down by a factor of $1.3 \cdot 10^{-14}$ ($1.1 \cdot 10^{-7}$). These results are likely too optimistic, since imperfections in the surfaces of the intervening vacuum port window, multiple reflections from these windows, and diffraction will typically distribute laser intensity outside of the theoretical waist of the beam. The degree to which this occurs depends on the details of window surfaces, etc. and must be resolved experimentally.

Tightly focussed Gaussian beams possess high transverse intensity gradients, resulting in the potential for significant intensity fluctuations at the selected ion if the relative position of the beam with respect to the ion is not stable on the time scale of the computation. An alternative to using tightly focussed Gaussian laser beams is to first feed the (expanded) laser beam through a sharply defined aperture (slit or aperture), and use a lens to image the aperture at the position of the ions. With this technique, the beam intensity can be distributed more smoothly around the selected ion and have very steep intensity edges (on the order of the original aperture sharpness) away from the ion, thus suppressing beam vibration problems and confining the radiation to a single ion. This technique has been used to make relatively "hard" walls for an optical dipole trap [42]. For this technique to work well, the imaging lens must collect a large fraction of the light transmitted through the aperture or else diffraction effects will result in light intensity outside the image of the aperture. To address individual ions, we require very small aperture images, which gives rise to a design tradeoff. If a one-to-one relay lens is used to image a small object aperture, effects of diffraction are enhanced. If a demagnifying lens is used to reduce a large object aperture, then the aperture must be placed a large distance from the lens, requiring a relatively large lens. For two ions, imaging a sharp edge such as a razor blade at the space between the ions may be sufficient. We might also consider having every other ion in a string be a "garbage" ion which is not used in the computation, thereby increasing the spacing between qubit ions by a factor of two (or more, if more garbage ions are used between each qubit ion). This has the disadvantage that total number of ions (and spectator modes) increases, aggravating the problems associated with large quantum registers. If sufficiently good addressing on one ion in a string can be accomplished, it may be simpler to shift the ions, rather than the laser beams, in order to address different ions. This could be accomplished by applying different static potentials $U_0$ and $U_0'$ to the end segments of the rods in Fig. 2. However, changes in $U_0$ and $U_0'$ would have to be coordinated to keep the COM axial frequency constant or else additional phase shifts would be introduced. Stimulated-Raman transitions have the advantage that the effective wavevector $\delta\boldsymbol{k} = \boldsymbol{k}_1 - \boldsymbol{k}_2$ can be made parallel to the axis of the trap even though each beam is at an angle with respect to the trap axis. This would allow selection of a particular ion, while eliminating coupling to transverse modes.

Another method of optically addressing individual ions is to cause a destructive optical interference at the position of a specific ion, with a net coupling at the other ion(s). For instance, if ion $j$ is positioned at the node of a resonant standing wave laser field, the coupling between states $|n\rangle\,|\downarrow\rangle_j$ and $|n'\rangle\,|\uparrow\rangle_j$ is proportional to $\langle n'|\sin[\eta_j(a + a^\dagger)]\,|n\rangle$. In this case, the coupling of the standing wave to ion $j$ vanishes when the laser frequency is tuned to an even order sideband such as the carrier ($n' = n$). If, instead, the ion is positioned at an antinode, the coupling is proportional to $\langle n'|\cos[\eta_j(a + a^\dagger)]\,|n\rangle$; thus, the coupling

vanishes when the laser frequency is tuned to an odd order sideband, such as the first blue or red sideband ($n' = n \pm 1$). By choosing the angles of focussed laser beams relative to the trap axis appropriately, it should be possible to position an antinode (node) at ion $j$ while approximately positioning nodes (antinodes) at the ions adjacent to ion $j$ (for equally spaced ions). In the case of two-photon stimulated Raman transitions, we desire to place ion $j$ at a common node or antinode of two standing waves. Although this interference technique should allow individual access to each of two trapped ions, it appears technically difficult to extend this technique to more than three ions.

Next, we consider the application of external field gradients which shift the internal energy levels of ions depending on their position. For a magnetic field gradient to give this selectivity, we require the Zeeman splitting between adjacent ions to be much larger than the Rabi frequency, or $\Delta\mu(\partial|\boldsymbol{B}|/\partial z)\, s/\hbar \gg \Omega$, where $\Delta\mu$ is the difference in $\langle \mu \cdot \boldsymbol{B}\rangle/|\boldsymbol{B}|$ between the two levels of interest, and $s$ is the ion separation along the $z$ direction. For $\Delta\mu = \mu_B$, $s = 10\,\mu\text{m}$, and a Rabi frequency of $\Omega/2\pi \approx 1$ MHz, this requires $\partial|\boldsymbol{B}|/\partial z \gg 0.1$ T/cm. Field gradients of this magnitude can be achieved; however, they might introduce large and uncontrollable phase shifts for the other ions in a quantum register.

The laser beam itself can provide ion selectivity by employing the transverse gradient in the optical field intensity. For instance, if we desire to perform a $\theta$-pulse on ion $j$ without affecting neighboring ion $k$, the intensity profile of the laser beam can be set so that the ratio of field strengths (intensities for the case of two-photon stimulated-Raman transitions) at ion $j$ vs. ion $k$ is $\theta/2\pi m$, where $m$ is an integer. Now if the pulse duration is set so that ion $j$ is rotated by $\theta$, ion $k$ receives a rotation of $2\pi m$ and hence returns back to its initial state (with an extra phase factor of $(-1)^m$).

For the case of two-photon stimulated-Raman transitions, the laser beam can provide ion frequency selectivity by employing the Stark shift and the transverse gradient of the optical field. Here, for example, we could assume that the two counterpropagating Raman beams of equal intensities and spatial profiles are offset so that beam 1 is centered on ion $j$, and beam 2 is centered on adjacent ion $k$ as depicted in Fig. 5. Let $\varepsilon$ be the fraction of peak intensity seen by the offset ions (that is, the intensity of beam 2 at ion $j$ and beam 1 at ion $k$). Assume that when either beam is centered on either ion, the single photon resonant Rabi frequencies are equivalent: $g_1 = g_2 = g$. When the beams are offset, the two-photon Rabi frequency at each ion is $\Omega = \varepsilon^{1/2}(g^2/\Delta_R)$, where $g^2/\Delta_R$ is the Rabi frequency expected if both beams were centered on a given ion. The Stark shifts of the two ions are in opposite directions: $\delta_j = +\delta_0$, $\delta_k = -\delta_0$, where $\delta_0 = \Omega(1-\varepsilon)/\varepsilon^{1/2}$. If we make $\delta_0 \gg \Omega$ ($\varepsilon \ll 1$), then by appropriately tuning the difference frequency of the laser beams, we can selectively drive transitions on either ion $j$ or $k$. Alternatively, if we desire to perform a $\theta$-pulse to ion $j$ without affecting ion $k$ in an "unrepairable" way, $\varepsilon$ can be tuned to a particular value which results in ion $k$ returning to within a phase factor to its initial state. For square pulses in time, we require $\theta/2(1+\delta^2/\Omega^2)^{1/2} = m\pi$, or $\varepsilon^2 - [1 + (2m\pi/\theta)^2]\,\varepsilon + 1 = 0$, where $m$ is an integer. For $m = 1$ and $\theta = \pi$ (a $\pi$-pulse on ion $j$), this occurs for $\varepsilon = 0.208$. Generalizing this to more than two ions becomes difficult if the laser beams also overlap other qubit ions. This scheme places an additional premium on laser power stability, since the light shifts are bigger than the Rabi frequencies by $1/\varepsilon^{1/2}$ for $\varepsilon \ll 1$. In addition, in both of the above schemes, employing the laser beams to differentially affect neighboring ions, one major drawback is that the positions and profiles of the laser beams must be accurately controlled.

Finally, we consider a method of addressing which utilizes rf micromotion. In a conventional Paul trap, generalized to the case of asymmetric electrodes ($\Phi \propto V_0 \cos(\Omega_T t) \times(\varepsilon x^2 + (1-\varepsilon)\, y^2 - z^2)$, $0 < \varepsilon < 1$) [43], the rf fields vanish only at a single point in space. When multiple ions are crystalized in such a trap, each ion experiences a different rf field, leading to different amounts of micromotion. In general, this effect causes each ion to have a unique Rabi frequency when a laser is applied, allowing the possibility of differen-

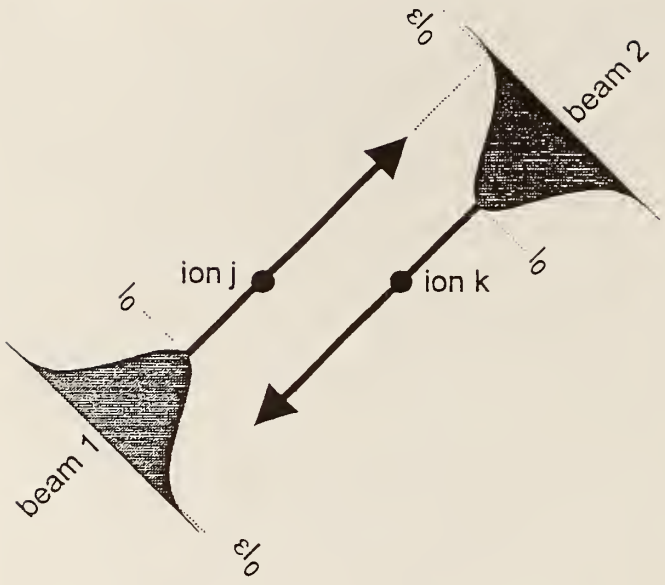


Fig. 5: Differential AC Stark shifting of neighboring ions. Equal intensity counter propagating beams 1 and 2 are centered on ions $j$ and $k$, respectively. A fraction $\varepsilon$ of the peak intensity $I_0$ of each beam is applied to the other ion. This results in a differential AC Stark shift of ions $j$ and $k$, allowing the possibility of individually accessing the ions by tuning the frequency of the laser beams.

tial addressing of the ions. If we assume that each ion sees the same intensity laser field, the Rabi frequency of ion $j$ is proportional to $J_0(\boldsymbol{k}\cdot\zeta_j)$ [11, 44], where $J_0(X)$ is the zeroth Bessel function of argument $X$, $\boldsymbol{k}$ is the effective laser wavevector, and $\zeta_j$ is the amplitude of micromotion associated with the $j$th ion. We assume that ion $j$ experiences a static electric field $E_{sj}$ (due to the Coulomb field of the other ions in addition to background static fields) which prevents the ion from occupying the trap center defined by the rf fields. For simplicity, we assume that $E_{sj} = E_{sj}\hat{x}$ is along the $x$ axis of the trap, which should be the case if the ions crystalize along the $x$-axis ($\varepsilon < 0.5$). To estimate $\zeta_j$, we solve the classical equations of motion in the trap for $U_0 = 0$ and find $= \zeta_j \cdot \hat{x} = \sqrt{2}\,qE_{sj}/m\omega_x\Omega_T$, where $\omega_x$ is the $x$-axis COM secular harmonic frequency. Thus, the Rabi frequency of the $j$th ion is

$$\Omega^j = \Omega_0^j J_0\left(\frac{\sqrt{2}\,k_x q E_j}{m\omega_x\Omega_T}\right), \tag{15}$$

where $\Omega_0^j$ is the Rabi frequency in absence of micromotion. (This reduction of the Rabi frequency due to ion motion is treated in section IV.B.1. under a different context.) Thus by controlling the electric field $E_j$ at the $j$th ion, some degree of differential addressing of the ions is possible. For example, for three ions held along the $x$-axis with the middle ion placed exactly at the rf null position, we find that the ratio of Rabi frequencies of the outer ions to the middle ion is $J_0(\beta)$, where $\beta = 1.52k_x(q^2\omega_x/4\pi\varepsilon_0 m)^{1/3}/\Omega_T$. An interesting case for individual addressing occurs when $\beta = 2.405$, in which case $J_0(\beta) = 0$, and the laser interaction with the outer two ions is effectively shut off. For three $^9Be^+$ ions held in a trap with a rf drive frequency of $\Omega_T \approx 240$ MHz, we find that the Rabi frequency of the outer two ions vanishes at a COM secular frequency of $\omega_x/2\pi \approx 6.1$ MHz. Here we assume that the Rabi frequency describes a stimulated Raman coupling between hyperfine ground states with $k_x = \sqrt{2}\,(2\pi/\lambda)$ and $\lambda \approx 313$ nm, relevant to recent experiments [10].

Many of the above individual addressing schemes are improved greatly when dealing with only two ions instead of a string of many. This leads us to seriously consider systems where quantum logic operations are performed on accumulators consisting of only two ions, with the other ions located somewhere else. For example, pairs of ions may be held in different regions of the same trap structure [11], or quantum information may be transferred from one register of ions to another by optical means [45].

### B. Multimode interference

Each additional ion in a quantum register adds three more motional modes. The simplest form of the Cirac/Zoller scheme ideally uses just a single mode as the bus. In this section, a few potential problems associated with the $3N-1$ spectator modes are considered. First, we must generalize the interaction with electromagnetic fields discussed in section II.B to consider motion in all $3N$ modes of motion for $N$ trapped ions. Here, as was assumed by CIRAC and ZOLLER [9], we consider that, on any given operation, the laser beam(s) interacts with only the $j$th ion; however, that ion will, in general, have components of motion from all modes. In this case Eq. (3) for the $j$th ion becomes

$$H_I^j = \hbar\Omega^j(S_+^j + S_-^j)\,[e^{i(\boldsymbol{k}\cdot\boldsymbol{x}_j-\omega t+\varphi_j)} + \text{h.c.}]\,. \tag{16}$$

We write the position operator of the $j$th ion (which represents the deviation from its equilibrium position) as

$$\boldsymbol{x}_j = u_j\hat{\boldsymbol{x}} + u_{N+j}\hat{\boldsymbol{y}} + u_{2N+j}\hat{\boldsymbol{z}}\,, \quad j\in\{1,2,,\ldots N\}\,, \tag{17}$$

where the $u_p$ are related to the $3N$ normal mode coordinates $q_k$ ($k\in\{1,2,\ldots 3N\}$ by the following relations [46]

$$u_p = \sum_{k=1}^{3L} D_k^p q_k\,, \qquad q_k = \sum_{p=1}^{3L} D_k^p u_p\,, \quad q_k \equiv q_{k0}(a_k\,e^{-i\omega_k t} + a_k^\dagger\,e^{i\omega_k t})\,. \tag{18}$$

In this expression, $q_k$ is the position operator and $a_k$ and $a_k^\dagger$ are the associated lowering and raising operators for for the $k$th normal mode, and the matrix $D_k^p$ is the transformation matrix between physical coordinates of the individual ions and normal coordinates of the string. Following the procedure of section II.C, we find

$$H_I^j = \hbar\Omega^j\left(S_+^j \exp\left[i\sum_{k=1}^{3L}\eta_k^j(a_k\,e^{-i\omega_k t} + a_k^\dagger\,e^{i\omega_k t}) - i(\delta t-\varphi_j)\right] + \text{h.c.}\right), \tag{19}$$

where we have kept the time dependence to allow consideration of all motional modes with different frequencies, and $\delta=\omega_L-\omega_0$ is the detuning of the applied radiation frequency (or difference frequency for the Raman coupling). The generalized Lamb-Dicke parameters are $\eta_k^j \equiv (\boldsymbol{k}\cdot\hat{\boldsymbol{x}}D_k^j + \boldsymbol{k}\cdot\hat{\boldsymbol{y}}D_k^{N+j} + \boldsymbol{k}\cdot\hat{\boldsymbol{z}}D_k^{2N+j})\,q_{k0}$, but for the linear trap case, motion will be separable in the $x$, $y$, and $z$ directions and $\eta_k^j$ will consist of one of these terms. We are typically interested in coupling the internal states of a given ion $j$ to a selected mode of collective motion $k$. In this case, the Rabi frequency coupling the states $|n_k\rangle\,|\downarrow\rangle_j$ to $|n_k'\rangle\,|\uparrow\rangle_j$ is

$$\Omega_{n_k',n_k}^j \equiv \Omega^j\,|\langle\{n_{p\neq k}\},\,n_k'|\prod_{l=1}^{3N} e^{i\eta_l^j(a_l+a_l^\dagger)}\,|\{n_{p\neq k}\},\,n_k\rangle|\,. \tag{20}$$

where $|\{n_{p\neq k}\}\rangle$ denotes the state of motion of the $3N-1$ spectator modes excluding mode $k$.

#### 1. Effects of motion in spectator modes on logic gates (Debye-Waller factors)

From the last equation, the Rabi frequency of a particular operation will in general depend on the motional state of the spectator modes. For instance, the conventional controlled-not gate employs two carrier pulses (steps (a) and (c) in Sec. III) which ideally do not depend

on the state of motion; this requires the Lamb-Dicke parameter $\eta$ to be small (see Eq. (10)). In the Raman configuration, $\eta$ is proportional to the difference in two wavevectors and can be made negligible by using co-propagating beams ($\delta k \approx 0$). On the other hand, with single-photon optical transitions, the Rabi frequencies depend on the motion of all modes which have a component of motion along the direction of $k$. We can take advantage of the motional dependence of the carrier to construct a logic gate, but in this case also, the Rabi frequency will depend on the motion in the other modes along the direction of $k$ or $\delta k$. Similarly, for sideband operations, such as steps (1) and (3) of the CN scheme discussed in Sec. III, it will, in general, be impossible to have $\Omega^j_{n',n}$ depend on only one mode of motion. In this section, we examine the influence of extraneous modes on the Rabi frequencies $\Omega^j_{n',n}$.

In a collection of $N$ ions, the motion in the $3N-1$ spectator modes reduces the Rabi frequency in much the same way as lattice vibrations affect a single emitter or scatterer embedded in a crystal, as described by the Debye-Waller effect [47]. Typically, the motional quantum numbers of the spectator modes in Eq. (20) will be thermally distributed (i.e., $P(n_p) \propto \gamma^{n_p}$ where $\gamma = \bar{n}_p/(1+\bar{n}_p)$ with $\bar{n}_p$ the mean number of phonons in mode p), so we can calculate the rms and mean values of the Rabi frequency given this distribution. For simplicity, we assume that all spectator modes are in the Lamb-Dicke regime ($\eta_p^j \bar{n}_p^{1/2} \ll 1$), but see Ref. [11] for the more general case. If the frequencies and amplitudes of all modes contributing to the axial motion of ion $j$ are assumed to be about the same, we can write $\eta_p^j \simeq \eta/N^{1/2}$ and $\bar{n}_p \simeq \bar{n}$ where $\eta$ and $\bar{n}$ are the Lamb-Dicke parameter and mean occupation for the axial motion of a single (thermalized) trapped ion. In this case, the fractional fluctuation in the Rabi frequency from run to run is

$$\frac{\Delta\Omega^{j,\,rms}_{n'_k,n_k}}{\bar{\Omega}^j_{n'_k,n_k}} \simeq \eta^2 \sqrt{\frac{\bar{n}(\bar{n}+1)}{N}} \,. \tag{21}$$

This expression indicates that a large number of ions is beneficial because it tends to average out the effects of motion in the $N-1$ spectator modes. Eq. (21) is an overestimate of the fluctuations since the spectator modes will have higher frequency than the COM mode, leading to smaller amplitudes of motion than assumed in this crude estimate. In any case, it is clearly desirable to cool all modes (whose motion is parallel to $\delta k$) to the zero-point state ($\bar{n}_p = 0$) to suppress the effects of these Debye-Waller factor fluctuations.

## 2. Mode cross-coupling from static electric field imperfections

If the $3N-1$ spectator modes of oscillation are not all laser-cooled to their zero-point energy, then energy can be transferred to the $k$th mode of interest. Even when the spectator modes are cooled to the zero-point state, they can act as a reservoir for energy from the COM mode. This does not lead to heating but can cause decoherence.

Ideally, the ions are subjected to quadratic potentials as in Sec. II.B. In practice, higher-order static potential terms are present; these terms can induce a coupling between the modes. Similar couplings are induced by the time varying fields necessary for providing entanglement; these are discussed below. We will assume that the higher order field gradients act as a perturbation to the (harmonic) normal mode solution. Following the convention in the above introduction to Sec. IV.B, these fields will be specified by $E_i$ for $i \in \{1, 2, \ldots 3N\}$ where the index $i$ specifies both the ion and direction of $E$. We write the electric field at the $j$th ion as

$$E_j = E_j\hat{x} + E_{N+j}\hat{y} + E_{2N+j}\hat{z}\,, \quad j \in \{1, 2, \ldots N\}\,. \tag{22}$$

From Eqs. (18) and (21), we can write the equation of the $k$th normal mode as [46]

$$\frac{\partial^2 q_k}{\partial t^2} + \omega_k^2 q_k = \frac{q}{m} \sum_{i=1}^{3N} D_k^i E_i \,. \tag{23}$$

In general, we can write

$$\begin{aligned} E_i &= E_i(\{u_p\}) = E_i(\{q_j\}) \\ &= E_i(\{q_j\} = 0) + \sum_{m=1}^{3N} q_m \left[\frac{\partial E_i}{\partial q_m}\right]_{\{q_j\}=0} + \frac{1}{2} \sum_{l=1}^{3L} \sum_{m=1}^{3N} q_l q_m \left[\frac{\partial^2 E_i}{\partial q_l \, \partial q_m}\right]_{\{q_j\}=0} + \cdots , \end{aligned} \tag{24}$$

where the derivatives are evaluated at the equilibrium positions. The first term on the right side of the last equation just gives rise to a shift of the equilibrium positions, and the second term can be absorbed into new definitions of the normal mode frequencies $\omega_i$. The second-order term (last term shown in this equation) can resonantly couple two modes of oscillation ($l$ and $m$) to the normal mode of interest $k$. We find a possible resonant term:

$$\frac{\partial^2 q_k}{\partial t^2} + \omega_k^2 q_k = \frac{q}{m} \sum_{i=1}^{3N} D_k^i q_l q_m \left[\frac{\partial^2 E_i}{\partial q_l \, \partial q_m}\right]_{\{q_j\}=0} , \tag{25}$$

where the $l$ and $m$ mode frequencies satisfy $|\omega_l \pm \omega_m| = \omega_k$. This type of coupling can either add to or extract energy from mode $k$, depending on the relative phases of motion in the three modes. By substituting the free solution to modes $l$ and $m$ ($q_j(t) = Q_k \exp(\pm i(\omega_j t + \varphi_j))$ into the second-order term, we find that if $q_k(t=0) = (dq_k/dt)_{t=0} = 0$, the driven solution to the amplitude of mode $k$ initially grows linearly with time:

$$|q_k(t)| = \left| \frac{qt}{2m\omega_k} \sum_{i=1}^{3N} D_k^i Q_l Q_m \left[\frac{\partial^2 E_i}{\partial q_l \, \partial q_m}\right]_{\{q_j\}=0} \right| . \tag{26}$$

We illustrate with an approximate numerical example which might have been expected to play a role in the motional heating that was observed in the NIST experiments [10, 17] (see section V.B below). In those experiments, performed on single $^9Be^+$ ions, the heating that was observed on the motion in the $x$ direction was such that the ion made a transition from the $n = 0$ to $n = 1$ level in about 1 ms. For a single ion, the three normal modes are just the oscillation modes along the $x$, $y$, and $z$ directions ($q_1 = x$, $q_2 = y$, $q_3 = z$; $D_k^i = \delta_k$). The mode frequencies were $(\omega_x, \omega_y, \omega_z)/2\pi \simeq (11.2,\ 18.2,\ 29.8)$ MHz, thus approximately satisfying the condition $\omega_x + \omega_y = \omega_z$. For sake of argument, we assume this resonance condition to be exactly satisfied. We consider heating of the $x$ motion assuming both the $y$ and $z$ modes are excited. From Eq. (26), we find $|x(t)| = |qtA_yA_z[\partial^2 E_x/\partial y\,\partial z]_{(y=z=0)}/(2m\omega_x)|$ where $A_y$ and $A_z$ are the amplitudes of motion in the $y$ and $z$ directions. Here, we neglect the fact that energy is exchanged between the three modes; for simplicity we assume the amplitudes of the $y$ and $z$ motion remain fixed. In this approximation, if $A_y = A_z = \xi$, the time it takes to excite the $x$ motion to the same amplitude is given by $t = |2m\omega_x/(q\xi[\partial^2 E_x/\partial y\,\partial z]_{(y=z=0)})|$. If $\xi = 10$ nm (corresponding to $\langle n_y \rangle \simeq \langle n_z \rangle \simeq 1$ for the conditions of the single $^9Be^+$ ion NIST experiments, the field gradient required to drive the $x$ motion to an amplitude of 10 nm ($\langle n_x \rangle \simeq 1$) in the

observed time of 1 ms is approximately $\partial^2 E_x/\partial y\,\partial z = 1000\ \mathrm{V/mm^3}$. It is highly unlikely the gradient was this large for the NIST experiments, and, furthermore, the resonance condition was only approximately satisfied. Moreover, this source of heating was easily tested by varying the initial values of $A_y$ and $A_z$ (by varying the Doppler-cooling minimum temperature through laser detuning) and studying the heating rate of the $x$ motion which had previously been cooled to the zero point of motion. No dependence on the initial values of $A_y$ and $A_z$ was found. In any case, if all modes of motion are initially cooled to the zero-point state this source of heating vanishes because the assumed coupling only provides an exchange of energy between modes. This places a premium on cooling all modes to as low an energy as possible. Finally, it appears that this single-ion example gives a worst case scenario since, for large numbers of ions, the force on the generalized coordinates (right hand side of Eq. (23)) requires a high-order field gradient to be nonzero. These gradients are highly suppressed in the typical case where ion-ion separation is much smaller than the distance between the ions and the trap electrodes.

## 3. Mode cross coupling induced by logic operations

In the preceding sections, we have assumed that when transitions are driven between $|n_k\rangle\,|\downarrow\rangle_j$ and $|n'_k\rangle\,|\uparrow\rangle_j$ involving a single mode of motion $k$, the other $3N-1$ spectator modes of motion are not affected because coupling to them is nonresonant. However, when the sum or difference frequency of two or more spectator modes is near the frequency of the desired mode-$k$ transition ($\omega_k\,|n'_k - n_k|$), higher order couplings can entangle the $|n_k\rangle\,|\downarrow\rangle_j$ and $|n'_k\rangle\,|\uparrow\rangle_j$ states with the spectator mode states.

Equation (19) describes the general interaction Hamiltonian between the internal levels of ion $j$ and all $3N$ modes of motion. By expanding the exponential in Eq. (19) to all orders, we find

$$H_I^j = \hbar\Omega'_j \left[ S_+^j \left( \prod_{l=1}^{3N} \sum_{b_l,\,d_l=0}^{\infty} \frac{(i\eta_l^j a_l^\dagger)^{b_l}\,(i\eta_l^j a_l)^{d_l}}{b_l!\,d_l!}\; e^{i(b_l-d_l)\,\omega_l t} \right) e^{i(\delta t-\varphi_j)} + \mathrm{h.c.} \right]; \qquad (27)$$

where $\Omega'_j = \Omega^j \exp\left[-\frac{1}{2}\,\Sigma_l(\eta_l^j)^2\right]$. This equation describes the processes of each mode $l$ gaining or losing $(b_l - d_l)$ vibrational quanta, accompanied by the raising or lowering of the internal electronic levels of ion $j$. We must account for all terms in Eq. (27) which do not vary rapidly in time, or terms in which the resonance condition is nearly met: $\Sigma_l(b_l - d_l)\,\omega_1 \simeq \delta = \omega_k(n'_k - n_k)$. Although detailed treatment of this problem is beyond our intent, a couple of comments may be made.

In general, we must account for all the terms in Eq. (27) which cause significant errors in the overall computation we are trying to carry out. For two or more trapped ions, some combination of modes will nearly always satisfy the resonance condition. However, this may occur only for high orders of $b_l$ and $d_l$, and if the Lamb-Dicke criterion is met, the contributions are vanishingly small. The terms that will cause problems are the ones that are close to satisfying the resonance condition and are relatively low order in $b_l$ and $d_l$. If the Lamb-Dicke criterion is satisfied, it will always be possible to avoid these spurious couplings, but it may be at the expense of making the Rabi frequency so small (in order to avoid coupling to relatively nearby off-resonant terms) that the operations will become too slow.

To understand this problem in the context of a simple example, we assume that a cross-mode coupling of this type occurs when two modes, $p$ and $q$, have frequencies which satisfy the condition $n_p\omega_p - n_q\omega_q \simeq 0$, $\omega_k$, or $-\omega_k$ corresponding to possible extraneous mode coupling on the carrier, first blue sideband, or first red sideband of the logic operations (assumed to utilize mode $k$). This additional resonance condition yields, to lowest

order in the Lamb-Dicke parameters, the effective Hamiltonian

$$H_I^j = \hbar\Omega_j' S_+^j \left\{ 1 + i\eta_k^j (a_k\, e^{-i\omega_k t} + a_k^\dagger\, e^{i\omega_k t}) + \frac{(i\eta_p a_p^\dagger)^{n_p}\,(i\eta_q a_q)^{n_q}}{n_p! n_q!}\, e^{i(n_p\omega_p - n_q\omega_q)t} \right\} e^{-i(\delta t - \varphi_j)} + \text{h.c.}\,, \tag{28}$$

where the resonance conditions are given by $\delta \equiv \omega_L - \omega_0 = 0$, $+\omega_k$, or $-\omega_k$. A specific example is relevant to the NIST single $^9Be^+$ ion experiments. Here, mode $k$ was the $x$ oscillation, and modes $p$ and $q$ are identified with the $z$ and $y$ oscillations of the single ion in the trap. In this experiment $\eta_x = \delta\boldsymbol{k}\cdot\hat{\boldsymbol{x}}x_0$, $\eta_y = \delta\boldsymbol{k}\cdot\hat{\boldsymbol{y}}y_0$, $\eta_z = \delta\boldsymbol{k}\cdot\hat{\boldsymbol{z}}z_0$, and $\omega_x \simeq \omega_z - \omega_y$. (The frequency relationship $\omega_x = \omega_z - \omega_y$ is a consequence of Maxwell's equations for a quadrupole rf trap in the absence of static potentials applied to the electrodes [43]) We assume that the desired transition is the first blue sideband of mode $x\,(\delta = \omega_x)$. In this case, the resonant part of Eq. (28) becomes

$$H_I^j = \hbar\Omega_j'[S_+^j\{i\eta_x a_x^\dagger - \eta_z\eta_y a_z^\dagger a_y + O(\eta^3)\} + \text{h.c.}]\,. \tag{29}$$

The term proportional to $a_x^\dagger$ is the desired anti-Jaynes-Cummings operator, and the term proportional to $a_z^\dagger a_y$ can entangle the internal state with the other spectator modes ($z$ and $y$), leading to errors.

For logic operations on a string of ions in a linear trap, we will assume that all other mode frequencies are higher. With the use of stimulated-Raman transitions, we can make $\delta\boldsymbol{k} \parallel \hat{\boldsymbol{z}}$ and restrict our attention to spectator modes along the $z$ axis. Nevertheless, as $N$ becomes large, nearby resonances of the type shown in Eq. (28) will become harder to avoid. These coupling terms always scale as products of Lamb-Dicke parameters. Thus if the spectator mode Lamb-Dicke parameters are small enough, or if at least one Lamb-Dicke parameter is approximately zero, the higher order unwanted resonances may be sufficiently suppressed. Furthermore, if the spectator modes are cooled to near the zero-point energy ($\langle n\rangle \ll 1$), then any couplings in Eq. (28) with powers of the annihilation operator $a_q$ will be absent most of the time. Hence, in large registers, it will probably be important to cool all modes to near the zero-point energy.

## V. Decoherence

### A. Internal state decoherence from spontaneous emission

The internal atomic states of trapped ions, which store quantum bits of information, must be protected from spontaneous emission, at least for the duration of the computation. This excludes the possibility of "error correction," [48] which can tolerate a certain level of errors due to spontaneous emission. For qubit levels coupled by single photon optical transitions, this may be accomplished by employing long-lived energy levels which do not have an allowed electric dipole coupling, such as metastable electronic levels with a quadrupole or intercombination coupling to the ground state. Although the interaction of these states with the vacuum (causing spontaneous emission) is reduced, their interaction with an external field for use in quantum logic operations is also reduced. This results in a fundamental limit on the accuracy of each operation by roughly the ratio of the spontaneous emission rate to the Rabi frequency $\xi = \Gamma/\Omega$. In the case of optical transitions, $\Omega$ cannot be increased indefinitely, since at optical intensities beyond about $10^{14}$ W/cm$^2$, the atom is quickly photoionized. This amounts to inaccuracies due to spontaneous emission on the order of $\xi = 10^{-6} - 10^{-7}$ [49]. Even this limit may be too optimistic, as the two-level

approximation breaks down before photoionization occurs, and the coupling to other electronic levels must also be considered [49]. This results in inaccuracies due to spontaneous emission on the order of $\xi = 10^{-5} - 10^{-6}$, depending on the particular ion used.

In the case of two-photon stimulated-Raman transitions between stable electronic ground states, the ratio of spontaneous emission rate to Rabi frequency is approximately $\xi_{SR} = \gamma_{se}/(g^2/\Delta)$, where $\gamma_{se} \approx \Gamma g^2/\Delta^2$ is the off-resonant spontaneous emission rate, $g$ is the resonant single-photon Rabi frequency of each laser beam, and $\Delta$ is the detuning of the Raman beams from the excited state. This results in an inaccuracy $\Gamma/\Delta$ due to spontaneous emission, which is independent of optical intensity. Since Raman transitions between $S$ electronic ground states are effective only when the detuning $\Delta$ is not much greater than the fine structure splitting of the atom [50]; this results in an inaccuracy $\xi_{SR}$ due to spontaneous emission in range from about $10^{-4}$ ($^9Be^+$) to $10^{-7}$ ($^{199}Hg^+$), depending on the particular ion used. Spontaneous emission from spectator electronic levels should not significantly affect this limit, provided that their splitting from the virtual excited state significantly exceeds $\Delta$ and that the single photon resonant Rabi frequencies coupling the ground states to the spectator levels are not much bigger than $g$ [49]. These appear to be reasonable assumptions for most candidate ions.

The decohering effects of spontaneous emission can be overcome by error correction schemes. Error correction is complicated by the fact that when spontaneous emission occurs, the atoms may decay to states outside the original set of computational basis states. However, this situation can, in principle, be detected by optically pumping the ions back to the computational basis and applying the error correction schemes [49, 51].

Spontaneous emission decoherence could, in principle, be nearly eliminated by driving single-photon transitions between ground-state-hyperfine or Zeeman levels with rf or microwave radiation since spontaneous emission from these levels is negligible. This may be accomplished by coupling the internal and motional states with inhomogeneous magnetic fields [52]. The speed of sideband operations is limited by the size of the field inhomogeneity one can obtain. For example, consider an ion moving along the $z$-axis with a magnetic field gradient $\partial B_x/\partial z$ applied on top of a uniform magnetic field $B_z$ along the direction of motion. In the ion's reference frame, there is an rf magnetic field which can induce transitions between the internal states. The interaction Hamiltonian is then

$$\mathcal{H} = -\boldsymbol{\mu} \cdot \boldsymbol{B} = -\mu B_z S_z - \frac{\mu(\partial B_x/\partial z)\, z_0}{4} (S_+ + S_-)(a^\dagger + a), \tag{30}$$

where $\mu \approx \mu_B$ is the magnitude of the ion magnetic moment, typically near one Bohr magneton, $z_0$ is the spatial spread of the zero-point ion wavepacket, $S_\pm$ are the spin raising and lowering operators from Sec. II.C and $a$ and $a^\dagger$ are the usual motional raising and lowering operators. The coupling (last term in Eq. (30)) is analogous to Eq. (3), allowing the construction of logic gates as described above. Unfortunately, this method requires very high magnetic field gradients $\partial B_x/\partial z$. For instance, in order to realize an effective Rabi frequency of 0.1 MHz ($\Omega_{\text{eff}} \approx \mu_B(\partial B_x/\partial z)\, z_0/4$), a magnetic field gradient of around 10 T/cm would be necessary, where we have assumed that the motional frequency is 1 MHz. Although these gradients aren't unreasonable in the laboratory, the residual fields that accompany the gradient will dramatically shift the internal electronic levels of the trapped ions. Moreover, it would be difficult to address selected ions because of the long wavelength of the radiation relative to typical ion spacings.

### B. Motional decoherence

Although the internal states of ions may be well isolated from environmental influences, the motional states of a collection of trapped ions are expected to be more susceptible to deco-

herence. The Cirac/Zoller scheme for quantum logic [9] transfers quantum information transiently through the motional states, so any decoherence of the motion will compromise operation of any multi bit quantum gate and must be minimized. In the NIST experiments with a single ion, the motional state of all three modes was observed to absorb energy from the environment at the rate of about 1 phonon (energy $\hbar\omega_z$, where $\omega_z/2\pi \approx 10$ MHz) per millisecond from the ground state [10, 17]. Although this as of yet unexplained heating rate is not believed to be fundamental, it is of considerable interest to characterize the possible sources. There are several potential mechanisms for motional decoherence; for instance "rf heating" from rf fields in the trap [53], collisions with background atoms, fluctuating patch and contact potentials on the trap electrodes, electron field emission from the electrodes, and Ohmic loss of induced image currents in the trap electrodes [54, 55]. These and other effects, considered in Ref. [11], are not expected to be major obstacles to motional coherence in a linear ion trap.

By virtue of the electric charge of trapped ions, it is natural to consider the coupling of spurious electric fields to the motion of the ion string. In this section we relate the size of electric field noise to the expected transition rate from the quantum ground state of motion in the ion trap. Such noisy electric fields might be generated from unstable trap parameters, external radiation, thermal (Johnson) noise from resistive losses in the trap electrodes, or patch potentials from nearby surfaces.

We first consider the axial COM harmonic motion of a string of $N$ ions at frequency $\omega_z$. An external uniform electric field will shift the position of the trap center; an external electric field gradient will change the effective spring constant of the trap. Following the approach of SAVARD, O'HARA and THOMAS [56], who considered heating mechanisms in the context of neutral atom dipole traps, we can similarly calculate the rate $\Gamma_0$ at which the ground state of ion motion is vacated due to noisy electric fields. We find

$$\Gamma_0^{\text{axial}} = \frac{Nq^2}{4m\hbar\omega_z}\left[S_E(\omega_z) + \frac{\hbar}{4Nm\omega_z} S_{E'}(2\omega_z)\right], \tag{31}$$

where $S_E(\omega)$ is the electric field noise spectral density in $(\text{V/cm})^2/\text{Hz}$ and $S_{E'}(\omega)$ is the electric field gradient noise spectral density in $(\text{V/cm}^2)^2/\text{Hz}$. The noise densities are defined so that the mean-squared electric field and field gradient are $(2\pi)^{-1}\int_0^\infty d\omega\, S_E(\omega)$ and $(2\pi)^{-1}\int_0^\infty d\omega\, S_{E'}(\omega)$, respectively [56].

Note that contributions of electric field noise to motional heating is concentrated near resonance ($\omega_z$) in Eq. (31), as expected for a resonantly driven harmonic oscillator. Contributions of electric field gradient noise to heating is concentrated near twice the resonant frequency ($2\omega_z$), as expected for a parametrically driven harmonic oscillator. For modes of motion with secular frequency $\omega_x$ derived from ponderomotive rf forces (i.e., the radial modes of a linear trap), there are additional contributions to heating from noisy fields at frequencies $\Omega_T \pm \omega_x$ and gradients at frequencies $\Omega_T \pm 2\omega_x$, to lowest order in the pseudopotential approximation $[(\omega_x/\Omega_T) \ll 1]$ [21]. We find

$$\Gamma_0^{\text{radial}} = \frac{Nq^2}{4m\hbar\omega_x}\left[S_E(\omega_x) + \frac{\omega_x^2}{2\Omega_T^2} S_E(\Omega_T \pm \omega_x) + \frac{\hbar}{4Nm\omega_x}\left(S_{E'}(2\omega_x) + \frac{2\omega_x^2}{\Omega_T^2} S_{E'}(\Omega_T \pm 2\omega_x)\right)\right]. \tag{32}$$

Given a source of electric field noise $S_E(\omega)^{1/2}$, we may expect the corresponding gradient noise spectrum $S_{E'}(\omega)^{1/2}$ to be no larger than $S_E(\omega)^{1/2}/d$, where $d$ is the characteristic ion trap electrode size. From the above equations, we find that this implies that the heating rate from gradient noise is expected to be a factor of $\approx (z_0/2d)^2$ smaller than the heating

rate from electric field noise, where we recall that $z_0 = (\hbar/2Nm\omega_z)^{1/2}$ is the size of the ground state wavepacket of the mode of interest. This ratio is typically very small in ion traps (in the NIST $^9Be^+$ experiments, $z_0 \approx 7$ nm, $d \approx 250\,\mu$m, and $(z_0/2d)^2 \approx 2 \times 10^{-10}$). Noise in the electric field gradient is therefore expected to be much less of a concern than noise in the electric field, unless the electric potentials on the trap electrodes possess an unusually high degree of symmetry. It also follows that the COM modes should be most susceptible to heating, as the non-COM modes do not respond to uniform electric fields. For instance, in the case of two ions confined along the $z$ axis, the COM mode along $z$ is sensitive to resonant uniform electric fields. The "stretch" mode along $z$ (where the two ions' motions are out of phase) on the other hand, is only sensitive to resonant electric field gradients. Therefore, if quantum logic operations are limited by motional heating due to uniform electric fields, higher-order (non-COM) motional modes should be used for quantum logic. COM heating will still indirectly affect the fidelity of operations on other modes, but this effect should be of higher order, as discussed in section IV.B.1.

We examine two expected sources of electric field noise, and estimate their effects on the heating rate of COM modes. These results are compared to the NIST experiment on a single $^9Be^+$ ion [17], where we observed a heating rate $\Gamma_0 \approx 10^3$/sec, corresponding to an electric field noise of $S_E(\omega_x)^{1/2} \approx 4 \cdot 10^{-8}$ V/cm/Hz$^{1/2}$ or electric field gradient noise of $S_{E'}(2\omega_x)^{1/2} \approx 0.07$ V/cm$^2$/Hz$^{1/2}$.

### 1. Thermal or blackbody noise

Thermal fluctuations from lossy elements of the trap electrode structure may lead to electric field noise at the ions. This is essentially the effect of blackbody radiation on the ion motion, altered by the "cavity" formed from the trap electrodes [11, 54, 57]. Lossy or resistive elements of the trap electrodes will only give rise to a noisy electric field only if the effective resistive current path is asymmetrically oriented with respect to the ions; otherwise only neglegible field gradients will contribute, as discussed above. The voltage noise spectral density from a resistor $R$ at temperature $T$ is $4kTR$. For an electrode structure of characteristic size $d$, we thus expect an electric field noise density of $S_E(\omega) \approx 4kTR(\omega)/d^2$, where $R(\omega)$ describes the resistance seen by the ion from the surrounding electrode structure, or, equivalently, the resistance through which currents induced by ion motion flow. Neglecting the gradient terms in Eqs. (31) and (32), this results in axial and radial mode heating rates of [7, 11]

$$\Gamma_0^{\text{axial}} \approx \frac{Nq^2kTR(\omega_z)}{md^2\hbar\omega_z} \tag{33}$$

and

$$\Gamma_0^{\text{radial}} = \frac{Nq^2kT}{m\hbar\omega_x d^2}\left(R(\omega_x) + \frac{\omega_x^2}{2\Omega_T^2}\,R(\Omega_T \pm \omega_x)\right). \tag{34}$$

We now use this last equation to estimate the heating rate which might have been expected in the NIST single ion $^9Be^+$ experiments [17], where all modes were confined from ponderomotive forces. We consider two current paths in the electrode structure which would likely have provided the largest resistances. The first is a direct path between the endcap electrodes, which were positioned around the ring electrode [11, 43]. Since this path length is only about $l \approx 0.5$ cm and much smaller than the wavelengths associated with the frequencies of interest $\omega_x/2\pi \approx 10$ MHz and $(\Omega_T \pm \omega_x)/2\pi \approx 230$ MHz, we can

treat this path as a lumped resistor with resistance $R(\omega) \approx \varrho l/A(\omega)$. Here, $\varrho$ is the resistivity of the electrode material and $A(\omega)$ is the effective cross-sectional area of the resistive path, proportional to the skin depth at frequency $\omega$. We conservatively estimate $R(\omega_x) \approx 0.04\ \Omega$ and $R(\Omega_T \pm \omega_x) \approx 0.20\ \Omega$ in the experiment [11, 43] and calculate a heating rate of $\Gamma_0 \approx 0.7/\text{s}$, dominated by the first term of Eq. (34) and much smaller than observed.

The rf and static electrodes in an rf trap are typically joined through an rf step-up transformer. This leads us to consider a resistive path from the rf to the static electrode, as the resistance between these electrodes can be high at frequencies near the resonant rf drive frequency $\Omega_T$. In a linear trap, these fields should not have a component along the axial modes of motion; moreover, these fields will vanish at trap center and only provide a gradient, unless there is an extreme asymmetry in the electrode structure. We thus consider noise fields resulting from a geometrical asymmetry $\beta$ between the ring and endcap electrodes ($0 \leq \beta \leq 1$, where $\beta$ is proportional to the electric field at the ion if a potential is applied between the ring and endcaps; $\beta = 0$ for perfect symmetry). In the NIST $^9Be^+$ experiments [10, 17], a quarter-wave transmision line acts as the step-up transformer [43], thus the impedance between the rf and static trap electrodes as a function of frequency $\omega$ is

$$Z_{\text{trap}}(\omega) = Z_0 \tanh\left[\frac{\pi}{4Q}\sqrt{\frac{\omega}{\Omega_T}} + i\frac{\pi}{2\Omega_T}\right], \tag{35}$$

where $Z_0$ is the characteristic line impedance, and $Q$ is the loaded quality factor of the transmission line of length $\pi c/2\Omega_T$ at resonance ($\omega = \Omega_T$). The resistance is the real part of Eq. (35), and at the frequencies of interest which might couple to the ion motion, $\omega_x$ and $\Omega_T \pm \omega_x$, we have $R(\omega_x) \approx (\pi Z_0/4Q)(\omega_x/\Omega_T)^{1/2} \approx 0.03\ \Omega$ and $R(\Omega_T \pm \omega_x) \approx (Z_0/\pi Q)(\Omega_T/\omega_x)^2 \approx 34\ \Omega$. In these expressions, $Z_0 \approx 100\ \Omega$ and $Q \approx 500$ are the characteristic impedance and quality factor of the transformer, and $\omega_x/2\pi$ and $\Omega_T/2\pi$ are taken to be 10 MHz and 230 MHz respectively [43]. Note the estimated resistance $R(\omega_x)$ is nearly equivalent to the value in the skin-depth model above, since this path length is still only a small fraction of the wavelength associated with $\omega_x$. We find that the two terms in Eq. (34) contribute roughly equal amounts to a total heating rate of approximately $\Gamma_0 \approx 0.8\beta^2/\text{s}$. Again, this rate is much smaller than the observed rate, even for large asymmetries.

### 2. Noise on trap voltages

Fluctuations in the trap voltages ($U_0$ and $V_0$ in Eq. (1)) will nominally only give rise to a noisy field gradient. However, in some cases, asymmetric fluctuations in trap parameters can give rise to a noisy electric field. For instance, noise on the static potentials of the end segments of a linear trap (Fig. 2) may not be common mode if the potentials are provided from uncorrelated power supplies, or if the leads connecting to the end segments experience different amounts of noise from pickup. In these cases, we can relate the electric field noise density to a differential potential noise density defined by $S_{\delta U_0}(\omega) = d^2 S_E(\omega)$, where $\delta U_0$ is the difference in potentials between the rod end segments. From Eq. (31), this would give rise to a heating rate of

$$\Gamma_0 = \frac{Nq^2}{4m\hbar\omega_z d^2} S_{\delta U_0}(\omega_z). \tag{36}$$

For example, a typical power supply might have rms noise of 0.1 mV uniformly distributed across a 20 MHz bandwidth. If the supply is filtered so that signal amplitude at frequency

$\omega_x$ is attenuated by a factor $F < 1$, we find $[S_{\delta U_0}(2\omega_z)]^{1/2} \approx 20F$ (nV/Hz$^{1/2}$), leading to a heating rate of the axial COM mode of $\Gamma_0 \approx 4 \cdot 10^6 N \cdot F^2/\mathrm{s}$. Here we have assumed trap parameters $\omega_z/2\pi \approx 1$ MHz and $d \approx 0.025$ cm.

If there exist asymmetric static patch or contact potentials on the electrodes, this could lead to a static electric field $\boldsymbol{E}_{\mathrm{static}}$ which would push the ions away from at the geometrical trap center defined by $x = y = z = 0$ in Eq. (1). In this case, fluctuations in the potentials $U_0$ and $V_0$ will be converted into a noisy electric field at the ions. If $\boldsymbol{E}_{\mathrm{static}}$ is in the axial direction, then a noise density of the static voltage $S_{U_0}(\omega)$ would be equivalent to a field noise density of $S_E(\omega) = (E_{\mathrm{static}}/\langle U_0\rangle)^2 S_{U_0}(\omega)$. If we assume $E_{\mathrm{static}} \approx \varphi/d$, where $\varphi$ is an effective axial potential difference across the electrodes (due to patch potentials for instance), then we find from Eq. (31)

$$\Gamma_0 = \frac{Nq^2}{4m\hbar\omega_z d^2} \left(\frac{\varphi}{\langle U_0\rangle}\right)^2 S_{U_0}(\omega_z)\,. \tag{37}$$

Similar to above, this leads to a heating rate of $\Gamma_0 \approx 4 \cdot 10^6 N \cdot F^2(\varphi/\langle U_0\rangle)^2/\mathrm{s}$ assuming the above values of the trap parameters. Controlling these potentially troublesome heating rates clearly points to the importance of heavily filtering the static electrodes at frequency $\omega_z$. The filtering is best accomplished as close as possible to the trap electrodes, and for reasonable filter factors of $F < 10^{-4}$, these heating sources should be negligible.

For fluctuations in the rf potential $V_0$, we can derive a similar heating rate of motional modes confined by ponderomotive rf forces, which would be relevant to the NIST experiments. For simplicity, we consider the COM radial mode at frequency $\omega_x$ and assume the confinement is dominated by the ponderomotive force ($\omega_p$ term in Eq. (2)). We consider the case of a patch field $E_{\mathrm{static}} = \varphi/R$. The equivalent electric field noise density is then $S_E(\omega) = (2E_{\mathrm{static}}/\langle V_0\rangle)^2 S_{V_0}(\omega)$, which from Eq. (32) results in a heating rate

$$\Gamma_0^{\mathrm{radial}} = \frac{Nq^2}{4m\hbar\omega_x R^2} \left(\frac{2\varphi}{\langle V_0\rangle}\right)^2 \left(S_{V_0}(\omega_x) + \frac{\omega_x^2}{2\Omega_T^2} S_{V_0}(\Omega_T \pm \omega_x)\right), \tag{38}$$

where $S_{V_0}(\omega)$ refers to the rf potential noise density at the trap rf electrode. To estimate the effect of rf amplitude noise at the input, we again assume that the rf input lead is connected to a step-up transformer. For a transformer of characteristic impedance $Z_0$ and quality factor $Q \gg \Omega_T/2\omega_x \gg 1$, input signals of frequency $\omega_x$ are essentially filtered out, and signals at $\Omega_T \pm \omega_x$ are multiplied by the factor $[Z_0/(2\pi R_s Q)]^{1/2}\, \Omega_T/\omega_x$, where $R_s$ is the source impedance. We thus neglect the first term of Eq. (38) and replace $S_{V_0}(\Omega_T \pm \omega_x)$ by $[Z_0/(2\pi R_s Q)]\,(\Omega_T/\omega_x)^2\, S_{V_0,\,\mathrm{input}}(\Omega_T \pm \omega_x)$ in the second term. If the rf source feeding the input has an effective noise figure of $NF \approx 10$ dB above the Johnson noise of a $R_s = 50\ \Omega$ source impedance, we have $S_{V_0,\,\mathrm{input}} \approx 10(4kTR_s) \approx 10^{-17}\ \mathrm{V}^2/\mathrm{Hz}$. Assuming $\omega_x/2\pi \approx 10$ MHz, we find $\langle V_0\rangle \approx 750$ V and a heating rate of $\Gamma_0 \approx 10(\varphi/\langle V_0\rangle)^2/\mathrm{s}$. Since $\varphi \ll \langle V_0\rangle$ for typical patch potentials of $< 1$ V, this source of heating is again much smaller than observed. Moreover, in the NIST experiments, $\varphi$ was varied over a wide range without an observed dependence on heating rate.

Although we have tried to characterize the more obvious sources of electric field noise, the actual electric field noise spectral density in an ion trap may have a complicated structure and may be difficult to characterize. The motional modes of a string of ions are most susceptible to electric field noise near the motional frequency of interest, as expected. If spurious resonances should occur at these frequencies due to background electric fields, it might be possible to avoid them by simply changing the trap param-

eters. As stated above, heavy filtering of the electrodes should provide adequate noise suppression at these frequencies and the COM motion of ions trapped in electrode structures with a high degree of symmetry will be less susceptible to electric field noise.

### C. Induced decoherence from applied field amplitude noise

In the ion trap quantum computer, all operations can be traced back to Eq. (5), the coupling of states $|n\rangle|\downarrow\rangle$ to $|n'\rangle|\uparrow\rangle$. The fidelity of these operations will depend, in part, on how accurately the coupling strength $\Omega^j$ and the application time can be set. For instance, in the rotation gate of Eq. (7), the rotation angle $\theta = 2\Omega^j t$, and noise in these parameters will lead to evolution to an undesired quantum state. The effects of (Gaussian) noise on laser intensity have been treated by SCHNEIDER and MILBURN [58]. These effects show up in a well-characterized way for transitions involving Fock states. Here we briefly investigate the size of laser power fluctuations, as the Rabi frequency is proportional to the laser power in the Raman configuration. We do not examine how such errors might propagate in an extended gate structure [9, 11, 59].

Fluctuations in the laser intensity at the site of a given ion can arise from both fluctuations in the relative position of the beam with respect to the ion and fluctuations in laser power. Laser/ion position stability is particularly important since the Cirac/Zoller scheme of quantum logic assumes that ions in an array be selectively addressed, thereby requiring a high degree of control of the laser beam spatial profile (Sec. IV.A). Of course, the simplest method for minimizing position fluctuations is to employ mechanically stiff mounts for the optics and ion trap electrodes, and have the laser source as close as possible to the ions. A quadrant detector indexed to the trap electrodes and placed near the ion may also be used to actively stabilize the beam position by feeding back to a galvanometer or acousto-optic modulator. If optical fibers are used to deliver laser beams to the ions, position fluctuations between the fiber and the ions could be made small; however, we must also consider position fluctuations between the laser source and the input to the fiber. If the position tolerances can be adequately controlled, the dominant source of intensity noise at the ion would likely be given by fluctuations in optical power and laser mode. Here, we estimate limits on laser amplitude noise.

If we assume the laser fields responsible for quantum logic operations are coherent states, the fundamental noise floor is photon shot noise. For a laser beam of average power $P_0$ the fractional level of shot noise is

$$\frac{\delta P}{P_0} = \sqrt{\frac{\hbar\omega}{P_0\tau_{\text{op}}}}. \tag{39}$$

where $\omega$ is the (optical) photon frequency, $\tau_{\text{op}}$ is the time the radiation is applied, and, for simplicity, we assume square pulse envelopes. Almost all laser sources have significant amplitude noise well above the shot-noise limit in the 10 Hz—10 kHz range due to acoustic vibrations which, for example, affect the laser cavity resonators. Much of this noise can be removed by active power stabilization, where a beamsplitter directs a portion of the laser power to a photodetector, and an error signal is derived and fed back to an upstream modulator or, in the case of a diode laser, directly to the amplitude of the laser source [60]. The limiting noise of this stabilization scheme is degraded slightly by the imperfect quantum efficiency of the photodetector as well as the beamsplitter. If the beamsplitter directs a fraction, of the input optical power to the stabilizer (which then gives an optical power

$P_u \simeq (1-\varepsilon) P_0$ directed to the ion), and the quantum efficiency of the photo detector is $\eta_{\text{det}}$, the limit of fractional power noise in the logic pulse is (assuming no added electronic noise in the feedback loop)

$$\frac{\delta P_u}{P_u} \geq \sqrt{\frac{\hbar\omega}{P_u \tau_{\text{op}} \eta_{\text{det}} \varepsilon (1-\varepsilon)}} \,. \tag{40}$$

For a laser wavelength of 313 nm, and assuming, $\varepsilon = 0.5$, and $\eta_{\text{det}} = 0.5$, we have $\delta P_u / P_u \geq 2.3 \cdot 10^{-9} (P_\mu \tau_{\text{op}})^{-1/2}$. For 1 W of usable laser power and $\tau_{\text{op}} = 1\,\mu\text{s}$, this corresponds to a fractional power fluctuation of $\geq 2.3 \cdot 10^{-6}$.

This estimate applies only to the laser power fluctuations at the beamsplitter and assumes no additional noise is introduced between the beamsplitter and the photo detector or the beam splitter and the ions. Typically, the usable part of the laser beam must be directed further through optics, the air, and a window to the vacuum envelope enclosing the ion trap. Fluctuating etalon effects in the optics and air currents may therefore seriously increase the power fluctuations beyond Eq. (39).

Fluctuations in timing errors may also be important. Clearly, fractional fluctuations in the duration of laser pulses will correspond directly to the same fractional fluctuations in the desired value of the gate parameters (e.g., rotation angles in Eq. (7)). If we require fractional fluctuations of $10^{-6}$ on these parameters, then we require timing precision of 1 ps on a 1 s pulse. Similar considerations apply to the stability of pulse envelope shapes.

For both amplitude and timing fluctuations, it may be possible to sample a portion of the beam used for logic and apply it to a "check bit" ion. The response of this ion could then be used to monitor and control the amplitude and timing of the pulses.

## VI. Conclusion

A system of trapped and cooled atomic ions is one of the few viable experimental candidates for quantum computation. Internal levels of the ions can coherently store quantum bits for extremely long times. Preserving coherence during logic gates will clearly be more difficult, because (1) the quantum bits are distributed through a collective motional degree of freedom in the trap which more readily couples to the environment, and (2) technical noise on the logic gates degrades gate operation. Nevertheless, to our knowledge, these difficulties appear to be technical, not fundamental. The maximum number of gates which can be applied coherently, and the maximum number of ions which can be packed into a trap, will undoubtedly be determined by technical limits. Although it appears that the quantum factoring algorithm would be extremely difficult to implement, we conclude that an ion trap quantum computer of very modest numbers of bits and gates looks quite promising.

In this paper, we have attemped to identify some of the more important experimental concerns with the ion trap system, and expect that their resolution will likely be determined in the laboratory. We summarize with a few general observations regarding the ion trap quantum computer.

(1) The most attractive coupling scheme appears to involve two-photon stimulated Raman transitions between hyperfine (or Zeeman) ground states separated by rf or microwave frequencies. This not only relaxes the laser frequency stability requirements when compared to single-photon optical transitions, but also allows more geometrical control of the effective wavevector $\delta k = k_1 - k_2$, which determines the coupling to particular motional modes.

(2) Laser cooling of all modes having a component of motion along $\delta k$ to their ground state energy will minimize cross coupling between the modes.

(3) The axial COM motional mode may not be the best choice for a "data bus" which couples the quantum bits between ions. First, although the COM mode is most resolved from the other modes, it has the lowest motional frequency, which may ultimately set a limit on the quantum gate speed. Second, the non-COM motional modes should be less sensitive to heating from external electric fields.

(4) For a given number of ions, the optimum value of the mode frequencies will likely involve a key tradeoff. Larger frequencies might minimize the effect of some sources of motional decoherence, as the motional energy levels would be further separated. This would also allow gate operations (and laser cooling) to proceed faster, as the Rabi frequency can be no larger than the mode frequency. On the other hand, smaller frequencies will increase the spatial separation of the ions, thus easing the problem of optical addressing of individual ions in a string.

(5) Internal state decoherence will likely be small, and it does not appear that motional decoherence will be a fundamental problem, notwithstanding the heating problem observed in the NIST experiments. It is important to heavily filter the ion trap static electrodes at $\omega_z$ to minimize environmental influences on the ion string COM motion.

## Acknowledgements

We gratefully acknowledge the support of the U.S. National Security Agency, Army Research Office, and Office of Naval Research. We acknowledge useful discussions with P. Bardroff, R. Blatt, I. Cirac, T. Darling, L. Davidovich, A. Despain, D. DiVincenzo, A. Ekert, B. Esry, N. Gisin, S. Haroche, M. Holland, M. Holzscheiter, R. Hughes, D. James, J. Kimble, P. Knight, S. Lloyd, G. Milburn, J. Preskill, W. Schleich, A. Steane, W. Vogel, P. Zoller, and W. Zurek.

## References

[1] D. P. DIVINCENZO, *Science* **270**, 255 (1995); S. LLOYD, *Scientific American* **273**, 140 (October 1995).
[2] A. EKERT and R. JOZSA, 1996, Rev. Mod. Phys. **68**, 733.
[3] D. DEUTSCH, Proc. R. Soc. London A **425**, 73 (1989); D. DEUTSCH and R. JOZSA, Proc. R. Soc. London A **439**, 554 (1992).
[4] P. SHOR, 1994, Proc. 35th Ann. Symp. Found. Comp. Sci. (IEEE Computer Society Press, New York), p. 124.
[5] S. LLOYD, *Science* **261**, 1569 (1993); **273**, 1073 (1996); L. K. GROVER, Phys. Rev. Lett. **79**, 325 (1997).
[6] *Quantum Theory and Measurement*, J. A. Wheeler and W. H. Zurek, Eds. (Princeton Univ. Press, Princeton, NJ, 1983).
[7] D. J. WINELAND, J. J. BOLLINGER, W. M. ITANO, and D. J. HEINZEN, Phys. Rev. A **50**, 67 (1994).
[8] J. J. BOLLINGER, D. J. WINELAND, W. M. ITANO, and D. J. HEINZEN, Phys. Rev. A **54**, R4649 (1996).
[9] J. I. CIRAC and P. ZOLLER, Phys. Rev. Lett. **74**, 4091 (1995).
[10] C. MONROE, D. MEEKHOF, B. KING, W. ITANO, and D. WINELAND, *Phys. Rev. Lett.* **75**, 4714 (1995).
[11] D. J. WINELAND, C. MONROE, W. M. ITANO, D. LEIBFRIED, B. E. KING, and D. M. MEEKHOF, quant-ph/9710025.
[12] A. STEANE, Appl. Phys. B **64**, 623 (1997).
[13] D. F. JAMES, Appl. Phys. B (in press), quant-ph/9702053.
[14] P. DOMOKOS, J. M. RAIMOND, M. BRUNE, and S. HAROCHE, Phys. Rev. A **52**, 3554 (1995); Q. A. TURCHETTE, C. J. HOOD, W. LANGE, H. MABUCHI, and H. J. KIMBLE, Phys. Rev. Lett. **75**, 4710 (1995); P. R. BERMAN, Ed., *Cavity Quantum Electrodynamics*, (Academic, Boston, MA, 1994).

[15] N. A. Gershenfeld and I. L. Chuang, Science **275**, 350 (1997); D. G. Cory, A. F. Fahmy, and T. F. Havel, Proc. Nat. Acad. Sci. USA **94**, 1634 (1997).
[16] J. J. Bollinger, D. J. Heinzen, W. M. Itano, S. L. Gilbert, and D. J. Wineland, IEEE *Trans. on Instrum. and Measurement* **40**, 126 (1991).
[17] C. Monroe, D. M. Meekhof, B. E. King, S. R. Jefferts, W. M. Itano, D. J. Wineland, and P. Gould, *Phys. Rev. Lett.* **75**, 4011 (1995).
[18] W. Nagourney, J. Sandberg, and H.G. Dehmelt, Phys. Rev. Lett. **56**, 2797 (1986); Th. Sauter, R. Blatt, W. Neuhauser, and P. E. Toschek, Phys. Rev. Lett. **57**, 1696 (1986); J. C. Bergquist, R. G. Hulet, W. M. Itano, and D. J. Wineland, Phys. Rev. Lett. **57**, 1699 (1986).
[19] M. G. Raizen, J. M. Gilligan, J. C. Bergquist, W. M. Itano, and D. J. Wineland, Phys. Rev. A**45**, 6493 (1992).
[20] W. Paul, H. P. Reinhard, and U. von Zahn, Z. Phys. **152**, 143 (1958).
[21] H. G. Dehmelt, Adv. At. Mol. Phys. **3**, 53 (1967); **5**, 109 (1967).
[22] M. E. Poitzsch, J. C. Bergquist, W. M. Itano, and D.J. Wineland, Rev. Sci. Instrum. **67**, 129 (1996).
[23] B. Esry and B. Paul (private communication).
[24] K. E. Kahill and R. J. Glauber, *Phys. Rev.* **177**, 1857 (1969); D. J. Wineland and W. M. Itano, *Phys. Rev.* A **20**, 1521 (1979); W. Vogel and R. L. De Matos Filho, *Phys. Rev.* A **52**, 4214 (1995).
[25] D. J. Wineland and H. G. Dehmelt, Bull. Am. Phys. Soc. **20**, 637 (1975).
[26] J. E. Thomas, P. R. Hemmer, S. Ezekiel, C. C. Leiby, R. H. Picard, and C. R. Willis, *Phys. Rev. Lett.* **48**, 867 (1982).
[27] M. Kasevich and S. Chu, Phys. Rev. Lett. **69**, 1741 (1992).
[28] F. Diedrich, J. C. Bergquist, W. M. Itano, and D. J. Wineland, Phys. Rev. Lett. **62**, 403 (1989).
[29] D. J. Wineland, R. E. Drullinger, and F. L. Walls, Phys. Rev. Lett. **40**, 1639 (1978); W. Neuhauser, M. Hohenstatt, P. Toschek, and H. Dehmelt, Phys. Rev. Lett **41**, 233 (1978); D. J. Wineland, and W. M. Itano, *Physics Today*, vol. 40, no. 6, p. 34 (1987)
[30] B. Appasamy, J. Siemers, Y. Stalgies, J. Eschner, R. Blatt, W. Neuhauser, and P. E. Toschek, Appl. Phys. B **60**, 473 (1995).
[31] R. Dum, P. Marte, T. Pellizzari, and P. Zoller, Phys. Rev. Lett. **73**, 2829 (1994); J. Eschner, B. Appasamy, and P. E. Toschek, Phys. Rev. Lett. **74**, 2435 (1995).
[32] G. Morigi, J. I. Cirac, M. Lewenstein, and P. Zoller, Europhys. Lett. **39**, 13 (1997).
[33] D. P. DiVincenzo, *Phys. Rev.* A **51**, 1015 (1995); A. Barenco, *et al.*, *Phys. Rev.* A **52**, 3457 (1995); S. Lloyd, *Phys. Rev. Lett.* **75**, 346 (1995).
[34] R. P. Feynman, Opt. News **11**, 11 (1985).
[35] D. M. Meekhof, C. Monroe, B. E. King, W. M. Itano, and D. J. Wineland, *Phys. Rev. Lett.* **76**, 1796 (1996).
[36] N. F. Ramsey, *Molecular Beams*, (Oxford University, London, 1963).
[37] C. Monroe, D. Leibfried, B. E. King, D. M. Meekhof, W. M. Itano, and D. J. Wineland, Phys. Rev. A **55**, R2489 (1997).
[38] C. Monroe, D. M. Meekhof, B. E. King, and D. J. Wineland, *Science* **272**, 1131 (1996).
[39] D. Leibfried, D. M. Meekhof, C. Monroe, B. E. King, W. M. Itano, and D. J. Wineland, Phys. Rev. Lett. **77**, 4281 (1996); J. Mod. Optics **44**, 2485 (1997).
[40] A. Einstein, B. Podolsky, and N. Rosen, Phys. Rev. **47**, 777 (1935).
[41] A. E. Siegman, *Lasers* (University Science Books, Mill Valley, CA, 1986).
[42] S. Chu, private communication (1997).
[43] S. R. Jefferts, C. Monroe, E. W. Bell, and D. J. Wineland, Phys. Rev. A **51**, 3112 (1995).
[44] D. J. Wineland and W. M. Itano, Phys. Rev. A **20**, 1521 (1979).
[45] J. I. Cirac, P. Zoller, H. J. Kimble, and H. Mabuchi, Phys. Rev. Lett. **78**, 3221 (1997); S. J. van Enk, J. I. Cirac, and P. Zoller, Phys. Rev. Lett. **78**, 429 (1997).
[46] H. Goldstein, *Classical Mechanics* (Addison-Wesley, Reading, MA, 1950).
[47] H. Frauenfelder, *The Mossbauer Effect*, (Benjamin, New York, 1963); H. J Lipkin, *Quantum Mechanics* (North Holland, Amsterdam, 1973), Chaps. 2–4.
[48] P. W. Shor, Phys. Rev. A **52**, R2493 (1995); A. Steane, Phys. Rev. Lett. **77**, 793 (1996); Proc. R. Soc. Lond. A **452**, 2551 (1996); R. LaFlamme, C. Miquel, J. P. Paz, and W. H. Zurek, Phys. Rev. Lett. **77**, 198 (1996); D. P. DiVincenzo and P. W. Shor, Phys. Rev. Lett. **77**, 3260 (1996).

[49] M. B. PLENIO and P. L. KNIGHT, Phys. Rev. A **53**, 2986 (1996); M. B. PLENIO, V. VEDRAL, and P. L. KNIGHT, Phys. Rev. A **55**, 67 (1997).
[50] R. A. CLINE, J. D. MILLER, M. R. MATTHEWS, and D. J. HEINZEN, Optics Letters, **19**, 207 (1994).
[51] J. I. CIRAC, T. PELLIZZARI, and P. ZOLLER, *Science* **273**, 1207 (1996).
[52] H. HARDE, H. LEHMITZ, J. HATTENDORF-LEDWOCH, and R. BLATT, Appl. Phys. B **53**, 131 (1991); D. J. WINELAND, J. J. BOLLINGER, W. M. ITANO, F. L. MOORE, and D. J. HEINZEN, Phys. Rev. A **46**, R6797 (1992).
[53] H. WALTHER, *Adv. At. Mol. Phys.* **31**, 137 (1993).
[54] D. J. WINELAND and H. G. DEHMELT, J. Appl. Phys. **46**, 919 (1975).
[55] J. R. ANGLIN, J. P. PAZ, and W. H. ZUREK, Phys. Rev. A **55**, 4041 (1997).
[56] T. A. SAVARD, K. M. O'HARA, and J. E. THOMAS, Phys. Rev. A **56**, R1095 (1997).
[57] A. J. DAHM and D. N. LANGENBERG, Am. J. Phys. **43**, 1004 (1975).
[58] S. SCHNEIDER and G. J. MILBURN, quant-ph/9710044.
[59] C. MIQUEL, J. P. PAZ, and W. H. ZUREK, Phys. Rev. Lett. **78**, 3971 (1997).
[60] N. C. WONG, J. L. HALL, J. Opt. Soc. Am. **B2**, 1527 (1985); C. C. HARB, M. B. GRAY, H.-A. BACHOR, R. SCHILLING, P. ROTTENGATTER, I. FREITAG, and H. WELLING, IEEE J. Quant. Elec. **30**, 2907 (1994).

(Manuscript received: September 19, 1997)

# Trapped ions, entanglement, and quantum computing*

C. J. Myatt, B. E. King, D. Kielpinski, D. Leibfried†, Q. A. Turchette, C. S. Wood, W. M. Itano, C. Monroe, and D. J. Wineland

Time and Frequency Division, National Institute of Standards and Technology, Boulder, CO 80303

## ABSTRACT

A miniature, elliptical ring rf (Paul) ion trap has been used in recent experiments toward realizing a quantum computer in a trapped ion system. With the combination of small spatial dimensions and high rf drive potentials, around 500 V amplitude, we have achieved secular oscillation frequencies in the range of 5-20 MHz. The equilibrium positions of pairs of ions that are crystallized in this trap lie along the long axis of the ellipse. By adding a static potential to the trap, the micromotion of two crystallized ions may be reduced relative to the case of pure rf confinement. The presence of micromotion reduces the strength of internal transitions in the ion, an effect that is characterized by a Debye-Waller factor, in analogy with the reduction of Bragg scattering at finite temperature in a crystal lattice. We have demonstrated the dependence of the rates of internal transitions on the amplitude of micromotion, and we propose a scheme to use this effect to differentially address the ions.

**Keywords:** quantum computing, quantum logic, ion traps, laser cooling and trapping

## 1. INTRODUCTION

Since the development of useful algorithms for quantum computation[1,2], there has been an explosion of work toward realizing a practical quantum computer. One of the more attractive systems for implementation is a string of trapped ions[3,4], and already a quantum logic gate has been demonstrated with a single trapped ion[5]. In this paper, we report on further progress toward achieving quantum logic in a trapped ion system. We describe a miniature, elliptical ring, rf (Paul) trap used in our current experiments. The addition of a static potential can be used to reduce the micromotion of several ions confined in this type of trap. We then describe progress toward individual addressing of ions using the Debye-Waller factors due to rf micromotion. Other recent results, including cooling two ions to their collective motional ground state as well as observations of heating, will be described in a separate publication[6].

## 2. ELLIPTICAL RF PAUL TRAP

The ion trap used in our current experiments, shown schematically in Figure 1, is based closely on the trap used in previous experiments[7]. The ring and endcap electrodes are made from 125 μm thick beryllium foil. The ring electrode was formed by punching a hole in the foil with a pinpoint and then widening the hole into an elliptical shape using a thin tungsten wire as a file. The edges of the hole were smoothed by "flossing" the hole with the tungsten wire. The aspect ratio of the ring is approximately 3:2, and the elongated axis is approximately 525 μm long. The endcaps are made by cutting a 250 μm slot in a similar piece of foil.

---



† Present address: Inst. für Exp. Physik, Universität Innsbruck, 6020 Innsbruck, Austria.

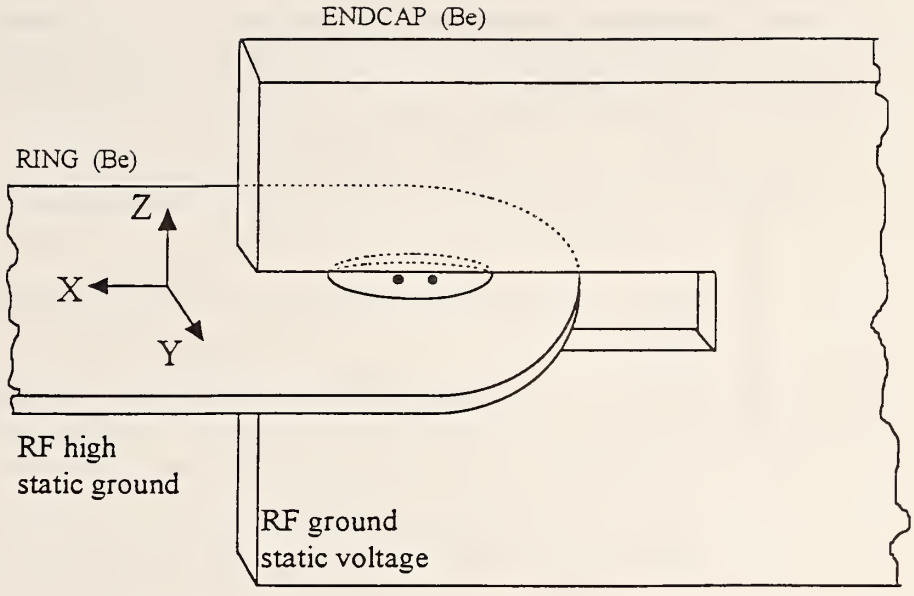


Figure 1. A schematic of the elliptical ion trap used in recent studies. Ions align along the elgongated, weak direction of the elliptical ring electrode. The endcaps may be biased with a static electric potential to adjust the spring constants of the trap.

The rf drive is generated by feeding a copper quarter-wave coaxial line, resonant at about 240 MHz, that is inside the vacuum system[7]. The rf is coupled in at the base of the resonator with a single loop of wire, the shape of which is empirically adjusted to impedance-match the 50 Ω rf source. The ring is clamped to the end of the center conductor, and the typical voltage amplitude on the ring is 550 V for 1 W input rf power. The endcaps may be biased with a static potential to adjust the trap frequencies. There are, in addition, four shim electrodes (not shown) that allow us to null out stray electric fields.

The classical motion of an ion in a rf quadrupole trap is described by the Mathieu equation.[8,9] In the pseudopotential approximation, the solution for the motion may be broken up into a fast, small amplitude motion at the rf drive frequency, termed the micromotion, and a slower, larger amplitude motion that describes the position of the ion averaged over a period of the rf drive, which is called the secular motion. The secular oscillation frequencies are observed through resonant detection[7,10]. A plot of the secular frequencies as a function of the electrical potential applied to the endcaps is shown in Figure 2. The measured frequencies have been fit with the functions

$$\omega_x = \frac{\Omega}{2}\sqrt{\alpha a + (\alpha q)^2/2}\,, \tag{1}$$

$$\omega_y = \frac{\Omega}{2}\sqrt{(1-\alpha)a + (1-\alpha)^2 q^2/2}\,, \text{ and} \tag{2}$$

$$\omega_z = \frac{\Omega}{2}\sqrt{-a + q^2/2}\,, \tag{3}$$

where $\Omega = 2\pi \times 238.3$ MHz is the rf drive frequency, $\alpha$ is the geometric ellipticity parameter, and $a$

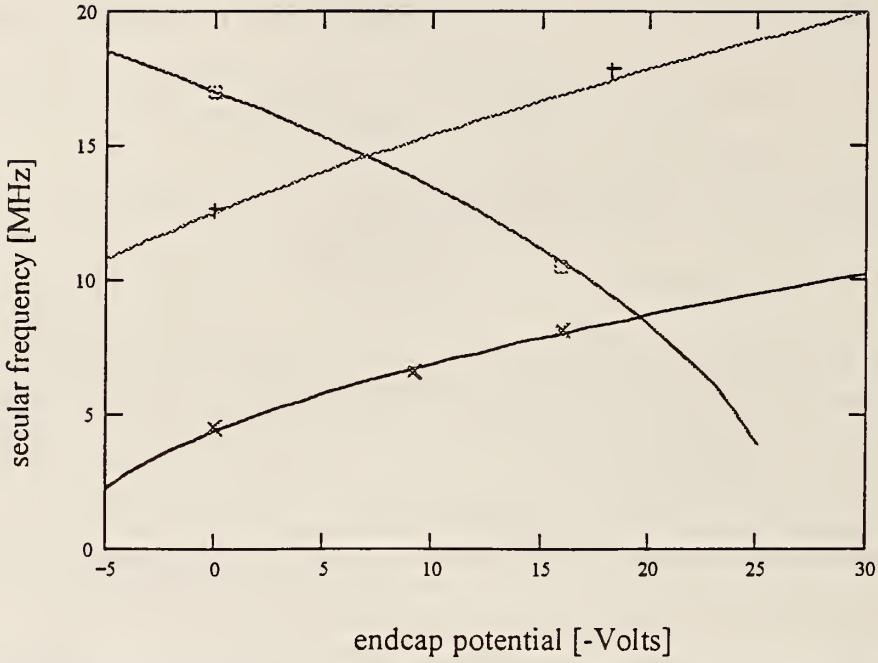


Figure 2. The secular motional frequencies as a function of the voltage applied to the endcaps. Note that the voltage is actually negative with respect to the ring electrode. The x symbols are for the $x$ frequencies, the open squares are for the $z$ frequencies, and the crosses are for the $y$ frequencies. The lines are fits to Equations 1 through 3.

and $q$ are static and rf parameters in the Mathieu equation for the classical amplitude of motion[9]. The parameter $\alpha$ is defined so that the electrical potential has the form $\Phi \propto \left[\alpha x^2 + (1-\alpha)y^2 - z^2\right]$. Thus, for a spherical quadrupole trap, $\alpha = 0.5$. Due to the asymmetry of the endcaps, the ellipticity parameter is $\alpha = 0.36$ even when the ring is circular[7]. The elliptical ring used in the current trap enhances the ellipticity of the fields, and we extract $\alpha = 0.26$ from a fit to the data.

In the type of trap described here, the electric fields vanish at a single point. In the absence of stray fields, a single ion in the trap is confined in the vicinity of this zero-field point. Thus, in the pseudopotential approximation ($q \ll 1$), there is almost negligible micromotion when a single ion is cooled to the zero-point state of secular motion. In the case of two ions crystallized in the trap, Coulomb repulsion pushes the ions away from this zero-field region. Thus there is significant micromotion even when two ions are cooled to the zero point of secular motion. The kinetic energy $T_\mu$ of micromotion is equal to the rf pseudopotential energy $U_{\mathrm{rf}}$ at the ion equilibrium positions[11]. However, the addition of a static potential $U_0$ can reduce the micromotion of two ions relative to the case of a pure rf trap. The ion separation is reduced by using a static potential to strengthen the confinement along the axis on which the ions lie, which in turn decreases the amplitude of the rf fields at the ion equilibrium positions. The potential energy at the "squeezed" equilibrium is a sum of the rf pseudopotential and static potential contributions, $U = U_{\mathrm{rf}} + U_0$, and the ratio of micromotion kinetic energy to total potential energy, $T_\mu / U = U_{\mathrm{rf}} / \left(U_{\mathrm{rf}} + U_0\right)$, is less than 1.

In the elliptical rf trap, the equilibrium positions of two cold crystallized ions lie along the direction of the weakest spring constant. In the absence of a static potential, the weakest confinement is

on the long axis of the elliptical ring, which we label the $\hat{x}$ axis (see Figure 1). As Figure 2 shows, the three trap frequencies may be altered by applying a voltage to the endcaps. In particular, a negative potential on the endcaps decreases the $\hat{z}$ confinement while strengthening the confinement in the plane of the ring. As the ions are squeezed together, they maintain their equilibria along the $\hat{x}$ axis so long as $\omega_x < \omega_z$. To determine the maximum reduction in micromotion, consider the limiting case $\omega_x = \omega_z$. In this case, the ratio of micromotion kinetic energy to total potential energy is $T_\mu/U = \alpha$. Thus the physical geometry of the trap determines the maximum suppression of micromotion, which can be substantial for small values of $\alpha$.

## 3. MICROMOTION AND DEBYE-WALLER FACTORS

Quantum logic operations on a string of ions require the ability to differentially address the ions. This can be accomplished by focusing a laser so that only one ion is illuminated and the others are in the dark. However, the scheme outlined in the previous section to reduce the micromotion, whereby the ions are squeezed together using a static potential, excacerbates the problems of illuminating only one ion. In this section we present an alternative method for differential addressing that does not require tight focussing of a laser beam. In this scheme, the ions are uniformly illuminated, and the internal transition strengths are differentially modified by the motion of the ions. This sort of effect is familiar in crystallography, where the amplitude of the Bragg diffraction peak is a sensitive function of the random motion of the atoms in the crystal. The reduction of Bragg scattering at elevated temperatures is governed by the Debye-Waller factor.

In the case of two ions, the amplitude for driving stimulated Raman transitions between two internal states is sensitive to the motion of the ion, and we call the motional terms that modify the Raman transition rate the Debye-Waller factors[4]. For our system of trapped ions, both the thermal motion of the ion and the micromotion contribute to a reduction in the rate of stimulated Raman transitions. In the frame of the oscillating ion, the applied laser light is frequency modulated at the ion motional frequencies due to the Doppler shift. We are here concerned with the micromotion, so the applied laser light appears to have sidebands at the rf frequency, and the power in the central frequency is depleted. If the modulation index due to the motion is $m$, then matrix elements of transitions driven by the central, or carrier, frequency are proportional[12] to the Bessel function $J_0(m)$. This reduction of the transition strength can be manipulated by applying external fields. In particular, an applied electric field along the $\hat{x}$ direction displaces the ions so that the micromotion of one ion is reduced while that of the other is increased. This will increase the Rabi frequency of one ion at the expense of reducing the Rabi frequency of the other ion. If the ratio of the Rabi frequencies can be made equal to 2, then a pulse of radiation can be a $\pi$ pulse for one ion and a $2\pi$ pulse for the other ion. Alternatively, the micromotion amplitude of one ion may be so large that $J_0(m) = 0$, allowing individual addressing of the other ion. The applied electric field may then be reversed to address the second ion.

In the experiment, an electric field along the $\hat{x}$ direction is generated by applying a potential to the four shim electrodes. For a variety of applied fields, the Rabi frequencies of the two ions on the carrier transition was observed[6,10], as shown in Figure 3. The data are fitted to a simple function with two independent frequencies. These pairs of frequencies are plotted in Figure 4 as a function of applied voltage on the shim electrodes. This clearly demonstrates the ability to adjust the Rabi frequencies. The implementation of quantum logic with this scheme is now under experimental investigation.

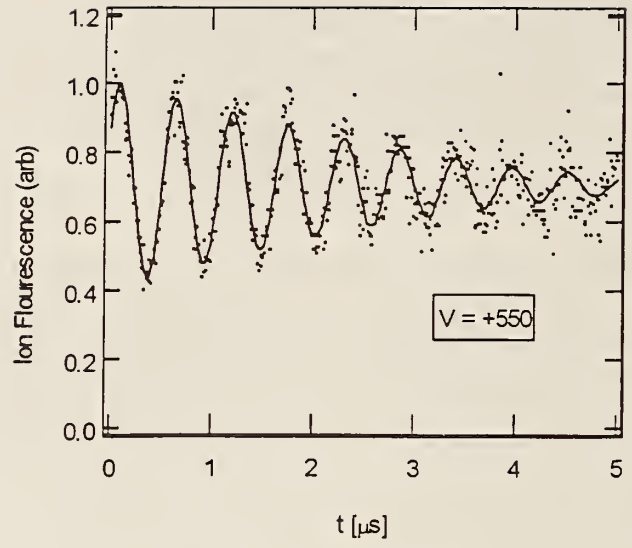


(a)

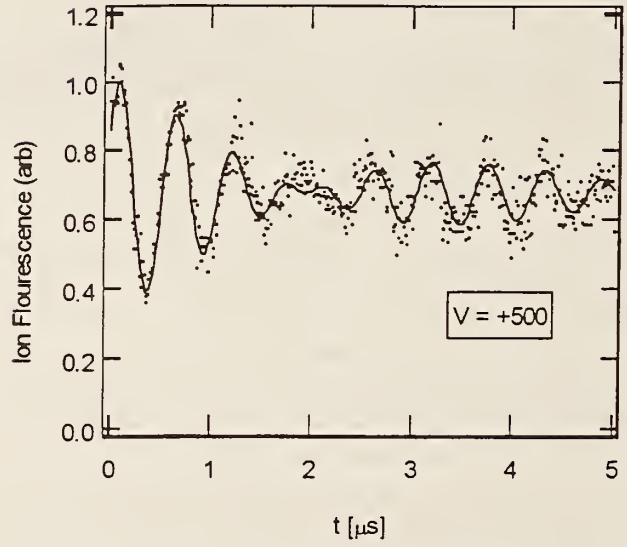


(b)

Figure 3. Rabi flopping on the carrier Raman transition for two ions. The detected flourescence oscillates in time as the ions flop between a "bright" state and a "dark" state.[6,10] In the upper trace, the ions have equal amplitudes of micromotion, and hence their Rabi frequencies are identical. In the lower curve, the ions have different amplitudes of micromotion, and this is reflected in two different Rabi frequencies. The fit is to two decaying sinusoids. The electric potential applied to the shim electrodes is indicated.

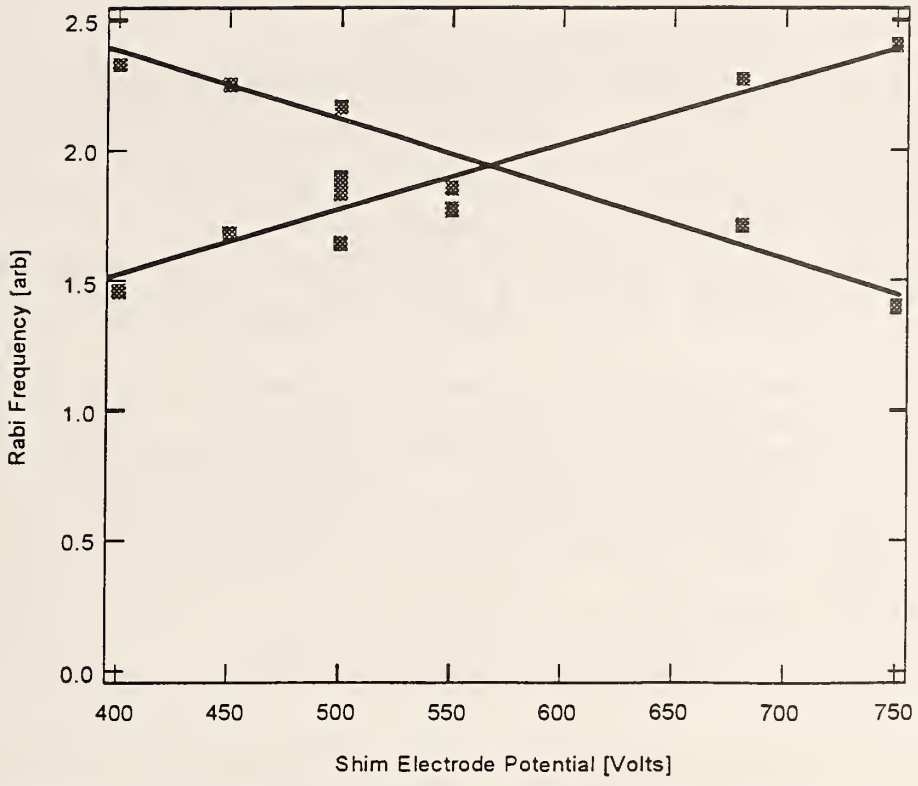


Figure 4. As the ions are displaced by an applied voltage on the shim electrodes, the Rabi frequencies are different for the two ions. The lines are only to guide the eye.

## 4. OUTLOOK

Achieving nontrivial quantum computation in a trapped-ion system requires a number of difficult steps. In this paper, we have discussed one possibility for individual addressing. Combined with our recent achievement of cooling two ions to the ground state of their collective motion[6], this puts simple quantum logic operations on two ions within reach. Future work will revolve around implementing some scheme for individual addressing in order to entangle the states of the ions. In the longer term, linear ion traps will be pursued in order to achieve quantum logic with more than two or three ions.

## 5. ACKNOWLEDGEMENTS

We thank the U. S. National Security Agency, the U. S. Army Research Office, and the U. S. Office of Naval Research for funding this work.

## 6. REFERENCES


1. P. W. Shor, in *Proc. of the 35th Annual Symposium on the Foundations of Computer Science,* edited by S. Goldwasser, pp. 124-134, 1994.
2. L. K. Grover, *Phys. Rev. Lett.* **79**, pp. 325-328, 1997.
3. J. I. Cirac and P. Zoller, *Phys. Rev. Lett.* **74**, pp. 4091-4094, 1995.
4. D. J. Wineland, C. Monroe, W. M. Itano, D. Leibfried, B. E. King, and D. M. Meekhof, submitted to *J. Res. Natl. Inst. Stand. Tech.*
5. C. Monroe, D. M. Meekhof, B. E. King, W. M. Itano, and D. J. Wineland, *Phys. Rev. Lett.* **75**, pp. 4714-4717, 1995.
6. B. E. King, C. S. Wood, C. J. Myatt, Q. A. Turchette, D. L. Leibfried, W. M. Itano, C. Monroe, and D. J. Wineland, submitted to *Phys. Rev. Lett.*
7. S. R. Jefferts, C. Monroe, E. W. Bell, and D. J. Wineland, *Phys. Rev. A* **51**, pp. 3112-3116, 1995.
8. H. Dehmelt, *Adv. At. Mol. Phys.* **3**, p. 53, 1967.
9. R. F. Wuerker, H. Shelton, and R. V. Langmuir, *J. Appl. Phys.* **30**, pp. 342-349, 1959.
10. D. M. Meekhof, C. Monroe, B. E. King, W. M. Itano, and D. J. Wineland, *Phys. Rev. Lett.* **76**, pp. 1796-1800, 1996.
11. F. G. Major and H. G. Dehmelt, *Phys. Rev.* **170**, pp. 91-107, 1968.
12. D. J. Wineland and W. M. Itano, *Phys. Rev. A* **20**, pp. 1521-1540, 1979.

# Shadows and Mirrors: Reconstructing Quantum States of Atom Motion

**Quantum mechanics allows us only one incomplete glimpse of a wavefunction, but if systems can be identically prepared over and over, quantum equivalents of shadows and mirrors can provide the full picture.**

Dietrich Leibfried, Tilman Pfau and Christopher Monroe

Imagine that a pair of coins are tossed in a black box. The box reports only one of the following three results at random: (1) the outcome of the first coin (heads or tails), (2) the outcome of the second coin (heads or tails), or (3) whether the outcomes of the two coins matched or were different. Our task is to construct a joint probability distribution of the four possible outcomes of the coins (HH, TT, HT, TH) based on many observations of the black box outputs. Now suppose that after many trials, the black box reports that each coin comes up heads two-thirds of the time when measured individually, yet the coins *never* match when they are compared. (Clearly the results of the coin tosses have been correlated—perhaps a joker in the black box flips the coins and then changes the outcomes appropriately.) We seek a distribution that both reflects this correlation and obeys the marginal distributions of each coin as two-thirds heads, one-third tails (see the three tables on page 23). The only way to satisfy both requirements is to force the joint probability $P(\mathrm{TT})$ of getting two tails to be negative! Mathematically, this is because $P(\mathrm{HH}) + P(\mathrm{TT})$ is observed to be zero, yet we expect $P(\mathrm{HH})$ to be greater than $P(\mathrm{TT})$, because the individual coins are weighted toward heads.

The sleight of hand giving rise to negative probabilities is that we have attempted to reconstruct a joint probability distribution without ever having observed individual joint outcomes of the coins. The only measured events are described by sums of joint probabilities such as $P(\mathrm{HT}) + P(\mathrm{TH}) = 1$ or $P(\mathrm{HH}) + P(\mathrm{HT}) = \frac{2}{3}$. One way to interpret the distribution of table 3 is to note that, since individual joint outcomes of the coins are inaccessible, nothing prevents us from assigning negative probabilities to such immeasurable events. With this rule in mind, this joint "quasi-probability" distribution may be a useful bookkeeping tool, as it not only characterizes the hidden correlations within the black box, but also retains information about the marginal probabilities of the individual coins.[1]

Although this example of coins in a black box is highly artificial, a similar situation arises in nature when we describe the probability distribution of a quantum mechanical particle in position–momentum phase space. A classical particle occupies a single point in phase space, and an ensemble of classical particles can be characterized by a phase-space probability distribution. On the other hand, the Heisenberg uncertainty relationship requires that a quantum mechanical particle be described by an area of uncertainty in phase space no smaller than $\Delta x\,\Delta p = \hbar/2$. If a particle's position is known well, then its momentum is not, and vice versa. In mathematical language, the position wavefunction $\Psi_x(x)$ and momentum wavefunction $\Psi_p(p)$ are related by a Fourier transform; thus, localized position wavefunctions lead to delocalized momentum wavefunctions, and vice versa. A probability distribution in quantum phase space must somehow incorporate this feature.

## Wigner distribution and 'negative probabilities'

In 1932, Eugene Wigner presented a convenient mathematical construct for visualizing quantum trajectories in phase space.[2] The Wigner distribution, or Wigner function $W(x, p)$, retains many of the features of a probability distribution, except that it can be negative in some regions of phase space. In the coin example above, practical use of the quasi-probability distribution of table 3 is limited to events described by sums of any two entries. Similarly, when we apply the Wigner distribution to measurements in quantum phase space, the probability distribution for the outcome of a measurement is obtained essentially by convolving $W(x, p)$ with a distribution of possible states of the measurement device, which must be distributed over an area of order $\hbar$ or larger. This prescription leads to a natural connection between quantum and classical phase space: As the measurement resolution is degraded away from the quantum limit so that the Heisenberg uncertainty relationship plays no role, localized regions of $W(x, p)$ (with possible negative values) become washed out, and the convolved Wigner distribution approaches the usual classical phase-space probability distribution. Similar to the quasi-distribution of the coins above, the Wigner distribution is not a *bona fide* probability distribution, but can be a useful bookkeeping tool that high-

Dietrich Leibfried *is a physicist at Innsbruck University in Austria. He was a guest researcher at the National Institute of Standards of Technology in Boulder, Colorado, during the writing of this article.* Tilman Pfau *is a physicist at the University of Konstanz in Germany.* Christopher Monroe *is a staff physicist at the National Institute of Standards and Technology in Boulder, Colorado.*

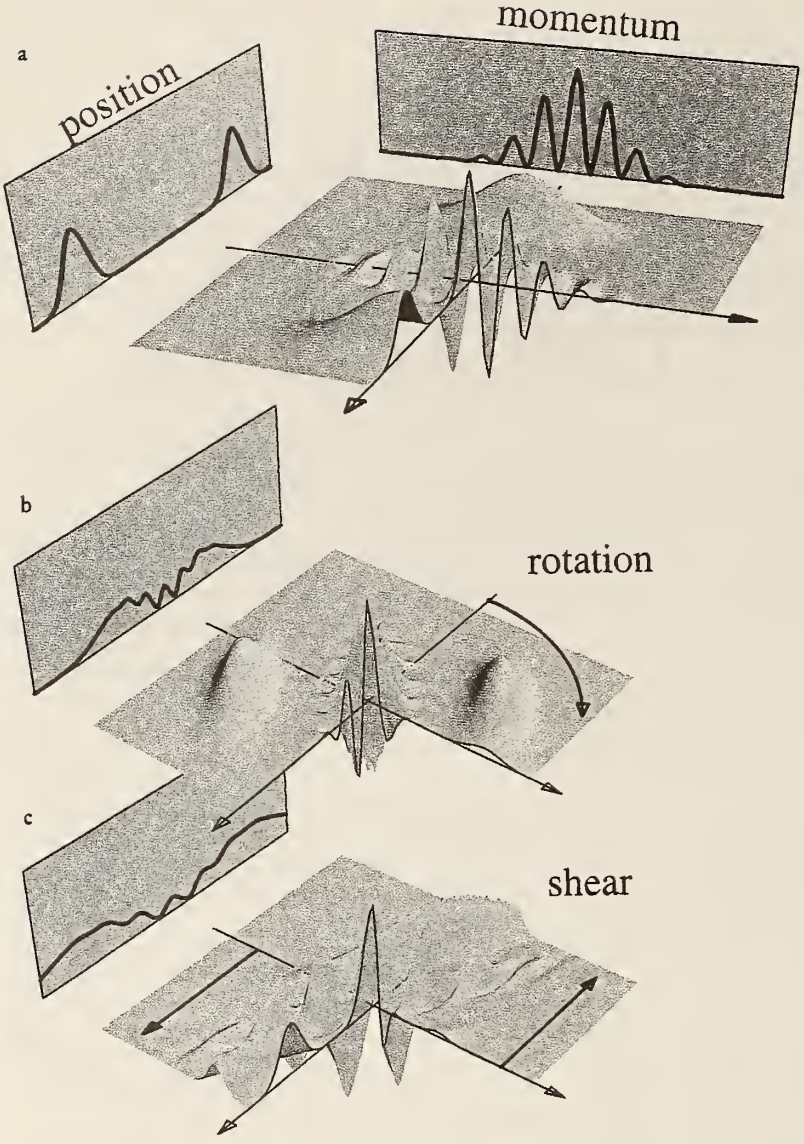


FIGURE 1: WIGNER FUNCTION FOR THE DOUBLE-SLIT EXPERIMENT, visualized in phase space. a: The initial Wigner distribution representing the superposition of two Gaussian lobes directly behind the slits. The oscillating part in the center is due to the spatial coherence between the two lobes. The "spacelike shadow" (on the orange screen, at left) shows the spatial marginal distribution $|\Psi_x(x)|^2$ of the state, obtained by ignoring the momentum information. The pale burgundy shadow at rear shows the corresponding "momentum-like shadow" $|\Psi_p(p)|^2$. With a position-sensitive detector measuring the spacelike shadow, we can view the initial Wigner distribution from different angles by either rotating it (b) or shearing it (c).

lights the inherent anticorrelation of position and momentum uncertainty.

For a pure quantum state, the Wigner distribution is related to the position or momentum wavefunction by

$$W(x,p) = \frac{1}{2\pi}\int_{-\infty}^{\infty} \Psi_x^*\left(x-\frac{s}{2}\right)\Psi_x\left(x+\frac{s}{2}\right)e^{-isp}\,ds$$

$$= \frac{1}{2\pi}\int_{-\infty}^{\infty} \Psi_p^*\left(p+\frac{s}{2}\right)\Psi_p\left(p-\frac{s}{2}\right)e^{-isx}\,ds\,, \qquad (1)$$

where we have set $\hbar = 1$. The Wigner distribution of a mixed quantum state is a weighted sum of either expression over the appropriate wavefunctions. These expressions may not be very illuminating, and the equivalent of the Schrödinger equation describing the time evolution of $W(x, p)$ is even less so. (However, Wolfgang Schleich and Georg Süssmann discussed a physical interpretation of this form of the Wigner distribution in PHYSICS TODAY, October 1991, page 146.) Nevertheless, Wigner showed that $W(x, p)$ is indeed the closest thing we have to a probability distribution in quantum phase space, as it corresponds to the phase-space probability distribution in the classical

TABLES: **Joint probability distributions of the outcomes of tossing two coins.** (1) Probability distribution given that the two coins are tossed independently, both weighted toward heads with $P(H) = \frac{2}{3}$ and $P(T) = \frac{1}{3}$. The marginal probabilities of the outcomes of either coin (obtained by adding the entries vertically or horizontally) result in two-thirds heads and one-third tails. (2) Probability distribution given that the coins are tossed in a black box that reports that the coins never match—that is, $P(HH) + P(TT) = 0$. The off-diagonals add to 1 as required, with $p$ arbitrary. The marginal probabilities can no longer be two-thirds heads for both coins. (3) "Quasi-probability" distribution under same conditions as (2) and also exhibiting marginal probabilities of each coin as two-thirds heads and one-third tails. The price paid is that one of the entries is negative!

(1)

| | H | T |
|---|---|---|
| H | 4/9 | 2/9 |
| T | 2/9 | 1/9 |

(2)

| | H | T |
|---|---|---|
| H | 0 | $p$ |
| T | $1-p$ | 0 |

(3)

| | H | T |
|---|---|---|
| H | 1/6 | 1/2 |
| T | 1/2 | −1/6 |

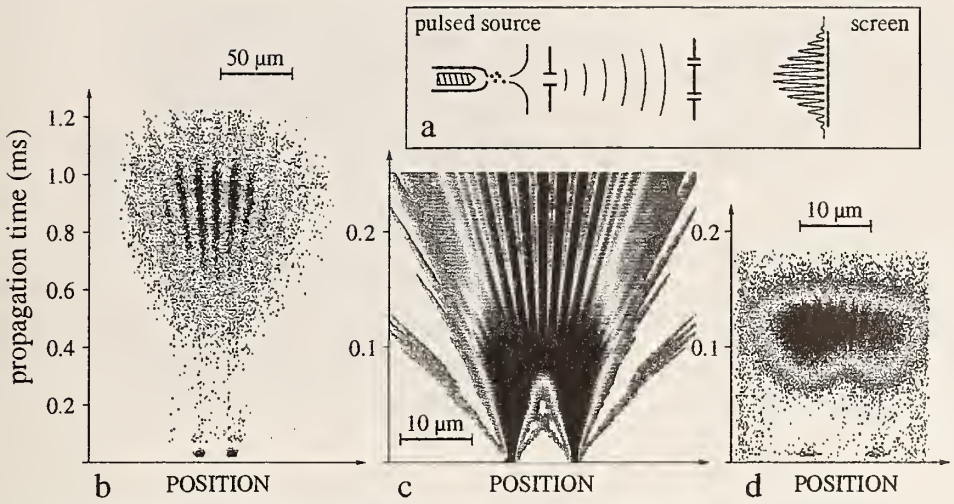


FIGURE 2: DOUBLE-SLIT ATOM INTERFEROMETRY. **a:** The experimental arrangement. Atoms from a collimated source propagate through a double slit with 8 $\mu$m separation and strike a position-sensitive detector screen. The source produces fast-moving atoms and a range of slower atoms. **b:** Diffraction pattern of the atomic matter waves plotted as a function of position and of the propagation time $t_d$ for the atoms to travel from the double slit to the detector. The distance from double slit to detector is $d$ = 195 cm, for which the slow atoms propagate long enough to produce a Fraunhofer (far-field) diffraction pattern. The fast atoms produce the near-field shadow of the slits at the bottom. (This shadow is magnified because of the geometry of the apparatus.) **c:** Calculated diffraction pattern for atoms having a wide range of velocities (and propagation times $t_d$), showing the transition between Fresnel (near-field) and Fraunhofer diffraction. **d:** Data for $d$ = 25 cm, where the transition between Fresnel and Fraunhofer diffraction becomes visible in the slow atoms' pattern.

limit, and also preserves the marginal probability distributions of position and momentum $|\Psi_x(x)|^2$ and $|\Psi_p(p)|^2$:

$$|\Psi_x(x)|^2 = \int_{-\infty}^{\infty} W(x,p)\,dp \quad \text{and} \quad |\Psi_p(p)|^2 = \int_{-\infty}^{\infty} W(x,p)\,dx\,. \quad (2)$$

Can the Wigner distribution $W(x,p)$ of a quantum particle be measured? At first glance, the answer appears to be no. The probability distribution of any physical observable corresponds to an integral over $W(x,p)$, as in equation 2, so a single measurement cannot provide localized values of $W(x,p)$. But if we prepare a particle in the same quantum state in repeated experiments, we can perform a large number of measurements on effectively the same quantum system. We can then reconstruct the Wigner distribution by measuring various shadows or projection integrals of $W(x,p)$ in separate experiments, or by averaging an observable whose expectation value is proportional to $W(x,p)$ in repeated experiments.[3]

In the following, we describe two methods for reconstructing the Wigner distribution of atomic motion in phase space from such a set of repeated measurements. In one experiment, identically prepared atoms from a beam travel through a double-slit interferometer, and different measurements are performed on them. In another experiment, a single trapped atom is repeatedly prepared in an identical state of motion, and a different measurement is performed after each preparation. The atoms in both experiments are prepared in nonclassical states of phase space; thus their corresponding Wigner distributions have features not found in classical phase-space distributions, such as negative values.

## Quantum shadows and the double slit

Detecting the positions of many identically prepared atoms yields the spatial marginal distribution $|\Psi_x(x)|^2$ as a "spacelike shadow" of the Wigner distribution; likewise, a momentum-sensitive detector yields the "momentum-like shadow" $|\Psi_p(p)|^2$. As shown in figure 1a, we can observe shadows across different angles in phase space either by rotating the detector's point of view or by rotating the Wigner distribution and keeping the detector fixed. For example, figure 1b shows the Wigner distribution rotated by 60° and measured with a position detector. The spacelike shadow on the screen now contains information about both $x$ and $p$ of the initial distribution. The Wigner distribution can be sheared in phase space as shown in figure 1c by allowing the particle to evolve freely. A shear rotates the spacelike shadow and gives an additional stretching, which can easily be compensated for. Thus, we can observe different shadows of the initial Wigner distribution by allowing particles to evolve freely for different times before we measure their position.

Tomography is a general technique for reconstructing the shape of an inaccessible object from a set of different shadows of that object. For instance, medical imaging uses this technique to obtain a full three-dimensional picture of the brain by piecing together various two-dimensional shadows from x rays or nuclear magnetic resonance techniques. Quantum state tomography has been used to reconstruct the quantum state of light waves[4] and molecular vibration,[5] and has also been theoretically considered for the reconstruction of the Wigner distribution of atoms from an atomic beam.[6] All these applications use a mathematical device called the inverse Radon transformation to generate an image of the higher dimensional object from a full set of shadows. In this sense, quantum mechanics places the observer in the situation of Plato's prisoner—chained in a cave so he can see only the shadows of objects outside the cave, not the objects themselves. However, when the objects are rotated or sheared, even Plato's prisoner can obtain a full picture of the objects.

At the University of Konstanz, Jürgen Mlynek's group use this tomographic technique in sending an atomic beam through a double-slit apparatus and reconstructing the Wigner distribution of the atoms immediately behind the slit.[7] The theoretical Wigner distribution in figure 1a depicts the idealized quantum state of the transverse position and momentum of each atom as it leaves the double slit. For a plane matter wave, the emerging quantum state is a linear superposition of one atomic wavepacket going through one slit and another such packet going through the other. The coherence between these two wavepackets leads to an interference pattern in the momentum distribution. The signature of this coherence in the Wigner distribution is the oscillating positive and negative values between the two main lobes. In the experiment, the spatial distribution of the atoms is measured on a screen. As the atoms freely propagate between the double slit and the screen, the corresponding quantum

state is sheared in phase space as shown in figure 1c. Different atoms experience different shear, since they are distributed over a broad range of velocities and therefore evolve for different times as they travel from the double slit to the detector. A velocity-selective experiment can therefore yield the full information about the quantum state of the motion.

The Konstanz experiment is sketched in figure 2a. A discharge source for metastable helium atoms fires for 10 $\mu$s, generating a double-peaked distribution of atomic velocities consisting of slow atoms between about 1000 and 3000 m/s and fast atoms near 33 000 m/s. The corresponding de Broglie wavelengths are concentrated near 3 picometers for the fast atoms and between 20 and 70 pm for the slow atoms. A 5 $\mu$m wide entrance slit collimates this beam. Farther downstream, the beam passes through a microfabricated double-slit structure with a slit separation of 8 $\mu$m and openings of 1 $\mu$m. The combination of entrance slit and double slit acts as a preparation tool for the transverse motional quantum state of the atoms. After emerging from this preparation tool, the atoms propagate over a distance $d$ to a time- and space-resolving detector. When each metastable atom strikes the detector, it releases a large amount of energy, allowing nearly every atom to be detected. The spatial and temporal coordinates of each such event at the detector are recorded. This data provides a measurement of spatial atomic distributions for different longitudinal velocities $v$ in the beam, or equivalently, different propagation times $t_d = d/v$ from the double slit to the detector.

As discussed above, different propagation times $t_d$ lead to different views of the Wigner distribution. Another way to look at this situation is to treat the atomic wavepacket evolution as an optical diffraction problem, in which the shear of the Wigner distribution corresponds to the transition from the Fresnel (near-field) regime to the Fraunhofer (far-field) regime. Figure 2c shows the results predicted by theory for atoms with a wide range of propagation times. In the extreme Fresnel regime, we recognize the spacelike shadow of the two slits. With increasing $t_d$, the wavepackets start to overlap and interfere until, for large $t_d$, we arrive at the Fraunhofer regime in which the diffraction pattern embodies the momentum-like shadow of the state. In figure 2, experimental measurements of the time-resolved diffraction patterns are shown on both sides of the theoretical plot. On the left, figure 2b corresponds to a distance $d$ = 195 cm, the Fraunhofer regime for slow atoms. It shows nicely a resolved interference pattern that corresponds to the momentum-like shadow. The very fast atoms produce the spacelike shadow of the double slit at the bottom of figure. This measurement corresponds to two separate ranges of propagation times, or view angles, of the quantum state's Wigner distribution. The other view angles are missing because their respective atom velocities are absent from the atomic beam. To fill in these views, a second experiment is performed with the detector screen placed only $d$ = 25 cm behind the double slit. Figure 2d shows the result of this experiment, which features the transition between the spreading individual wavepackets and the overlapping and interference of the slow atoms, in addition to the usual spacelike shadow of the very fast atoms at the bottom.

Figure 3 displays the Wigner distribution that is reconstructed by binning the data according to the different propagation times $t_d$ and performing the inverse Radon transformation. Figure 3a shows the Wigner distribution reconstructed from the $d$ = 25 cm data, and figure 3b shows the Wigner distribution derived from the $d$ = 195 cm data. In both cases, we recognize two positive ridges corresponding to the spatial distribution of the atoms

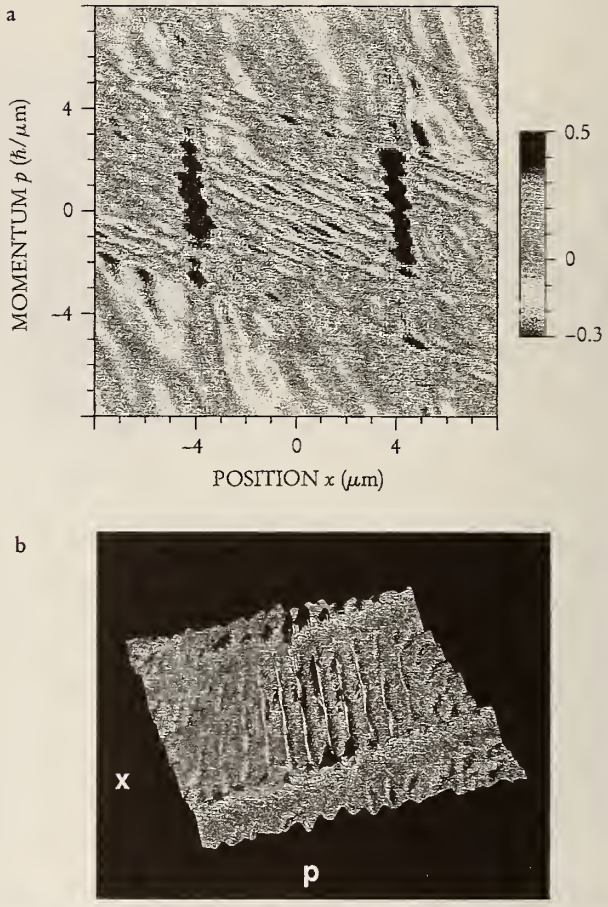


FIGURE 3: RECONSTRUCTED WIGNER DISTRIBUTIONS derived from the experimental data sets shown in figure 2d (corresponding to $d$ = 25 cm) (a) and figure 2b ($d$ = 195 cm) (b). Both reconstructions show the expected two lobes separated by the slit separation of 8 $\mu$m. Between the lobes, the Wigner distribution oscillates between positive and negative values, indicating the spatial coherence and nonclassical character of the state immediately behind the double slit.

immediately behind the double slit. These ridges are separated by 8 $\mu$m—the spacing of the double slit. The coherence between the two spatially separated parts of the wavefunction at the double slit leads to interference, reflected by the oscillations in the Wigner distribution in the region between the ridges. In this region, the reconstructed Wigner distribution assumes negative values, indicating a property that cannot be obtained by classical phase-space distributions and revealing the quantum nature of the observed ensemble of atoms. The reconstructed Wigner distributions, determined from about 500 000 atoms, exhibit all the features of a superposition state expected from an atom interferometer. The measured Wigner distributions differ in some respects from what is theoretically expected, including residual shear and spurious negative regions close to the two largé positive ridges. These artifacts occur primarily because the reconstructions are from an incomplete range of projection angles.

## Quantum mirrors and a trapped atom

To reconstruct the quantum state of motion of a single harmonically trapped atom, we turn to a more direct method that does not require the transformations involved in the tomographic technique described above. Instead,

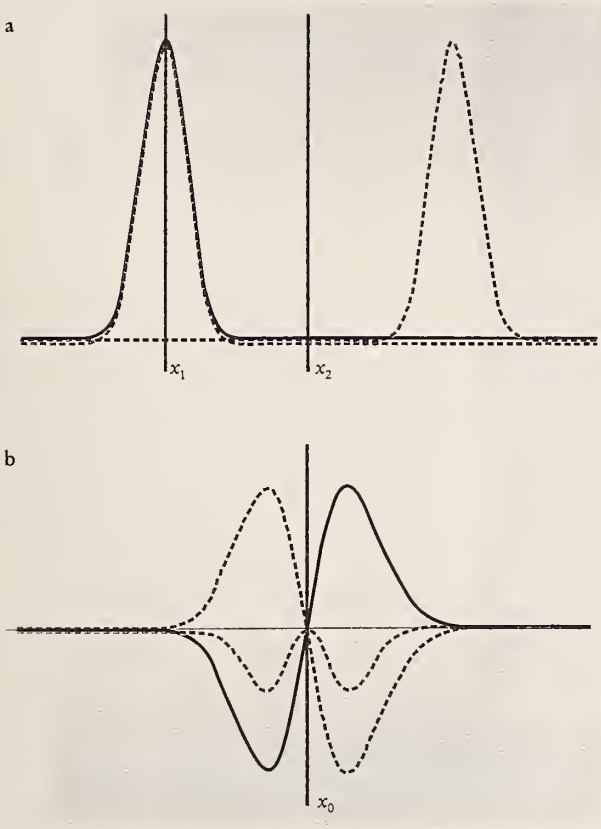


FIGURE 4: THE QUANTUM MIRROR. a: The classical-like case of a localized particle. If the initial wavefunction (solid black line) is mirrored around $x_1$, where the particle is localized, the mirror image (blue dashed line) lies right on top of the original and the overlap is large. If the mirror is at $x_2$, the image (red dashed line) has essentially no overlap with the original. Thus, the overlap is localized like the particle's probability distribution. b: The quantumlike case of a particle with coherent amplitudes in different locations. The wavefunction of the first excited ($n = 1$) energy eigenstate of a harmonic oscillator has a valley and a peak left and right of the origin (solid black line) and exhibits odd parity. Peak and valley are interchanged on the mirror image around $x_0 = 0$ (blue dashed line) and the overlap product of the two functions (dashed green line) is zero or negative everywhere. The value of the Wigner distribution at the origin of phase space is the area of the green curve, and is thus maximally negative for the $n = 1$ state.

the Wigner distribution at a particular point in phase space is extracted directly by performing several different measurements on an identically prepared system. This method is based upon a simple and powerful picture of the Wigner distribution that was first pointed out in 1977 by Antoine Royer.[8]

Suppose we create a mirror image of the wavefunction $\Psi_x(x)$ about the point $x_0$ and then measure the overlap of the mirror image $\mathcal{M}(x_0)\Psi_x(x) = \Psi_x(2x_0 - x)$ with the original $\Psi_x(x)$. Formally, this is a measurement of the expectation value $m$ of the mirror operation $\mathcal{M}$,

$$m(x_0) = \langle\Psi_x|\mathcal{M}(x_0)|\Psi_x\rangle$$

$$= \frac{1}{2}\int ds\, \Psi_x^*\left(x_0 + \frac{s}{2}\right)\Psi_x\left(x_0 - \frac{s}{2}\right). \qquad (3)$$

If $\Psi_x(x)$ is localized around $x_1$, the mirror operation about $x_0 = x_1$ will largely map this area onto itself, resulting in a nonzero overlap. But if we perform the mirror operation about some other point $x_2$—far from $x_1$—the overlap with the original wavefunction will nearly vanish. (See figure 4a.) Thus, we might expect that the observed overlap $m(x_0)$ will be nonzero only for positions $x_0$ where $\Psi_x(x)$ is localized. But now suppose that the wavefunction is localized in two separated regions, centered at $-\tilde{x}$ and $\tilde{x}$. If we perform the mirror operation halfway in between, at $x_0 = 0$, the lobes of the mirrored wavefunction will nearly coincide with the original lobes, resulting in a large overlap. Moreover, the overlap will contain information about the phase difference between the original and mirrored wavefunction. For instance, in figure 4b, the two pieces of the wavefunction are 180° out of phase (a mountain and a valley), resulting in a negative value of the overlap between the wavefunction and its image.

Returning to equation 3, we note that the mirror expectation $m(x_0)$ is proportional to the Wigner distribution at zero momentum $W(x_0, 0)$. If the mirror operation could be performed about the phase-space coordinates $(x_0, p_0)$, we might hope the Wigner distribution $W(x_0, p_0)$ could be extracted directly from a measurement of this modified overlap. Royer made this connection and saw that the mirror operator about the origin of phase space is just the parity operator $\Pi$. Therefore the Wigner distribution at $(x_0, p_0)$ can be interpreted as the expectation of the displaced parity operator,

$$W(x_0, p_0) = \frac{1}{\pi}\langle\Psi|\mathcal{D}^\dagger(-x_0, -p_0)\,\Pi\,\mathcal{D}(-x_0, -p_0)|\Psi\rangle\,, \qquad (4)$$

where $\mathcal{D}(x, p)$ is the coherent displacement operator, which displaces a state across phase space by an amount $(x, p)$ or, equivalently, shifts the origin of phase space from $(0, 0)$ to $(-x, -p)$.[9] The examples of figure 4 illustrate the connection between the overlap of wavefunction mirrors and the Wigner distribution, and figure 4b highlights a particular case in which the Wigner distribution can take on its peculiar negative values. These negative values occur only when the wavefunction is nonlocally distributed, thereby highlighting the nonclassical or delocalized features of the quantum state.

In experiments conducted by David Wineland's group at the National Institute of Standards and Technology in Boulder, Colorado,[10] a single $^9Be^+$ ion is confined in a radio frequency (Paul) ion trap. The trapping potential is well characterized by a three-dimensional anisotropic harmonic oscillator. We describe the measurement of the Wigner distribution for motion in one of the dimensions, characterized by the ladder of energy eigenstates $|n\rangle$ of energy $(n + \frac{1}{2})\hbar\omega$, where $n = 0, 1, 2, \ldots$, and $\omega/2\pi \approx 11$ MHz is the harmonic oscillation frequency. To reconstruct $W(x_0, p_0)$ in this system, the same quantum state must be prepared over and over. First, the ion is initialized in the harmonic oscillator ground state by laser cooling. (See the article by Wineland and Wayne Itano in PHYSICS TODAY, June 1987, page 34.) Next, a particular motional state is prepared in a controlled fashion by applying laser pulses and RF fields. A variety of harmonic oscillator states can be created, including thermal, coherent, squeezed and energy eigenstates (number states),[11] and superpositions of these types of states, including "Schrödinger's cat" states.[12] The relative phases of these states of motion can be controlled by the stable relative phases of the laser and RF fields used in their creation.

The quantum mirror measurement of the Wigner distribution requires two ingredients: a coherent displacement of the state (equivalent to a displacement of the phase-space origin), and a way to determine the expectation value of the parity operator of this displaced state.

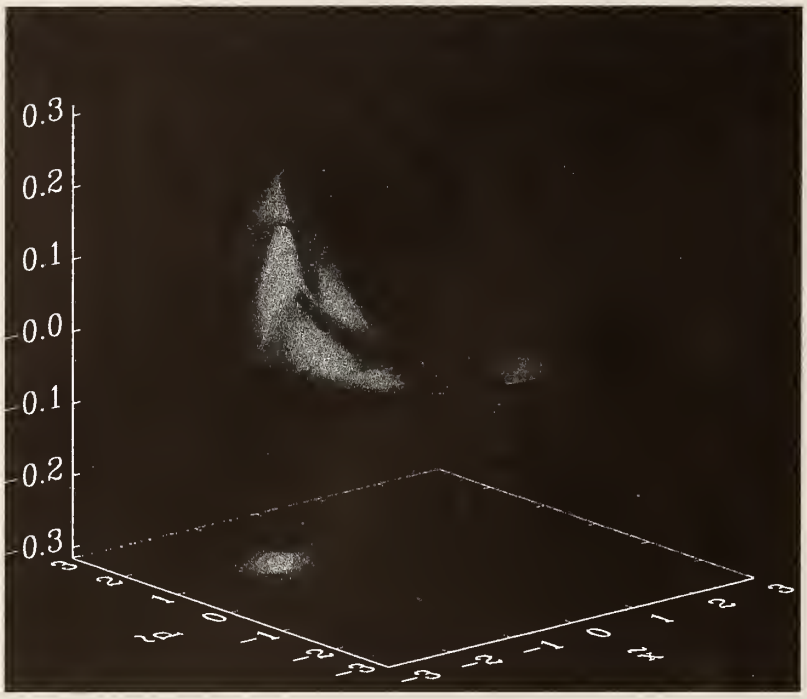


FIGURE 5: A CLASSICAL-LIKE COHERENT STATE of a harmonic oscillator (in this case an ion of mass $m$ in a trap) produces this experimentally reconstructed Wigner distribution. The ion's coordinates of position $x$ and momentum $p$ are scaled to $x' = x\sqrt{m\omega/\hbar}$ and $p' = p/\sqrt{m\hbar\omega}$ and further transformed to a frame $(\tilde{x}, \tilde{p})$ that rotates at the harmonic trap frequency $\omega$, in which the Wigner distribution is stationary. The center of gravity is about 2 scaled units from the origin, and the roughly circular Gaussian shape has nearly the minimum uncertainty width allowed by the Heisenberg uncertainty relationship ($\Delta\tilde{x}\Delta\tilde{p} \approx \frac{1}{2}$).

The displacement operator is achieved by applying an oscillating (resonant) electric field, which couples to the ion's harmonic motion, similar to pushing (or stopping) a child on a swing. In principle, the state can be coherently displaced by any amount $(x_0, p_0)$ in phase space by varying the amplitude of the applied field and its phase with respect to that of the initial state of motion. The expectation value of the parity operator after the displacement can be determined by measuring the populations of energy eigenstates, which, for a harmonic oscillator, are also parity eigenstates. That is, states $|n\rangle$ with an even or odd number of energy quanta $n$ have even or odd parity, respectively. Therefore, the expectation of the parity operator can be deduced by simply measuring the probability distribution $P_n(x_0, p_0)$ of energy eigenstates of the displaced state and performing an alternating sum over these probabilities. Substituting this result in equation 4, we find that the Wigner distribution is

$$W(x_0, p_0) = \frac{1}{\pi} \sum_{n=0}^{\infty} (-1)^n P_n(x_0, p_0) . \qquad (5)$$

The measurement of the motional state occupation probabilities $P_n(x_0, p_0)$ is tricky, because it is very difficult to detect a single ion's motion directly. Instead, features of the motional state are encoded onto two internal electronic (hyperfine) levels of the ion, labeled $|\downarrow\rangle$ and $|\uparrow\rangle$. The occupation of these states can be detected with nearly 100% quantum efficiency by applying laser radiation that connects one of the hyperfine levels (say $|\downarrow\rangle$) to an excited electronic state. If the ion is in state $|\downarrow\rangle$, it scatters thousands of photons, an event that can easily be detected. If, on the other hand, the ion is in state $|\uparrow\rangle$, essentially no photons will be scattered.[13] To encode the motional states onto the internal states of the ion, a "mapping interaction" is realized with laser beams. For an appropriate tuning of the lasers, the external motion is coupled to the internal hyperfine levels, and energy is periodically exchanged between the two systems, similarly to energy exchange between two coupled pendulums. The exchange frequency (or Rabi frequency) $\Omega_n$ between $|\downarrow\rangle$ and $|\uparrow\rangle$ due to this mapping interaction is different for each motional eigenstate $|n\rangle$, and if the atom is initially in state $|\downarrow\rangle$, after the mapping interaction is applied for a time $\tau$, its probability of being in state $|\downarrow\rangle$ is[11]

$$P_{\downarrow}(\tau) = \sum_{n=0}^{\infty} P_n(x_0, p_0) \cos^2(\Omega_n \tau) . \qquad (6)$$

This whole process—initial state preparation, displacement by $(x_0, p_0)$, mapping interaction for time $\tau$, measurement of $P_{\downarrow}(\tau)$—is repeated for different values of interaction time $\tau$. The motional probabilities $P_n(x_0, p_0)$ are then extracted from equation 6 by Fourier transforming the measured $P_{\downarrow}(\tau)$ at the known frequencies $\Omega_n$.

Figure 5 shows the reconstructed Wigner distribution for the single trapped ion in a classical-like coherent state, which is simply a wavepacket oscillating in the harmonic potential without changing shape. In the laboratory frame, the Wigner distribution rotates in phase space at the harmonic trap frequency $\omega$, but here the reconstruction is performed in the rotating frame (rotating in phase space), where $W(x, p)$ is stationary. Within the limits of experimental uncertainty, the reconstructed Wigner distribution is positive everywhere and the nearly Gaussian hump has a width close to the Heisenberg limit, which is $\Delta\tilde{x}\,\Delta\tilde{p} \approx \frac{1}{2}$ in the scaled coordinates (this is most obvious in the contour plot at the bottom of the figure).

Figure 6 shows the reconstructed Wigner distribution of the first excited energy eigenstate of the harmonic oscillator (that is, the $n = 1$ Fock state). Although Fock states of the harmonic oscillator are treated in every introductory quantum mechanics textbook, the NIST experiments represent the first time Fock states (other than the $n = 0$ ground state) have been created on demand and fully characterized. (In many quantum optics experiments, single-photon states have been produced using down-conversion, but such states are not created on demand—they occur at random moments in a nonlinear crystal—and their mode identity is not well defined.) In accord with the nonclassical nature of this state, the Wigner distribution is negative around the origin. The experimental reconstruction in the figure reaches approximately −0.25 at the origin of phase space, not far from the theoretical value of $-1/\pi$, which is in fact the largest negative value the Wigner distribution (as defined in

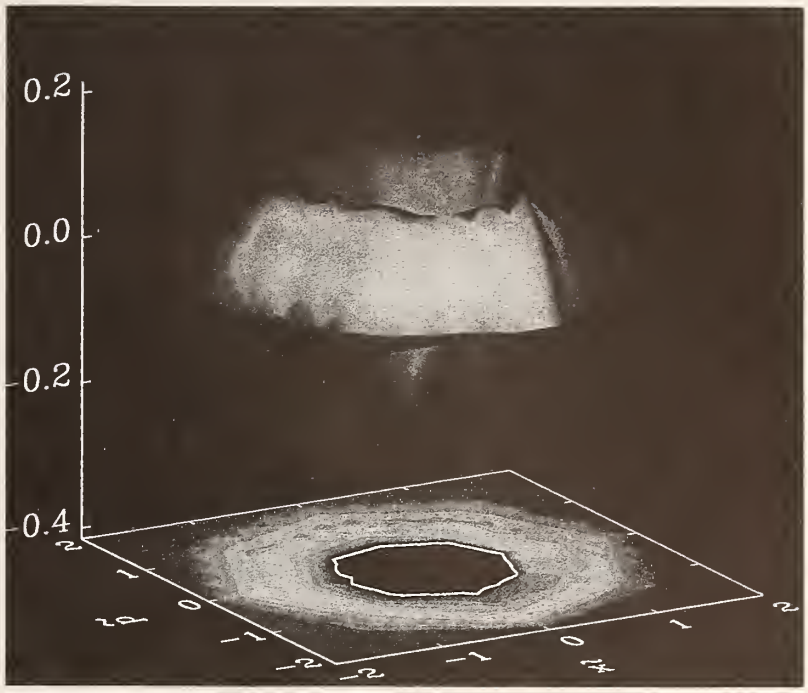


FIGURE 6: THE FIRST EXCITED ENERGY eigenstate of a harmonic oscillator produces this experimentally reconstructed Wigner distribution. The coordinates $\bar{x}$ and $\bar{p}$ are scaled and in a rotating frame, as in figure 5. Because energy and phase are complementary, the measured function is nearly rotationally symmetric, providing no phase information. The measured values of the Wigner distribution near the origin are negative and reach a minimum value of about −0.25 at the origin. This is close to the largest negative value possible ($-1/\pi$) for a Wigner distribution.

equation 1) can reach in any physical system. Discrepancies with respect to theory can be traced to slight imperfections in the preparation and are not surprising, considering the stability required of the experimental parameters—the reconstructions are the result of about 24 million preparations of the same state. Nevertheless, the reconstructed Wigner distributions correspond very closely to that of a pure quantum state.

## Applications for quantum trickery

The Wigner distribution $W(x, p)$ corresponds most closely to the idea of a phase-space probability distribution in quantum mechanics, making it a useful tool for characterizing quantum states. We've seen that the Wigner distribution is not a real probability distribution, because certain joint events (such as simultaneous position and momentum states) are inaccessible. Localized negative values of $W(x, p)$ emphasize this fact. To make a connection between the quantum Wigner distribution and the "negative probabilities" derived in table 3 for flipping coins in a black box, we're tempted to identify the joker in the black box as Heisenberg himself, who somehow knows what is to be measured each time, and changes the results of the coin tosses accordingly. And yet, in a sense, quantum mechanics is stranger still than this picture, for the wavefunction or the Wigner distribution ensures the consistency of different measurements without any need for such a trickster behind the scenes.

The recent experiments we have discussed, in which quantum states of matter waves have been reconstructed by mapping their Wigner distributions, were made possible by advances in quantum state preparation and manipulation. These newly developed measurement techniques have abundant future applications. For instance, in the fields of quantum control and quantum computing, these techniques could be extended to provide a complete picture of the evolution of a quantum logic gate. Control and diagnostics of an atomic beam at the quantum level might be a helpful tool in deposition techniques reaching quantum-limited resolution. An intriguing prospect would be to reconstruct the output state of laserlike sources of atoms that might evolve from the current research in Bose–Einstein condensates of dilute gases. A fundamental application of these techniques will be the study of quantum decoherence. The reconstruction of a quantum state as it loses coherence may someday shed light on the elusive mechanisms at work when a wavefunction "collapses."

*We thank our coworkers David Wineland, Wayne Itano, Dawn Meekhof and Brian King at NIST; and Christian Kurtsiefer, Martin Wilkens, Ulf Janicke and Jürgen Mlynek at the University of Konstanz. We give special thanks to Ben Stein of the American Institute of Physics for suggesting this article and Matt Young at NIST for carefully reading the manuscript. The work at NIST was supported by the National Security Agency, the Army Research Office and the Office of Naval Research. One of us (Leibfried) acknowledges a German Research Foundation (DFG) research grant. The work at the University of Konstanz was supported by the DFG.*

## References

1. This example was inspired by an article by R. P. Feynman, "Negative Probabilities," in *Quantum Implications: Essays in Honor of David Bohm*, B. J. Hiley, F. D. Peat, eds., Routledge & Kegan Paul, London (1987), p. 235. See also R. P. Feynman, Int. J. Theor. Phys. **21**, 467 (1982).
2. E. P. Wigner, Phys. Rev. **40**, 749 (1932).
3. For general references on this subject, see Ulf Leonhardt, *Measuring the Quantum State of Light*, Cambridge U. P., New York (1997). M. G. Raymer, Contemp. Physics **38**, 343 (1997). W. P. Schleich, M. G. Raymer, eds., special issue of J. Mod. Opt., **44**, no. 11/12 (1997).
4. D. T. Smithey, M. Beck, M. G. Raymer, A. Faridani, Phys. Rev. Lett. **70**, 1244 (1993).
5. T. J. Dunn, I. A. Walmsley, S. Mukamel, Phys. Rev. Lett. **74**, 884 (1995).
6. M. G. Raymer, M. Beck, D. F. McAlister, Phys. Rev. Lett. **72**, 1137 (1994). U. Janicke, M. Wilkens, J. Mod. Opt. **42**, 2183 (1995).
7. C. Kurtsiefer, T. Pfau, J. Mlynek, Nature **386**, 150 (1997).
8. A. Royer, Phys. Rev. A **15**, 449 (1977).
9. R. J. Glauber, Phys. Rev. **131**, 2766 (1963).
10. D. Leibfried, D. M. Meekhof, B. E. King, C. Monroe, W. M. Itano, D. J. Wineland, Phys. Rev. Lett. **77**, 4281 (1996).
11. D. M. Meekhof, C. Monroe, B. E. King, W. M. Itano, D. J. Wineland, Phys. Rev. Lett. **76**, 1796 (1996).
12. C. Monroe, D. M. Meekhof, B. E. King, D. J. Wineland, Science **272**, 1131 (1996).
13. R. Blatt, P. Zoller, Eur. J. Phys. **9**, 250 (1988). ■

# Complementarity and Young's interference fringes from two atoms

W. M. Itano, J. C. Bergquist, J. J. Bollinger, and D. J. Wineland
*Time and Frequency Division, National Institute of Standards and Technology, Boulder, Colorado 80303*

U. Eichmann
*Max-Born-Institut for Non-linear Optics and Short Pulse Spectroscopy, Rudower Chaussee 6, 12489 Berlin, Germany*

M. G. Raizen
*Department of Physics, University of Texas, Austin, Texas 78712*
(Received 18 November 1997)

The interference pattern of the resonance fluorescence from a $J=1/2$ to $J=1/2$ transition of two identical atoms confined in a three-dimensional harmonic potential is calculated. The thermal motion of the atoms is included. Agreement is obtained with experiments [U. Eichmann *et al.*, Phys. Rev. Lett. **70**, 2359 (1993)]. Contrary to some theoretical predictions, but in agreement with the present calculations, a fringe visibility greater than 50% can be observed with polarization-selective detection. The dependence of the fringe visibility on polarization has a simple interpretation, based on whether or not it is possible in principle to determine which atom emitted the photon. [S1050-2947(98)01606-0]

PACS number(s): 03.65.Bz, 32.80.Pj, 42.50.Ct

## I. INTRODUCTION

Many variants of two-slit interference experiments, often "thought experiments," have been used to illustrate fundamental principles of quantum mechanics. Recently, Eichmann *et al.* [1] have observed interference fringes in the resonance fluorescence of two trapped ions, analogous to those seen in Young's two-slit experiment. Of particular interest was the fact that the interference fringes appeared when it was impossible in principle to determine which ion scattered the photon and disappeared when it was possible to do so. This is in agreement with Bohr's principle of complementarity, which requires that the wave nature of the photon (the interference fringes) cannot be observed under the same conditions as its particle nature (the possibility of assigning to the photon a trajectory that intersects just one of the ions). In contrast to many thought experiments [2], the disappearance of the fringes when the path of the particle can be determined cannot be understood in terms of random classical momentum kicks. The experiment contains features from some thought experiments of Scully and Drühl [3], regarding the interference of light scattered by two multilevel atoms.

Recently, controversy has arisen over the mechanism by which complementarity is enforced in a two-slit interference experiment. Some claim that the destruction of interference by a determination of the particle's path is *always* due to a random momentum transfer necessitated by the indeterminacy relations [4–6]. Others claim that the mere *existence* of the path information can be sufficient to destroy the interference [7]. Englert *et al.* claim that the experiment of Eichmann *et al.* supports the second position [8].

Published calculations explain some aspects of the observations of Eichmann *et al.* [9–13]. However, none of those calculations include all of the factors required to make a comparison with the experimental data. Here we calculate the scattering cross section for arbitrary directions and polarizations of the incident and outgoing light. While the results were used in the analysis of the data in Ref. [1], the details of the calculations were not given. The main limitation of the calculation is the use of perturbation theory, so that it is valid only for low light intensities. However, it includes the effect of thermal motion more precisely than has been done elsewhere, taking into account the actual normal modes of the system. Also, the actual experimental geometry is fully taken into account, which is not always the case in the other calculations.

Finally, we clarify the sense in which the loss of the fringe visibility [defined as $(I_{\max}-I_{\min})/(I_{\max}+I_{\min})$] for certain detected polarizations is due to the existence of "which path" information in the ions. This is an application of the fundamental quantum principle that transition amplitudes are to be added before squaring if and only if they connect the same initial and final states.

## II. EXPERIMENT

The experimental apparatus has been described previously [1,14]. Figure 1 shows the geometry. Two $^{198}Hg^+$ ions were confined in a linear Paul (rf) trap by a combination of static and rf electric fields. The ions were laser cooled to temperatures of a few mK with a beam of linearly polarized, continuous-wave light, nearly resonant with the 194-nm transition from the ground $6s\ ^2S_{1/2}$ level to the $6p\ ^2P_{1/2}$ level. The laser beam diameter was about 50 $\mu$m and the power was 50 $\mu$W or less. The same beam was the coherent source for Young's interference. Cooling in the trap resulted in strong localization of the ions, which was essential for observation of interference fringes. The trap potentials were arranged so that a pair of ions would be oriented along the symmetry ($Z$) axis of the trap. The incoming photons, with wave vector $\mathbf{k}_{\rm in}$ and polarization vector $\hat{\boldsymbol{\epsilon}}_{\rm in}$, made an angle $\Theta$ of 62° with respect to the $Z$ axis. The $X$ axis is oriented so that the $X$-$Z$ plane contains $\mathbf{k}_{\rm in}$. Light emitted by the ions was collimated by a lens and directed to the surface of an

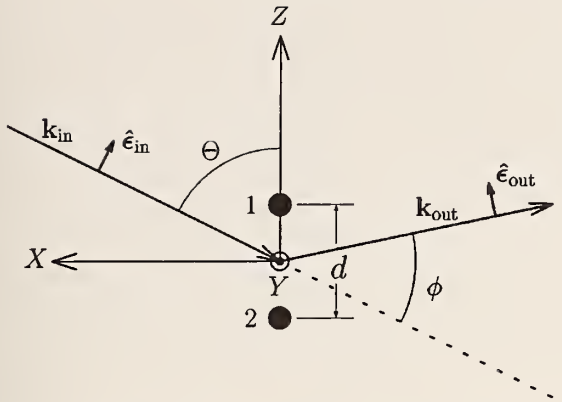


FIG. 1. Geometry of Young's interference experiment, projected onto the $X$-$Z$ plane. The equilibrium positions of the two ions, represented by the filled circles, lie along the $Z$ axis. The wave vector $\mathbf{k}_{in}$ of the incoming photon is in the $X$-$Z$ plane, making an angle $\Theta$ with the $Z$ axis. The $Y$ axis is out of the plane of the figure. The projection of the wave vector $\mathbf{k}_{out}$ onto the $X$-$Z$ plane makes an angle $\phi$ with $\mathbf{k}_{in}$. The angle that $\mathbf{k}_{out}$ deviates from the $X$-$Z$ plane in the $+Y$ direction is $\Phi$ (not shown). The polarization vectors of the incoming and outgoing photons are $\hat{\epsilon}_{in}$ and $\hat{\epsilon}_{out}$.

imaging photodetector, which was used to observe the fringes. The wave vector and polarization of an outgoing photon are $\mathbf{k}_{out}$ and $\hat{\epsilon}_{out}$. The projection of $\mathbf{k}_{out}$ onto the $X$-$Z$ plane makes an angle $\phi$ with respect to $\mathbf{k}_{in}$. The deviation of $\mathbf{k}_{out}$ from the $X$-$Z$ plane in the $+Y$ direction is $\Phi$ (not shown in Fig. 1). The sensitive area of the photodetector included a range of $\phi$ from about 15° to 45° and a range of $\Phi$ from about −15° to +15°. For polarization-selective detection, a glass plate oriented at Brewster's angle was placed in the detection path so that nearly all of the light with $\hat{\epsilon}_{out}$ in the $X$-$Z$ plane was transmitted into the glass, while some of the light polarized along the $Y$ axis was reflected to the imaging detector. The input polarization $\hat{\epsilon}_{in}$ was varied. Another lens system formed a real image of the ions on a second imaging detector. This image was used to determine when there were precisely two ions in the trap.

## III. TWO-ION HARMONIC-OSCILLATOR SYSTEM

In the pseudopotential approximation, the Hamiltonian for the translational motion of the two ions in the harmonic trap is

$$H_{\text{trans}}=\frac{\mathbf{P}_1^2}{2m}+\frac{\mathbf{P}_2^2}{2m}+V(\mathbf{R}_1)+V(\mathbf{R}_2)+\frac{e^2}{4\pi\epsilon_0|\mathbf{R}_1-\mathbf{R}_2|}, \tag{1}$$

where $\mathbf{R}_i$ and $\mathbf{P}_i$ are the position and momentum of the $i$th ion, $e$ and $m$ are the charge and mass of an ion, and

$$V(\mathbf{R})\equiv\frac{1}{2}m\omega_R^2(X^2+Y^2)+\frac{1}{2}m\omega_Z^2Z^2 \tag{2}$$

is the potential energy of a single ion in the trap. In Eq. (2) we have made the approximation that the trap pseudopotential is cylindrically symmetric. Here $\mathbf{R}=(X,Y,Z)$, in the Cartesian coordinate system shown in Fig. 1. The classical

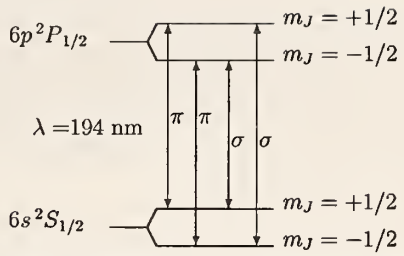


FIG. 2. Zeeman sublevels involved in the 194-nm, $6s\ ^2S_{1/2}$ to $6p\ ^2P_{1/2}$ transition of $^{198}Hg^+$. The allowed $\pi$ and $\sigma$ transitions are labeled. The Zeeman splitting of the levels is exaggerated.

equilibrium positions of the ions, found by minimizing the total potential energy, are $\mathbf{R}_1^0=(d/2)\hat{\mathbf{Z}}$ and $\mathbf{R}_2^0=-(d/2)\hat{\mathbf{Z}}$, where $d=(e^2/2\pi\epsilon_0 m\omega_Z^2)^{1/3}$, and it is assumed that $\omega_R>\omega_Z$.

For small displacements $\mathbf{u}_1=\mathbf{R}_1-\mathbf{R}_1^0$ and $\mathbf{u}_2=\mathbf{R}_2-\mathbf{R}_2^0$ about the equilibrium positions, a harmonic approximation can be made. The Hamiltonian separates into terms involving either center-of-mass (c.m.) or relative coordinates and momenta defined by

$$\begin{aligned}\mathbf{u}^{\text{c.m.}}&\equiv(\mathbf{u}_1+\mathbf{u}_2)/2,\\ \mathbf{u}^{\text{rel}}&\equiv(\mathbf{u}_1-\mathbf{u}_2)/2,\\ \mathbf{P}^{\text{c.m.}}&\equiv\mathbf{P}_1+\mathbf{P}_2,\\ \mathbf{P}^{\text{rel}}&\equiv\mathbf{P}_1-\mathbf{P}_2.\end{aligned} \tag{3}$$

The translational Hamiltonian, in the harmonic approximation, is

$$\begin{aligned}H_{\text{trans}}=&\hbar\omega_Z(N_Z^{\text{c.m.}}+1/2)+\hbar\omega_R(N_X^{\text{c.m.}}+N_Y^{\text{c.m.}}+1)\\&+\hbar\omega_S(N_Z^{\text{rel}}+1/2)+\hbar\omega_T(N_X^{\text{rel}}+N_Y^{\text{rel}}+1).\end{aligned} \tag{4}$$

The number operators are defined in the usual way by $N_i^{\text{c.m.}}\equiv(a_i^{\text{c.m.}})^\dagger a_i^{\text{c.m.}}$ and $N_i^{\text{rel}}\equiv(a_i^{\text{rel}})^\dagger a_i^{\text{rel}}$ for $i=X,Y,Z$. The annihilation operators are defined in the usual way, for example,

$$a_Z^{\text{c.m.}}\equiv\sqrt{\frac{m\omega_Z}{\hbar}}u_Z^{\text{c.m.}}+\frac{i}{\sqrt{4\hbar m\omega_Z}}P_Z^{\text{c.m.}}. \tag{5}$$

The three center-of-mass modes have the same frequencies as those of a single ion in the trap: $\omega_Z$ and $\omega_R$. The three relative modes include a symmetric stretch mode along the $Z$ direction at frequency $\omega_S=\sqrt{3}\omega_Z$ and two tilting or rocking modes along the $X$ and $Y$ directions at frequency $\omega_T=(\omega_R^2-\omega_Z^2)^{1/2}$. The eigenstates of $H_{\text{trans}}$ are the simultaneous eigenstates of the set of number operators $|n_X^{\text{c.m.}},n_Y^{\text{c.m.}},n_Z^{\text{c.m.}},n_X^{\text{rel}},n_Y^{\text{rel}},n_Z^{\text{rel}}\rangle$ with eigenvalues $\hbar[\omega_Z(n_Z^{\text{c.m.}}+1/2)+\omega_R(n_X^{\text{c.m.}}+n_Y^{\text{c.m.}}+1)+\omega_S(n_Z^{\text{rel}}+1/2)+\omega_T(n_X^{\text{rel}}+n_Y^{\text{rel}}+1)]$.

## IV. ATOMIC LEVEL STRUCTURE

Figure 2 shows the magnetic sublevels involved in the $6s\ ^2S_{1/2}$ to $6p\ ^2P_{1/2}$ transition. These levels form an approximately closed system since the probability that the $6p\ ^2P_{1/2}$

level radiatively decays to the $5d^9 6s^2\ ^2D_{3/2}$ level is only $1.4\times10^{-7}$ [15]. The rest of the time it returns to the ground $6s\ ^2S_{1/2}$ level. The $5d^9 6s^2\ ^2D_{3/2}$ level has a lifetime of 9-ms and decays with about equal probability to the ground level or to the $5d^9 6s^2\ ^2D_{5/2}$, which has a lifetime of 86-ms and decays only to the ground level.

Since the static magnetic field is small, we are free to define the quantization axis of the ions to be along the electric polarization vector $\hat{\boldsymbol{\epsilon}}_{\rm in}$ of the incident light. If the static magnetic field is along some other direction, then the Zeeman sublevels defined according to the electric polarization vector are not stationary states. This does not change the analysis as long as the Zeeman precession frequency is much less than the inverse of the scattering time, which is approximately equal to the $6p\ ^2P_{1/2}$ state lifetime (2.3 ns). In the experiments described here, the magnetic field was small enough that this was always the case.

Figure 3 shows a Cartesian coordinate system having its $z$ axis oriented along $\hat{\boldsymbol{\epsilon}}_{\rm in}$. The $x$ axis is parallel to $\mathbf{k}_{\rm in}$. The $y$ axis is defined so that $(x,y,z)$ forms a right-handed coordinate system. This coordinate system is more useful than the trap-oriented $(X,Y,Z)$ coordinate system of Fig. 1 for describing the angular distribution of the scattered light.

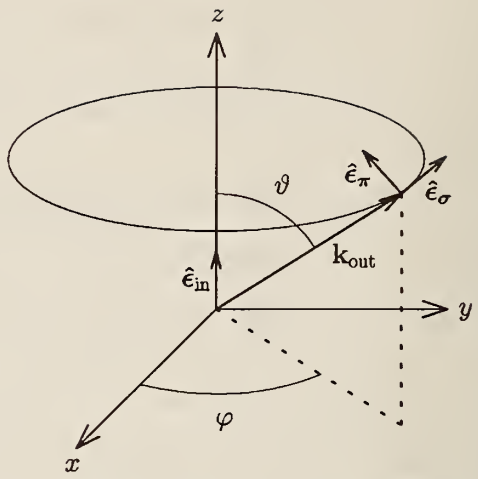


FIG. 3. Coordinate system for description of the direction and polarization of the outgoing photon. The $z$ axis is parallel to $\hat{\boldsymbol{\epsilon}}_{\rm in}$ and the $x$ axis is parallel to $\mathbf{k}_{\rm in}$. The polarization vector $\hat{\boldsymbol{\epsilon}}_\pi$ lies in the plane containing $\hat{\boldsymbol{\epsilon}}_{\rm in}$ and $\mathbf{k}_{\rm out}$, while $\hat{\boldsymbol{\epsilon}}_\sigma$ is perpendicular to that plane.

## V. SCATTERING CROSS SECTION

Consider the process in which two ions, initially in their ground electronic states, absorb a photon having a wave vector $\mathbf{k}_{\rm in}$ and polarization $\hat{\boldsymbol{\epsilon}}_{\rm in}$, emit a photon having a wave vector $\mathbf{k}_{\rm out}$ and polarization $\hat{\boldsymbol{\epsilon}}_{\rm out}$ and are left in their ground electronic states. The ions may change their Zeeman sublevels during the process. Also, the motional state of the two ions may change.

The electric-dipole Hamiltonian that causes the transitions is

$$H_{\rm ED}=-\mathbf{D}_1\cdot\mathbf{E}(\mathbf{R}_1,t)-\mathbf{D}_2\cdot\mathbf{E}(\mathbf{R}_2,t), \tag{6}$$

where $\mathbf{D}_1$ and $\mathbf{D}_2$ are the electric-dipole moment operators for ions 1 and 2 and $\mathbf{E}(\mathbf{R},t)$ is the electric field, consisting of a classical part, representing the incident laser beam, and the quantized free field operator

$$\mathbf{E}(\mathbf{R},t)=\hat{\boldsymbol{\epsilon}}_{\rm in}{\rm Re}\mathcal{E}_0 e^{i\mathbf{k}_{\rm in}\cdot\mathbf{R}-i\omega_{\rm in}t} + \sum_s i\sqrt{\frac{\hbar\omega_s}{2\epsilon_0 V}}[a_s\hat{\boldsymbol{\epsilon}}_s e^{i\mathbf{k}_s\cdot\mathbf{R}}-a_s^\dagger\hat{\boldsymbol{\epsilon}}_s e^{-i\mathbf{k}_s\cdot\mathbf{R}}], \tag{7}$$

where Re denotes the real part, $\mathcal{E}_0$ is the amplitude of the laser electric field, $a_s$ is the annihilation operator for a photon of wave vector $\mathbf{k}_s$, frequency $\omega_s$, and polarization $\boldsymbol{\epsilon}_s$, and $V$ is the quantization volume.

The electric-dipole Hamiltonian, in second-order perturbation theory, gives the cross section for the two ions to scatter a photon in a particular direction:

$$\frac{d\sigma_i}{d\Omega_{\rm out}}=\sum_f C_1\left|\sum_j \frac{\langle\Psi_f|(\mathbf{D}_1\cdot\hat{\boldsymbol{\epsilon}}_{\rm out})e^{-i\mathbf{k}_{\rm out}\cdot\mathbf{R}_1}|\Psi_j\rangle\langle\Psi_j|(\mathbf{D}_1\cdot\hat{\boldsymbol{\epsilon}}_{\rm in})e^{i\mathbf{k}_{\rm in}\cdot\mathbf{R}_1}|\Psi_i\rangle}{\omega_0-\omega_{\rm in}+(E_j-E_i)/\hbar-i\gamma/2} + \sum_j \frac{\langle\Psi_f|(\mathbf{D}_2\cdot\hat{\boldsymbol{\epsilon}}_{\rm out})e^{-i\mathbf{k}_{\rm out}\cdot\mathbf{R}_2}|\Psi_j\rangle\langle\Psi_j|(\mathbf{D}_2\cdot\hat{\boldsymbol{\epsilon}}_{\rm in})e^{i\mathbf{k}_{\rm in}\cdot\mathbf{R}_2}|\Psi_i\rangle}{\omega_0-\omega_{\rm in}+(E_j-E_i)/\hbar-i\gamma/2}\right|^2, \tag{8}$$

where $\omega_{\rm in}=c|\mathbf{k}_{\rm in}|$, $\omega_{\rm out}=c|\mathbf{k}_{\rm out}|$, $\hbar\omega_0$ is the separation between the ground and excited electronic states of an ion, $\gamma$ is the decay rate of the excited state, and $C_1\equiv\omega_{\rm out}^3/16\pi^2c^4\hbar^2\epsilon_0^2$. The initial, final, and intermediate states describing the electronic and motional degrees of freedom of the system are $|\Psi_i\rangle$, $|\Psi_f\rangle$, and $|\Psi_j\rangle$. The energies $E_i$, $E_f$, and $E_j$ are the motional energies of the ions in the initial, final, and intermediate states. They depend on the values of the six harmonic-oscillator quantum numbers, which we denote by $\{n_{\rm HO}\}$. Because of energy conservation, the frequency of the outgoing photon depends on the final state

$$\omega_{\rm out}=\omega_{\rm in}+(E_i-E_f)/\hbar. \tag{9}$$

Thus the scattered light has a discrete frequency spectrum and the different components could, in principle, be detected separately. In Eq. (8) all frequency components are summed,

which is appropriate if the detection is frequency insensitive. The laser frequency is assumed to be nearly resonant with an optical transition in the ion, so that only one intermediate electronic state has to be included in the sums and we can neglect the counterrotating terms. We ignore dipole-dipole interactions between the ions because they were separated by many wavelengths in the experiment. Here we specialize to the case of an ion that has no nuclear spin and has a $^2S_{1/2}$ ground state and a $^2P_{1/2}$ excited state, like the $^{198}Hg^+$ ions used in Ref. [1]. We denote a state in which ion 1 is in the $^2S_{1/2}$, $m_J=+1/2$ state, ion 2 is in the $^2P_{1/2}$, $m_J=-1/2$ state, and has the harmonic-oscillator quantum numbers $\{n_{HO}\}$ by

$$|\Psi\rangle=|(^2S_{1/2},+1/2)_1(^2P_{1/2},-1/2)_2\{n_{HO}\}\rangle. \quad (10)$$

There are four possible sets of initial $m_J$ quantum numbers for the two ions and four possible final sets. There are two basic kinds of scattering processes, those that preserve the $m_J$ quantum numbers of the ions and those that change $m_J$ of one ion. We treat these cases separately. The form of Eq. (8) excludes the possibility of both ions changing their $m_J$ quantum numbers.

**A. Both $m_J$ quantum numbers remain the same ($\pi$ case)**

In order to be definite, we set $m_J=+1/2$ for both ions, both before and after the scattering, that is,

$$|\Psi_i\rangle=|(^2S_{1/2},+1/2)_1(^2S_{1/2},+1/2)_2\{n_{HO}\}_i\rangle, \quad (11)$$

$$|\Psi_f\rangle=|(^2S_{1/2},+1/2)_1(^2S_{1/2},+1/2)_2\{n_{HO}\}_f\rangle. \quad (12)$$

We call this the $\pi$ case because it involves only $\pi$ transitions, that is, transitions that leave $m_J$ unchanged. Because of the electric-dipole selection rules, the only intermediate states that contribute nonzero terms are of the form

$$|\Psi_j\rangle=|(^2P_{1/2},+1/2)_1(^2S_{1/2},+1/2)_2\{n_{HO}\}_j\rangle \quad (13)$$

for the first sum and

$$|\Psi_j\rangle=|(^2S_{1/2},+1/2)_1(^2P_{1/2},+1/2)_2\{n_{HO}\}_j\rangle \quad (14)$$

for the second sum. The matrix elements connecting the initial states to the intermediate states are

$$\langle\Psi_j|(\mathbf{D}_p\cdot\hat{\boldsymbol{\epsilon}}_{in})e^{i\mathbf{k}_{in}\cdot\mathbf{R}_p}|\Psi_i\rangle=\langle(^2P_{1/2},+1/2)_p|D_{pz}|(^2S_{1/2},+1/2)_p\rangle\langle\{n_{HO}\}_j|e^{i\mathbf{k}_{in}\cdot\mathbf{R}_p}|\{n_{HO}\}_i\rangle$$

$$=\frac{1}{\sqrt{6}}(^2P_{1/2}\|D^{(1)}\|^2S_{1/2})\langle\{n_{HO}\}_j|e^{i\mathbf{k}_{in}\cdot\mathbf{R}_p}|\{n_{HO}\}_i\rangle, \quad (15)$$

where $p=1$ or 2, $D_{pz}$ is the $z$ component of the $\mathbf{D}_p$ operator, and $(^2P_{1/2}\|D^{(1)}\|^2S_{1/2})$ is the reduced matrix element of the dipole moment operator (the same for both ions).

The angular distribution of the outgoing photon is contained in the matrix elements connecting the intermediate states to the final states. The unit propagation vector for the outgoing photon is

$$\hat{\mathbf{k}}_{out}=(\sin\vartheta\cos\varphi,\sin\vartheta\sin\varphi,\cos\vartheta), \quad (16)$$

where $\vartheta$ and $\varphi$ are spherical polar angles with respect to the $(x,y,z)$ coordinate system of Fig. 3. The polarization vector $\hat{\boldsymbol{\epsilon}}_{out}$ must be perpendicular to $\hat{\mathbf{k}}_{out}$. We define two mutually orthogonal unit polarization vectors, both perpendicular to $\hat{\mathbf{k}}_{out}$, by

$$\hat{\boldsymbol{\epsilon}}_\pi=(-\cos\vartheta\cos\varphi,-\cos\vartheta\sin\varphi,\sin\vartheta) \quad (17)$$

and

$$\hat{\boldsymbol{\epsilon}}_\sigma=(-\sin\varphi,\cos\varphi,0). \quad (18)$$

Since only the $z$ components of $\mathbf{D}_1$ and $\mathbf{D}_2$ contribute to the matrix elements connecting the intermediate and final states for this case, light with polarization vector $\hat{\boldsymbol{\epsilon}}_\sigma$ cannot be emitted.

With the choice of $\hat{\boldsymbol{\epsilon}}_{out}=\hat{\boldsymbol{\epsilon}}_\pi$, the matrix elements connecting the intermediate states to the final states are

$$\langle\Psi_f|(\mathbf{D}_p\cdot\hat{\boldsymbol{\epsilon}}_\pi)e^{-i\mathbf{k}_{out}\cdot\mathbf{R}_p}|\Psi_j\rangle=\sin\vartheta\langle(^2S_{1/2},+1/2)_p|D_{pz}|(^2P_{1/2},+1/2)_p\rangle\langle\{n_{HO}\}_f|e^{-i\mathbf{k}_{out}\cdot\mathbf{R}_p}|\{n_{HO}\}_j\rangle$$

$$=\frac{\sin\vartheta}{\sqrt{6}}(^2S_{1/2}\|D^{(1)}\|^2P_{1/2})\langle\{n_{HO}\}_f|e^{-i\mathbf{k}_{out}\cdot\mathbf{R}_p}|\{n_{HO}\}_j\rangle. \quad (19)$$

Equation (8) for the cross section becomes

$$\frac{d\sigma^{(1)}}{d\Omega_{\rm out}}=\frac{\sin^2\vartheta}{36}|(^2S_{1/2}\|D^{(1)}\|^2P_{1/2})|^4\sum_f C_1\left|\sum_j \frac{\langle\{n_{\rm HO}\}_f|e^{-i\mathbf{k}_{\rm out}\cdot\mathbf{R}_1}|\{n_{\rm HO}\}_j\rangle\langle\{n_{\rm HO}\}_j|e^{i\mathbf{k}_{\rm in}\cdot\mathbf{R}_1}|\{n_{\rm HO}\}_i\rangle}{\omega_0-\omega_{\rm in}+(E_j-E_i)/\hbar-i\gamma/2}\right.$$
$$\left.+\sum_j \frac{\langle\{n_{\rm HO}\}_f|e^{-i\mathbf{k}_{\rm out}\cdot\mathbf{R}_2}|\{n_{\rm HO}\}_j\rangle\langle\{n_{\rm HO}\}_j|e^{i\mathbf{k}_{\rm in}\cdot\mathbf{R}_2}|\{n_{\rm HO}\}_i\rangle}{\omega_0-\omega_{\rm in}+(E_j-E_i)/\hbar-i\gamma/2}\right|^2. \tag{20}$$

The (1) superscript on the cross section is to label it as the $\pi$ case. The same result would have been obtained for any of the other three possible sets of initial $m_J$ quantum numbers, so this is the general result for the case in which the $m_J$ values do not change. The presence of two terms in Eq. (20), which are added and then squared, is the source of Young's interference fringes. These two terms can be identified with the two possible paths for the photon, each intersecting one of the two ions.

The sums over intermediate harmonic-oscillator states can be done by closure if the energy denominators are constant. While they are not constant, because $E_j-E_i$ varies, it can be shown (see, for example, Ref. [16]) that the main contributions to the sum come from terms where $|E_j-E_i|$ is less than or on the order of $\sqrt{RE_i}$, where $R$ is the photon recoil energy $(\hbar k_{\rm out})^2/2m$. For the $Hg^+$ 194.2-nm transition, $R=h\times 26.7$ kHz. For Doppler cooling, $E_i$ will be on the order of $\hbar\gamma$, where, for this transition, $\hbar\gamma=h\times 70$ MHz. Thus the rms value of $E_j-E_i$ will be on the order of $h\times 1.4$ MHz, which is much less than $\hbar\gamma/2$. Therefore, while the denominators are not strictly constant, they are nearly constant for the terms that contribute significantly to the sums.

If we neglect $(E_j-E_i)/\hbar$ compared to $\gamma/2$ and use closure to evaluate the sums, Eq. (20) simplifies to

$$\frac{d\sigma^{(1)}}{d\Omega_{\rm out}}=\frac{\sin^2\vartheta}{36}\frac{|(^2S_{1/2}\|D^{(1)}\|^2P_{1/2})|^4}{(\omega_0-\omega_{\rm in})^2+\gamma^2/4}\sum_f C_1|\langle\{n_{\rm HO}\}_f|e^{-i\mathbf{k}_{\rm out}\cdot\mathbf{R}_1}e^{i\mathbf{k}_{\rm in}\cdot\mathbf{R}_1}|\{n_{\rm HO}\}_i\rangle+\langle\{n_{\rm HO}\}_f|e^{-i\mathbf{k}_{\rm out}\cdot\mathbf{R}_2}e^{i\mathbf{k}_{\rm in}\cdot\mathbf{R}_2}|\{n_{\rm HO}\}_i\rangle|^2$$
$$=\frac{\sin^2\vartheta}{36}\frac{(^2S_{1/2}\|D^{(1)}\|^2P_{1/2})|^4}{(\omega_0-\omega_{\rm in})^2+\gamma^2/4}\sum_f C_1|\langle\{n_{\rm HO}\}_f|e^{-i\mathbf{q}\cdot\mathbf{R}_1}|\{n_{\rm HO}\}_i\rangle+\langle\{n_{\rm HO}\}_f|e^{-i\mathbf{q}\cdot\mathbf{R}_2}|\{n_{\rm HO}\}_i\rangle|^2$$
$$=\frac{\sin^2\vartheta}{36}\frac{|(^2S_{1/2}\|D^{(1)}\|^2P_{1/2})|^4}{(\omega_0-\omega_{\rm in})^2+\gamma^2/4}\sum_f C_1|\langle\{n_{\rm HO}\}_f|e^{-i\mathbf{q}\cdot\mathbf{R}_1}+e^{-i\mathbf{q}\cdot\mathbf{R}_2}|\{n_{\rm HO}\}_i\rangle|^2, \tag{21}$$

where $\mathbf{q}\equiv\mathbf{k}_{\rm out}-\mathbf{k}_{\rm in}$. Since the branching ratio for decay of the excited $^2P_{1/2}$ states to the ground $^2S_{1/2}$ states is nearly 100%, the spontaneous decay rate $\gamma$ is

$$\gamma=\frac{\omega_0^3}{6\pi\epsilon_0\hbar c^3}|(^2S_{1/2}\|D^{(1)}\|^2P_{1/2})|^2. \tag{22}$$

Equation (21) for the cross section becomes

$$\frac{d\sigma^{(1)}}{d\Omega_{\rm out}}=\frac{\sin^2\vartheta}{8\pi}\sigma_0\mathcal{L}(\omega_{\rm in}-\omega_0)$$
$$\times\sum_f|\langle\{n_{\rm HO}\}_f|e^{-i\mathbf{q}\cdot\mathbf{R}_1}+e^{-i\mathbf{q}\cdot\mathbf{R}_2}|\{n_{\rm HO}\}_i\rangle|^2, \tag{23}$$

where $\sigma_0=\lambda_0^2/2\pi$ is the resonance cross section, $\lambda_0=2\pi c/\omega_0$ is the resonance wavelength, and $\mathcal{L}(\omega_{\rm in}-\omega_0)$ is a Lorentzian of unit height and width $\gamma$:

$$\mathcal{L}(\omega_{\rm in}-\omega_0)\equiv\frac{(\gamma/2)^2}{(\omega_{\rm in}-\omega_0)^2+(\gamma/2)^2}. \tag{24}$$

In deriving Eq. (23) we have assumed that $\omega_0/\omega_{\rm out}\approx 1$. The sum over final harmonic-oscillator states can be done by closure:

$$\frac{d\sigma^{(1)}}{d\Omega_{\rm out}}=\frac{\sin^2\vartheta}{8\pi}\sigma_0\mathcal{L}(\omega_{\rm in}-\omega_0)\langle\{n_{\rm HO}\}_i|(e^{i\mathbf{q}\cdot\mathbf{R}_1}+e^{i\mathbf{q}\cdot\mathbf{R}_2})$$
$$\times(e^{-i\mathbf{q}\cdot\mathbf{R}_1}+e^{-i\mathbf{q}\cdot\mathbf{R}_2})|\{n_{\rm HO}\}_i\rangle$$
$$=\frac{\sin^2\vartheta}{8\pi}\sigma_0\mathcal{L}(\omega_{\rm in}-\omega_0)\langle\{n_{\rm HO}\}_i|2+e^{i\mathbf{q}\cdot(\mathbf{R}_1-\mathbf{R}_2)}$$
$$+e^{-i\mathbf{q}\cdot(\mathbf{R}_1-\mathbf{R}_2)}|\{n_{\rm HO}\}_i\rangle. \tag{25}$$

The exponentials can be combined in Eq. (25) because the components of $\mathbf{R}_1$ and $\mathbf{R}_2$ commute. The cross section can be written in terms of the equilibrium ion separation $\mathbf{d}$ and the displacement coordinates $\mathbf{u}_1$ and $\mathbf{u}_2$ as

$$\frac{d\sigma^{(1)}}{d\Omega_{\rm out}}=\frac{\sin^2\vartheta}{8\pi}\sigma_0\mathcal{L}(\omega_{\rm in}-\omega_0)\langle\{n_{\rm HO}\}_i|2+e^{i\mathbf{q}\cdot(\mathbf{d}+\mathbf{u}_1-\mathbf{u}_2)}$$
$$+e^{-i\mathbf{q}\cdot(\mathbf{d}+\mathbf{u}_1-\mathbf{u}_2)}|\{n_{\rm HO}\}_i\rangle. \tag{26}$$

The exponential factors in Eq. (26) depend on the relative coordinates of the two ions and not on their center-of-mass coordinates.

In order to compare with the experiment, we compute the cross section averaged over a thermal distribution of $|\{n_{\rm HO}\}_i\rangle$ initial states:

$$\left\langle \frac{d\sigma^{(1)}}{d\Omega_{\rm out}} \right\rangle = \frac{\sin^2\vartheta}{8\pi}\sigma_0 \mathcal{L}(\omega_{\rm in}-\omega_0)[2+e^{i\mathbf{q}\cdot\mathbf{d}}\langle e^{i\mathbf{q}\cdot(\mathbf{u}_1-\mathbf{u}_2)}\rangle + e^{-i\mathbf{q}\cdot\mathbf{d}}\langle e^{-i\mathbf{q}\cdot(\mathbf{u}_1-\mathbf{u}_2)}\rangle], \quad (27)$$

where $\langle A\rangle$ denotes the thermal average of the operator $A$. For harmonic oscillators, the thermal averages have a simple form [17,18]

$$\langle e^{\pm i\mathbf{q}\cdot(\mathbf{u}_1-\mathbf{u}_2)}\rangle = e^{-\langle[\mathbf{q}\cdot(\mathbf{u}_1-\mathbf{u}_2)]^2\rangle/2}. \quad (28)$$

While Refs. [17,18] assume a common temperature for all of the harmonic-oscillator modes, Eq. (28) is still valid if different modes have different temperatures. Different modes are laser cooled at different rates depending on the direction of the laser beam. Hence the modes have different temperatures unless the energy transfer rate between them is fast [19]. The thermally averaged cross section is

$$\left\langle \frac{d\sigma^{(1)}}{d\Omega_{\rm out}} \right\rangle = \frac{\sin^2\vartheta}{4\pi}\sigma_0 \mathcal{L}(\omega_{\rm in}-\omega_0) \times[1+\cos(\mathbf{q}\cdot\mathbf{d})e^{-\langle[\mathbf{q}\cdot(\mathbf{u}_1-\mathbf{u}_2)]^2\rangle/2}], \quad (29)$$

which is equivalent to Eq. (1) of Ref. [1], except that it includes the $\sin^2\vartheta$ angular dependence. The interference fringe visibility is given by the exponential factor multiplying $\cos(\mathbf{q}\cdot\mathbf{d})$. This factor decreases with increasing temperature and is analogous to the Debye-Waller factor for x-ray scattering from a crystal. It can be rewritten as

$$\begin{aligned} e^{-\langle[\mathbf{q}\cdot(\mathbf{u}_1-\mathbf{u}_2)]^2\rangle/2} &= \exp\left[-\frac{\hbar q_X^2}{m\omega_T}\left(\langle N_X^{\rm rel}\rangle+\frac{1}{2}\right)-\frac{\hbar q_Y^2}{m\omega_T}\left(\langle N_Y^{\rm rel}\rangle+\frac{1}{2}\right)-\frac{\hbar q_Z^2}{m\omega_S}\left(\langle N_Z^{\rm rel}\rangle+\frac{1}{2}\right)\right] \\ &= \exp\left[-\frac{\hbar q_X^2}{2m\omega_T}\coth\left(\frac{\hbar\omega_T}{2k_BT_X^{\rm rel}}\right)-\frac{\hbar q_Y^2}{2m\omega_T}\coth\left(\frac{\hbar\omega_T}{2k_BT_Y^{\rm rel}}\right)-\frac{\hbar q_Z^2}{2m\omega_S}\coth\left(\frac{\hbar\omega_S}{2k_BT_Z^{\rm rel}}\right)\right] \\ &\approx \exp\left(-\frac{q_X^2k_BT_X^{\rm rel}}{m\omega_T^2}-\frac{q_Y^2k_BT_Y^{\rm rel}}{m\omega_T^2}-\frac{q_Z^2k_BT_Z^{\rm rel}}{m\omega_S^2}\right), \end{aligned} \quad (30)$$

where $T_Z^{\rm rel}$ is the temperature of the $u_Z^{\rm rel}$ mode, etc., and the approximation in the last line is valid when the mean harmonic-oscillator quantum numbers are large. In the limit of small thermal motion or small $|\mathbf{q}|$ (near-forward scattering), the visibility can approach 100% (with polarized detection), in agreement with Ref. [13], but in contradiction to Ref. [11], where it was claimed that the visibility could not exceed 50%.

### B. One $m_J$ quantum number changes ($\sigma$ case)

Here we consider the case in which one of the ions changes its $m_J$ quantum number in the scattering process. We call this the $\sigma$ case since it involves a $\sigma$ transition, that is, a transition that changes $m_J$ by $\pm 1$ in one of the ions. There are eight cases since there are four possible initial states and two ions that could change quantum numbers.

In order to be definite, we pick the case where $m_J = +1/2$ for both ions before the scattering and ion 1 changes to $m_J = -1/2$ after the scattering, that is,

$$|\Psi_i\rangle = |(^2S_{1/2},+1/2)_1(^2S_{1/2},+1/2)_2\{n_{\rm HO}\}_i\rangle, \quad (31)$$

$$|\Psi_f\rangle = |(^2S_{1/2},-1/2)_1(^2S_{1/2},+1/2)_2\{n_{\rm HO}\}_f\rangle. \quad (32)$$

Only the first sum over $j$ in Eq. (8) contributes since only it contains $\mathbf{D}_1$, the dipole moment that leads to the change in $m_J$ of ion 1.

As in the previous case, the only intermediate states that contribute nonzero terms are of the form

$$|\Psi_j\rangle = |(^2P_{1/2},+1/2)_1(^2S_{1/2},+1/2)_2\{n_{\rm HO}\}_j\rangle. \quad (33)$$

The matrix elements connecting the initial states to the intermediate states are

$$\begin{aligned} &\langle\Psi_j|(\mathbf{D}_1\cdot\hat{\boldsymbol{\epsilon}}_{\rm in})e^{i\mathbf{k}_{\rm in}\cdot\mathbf{R}_1}|\Psi_i\rangle \\ &\quad = \langle(^2P_{1/2},+1/2)_1|D_{1z}|(^2S_{1/2},+1/2)_1\rangle \\ &\qquad \times\langle\{n_{\rm HO}\}_j|e^{i\mathbf{k}_{\rm in}\cdot\mathbf{R}_1}|\{n_{\rm HO}\}_i\rangle \\ &\quad = \frac{1}{\sqrt{6}}(^2P_{1/2}\|D^{(1)}\|^2S_{1/2})\langle\{n_{\rm HO}\}_j|e^{i\mathbf{k}_{\rm in}\cdot\mathbf{R}_1}|\{n_{\rm HO}\}_i\rangle. \end{aligned} \quad (34)$$

In the $\vartheta=\pi/2$ plane, only the polarization corresponding to $\hat{\boldsymbol{\epsilon}}_\sigma$ is emitted, but, in general, light with both $\hat{\boldsymbol{\epsilon}}_\sigma$ and $\hat{\boldsymbol{\epsilon}}_\pi$ contributes to the scattered intensity. We consider these two cases separately.

For $\hat{\boldsymbol{\epsilon}}_{\rm out}=\hat{\boldsymbol{\epsilon}}_\sigma$, the matrix elements connecting the intermediate states to the final states are

$$\langle \Psi_f | (\mathbf{D}_1 \cdot \hat{\epsilon}_\sigma) e^{-i\mathbf{k}_{\text{out}} \cdot \mathbf{R}_1} | \Psi_j \rangle$$
$$= \frac{-ie^{i\varphi}}{\sqrt{2}} \langle ({}^2S_{1/2}, -1/2)_1 | D^{(1)}_{1-1} | ({}^2P_{1/2}, +1/2)_1 \rangle$$
$$\times \langle \{n_{\text{HO}}\}_f | e^{-i\mathbf{k}_{\text{out}} \cdot \mathbf{R}_1} | \{n_{\text{HO}}\}_j \rangle$$
$$= \frac{-ie^{i\varphi}}{\sqrt{6}} ({}^2S_{1/2} \| D^{(1)} \| {}^2P_{1/2}) \langle \{n_{\text{HO}}\}_f | e^{-i\mathbf{k}_{\text{out}} \cdot \mathbf{R}_1} | \{n_{\text{HO}}\}_j \rangle, \tag{35}$$

where $D^{(1)}_{p-1}$ is the $(1,-1)$ spherical tensor component of the dipole moment operator for ion $p$. The rest of the calculation is very similar to the $\pi$ case. The final result, analogous to Eq. (29) for the $\pi$ case, is

$$\left\langle \frac{d\sigma^{(2)}}{d\Omega_{\text{out}}} \right\rangle = \frac{1}{8\pi} \sigma_0 \mathcal{L}(\omega_{\text{in}} - \omega_0), \tag{36}$$

which is independent of $\hat{\mathbf{k}}_{\text{out}}$ and shows no interference fringes. The same result would have been obtained for any of the other three initial states since the absolute squares of the matrix elements are the same.

For $\hat{\boldsymbol{\epsilon}}_{\text{out}} = \hat{\boldsymbol{\epsilon}}_\pi$, the matrix elements connecting the intermediate states to the final states are

$$\langle \Psi_f | (\mathbf{D}_1 \cdot \hat{\boldsymbol{\epsilon}}_\pi) e^{-i\mathbf{k}_{\text{out}} \cdot \mathbf{R}_1} | \Psi_j \rangle = \frac{-\cos\vartheta e^{i\varphi}}{\sqrt{2}} \langle ({}^2S_{1/2}, -1/2)_1 | D^{(1)}_{1-1} | ({}^2P_{1/2}, +1/2)_1 \rangle \langle \{n_{\text{HO}}\}_f | e^{-i\mathbf{k}_{\text{out}} \cdot \mathbf{R}_1} | \{n_{\text{HO}}\}_j \rangle$$
$$= \frac{-\cos\vartheta e^{i\varphi}}{\sqrt{6}} ({}^2S_{1/2} \| D^{(1)} \| {}^2P_{1/2}) \langle \{n_{\text{HO}}\}_f | e^{-i\mathbf{k}_{\text{out}} \cdot \mathbf{R}_1} | \{n_{\text{HO}}\}_j \rangle. \tag{37}$$

The final result is

$$\left\langle \frac{d\sigma^{(3)}}{d\Omega_{\text{out}}} \right\rangle = \frac{\cos^2\vartheta}{8\pi} \sigma_0 \mathcal{L}(\omega_{\text{in}} - \omega_0), \tag{38}$$

which shows no interference fringes. The same result would have been obtained for any of the other initial states.

For the $\sigma$ case, Young's interference fringes are not observed because only one of the two terms inside the absolute value bars in Eq. (8) is nonzero. There is only one path for the photon, intersecting the ion whose state is changed in the scattering process.

### C. Total cross section with or without polarization-selective detection

In Ref. [1] a linear polarizer was sometimes placed before the photon detector. For experimental convenience, the orientation of this polarizer was fixed, while the input polarization could be varied. To obtain the total cross section describing a given experimental situation, we sum over all final atomic states and average over all initial states. For polarization-insensitive detection, we also sum over the polarizations of the outgoing photon.

The cross section for polarization-insensitive detection is

$$\left\langle \frac{d\sigma^{\text{unpol}}}{d\Omega_{\text{out}}} \right\rangle = \left\langle \frac{d\sigma^{(1)}}{d\Omega_{\text{out}}} \right\rangle + 2\left\langle \frac{d\sigma^{(2)}}{d\Omega_{\text{out}}} \right\rangle + 2\left\langle \frac{d\sigma^{(3)}}{d\Omega_{\text{out}}} \right\rangle$$
$$= \frac{\sigma_0}{4\pi} \mathcal{L}(\omega_{\text{in}} - \omega_0) \{ 1 + \cos^2\vartheta$$
$$+ \sin^2\vartheta [ 1 + \cos(\mathbf{q}\cdot\mathbf{d}) e^{-\langle [\mathbf{q}\cdot(\mathbf{u}_1 - \mathbf{u}_2)]^2 \rangle / 2} ] \}. \tag{39}$$

The fringe visibility in this case cannot exceed 50%.

The cross section for detection of light with polarization $\hat{\boldsymbol{\epsilon}}_\pi$ is

$$\left\langle \frac{d\sigma^{(\pi)}}{d\Omega_{\text{out}}} \right\rangle = \left\langle \frac{d\sigma^{(1)}}{d\Omega_{\text{out}}} \right\rangle + 2\left\langle \frac{d\sigma^{(3)}}{d\Omega_{\text{out}}} \right\rangle$$
$$= \frac{\sigma_0}{4\pi} \mathcal{L}(\omega_{\text{in}} - \omega_0) \{ \cos^2\vartheta$$
$$+ \sin^2\vartheta [ 1 + \cos(\mathbf{q}\cdot\mathbf{d}) e^{-\langle [\mathbf{q}\cdot(\mathbf{u}_1 - \mathbf{u}_2)]^2 \rangle / 2} ] \}. \tag{40}$$

The fringe visibility in this case can approach 100% in the $\vartheta = \pi/2$ plane if the Debye-Waller factor is close to 1. The cross section for detection of light with polarization $\hat{\boldsymbol{\epsilon}}_\sigma$ is

$$\left\langle \frac{d\sigma^{(\sigma)}}{d\Omega_{\text{out}}} \right\rangle = 2\left\langle \frac{d\sigma^{(2)}}{d\Omega_{\text{out}}} \right\rangle = \frac{\sigma_0}{4\pi} \mathcal{L}(\omega_{\text{in}} - \omega_0), \tag{41}$$

which is totally isotropic and shows no fringes.

### D. Which-path interpretation

The presence of interference fringes in the $\pi$ case and their absence in the $\sigma$ case have a simple explanation in terms of the possibility, in principle, of determining which of the two ions scattered the photon. Consider the sequence of transitions in Fig. 4(a), representing the $\pi$ case. Each box represents the combined state of the two ions. Ion 1 is represented by the diagram on the left side of a box and ion 2 by that on the right. The ordering of energy levels is the same as in Fig. 2. For simplicity, we neglect the translational degrees of freedom, which lead to the appearance of the Debye-Waller factor in Eq. (29). The system begins in the state

$$|\Psi_i\rangle = |(^2S_{1/2}, +1/2)_1 (^2S_{1/2}, -1/2)_2\rangle. \quad (42)$$

One ion or the other absorbs a photon from the laser beam and undergoes a $\pi$ transition to the excited state. That ion emits a photon and undergoes a $\pi$ transition back to the ground state. The two paths, corresponding to either ion 1 or ion 2 scattering the photon, lead to the same final state. Therefore, the amplitudes for these two paths must be added and this leads to interference. Since the final states of the ion are the same as the initial states, it is not possible to determine which of the ions scattered the photon by examining their states.

Now consider the sequence of transitions in Fig. 4(b), representing the $\sigma$ case. As in the previous case, one ion or the other absorbs a photon and undergoes a $\pi$ transition to the excited state. However, in this case, that ion undergoes a $\sigma$ transition when it emits a photon and changes its $m_J$ quantum number. The final states differ, depending on which of the ions scattered the photon. Hence there is no interference between the two paths. It would be possible to tell which ion scattered the photon by examining the states of the ions before and after the scattering.

The preceding analysis is valid only in the limit of low laser intensity, so that the probability of both ions being excited at the same time is negligible and stimulated emission can be neglected. It is not necessary that the two ions be in the same quantum state for interference to occur, only that the final combined states for the two paths be indistinguishable. For definiteness, a particular initial state [Eq. (42)] was chosen. For each of the three other possible initial states, there is a process like Fig. 4(a) in which the ions scatter a photon and return to their original states and one like Fig. 4(b) in which one of them scatters a photon and changes its state. Processes of the former type lead to interference; those of the latter type do not.

## VI. COMPARISON WITH EXPERIMENT

Figure 5 shows an image of the fringes observed for the $\pi$ case in which $\hat{\epsilon}_{\text{in}}$ was perpendicular to the $X$-$Z$ plane and the detector was sensitive only to light polarized parallel to $\hat{\epsilon}_{\text{in}}$. The dark spots are due to stray reflections of the laser beams. When $\hat{\epsilon}_{\text{in}}$ was rotated by 90° without changing the polarizer in front of the detector ($\sigma$ case), the image showed no fringes. The image data from a single ion, which shows no interference fringes, were used to correct the data of Fig. 5 for a slowly spatially varying detection efficiency. The data within the rectangle in Fig. 5 were summed along the vertical direction and divided by the detection-efficiency function.

The normalized data points are shown in Fig. 6 together with a least-squares fit. In this fit, as in Ref. [1], the temperatures of the stretch and tilt modes were assumed to have the ratio expected from theory [19],

$$T_Z^{\text{rel}}/T_X^{\text{rel}} = \{1+[3\cos^2(\Theta)]^{-1}\}/\{1+[3\sin^2(\Theta)]^{-1}\}, \quad (43)$$

and both temperatures were allowed to vary together in the fit. The fringe visibility in the vicinity of the $X$-$Z$ plane is insensitive to the temperature of the $Y$ motion, which is cooled indirectly by coupling to the other modes. The mean ion separation was calculated from knowledge of the trap parameters. The dependence of Eq. (29) on the out-of-plane angle $\Phi$ is small and $\Phi$ was set to 0 in the fit. The fitted value of $T_X^{\text{rel}}$ was $1.08\pm0.12$ mK, or $0.92\pm0.10$ times the Doppler-cooling limit. The fringe visibility, extrapolated to $\phi=0$, would be 100% if it followed Eq. (29). The fitted value for this parameter was $(71\pm4)\%$. The errors represent the standard deviations estimated from the fit. The maximum *observed* visibility at the minimum value of $\phi$ in Fig. 6 is approximately 60%.

There are several likely causes of the difference between the observed and predicted values of the fringe visibility. First, the theory was derived for the limit of low intensity. The saturation parameter was measured to be $s=0.078\pm0.025$ (see the Appendix). By itself, this would reduce the maximum visibility to $(1+s)^{-1}\approx93\%$ because the spectrum of the resonance fluorescence in this polarization contains an incoherent part [20]. Other likely causes of reduced visibility are unequal laser intensities at the two ions, imperfect polarizers, stray background light, and quantum jumps of one of the ions to a metastable state, leaving only one ion fluorescing. Each of these effects might reduce the visibility by a few percent.

## VII. DISCUSSION

The fact that the resonance fluorescence from a two-level atom illuminated by weak, monochromatic light is coherent with the applied field was noted by Heitler [21]. The spectrum of the resonance fluorescence for arbitrary applied intensities was calculated by Mollow [22]. In the limit of low applied intensity, the spectrum is monochromatic and coherent with the applied field (a $\delta$ function). At higher intensities, the coherent component decreases in amplitude and a component not coherent with the applied field and having a width equal to the natural linewidth appears. At very high intensities, the coherent component continues to decrease in amplitude and the incoherent component splits into three separate Lorentzians. The existence of a coherent component in the resonance fluorescence of a single ion was confirmed directly by Höffges *et al.* by a heterodyne measurement [23].

Classically, we would expect the resonance fluorescence from two two-level atoms at fixed positions, excited by the same monochromatic field, to generate interference fringes having 100% visibility in the limit of low applied intensity since the radiated fields are coherent with each other. At higher applied intensities, the visibility should decrease since more of the resonance fluorescence intensity belongs to the incoherent component. Quantum treatments for two two-level atoms have been given by Richter [24] and by Kochan *et al.* [25], who predict a visibility equal to $(1+s)^{-1}$, where $s$ is the saturation parameter defined in Ref. [26]. This is just the ratio of the intensity of the coherent component to the total resonance fluorescence intensity for a single atom.

Polder and Schuurmans [20] calculated the spectrum of the resonance fluorescence of a $J=1/2$ to $J=1/2$ transition for a single atom. The spectrum of the light having polarization $\hat{\epsilon}_\pi$ is like that for a two-level atom. Hence interference fringes would be expected in the $\hat{\epsilon}_\pi$-polarized resonance fluorescence from two such atoms for low applied intensity.

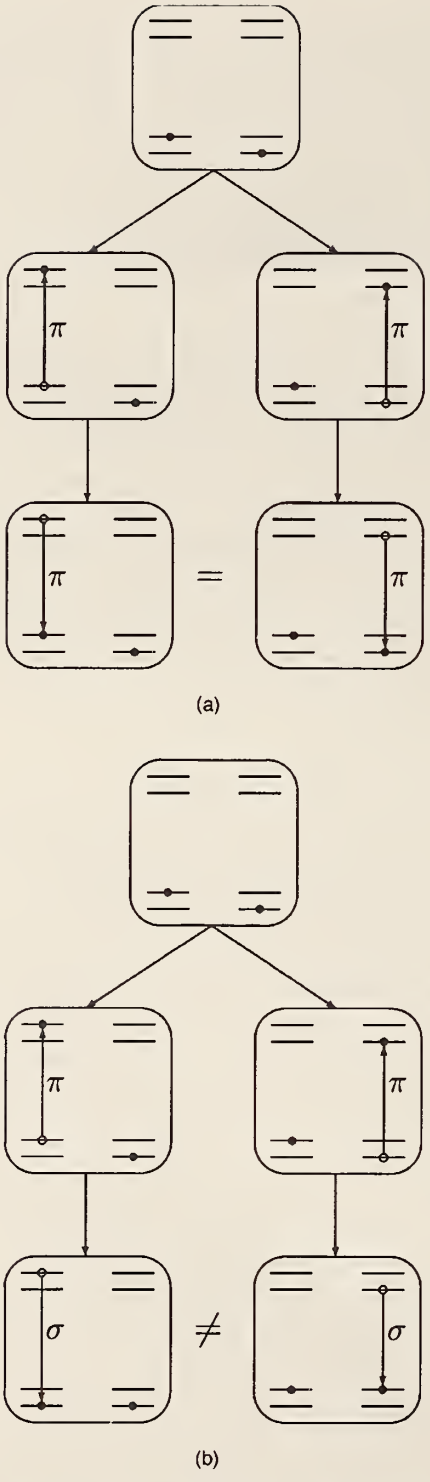


FIG. 4. Each box represents the combined state of the two ions. The ordering of energy levels is the same as in Fig. 2. In (a) (the $\pi$ case), one ion or the other undergoes a $\pi$ transition from the ground to the excited state. That ion undergoes a $\pi$ transition back to the ground state. The two paths lead to the same final state of the two ions. Hence the probability amplitudes must be added and interference is possible. In (b) (the $\sigma$ case), one ion or the other undergoes a $\pi$ transition to the excited state, but the excited ion undergoes a $\sigma$ transition to the ground state. The two paths lead to different final states of the two ions. Hence there is no possibility of interference. In order for interference to occur, it is *not* necessary that the initial states of the two ions be the same, only that the final combined states for the two paths be the same.

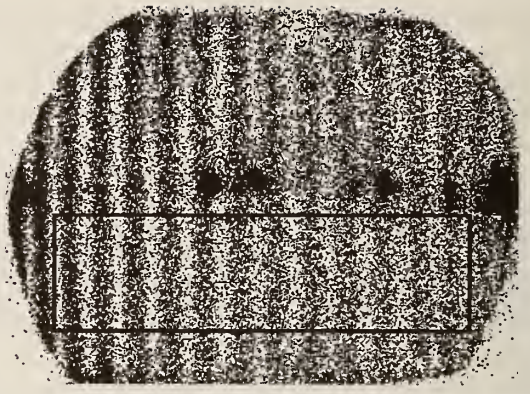

FIG. 5. Experimental fringe data for the case in which the detected light is polarized in the same direction as the incoming light ($\pi$ case). The ion separation $d=4.17$ $\mu$m. The angle $\phi$ (the deviation from the forward-scattering direction) increases to the right. The decrease in visibility with increasing $\phi$ is due to thermal motion of the ions. The dark spots are due to stray reflections of the laser beams. The data within the rectangle were summed along the vertical direction and least-squares fitted.

The spectrum of the light having polarization $\hat{\epsilon}_\sigma$ does not contain a $\delta$ function. In the limit of low applied intensity, it is a Lorentzian having a width approximately equal to the photon scattering rate, which can be much less than the natural linewidth. Even for applied intensities approaching $s=1$, the coherence length is on the order of $c/\gamma$, where $\gamma$ is the spontaneous decay rate of the excited state. For the $Hg^+$ $6p\ ^2P_{1/2}$ level, this is about 70 cm. For interference fringes to exist, the radiation from the two atoms must be *mutually* coherent. Whether or not fringes should exist in the $\hat{\epsilon}_\sigma$-polarized light from two atoms is not immediately obvious from a classical analysis. However, the perturbative quantum treatment of Sec. V predicts that there should be no interference since there is only one probability amplitude connecting the initial and final states. The absence of interference in this case is fundamentally a quantum effect, though one having more to do with the quantum nature of the atom and the existence of degenerate, orthogonal ground

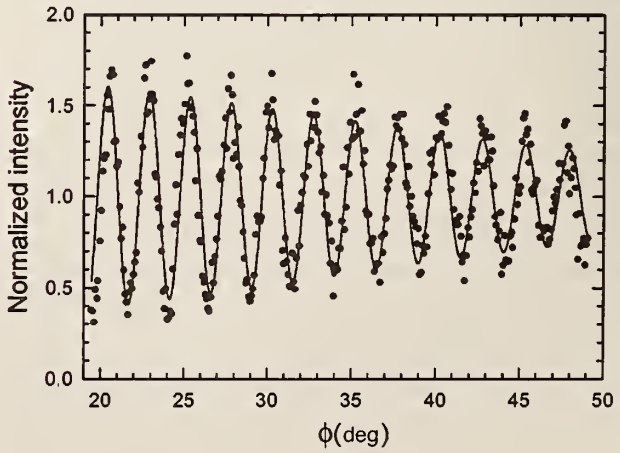


FIG. 6. Experimental fringe data (dots) from the image of Fig. 5 and a least-squares fit (line) to the sum of the theoretical intensity [Eq. (29)] and a constant background. The fitted temperature is approximately equal to the Doppler-cooling limit.

states, than with the quantum nature of the electromagnetic field. Precisely the same point was made by Scully and Drühl when they showed that interference fringes are not present in the Raman radiation emitted by two three-level atoms having a $\Lambda$ configuration [3].

Wong *et al.* [13] calculated the interference of resonance fluorescence from two four-level atoms having a level structure like that of $^{198}Hg^+$. Their analytic calculations are for a simpler geometry than the one actually used by Eichmann *et al.* [1] and ignore the motion of the ions. They do, however, include the effect of the decrease in visibility due to the incoherent component of the resonance fluorescence, which is not included in the perturbative calculation of Sec. V. The analytic calculations of Wong *et al.* and the present calculations agree in the limits in which they are both valid, that is, for low applied intensities and for no ion motion. In particular, Wong *et al.* show that the fringe visibility can approach 100% at low applied intensities, with polarization-selective detection. Wong *et al.* also made Monte Carlo wave-function simulations, in which the motion of the ions was included classically, and observed a decrease in visibility due to this effect.

Huang *et al.* [12] calculated the effect of thermal motion on the interference fringe visibility for two two-level atoms, each trapped in a separate harmonic well. They obtained an expression equivalent to Eq. (1) of Eichmann *et al.* [1] for this model. However, the treatment of Eichmann *et al.*, the details of which are given in the present article, is more useful for the analysis of the experiment of Ref. [1] since it deals explicitly with the actual normal mode structure of the two trapped ions.

Brewer has published a theory of interference in the light scattered from two four-level atoms [11]. One prediction of this theory is that the fringe visibility cannot exceed 50%, even with polarization-selective detection. This contradicts the experimental results of Sec. VI shown in Fig. 6. While the maximum visibility is about 60%, only slightly exceeding 50%, *no* background has been subtracted from the data and there are several known sources of decreased visibility, including thermal motion of the ions, the incoherent component of the resonance fluorescence, and stray scattered light. The data were normalized by division by a slowly varying detection sensitivity function, a process that cannot enhance the visibility.

The basic flaw in Brewer's argument can be seen in Eq. (2) of Ref. [11], where he lists the basis states for the two-atom system. The states $|5\rangle$–$|8\rangle$ are the four states in which both atoms are in the ground electronic state. The states $|1\rangle$–$|4\rangle$ are linear combinations of states in which one atom is in the ground state and one is in the excited state. However, most of the possible states of this type are missing, apparently because of a false assumption that the allowed states must have a particular kind of exchange symmetry. For example, the intermediate superposition state shown in Fig. 4(a) is, in his notation,

$$\frac{1}{\sqrt{2}}(|c_1 b_2\rangle \pi_{nn,1} + |a_1 d_2\rangle \pi_{nn,2}) \tag{44}$$

and is not contained in the list. The neglect of these basis states leads to the neglect of processes like that of Fig. 4(a), in which the two atoms are initially in different $m_J$ states. Thus he reaches the false conclusion that the two atoms must initially be in the same $m_J$ state in order for interference to occur. Since he misses half of the processes that lead to interference, he predicts a maximum visibility, with polarization-sensitive detection, of 50% rather than 100%.

We conclude with some remarks regarding the principle of complementarity. Wave and particle properties of light are complementary and hence cannot be observed at the same time. If it is possible to determine which atom scattered the photon, the interference fringes must vanish. Feynman's thought experiments, in which various methods of determining the path of an electron through a two-slit Young interferometer lead to the destruction of interference fringes due to a random momentum transfer, are often quoted (see Ref. [2], pp. 1-6–1-11). However, in Chap. 3 of the same textbook, Feynman emphasizes the seemingly more fundamental viewpoint that interference is present only if there exist different indistinguishable ways to go from a given initial state to the *same* final state. His example of the scattering of neutrons from a crystal is very similar to the experiment of Eichmann *et al.* If the nuclei of the atoms in the crystal have a nonzero spin, the angular distribution of scattered neutrons is the sum of a featureless background and some sharp diffraction peaks. The sharp diffraction peaks are associated with neutrons that do not change their spin orientations in the scattering. The featureless background is associated with neutrons whose spins change their orientations in the scattering. In this case, there must also be a change in the spin orientation of one of the nuclei in the crystal. It would be possible in principle to determine the nucleus which scattered the neutron, so there is no interference.

## ACKNOWLEDGMENTS

This work was supported by the Office of Naval Research. U.E. acknowledges financial support from the Deutsche Forschungsgemeinschaft. Dr. J. M. Gilligan assisted in the early stages of the experiment and suggested the method that was used for the polarization-selective detection.

## APPENDIX: CALIBRATION OF THE SATURATION PARAMETER

For the case where an electric-dipole transition between a $^2S_{1/2}$ ground state and a $^2P_{1/2}$ excited state is excited by linearly polarized light, we define the saturation parameter $s$ similarly to the way in which it is defined for a two-level system [26]. The magnetic field is assumed to be small and the quantization axis for the ion is along the electric field. We define

$$s = \frac{\Omega_1^2/2}{(\omega_0 - \omega_{\text{in}})^2 + (\gamma/2)^2}, \tag{A1}$$

where $\Omega_1 = 6^{-1/2}|\mathcal{E}_0(^2S_{1/2}\|D^{(1)}\|^2P_{1/2})|\hbar^{-1}$ is the Rabi frequency, and the other terms have been defined previously. In order for the perturbative analysis of Sec. V to be valid, we

must have $s \ll 1$. In the case of $Hg^+$, the $^2P_{1/2}$ state has a small (approximately $10^{-7}$) probability of decaying to the metastable $^2D_{3/2}$ state, which decays either directly to the ground state or to the metastable $^2D_{5/2}$ state, which decays to the ground state. The 194.2-nm fluorescence intensity from a single ion is bistable since it has a steady level when the ion is cycling between the $^2S_{1/2}$ and $^2P_{1/2}$ states and vanishes when the ion drops to a metastable state. The fractional population of the $^2P_{1/2}$ state, summed over both $m_J$ values, is $s/2(1+s)$ while the ion is cycling between the $^2S_{1/2}$ and $^2P_{1/2}$ states. The quantum jump statistics have been discussed in several previous articles [15,27,28]. For a single ion, we define $p_{on}$ to be the fraction of the time that the ion is cycling between the $^2S_{1/2}$ and $^2P_{1/2}$ states and $p_{off} = (1 - p_{on})$ to be the fraction of the time that it spends in either of the metastable states. It can be shown, from the steady-state solutions of the differential equations for the populations [Eqs. (2a)–(2c) of Ref. [28]], that $s$ is related to the ratio $p_{off}/p_{on}$ according to

$$\frac{1}{2}\frac{s}{(1+s)} = \frac{\gamma_1\gamma_2(p_{off}/p_{on})}{\gamma_3(\gamma_2+f_2\gamma_1)} \approx 0.36\,\frac{p_{off}}{p_{on}}, \qquad \text{(A2)}$$

where the parameters $\gamma_1$, $\gamma_2$, $\gamma_3$, and $f_2$ have been measured [15] and the uncertainty in the coefficient (0.36) is about 30%, due mostly to the uncertainty in $\gamma_3$.

For two ions, the fluorescence will be tristable since zero, one, or two ions may be in a metastable state. During an interference fringe measurement, the number of photons detected in each successive period of a few milliseconds was recorded. Figure 7 shows a plot of the probability distribution of the 5-ms photon counts during the measurement of Fig. 5. The three peaks correspond, from left to right, to two, one, or zero ions being in a metastable state. The leftmost peak corresponds to the signal from stray background light since there is no fluorescence from the ions. The curve is a least-squares fit to a sum of three Gaussians. The areas under the peaks should be in the ratio $p_{off}^2 : 2p_{off}p_{on} : p_{on}^2$. The ratios of the areas obtained from the fit are 0.011:0.160:0.828, so $p_{off}/p_{on} = 0.10 \pm 0.01$ and, from Eq. (A2), $s = 0.078 \pm 0.025$, so the perturbative analysis should be a good approximation.

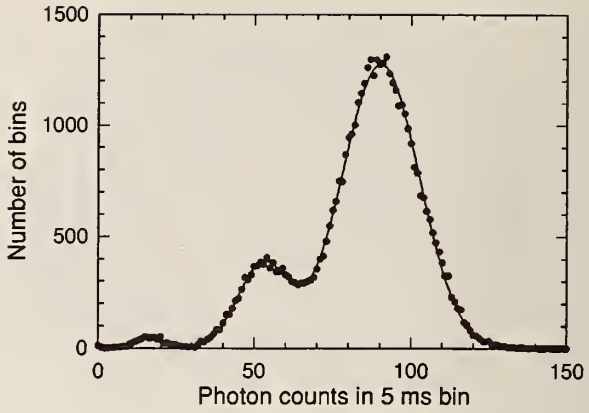


FIG. 7. Plot of the probability distribution of the fluorescence intensity for two ions, used to determine the saturation parameter $s$. The horizontal axis corresponds to the number of photons counted in a 5-ms interval. The vertical axis corresponds to the number of 5-ms intervals in which a given number of photons was counted. This was measured simultaneously with the interference fringes shown in Fig. 5. The curve is a least-squares fit to a sum of three Gaussians. The areas under the Gaussians, from left to right, are proportional to the probabilities that two, one, or none of the ions are in a metastable state. Higher values of $s$ correspond to higher populations in the metastable states.

During this measurement period, the interference fringe detection was gated off for 5 ms if the number of photons detected in the previous 5 ms was less than 80. This helped to prevent loss of the fringe visibility due to background from single-ion fluorescence, which would have no interference fringes.

[1] U. Eichmann, J. C. Bergquist, J. J. Bollinger, J. M. Gilligan, W. M. Itano, D. J. Wineland, and M. G. Raizen, Phys. Rev. Lett. **70**, 2359 (1993).
[2] R. Feynman, R. Leighton, and M. Sands, *The Feynman Lectures on Physics* (Addison-Wesley, Reading, MA, 1965), Vol. III.
[3] M. O. Scully and K. Drühl, Phys. Rev. A **25**, 2208 (1982).
[4] P. Storey, S. Tan, M. Collet, and D. Walls, Nature (London) **367**, 626 (1994).
[5] E. P. Storey, S. M. Tan, M. J. Collet, and D. F. Walls, Nature (London) **375**, 368 (1995).
[6] H. W. Wiseman, F. E. Harrison, M. J. Collett, S. M. Tan, D. F. Walls, and R. B. Killip, Phys. Rev. A **56**, 55 (1997).
[7] M. O. Scully, B.-G. Englert, and H. Walther, Nature (London) **351**, 111 (1991).
[8] B.-G. Englert, M. O. Scully, and H. Walther, Nature (London) **375**, 367 (1995); Sci. Am. (Int. Ed.) **271**(6), 56 (1994).
[9] R. G. Brewer, Phys. Rev. A **52**, 2965 (1995).
[10] R. G. Brewer, Phys. Rev. A **53**, 2903 (1996).
[11] R. G. Brewer, Phys. Rev. Lett. **77**, 5153 (1996).
[12] H. Huang, G. S. Agarwal, and M. O. Scully, Opt. Commun. **127**, 243 (1996).
[13] T. Wong, S. M. Tan, M. J. Collett, and D. F. Walls, Phys. Rev. A **55**, 1288 (1997).
[14] M. G. Raizen, J. M. Gilligan, J. C. Bergquist, W. M. Itano, and D. J. Wineland, Phys. Rev. A **45**, 6493 (1992).
[15] W. M. Itano, J. C. Bergquist, R. G. Hulet, and D. J. Wineland, Phys. Rev. Lett. **59**, 2732 (1987).
[16] H. J. Lipkin, Ann. Phys. (N.Y.) **18**, 182 (1962).
[17] N. D. Mermin, J. Math. Phys. **7**, 1038 (1966).
[18] D. S. Bateman, S. K. Bose, B. Dutta-Roy, and M. Bhattacharyya, Am. J. Phys. **60**, 829 (1992).
[19] W. M. Itano and D. J. Wineland, Phys. Rev. A **25**, 35 (1982).
[20] D. Polder and M. F. H. Schuurmans, Phys. Rev. A **14**, 1468 (1976).
[21] W. Heitler, *The Quantum Theory of Radiation*, 3rd ed. (Oxford University Press, London, 1954), pp. 201 and 202.
[22] B. R. Mollow, Phys. Rev. **188**, 1969 (1969).

[23] J. T. Höffges, H. W. Baldauf, T. Eichler, S. R. Helmfrid, and H. Walther, Opt. Commun. **133**, 170 (1997).
[24] Th. Richter, Opt. Commun. **80**, 285 (1991).
[25] P. Kochan, H. J. Carmichael, P. R. Morrow, and M. G. Raizen, Phys. Rev. Lett. **75**, 45 (1995).
[26] C. Cohen-Tannoudji, J. Dupont-Roc, and G. Grynberg, *Atom-Photon Interactions* (Wiley, New York, 1992), p. 369.
[27] W. M. Itano, J. C. Bergquist, R. G. Hulet, and D. J. Wineland, Phys. Scr. **T22**, 79 (1988).
[28] W. M. Itano, J. C. Bergquist, and D. J. Wineland, Phys. Rev. A **38**, 559 (1988).

# Cooling the Collective Motion of Trapped Ions to Initialize a Quantum Register

B. E. King,* C. S. Wood, C. J. Myatt, Q. A. Turchette, D. Leibfried,† W. M. Itano, C. Monroe, and D. J. Wineland

*Time and Frequency Division, National Institute of Standards and Technology, Boulder, Colorado 80303*

(Received 6 March 1998)

We report preparation in the ground state of collective modes of motion of two trapped $^9Be^+$ ions. This is a crucial step towards realizing quantum logic gates which can entangle the ions' internal electronic states. We find that heating of the modes of relative ion motion is substantially suppressed relative to that of the center-of-mass modes, suggesting the importance of these modes in future experiments. [S0031-9007(98)06838-0]

PACS numbers: 03.67.Lx, 03.65.–w, 32.80.Pj

In physics, quantum computation [1] provides a general framework for fundamental investigations into subjects such as entanglement, quantum measurement, and quantum information theory. Since quantum computation relies on entanglement between qubits, any implementation of a quantum computer must offer isolation from the effects of decoherence, but also allow controllable and *coherent* interaction between the qubits. Cirac and Zoller [2] have proposed an attractive scheme for realizing a quantum computer, which is scalable to an arbitrary number of qubits. Their scheme is based on a collection of trapped atomic ions, where each qubit (one per ion) is comprised of a pair of the ions' internal states, while quantum information is transferred between different ions using a particular quantized mode of the ions' collective motion. This "quantum data bus" must first be initialized in a pure quantum state [2]: for example, its ground state [3]. The basics of this scheme have been demonstrated experimentally in a fundamental logic gate (a Controlled-NOT) operating between a motional mode of a single trapped ion and two of the ion's internal states [4]. In that work, the motional state was initialized in the ground state by laser cooling [5]. The next step towards implementing the Cirac-Zoller scheme is to cool at least one mode of collective motion of multiple ions to the ground state. In this Letter, we describe the first experiments to realize this goal. We also report a significant difference between the decoherence rates of the center-of-mass and non-center-of-mass modes of motion.

We confine $^9Be^+$ ions in a coaxial-resonator-based rf (Paul) trap, similar to that described in Ref. [6]. The electrodes in this trap are made from 125-$\mu$m-thick sheets of Be metal, as shown in Fig. 1. We apply a potential $\phi(t) = V_0 \cos(\Omega_T t) + U_0$ to the (elliptical) ring electrode relative to the end cap electrodes. If several ions are trapped and cooled, they will naturally align themselves along the major axis of the ring electrode. The electrode's elliptical shape, in combination with $U_0 > 0$, allows a linear crystal to be maintained while suppressing rf micromotion of the ions along this direction [7]. With $V_0 \approx 520$ V, $\Omega_T/2\pi \approx 238$ MHz, and $U_0 = 0$ V, the pseudopotential oscillation frequencies are $(\omega_x, \omega_y, \omega_z)/2\pi \approx (4.6, 12.7, 17.0)$ MHz. With $U_0 = 18.2$ V, the frequencies become (8.6, 17.6, 9.3) MHz. Figure 1 shows two ions confined in the trap and imaged with an $f/3$ lens system onto a position-sensitive photomultiplier tube.

The ions are cooled and probed with laser beams whose geometry is indicated in Fig. 2(a). The relevant level structure of $^9Be^+$ is shown in Fig. 2(b). The quantization axis is defined by an applied static magnetic field; $|\boldsymbol{B}| \approx 0.2$ mT. The levels of interest for quantum logic operations are the $2s\,^2S_{1/2}|F = 2, m_F = 2\rangle$ and $2s\,^2S_{1/2}|F = 1, m_F = 1\rangle$ states, abbreviated by $|\downarrow\rangle$ and $|\uparrow\rangle$, respectively. Laser beams D1, D2, and D3 are $\sigma^+$ polarized and focused to nearly saturate the ions ($I_{\text{sat}} \approx 85$ mW cm$^{-2}$). Beams D1 and D2 provide Doppler precooling in all three dimensions, and beam D3 prevents optical pumping to the $|F = 2, m_F = 1\rangle$ state. The $|\downarrow\rangle \rightarrow 2p\,^2P_{3/2}|F = 3, m_F = 3\rangle$ transition (radiative linewidth $\gamma/2\pi \approx 19.4$ MHz), driven by D2, is a cycling transition, which allows us to detect the ion's electronic state ($|\downarrow\rangle$ or $|\uparrow\rangle$) with nearly unit detection efficiency.

Beams R1 ($\sigma^+/\sigma^-$ polarized) and R2 ($\pi$ polarized) are used to drive stimulated Raman transitions between

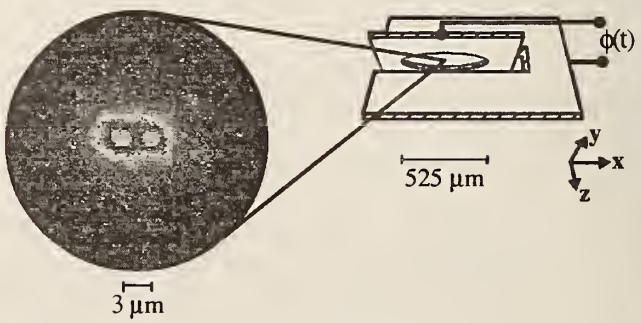


FIG. 1(color). Two ions trapped in an elliptical rf (Paul) trap. The ring has an aspect ratio of 3:2 and the major axis is 525 $\mu$m long. The slot which forms the end caps is 250 $\mu$m across. A potential $\phi(t)$ is applied to the ring (see text). The Be sheets are ≈125 $\mu$m thick. With an $x$-axis pseudopotential oscillation frequency $\omega_x/2\pi = 4.6$ MHz, the ion-ion spacing is approximately 3 $\mu$m.

$|\downarrow\rangle$ and $|\uparrow\rangle$, through the virtual $2p\,^2P_{1/2}$ state [5]. These beams are derived from a single laser, whose output is split by an acousto-optic modulator [8]. The beams are detuned by $\Delta/2\pi \approx 40$ GHz to the red of the $2s\,^2S_{1/2} \rightarrow 2p\,^2P_{1/2}$ transition, and their frequency difference is tuned around the $2s\,^2S_{1/2}$ hyperfine splitting of $\omega_0/2\pi \approx 1.25$ GHz. (Here, $\omega_0$ includes stable shifts of a few megahertz from the Zeeman and ac Stark effects.) R2 is directed along $(-1/\sqrt{2})\hat{x} + (1/2)(-\hat{y} + \hat{z})$. If R1 $\perp$ R2 as in Fig. 2, then the Raman beam wave vector difference $\delta k \parallel \hat{x}$, and the transitions are sensitive to ion motion only in this direction. If, however, R1 is counterpropagating to R2, the transitions become sensitive to motion in all three dimensions.

When two cold ions are held in the trap and undergo small oscillations about their equilibrium positions, we may solve the equations of motion using normal mode coordinates. For two ions lying along the $x$ axis there are two modes involving motion along this axis: the center-of-mass (COM) mode (in which the ions move together with frequency $\omega_{\mathrm{COM}} = \omega_x$) and the stretch mode (wherein the ions move out of phase, with frequency $\omega_{\mathrm{str}} = \sqrt{3}\,\omega_{\mathrm{COM}}$). The other motional frequencies are $\omega_y$ ($y$ center of mass), $\omega_z$ ($z$ center of mass), $\sqrt{\omega_y^2 - \omega_x^2}$ ($xy$ rocking), and $\sqrt{\omega_z^2 - \omega_x^2}$ ($xz$ rocking).

The lower traces in Fig. 3, taken with $\delta k \parallel \hat{x}$, show an $x$-axis normal mode spectrum; results for the $y$ and $z$ modes are very similar. We take the data with the following steps: first we turn on beams D1, D2, and D3 for approximately 10 $\mu$s to Doppler cool the ions to the Lamb-Dicke regime, where the ions' confinement is much smaller than the laser wavelength. Next, we turn off beam D2, and leave beams D1 and D3 on for 5 $\mu$s to optically pump both ions to the $|\downarrow\rangle$ state. We then turn on only the Raman beams R1 and R2 for a time $t_{\mathrm{pr}}$, with relative detuning $\omega_0 + \delta_{\mathrm{pr}}$ (the "Raman probe" pulse). Finally, we drive the cycling transition with D2 and measure the ions' fluorescence. We repeat the experiment at a rate of a few kilohertz while slowly sweeping $\delta_{\mathrm{pr}}$. If the Raman beam difference frequency is resonant with a transition, then an ion is driven from $|\downarrow\rangle \rightarrow |\uparrow\rangle$ and the D2-driven fluorescence rate drops.

For a *single* ion, the carrier transition ($\delta_{\mathrm{pr}} = 0$) causes the population to undergo sinusoidal Rabi oscillations between $|\downarrow\rangle$ and $|\uparrow\rangle$ [9]. The effective Rabi frequency is $\Omega = g_1 g_2/\Delta \approx 2\pi \times 250$ kHz, where $g_1$, $g_2$ are the single-photon resonant Rabi frequencies of beams R1 and R2. (We assume $\Delta \gg \gamma, \omega_m \gg \Omega$, where $\omega_m$ is the frequency of the motional mode of interest.) If $\delta_{\mathrm{pr}} = -\omega_x$ (the first lower $x$ sideband), then the transition couples the states $|\downarrow, n_x\rangle$ and $|\uparrow, n_x - 1\rangle$, where $n_x$ is the vibrational level of the quantized motion along $\hat{x}$. In the Lamb-Dicke regime, the corresponding Rabi frequency is given by $\Omega_{n_x,n_x-1} = \eta_x\sqrt{n_x}\,\Omega$ [9]. Here, $\eta_x = x_0|\delta k \cdot \hat{x}|$ is the Lamb-Dicke parameter (= 0.23 when $\omega_x/2\pi = 8.6$ MHz) and $x_0 = \sqrt{\hbar/(2m\omega_x)}$ is the spread of the $n_x = 0$ wave function, with $m$ being the ion's mass). (Note that if the ion is in the $n_x = 0$ state of motion, this lower sideband vanishes.) The first upper $x$ sideband transition ($\delta_{\mathrm{pr}} = +\omega_x$) couples $|\downarrow, n_x\rangle$ and $|\uparrow, n_x + 1\rangle$ with Rabi frequency $\Omega_{n_x,n_x+1} = \eta_x\sqrt{n_x + 1}\,\Omega$.

In the case of *two* ions driven on the carrier transition, each ion independently undergoes Rabi oscillations

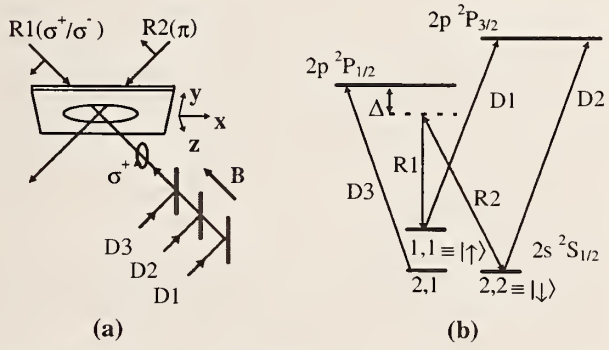


FIG. 2. (a) Laser beam geometry. The trap ring electrode is shown rotated 45° out of the page. The end cap electrodes are omitted for clarity (see Fig. 1). A magnetic field $\boldsymbol{B}$ of magnitude 0.2 mT defines the quantization axis along $-(1/\sqrt{2})\hat{x} + (1/2)(\hat{y} - \hat{z})$, and laser beam polarizations are indicated. (b) Relevant $^9Be^+$ energy levels (not to scale), indicated by $F$, $m_F$ quantum numbers in the ground state. $^2P$ fine structure splitting is ≈197 GHz, $^2S_{1/2}$ hyperfine splitting is $\omega_0/2\pi \approx 1.25$ GHz, $2P_{1/2}$ hyperfine splitting is ≈237 MHz, and the $^2P_{3/2}$ hyperfine structure ($\ll\gamma/2\pi \approx 19.4$ MHz) is not resolved. All optical transitions are near $\lambda \approx 313$ nm, and $\Delta/2\pi \approx 40$ GHz.

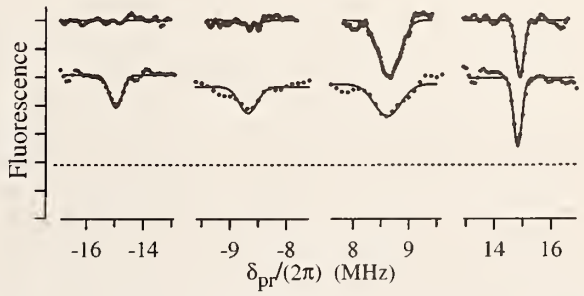


FIG. 3. Spectrum of sidebands due to two-ion $x$-axis normal mode motion: (from left to right) lower stretch, lower COM, upper COM, and upper stretch. The ordinate is the detuning of the Raman probe beam difference frequency from the carrier transition. The abscissa shows the ion fluorescence (proportional to the expectation value of the number of atoms in the state $|\downarrow\rangle$), plus a constant background (whose approximate level for the lower curves is indicated by the dashed line). The solid lines, meant as guides to the eye, are fits to Gaussians. The lower traces show the effects of Doppler cooling. The upper traces, offset vertically for clarity, show the effects of several pulses of Raman cooling on the mode which is displayed. Vanishing lower motional sidebands indicate cooling to the ground state of motion. The peak widths are consistent with the Raman probe pulse lengths (≈3 $\mu$s).

between $|\downarrow\rangle$ and $|\uparrow\rangle$ with Rabi frequency $\Omega$. Since the laser beam waists ($\approx 20\ \mu$m) are much larger than the ion-ion separation ($\approx 2\ \mu$m), the ions are equally illuminated. Nonetheless, if the micromotion of the two ions is different, then the reduction of the carrier (and sideband) transition strengths due to the micromotion will give a different Rabi frequency for each ion [7,10]. This could be used as a means of selectively addressing the ions [11]; however, in the present work the two ions' Rabi frequencies were equal.

Since the sideband transitions affect the motional state, which is a shared property of both ions, such transitions produce entanglement between the ions' spins and their collective motion [12]. The system can no longer be treated as two, independent, two-level systems and the measured fluorescence following the Raman probe is a complicated function of the probe pulse duration $t_{\mathrm{pr}}$. For example, given an initial state $|\downarrow,\downarrow,n\rangle$ (where $n$ is the vibrational level of the COM or stretch motion along the $x$ axis) driven on the corresponding lower sideband for a time $t_{\mathrm{pr}}$, the wave function evolves as

$$|\psi_n(t_{\mathrm{pr}})\rangle = \left\{1 - \frac{n}{2n-1}[1-\cos(Gt_{\mathrm{pr}})]\right\}|\downarrow,\downarrow,n\rangle - ie^{i(\theta-\phi)/2}\sqrt{\frac{n}{2n-1}}\sin(Gt_{\mathrm{pr}})\frac{(|\downarrow,\uparrow\rangle \pm e^{i\phi}|\uparrow,\downarrow\rangle)|n-1\rangle}{\sqrt{2}}$$
$$\mp e^{i\theta}\frac{\sqrt{n^2-n}}{2n-1}[1-\cos(Gt_{\mathrm{pr}})]|\uparrow,\uparrow,n-2\rangle, \quad (1)$$

where $G = \sqrt{2(2n-1)}\,\Omega\,\eta_{x,m}$ and $\theta$, $\phi$ are the sum and difference of the Raman beam phases at the ions. On the COM sideband [top sign in Eq. (1)], $\eta_{x,m} = \eta_{x,\mathrm{COM}} = \eta_x/\sqrt{2}$ (down by a factor of $\sqrt{2}$ from the single-ion case due to the extra mass of the two-ion string), whereas on the stretch sideband (lower sign), $\eta_{x,m} = \eta_{x,\mathrm{str}} = \eta_x/\sqrt{2\sqrt{3}}$. The expressions for transitions on the upper motional sidebands are similar. If, before the Raman probe pulse, the ions have probability $p_n$ of being in the motional state $|n\rangle$, the subsequently measured average fluorescence from the cycling transition is

$$S(t_{\mathrm{pr}}) = \sum_n p_n(2|\langle\downarrow,\downarrow,n|\psi_n(t_{\mathrm{pr}})\rangle|^2 + |\langle\downarrow,\uparrow,n-1|\psi_n(t_{\mathrm{pr}})\rangle|^2 + |\langle\uparrow,\downarrow,n-1|\psi_n(t_{\mathrm{pr}})\rangle|^2). \quad (2)$$

This signal is proportional to the expectation value of the number of atoms in the state $|\downarrow\rangle$. For the data shown in Fig. 3, $t_{\mathrm{pr}}$ was chosen to maximize the sideband features.

The upper traces in Fig. 3 show the effects of adding several cycles of Raman cooling [5] on one particular $x$ mode after the Doppler cooling but before the probe pulse. The reduction in the mean vibrational number $\langle n\rangle$ is indicated by the reduction in size of the lower sideband, which vanishes in the limit $\langle n\rangle \to 0$. The data are consistent with a thermal state of $\langle n_{\mathrm{COM}}\rangle = 0.11^{+0.17}_{-0.03}$ or $\langle n_{\mathrm{str}}\rangle = 0.01^{+0.08}_{-0.01}$. This implies that the COM and stretch modes are in their ground states $90^{+3}_{-12}\%$ and $99^{+1}_{-7}\%$ of the time, respectively. We have also *simultaneously* cooled the COM and stretch modes along $x$, to comparable values of $\langle n\rangle$ (and have separately cooled the other four motional modes—$y$ and $z$ COM, $xy$ rocking, and $xz$ rocking—to near their ground states).

Each cycle of Raman cooling consists of (i) a pulse of the Raman beams with their difference frequency tuned to one of the lower sidebands (COM or stretch mode) and (ii) optical repumping to the $|\downarrow\rangle$ state driven by beams D1 and D3. The Raman transition reduces the vibrational energy by $\hbar\omega_m$, whereas the repumping, on average, heats each mode by approximately the recoil energy ($\ll\hbar\omega_m$). Therefore, the ion is cooled through this process. Five pulses of Raman cooling were used for the data shown in Fig. 3. The exact durations of the Raman pulses were chosen to optimize the cooling rate—each pulse was approximately 5 $\mu$s long.

For an ion-trap implementation of a quantum computer, the motional modes are most susceptible to decoherence. The ions' motional states lose coherence if they couple to (stochastic) electric fields caused by fluctuating potentials on the electrodes. This leads to heating, which has previously been observed in single ions [5,10,13]; in Ref. [5], the heating drove the ion out of the motional (COM) ground state in approximately 1 ms. We have performed similar heating measurements on the COM and non-COM modes of motion of two ions. The results are summarized in Table I. The heating rate was determined by inserting a delay between laser cooling and the Raman

TABLE I. Heating rates of the six normal modes of two trapped ions. The Raman beams were counterpropagating for the $y$- and $z$-axis data, making the Raman probe sensitive to motion in all three dimensions. Note that the COM modes are heated at a much higher rate than the non-COM modes (see text). (The precision with which the heating rates are given for the last five modes is limited by measurement noise.)

| Mode | $\omega_m/2\pi$ (MHz) | $\delta\langle n\rangle/\delta t$ (ms$^{-1}$) |
|---|---|---|
| $x_{\mathrm{COM}}$ | 8.6 | $19^{+40}_{-13}$ |
| $y_{\mathrm{COM}}$ | 17.6 | $>10$ |
| $z_{\mathrm{COM}}$ | 9.3 | $>20$ |
| $x_{\mathrm{str}}$ | 14.9 | $<0.18$ |
| $xy_{\mathrm{rocking}}$ | 15.4 | $<1$ |
| $xz_{\mathrm{rocking}}$ | 3.6 | $<0.5$ |

probe. The main results from these data are that the COM modes are heated out of the ground state much more quickly than the non-COM modes. This can be explained as follows.

The COM modes, in which both ions move in phase, can be excited by a uniform electric field. However, no non-COM mode can be excited by a uniform electric field [14]—since these modes involve *differential* motion of the ions, they can be driven only by field gradients. If the fluctuating field at the ion (along the direction of motion of the mode of interest) is $E(t)$, an estimate of the corresponding field gradient is $E(t)/d$, where $d$ is a characteristic internal dimension of the trap. For stochastic fields, the COM heating rate scales as $\langle E^2(t)\rangle$; the non-COM mode heating rates scale as $\langle[\frac{E(t)}{d}\Delta x]^2\rangle$ (where $\Delta x$ is the ion-ion separation), down by a factor of $10^4$ for the present trap. Similarly, other non-COM modes for more than two ions can be excited only by higher-order field gradients, leading to further reductions in their heating.

This suggests using non-COM modes for the quantum data bus in the Cirac-Zoller scheme. Excitation of the "spectator" COM modes along the direction to which the Raman transitions are sensitive will still alter the Rabi frequencies, but these effects will be higher order in the Lamb-Dicke parameter [10]. In the two-ion example, in the Lamb-Dicke regime, the Rabi frequency for a first sideband transition $|n_1\rangle \rightarrow |n_1'\rangle$ on (cold) mode 1, given that (hotter) mode 2 is in the state $|n_2\rangle$, is [10]

$$\Omega_{n_1,n_1'}(n_2) = \Omega\,\eta_1\sqrt{n_{1>}}\,e^{-(\eta_1^2+\eta_2^2)/2}(1 - n_2\eta_2^2), \quad (3)$$

where $n_{1>}$ denotes the larger of $n_1'$ or $n_1$, and $\eta_1$ and $\eta_2$ are the Lamb-Dicke parameters for modes 1 and 2, respectively. Fluctuations in the Rabi frequency of mode 1 due to fluctuations in $n_2$ therefore occur in order $\eta_2^2$. However, for the conditions of the present experiment, even if quantum logic operations were performed using the $x$-stretch mode, the $x$-COM mode heating would still limit the number of operations to around ten by the above mechanism. Clearly, this heating must be eliminated in future experiments.

The two-ion cooling results presented here are comparable to our previous single-ion results [5], indicating that rf heating should not be a concern for small numbers of ions [10]. Comparable cooling for $N > 2$ ions should not present any fundamental difficulties, as long as spurious overlaps of motional modes are avoided.

The preparation of a pure state of motion (the ground state) of multiple trapped ions represents the first step towards realizing quantum logic operations on them. Such operations should lead to the creation of arbitrary entangled states of massive particles, including EPR- or GHZ-like spin states [15]. Unlike other systems in which EPR states have been generated, it should be possible to reliably create these states on demand [11] rather than by a selection process, and to detect them with nearly perfect efficiency [16].

We acknowledge support from the U.S. National Security Agency, Office of Naval Research, and Army Research Office. We thank Kristan Corwin, David Kielpinski, and Matt Young for critical readings of the manuscript.

*Electronic address: kingb@ucsu.Colorado.EDU
†Present address: Institut für Experimentalphysik, Universität Innsbruck, Innsbruck, Austria.

[1] A. Ekert and R. Jozsa, Rev. Mod. Phys. **68**, 733 (1996); A. Steane, Rep. Prog. Phys. **61**, 117 (1998).
[2] J. I. Cirac and P. Zoller, Phys. Rev. Lett. **74**, 4091 (1995).
[3] If the "data bus" is in a thermal state with probability $P_0$ of being in the ground state then, if we ignore all other sources of error, a given quantum computation must be repeated $1/P_0$ times, on average, to give a correct answer.
[4] C. Monroe *et al.*, Phys. Rev. Lett. **75**, 4714 (1995).
[5] C. Monroe *et al.*, Phys. Rev. Lett. **75**, 4011 (1995).
[6] S. R. Jefferts, C. Monroe, E. Bell, and D. J. Wineland, Phys. Rev. A **51**, 3112 (1995).
[7] C. J. Myatt *et al.*, in *Methods for Ultrasensitive Detection,* SPIE Proceedings Vol. 3270, edited by Bryan L. Fearey (SPIE–International Society for Optical Engineering, Bellingham, WA, 1998) p. 131; R. G. Devoe, Phys. Rev. A **58**, 910–914 (1998).
[8] J. E. Thomas *et al.*, Phys. Rev. Lett. **48**, 867 (1982).
[9] D. M. Meekhof *et al.*, Phys. Rev. Lett. **76**, 1796 (1996).
[10] D. J. Wineland *et al.*, J. Res. Natl. Inst. Stand. Technol. **103**, 259 (1998); Forschr. Phys. **46**, 363 (1998).
[11] Q. A. Turchette *et al.*, quant-phy/9806012.
[12] D. J. Wineland, J. J. Bollinger, W. M. Itano, and D. J. Heinzen, Phys. Rev. A **50**, 67 (1994).
[13] F. Diedrich, J. C. Bergquist, W. M. Itano, and D. J. Wineland, Phys. Rev. Lett. **62**, 403 (1989).
[14] D. J. Wineland and H. G. Dehmelt, J. Appl. Phys. **46**, 919 (1975); D. F. V. James, Phys. Rev. Lett. **81**, 317 (1998).
[15] A. Einstein, B. Podolsky, and N. Rosen, Phys. Rev. **47**, 777 (1935); D. M. Greenberger, M. A. Horne, A. Shimony, and A. Zeilinger, Am. J. Phys. **58**, 1131 (1990); M. Lamehi-Rachti and W. Mittig, Phys. Rev. D **14**, 2543 (1976); E. Hagley *et al.*, Phys. Rev. Lett. **79**, 1 (1997).
[16] R. Blatt and P. Zoller, Eur. J. Phys. **9**, 250 (1988).

# Deterministic Entanglement of Two Trapped Ions

Q. A. Turchette,* C. S. Wood, B. E. King, C. J. Myatt, D. Leibfried,† W. M. Itano, C. Monroe, and D. J. Wineland

*Time and Frequency Division, National Institute of Standards and Technology, Boulder, Colorado 80303*

(Received 26 May 1998)

We have prepared the internal states of two trapped ions in both the Bell-like singlet and triplet entangled states. In contrast to all other experiments with entangled states of either massive particles or photons, we do this in a deterministic fashion, producing entangled states *on demand* without selection. The deterministic production of entangled states is a crucial prerequisite for large-scale quantum computation. [S0031-9007(98)07411-0]

PACS numbers: 42.50.Ct, 03.65.Bz, 03.67.Lx, 32.80.Pj

Since the seminal discussions of Einstein, Podolsky, and Rosen, two-particle quantum entanglement has been used to magnify and confirm the peculiarities of quantum mechanics [1]. More recently, quantum entanglement has been shown to be not purely of pedagogical interest, but also relevant to computation [2], information transfer [3], cryptography [4], and spectroscopy [5,6]. Quantum computation (QC) exploits the inherent parallelism of quantum superposition and entanglement to perform certain tasks more efficiently than can be achieved classically [7].

Relatively few physical systems are able to approach the severe requirements of QC: Controllable coherent interaction between the quantum information carriers (quantum bits or qubits), isolation from the environment, and high-efficiency interrogation of individual qubits. Cirac and Zoller have proposed a *scalable* scheme utilizing trapped ions for QC [8]. In it, the qubits are two internal states of an ion; entanglement and computation are achieved by quantum logic operations on pairs of ions involving shared quantized motion. Previously, trapped-ion quantum logic operations were demonstrated between a single ion's motion and its spin [9]. In this Letter, we use conditional quantum logic transformations to entangle and manipulate the qubits of two trapped ions.

Previous experiments have studied entangled states of photons [10,11] and of massive particles [12–14]. These experiments rely on *random processes,* either in creation of the entanglement in photon cascades [10], photon down-conversion [11], and proton scattering [12], or in the selection of appropriate atom pairs from a larger sample of trials in cavity QED [13]. Recent results in NMR of bulk samples have shown entanglement of particle spins [14,15], but because pseudopure states are selected through averaging over a thermal distribution, the signal is exponentially degraded as the number of qubits is increased. In the preceding experiments the efficiency of state generation will exponentially decrease with the system size (both particles and operations). This is because the preceding processes are *selectable* but not *deterministic* generators of entanglement. We mean deterministic as defined in Ref. [16] which in the present context is "the property that if the [entanglement] source is switched on, then with a high degree of certainty [the desired quantum state of all of a given set of particles is generated] at a known, user-specified time." Deterministic entanglement coupled with the ability to store entangled states for future use is crucial for the realization of large-scale quantum computation. Ion-trap QC has no fundamental scaling limits; moreover, even the simple two-ion manipulations described here can, in principle, be incorporated into large-scale computing by coupling two-ion subsystems via cavities [17], or by using accumulators [6].

In this Letter, we describe the deterministic generation of a state which under ideal conditions is given by

$$|\psi_e(\phi)\rangle = \tfrac{3}{5}\,|{\downarrow\uparrow}\rangle - e^{i\phi}\,\tfrac{4}{5}\,|{\uparrow\downarrow}\rangle, \qquad (1)$$

where $|{\downarrow}\rangle$ and $|{\uparrow}\rangle$ refer to internal electronic states of each ion (in the usual spin-1/2 analogy) and $\phi$ is a controllable phase factor. For $\phi = 0$ or $\pi$, $|\psi_e(\phi)\rangle$ is a good approximation to the usual Bell singlet $(-)$ or triplet $(+)$ state $|\psi_B^{\mp}\rangle = [|{\downarrow\uparrow}\rangle \mp |{\uparrow\downarrow}\rangle]/\sqrt{2}$ since $|\langle\psi_B^{-}|\psi_e(0)\rangle|^2 = |\langle\psi_B^{+}|\psi_e(\pi)\rangle|^2 = 0.98$ and $E[\psi_e(\phi)] = 0.94$ where $E$ is the *entanglement* defined in [18]. We also describe a novel means of differentially addressing each ion to generate the entanglement and a state-sensitive detection process to characterize it, leading to a measured fidelity of our experimentally generated state described by density matrix $\rho^{\pm}$ of $\langle\psi_e(\pi,0)|\rho^{\pm}|\psi_e(\pi,0)\rangle \approx \langle\psi_B^{\pm}|\rho^{\pm}|\psi_B^{\pm}\rangle \approx 0.70$.

The apparatus is described in Ref. [19]. We confine $^9Be^+$ ions in an elliptical rf Paul trap (major axis $\approx 525\ \mu$m, aspect ratio 3:2) with a potential applied between ring and end caps of $V_0 \cos\Omega_T t + U_0$ with $\Omega_T/2\pi \approx 238$ MHz, $V_0 \approx 520$ V. The trap is typically operated over the range $12 < U_0 < 17$ V leading to secular frequencies of $(\omega_x, \omega_y, \omega_z)/2\pi = (7.3, 16, 12.6)$ to $(8.2, 17.2, 10.1)$ MHz. The ion-ion spacing (along $\hat{x}$) is $l \approx 2\ \mu$m.

The relevant level structure of $^9Be^+$ is shown in Fig. 1a. The qubit states are the $2s\ ^2S_{1/2}\ |F = 2, m_F = 2\rangle \equiv |{\downarrow}\rangle$ and $2s\ ^2S_{1/2}\ |F = 1, m_F = 1\rangle \equiv |{\uparrow}\rangle$ states. Laser beams D1 and D2 provide Doppler precooling and beam D3 prevents optical pumping to the $|F = 2, m_F = 1\rangle$ state. The cycling $|{\downarrow}\rangle \rightarrow 2p\ ^2P_{3/2}$

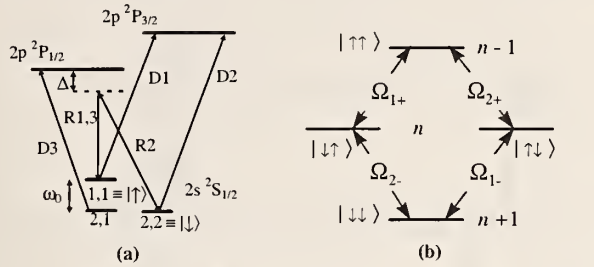


FIG. 1. (a) Relevant $^9Be^+$ energy levels. All optical transitions are near $\lambda = 313$ nm, $\Delta/2\pi = 40$ GHz, and $\omega_0/2\pi = 1.25$ GHz. R1–R3: Raman beams. D1–D3: Doppler cooling, optical pumping, and detection beams. (b) The internal basis qubit states of two spins shown with the vibrational levels connected on the red motional sideband. The labeled atomic states are as in (a); $n$ is the motional-state quantum number (note that the motional mode frequency $\omega_{str} \ll \omega_0$). $\Omega_{i\pm}$ are the Rabi frequencies connecting the states indicated.

$|F = 3, m_F = 3\rangle$ transition driven by the $\sigma^+$-polarized D2 laser beam allows us to differentiate $|\uparrow\rangle$ from $|\downarrow\rangle$ in a single ion with ≈90% detection efficiency by observing the fluorescence.

Transitions $|\downarrow\rangle|n\rangle \leftrightarrow |\uparrow\rangle|n'\rangle$ (where $n, n'$ are vibrational quantum numbers) are driven by stimulated Raman processes from pairs of laser beams in one of two geometries. Additionally, two types of transitions are driven: the "carrier" with $n' = n$, and the red motional sideband (rsb) with $n' = n - 1$ [20]. With reference to Fig. 1a, the pair of Raman beams R1⊥R2 has difference wave vector $\delta\vec{k} \parallel \hat{x}$ and is used for sideband cooling (to prepare $|\downarrow\downarrow\rangle|0\rangle$), driving the $\hat{x}$ rsb, and to drive the "$\hat{x}$ carrier." Beam pair R2 ∥ R3 with $\delta\vec{k} \approx 0$ drives the "copropagating carrier" and is insensitive to motion.

Two trapped ions aligned along $\hat{x}$ have two modes of motion along $\hat{x}$: the center-of-mass (c.m.) mode (at $\omega_x$) and the stretch mode (at $\omega_{str} = \sqrt{3}\,\omega_x$) in which the two ions move in opposite directions. We sideband cool both of these modes to near the ground state, but use the stretch mode on transitions which involve the motion since it is colder (99% probability of $|n = 0\rangle$) than the c.m. and heats at a significantly reduced rate [19]. Figure 1b shows the relevant states coupled on the rsb with Rabi frequencies (in the Lamb-Dicke limit)

$$\Omega_{i+} = \sqrt{n}\,\eta'\Omega_i; \qquad \Omega_{i-} = \sqrt{n+1}\,\eta'\Omega_i, \quad (2)$$

where $\eta' = \eta/\sqrt{2\sqrt{3}}$ is the stretch-mode two-ion Lamb-Dicke parameter (with single-ion $\eta \approx 0.23$ for $\omega_x/2\pi \approx 8$ MHz) and $\Omega_i$ is the carrier Rabi frequency of ion $i$ [9]. On the carrier the time evolution is simply that of independent Rabi oscillations with Rabi frequencies $\Omega_i$. On the copropagating carrier, $\Omega_1 = \Omega_2 \equiv \Omega_c$.

In the Cirac-Zoller scheme, each of an array of tightly focused laser beams illuminates one and only one ion for individual state preparation. Here, each ion is equally illuminated, and we pursue an alternative technique to attain $\Omega_1 \neq \Omega_2$. Differential Rabi frequencies can be used conveniently for individual addressing on the $\hat{x}$ carrier: for example, if $\Omega_1 = 2\Omega_2$, then ion 1 can be driven for a time $\Omega_1 t = \pi$ ($2\pi$ pulse, no spin flip) while ion 2 is driven for a $\pi$ pulse resulting in a spin flip.

For differential addressing, we control the ion micromotion. To a good approximation, we can write [21]

$$\Omega_i = \Omega_c J_0(|\delta\vec{k}|\xi_i), \quad (3)$$

where $J_0$ is the zero-order Bessel function and $\xi_i$ is the amplitude of micromotion at $\Omega_T$ (along $\hat{x}$) associated with ion $i$, proportional to the ion's mean $\hat{x}$ displacement from trap center. The Bessel function arises because the micromotion effectively smears out the position of an ion, thereby suppressing the laser-atom interaction [21]. The micromotion is controlled by applying a static electric field to push the ions [22] along $\hat{x}$, moving ion 2 (ion 1) away from (toward) the rf null position, inducing a smaller (larger) Rabi frequency. The range of Rabi frequencies explored experimentally is shown in Fig. 2a.

We determine $\Omega_{1,2}$ by observing the Rabi oscillations of the ions (between $|\downarrow\rangle$ and $|\uparrow\rangle$) driven on the $\hat{x}$ carrier. An example with $\Omega_1 = 2\Omega_2$ is shown in Fig. 2b. We

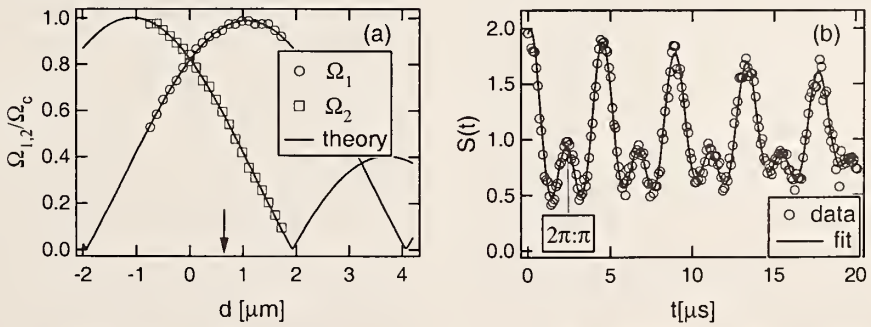


FIG. 2. (a) Normalized $\hat{x}$-carrier Rabi frequencies $\Omega_i/\Omega_c$ of each of two ions as a function of center-of-mass displacement $d$ from the rf-null position. The solid curves are Eq. (3) where the distance between the maxima of the two curves sets the scale of the ordinate, based on the known ion-ion spacing of $l \approx 2.2$ $\mu$m at $\omega_x/2\pi = 8.8$ MHz. (b) Example of Rabi oscillations starting from the initial state $|\downarrow\downarrow\rangle|n = 0\rangle$ with $\Omega_1 = 2\Omega_2$. A fit to Eq. (4) determines that $\Omega_1/2\pi = 2\Omega_2/2\pi \approx 225$ kHz, $\gamma/2\pi \approx 6$ kHz, and $\alpha \approx -0.05$. The arrow in (a) indicates the conditions of (b).

detect a fluorescence signal $S(t) = 2P_{\downarrow\downarrow} + (1 + \alpha)P_{\downarrow\uparrow} + (1 - \alpha)P_{\uparrow\downarrow}$ where $P_{kl} = |\langle\psi(t)|kl\rangle|^2$, $k, l \in \{\uparrow, \downarrow\}$, $\psi(t)$ is the state at time $t$ and $|\alpha| \ll 1$ describes a small differential detection efficiency due to the induced differential micromotion. Driving on the $\hat{x}$ carrier for time $t$ starting from $|\downarrow\downarrow\rangle|0\rangle$, $S(t)$ can be described by

$$S(t) = 1 + (1/2)(1 + \alpha)\cos(2\Omega_1 t)e^{-\gamma t} + (1/2)(1 - \alpha)\cos(2\Omega_2 t)e^{-(\Omega_2/\Omega_1)\gamma t}, \quad (4)$$

where $\gamma$ allows for decay of the signal [20]. The local maximum at $t = 2.4$ $\mu$s on Fig. 2b is the $2\pi{:}\pi$ point at which ion 1 has undergone a $2\pi$ pulse while ion 2 has undergone a $\pi$ pulse resulting in $|\downarrow\downarrow\rangle|0\rangle \rightarrow |\downarrow\uparrow\rangle|0\rangle$. Driving a $\pi{:}\pi$ pulse on the copropagating carrier transforms $|\downarrow\uparrow\rangle|0\rangle$ to $|\uparrow\downarrow\rangle|0\rangle$ and $|\downarrow\downarrow\rangle|0\rangle$ to $|\uparrow\uparrow\rangle|0\rangle$, completing the generation of all four internal basis states of Fig. 1b.

Now consider the levels coupled by the first rsb [20] shown in Fig. 1b. If we start in the state $|\psi(0)\rangle = |\downarrow\uparrow\rangle|0\rangle$ and drive on the (stretch mode) rsb for time $t$, the Schrödinger equation can be integrated to yield

$$|\psi(t)\rangle = -\frac{i\Omega_{2-}}{G}\sin(Gt)|\downarrow\downarrow\rangle|1\rangle + \left[\frac{\Omega_{2-}^2}{G^2}(\cos Gt - 1) + 1\right]|\downarrow\uparrow\rangle|0\rangle + e^{i\phi}\left[\frac{\Omega_{2-}\Omega_{1-}}{G^2}(\cos Gt - 1)\right]|\uparrow\downarrow\rangle|0\rangle, \quad (5)$$

where $G = (\Omega_{2-}^2 + \Omega_{1-}^2)^{1/2}$ and $\Omega_{i-}$ is from Eq. (2) with $n = 0$. The phase factor $\phi = \delta\vec{k}\cdot\langle\vec{x}_1 - \vec{x}_2\rangle$ depends on the spatial separation of ions and the arises because each ion sees different laser phases. The ion-ion spacing varies by $\delta l \approx 100$ nm over the range of $U_0$ cited previously ($\phi = 0$ for $U_0 = 16.3$ V and $\phi = \pi$ for $U_0 = 12.6$ V, with $d\phi/dU_0$ in good agreement with theory). For $Gt = \pi$ and $\Omega_1 = 2\Omega_2$, the final state is $\psi_e(\phi)$ from Eq. (1). Note that $\Omega_1 = (\sqrt{2} + 1)\Omega_2$ would generate the Bell states (but we would not have access to the initial state $|\downarrow\uparrow\rangle$, since $\Omega_i$ are fixed throughout an experiment).

We now describe our two-ion state-detection procedure. We first prepare a two-ion basis state $|kl\rangle$, apply the detection beam D2 for a time $\tau_d \approx 500$ $\mu$s, and record the number of photons $m$ detected in time $\tau_d$. We repeat this sequence for $N \approx 10^4$ trials and build a histogram of the photons collected (Fig. 3). To determine the population of an unknown state, we fit its histogram to a weighted sum of the four basis histograms with a simple linear least-squares procedure.

We observe that the $|\uparrow\uparrow\rangle$ count distribution (Fig. 3a) is not the expected single peak at $m = 0$, but includes contributions at $m = 1$ and $m = 2$ due to background counts. The signal in bins $m > 2$ (which accounts for $\sim$10% of the area) is due to a depumping process in which

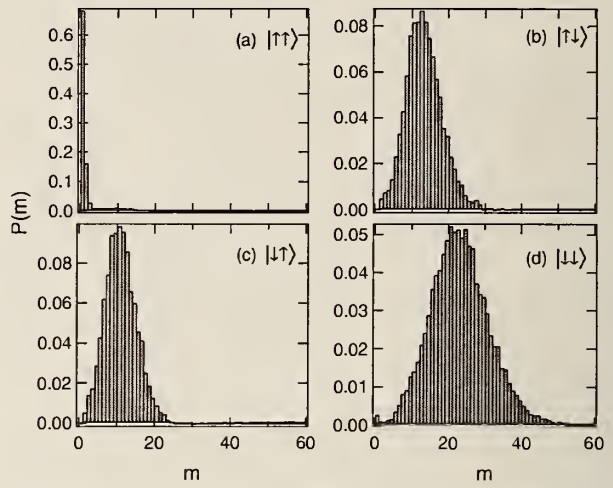


FIG. 3. Photon-number distributions for the four basis qubit states. Plotted in each graph is the probability of occurrence $P(m)$ of $m$ photons detected in 500 $\mu$s vs $m$, taken over $\sim 10^4$ trials. Note the different scales for each graph.

D2 off-resonantly drives an ion out of $|\uparrow\rangle$, ultimately trapping it in the cycling transition. We approximately double the depumping time by applying two additional Raman "shelving" pulses ($|\uparrow\rangle \rightarrow {}^2S_{1/2}|F = 2, m_F = 0\rangle \rightarrow {}^2S_{1/2}|F = 1, m_F = -1\rangle$; $|\downarrow\rangle$ unaffected) after every state preparation. This results in an average difference of 10–15 detected photons between an initial $|\downarrow\rangle$ and $|\uparrow\rangle$ state, as shown in Fig. 3. The distributions associated with $|\downarrow\uparrow\rangle$, $|\uparrow\downarrow\rangle$, and $|\downarrow\downarrow\rangle$ are non-Poissonian due to detection laser intensity and frequency fluctuations, the depumping described previously and $|\downarrow\rangle \rightarrow |\uparrow\rangle$ transitions from imperfect polarization of D2.

One may ask: What is our overall two-ion state-detection efficiency on a *per experiment* basis? To address this issue, we distinguish three cases: (1) $|\uparrow\uparrow\rangle$, (2) $|\uparrow\downarrow\rangle$ or $|\downarrow\uparrow\rangle$, and (3) $|\downarrow\downarrow\rangle$. Now define case 1 to be true when $m \leq 3$, case 2 when $3 < m < 17$, and case 3 when $m \geq 17$. This gives an optimal 80% probability that the correct case is diagnosed.

We have generated states described by density operators $\rho^{\pm}$ in which the populations (diagonals of $\rho^{\pm}$) are measured to be $P_{\downarrow\uparrow} \approx P_{\uparrow\downarrow} \approx 0.4$, $P_{\downarrow\downarrow} \approx 0.15$, and $P_{\uparrow\uparrow} \approx 0.05$. To establish coherence, consider first the Bell singlet state $\psi_B^-$ which has $P_{\downarrow\uparrow} = P_{\uparrow\downarrow} = 1/2$. Since $\psi_B^-$ has total spin $J = 0$, any $J$-preserving transformation, such as an equal rotation on both spins, must leave this state unchanged, whereas such a rotation on a mixed state with populations $P_{\downarrow\uparrow} = P_{\uparrow\downarrow} = 1/2$ and no coherences will evolve quite differently. We perform a rotation on both spins through an angle $\theta$ by driving on the copropagating carrier for a time $t$ such that $\theta = \Omega_c t$. Figure 4a shows the time evolution of an experimental state which approximates the singlet Bell state. Contrast this with the approximate "triplet" state shown in Fig. 4b. The data show that $\rho^{\pm}$ is decomposed as $\rho^{\pm} = C|\psi_B^{\pm}\rangle\langle\psi_B^{\pm}| + (1 - C)\rho_m$

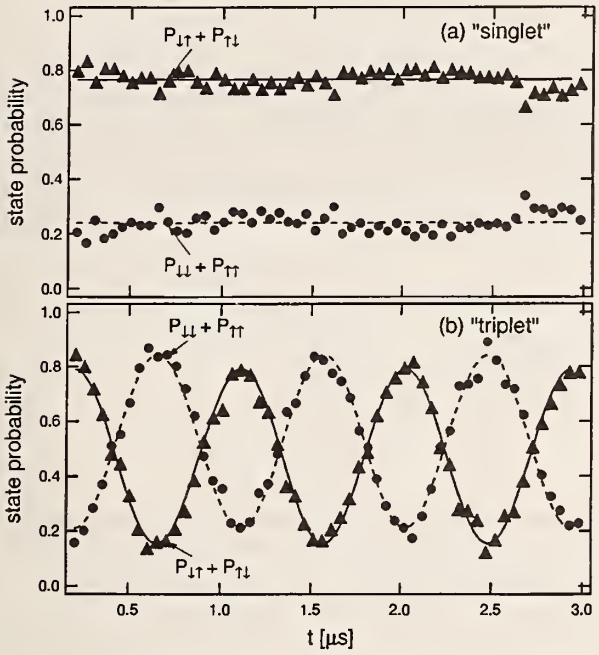


FIG. 4. Probabilities $P_{\Uparrow} + P_{\Downarrow}$ and $P_{\Downarrow} + P_{\Uparrow}$ as a function of time $t$ driving on the copropagating carrier, starting from (a) the "singlet" $\psi_e(0)$ and (b) the "triplet" $\psi_e(\pi)$ entangled states. The equivalent rotation angle is $2\Omega_c t$ ($\Omega_c/2\pi \approx 200$ kHz for these data). The solid and dashed lines in (a) and (b) are sinusoidal fits to the data, from which the contrast is extracted.

in which $\rho_m$ has no coherences which contribute to the measured signal (off-diagonal elements connecting $|\uparrow\downarrow\rangle$ with $|\downarrow\uparrow\rangle$ and $|\uparrow\uparrow\rangle$ with $|\downarrow\downarrow\rangle$), and $C = 0.6$ is the contrast of the curves in Fig. 4. This leads to a fidelity of $\langle\psi_B^{\pm}|\rho^{\pm}|\psi_B^{\pm}\rangle = (P_{\Uparrow} + P_{\Downarrow} + C)/2 \approx 0.7$.

The nonunit fidelity of our states arises from Raman laser intensity noise and a second-order (in $\eta$) effect on $\Omega_i$ due to excitation of the c.m. mode [19]. These effects can be seen in Fig. 2b as a decay envelope on the data [modeled by $\gamma$ of Eq. (4)] and cause a 10% loss of fidelity in initial state preparation [23].

The micromotion-induced selection of Rabi frequencies as here demonstrated is sufficient to implement two-ion universal quantum logic with individual addressing [8]. To start, we arrange the trap strength and static electric field in such a way that $|\delta\vec{k}|\xi_1 = 0$ and $|\delta\vec{k}|\xi_2 = a_0$, where $J_0(a_0) = 0$. To isolate ion 1, note that by Eq. (3) $\Omega_1 = \Omega_c J_0(0) = \Omega_c$ and $\Omega_2 = \Omega_c J_0(a_0) = 0$. To isolate ion 2, we add $\Omega_T/2\pi = \pm 238$ MHz to the difference frequency of the Raman beams. This drives the first sideband of the rf micromotion so that the $J_0$ of Eq. (3) is replaced by $J_1$, resulting in $\Omega_1 = \Omega_c J_1(0) = 0$ and $\Omega_2 = \Omega_c J_1(a_0) \neq 0$.

In conclusion, we have taken a first step which is crucial for quantum computations with trapped ions. We have *engineered* entangled states deterministically; that is, there is no inherent probabilistic nature to our quantum entangling source. We have developed a two-ion state-sensitive detection technique which allows us to measure the diagonal elements of the density matrix $\rho^{\pm}$ of our states, and have performed transformations which directly measure the relevant off-diagonal coherences of $\rho^{\pm}$.

We acknowledge support from the U.S. National Security Agency, Office of Naval Research, and Army Research Office. We thank Eric Cornell, Tom Heavner, David Kielpinski, and Matt Young for critical readings of the manuscript.

*Electronic address: quentint@boulder.nist.gov.
†Present address: Univ. Innsbruck, Innsbruck, Austria.

[1] A. Einstein, B. Podolsky, and N. Rosen, Phys. Rev. **47**, 777 (1935); J. S. Bell, *Speakable and Unspeakable in Quantum Mechanics* (Cambridge University Press, Cambridge, England, 1987).
[2] P. W. Shor, SIAM J. Comput. **26**, 1484 (1997); L. K. Grover, Phys. Rev. Lett. **79**, 325 (1997).
[3] A. Barenco and A. Ekert, J. Mod. Opt. **42**, 1253 (1995); C. H. Bennett, Phys. Today **48**, No. 10, 24 (1995).
[4] A. Ekert, Phys. Rev. Lett. **67**, 661 (1991); C. H. Bennett, Sci. Am. **267**, No. 4, 50 (1992).
[5] J. J. Bollinger *et al.*, Phys. Rev. A **54**, R4649 (1996); S. F. Huelga *et al.*, Phys. Rev. Lett. **79**, 3865 (1997).
[6] D. J. Wineland *et al.*, J. Res. Natl. Inst. Stand. Technol. **103**, 259 (1998).
[7] A. Ekert and R. Jozsa, Rev. Mod. Phys. **68**, 733 (1996); A. Steane, Rep. Prog. Phys. **61**, 117 (1998).
[8] J. I. Cirac and P. Zoller, Phys. Rev. Lett. **74**, 4091 (1995).
[9] C. Monroe *et al.*, Phys. Rev. Lett. **75**, 4714 (1995).
[10] S. J. Freedman and J. F. Clauser, Phys. Rev. Lett. **28**, 938 (1972); E. S. Fry and R. C. Thompson, Phys. Rev. Lett. **37**, 465 (1976); A. Aspect, P. Grangier, and G. Roger, Phys. Rev. Lett. **49**, 91 (1982).
[11] Z. Y. Ou and L. Mandel, Phys. Rev. Lett. **61**, 50 (1988); Y. H. Shih and C. O. Alley, Phys. Rev. Lett. **68**, 3663 (1992); Z. Y. Ou *et al.*, Phys. Rev. Lett. **68**, 3663 (1992); P. Kwiat *et al.*, Phys. Rev. Lett. **75**, 4337 (1995); W. Tittel *et al.*, Europhys. Lett. **40**, 595 (1997); D. Bouwmeester *et al.*, Nature (London) **390**, 575 (1997).
[12] M. Lamehi-Rachti and W. Mittig, Phys. Rev. D **14**, 2543 (1976).
[13] E. Hagley *et al.*, Phys. Rev. Lett. **79**, 1 (1997).
[14] R. Laflamme *et al.*, quant-ph/9709025 (unpublished).
[15] I. L. Chuang, N. Gershenfeld, and M. Kubinec, Phys. Rev. Lett. **80**, 3408 (1998); I. L. Chuang *et al.*, Nature (London) **393**, 143 (1998); D. G. Cory, M. D. Price, and T. F. Havel, Physica (Amsterdam) **120D**, 82 (1998); D. G. Cory *et al.*, Phys. Rev. Lett. **81**, 2152 (1998).
[16] C. K. Law and H. J. Kimble, J. Mod. Opt. **44**, 2067 (1997).
[17] J. I. Cirac *et al.*, Phys. Rev. Lett. **78**, 3221 (1997).
[18] C. H. Bennett *et al.*, Phys. Rev. A **53**, 2046 (1996).
[19] B. E. King *et al.*, Phys. Rev. Lett. **81**, 1525 (1998).
[20] D. M. Meekhof *et al.*, Phys. Rev. Lett. **76**, 1796 (1996); **77**, 2346 (1996).
[21] D. J. Wineland and W. M. Itano, Phys. Rev. A **20**, 1521 (1979).
[22] S. R. Jefferts *et al.*, Phys. Rev. A **51**, 3112 (1995).
[23] The reference histograms for $|\downarrow\uparrow\rangle$ and $|\uparrow\downarrow\rangle$ (Figs. 3b and 3c) have had this 10% contamination from $|\uparrow\uparrow\rangle$ and $|\downarrow\downarrow\rangle$ removed.

# Grating-tuned semiconductor MOPA lasers for precision spectroscopy*

J. H. Marquardt, F. C. Cruz, M. Stephens, C. W. Oates, L. W. Hollberg, J. C. Bergquist
National Institute of Standards and Technology
Boulder, CO 80303

D. F. Welch, D. Mehuys, and S. Sanders
SDL, Inc.
80 Rose Orchard Way, San Jose, CA 95134

## ABSTRACT

A standard grating-tuned extended-cavity diode laser is used for injection seeding of a tapered semiconductor laser/amplifier. With sufficient injection power the output of the amplifier takes on the spectral characteristics of the master laser. We have constructed master-oscillator power-amplifier (MOPA) systems that operate near 657 nm, 675 nm, 795 nm, and 850 nm. Although the characteristics vary from system to system, we have demonstrated output powers of greater than 700 mW in a single spatial mode, linewidths less than 1 kHz, coarse tuning greater than 20 nm, and continuous single-frequency scanning greater than 150 GHz. We discuss the spectroscopic applications of these high power, highly coherent, tunable diode lasers as applied to Ca, $Hg^+$, $I_2$, and two-photon transitions in Cs.

Keywords: diode lasers, tapered amplifiers, injection locking, high resolution spectroscopy, MOPA



## 1. INTRODUCTION

Many scientific and technical applications of tunable diode lasers require higher powers than have been available from semiconductor laser sources. Recent advances in tapered gain structures have opened a new frontier in single-mode, single-frequency, tunable, semiconductor laser capabilities.[1] Tapered amplifiers (TA) can have broad gain-bandwidths, providing tremendous potential for tunable lasers with high power. They provide roughly one order of magnitude more power than previous single-spatial-mode devices. However, these tapered amplifiers/oscillators usually operate with many simultaneous longitudinal modes, which limits their usefulness for coherent and high-resolution applications. Using tapered amplifiers in extended cavities for wavelength control (such as optical feedback from diffraction gratings) allows good coarse tuning at high power,[2] but it is difficult to maintain true single-frequency operation. Extended-cavity TAs often exhibit instabilities which can cause jumps among a few nearby longitudinal modes or result in lasing on a few modes simultaneously.

One powerful solution to these problems is to separate the function of the high-power generation from that of the high-precision single-frequency tuning. A few modern examples of this type of system can be found in the literature and include: distributed Bragg reflector (DBR) laser diode plus tapered amplifier,[3] solitary diode laser plus tapered amplifier,[4] and grating-tuned extended-cavity diode laser (ECDL) plus tapered amplifier. In this paper we describe the applications of extended-cavity diode-laser plus master-oscillator power-amplifier (ECDL-MOPA) systems that are currently under way at NIST. The characteristics of these systems are discussed from a user's perspective, where our applications are primarily in high resolution spectroscopy. Other related systems and applications have been described by Zimmermann et al.[5] and Goldberg and Burns.[6]

## 2. EXPERIMENT

By using several different experimental setups we gain some insight into the general characteristics of injection-locked MOPAs. A typical experimental setup is shown in Figure 1; it consists of a standard grating-tuned ECDL in the Littman-



0-8194-2222-3/96/$6.00

Metcalf (grazing incidence) configuration, which acts as the master laser to inject the TA slave. The light from the master laser is sent through an optical isolator and spatially mode-matched to the beam emitted from the back facet of the TA. Since the front output aperture of the TA is very asymmetric (~ 1 μm by 100 μm), a cylindrical lens, in addition to the standard spherical lens is needed to collimate the output beam. (In addition the output beam can have large astigmatism which may be compensated.)

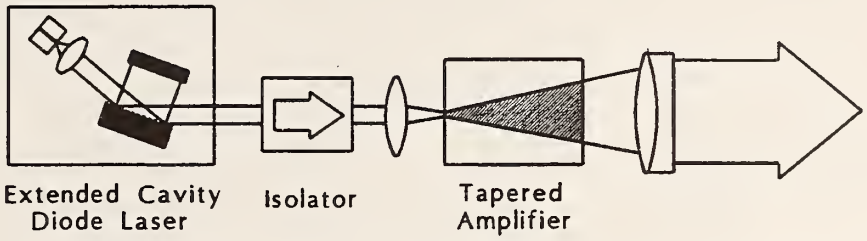


Figure 1. General ECDL-MOPA set-up. The ECDL output is sent through an isolator and then mode-matched to the beam emitted from the rear facet of the tapered amplifier. The collimating optics consist of one spherical and one cylindrical lens.

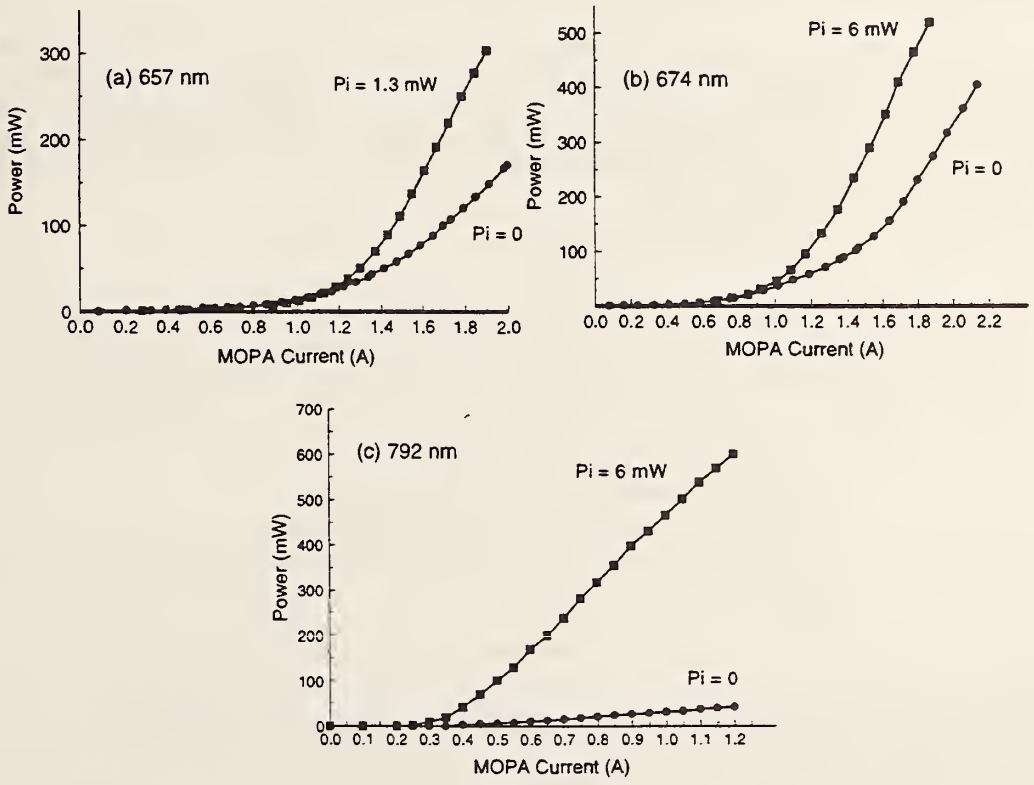


Figure 2. This figure shows the power versus injection current for three of our ECDL-MOPA systems (a) 657 nm, (b) 674 nm, and (c) 792 nm. Each graph is shown with and without optical injection power. Graph (a) and (b) show clearly a lasing threshold of the TA at high currents even without optical injection. The thresholds of all of the systems are lowered, and the slope efficiencies increase with increasing injection power. The optical injection power $P_i$ used in these systems is (a) 1.3 mW, (b) 6 mW, and (c) 6 mW.

With optical injection from the master laser into the TA, the threshold of the TA decreases, resulting in more emitted power and the slope efficiency increases to as much as 0.7 W/A for the 674 nm and 792 nm systems (Figure 2). The MOPA output power quickly saturates with injection power from the master laser. Figure 3 shows the output power of the MOPA as a function of injected optical power. With good mode matching of the master into the TA, the output power saturates with about 2-3 mW of injected power. The different ECDL-MOPA systems vary slightly in this characteristic but they all saturate with less than ~5 mW of injection power due to the high gain and strongly asymmetric nature of the TA.

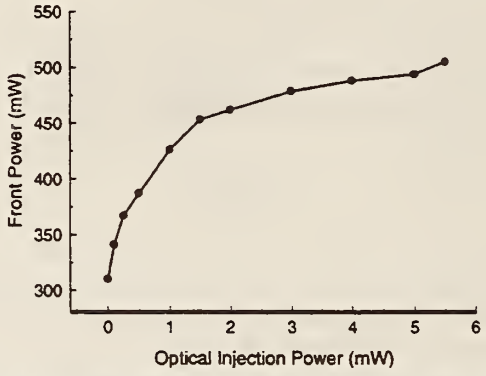


Figure 3. Dependence of output power with optical injection power for the 674 nm system. The output power saturates quickly with as little as 2-3 mW (solid circles).

The isolation required between the master and the slave depends somewhat on system parameters such as master laser power, mode matching, and the power emitted out of the back of the amplifier. We often use another isolator on the output of the amplifier to eliminate feedback into the high power amplifier. Although good quality isolators are needed between the master and the slave for relatively low injection powers (<5 mW), this requirement may be relaxed with higher injection powers. With optical injection from the master laser we have observed a decrease in temperature of the TA due to the large increase in optical power and high efficiency of the TA.

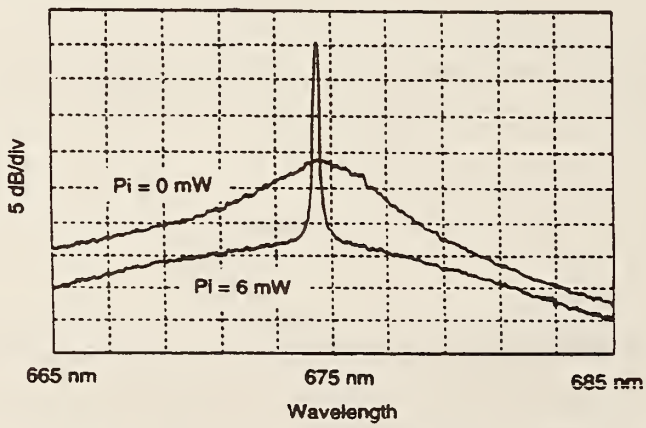


Figure 4. Optical spectrum analyzer trace showing the output of the ECDL-MOPA with and without 6 mW of injection power. The vertical scale is 5 dB/div and the horizontal scale is 2 nm/div. The instrument resolution is 0.1 nm.

The MOPA output power can be quite high (up to 700 mW), in a single spatial mode, while retaining the spectral properties of the master laser. Figure 4 shows an optical spectrum of the TA at 674 nm with and without injection. With injection the broad spectrum collapses into the single strong mode of the master laser. The single-frequency output takes power away from nearby regions and rises 25-30 dB above the background pedestal as measured with a 0.1 nm resolution bandwidth. As the master laser is tuned, the single-mode, coherent output of the MOPA follows exactly.

The residual facet reflectance of the TA can significantly affect the tuning characteristics of the MOPA and varies somewhat with each system. When injection current in the TA is brought above its own lasing threshold, the residual chip modes of the amplifier become important. Since these chip modes tune with slave current and temperature, it is straightforward to reach the desired wavelength and be centered on a "good" MOPA chip mode as well. When the TA shows no threshold behavior (as for the 792 nm system), these chip modes can be suppressed by the optical injection. For those TAs that can operate well above their threshold, the modulation is always present. These characteristics represent two different operating regimes for the MOPA: below the threshold of the TA the system acts like an optical amplifier, while above the threshold of the TA the system behaves like an injection locked laser. Using the 674 nm system near its own lasing threshold (~1.2 A) and with ~6 mW of injection power, we were able to scan continuously over 150 GHz with an output power of ~100 mW.[7] As a demonstration of this capability, Figure 5 shows absorption of $I_2$ near 674 nm. Although there is some modulation in the power, the sweep remains single mode for greater than 150 GHz. Even when the chip modes are strong, the system can be scanned ~20-30 GHz without mode jumps. This performance is comparable to that of many single-frequency tunable dye lasers. For most high resolution spectroscopy, this scan range is more than adequate, but some applications, such as molecular spectroscopy, may need longer single mode scanning ranges. In addition, active control of the injection current of the slave can be used to suppress the power modulation due to the residual facet reflectance.

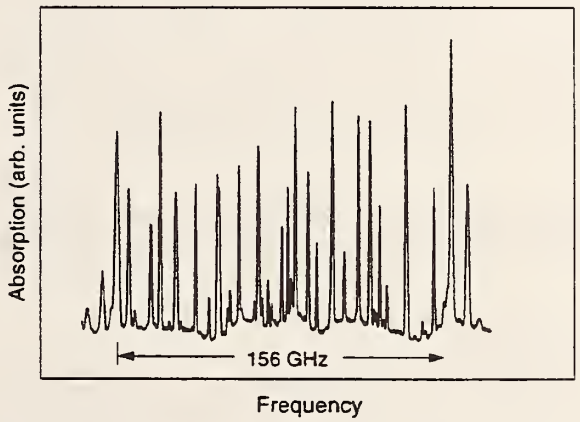


Figure 5. Absorption spectrum of $I_2$ near 674 nm taken with an ECDL-MOPA system (adapted from ref (7)). A specially designed long-scanning ECDL was used as the master oscillator to obtain this spectrum. The peak absorption was about 30% for a 5 cm long cell with a temperature of about 80°C.

## 3. APPLICATIONS

Applications of these ECDL-MOPAs provide "real-world" tests of the practicality and usefulness of these systems. The following examples from our laboratory are used to illustrate the performance characteristics of these systems.

The first system at 792 nm is used to generate 194 nm light for use in a $Hg^+$ frequency standard. In this experiment $Hg^+$ ions are held in electromagnetic traps and laser-cooled to temperatures on the order of 1 mK. Single-frequency radiation at 194 nm, required for laser-cooling the ions, is generated by sum-frequency mixing of radiation at 257 and 792 nm in an external build-up cavity. Radiation at 257 nm is obtained by frequency-doubling 515 nm radiation from an $Ar^+$ laser. Single-frequency radiation at 792 nm is generated from the ECDL-MOPA system. More than 700 mW of light at 792 nm is generated with optical injection between 3 mW and 20 mW from the master laser. Greater than 90% of the slave laser power can be mode-matched into the sum-frequency cavity, and negligible variation of the mode quality is observed as the slave laser's output power or frequency is varied. The ability to couple such a high percentage of light into the external ring cavity illustrates the excellent spatial mode these systems can provide. Two isolators (net isolation of about 60 dB) were used between the master and the slave laser, but no isolator was used on the output of the ECDL-MOPA. This high level of isolation was required to prevent instabilities of the ECDL-MOPA caused by a small amount of optical feedback from the

build-up cavity.

Using the 792 nm system an experiment to check for the relative coherence between the injection beam and the TA output was performed. We split off part of the master laser beam, frequency-shifted it in an acousto-optic modulator (AOM), and then heterodyned this beam with the output of the TA (Figure 6). The beat signal at the modulation frequency was then heterodyned with the signal driving the AOM, and the resulting DC signal (proportional to the relative optical phase between the master and the slave) was observed on an oscilloscope. In this way phase variations between the master and slave lasers were observed directly. Phase locking between the master and slave laser was observed. The phase difference never exceeded $\pi$ rad for times of the order of minutes. Similar results have also been reported by Kikuchi et al.[8]

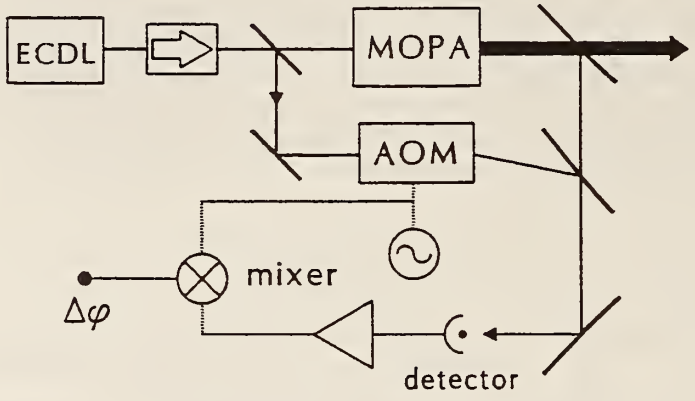


Figure 6. Schematic diagram of the method used to measure the relative phase coherence between the master laser and the slave.

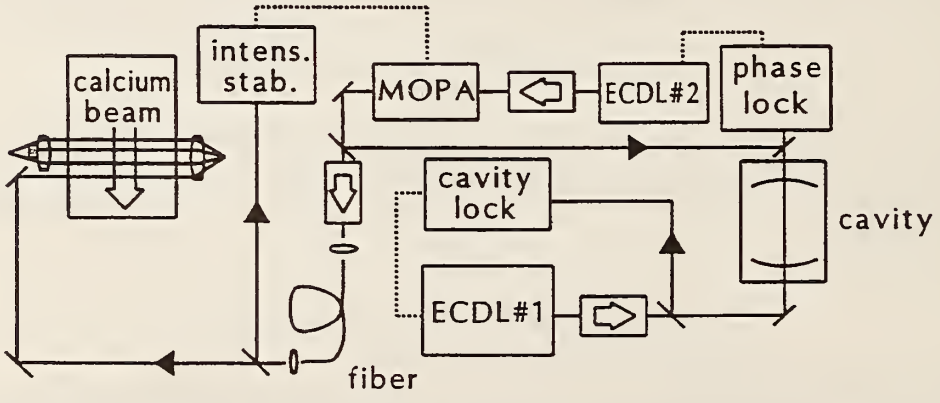


Figure 7. Calcium spectroscopy set-up. The solid lines represent the laser light and the dotted lines represent the servo loops.

A good demonstration of the narrow linewidths and high optical resolution that can be achieved with these ECDL-MOPAs is provided by the 657 nm system we use for Ca spectroscopy. The system is shown in Figure 7. ECDL1 is locked to an ultra-stable high finesse Fabry-Perot cavity (fringe width ~ 50 kHz FWHM) using the Pound-Drever-Hall technique. The beam transmitted through the cavity is used to phase-lock the 657 nm ECDL2-MOPA. This ECDL-MOPA output is then spatially filtered using an optical fiber which delivers the light to the Ca atomic beam system. In addition, the output of the fiber is intensity-stabilized by active feedback control to the MOPA current. This is done to compensate for the intensity fluctuations due to polarization changes and thermal drifts of the fiber system. The very high resolution achievable with this system is evident in Figure 8. This figure shows the optical Ramsey spectra of the 657 nm calcium line. The FWHM of

approximately 11.5 kHz, with a signal-to-noise ratio of about 30 in a 1 Hz bandwidth, corresponds to what would be a noise-limited frequency stability $\delta\nu/\nu$ of about $8\times10^{-13}\,\tau^{-1/2}$ (where $\tau$ is the averaging time). The resolution is limited here by the physical size of the windows on the atomic beam apparatus which limits the distance between interaction regions. Using the Ca lineshape and the Fabry-Perot cavity as frequency discriminators we measure the residual FM noise of the ECDL-MOPA to be $\leq$ 1 kHz dominated by the acoustical mode coupling between the laser table and the reference Fabry-Perot cavity (at about 1-2 Hz).

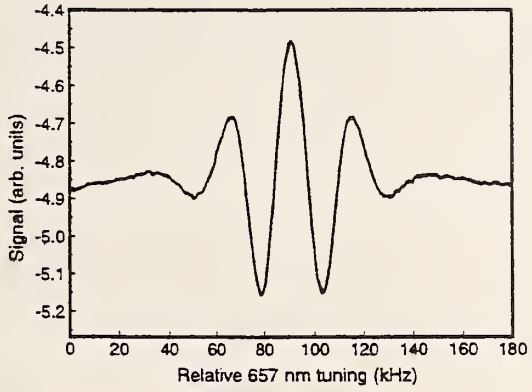


Figure 8. Ramsey fringe of calcium using the ECDL-MOPA setup shown in Figure 7. The FWHM of the fringe is ~11.5 kHz, at an optical frequency of 456 THz.

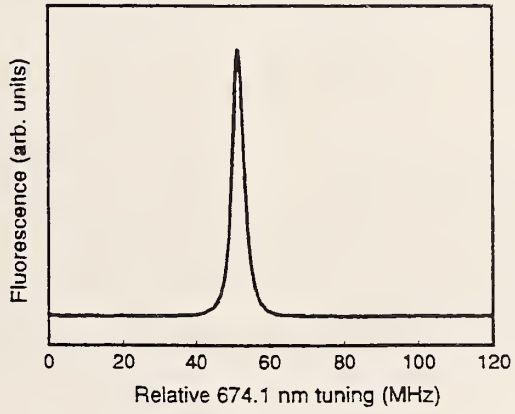


Figure 9. Fluorescence spectroscopy of the $6S_{1/2}$, F=4 -> $12S_{1/2}$, F=5 two-photon transition in cesium (1 Hz bandwidth).

A third ECDL-MOPA system is used for high resolution and high sensitivity nonlinear spectroscopy in cesium atoms. The 674 nm system provides 500 mW of usable output power which is sufficient for two-photon spectroscopy on weak optical transitions without the need of a build-up cavity. The 674 nm light is scanned over the $6S_{1/2}$ -> $12S_{1/2}$ two-photon transition in a cesium vapor cell heated to ~80 °C; the transition is detected by the decay fluorescence from the $12S_{1/2}$ state to the $6P_{1/2}$ state at 541 nm (Figure 9). The nonlinear signal is quadratic in laser power, yet the signal-to-noise ratio is excellent (>1000 in a 1 Hz bandwidth). This demonstrates that the MOPA output has low AM noise.

## 4. LIMITATIONS

This new technology is exciting and appears to have a bright future. However, there are some limitations. One limitation is that the ECDL-MOPA systems are roughly one order of magnitude more costly to build than the standard low power counterparts. Although more expensive they are still an order of magnitude less expensive than many other high-power tunable laser systems such as dye and $Ti:Al_2O_3$ lasers. As with low power diode lasers, these ECDL-MOPAs are very susceptible to optical feedback and often require good quality isolators.

## 5. CONCLUSIONS

With these ECDL-MOPA lasers a new era in diode laser spectroscopy is opened. Power is increased by an order of magnitude or more over conventional diode lasers while the systems retain the good spectral characteristics and tunability of the lower power ECDL lasers. We have demonstrated the ability to use these lasers in several different experiments including the high resolution spectroscopy of Ca, $Hg^+$, $I_2$, and Cs. Although the systems have slightly different characteristics, our experiments demonstrate that tunable, highly coherent, spatially single-mode, high power laser systems are achievable. These lasers will undoubtedly play an increasingly important role in the high resolution spectroscopy and nonlinear optics of the future.

## 6. ACKNOWLEDGMENTS

We acknowledge the support of the U.S. Air Force Office of Scientific Research.

## 7. REFERENCES

1. J. N. Walpole, "Semiconductor amplifiers and lasers with tapered gain regions," *Opt. Quantum Electron.*, **28**, pp. 623-645 (1996).
2. D. Mehuys, D. Welch, and D. Scifres, "1 W CW, Diffraction-Limited, Tunable External-Cavity Semiconductor Laser," *Electron. Lett.*, **29**, pp. 1254-1255 (1992).
3. S. O'Brien et al., "Operating characteristics of a high-power monolithically integrated flared amplifier master oscillator power amplifier," *IEEE J. Quantum Electron.*, **29**, 2052 (1993).
4. D. Mehuys, D.F. Welch, and L. Goldberg, "2.0 W CW, diffraction-limited tapered amplifier with diode injection," *Elec. Lett.*, **28**, 1944 (1992).
5. C. Zimmermann, V. Vuletic, A. Hemmerich, and T.W. Hänsch, "All solid state laser source for tunable blue and ultraviolet radiation," *Appl. Phys. Lett.*, **66**, pp. 2318-2320 (1995).
6. Lew Goldberg and W. K. Burns, "Deep UV to mid-IR generation with laser diodes and non-linear frequency conversion," in *Proc. LEOS '95*, edited by T. Fan, pp. 459-460 (IEEE, Piscatoway, NJ, 1995).
7. L. Hollberg, J. Marquardt. M. Stephens, and R. W. Fox, "Diode lasers and spectroscopy," in *Proc. LEOS '95*, edited by T. Y. Fan, pp. 327-328 (IEEE Piscatoway, NJ, 1995).
8. K. Kikuchi, C.-E. Zah, and T.-P. Lee, "Measurement and analysis of phase noise generated from semiconductor optical amplifiers," *IEEE J. Quantum Electron.*, **27**, 416 (1991).

15 January 1996

ELSEVIER

Optics Communications 123 (1996) 207–214

OPTICS COMMUNICATIONS

# CW second harmonic generation with elliptical Gaussian beams

A. Steinbach, M. Rauner [1], F.C. Cruz, J.C. Bergquist

*Time and Frequency Division, National Institute of Standards and Technology, Boulder, CO 80303, USA*

Received 28 April 1995; revised version received 27 September 1995

**Abstract**

We present a study of the efficiency and optimization of cw second harmonic generation by elliptical Gaussian laser beams. Elliptical focusing slightly improves conversion efficiency and reduces crystal damage risk when heavy walk-off is present. Single-pass measurements of the efficiency for doubling 515-nm radiation in beta-barium borate (BBO) agree with theory. Thermal effects, caused by radiation absorption, limit the doubling efficiency of single-frequency radiation in an external enhancement ring cavity.

## 1. Introduction

Second harmonic generation (SHG) has become a very useful and widely employed technique to provide monochromatic light sources at wavelengths that are difficult or even inaccessible with conventional lasers. Literature on cw SHG is extensive and explores many possible schemes toward high conversion efficiencies from radiation at the fundamental frequency into radiation at the harmonic. The optimization of cw SHG using spherically focused Gaussian beams was first treated in the most general case by Boyd and Kleinman [1], but SHG using focused Gaussian beams with elliptical cross section offers advantages in some cases. Librechet and Simons [2] show that when critical phase-matching is required, a small increase in doubling efficiency can be expected by using an optimally focused elliptical laser beam rather than an optimally focused circular beam. Asymptotic and exact solutions are found for an ADP crystal with a length of 2 cm and for different values of ellipticity. Comparisons are made between theoretical predictions and experimental values for three choices of ellipticity. Kuizenga [3] treats elliptical focusing for the case of a parametric amplifier and finds that by optimizing the confocal parameters, the threshold for gain can be lowered from that obtained for optimum spherical focusing. This result is valid only when the walk-off parameter $B$ exceeds 1. He also finds that the signal and idler beams remain almost circular while the pump beam grows increasingly elliptical as $B$ increases. Recently, Taira [4,5] has reported high power generation for the second harmonic of a 515-nm argon-ion laser using elliptically focused beams. Motivated by these results, we sought to more rigorously study the generation of second harmonic radiation using cylindrical focusing. We examine conversion efficiencies for a wide range of practical confocal parameters in the critical and noncritical directions and for various values of the walk-off parameter $B$. For heavy walk-off, we find the the diameter of the light beam in the noncritical direction must remain within a factor 2 of optimum elliptical focusing, otherwise, less harmonic power is generated than for optimum spherical focusing. Our study also

[1] Present address: Institut für Quantenoptik, Universität Hannover, 30167-Hannover, Germany.


*SSDI* 0030-4018(95)00626-5

reveals no fundamental difference in the far-field mode pattern whether the harmonic radiation is generated by cylindrically or spherically focused light. Measurements of the nonlinear conversion efficiency obatined by single-pass doubling of 515-nm radiation in angle-tuned beta-barium borate (BBO) are presented and compared to theory. We also discuss experimental results obtained by doubling the 515-nm radiation in a Brewster-cut BBO crystal placed in a low-loss external ring cavity using cylindrical mirrors. Although high circulating powers are possible in the absence of harmonic generation, absorption of the UV radiation at 257 nm causes thermal lensing in the crystal that limits the generation of harmonic radiation at higher powers.

## 2. Theory

In order to calculate the second harmonic power generated by an arbitrary elliptical Gaussian beam passing through a uniaxial nonlinear crystal, we allow fundamental electric fields of the form [6]:

$$E_1(x,y,z) = \frac{E_0 \exp(ik_1 z)}{\sqrt{(1+i\tau_x)}\sqrt{(1+i\tau_y)}} \times \exp\left(\frac{-x^2}{w_{0x}^2(1+i\tau_x)} - \frac{y^2}{w_{0y}^2(1+i\tau_y)}\right), \quad (1)$$

where

$$\tau_i = 2\left(\frac{z-f_i}{b_i}\right), \quad b_i = w_{0i}^2 k_1.$$

Eq. (1) represents an elliptical $TEM_{00}$ Gaussian beam whose focal points ($f_x$ and $f_y$) and beam waists ($w_{0x}$ and $w_{0y}$) in the $x$ and $y$ transverse directions are independently adjustable. $k_1$ is the magnitude of the wave vector inside the crystal. Here we neglect absorption of radiation by the crystal.

In analogy to the heuristic treatment of Boyd and Kleinman, we derive the second harmonic field amplitude in the far field outside the crystal and obtain the power of the second harmonic by integrating over the intensity distribution $(n_2 c/8\pi)|E_2|^2$:

$$P_2 = K P_1^2 l k_1 \cdot \tilde{h}(B, \Delta k, \xi_x, \xi_y), \quad (2)$$

where

$$\tilde{h}(B,\Delta k,\xi_x,\xi_y) = \frac{\sqrt{\xi_x \xi_y}}{l^2} \times \int_0^l \int_0^l \frac{e^{i\Delta k(z'-z)}\, e^{-4B^2(z'-z)^2\xi_x/l^2}\, dz\, dz'}{\sqrt{1+i\tau_x'}\sqrt{1+i\tau_y'}\sqrt{1-\tau_x}\sqrt{1-\tau_y}}, \quad (3)$$

and

$$K = (128\pi^2\omega_1^2/c^3 n_1^2 n_2)\, d_{\text{eff}}^2$$

$$\xi_i = l/b_i, \quad B = \rho\sqrt{lk_1}/2.$$

$\tau'$ differs from $\tau$ by replacing $z$ with $z'$. We use the same coordinate system as in Fig. 1 of Ref. [1] where the optical beam axis is the $z$ direction, the origin is the point where this axis enters the crystal, and the $xy$-plane is parallel to the crystal faces. The crystal length is $l$, $\rho$ is the walk-off angle in radians, and $n_2$ is the extraordinary index of refraction at the doubled frequency. The optic axis of the crystal lies in the $xz$-plane, and $\Delta k$ is the wave vector mismatch $(2k_1 - k_2)$. $P_1$ is the power of the fundamental radiation, $d_{\text{eff}}$ is the effective nonlinear coefficient, and $n_1$ is the ordinary-ray index of refraction.

The second harmonic power is proportional to the function $\tilde{h}(B,\Delta k,\xi_x,\xi_y)$ which, for a given crystal length and amount of input power, contains all variables for optimization. Our numerical calculations show that harmonic power is maximized by adjusting both beam waists to lie at the crystal's midpoint ($f_x = f_y = l/2$). Further, in calculating the harmonic power for a given set of parameters, we use the value of $\Delta k$ that maximizes the harmonic power. Experimentally $\Delta k$ can be optimized by temperature or angle-tuning the crystal. Thus, once a particular crystal type is chosen, the waist size in each transverse direction is the only remaining optimizable parameter.

We can solve for second harmonic power as a function of $\xi_x$, with $\xi_y$ fixed at the value that maximizes $\tilde{h}(B,\Delta k,\xi_x,\xi_y)$ for a given $B$ and $\Delta k$. $\tilde{h}$ is plotted in Fig. 1 for a variety of walk-off strengths $B$ and for $\Delta k = \Delta k_m$, the optimum phase-match angle. Comparing these curves to the theoretical predictions for optimized spherical focusing [1] reveals perhaps the most atractive feature of cylindrical focusing: For crystals with heavy walk-off, it is possible to decrease the focusing parameter $\xi_x$ by several orders of magnitude without dropping below the harmonic power that

would be obtained by optimal spherical focusing. It is thus possible to reduce the peak field intensity by several orders of magnitude without lowering conversion efficiency. This reduces the risk of radiation damage to the crystal as well as possible thermal effects.

Optimal cylindrical focusing also improves harmonic conversion efficiency as compared to optimized spherical focusing. For example, for $B = 16$ the optimum focusing parameters are $\xi_x = 0.25$, $\xi_y = 3.3$. This generates 27% more power than that generated for the spherical optimum at $\xi = \xi_x = \xi_y = 1.39$. In all cases where $B \neq 0$, optimal focusing is achieved by a softer focus than the spherical optimum in the transverse direction sensitive to phase matching. When $B = 0$, the cylindrical optimum reduces to the well known spherical focusing optimum given by $\xi = 2.84$. The curves in Fig. 1 are essentially those in Fig. 2 of Ref. [3], which give optimum focusing conditions for parametric gain, and resemble efficiency curves for SHG with spherical focusing in the case that both the harmonic and fundamental power are enhanced in resonant cavities placed around the nonlinear crystal [7–9].

Fig. 2 gives a direct comparison of harmonic power generated by cylindrical and spherical focusing for the case of heavy walk-off. The solid curve gives relative harmonic power versus the spherical focusing parameter $\xi = l/b$ for $B = 16$. The dashed curve represents cylindrical focusing versus $\xi_x$, also for $B = 16$. $\xi_y$ is fixed at its optimum value of 3.3. Although the increase in efficiency is apparent here (27% for $B = 16$), in practice it may be preferable to decrease the peak field intensity at the crystal surface by decreasing $\xi_x$, since the loss in second harmonic power can be small. For example, with $B = 16$ it is possible to decrease $\xi_x$ to 0.007 before the harmonic power drops to the maximum possible with spherical focusing. This assumes that $\xi_y$ is fixed at its optimum value of 3.3. The dotted curve in Fig. 2 shows the relative second harmonic power obtained for $\xi_y$ fixed at 1.39, which is the optimal value of $\xi$ for spherical focusing. In this case the somewhat softer focus in the noncritical direction only slightly lowers the nonlinear efficiency from the optimized cylindrical case. But even this nonoptimum curve still rises above the optimum for spherical focusing. Hence, $\xi_x$ can be decreased without sacrificing conversion efficiency, and the lower fundamental intensity reduces the likelihood of crystal damage and the amount of thermal effects.

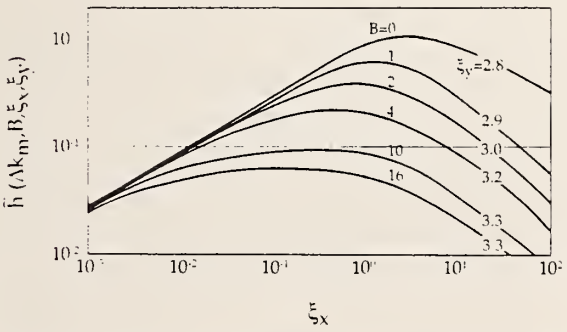


Fig. 1. $\bar{h}$ maximized with respect to $\xi_y$ for different walk-off parameters $B$. $\Delta k_m$ is the optimized value of $\Delta k$. For zero walk-off, $B = 0$, the maximum power is the same as in the spherical case; same coordinate system as in Fig. 1 of Ref. [1] where the optical cylindrical focusing technique is only of advantage if energy walk-off occurs. $\xi_x$ approaching zero corresponds to the plane wave limit.

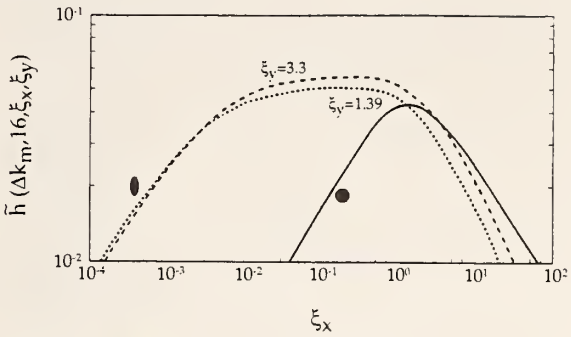


Fig. 2. Cylindrical versus spherical focusing for $B = 16$ and $\Delta k = \Delta k_m$. The focusing parameters which maximize SHG conversion efficiency are $\xi_y = 3.3$ and $\xi_x = 0.25$. For cylindrical focusing $\xi_x$ can be as small as 0.01 before conversion efficiency returns to the maximum value obtained for spherical focusing. The dashed curve represents cylindrical focusing with $\xi_y = 1.39$.

In general, it may not be possible to attain the optimum focusing in either the critical or noncritical direction (for example, in internal or external SHG-setups that use cylindrical elements [4]). For these cases, it would be useful to compare second harmonic generation for non-optimum focusing. In Fig. 3, we show relative harmonic power generation for the case of heavy walk-off ($B = 16$) and various focusing parameters $\xi_x$ and $\xi_y$. A factor 2 change in the waist size in the noncritical direction away from optimum reduces the maximum harmonic power for cylindrical

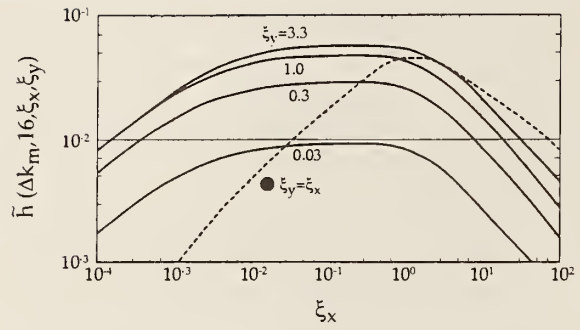


Fig. 3. Dependence of $\tilde{h}$ upon focusing. The conversion efficiency for $B = 16$ is plotted for different $\xi_y$ corresponding to a variation of the waist size in the sagittal ($yz$) plane. The optimum conversion efficiency can be achieved with $\xi_y = 3.3$. In our experiment, cylindrical mirrors with radius of curvature of 10 cm are used. In this case the values for $\xi_y$ are on the order of 0.1. For comparison, the curve for spherical focusing (•) is also shown.

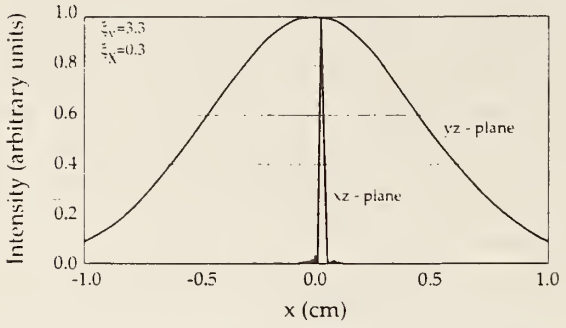


Fig. 4. Second harmonic intensity distribution in the far-field for $B = 12$. The intensity profiles are shown in th $x$- and $y$-direction for optimized cylindrical focusing. Whereas the profile in the $y$-direction is Gaussian, the intensity distributions in the walk-off plane exhibit interference patterns in the wings. An integration over the tangential intensity profile shows that the main lobe contains 96.6% of the total power.

focusing below that obtained for optimum spherical focusing. Clearly it is desirable to remain near optimum focusing in the noncritical direction to realize the full advantages of cylindrical focusing.

The far-field intensity pattern is fundamentally the same for either spherical focusing or cylindrical focusing. Fig. 4 shows the far-field intensity profiles of the harmonic radiation along the $x$-axis and the $y$-axis for cylindrical focusing. The interference pattern along the $x$-axis (the walk-off direction) is due to second harmonic light emitted at different points along the path of the fundamental beam inside the crystal. Since the generated harmonic radiation is emitted under a certain angle relative to the surfaces of equal phase of the fundamental, fringes appear in the intensity distribution. They are also present in the spherical focusing case. However, the amplitude of these fringes is small compared to the amplitude of the main lobe. For both cylindrical and spherical focusing, the main lobe contains over 95% of the total power. In the absence of energy walk-off, the generated radiation would be in phase throughout the crystal and there would be no interference.

The intensity distribution in the walk-off direction is much narrower than the Gaussian intensity distribution in the $y$-direction. This feature is also common to both methods of focusing. In the spherical case, beam walk-off of the harmonically generated light enlarges the tangential waist of the harmonic compared to the waist in the sagittal plane. In the cylindrical case, both the asymmetric focusing and beam walk-off contribute to the larger waist in the tangential plane. The elliptical cross-section of the second harmonic beam in the far-field is not a serious obstacle. It can be made nearly spherical-Gaussian by means of suitable lenses or mirrors. It has been shown that approximately 89% of the second harmonic radiation can be mode-matched into external resonators that support spherical Gaussian modes [10].

## 3. Experimental results and discussion

We compared our theoretical predictions to measurements of single-pass SHG conversion efficiencies for various cylindrical focusing geometries. Light from a single-frequency argon-ion laser at 515 nm was doubled to 257 nm in an angle-tuned, Brewster-cut BBO crystal. Combinations of cylindrical and spherical lenses and mirrors were used to create the various $TEM_{00}$ elliptical Gaussian beams. The BBO crystal length is 6.5 mm and the walk-off angle $\rho$ is 0.085 rad; hence, $B = 15.6$. In Fig. 5, the solid line represents the theoretical SHG conversion efficiency for $B = 15.6$ as a function of $\xi_x$. $\xi_y$ is fixed at 2.4, which corresponds to the 15 $\mu$m value of $w_{0y}$ that was used for all our experimental data points (this value is near the optimum value for cylindrical focusing that gives $\xi_y = 3.3$ and $w_{0y} \simeq 13$ $\mu$m ). The single-pass conversion efficiency $\eta$ is given by $P_2 = \eta P_1^2$, where

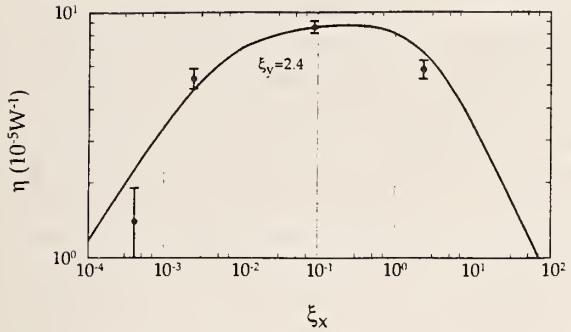


Fig. 5. Comparison of theoretically predicted values and experimental data for the single-pass conversion efficiency. In the experiment, the waist size and position in the (noncritical) $yz$-plane is kept fixed at 11.5 $\mu$m, while the waist size in the walk-off plane is varied by means of different lens combinations. The theoretical curve is calibrated by deriving $d_{\text{eff}}$ for our BBO crystal from a single-pass conversion efficiency measurement under optimum spherical focusing conditions.

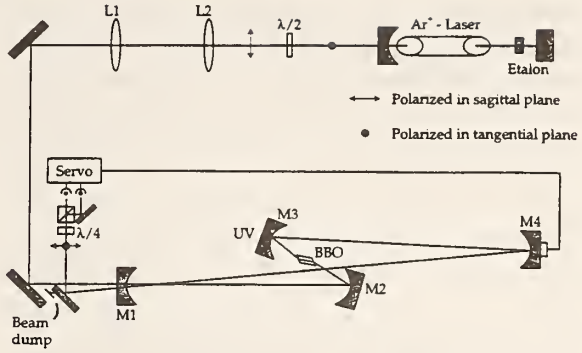


Fig. 6. The experimental setup for generating high-power 257-nm radiation. The single-frequency green light ($\lambda \simeq 515$ nm) of an argon-ion laser is doubled with a Brewster cut and polished BBO crystal placed in an external ring resonator. M1 (input coupler) and M4 are spherical mirrors with a radius of curvature of 30 cm. In order to produce a Gaussian mode with an elliptical cross section, M2 and M3 are cylindrical mirrors with a radius of curvature of 10 cm in the plane of the drawing. M3 is highly reflecting for 515 nm and highly transmitting for 257 nm.

$P_2$ is the output harmonic power. The theoretical peak height depends on the value of $d_{\text{eff}}$ used. The value of $d_{\text{eff}}$ for our crystal was derived from a single-pass measurement under optimum spherical focusing conditions ($w_0 \simeq 20$ $\mu$m). We measured the efficiency to be $7.0 \times 10^{-5}$ W$^{-1}$ which gives $d_{\text{eff}} \simeq 0.32$ pm/V (subsequently we obtained a second BBO crystal from another vendor and measured its single pass efficiency to give $d_{\text{eff}} \simeq 0.4$ pm/V). In Fig. 5 the data points represent the measurements of single-pass efficiency as a function of $\xi_x$. The agreement between the theoretical curve ($B = 15.6$, $\xi_x$=2.4) and the experimentally obtained values is good. The error bars account for statistical error.

In applications that need high second harmonic power, cylindrical focusing can be achieved easily with optical cavities that boost the amount of fundamental power incident on the crystal. High power, cw 257-nm generation, obtained by doubling the frequency of an argon-ion laser in an intracavity setup, has been demonstrated [4] with cylindrical lenses as focusing elements. In Fig. 6 we show a simple frequency doubling scheme where the crystal is placed between two cylindrical mirrors in an external ring resonator. This configuration avoids the additional losses introduced by intracavity lenses and the complications and expense of low-loss AR coatings for both the fundamental and the harmonic. Mirrors M2, M3 and M4 have a high reflectivity ($R \geq 0.998$) at the 515-nm wavelength of the argon-ion laser and the transmission of the input coupler M1 is about 1.8%. The cylindrical mirror M3 transmits 94% of the generated UV at 257 nm. Two spherical lenses, L1 and L2, constitute a telescope to establish mode-matching into the cavity. The cavity is locked to resonance by means of the Hänsch-Couillaud locking scheme [11].

M1 and M4 are spherical mirrors with matching radii of curvature of 30 cm. M2 and M3 are cylindrical mirrors with a radius of curvature of 10 cm. The eigenmode of the resonator is spherical-Gaussian, except in the region between the two cylindrical mirrors where the cross section of the beam is elliptical. Since M2 and M3 act as flat mirrors for the tangential component of the beam, the cavity is free of astigmatism other than the small amount due to the off-axis incidence on mirrors M1 and M4. The angles of incidence on all mirrors can be made small to minimize most higher-order aberrations. Maximum conversion efficiency is obtained when both the tangential and the sagittal focus are centered inside the crystal. Therefore the ideal alignment is symmetric about the crystal.

The lowest order $\text{TEM}_{00}$ eigenmode of the resonator exhibits comparatively soft focii ($w_{0x} \simeq 200$ $\mu$m) at the middle of the crystal as well as halfway between M4 and M1. In the sagittal plane the cylindrical mirrors focus the beam more tightly ($w_{0y} \simeq 50$ $\mu$m).

Faster cylindrical mirrors are needed to come closer to the optimum focusing condition where $w_{0x} \simeq 46$ $\mu$m, $w_{0y} \simeq 13$ $\mu$m for $B = 15.6$ and $l = 6.5Z$ mm. A cavity using cylindrical mirrors with a radius of curvature of about 3 cm in combination with a pair of spherical mirrors with a radius of curvature of 30 to 50 cm can establish near optimum focusing conditions. Theoretically, an improvement in the doubling efficiency of about 2.5 can be expected as compared to our current setup.

For Brewster cut, highly transparent crystals, linear intracavity losses are usually dominated by light scattering from the crystal surfaces due to imperfect polishing and by a small transmission of the fundamental radiation through the highly reflecting mirrors. We determined the round-trip linear loss term of the cavity to be about 0.7% (for the second, more efficient BBO crystal) from the mode-matched power enhancement factor of about 115. For this measurement, the angle of the BBO crystal is adjusted so that no harmonic radiation is generated. Since the transmission of the input coupler is 1.8%, not all of the fundamental power is coupled into the cavity. Ideal coupling (no power reflected from the input coupler) is obtained when the transmission of the input coupler equals the round-trip intracavity loss term [12]. However, when the BBO crystal is again angle tuned so that harmonic radiation is generated, the impedance match improves as the fundamental power is increased, because the nonlinear loss term increases as a greater fraction of the circulating fundamental power is converted to UV light [13,14]. The losses due only to the mirrors were determined to be 0.35% by measuring a power enhacement factor of about 156 for the cavity without the crystal. Therefore the linear losses due solely to the crystal are also about 0.35%.

We measure the fundamental power enhancement in two ways; either by sweeping the cavity through resonance or by locking the cavity to resonance. In both cases, the power leaking through one of the highly reflecting cavity mirrors is compared to the power transmitted by the same mirror with the input coupler to the cavity removed. We expect both methods to give identical results unless there are thermal problems which degrade the power enhancement when the cavity is locked to resonance [14]. For input powers less than 250 mW, the power enhancement factor in the fundamental mode, measured by either method, is about 110 ($\sim$ 5% of the input power was coupled into higher-order modes). As the input power is increased, the enhancement factor (again measured by either method) begins to decline as the loss term due to nonlinear conversion of fundamental radiation into second harmonic light increases. However, for input powers exceeding approximately 1 W (85-90 W intracavity), the power amplification factors measured by the swept method and the locked method begin to diverge. When locked to resonance, the circulating power is less than that measured for the swept case, presumably due to radiation absorption that causes thermal lensing in the crystal [14]. The divergence increases as the input power is raised (2.1 W is the single-mode power limit of our present laser). If the crystal is angle detuned so that harmonic generation does not occur, than the power enhancement factor remains about 110 for all input powers whether measured when locked to resonance or swept . Interestingly, the conversion efficiency $\eta$ also drops for higher powers as the thermal effects become more prominent. $\eta$ remains near $4.5 \times 10^{-5}$ W$^{-1}$ for our cavity focusing conditions and for power inputs up to 1 W, then begins to decrease (remember that $\eta$ depends on the focusing parameters which change as the thermal lensing increases). At 2 W into the cavity the build-up on resonance is only 63. The amount of absorption and radiative heating seems to vary widely from crystal to crystal, even for BBO [15,16]. The cavity power enhancement for our poorer crystal drops from about 90 to nearly 40 at 2 W input power and we are unable to stably lock the cavity to resonance at 2 W input power. For the better BBO crystal, an input power of 380 mW generates 64 mW of UV power; at a fundamental input power of 1.9 W, the cavity can still be stably locked to resonance and approximately 500 mW of harmonic power is produced. Although we made no long term measurements of the stability of the harmonic power, the 500 mW was reproducible day-to-day and stable for 30 minute periods. These and other values for different input powers are plotted in Fig. 7a. The values for the UV power have been corrected for the 94% mirror transmission and the 20% Fresnel loss at the exit face of the Brewster cut crystal. The solid line in Fig. 7a represents the theoretical expectation for the harmonic output obtained from :

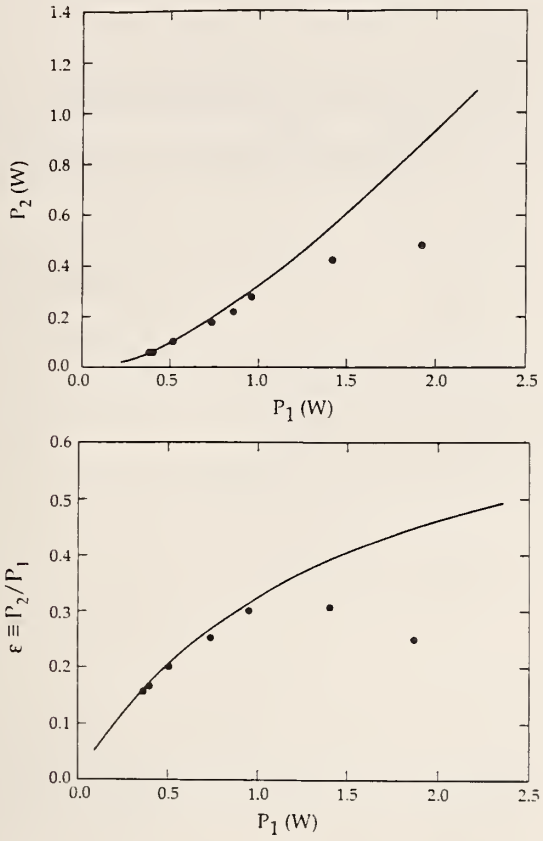


Fig. 7. (a) Second harmonic power $P_2$ as a function of fundamental input power $P_1$ at $\lambda = 515$ nm. (b) Overall conversion efficiency $\epsilon \equiv P_2/P_1$ as a function of input power $P_1$ . The solid line curves are derived from Eq. (4) using the measured values $\eta = 4.2 \times 10^{-5}$ $W^{-1}$, $L = 0.7\%$ and $T = 1.8\%$.

$$\sqrt{\varepsilon} = \frac{4T\sqrt{\eta P_1}}{[2 - \sqrt{1-T}(2 - L - \sqrt{\varepsilon\eta P_1})]^2}, \qquad (4)$$

where $\varepsilon \equiv P_2/P_1$ denotes the overall conversion efficiency, $T$ the transmission of the input coupler, and $L$ the cavity round-trip linear loss term [13,14]. Eq. (4) includes the nonlinear loss factor in the last term in the denominator. The deviation of the experimental results from the theoretical prediction above 1 W of input power reveals the thermal effects due to absorption of harmonic radiation. In Fig. 7b, the theoretical (solid line) and experimental values of $\varepsilon$ are plotted which also clearly show the deviation caused by thermal effects in the BBO crystal. Our best values for overall conversion efficiency slightly exceed 30%. While better conversion efficiences can be expected for optimum focusing and better impedance matching at low input powers, the thermal effects caused by radiation absorption may worsen for the tighter focusing and severely limit $\eta$ at higher powers [2].

## 4. Conclusion

In conclusion, we have calculated efficiency curves for harmonic generation for the general case of cylindrical focusing for a wide range of confocal parameters and for practical values of beam walk-off. We have shown that, for angle-tuned harmonic generation, elliptical focusing can produce the same or slightly more harmonic power than spherical focusing for the same fundamental power. Also, since the intensity can be lower for elliptical focusing, the risk of radiation damage to the crystal can, in principle, be reduced. Measurements of single-pass efficiency are in agreement with these calculations. We have shown the the far-field intensity distribution for the harmonic radiation is the same whether the fundamental beam is cylindrically or spherically focused. We have also built a simple, low-loss external ring cavity using cylindrical mirrors and an intracavity, Brewster-cut BBO crystal. The cavity had a mode-matched power enhancement factor of about 110, for light at 515-nm. Thermal lensing in our crystal limited the overall conversion efficiency to about 30%. Even though we achieved slightly higher conversion efficiencies in BBO with cylindrical focusing, the thermal lensing effects limited the useful fundamental power in the external cavity to a level where a simpler spherical cavity would offer no risk of crystal damage. From our results, we conclude that the small increase in second harmonic power due to elliptical focusing probably does not warrant the expense and complication of cylindrical mirrors or lenses.

[2] We note that Kubota et al. [16] were able to achieve a stable output power of about 800 mW at 266 nm by doubling 532 nm radiation in BBO in an external ring cavity. This would either imply a better BBO crystal with extremely low absorption in the ultraviolet, or that the absorption at 266 nm is lower than at 257 nm.

## Acknowledgements

We thank H. Patrick and M. Young for careful reading of the manuscript. F.C. Cruz is pleased to acknowledge the financial support of CAPES (Brazil).

## References

[1] G.D. Boyd, D.A. Kleinman, J. Appl. Phys. 39 (1968) 3597.
[2] F.M. Librecht and J.A. Simons, IEEE J. Quantum Electron. 11 (1975) 850.
[3] D.J. Kuizenga, Appl. Phys. Lett. 21 (1972) 570.
[4] Y. Taira, Jpn. J. Appl. Phys. 31 (1992) L682.
[5] Y. Taira, CLEO'93 proceedings, pp. 634–637.
[6] A. Yariv, Quantum Electronics (Holt, Rinehart and Winston, New York, 1976) p. 51.
[7] C. Zimmermann, R. Kallenbach, T.W. Hänsch and J. Sandberg, Optics Comm. 71 (1989) 229.
[8] Z.Y. Ou and H.J. Kimble, Optics Lett. 13 (1993) 1053.
[9] K. Fiedler,S. Schiller, R. Paschotta, P. Kürz and J. Mlynek, Optics Lett. 18 (1993) 1786.
[10] M. Boshier, Ph.D. Thesis, University of Oxford (United Kingdom), 1988; available from UMI in association with the British Library.
[11] T.W. Hänsch and B. Couillaud, Optics Comm. 35 (1980) 441.
[12] J.C. Bergquist, H. Hemati and W.M. Itano, Optics Comm. 43 (1982) 437.
[13] W.J. Kolowsky, C.D. Nabors and R.L. Byer, IEEE J. Quantum Electron. 24 (1988) 913.
[14] E.S. Polzik and H.J. Kimble, Optics Lett. 16 (1991) 1400.
[15] Coherent, private communication;
Y. Taira, private communication.
[16] Kubota et al., Optics Lett. 19 (1994) 189.

# Sum-frequency generation of continuous-wave light at 194 nm

Dana J. Berkeland, Flavio C. Cruz, and James C. Bergquist

Over 2 mW of continuous-wave tunable 194-nm light is produced by sum-frequency mixing approximately 500 mW of 792-nm and 500 mW of 257-nm radiation in beta-barium borate (BBO). The powers in both fundamental beams are enhanced in separate ring cavities whose optical paths overlap in the Brewster-cut BBO crystal. Due to the higher circulating fundamental powers, the sum-frequency-generated power is nearly 2 orders of magnitude greater than previously reported values. 

*Key words:* Sum-frequency generation, second-harmonic generation, ultraviolet light, lasers, diode lasers, optical cavities.

Tunable narrowband sources of ultraviolet radiation have applications in laser cooling and in spectroscopy of atoms and molecules. In particular, light at 194.1 nm drives the $5d^{10}6s\ ^2S_{1/2}$–$5d^{10}6p\ ^2P_{1/2}$ resonance in singly ionized mercury. This allows laser-cooling, Raman-cooling, double-resonance experiments and other experiments on strings of electromagnetically trapped $Hg^+$ ions.[1,2] Because available nonlinear materials cannot be phase matched for second-harmonic generation (SHG) to 194 nm,[3] light at this wavelength is produced by sum-frequency generation (SFG). Also, because most materials absorb in the ultraviolet, only a few crystals are suitable for generation of light in this region. Previously, several microwatts of continuous-wave 194-nm radiation have been produced by SFG in potassium pentaborate (KB5)[4] and 31 μW in beta-barium borate (BBO).[5] Here we report the generation of over 2 mW of coherent cw radiation at 194 nm.

Figure 1 shows an overview of the apparatus. As in Refs. 4 and 5, the wavelengths of the fundamental beams are 792 and 257 nm, where the 257-nm light is produced by frequency doubling the 515-nm light from a single-frequency argon-ion laser. The fundamental beams are enhanced in separate resonant cavities whose smallest waists overlap. At this intersection, the beams propagate collinearly in a Brewster-cut, angle-tuned BBO crystal to produce the sum-frequency-generated 194-nm radiation.

Light at 515 nm is provided by an argon-ion laser made to run at a single frequency by a temperature-tuned intracavity étalon. An active servo adjusts the temperature of the étalon to maintain maximum power, which eliminates mode hops. Feedback to the position of a piezo-mounted cavity mirror stabilizes the laser frequency relative to a low-finesse reference cavity, reducing short-term fluctuations to less than 1 MHz. Long-term drift is removed by feedback to the reference cavity length so that the laser frequency maintains resonance with a hyperfine feature in molecular iodine.[6]

The 515-nm beam is mode matched into a power enhancement cavity in which a 3 mm × 3 mm × 5 mm, angle-tuned, Brewster-cut BBO crystal is placed. The cavity consists of two 10-cm radius of curvature mirrors, a 30-cm radius of curvature mirror, and a flat input coupler that transmits 1.8% of the input power. The round-trip length of the cavity is 1.35 m, and the 28-μm minimum beam waist is between the two 10-cm mirrors. The crystal is heat sunk when pressed into a slot in an aluminum block. Thin indium foil is placed between the crystal and the aluminum to ensure good thermal contact. The crystal is placed at the 28-μm waist so that the fundamental beam propagates as an *o* wave for type I phase matching. A dichroic beam splitter reflects 97% of the harmonically generated 257-nm light while transmitting the 515-nm light. The cavity is locked to resonance with the incident radiation by use of the Hänsch–Couillaud method,[7] as are all other cavities in this experiment. With the crystal in

The authors are with the Time and Frequency Division, National Institute of Standards and Technology, 325 Broadway, Boulder, Colorado 80303.

Received 12 September 1996; revised manuscript received 27 February 1997.

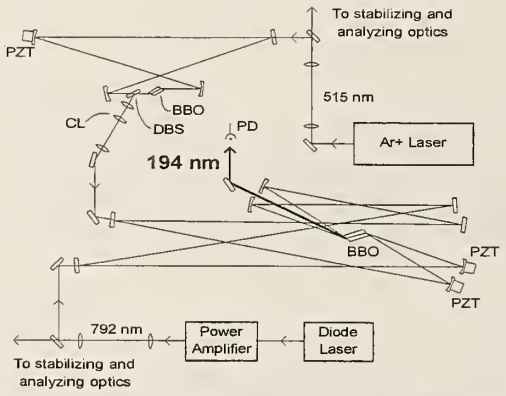


Fig. 1. Optical layout. DBS, dichroic beam splitter; CL, cylindrical lens; PD, photodiode; PZT, piezoelectric transducer. Not shown are optics and electronics for stabilizing and analyzing laser frequencies or for stabilizing enhancement cavities.

place and at low circulating powers, the power enhancement factor is 120.

However, with an incident power of 2 W, the enhancement is reduced to roughly 90 because of nonlinear conversion loss. As the circulating power increases, fractionally more of the fundamental power is transferred to the second-harmonic beam. This increases the cavity losses, lowering the power enhancement factor. Consequently, the overall conversion efficiency $\varepsilon = P_{257}/P_{515}$, where $P_{515}$ is the input power at 515 nm and $P_{257}$ is the output power at 257 nm, does not increase linearly with the input power. Rather, it is determined by[8,9]

$$\sqrt{\varepsilon} = \frac{4T\sqrt{\eta P_{515}}}{[2 - \sqrt{1 - T(2 - L - \sqrt{\varepsilon\eta P_{515}})}]^2}, \quad (1)$$

where $T$ is the transmission of the input coupler, $L$ is the round-trip loss not including conversion losses, and $\eta$ is the single-pass efficiency of the crystal measured at low powers. Figure 2 shows the theoretically expected values of $\varepsilon$ as a function of input power, along with our measured values of $\varepsilon$, corrected by the Fresnel loss of the second-harmonic beam at the exit face of the crystal. For 5.6 W of input power we obtain 2.0 W of second-harmonic radiation. The measured efficiencies, however, are significantly lower than the theoretical values for input powers of 2 W and greater.

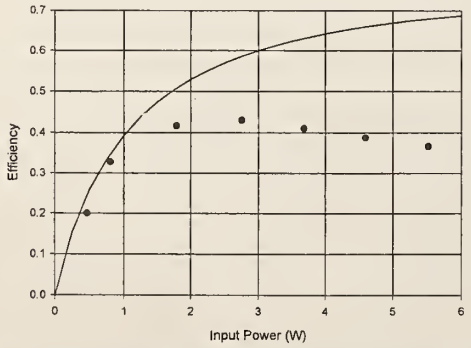


Fig. 2. Theoretically expected values of SHG efficiency from Eq. (1) (solid curve) and measured values (filled circles). Calculated values use $\eta = 6.0 \times 10^{-5}$ W$^{-1}$, $L = 0.007$ m, and $T = 0.015$.

This discrepancy is explained by the small, but finite, absorption of the harmonically generated UV light. As more 257-nm radiation is generated, the crystal develops an anisotropic temperature gradient that is due to the nonuniform intensity distribution of the harmonic power. Because the indices of refraction are temperature dependent, a thermal lens is created in the crystal. This changes the mode-matching efficiency between the input beam and the cavity, which decreases the circulating power.[10] The resulting feedback between the intracavity power and the thermal lens can in turn destabilize the cavity resonance.[8] The heat sink controls the crystal temperature sufficiently so that the cavity can be tightly locked with at least 6 W of input power. However, because the heat sink does not eliminate the thermal lens, our optimum conversion efficiency is limited to 40%.

Approximately 500 mW of 257-nm radiation is mode matched into a second power enhancement cavity containing a second, angle-tuned BBO crystal used for SFG to 194 nm. Because the 257-nm radiation is generated in angle-tuned BBO, its beam profile at the crystal surface is approximately rectangular along the walk-off direction.[8,11] The beam's width is the walk-off distance $\rho l$, where $\rho$ is the walk-off angle and $l$ is the length of the crystal. Because the overlap of this beam profile with a Gaussian distribution of width $w_0 = 1/2\rho l$ is[12]

$$\xi = \left[\int_{-w_0}^{w_0} \left(\frac{2}{\pi w_0}\right)^{1/4} \exp\left(-\frac{x^2}{w_0^2}\right)\sqrt{\frac{1}{2w_0}}\,dx\right]^2 = 0.89, \quad (2)$$

the second-harmonic beam can be mode matched with as much as $\xi = 89\%$ efficiency into a cavity with spherically symmetric Gaussian modes. After passing through suitably chosen spherical and cylindrical mode-matching lenses, approximately 85% of the input beam is coupled into the enhancement cavity's $TEM_{00}$ mode.

The 257-nm power enhancement cavity is formed by two 30-cm radius of curvature mirrors and two flat mirrors, which includes a 9% transmitting input coupler. The round-trip length is 1.79 m and the minimum waist, located midway between the two curved mirrors, is 39 $\mu$m. The power enhancement factor of the empty cavity is approximately 27. When the Brewster-cut BBO crystal is positioned at the cavity waist so that it is near Brewster's angle, the build-up factor can be as great as 21. Due to gradual UV-induced degradation of the cavity surfaces, the build-up factor at the time of this measurement was roughly 12. With 500-mW input, then, the circulating 257-nm power is 6 W.

As in the SHG cavity, the high power and intensity of the circulating 257-nm radiation (>240 kW cm$^{-2}$ for 6-W circulating power) has several adverse effects

on the 257-nm enhancement cavity. Thermal lensing in the SFG BBO crystal destabilizes the intracavity power as explained above. The baseline of the Hänsch–Couillaud dispersion signal also drifts significantly. This may be due to the increased intensity of reflected higher-order cavity modes combined with slight beam misalignments. It is also possible that changes in the crystal birefringence slightly alter the polarization of the light reflected from the cavity. Changes in the crystal's indices of refraction also alter the phase-matching conditions for SFG. Thus the difference in the 194-nm beam position when the cavity is locked into resonance versus when it is swept through resonance is roughly 3 mrad. The beam also moves as the crystal temperature fluctuates over the course of the day. These problems are reduced greatly when the SFG crystal is heat sunk in the same way as the SHG crystal, although the 257-nm intracavity power can still vary by more than 10% over tens of minutes.

Approximately 500 mW of narrowband single-frequency radiation at 792 nm is produced by a master oscillator power amplifier system.[13] The master laser is an external-cavity diode laser in the Littman configuration, whose free-running line width is less than 0.5 MHz. The frequency of the master laser is stabilized to an external cavity whose length is servoed to light from the iodine-stabilized argon-ion laser. Approximately 18 mW from the master laser are mode matched into a tapered amplifier[14] acting as a slave laser. With no more than 1.1 A into the slave laser, as much as 600 mW can be generated safely. We verified that the frequency of the slave laser is phase locked to the master laser with as little as 3 mW of injected power. The shape of the slave laser beam is transformed so that it is nearly spherically Gaussian, after which the beam is mode matched into a power enhancement cavity with greater than 90% efficiency.

The 792-nm enhancement cavity is formed by two 30-cm radius of curvature mirrors and two flat mirrors. The round-trip length of the cavity is 1.83 m, and the minimum cavity waist size is approximately 68 μm. The transmission of the input coupler is 1.5% and the build-up factor of the empty cavity is approximately 80. With the crystal placed near the cavity waist so that its surfaces are at Brewster's angle, the power enhancement is reduced only slightly. Thus for 600-mW input power, the circulating power is 48 W. Aside from a 10% decrease in intracavity power when the 257-nm cavity is locked to resonance, the 792-nm cavity is not affected by thermal lensing in the crystal at these powers.

The 792-nm and 257-nm cavities are situated so that the intracavity beams coincide at the crystal position near the minimum beam waists. The Brewster-cut SFG BBO crystal is 4 mm × 4 mm × 5.75 mm, and cut at 71.6° to the optic axis. Both fundamental beams propagate as *o* waves inside the crystal, while the SFG beam propagates as an *e* wave. To make the beams collinear inside the crystal, the incidence angles of the fundamental beams at the crystal are adjusted to account for the difference in refraction angles. Only the 792-nm beam is strictly at Brewster's angle. Because of the differences in refraction angles of the SFG and fundamental beams, the 194-nm beam is separated sufficiently from the 792-nm and 257-nm beams to pass the cavity optics easily. For the conditions described here, a National Institute of Standards and Technology calibrated photodiode measures 1.4 mW of 194-nm radiation 2.0 m from the crystal. If absorption in air and the Fresnel loss at the exit surface of the crystal are accounted for, approximately 2.2 mW of radiation is generated.

To conclude, we have produced more than 2 mW of 194-nm radiation, which is 2 orders of magnitude greater than previously reported. This is due partly to production of 500 mW of 257-nm radiation by SHG in BBO, whereas previous experiments produced only 20–30 mW by SHG in ammonium dihydrogen phosphate (ADP).[4,5] Furthermore, although the quality of the 257-nm power enhancement cavity is not improved over that reported in Ref. 5, the build-up factor of the 792-nm power enhancement cavity is seven times that of Refs. 4 and 5. The 194-nm power may still be increased by approximately a factor of 3 when the intracavity beam waist sizes are decreased closer to the optimum size of approximately 15 μm[11] and when the build-up factor of the 257-nm power enhancement cavity is increased. However, the higher intensities (especially at 257 nm) might cause crystal damage or severe thermal problems.

We thank S. Mioc, D. Meekhof, M. Young, and D. Sullivan for careful reading of this manuscript. F. C. Cruz acknowledges the support of Coordenadoria de Aperfeiçoamento de Pessoal de Nível Superior (CAPES) (Brazil).

### References and Notes

1. M. G. Raizen, J. M. Gilligan, J. C. Bergquist, W. M. Itano, and D. J. Wineland, "Ionic crystals in a linear Paul trap," Phys. Rev. A **45,** 6493–6501 (1992).
2. J. Miller, D. Berkeland, F. Cruz, J. Bergquist, W. Itano, and D. Wineland, "Cryogenic linear trap for accurate spectroscopy," in *Proceedings of the 1996 IEEE International Frequency Control Symposium* (Institute of Electrical and Electronics Engineers, New York, 1996), pp. 1086–1088.
3. The crystal $Sr_2Be_2B_2O_7$ (SBBO) has produced wavelengths as short as 177.3 nm by SHG. C. Chen, B. Wu, W. Zeng, Y. Wang, N. Ye, and L. Yu, "New nonlinear optical crystal $Sr_2Be_2B_2O_7$: growth and properties," in *Quantum Electronics & Laser Science Conference*, Vol. 10 of 1996 OSA Technical Digest Series (Optical Society of America, Washington, D.C.), pp. 229–230. The crystal $KBe_2BO_3F_2$(KBBF) has produced 184.7-nm SHG output. C. Chen, Z. Xu, D. Deng, J. Zhang, G. K. L. Wong, B. Wu, N. Ye, and D. Tang, "The vacuum ultraviolet phase-matching characteristics of nonlinear optical $KBe_2BO_3F_2$ crystal," Appl. Phys. Lett. **68,** 2930–2932 (1996).
4. H. Hemmati, J. C. Bergquist, and W. M. Itano, "Generation of continuous-wave 194-nm radiation by sum-frequency mixing in an external ring cavity," Opt. Lett. **8,** 73–75 (1983).
5. M. Watanabe, K. Hayasaka, H. Imago, and S. Urabe, "Continuous-wave sum-frequency generation near 194 nm with a collinear double enhancement cavity," Opt. Commun. **97,** 225–227 (1993).

6. J. C. Bergquist, H. Hemmati, and W. M. Itano, "High power second harmonic generation of 257 nm radiation in an external ring cavity," Opt. Commun. **43,** 437–442 (1982).
7. T. W. Hänsch and B. Couillaud, "Laser frequency stabilization by polarization spectroscopy of a reflecting reference cavity," Opt. Commun. **35,** 441–444 (1980).
8. A. Steinbach, M. Rauner, F. C. Cruz, and J. C. Bergquist, "CW second harmonic generation with elliptical Gaussian beams," Opt. Commun. **123,** 207–214 (1996).
9. W. J. Kozlovsky, C. D. Nabors, and R. L. Byer, "Efficient second harmonic generation of a diode-laser-pumped CW Nd:YAG laser using monolithic MgO:$LiNbO_3$ external resonant cavities," IEEE J. Quantum Electron. **24,** 913–919 (1988).
10. E. S. Polzik and H. J. Kimble, "Frequency doubling with $KNbO_3$ in an external cavity," Opt. Lett. **16,** 1400–1402 (1991).
11. G. D. Boyd and D. A. Kleinman, "Parametric interaction of focused Gaussian light beams," J. Appl. Phys. **39,** 3597–3639 (1968).
12. M. G. Boshier, "Precise laser spectroscopy of the hydrogen 1S-2S transition," Ph.D. dissertation. (University of Oxford, Oxford, England, 1988).
13. F. C. Cruz, M. Rauner, J. H. Marquardt, L. Hollberg, and J. C. Bergquist, "An all solid-state $Hg^+$ optical frequency standard," in *Proceedings of the Fifth Symposium on Frequency Standards and Metrology*, J. C. Bergquist, ed. (World Scientific, Singapore, 1996), pp. 511–513.
14. SDL-8630; the mention of brand names in this paper is for information purposes only and does not constitute an endorsement of the product by the authors or their institutions.

# Minimization of ion micromotion in a Paul trap

D. J. Berkeland,[a] J. D. Miller,[b] J. C. Bergquist, W. M. Itano, and D. J. Wineland
*National Institute of Standards and Technology, 325 Broadway, Boulder, Colorado 80303*

(Received 26 November 1997; accepted for publication 12 February 1998)

Micromotion of ions in Paul traps has several adverse effects, including alterations of atomic transition line shapes, significant second-order Doppler shifts in high-accuracy studies, and limited confinement time in the absence of cooling. The ac electric field that causes the micromotion may also induce significant Stark shifts in atomic transitions. We describe three methods of detecting micromotion. The first relies on the change of the average ion position as the trap potentials are changed. The second monitors the amplitude of the sidebands of a narrow atomic transition, caused by the first-order Doppler shift due to the micromotion. The last technique detects the Doppler shift induced modulation of the fluorescence rate of a broad atomic transition. We discuss the detection sensitivity of each method to Doppler and Stark shifts, and show experimental results using the last technique. [S0021-8979(98)05610-2]

## I. INTRODUCTION

Because of their low velocities, cooled and confined ions can provide the basis for accurate and stable frequency standards and atomic clocks. For example, for $^{199}Hg^+$ ions trapped in an rf Paul trap and laser cooled to the Doppler limit, the magnitude of the fractional second-order Doppler (time dilation) shift of transition frequencies can be as low as $2\times10^{-18}$.[1] However, due to the ion motion synchronous with the trap ac field (the "micromotion"), this shift can be orders of magnitude larger if the average ion position is not at the nodal position of the trap's ac electric field. To realize the high accuracy of a trapped-ion frequency standard, the ion micromotion must be minimized. In this article, we discuss ion micromotion in a Paul trap and its associated effects on stored ions and their transition frequencies. We also describe methods to detect and minimize micromotion, and present experimental data using one of these methods.

## II. MICROMOTION IN A PAUL TRAP

For brevity, we characterize motion of a single ion in one type of Paul trap that may be particularly useful for high-accuracy spectroscopy. The results in this section can be generalized to other types of Paul traps. If several ions are stored in the same trap, the equations of motion must be modified to include modes of collective motion. However, the conclusions about micromotion and its effects are still valid.

Figure 1 shows a schematic diagram of a linear Paul trap.[1–7] Electrodes 1 and 3 are held at ground potential, while the potential of electrodes 2 and 4 is $V_0\cos(\Omega t)$. Typically, for atomic ions, $\Omega/2\pi>100$ kHz and $|V_0|<1000$ V. Near the axis of the trap the potential due to the electrodes is

$$V(x,y,t)=\frac{V_0}{2}\left(1+\frac{x^2-y^2}{R'^2}\right)\cos(\Omega t). \tag{1}$$

$R$ is the perpendicular distance from the trap axis to the trap electrodes [shown in Fig. 1(b)], and $R'\cong R$ ($R'=R$ if the trap electrodes are hyperbolic cylinders of infinite length).[2,3] The gradient of the corresponding electric field confines the ion radially in a harmonic pseudopotential.[8] To confine the ion axially, two endcaps held at potential $U_0$ create a static potential $U(x,y,z)$. Near the center of the trap, $U(x,y,z)$ can be approximated by

$$U(x,y,z)=\frac{\kappa U_0}{Z_0^2}\left[z^2-\tfrac{1}{2}(x^2+y^2)\right], \tag{2}$$

where $\kappa(<1)$ is a geometrical factor and $Z_0$ is shown in Fig. 1(a). Here, for simplicity, we have neglected the (small) component of alternating electric field along the $z$ axis caused by the electrode configuration shown in Fig. 1. Linear trap electrode geometries which eliminate this field are discussed in Refs. 1 and 2 (see also Sec. V). From Eqs. (1) and (2), the total electric field is

$$\mathbf{E}(x,y,z,t)=-V_0\left(\frac{x\hat{x}-y\hat{y}}{R'^2}\right)\cos(\Omega t)$$
$$-\frac{\kappa U_0}{Z_0^2}\left[2z\hat{z}-x\hat{x}-y\hat{y}\right]. \tag{3}$$

The equations of motion for a single ion of mass $m$ and charge $Q$ in the above field are given by the Mathieu equation

$$\ddot{u}_i+[a_i+2q_i\cos(\Omega t)]\frac{\Omega^2}{4}u_i=0, \tag{4}$$

where $\mathbf{u}=u_x\hat{x}+u_y\hat{y}+u_z\hat{z}$ is the position of the ion using the coordinate system shown in Fig. 1(b), and from Eq. (3),

$$a_x=a_y=-\frac{1}{2}a_z=-\frac{4Q\kappa U_0}{mZ_0^2\Omega^2}, \tag{5}$$

and

$$q_x=-q_y=\frac{2QV_0}{mR'^2\Omega^2},\quad q_z=0. \tag{6}$$

[a]Electronic mail: dana.berkeland@boulder.nist.gov
[b]Present address: KLA, Austin, TX.

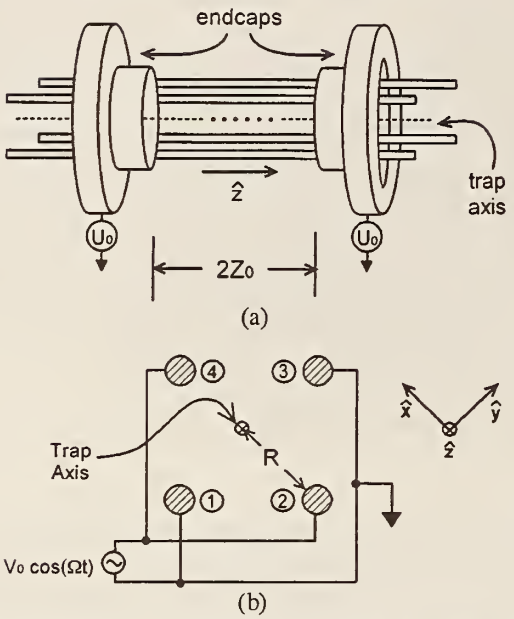


FIG. 1. Linear Paul trap (a) side view and (b) axial view. A string of trapped ions is shown schematically in (a). For clarity, the endcaps are not shown in (b). The trap electrodes are labeled 1, 2, 3, and 4. The trap axis defines the $z$-axis, and the origin of the $z$ axis is centered between the two endcaps.

For convenience, we also define the unit vectors

$$\hat{u}_x=\hat{x}, \quad \hat{u}_y=\hat{y}, \quad \text{and } \hat{u}_z=\hat{z}. \tag{7}$$

In the typical case where $|q_i|\ll 1$ and $|a_i|\ll 1$, the first-order solution to Eq. (4) is[9]

$$u_i(t)\approx u_{1i}\cos(\omega_i t+\varphi_{Si})\left[1+\frac{q_i}{2}\cos(\Omega t)\right], \tag{8}$$

where

$$\omega_i\cong\tfrac{1}{2}\Omega\sqrt{a_i+\tfrac{1}{2}q_i^2} \tag{9}$$

and $\varphi_{Si}$ is a phase determined by the initial conditions of the ion position and velocity. The "secular" motion of the ion is the harmonic oscillation at frequency $\omega_i$ and amplitude $u_{1i}$. The motion corresponding to the $\cos(\Omega t)$ term is driven by the applied ac field, and is called "micromotion."

From Eq. (8), the kinetic energy of the ion averaged over a period of the secular motion is

$$E_{Ki}=\tfrac{1}{2}m\langle \dot{u}_i^2\rangle\cong\tfrac{1}{4}mu_{1i}^2(\omega_i^2+\tfrac{1}{8}q_i^2\Omega^2)$$
$$\cong\tfrac{1}{4}mu_{1i}^2\omega_i^2\left(1+\frac{q_i^2}{q_i^2+2a_i}\right), \tag{10}$$

where the first term in the last two expressions is the kinetic energy due to the secular motion, and the second term is the kinetic energy due to the micromotion. For motion parallel to the trap axis, $q_z^2=0$, so the average kinetic energy is due entirely to secular motion. Because the secular motion is typically thermal, incoherent motion, the kinetic energy due to motion in the $z$ direction is

$$E_{Kz}=\tfrac{1}{2}k_BT_z\cong\tfrac{1}{4}mu_{1z}^2\omega_z^2, \tag{11}$$

where $k_B$ is the Boltzmann constant, and the kinetic energy is characterized by a temperature $T_z$. Typically, in the radial direction, $|a_i|\ll q_i^2 (i=x,y)$. The energy of the radial secular motion is then approximately equal to that of the radial micromotion. In this case,

$$E_{Ki}=k_BT_i\cong\tfrac{1}{2}mu_{1i}^2\omega_i^2 (i=x,y). \tag{12}$$

The energy of the secular motion can be reduced by cooling.[10] As the amplitude $u_{1i}$ of the secular motion is reduced, the micromotion and its corresponding energy are also reduced according to Eqs. (8) and (10). The Doppler-cooling limit of the ion temperature due to secular motion in one direction is[10]

$$T_D\cong\frac{\hbar\gamma}{2k_B}, \tag{13}$$

where $\gamma$ is the linewidth of the cooling transition. As an example, for the $^{199}Hg^+$ $5d^{10}6s\ ^2S_{1/2}\rightarrow 5d^{10}6p\ ^2P_{1/2}$ transition used for laser cooling, $\gamma=2\pi\cdot 70$ MHz. The Doppler-limited cooling temperature is $T_D\cong 1.7$ mK.

If, in addition to the trap fields described above, the ion is also subjected to a uniform static electric field $\mathbf{E}_{dc}$, Eq. (4) becomes

$$\ddot{u}_i+[a_i+2q_i\cos(\Omega t)]\frac{\Omega^2}{4}u_i=\frac{Q\mathbf{E}_{dc}\cdot\hat{u}_i}{m}. \tag{14}$$

To lowest order in $a_i$ and $q_i$, the solution to Eq. (14) is

$$u_i(t)\cong[u_{0i}+u_{1i}\cos(\omega_i t+\varphi_{Si})]\left[1+\frac{q_i}{2}\cos(\Omega t)\right], \tag{15}$$

where

$$u_{0i}\cong\frac{4Q\mathbf{E}_{dc}\cdot\hat{u}_i}{m(a_i+\frac{1}{2}q_i^2)\Omega^2}\cong\frac{Q\mathbf{E}_{dc}\cdot\hat{u}_i}{m\omega_i^2}. \tag{16}$$

The field $\mathbf{E}_{dc}$ displaces the average position of the ion to $\mathbf{u}_0=u_{0x}\hat{x}+u_{0y}\hat{y}+u_{0z}\hat{z}$, but does not directly change $u_{1i}$. The ac electric field at position $\mathbf{u}_0$ causes micromotion of amplitude $\frac{1}{2}u_{0i}q_i$ along $\hat{u}_i$. We will call this "excess micromotion," to distinguish it from the unavoidable micromotion that occurs when the secular motion carries the ion back and forth through the nodal line of the ac field. Unlike secular motion, excess micromotion cannot be significantly reduced by cooling methods because it is driven motion.

Excess micromotion can also be caused by a phase difference $\varphi_{ac}$ between the ac potentials applied to electrodes 2 and 4. For example, in the trap shown in Fig. 1, the potential applied to the electrode 4 may be $+V_0\cos(\Omega t+\frac{1}{2}\varphi_{ac})$, and to electrode 2, $V_0\cos(\Omega t-\frac{1}{2}\varphi_{ac})$. If $\varphi_{ac}\ll 1$, these potentials are approximately equal to $V_0\cos(\Omega t)-\frac{1}{2}V_0\varphi_{ac}\sin(\Omega t)$ and $V_0\cos(\Omega t)+\frac{1}{2}V_0\varphi_{ac}\sin(\Omega t)$, respectively. Near the trap axis, the additional field due to the $\pm\frac{1}{2}V_0\varphi_{ac}\sin(\Omega t)$ terms is approximately that of two parallel plates held at potentials $\pm\frac{1}{2}V_0\varphi_{ac}\sin(\Omega t)$ and separated by $2R/\alpha$.[11] The value of $\alpha$ depends on the geometry of the trap. We use the method of van Wijngaarden and Drake[12] to calculate the dipole moment for our trap ($R=0.81$ mm, electrode radius $r=0.38$ mm), and find $\alpha=0.75$. If we include a uniform static field, the total electric field near the center of the trap is

$$\mathbf{E}(x,y,z,t) \cong -\frac{V_0}{R'^2}(x\hat{x}-y\hat{y})\cos(\Omega t)-\frac{\kappa U_0}{Z_0^2} \times(2z\hat{z}-x\hat{x}-y\hat{y})+\mathbf{E}_{\rm dc} + \frac{V_0\varphi_{\rm ac}\alpha}{2R}\sin(\Omega t)\hat{x}. \quad (17)$$

With the additional oscillating electric field due to $\varphi_{\rm ac}$, the equations of motion in the $y$ and $z$ directions remain unchanged from Eq. (15). However, if we solve the equation of motion in the $x$ direction to lowest order in $a_x$, $q_x$ and $\varphi_{\rm ac}$, and use $R'=R$ in Eq. (6), then

$$u_x(t) \cong [u_{0x}+u_{1x}\cos(\omega_{xt}+\varphi_{Sx})][1+\tfrac{1}{2}q_x\cos(\Omega t)] - \tfrac{1}{4}q_x R\alpha\varphi_{\rm ac}\sin(\Omega t). \quad (18)$$

Equation (18) shows that unless $\varphi_{\rm ac}=0$, the excess micromotion in the $x$ direction will not vanish for any average ion position $\mathbf{u}_0$.

From Eqs. (15), (16), and (18), the average kinetic energy due to motion along $\hat{u}_i$ is

$$E_{Ki} \cong \tfrac{1}{4}mu_{1i}^2(\omega_i^2+\tfrac{1}{8}q_i^2\Omega^2)+\frac{4}{m}\left(\frac{Qq_i\mathbf{E}_{\rm dc}\cdot\hat{u}_i}{(2a_i+q_i^2)\Omega}\right)^2 + \tfrac{1}{64}m(q_xR\alpha\varphi_{\rm ac}\Omega)^2\delta_{i,x}. \quad (19)$$

In order to compare the size of the last two terms relative to the first, it is useful to write them as $k_BT_{\mu i}/2$, where $T_{\mu i}$ is the equivalent (pseudo) temperature for the kinetic energy due to the excess micromotion along $\hat{u}_i$. A uniform static field along the axial direction does not change $E_{Kz}$, since it only shifts the position of the minimum of the static potential $U(x,y,z)$. For a $^{199}Hg^+$ ion in a trap with $|a_i|\ll q_i^2\ll 1$ and $\omega_x=2\pi\cdot 100$ kHz, a 1 V mm$^{-1}$ uniform field along the $x$ direction increases $T_{\mu x}$ by $1.4\times10^4$ K. For $R=1.0$ mm and $\alpha=0.75$, a phase shift of $\varphi_{\rm ac}=1°$ between the trap electrode potentials increases $T_{\mu x}$ by 0.41 K. These effective temperatures are orders of magnitude greater than the 1.7 mK temperature associated with the secular motion at the Doppler-cooling limit.

These phase shifts and electric fields may be reasonably expected. A phase shift can be caused by asymmetries in the electrical impedances of the electrodes. For example, a phase shift will occur if the leads to the trap electrodes have different inductances due to different lengths or geometrical arrangements. A uniform electric field of magnitude 1 V mm$^{-1}$ may develop in a millimeter-sized trap in several ways. Often, an effusive oven located on one side of the trap is used with an electron-emitting filament to produce ions inside the trap. In this case, the trap electrodes may become unevenly coated with the oven contents, which could cause contact potentials of a fraction of a volt. Additionally, the trap electrodes may become unevenly charged when this coating or other dielectric or oxide layer is charged by the emitted electrons. Finally, patch effects due to different crystal planes at the surface of the electrodes also can produce surface potential variations of roughly 100 mV. Although the magnitude of stray fields caused by patch effects and charging of the trap electrodes can be reduced by heating the trap electrodes *in situ*,[13] no technique can eliminate these fields.

Below, we will give general expressions for the effects of excess micromotion and several methods to detect it. To provide examples, we consider the Doppler shifts and the ac Stark shift of the $^{199}Hg^+$ $5d^{10}6s\ ^2S_{1/2}\rightarrow 5d^96s^2\ ^2D_{5/2}$ electric quadrupole transition at 282 nm, and the sensitivity of the various methods used to detect these shifts. Because effects from excess micromotion are negligible in the limit that $|a_i|\gg q_i^2$, in the following sections all examples assume that $|a_i|\ll q_i^2\ll 1$ $(i=x,y)$. We take the physical trap parameters as $R'\approx R=1.0$ mm, $\alpha=0.75$, $\Omega=2\pi\cdot 10$ MHz, $\omega_x\approx\omega_y=2\pi\cdot 1.0$ MHz, and $q_x\approx q_y=0.28$.

## III. EFFECTS OF EXCESS ION MICROMOTION

The first-order Doppler shift due to excess micromotion can significantly alter the excitation spectrum of an atomic transition. The spectrum can even change so that a laser heats the ions at frequencies where laser cooling is normally expected.[14,15] Assume that the electric field of the laser used to excite the ion has amplitude $\mathbf{E}_0$, frequency $\omega_{\rm laser}$, phase $\varphi_{\rm laser}$, and wave vector $\mathbf{k}$. From Eqs. (15) and (18), in the rest frame of an ion undergoing excess micromotion, this laser field becomes

$$\mathbf{E}(t)=\mathrm{Re}\{\mathbf{E}_0\exp[i\mathbf{k}\cdot\mathbf{u}-i\omega_{\rm laser}t+\varphi_{\rm laser}]\} \cong \mathrm{Re}\{\mathbf{E}_0\exp[i\mathbf{k}\cdot(\mathbf{u}_0+\mathbf{u}')-i\omega_{\rm laser}t+\varphi_{\rm laser}]\}, \quad (20)$$

where $\mathbf{u}'$ is the amplitude of the excess micromotion. To isolate the effect of excess micromotion, we have assumed that $|u_{0i}|\gg|u_{1i}|$ and $|R\alpha\varphi_{\rm ac}|\gg|u_{1i}|$. From Eqs. (15) and (18),

$$\mathbf{k}\cdot\mathbf{u}'(t)=\beta\Omega\cos(\Omega t+\delta), \quad (21)$$

where

$$\beta=\sqrt{\left(\frac{1}{2}\sum_{i=x,y}k_iu_{0i}q_i\right)^2+\left(\frac{1}{4}k_xq_xR\alpha\varphi_{\rm ac}\right)^2}, \quad (22)$$

$$\sin\delta=\frac{k_xq_xR\alpha\varphi_{\rm ac}}{\sqrt{(2\Sigma_{i=x,y}k_iu_{0i}q_i)^2+(k_xq_xR\alpha\varphi_{\rm ac})^2}}, \quad (23)$$

and

$$\cos\delta=\frac{2\Sigma_{i=x,y}k_iu_{0i}q_i}{\sqrt{(2\Sigma_{i=x,y}k_iu_{0i}q_i)^2+(k_xq_xR\alpha\varphi_{\rm ac})^2}}. \quad (24)$$

With the Bessel function expansion

$$\exp[i\beta\cos(\Omega t+\delta)]=\sum_{n=-\infty}^{\infty}J_n(\beta)\exp[in(\Omega t+\delta+\pi/2)], \quad (25)$$

Eq. (20) can be written as

$$\mathbf{E}(t)=\mathrm{Re}\left\{\mathbf{E}_0\exp[i\mathbf{k}\cdot\mathbf{u}_0]\sum_{n=-\infty}^{\infty}J_n(\beta) \times\exp[-i\omega_{\rm laser}t+\varphi_{\rm laser}+in(\Omega t+\delta+\pi/2)]\right\}. \quad (26)$$

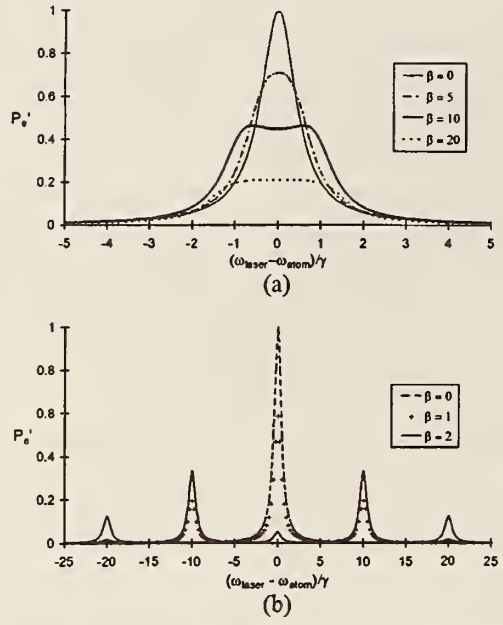


FIG. 2. Effect of micromotion on the spectrum of $P_e$ (excited state population). We plot $P_e'=P_e[\hbar\gamma/(2\mathscr{P}|E_0|)]^2$ for various values of $\beta$. For both graphs, we assume that the ion is driven below the saturation limit. (a) $\Omega/\gamma=0.1$. For $\beta=10$, heating occurs in the regions $<0.6<(\omega_{\text{laser}}-\omega_{\text{atom}})/\gamma<0$ and $(\omega_{\text{laser}}-\omega_{\text{atom}})/\gamma>0.6$. (b) $\Omega/\gamma=10$. For $\beta>0$, heating can occur when the laser frequency is tuned near, but above the center of, any of the sideband frequencies.

We define $\mathscr{P}|\mathbf{E}|$ as the amplitude of the interaction matrix element between atomic levels $|e\rangle$ and $|g\rangle$ coupled by an electric field $\text{Re}\{\mathbf{E}e^{i\omega+i\varphi}\}$. Here, $\omega$ is the field frequency and $\varphi$ is the field phase. If the field of Eq. (26) interacts with the atom in the low intensity limit

$$\frac{\mathscr{P}|\mathbf{E}_0|}{\hbar}\ll\gamma, \tag{27}$$

then the steady-state solution to the optical Bloch equation for the upper level population $P_e$ is[14,15]

$$P_e=\left(\frac{\mathscr{P}|\mathbf{E}_0|}{\hbar}\right)^2\sum_{n=-\infty}^{\infty}\frac{J_n^2(\beta)}{(\omega_{\text{atom}}-\omega_{\text{laser}}+n\Omega)^2+(\frac{1}{2}\gamma)^2}, \tag{28}$$

where $\omega_{\text{atom}}$ is the resonance frequency of the atomic transition. Figure 2(a) shows the excitation spectrum calculated from Eq. (28) for various magnitudes of micromotion, for $\Omega\ll\gamma$ and in the low intensity limit. As $\beta$ increases from 0, the frequency modulation from the excess micromotion first broadens the transition. This decreases the rate at which a laser can cool the ion. For larger values of $\beta$, the line shape can develop structure that causes the laser to heat, rather than cool the ion, even when $\omega_{\text{laser}}-\omega_{\text{atom}}<0$. Figure 2(b) shows the effect of micromotion when $\Omega\gg\gamma$. As $\beta$ increases, the excitation spectrum develops sidebands at $\pm n\Omega$ ($n=1,2,3,...$), and the strength of the carrier transition decreases. Heating now occurs when the laser frequency is tuned near, but above the center frequency of any of the sidebands.

Ion motion also produces a second-order Doppler (time-dilation) shift of atomic transition frequencies

$$\Delta\nu_{D2}=-\frac{E_K}{mc^2}\nu=-\frac{1}{2}\frac{\langle V^2\rangle}{\langle c^2\rangle}\nu, \tag{29}$$

where $\nu$ is the atomic transition frequency and $V$ is the ion velocity. From Eqs. (12) and (19), the fractional shift due to motion along $\hat{u}_i$ can be written as

$$\left(\frac{\Delta\nu_{D2}}{\nu}\right)_i\approx-\frac{1}{mc^2}\left[\frac{k_BT_i(a_i+q_i^2)}{(2a_i+q_i^2)}+\frac{4}{m}\left(\frac{Qq_i\mathbf{E}_{\text{dc}}\cdot\hat{u}_i}{(2a_i+q_i^2)\Omega}\right)^2+\frac{m(q_xR\alpha\varphi_{\text{ac}}\Omega)^2}{64}\delta_{i,x}\right]. \tag{30}$$

If $\mathbf{E}_{\text{dc}}=0$, $\varphi_{\text{ac}}=0$ and $T_x=1.7$ mK, motion in the $x$ direction for a $^{199}Hg^+$ ion contributes $-8\times10^{-19}$ to the fractional second-order Doppler shift. However, if $\varphi_{\text{ac}}=1°$, the fractional shift becomes $-9\times10^{-15}$. A 1 V mm$^{-1}$ field along the $x$ axis further increases the magnitude of the fractional shift by $3\times10^{-14}$.

The ac field that causes micromotion can also cause significant ac Stark shifts. The Stark shift due to the field the ion experiences is approximately

$$\Delta\nu_S\cong\sigma_S\langle E(\mathbf{u},t)^2\rangle, \tag{31}$$

where $\sigma_S$ is the static Stark shift constant and $\langle E(\mathbf{u},t)^2\rangle$ is the time-averaged square of the electric field at the ion position. To lowest order in $q_i$ and $a_i$, substituting Eq. (18) into Eq. (17) gives

$$\langle E_i^2(\mathbf{u},t)\rangle\cong\frac{m\Omega^2k_BT_i}{2Q^2}\frac{a_i^2+2q_i^2}{2a_i+q_i^2}+8\left(\frac{q_i\mathbf{E}_{\text{dc}}\cdot\hat{u}_i}{2a_i+q_i^2}\right)^2+\frac{1}{32}\left(\frac{mq_xR\alpha\varphi_{\text{ac}}\Omega^2}{Q}\right)^2\delta_{i,x}. \tag{32}$$

The second term is much greater than the square of $\mathbf{E}_{\text{dc}}\cdot\hat{u}_i$ when $|a_i|\ll q_i^2\ll1$, so a small uniform static field can induce a large Stark shift.

Stark shifts have been measured for the three Zeeman components of the 1.76 $\mu$m $6^2S_{1/2}\rightarrow5^2D_{5/2}$ transition in a single $^{138}Ba^+$ ion.[16] The ion, cooled to about 1 mK, was confined in a spherical Paul trap in which $\Omega=2\pi\cdot26$ MHz and $\omega_z=2\pi\cdot2.6$ MHz. A static electric field was applied along the $z$ direction, and the shift of the transition frequency was measured as a function of the field strength. The measured values of $\sigma_S$ were on the order of $+10^{-6}$ Hz/(V/m)$^2$ for each Zeeman component. With these values of $\sigma_S$, the fractional Stark shift of the transition frequency in the absence of uniform static electric fields was calculated to be $10^{-17}$. A 5 mV potential across the 0.3 mm diameter trap was predicted to cause a fractional shift of $+1.2\times10^{-15}$.

We have estimated the static Stark shift constant $\sigma_S$ of the 282 nm $^{199}Hg^+$ $5d^{10}6s\ ^2S_{1/2}\rightarrow5d^96s^2\ ^2D_{5/2}$ electric quadrupole transition. First, we calculate the matrix elements between the $5d^{10}6s\ ^2S_{1/2}$ ground state and the closest few states with the $5d^{10}6p$ configuration. This gives $\alpha_S=2.1\times10^{-24}$ cm$^3$ for the polarizability of the ground state. To estimate the polarizability of the $5d^96s^2\ ^2D_{5/2}$ state, we con-

sider transitions from the $5d^96s^2\ ^2D_{5/2}$ state to the various states with the configuration $5d^96s6p$. In the $5d^96s6p$ states, one of the two $6s$ electrons of the $^2D_{5/2}$ state has been excited to a $6p$ state. That transition is qualitatively similar to exciting the single $6s$ electron of the $5d^{10}6s\ ^2S_{1/2}$ state to one of the $5d^{10}6p$ states. Hence we assume that the matrix elements between the $5d^96s^2$ states and the $5d^9_{5/2}6s6p$ states are similar to those between the $5d^{10}6s$ and $5d^{10}6p$ states. The center of gravity of the $5d^96s^2 \rightarrow 5d^9_{5/2}6s6p$ transitions is about 208 nm. This wavelength is not much longer than that of the first $5d^{10}6s \rightarrow 5d^{10}6p$ transition at 194 nm. Thus we expect that the polarizability $\alpha_D$ of the $^2D_{5/2}$ state is on the order of that of the ground state. Both states will be shifted down in energy by a static electric field, since all electric dipole transitions connect them only to higher-lying states. For the electric quadrupole transition, then, we estimate that $|\sigma_S| \leqslant 1.0\times10^{-6}$ Hz/(V/m)$^2$.

This number lets us estimate the magnitude of the Stark shift for the 282 nm quadrupole transition, using the parameters stated earlier. If $\mathbf{E}_{dc}=0$, $\varphi_{ac}=0$, and the ion is cooled to the Doppler limit in the $x$ direction, then the Stark shift of the 282 nm quadrupole transition due to the electric field in the $x$ direction is $|\Delta\nu_S/\nu| \leqslant 1.1\times10^{-18}$. A 1 V mm$^{-1}$ static field along the $x$ direction causes a fractional Stark shift of $|\Delta\nu_S/\nu| \leqslant 9\times10^{-14}$. If $\varphi_{ac}=1°$, the magnitude of this shift increases by about $3\times10^{-14}$.

Under favorable circumstances, the second-order Doppler and ac Stark shifts from excess micromotion can be made to cancel. If we consider only the effects of excess micromotion, we have

$$Q\mathbf{E}(\mathbf{u},t)=m\frac{d^2\mathbf{u}'}{dt^2}=m\frac{d\mathbf{V}_\mu}{dt}, \tag{33}$$

where $\mathbf{V}_\mu$ is the velocity of the excess micromotion. From Eq. (31), the ac Stark shift can be written as

$$\Delta\nu_S \cong \sigma_S\left(\frac{m\Omega}{Q}\right)^2\langle V_\mu^2\rangle. \tag{34}$$

Using Eq. (29), we can write the sum of the fractional second-order Doppler and ac Stark shifts as

$$\frac{\Delta\nu_S}{\nu}+\frac{\Delta\nu_{2D}}{\nu}\cong\left[\frac{\sigma_S}{\nu}\left(\frac{m\Omega}{Q}\right)^2-\frac{1}{2c^2}\right]\langle V_\mu^2\rangle. \tag{35}$$

For $\sigma_S>0$, it might be possible to make the factor in brackets equal to 0. As an example, for the 282 nm quadrupole transition in $^{199}Hg^+$, if $\sigma_S=1\times10^{-6}$ Hz/(V/m)$^2$, this factor is 0 for $\Omega\cong 2\pi\cdot 8.4$ MHz, close to the condition of the experiment reported in Sec. V.

Finally, if several ions are stored in the same trap, excess micromotion can also increase the magnitude of the secular motion. The micromotion and secular motion of a single ion in a Paul trap are highly decoupled, so excess micromotion will typically not increase the secular motion. However, if two or more ions are in the trap, the energy of the excess micromotion of any ion can be parametrically coupled into the energy of the secular motion of the other ions.[7,14,15,17] Since the micromotion is driven by the ac field, this heating is continuous and can limit the lowest temperature attainable by cooling methods. In the absence of cooling mechanisms, the ions can gain enough energy to leave the trap.

## IV. DETECTION OF EXCESS MICROMOTION

Different techniques can be used to detect excess micromotion caused by a uniform static field $\mathbf{E}_{dc}$ or phase difference $\varphi_{ac}$ between the trap electrode potentials. In the first of these methods, which is sensitive to excess micromotion caused by static fields, the time-averaged ion position is monitored as the pseudopotential is raised and lowered.[18] If an imaging system is used to view the ion as it is translated, then the ion position in the plane of observation can be determined to the resolution limit of the optics. Translations can also be detected in any direction by monitoring the distance that a focused laser beam must be translated to maintain the maximum photon scattering rate from the ions. Let $\Delta u_{0i}$ be the measured translation along $\hat{u}_i$ when the secular frequency is reduced from $\omega_{i1}$ to $\omega_{i2}$. From Eqs. (16) and (30) (taking $|a_i| \ll q_i^2 \ll 1$), when the secular frequency is $\omega_{i1}$, the fractional second-order Doppler shift due to excess micromotion along $\hat{u}_i$ is

$$\left(\frac{\Delta\nu_{D2}}{\nu}\right)\cong-\frac{1}{2}\left(\frac{\omega_{i2}^2}{\omega_{i1}^2-\omega_{i2}^2}\frac{\Delta u_{0i}\omega_{i1}}{c}\right)^2. \tag{36}$$

From Eqs. (16) and (32), the Stark shift due to the ac field along $\hat{u}_i$ is

$$(\Delta\nu_S)_i\cong\sigma_S\left(\frac{\omega_{i2}^2}{\omega_{i1}^2-\omega_{i2}^2}\frac{m\Delta u_{0i}\omega_{i1}\Omega}{Q}\right)^2. \tag{37}$$

As an example of the sizes of the detectable shifts, we assume the same parameters for the trap and ion ($^{199}Hg^+$) as above. We assume also that the ion position changes by $|\Delta u_{0x}|=25\ \mu$m in the $x$ direction when the pseudopotential is lowered to $\omega_x=2\pi\cdot 0.5$ MHz. Then the second-order Doppler shift when $\omega_x=2\pi\cdot 1.0$ MHz is $\Delta\nu_{D2}/\nu\cong-1.5\times10^{-14}$, and the Stark shift of the electric quadrupole transition is $|\Delta\nu_S/\nu| \leqslant 4\times10^{-14}$.

This technique can also be used by modulating the pseudopotential (by modulating $V_0$ at frequency $\omega_{mod} \ll \Omega$) while the ion is located in the waist of a laser beam tuned to a cycling transition (for example, the Doppler-cooling transition). We assume that $|a_i| \ll q_i^2 \ll 1$ and that the modulation is adiabatic, so while the magnitude of the excess micromotion changes, the magnitude of the thermal motion is approximately constant Suppose that the laser beam has a transverse Gaussian intensity profile

$$I(r)=I_0\exp(-2r^2/w_0^2), \tag{38}$$

and that the ion lies on the half-intensity radius of the beam

$$r=r_0\cong\sqrt{\frac{\ln 2}{2}}\,w_0. \tag{39}$$

The secular frequency is given by

$$\omega_i'=\omega_i+\Delta\omega_i\cos(\omega_{mod}t+\varphi_{mod}), \tag{40}$$

where

$$\frac{\Delta\omega_x}{\omega_x}=\frac{\Delta\omega_y}{\omega_y}\cong\frac{\Delta V_0}{V_0}, \tag{41}$$

$\varphi_{\mathrm{mod}}$ is the phase of the modulation, and $\Delta V_0$ is the modulation of the trap rf amplitude. Here, for simplicity, we assume that $\Delta\omega_i/\omega_i\ll 1$. The ion position averaged over a cycle of the rf potential varies as

$$u'_{0i}=u_{0i}-\Delta u_{0i}\cos(\omega_{\mathrm{mod}}t+\varphi_{\mathrm{mod}}), \tag{42}$$

where

$$\Delta u_{0i}=\frac{2u_{0i}\Delta V_0}{V_0}\ (i=x,y). \tag{43}$$

We define $\mathbf{r}=r\hat{r}$ as the vector from the laser beam axis to the ion position (such that $\hat{r}\cdot\mathbf{k}=0$). If $\Delta\mathbf{u}_0\cdot\hat{r}\ll w_0$, then the laser intensity in the rest frame of the ion is

$$I\cong I_0\left[\frac{1}{2}-\frac{\sqrt{2\ln 2}\,\Delta\mathbf{u}_0\cdot\hat{r}\cos(\omega_{\mathrm{mod}}t+\varphi_{\mathrm{mod}})}{w_0}\right]$$

$$\equiv\tfrac{1}{2}I_0-\Delta I\cos(\omega_{\mathrm{mod}}t+\varphi_{\mathrm{mod}}). \tag{44}$$

In the low intensity limit, the detected fluorescence signal is $R_d=\frac{1}{2}R_{\max}-\Delta R_d\cos(\omega_{\mathrm{mod}}t+\varphi_{\mathrm{mod}})$. Here, $\Delta R_d$ is the amplitude of the signal synchronous with the pseudopotential modulation, and $R_{\max}$ is the signal when the ion is at the center of the laser beam profile. We can write

$$\frac{\Delta R_d}{R_{\max}}=\frac{\Delta I}{I_0}\cong\sqrt{2\ln 2}\,\frac{\Delta\mathbf{u}_0\cdot\hat{r}}{w_0}=\sqrt{2\ln 2}\,\frac{|\Delta u_0|}{w_0}\cos\theta_{\mu r}, \tag{45}$$

where $\theta_{\mu r}$ is the angle between $\Delta\mathbf{u}_0$ and $\hat{r}$. From the measured value of $\Delta R_d/R_{\max}$ and for a known value of $\Delta V_0/V_0$, we can determine $u_{0i}$ from Eqs. (43) and (45). From Eqs. (16), (30), and (32), we can then determine the corresponding values of $\Delta\nu_D/\nu$ and $\langle E_i^2\rangle$, analogous to Eqs. (36) and (37). Generally, $\cos\theta_{\mu r}$ is not known, but it can be maximized and the direction of $\Delta\mathbf{u}$ can be determined by moving the laser beam appropriately.

The main disadvantage to the above techniques is that they are not sensitive to excess micromotion caused by a phase shift $\varphi_{\mathrm{ac}}$ between the potentials applied to the trap electrodes. If $u_{0x}=0$ but $\varphi_{\mathrm{ac}}\neq 0$, the average ion position will not change as the pseudopotential is raised and lowered, as indicated in Eq. (18). Techniques that sense the magnitude of the first-order Doppler shift caused by the excess micromotion eliminate this problem.

We will assume that we measure the effects of the first-order Doppler shift on an optical transition with natural width $\gamma$. Previously, first-order Doppler shifts of microwave spectra have been used to determine the temperature of the secular motion of trapped ions.[19,20] We first take the case in which $\Omega\gg\gamma$. The micromotion can be monitored by measuring the scattering rate $R_0$ when the laser is tuned to the carrier ($\omega_{\mathrm{laser}}-\omega_{\mathrm{atom}}=0$) and $R_1$ when tuned to the first sideband ($\omega_{\mathrm{laser}}-\omega_{\mathrm{atom}}=\pm\Omega$)[21] [see Fig. 2(b)]. From Eq. (28), in the low intensity limit,

$$\frac{R_1}{R_0}=\frac{J_1^2(\beta)}{J_0^2(\beta)}, \tag{46}$$

where $\beta$ is defined in Eq. (22). For $\beta\ll 1$,

$$\frac{R_1}{R_0}\cong(\tfrac{1}{2}\beta)^2, \tag{47}$$

and since

$$\beta=|\mathbf{k}\cdot\mathbf{u}'|=\left|\frac{\mathbf{k}\cdot\mathbf{V}_\mu}{\Omega}\right|, \tag{48}$$

the fractional second-order Doppler shift can be written as

$$\frac{\Delta\nu_{D2}}{\nu}\cong-\left(\frac{\Omega}{ck\cos\theta_{\mu k}}\right)^2\frac{R_1}{R_0}, \tag{49}$$

where $\theta_{\mu k}$ is the angle between $\hat{k}$ and the direction of the excess micromotion. From Eqs. (34), (47), and (48), the corresponding Stark shift can be written

$$\Delta\nu_S\cong 2\sigma_S\left(\frac{m\Omega^2}{Qk\cos\theta_{\mu k}}\right)^2\frac{R_1}{R_0}. \tag{50}$$

As an example, we assume that we probe the sidebands on the 282 nm transition in $^{199}Hg^+$ in a trap with the parameters listed previously. If $\theta_{\mu k}=0$ and $R_1/R_0=0.1$, then the second-order Doppler shift is $\Delta\nu_{D2}/\nu\cong-9\times10^{-18}$. The corresponding Stark shift is $|\Delta\nu_S/\nu|\leqslant 2.5\times10^{-18}$.

In the limit $\Omega\ll\gamma$, a sensitive method to detect excess micromotion monitors the modulation of the ion's fluorescence signal due to the first-order Doppler shift.[22–24] We will call this the "cross-correlation" technique because the modulation is correlated to the ac potentials applied to the trap electrodes. For simplicity, we assume that the amplitude of the first-order Doppler shift is much less than the linewidth $\gamma$. From Eqs. (15) and (18), the velocity due to excess micromotion is given by

$$\mathbf{V}_\mu(t)=-\frac{1}{2}\sum_{i=x,y}u_{0i}q_i\Omega\sin(\Omega t)\hat{u}_i$$

$$-\frac{1}{4}q_xR\alpha\varphi_{\mathrm{ac}}\Omega\cos(\Omega t)\hat{x}. \tag{51}$$

In the frame of an ion undergoing excess micromotion, the frequency of the laser is Doppler shifted by $-\mathbf{k}\cdot\mathbf{V}_\mu=\beta\Omega\sin(\Omega t+\delta)$, where $\beta$ and $\delta$ are defined in Eqs. (22), (23), and (24). In the low intensity limit, the detected fluorescence rate is thus

$$R_d=R_{\max}\frac{(\frac{1}{2}\gamma)^2}{(\frac{1}{2}\gamma)^2+[\omega_{\mathrm{atom}}-\omega_{\mathrm{laser}}-\beta\Omega\sin(\Omega t+\delta)]^2}. \tag{52}$$

We take $\omega_{\mathrm{atom}}-\omega_{\mathrm{laser}}=\gamma/2$, which is a natural choice since this minimizes the temperature of the Doppler-cooled ions and because it maximizes the cross-correlation signal. If $\beta\Omega\ll\gamma$, then

$$\frac{R_d}{R_{\max}}\approx\frac{1}{2}+\frac{\beta\Omega\sin(\Omega t+\delta)}{\gamma}\equiv\frac{1}{2}+\frac{\Delta R_d\sin(\Omega t+\delta)}{R_{\max}}. \tag{53}$$

Using Eq. (48), we can write the fractional second-order Doppler shift as

$$\frac{\Delta\nu_{D2}}{\nu}\approx-\frac{1}{4}\left(\frac{\gamma}{ck\cos\theta_{\mu k}}\frac{\Delta R_d}{R_{\max}}\right)^2. \tag{54}$$

where, again, $\theta_{\mu k}$ is the angle between $\hat{k}$ and the direction of the excess micromotion. With Eqs. (34) and (48), the corresponding Stark shift can be written as

$$\Delta\nu_S=\sigma_S\frac{1}{2}\left(\frac{m\gamma\Omega}{Qk\cos\theta_{\mu k}}\frac{\Delta R_d}{R_{\max}}\right)^2. \tag{55}$$

As an example, we consider $^{199}Hg^+$ ions, using the previously stated trap parameters, and $\gamma=2\pi\cdot 70$ MHz for the 194 nm Doppler-cooling transition. If $\theta_{\mu k}=0$ and $\Delta R_d/R_{\max}=0.1$, then the second-order Doppler shift is $\Delta\nu_{D2}/\nu\cong-5\times10^{-18}$, and the Stark shift of the electric quadrupole transition is $|\Delta\nu_S/\nu|\leq 1.5\times10^{-17}$.

As opposed to the first method for sensing micromotion, the cross-correlation technique can determine whether the ac potential applied to electrode 2 is out of phase with that applied to electrode 4 (see Fig. 1). If a deliberately applied static electric field moves the ion to different positions in the trap, the phase of the fluorescence modulation at frequency $\Omega$ depends on $\varphi_{ac}$. The atomic velocity is 90° out of phase with the force due to the ac electric field. Thus if $\varphi_{ac}=0$, the phase of the cross-correlation signal jumps by 180° as the average position of the ion crosses the nodal line of the ac field. Also, when the ion is on the nodal line, the signal at frequency $\Omega$ vanishes. However, if $\varphi_{ac}\neq 0$, from Eq. (18), the phase of micromotion in the $x$ direction continuously varies as the varies as the average ion position is changed. Furthermore, the amplitude of the micromotion is never zero. This behavior can be used to determine the relative contributions of stray static electric fields and electrode potential phase shifts to the excess micromotion. In general, the effects of $\mathbf{E}_{dc}$ can be eliminated by purposely applying a static field $\mathbf{E}_{applied}=-\mathbf{E}_{dc}$; $\varphi_{ac}$ can be made zero by loading electrodes 2 and 4 with the appropriate reactances.

Still, avoidable effects may confuse the interpretation of the cross-correlation signal. For example, as the ion moves back and forth across a nonuniform laser beam intensity profile, the fluorescence is modulated at frequency $\Omega$, even if $\mathbf{k}\cdot\mathbf{V}_\mu=0$. This modulation is minimized when the ion is at the center of the (symmetric) laser beam, regardless of its average distance from the ac field's nodal position. However, this condition can be detected—the phase of this fluorescence modulation is sensitive to lateral translations of the laser beam, which is not true if the fluorescence modulation is due to the first-order Doppler shift.

It is also important to avoid tuning the laser frequency too close to the atomic frequency. In this case, the fluorescence modulation due to the first-order Doppler shift [Eq. (52)] is deceptively small. This situation, though, is easily checked by detuning the laser frequency farther from atomic resonance to see if the fluorescence modulation amplitude increases.

Finally, to determine that the micromotion is zero in all three dimensions, three laser beams must interact with the ion. These beams must not be coplanar, to ensure sensitivity to micromotion in every direction. Unless the three beams are orthogonal, this technique is not equally sensitive to ion motion in all directions, as illustrated below.

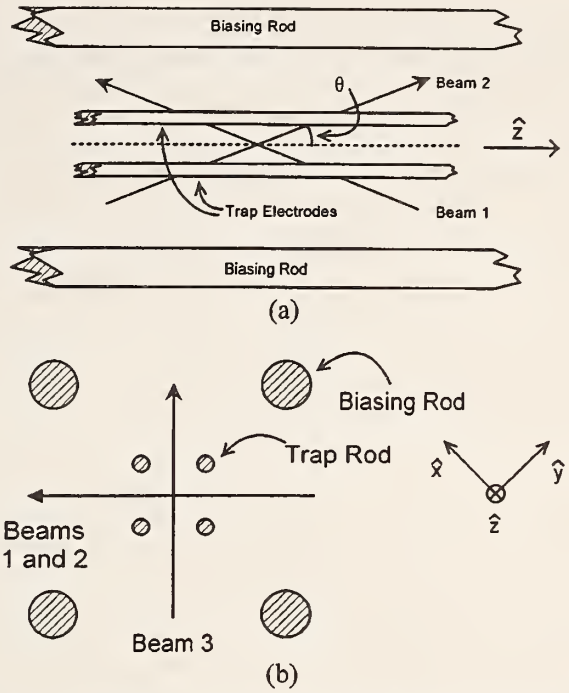


FIG. 3. Experimental setup to observe and minimize micromotion using the cross-correlation technique. The ions are at the intersection of the three laser beams. (a) Top view of the section of the trap in which the ions are located. Beam 3 is not shown. (b) View along the trap axis. For clarity, the origin of the coordinate system has been translated.

## V. EXPERIMENTAL DEMONSTRATION OF THE FLUORESCENCE MODULATION TECHNIQUE

Figure 3 illustrates the experimental configuration we use to detect and minimize micromotion of a string of ions in our linear Paul trap, using the cross-correlation technique. In this trap, $\varphi_{ac}=0$ within the experimental resolution. Typically, about ten ions, whose extent is small compared to their distance from the electrodes, are stored in the trap. In this case the fluorescence modulation signals from each ion add in phase. Laser beams 1 and 2 propagate along $\sin\theta[(\hat{x}-\hat{y})/\sqrt{2}]\mp\cos\theta\,\hat{z}$, where $\theta=20°$. Beam 3 propagates along $(\hat{x}+\hat{y})/\sqrt{2}$. The three beams intersect at the ions' position. Static electric potentials are applied to four biasing rods running parallel to the trap electrodes, creating an additional field that is nearly uniform at the site of the ions. When the potentials on the four rods are appropriately summed, the electric fields along the $(\hat{x}\pm\hat{y})/\sqrt{2}$ directions can be separately controlled.

We detect the fluorescence modulation with a START-STOP time-to-amplitude converter (TAC).[25] The TAC generates an analog pulse having a height proportional to the time delay between a START and a STOP pulse. A fluorescence photon, detected by a photomultiplier tube, generates the START pulse. An amplifier discriminator generates a STOP pulse for each negative-going zero crossing of the trap ac potential. The counting rate of fluorescence photons is

typically much less than the frequency of the ac field. Also, the time between photon detections is much greater than the time the TAC takes to reset for the next START pulse. Thus, each detected photon results in an output from the TAC, proportional to the time to the next STOP pulse. This process would be inefficient if the START and STOP trigger sources were reversed, because not every START pulse would be followed by a STOP pulse within a period of the ac electric field. Finally, the height of the output pulse from the TAC is measured by a triggered analog-to-digital converter and binned according to height by a computer, which acts as a multichannel analyzer.[25] A spectrum of the fluorescence intensity as a function of the phase of the ac electric field is typically built up within a few seconds.

The fluorescence modulation signals due to beams 1, 2, and 3 are separately measured, then the static fields are adjusted to minimize the fluorescence modulation for each beam. Since the micromotion is directed along the ac electric field, in general, the direction of the micromotion is not the direction of the ion displacement from the trap axis. For example, in the trap of Figs. 1 and 3, micromotion along $(\hat{x}+\hat{y})/\sqrt{2}$ indicates that the ions are displaced along $(\hat{x}-\hat{y})/\sqrt{2}$, and vice versa. To begin, we compare the cross-correlation signal $\Delta R_d/R_{\max}$ with only beam 1 present to $\Delta R_d/R_{\max}$ with only beam 2 present. The signals due to the two beams will differ if the ions experience micromotion along $\hat{z}$. Such axial micromotion is due to the endcaps, which produce a (small) component of the ac electric field along $\hat{z}$. From symmetry, this axial micromotion should be minimized when the ions are equidistant from the endcaps. A differential potential is applied between the two endcaps to translate the ions along the trap axis until the signals from beams 1 and 2 are nearly equal. Next, the static field along $(\hat{x}+\hat{y})/\sqrt{2}$ is adjusted to move the ions to a position at which $\Delta R_d/R_{\max}$ from beams 1 and 2 are each minimized. Typically, we must iterate these adjustments before $\Delta R_d/R_{\max} \approx 0$ for both beams 1 and 2. Finally, a static field along $(\hat{x}-\hat{y})/\sqrt{2}$ is applied to null the amplitude of the signal from beam 3. After this we check that the signals from beams 1 and 2 have remained negligible. If they have increased, we repeat the entire process until the micromotion is eliminated in all three dimensions.

Figure 4 shows some fluorescence modulation signals collected with the setup shown in Fig. 3, when only beam 1 is present. The laser is tuned near the 194 nm $5d^{10}6s\ ^2S_{1/2} \rightarrow 5d^{10}6p\ ^2P_{1/2}$ transition. Here, $\Omega = 2\pi \cdot 8.6$ MHz, $\omega_x \approx \omega_y \approx 2\pi \cdot 65$ kHz, and $\omega_{\text{laser}} - \omega_{\text{atom}} \cong -\gamma/2$. The micromotion has been nulled in all three dimensions as just described.

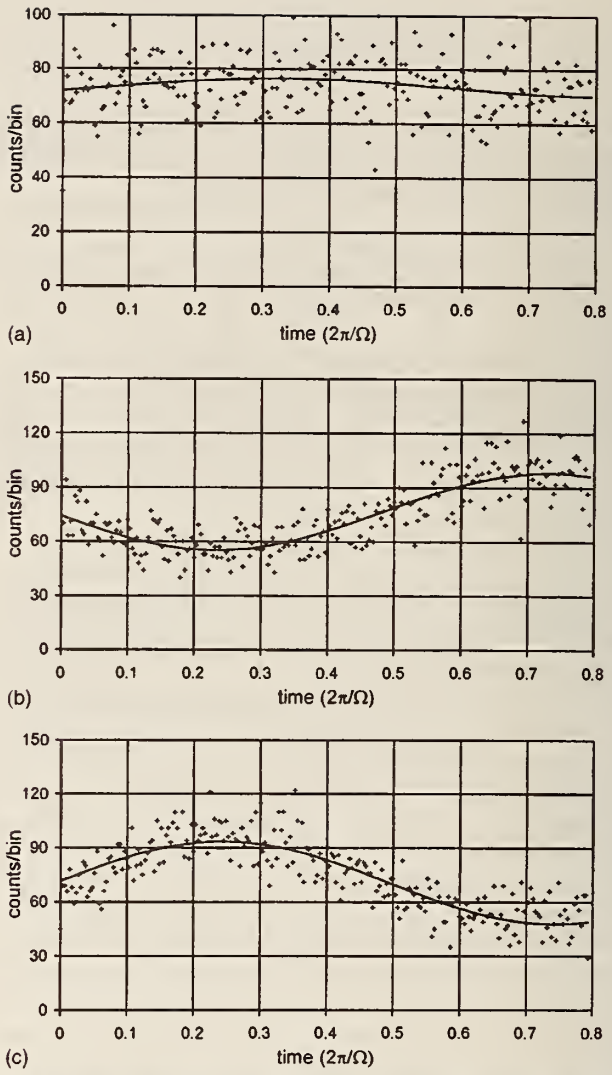


FIG. 4. Experimental fluorescence modulation signals for beam 1 of Fig. 3, using eight ions in the linear trap (points) and fit (solid line). Displacement of the ions from the trap axis along $(\hat{x}+\hat{y})/\sqrt{2}$ is (a) $0.9 \pm 0.3\ \mu$m, (b) $6.7 \pm 0.4\ \mu$m, and (c) $-6.7 \pm 0.4\ \mu$m.

TABLE I. Summary of the sensitivities of various techniques to the fractional second-order Doppler shift and the Stark shift. Formulas are approximations assuming $|a_i| \ll q_i^2 \ll 1$ $(i=x,y)$. Here, $(\Delta\nu_{2D}/\nu)_i$ is the fractional second-order Doppler shift due to motion along direction $\hat{u}_i$, $(\Delta\nu_S)_i$ the Stark shift due to the electric field along direction $\hat{u}_i$, $\mathbf{k}$ the wave vector, and $\gamma$ the width of the excited transition, $m$ the ion mass, $Q$ the ion charge, $\Omega$ the trap drive frequency, $\omega_i$ the secular frequency along direction $\hat{u}_i$, and $\theta_{\mu k}$ the angle between the direction of the micromotion and $\mathbf{k}$.

| Method | $\Delta\nu_{2D}/\nu$ | $\Delta\nu_S$ |
|---|---|---|
| Directly monitor ion displacement $\Delta u_{0i}$ along direction $\hat{u}_i$ as $\omega_i$ is changed from $\omega_{i1}$ to $\omega_{i2}$ | $\left(\frac{\Delta\nu_{D2}}{\nu}\right)_i \cong -\frac{1}{2}\left(\frac{\omega_{i2}^2}{\omega_{i1}^2-\omega_{i2}^2}\frac{\Delta u_{0i}\omega_{i1}}{c}\right)^2$ | $(\Delta\nu_S)_i \cong \sigma_S\left(\frac{\omega_{i2}^2}{\omega_{i1}^2-\omega_{i2}^2}\frac{m\Delta u_{0i}\omega_{i1}\Omega}{Q}\right)^2$ |
| Measure ratio $R_1/R_0$ of scattering rates of carrier and first sideband $(\Omega \gg \gamma)$ | $\approx -\left(\frac{\Omega}{ck\cos\theta_{\mu k}}\right)^2\frac{R_1}{R_0}$ | $2\sigma_S\left(\frac{2m\Omega^2}{Qk\cos\theta_{\mu k}}\right)^2\frac{R_1}{R_0}$ |
| Monitor cross-correlation signal $\Delta R_d/R_{\max}$ due to first-order Doppler shift $(\Omega \ll \gamma)$ | $\approx -\frac{1}{4}\left(\frac{\gamma}{ck\cos\theta_{\mu k}}\frac{\Delta R_d}{R_{\max}}\right)^2$ | $\frac{1}{2}\sigma_S\left(\frac{m\gamma\Omega}{Qk\cos\theta_{\mu k}}\frac{\Delta R_d}{R_{\max}}\right)^2$ |

Next, only beam 1 is used as the ions are translated along $(\hat{x}+\hat{y})/\sqrt{2}$ to induce excess micromotion along $(\hat{x}-\hat{y})/\sqrt{2}$. Figure 4(a) shows the cross-correlation signal when the ions are located near the trap axis. The fit to the data gives $\Delta R_d/R_{\max}=0.043\pm0.014$, corresponding to a fractional second-order Doppler shift of $\Delta\nu_{D2}/\nu\cong-(9\pm3)\times10^{-19}$ due to motion along the propagation direction of beam 1. Figures 4(b) and 4(c) are the fluorescence modulation signals when the ions are deliberately shifted by approximately $\pm6.7$ $\mu$m along $(\hat{x}+\hat{y})/\sqrt{2}$. For these signals, $|\Delta R_d/R_{\max}|\approx0.3$, corresponding to a second-order Doppler shift of $\Delta\nu_{D2}/\nu\cong-5\times10^{-17}$ due to motion along the propagation direction of beam 1. The Stark shift due to the ac field along the propagation direction of beam 1 is $|\Delta\nu_S/\nu|\leqslant1.0\times10^{-16}$.

The fluorescence modulation signals from all three laser beams can be reduced to the level shown in Fig. 4(a). We consider the case in which the signals from beams 1 and 2 have the same sign. Then from Eq. (54), the fractional second-order Doppler shifts due to excess micromotion is $-(0\pm0.2)\times10^{-18}$ along $\hat{z}$, $-(8\pm2)\times10^{-18}$ along $(\hat{x}-\hat{y})/\sqrt{2}$, and $-(0.9\pm0.3)\times10^{-18}$ along $(\hat{x}+\hat{y})/\sqrt{2}$. These values add to give a total shift of $\Delta\nu_{D2}/\nu\cong-(9\pm2)\times10^{-18}$. Similarly, from Eq. (55), these signals indicate a total Stark shift of $|\Delta\nu_S/\nu|\leqslant(1.9\pm0.4)\times10^{-17}$. These small shifts illustrate this method's effectiveness in reducing micromotion.

To conclude, the micromotion of ions in a Paul trap has several related adverse effects. In high-resolution spectroscopy, the most significant are the second-order Doppler shift and a possible Stark shift due to the ac electric fields. Because these shifts can be substantial, it is critical that micromotion be eliminated in all three dimensions. Table I lists the methods discussed in this article, and the corresponding formulas for determining the second-order Doppler shift and the Stark shift from the relevant signals. The first method monitors the spatial motion of the ions as the pseudopotential is varied, whereas the last two methods monitor the effects of first-order Doppler shift on the atomic line shape. The spatial-monitoring techniques are insensitive to micromotion caused by a phase shift between the ac potentials applied to the trap electrodes. Apart from this, which technique is most sensitive to micromotion depends on the parameters of the trap, laser beams, and atomic transition.

## ACKNOWLEDGMENTS

This work was supported by ONR and ARO. The authors thank Dietrich Leibfried, Don Sullivan, Brent Young, and Matt Young for helpful comments on the manuscript.

[1] D. J. Wineland, J. C. Bergquist, J. J. Bollinger, W. M. Itano, D. J. Heinzen, S. L. Gilbert, C. H. Manney, and M. G. Raizen, IEEE Trans. Ultrason. Ferroelectr. Freq. Control **37**, 515 (1990).
[2] J. Prestage, G. J. Dick, and L. Maleki, J. Appl. Phys. 66, 1013 (1989); R. L. Tjoelker J. D. Prestage, and L. Maleki, in *Fifth Symposium on Frequency Standards and Metrology*, edited by J. C. Bergquist, Woods Hole, MA, Oct. 1995 (World Scientific, Singapore, 1996), p. 33.
[3] M. G. Raizen, J. M. Gilligan, J. C. Bergquist, W. M. Itano, and D. J. Wineland, Phys. Rev. A **45**, 6493 (1992).
[4] P. T. H. Fisk, M. J. Sellars, M. A. Lawn, C. Coles, in *Fifth Symposium on Frequency Standards and Metrology*, edited by J. C. Bergquist, Woods Hole, MA, Oct. 1996 (World Scientific, Singapore, 1996), p. 27.
[5] M. E. Poitzsch, J. C. Bergquist, W. M. Itano, and D. J. Wineland, Rev. Sci. Instrum. **67**, 129 (1996).
[6] H. C. Naegerl, W. Bechter, J. Eschner, F. Schmidt-Kaler, and R. Blatt, Appl. Phys. B **66**, 603 (1998).
[7] H. Walther, Adv. At., Mol., Opt. Phys. **31**, 137 (1993).
[8] W. Paul, Rev. Mod. Phys. **62**, 531 (1990).
[9] L. D. Landau and E. M. Lifshitz, in *Mechanics* (Pergamon, New York, 1976), pp. 93–95.
[10] W. M. Itano, J. C. Bergquist, J. J. Bollinger, and D. J. Wineland, Phys. Scr. **T59**, 106 (1995).
[11] D. J. Wineland, W. M. Itano, J. C. Bergquist, and R. G. Hulet, Phys. Rev. A **36**, 2220 (1987).
[12] A. van Wijngaarden and G. W. F. Drake, Phys. Rev. A **17**, 1366 (1978).
[13] N. Yu, W. Nagourney, and H. Dehmelt, J. Appl. Phys. 69, 3779 (1991).
[14] R. G. DeVoe, J. Hoffnagle, and R. G. Brewer, Phys. Rev. A **39**, 4362 (1989).
[15] R. Blümel, C. Kappler, W. Quint, and H. Walther, Phys. Rev. A **40**, 808 (1989).
[16] N. Yu, X. Zhao, H. Dehmelt, and W. Nagourney, Phys. Rev. A **50**, 2738 (1994).
[17] D. A. Church and H. G. Dehmelt, J. Appl. Phys. **40**, 3421 (1969).
[18] C. Tamm (unpublished). Talk presented in *Proceedings of the Fifth Symposium on Frequency Standards and Metrology*, edited by C. Bergquist (World Scientific, Singapore, 1996).
[19] H. A. Schuessler and H. S. Lakkaraju, in *Precision Measurement and Fundamental Constants II*, edited by B. N. Taylor and W. D. Phillips, Natl. Bur. Stand. (U.S.), Spec. Publ. 617 (1984), p. 103.
[20] M. Jardino, F. Plumelle, M. Desaintfuscien, and J. L. Duchene, in *Proceedings of 38th Annual Symposium on Frequency Control*, IEEE 84CH2062-8 (IEEE, New York, 1984), p. 431; L. S. Cutler, C. A. Flory, R. P. Giffard, and M. D. McGuire, Appl. Phys. B 39, 251 (1986).
[21] J. C. Bergquist, Wayne M. Itano, and D. J. Wineland, Phys. Rev. A 36, 428 (1987).
[22] G. R. Janik, Ph.D. thesis, University of Washington (University Microfilms International, 1984).
[23] F. Diedrich and H. Walther, Phys. Rev. Lett. **58**, 203 (1987).
[24] J. T. Höffges, H. W. Baldauf, T. Eichler, S. R. Helmfrid, and H. Walther, Opt. Commun. **133**, 170 (1997).
[25] W. R. Leo, *Techniques for Nuclear and Particle Physics Experiments*, second revised edition (Springer, Berlin, 1994).



*U.S. GPO 2002-0-773-018/40206

The National Institute of Standards and Technology was established in 1988 by Congress to "assist industry in the development of technology . . . needed to improve product quality, to modernize manufacturing processes, to ensure product reliability . . . and to facilitate rapid commercialization . . . of products based on new scientific discoveries."

NIST, originally founded as the National Bureau of Standards in 1901, works to strengthen U.S. industry's competitiveness; advance science and engineering; and improve public health, safety, and the environment. One of the agency's basic functions is to develop, maintain, and retain custody of the national standards of measurement, and provide the means and methods for comparing standards used in science, engineering, manufacturing, commerce, industry, and education with the standards adopted or recognized by the Federal Government.

As an agency of the U.S. Commerce Department's Technology Administration, NIST conducts basic and applied research in the physical sciences and engineering, and develops measurement techniques, test methods, standards, and related services. The Institute does generic and precompetitive work on new and advanced technologies. NIST's research facilities are located at Gaithersburg, MD 20899, and at Boulder, CO 80303. Major technical operating units and their principal activities are listed below. For more information contact the Publications and Program Inquiries Desk, 301-975-3058.

## Office of the Director
- National Quality Program
- International and Academic Affairs

## Technology Services
- Standards Services
- Technology Partnerships
- Measurement Services
- Information Services

## Advanced Technology Program
- Economic Assessment
- Information Technology and Applications
- Chemistry and Life Sciences
- Electronics and Photonics Technology

## Manufacturing Extension Partnership Program
- Regional Programs
- National Programs
- Program Development

## Electronics and Electrical Engineering Laboratory
- Microelectronics
- Law Enforcement Standards
- Electricity
- Semiconductor Electronics
- Radio-Frequency Technology[1]
- Electromagnetic Technology[1]
- Optoelectronics[1]
- Magnetic Technology[1]

## Materials Science and Engineering Laboratory
- Intelligent Processing of Materials
- Ceramics
- Materials Reliability[1]
- Polymers
- Metallurgy
- NIST Center for Neutron Research

## Chemical Science and Technology Laboratory
- Biotechnology
- Physical and Chemical Properties[2]
- Analytical Chemistry
- Process Measurements
- Surface and Microanalysis Science

## Physics Laboratory
- Electron and Optical Physics
- Atomic Physics
- Optical Technology
- Ionizing Radiation
- Time and Frequency[1]
- Quantum Physics[1]

## Manufacturing Engineering Laboratory
- Precision Engineering
- Manufacturing Metrology
- Intelligent Systems
- Fabrication Technology
- Manufacturing Systems Integration

## Building and Fire Research Laboratory
- Applied Economics
- Structures
- Building Materials
- Building Environment
- Fire Research

## Information Technology Laboratory
- Mathematical and Computational Sciences[2]
- Advanced Network Technologies
- Computer Security
- Information Access
- Convergent Information Systems
- Information Services and Computing
- Software Diagnostics and Conformance Testing
- Statistical Engineering

[1] At Boulder, CO 80303.
[2] Some elements at Boulder, CO.

**U.S. Department of Commerce**
National Institute of Standards and Technology
325 Broadway
Boulder, CO 80305

Official Business
Penalty for Private Use $300